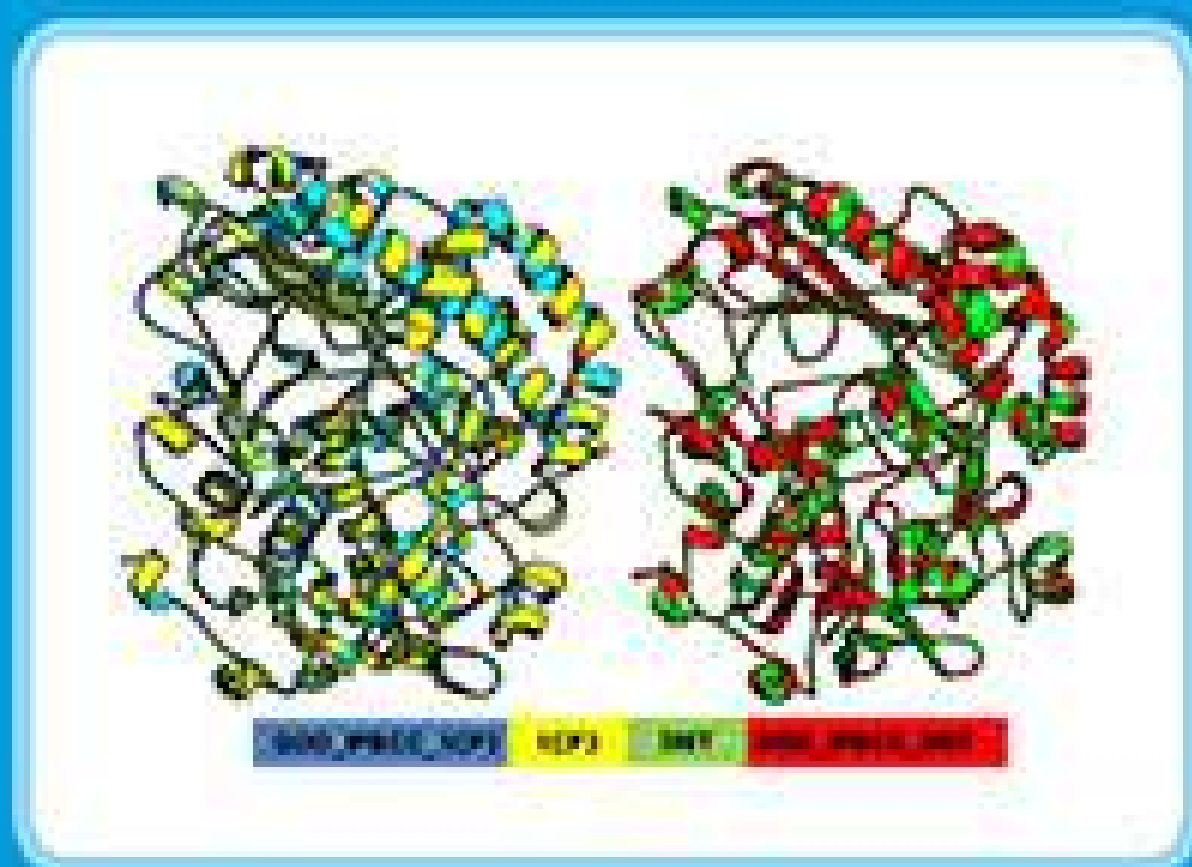
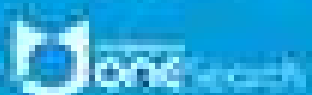
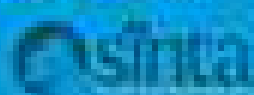


Indonesian Journal of Chemistry

Vol. 20, No. 1, February 2020



Google Scholar



Approved by IAIN Curup
No. 21/04/2019

Attenuated Total Reflectance-FTIR Spectra Combined with Multivariate Calibration and Discrimination Analysis for Analysis of Patchouli Oil Adulteration

Zaki Fahmi¹, Mudasir¹, and Abdul Rohman^{2,3,*}

¹Department of Chemistry, Faculty of Mathematics and Natural Sciences, Universitas Gadjah Mada, Sekip Utara, Yogyakarta 55281, Indonesia

²Department of Pharmaceutical Chemistry, Faculty of Pharmacy, Universitas Gadjah Mada, Sekip Utara, Yogyakarta 55281, Indonesia

³Institute of Halal Industry and Systems, Universitas Gadjah Mada, Sekip Utara, Yogyakarta 55281, Indonesia

* **Corresponding author:**

email: abdul_kimfar@ugm.ac.id

Received: July 12, 2018

Accepted: February 3, 2019

DOI: 10.22146/ijc.36955

Abstract: The adulteration of high priced oils such as patchouli oil with lower price ones is motivated to gain the economical profits. The aim of this study was to use FTIR spectroscopy combined with chemometrics for the authentication of patchouli oil (PaO) in the mixtures with Castor Oil (CO) and Palm Oil (PO). The FTIR spectra of PaO and various vegetable oils were scanned at mid infrared region (4000–650 cm^{-1}), and were subjected to principal component analysis (PCA). Quantitative analysis of PaO adulterated with CO and PO were carried out with multivariate calibration of Partial Least Square (PLS) regression. Based on PCA, PaO has the close similarity to CO and PO. From the optimization results, FTIR normal spectra in the combined wavenumbers of 1200–1000 and 3100–2900 cm^{-1} were chosen to quantify PaO in PO with coefficient of determination (R^2) value of 0.9856 and root mean square error of calibration (RMSEC) of 4.57% in calibration model. In addition, R^2 and root mean square error of prediction (RMSEP) values of 0.9984 and 1.79% were obtained during validation, respectively. The normal spectra in the wavenumbers region of 1200–1000 cm^{-1} were preferred to quantify PaO in CO with R^2 value of 0.9816 and RMSEC of 6.89% in calibration, while in validation model, the R^2 value of 0.9974 and RMSEP of 2.57% were obtained. Discriminant analysis was also successfully used for classification of PaO and PaO adulterated with PO and CO without misclassification observed. The combination of FTIR spectroscopy and chemometrics provided an appropriate model for authentication study of PaO adulterated with PO and CO.

Keywords: infrared spectroscopy; chemometrics; patchouli oil; castor oil; palm oil

■ INTRODUCTION

Patchouli Oil (PaO) is an essential oil obtained from dried and fermented young leaves of *Pogostemon cablin* (Blanco) Benth, a perennial herb belonging to family *Lamiaceae* and widely distributed in regions of tropical and subtropical, prior to be subjected to steam distillation. The yield of oil is typically 2–3% [1]. The oil is an important natural material used in the industries of perfumery, food, and has been historically used to repel clothes moths and as a cold treatment in Asia [2]. The major component composed of PaO is patchouli alcohol, a natural tricyclic

sesquiterpene isolated from volatile oil of PaO. Patchouli Oil has been reported to have some biological activities such as anti-inflammatory [3], anti-oxidative [4], anti-tumor [5], antibacteria, antifungus and antiviral [6-8], as well as as whitening agent [9]. The oil has high priced value in oil industry, therefore, PaO is subjected to be adulterated with other oils to gain economical profit.

The adulteration practice of essential oils is an emerging issue currently, not only for consumers but also for producers and regulatory bodies [10]. This practice included the addition of cheaper essential oils,

addition of vegetable oils such as castor oil and palm oils to increase the weight of essential oils and total or partial substitution of the original plant sources by other plants [11]. In order to assure quality, safety, and the authenticity of essential oils, different analytical techniques are needed. As a consequence, several analytical methods have been reported for the authentication of essential oils including organoleptic, physical, chemical, spectroscopic and chromatographic-based methods [12-15]. Fourier Transform Infrared (FTIR) spectroscopy is promising technique for authentication of essential oils due to its property as fingerprint analytical technique [16]. The fingerprinting analysis of essential oils represented qualitative approach to plant species authentication as well as quality evaluation [17].

FTIR spectroscopy in combination with chemometrics techniques have been reported for authentication of four essential oils namely wintergreen, rosemary, tea tree, and lemon eucalyptus oils adulterated with either lemongrass essential oil or peppermint essential oil [18], authentication of origano, thyme, and chamomile [18], geographical origin of lavandin var. Grosso essential oils [19], and authentication of camellia oil [20]. Few studies have been reported the authentication of patchouli oil, especially using FTIR spectroscopy. Therefore, this study was intended to use FTIR spectroscopy in combination with chemometrics of multivariate calibration of Partial Least Square (PLS) and Discriminant Analysis (DA) for the authentication of patchouli oil.

■ EXPERIMENTAL SECTION

Materials

Patchouli oil was purchased from CV. Surya Wulan (Yogyakarta, Indonesia). Olive oil, palm oil, castor oil and other oils used in this study were purchased from supermarkets around Yogyakarta, Indonesia. The solvents and reagents used were of pro-analytical grade and were purchased from Merck (Darmstadt, Germany).

Procedure

Compositional analysis of patchouli oil

The compositional analysis of patchouli oil was

performed using gas chromatography-mass spectrometry (GC-MS). Patchouli oil (1 μ L) was injected into Gas Chromatography GC-2014 (Shimadzu GC-2010, Shimadzu Corp., Tokyo, Japan) under the following conditions: DB-5 capillary column (30 m \times 0.25 mm I.D. and 0.25 μ m thickness; Agilents, Tokyo, Japan); carrier gas of He with 12.0 kPa with flow rate of 50 mL/min; a column temperature was set from 50–240 $^{\circ}$ C with rate of 5 $^{\circ}$ C/min, and the temperature was hold at 240 $^{\circ}$ C for 19 min; injection temperature of 250 $^{\circ}$ C; detection temperature of 320 $^{\circ}$ C. Helium was used as the carrier gas. GC-mass spectrometry (GC-MS) data were collected with a GCMS-QP 2010 (Shimadzu, Japan) under the following conditions: DB-1 capillary column (30 m \times 0.25 mm I.D. and 0.25 μ m; GL Sciences, Tokyo, Japan); column temperature from 50 $^{\circ}$ C (1 min) to 320 $^{\circ}$ C at 5 $^{\circ}$ C/min; injector temperature of 260 $^{\circ}$ C with *split ratio* of 1:50; MS detector temperature was set of 320 $^{\circ}$ C with acquisition mass range of 40–500 amu. Components were identified using the comparison of the experimental GCMS data with authentic compounds or the NIST MS library. Quantification of volatile compounds was determined using relative percentage, known as internal normalization technique.

Quantitative analysis of patchouli oil using FTIR spectroscopy

For quantitative analysis of patchouli oil (PaO) in the mixture with castor oil (CO) and palm oil (PO), a set of 21 calibration samples consisting of PaO-CO and PaO-PO in certain concentration covering 1.0–50.0% (v/v) was prepared. Another independent samples called with validation samples were also prepared. All samples were scanned using FTIR spectrophotometer.

Classification of PaO and PaO adulterated with CO and PO

Classification of PaO and PaO adulterated with CO and PO was carried out using discriminant analysis by preparing at concentration range of 1–50% of CO and PO. All pure PaO and PaO mixed with CO and PO were assigned as “unadulterated” and “adulterated”, respectively.

FTIR spectra measurement

FTIR spectra of were measured using FTIR spectrophotometer Nicolet 6700 equipped with detector of deuterated triglycine sulphate (DTGS) and beam splitter of KBr/Germanium. This instrument was interfaced to computer operating systems which include OMNIC operating system (Version 7.0 Thermo Nicolet) software. The sampling compartment was horizontal Attenuated Total Reflectance kit composed of ZnSe crystal. All FTIR spectra of tested samples were scanned at wavenumbers of 4000–650 cm^{-1}), using 32 scans with 4 cm^{-1} resolution. These spectra were recorded as absorbance mode at each data point in triplicate.

Data analyses

The software of TQ Analyst™ version 6 was used for the treatment of multivariate calibration of Partial Least Square (PLS) and Discriminant Analysis (DA). The spectral regions where the variations were observed were chosen during analysis (PLS and DA). In addition, Minitab software version 17 was used for principal component analysis (PCA).

RESULTS AND DISCUSSION

Each edible fats and oils are mainly composed from triglycerides (nearly 98%) along with some minor components including sterols, tocopherols, lipid-soluble vitamins, and other components in trace levels. The characterization of patchouli oil (PaO) was performed by determining volatile components present using Gas Chromatography-Mass Spectrometer (GC-MS), while palm and castor oils were characterized based on fatty acid composition. Table 1 revealed the volatile components in PaO, in which Patchouli alcohol was the main components accounting of 15.80%. The levels of volatile components were comparable with those reported by Akhila and Tewari [2]. Therefore, it can be concluded that the used PaO was not previously mixed with other components.

In order to decide the oil models used as adulterant in PaO, principal component analysis (PCA) was used. Fig. 1 showed PCA score plot using absorbance values at whole mid infrared region (4000–650 cm^{-1}) as variables, representing the projection of samples defined by the first

Table 1. The composition of volatile components in patchouli oil as determined using gas chromatography-mass spectrometry

Volatile components	Concentration (%)	
	Present study	Akhila and Tewari [2]
α -pinene	0.24	0.001-0.3
β -pinene	0.57	0.02-1
Limonene	0.05	0.01-0.3
λ -elemene	-	0.01-1.9
β -patchoulene	-	0.03-12
β -elemene	-	0.18-1.9
Cycloseychellene	-	0.02-0.8
β -caryophyllene	-	0.75-6.8
α -Guaiene	18.56	2.9-23
Seychellene	14.88	2.3-13
α -humulene	3.69	0.05-2
α -patchoulene	1.89	1.2-13
Germacrene	-	0.00-0.2
Aciphyllene	5.53	0.7-4.2
α -bulnesene	14.14	2.9-23
Caryophyllene oxide	0.60	0.0-4.6
Pogostol	-	0.2-6.2
Patchouli alcohol	15.80	11-72

Principle Component (PC 1) and the second Principle Component (PC 2). Among studied oils having low price values in the market, castor oil and palm oil had close similarity with PaO, therefore both oils were preferred as oil adulterants in PaO.

Quantitative Analysis of Adulterants in Patchouli Oil

In this study, authentication of PaO was carried out by quantifying PaO in the binary mixture with castor oil and palm oil using multivariate calibration and classifying PaO and PaO mixed with castor oil and palm oil using discriminant analysis using absorbance values at selected wavenumbers. Fig. 2 revealed FTIR spectra of patchouli

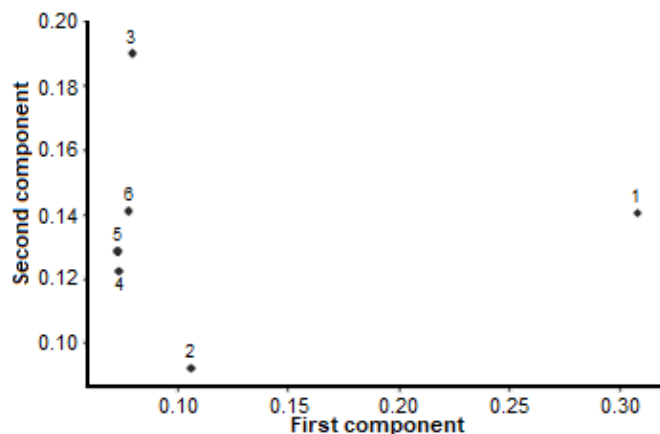


Fig 1. The PCA score plot of patchouli oil and some vegetable oils. (1) patchouli oil; (2) castor oil; (3) palm oil; (4) soybean oil; (5) corn oil and (6) coconut oil

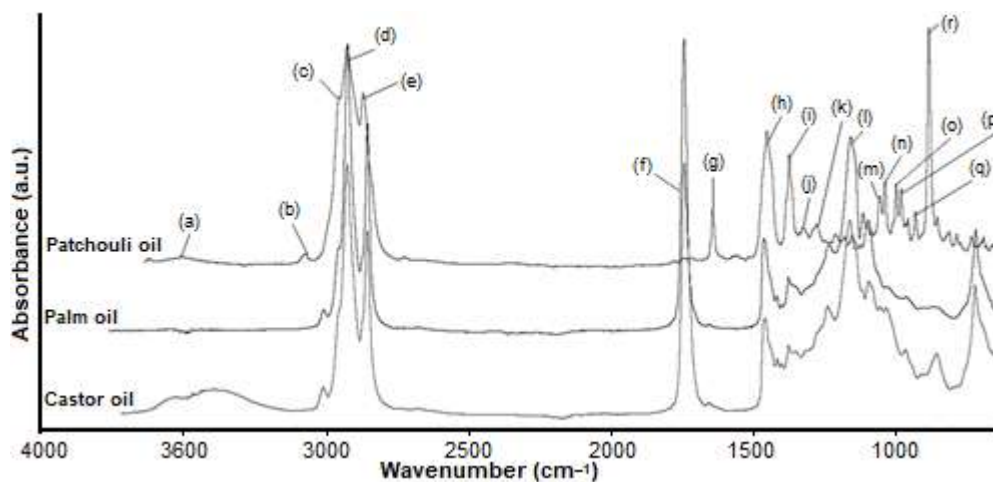


Fig 2. FTIR spectra of patchouli oil, palm oil and castor oil, scanned at mid infrared region (4000–650 cm^{-1})

Table 2. The functional groups responsible for infrared absorptions at wavenumbers of 4000–650 cm^{-1} [23-24]

Assignment	Wavenumber (cm^{-1})	Functional groups and modes of vibration
(a)	3503	O–H bonding, stretching
(b)	3069	<i>cis</i> C=CH Stretching
(c) and (e)	2953 and 2875	methyl ($-\text{CH}_3$) asymmetric and symmetric stretching vibration
(d)	2922	methylene ($-\text{CH}_2$) asymmetric stretching vibration
(f)	1741	carbonyl (C=O) stretching vibration, especially guaiene and seychellene
(g)	1643	<i>cis</i> C=C, stretching
(h)	1453	$-\text{CH}_2$ (methylene), Bending (scissoring)
(i)	1374	$-\text{CH}_3$ (methyl), Bending
(j)	1278	C–O alcohol, bending
(k) and (l)	1117 and 1097	C–O ether, bending
(m), (n), (o), and (p)	1057, 1039, 1032, and 999	C–O ether, bending
(q)	982	$-\text{HC}=\text{CH}-$ (<i>trans</i>), out of plane
(r)	885	$-\text{HC}=\text{CH}-$ (<i>cis</i>), out of plane

oil and the oil adulterants (castor oil and palm oil) at mid infrared region of 4000–650 cm^{-1} . Each bands and shoulder are corresponding to absorption of infrared radiation by functional groups present in PaO, CO and PO, as compiled in Table 2. The variation in FTIR spectra existed in PaO, CO and PO was exploited for selecting wavenumbers region used for quantitative and classification analyses.

Quantitative analysis of PaO in palm oil and castor oil was facilitated with the commonly used of multivariate calibration, namely Partial Least Square (PLS) regression. This regression was based on inverse regression in which concentration in y -axis was modelled using predictors of principle components, a linear combination of absorbance values in x -axis [21]. To get the optimum prediction, the optimization process in terms of selection of wavenumbers and FTIR spectral treatments offering best prediction models was performed. The wavenumbers selected to be optimized was based on the variation existed between PaO and oil adulterants (CO and PO). Table 3 revealed

the optimization results using different wavenumbers regions and FTIR spectral treatments. Because of its highest values of R^2 and lowest values of RMSEC and RMSEP, PaO in palm oil was quantified using normal spectra using variables of absorbance values at combined wavenumbers region of 1200–1000 cm^{-1} .

Similarly, Table 4 exhibited the results of quantification of PaO in castor oils using PLS regression with different wavenumbers and FTIR spectra models. Fig. 3 showed PLS regression models for the relationship between actual values of PaO (x -axis) and FTIR predicted values (y -axis) in either calibration or validation using wavenumbers region of 1200-1000 cm^{-1} . The equations obtained were $y = 0.9636x + 1.8435$ (R^2 of 0.9738) in calibration, and $y = 0.9414x + 2.9902$ ($R^2 = 0.9984$) in validation models, respectively. Residual analyses revealed that the difference between actual and predicted values fallen near zero, indicating that systematic errors were negligible.

Table 3. The performance of partial least square regression for quantification of patchouli oil in in palm oil

Frequency region (cm^{-1})	Spectral treatment	Number of factors	Calibration		Validation	
			R^2	RMSEC (%)	R^2	RMSEP (%)
943-863 and 1069-1033	Normal	3	0.9875	4.72	0.9999	4.33
1200-1000 and 3100-2900*	Normal	5	0.9901	4.20	0.9999	2.14
1200-1000	Normal	2	0.9862	4.96	0.9998	2.15
3100-2900	Normal	2	0.9821	5.65	0.9999	3.97
885-857, 982-964 and 1039-983	First derivative	2	0.9870	4.82	1.000	3.65
1200-1000 and 3100-2900	First derivative	2	0.9865	4.92	0.9999	4.11
1200-1000	First derivative	2	0.9873	4.77	0.9999	4.18
3100-2900	First derivative	2	0.9834	5.43	1.000	3.81

***Bold** = selected for quantification

Table 4. The performance of partial least square regression for quantification of patchouli oil in in castor oil

Frequency region (cm^{-1})	Spectral treatment	Number of factors	Calibration		Validation	
			R^2	RMSEC	R^2	RMSEP
870-811, 928-873 and 940-929	Normal	2	0.9684	7.07	0.9974	4.23
1200-1000 and 3100-2900	Normal	2	0.9694	7.56	0.9982	3.62
1200-1000	Normal	4	0.9738	6.89	0.9974	2.57
3100-2900	Normal	2	0.9512	10.1	0.9985	9.35
906-878, 1107-1093 and 1179-1163	First derivative	2	0.9693	7.57	0.9970	2.60
1200-1000 and 3100-2900	First derivative	2	0.9677	7.64	0.9979	5.30
1200-1000	First derivative	1	0.9650	7.95	0.9981	6.00
3100-2900	First derivative	2	0.9562	8.87	0.9982	8.36

***Bold** = selected for quantification

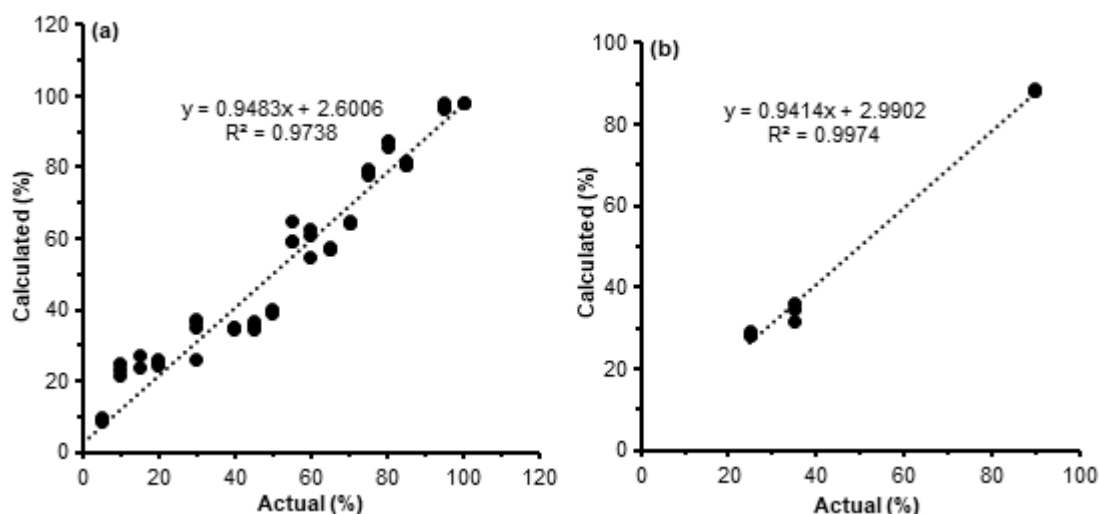


Fig 3. Partial least square regression for the relationship between actual values and FTIR calculated values of patchouli oil in castor oil either in calibration or in validation samples (a) calibration model; (b) validation model

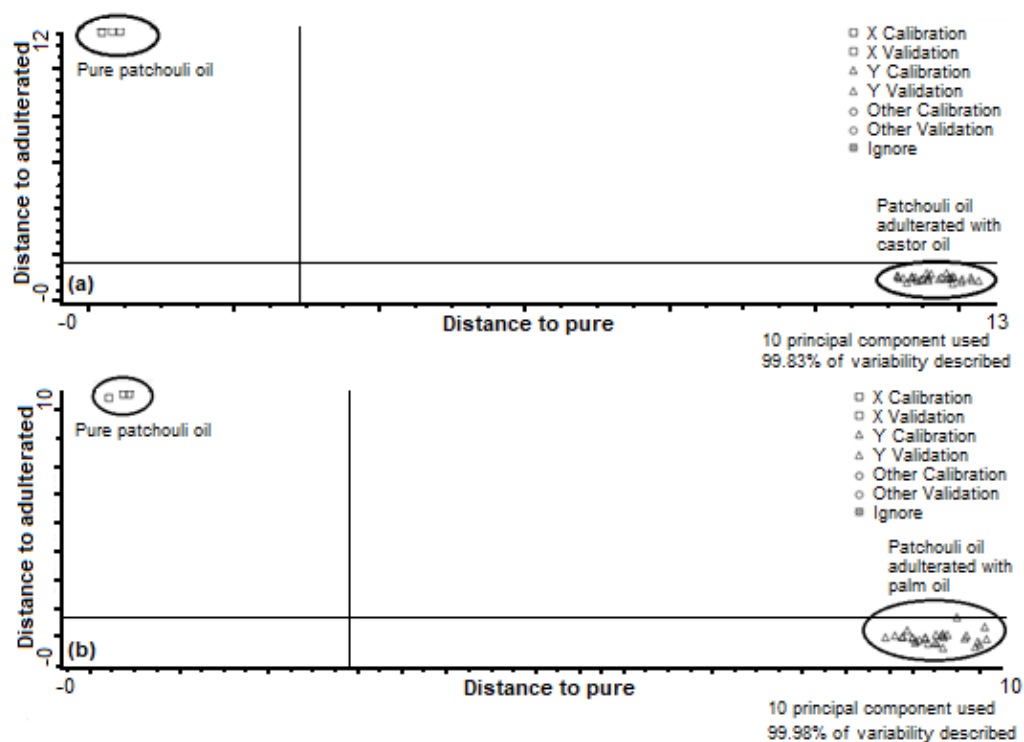


Fig 4. The Cooman plots obtained during discriminant analysis for classification of patchouli oil and that adulterated with (a) castor oil and (b) palm oil

Discriminant Analysis

In order to classify patchouli oil and that adulterated with castor oil and palm oil, discriminant analysis was used. DA is one of supervised pattern recognition technique [21]. The Mahalanobis distance using absorbancies at wavenumbers of 3933–717 cm^{-1} were

used as variables during classification of pure oil and that adulterated with DA. Fig. 4 revealed the Cooman's plot for classification results. DA can successfully classified patchouli oil and that adulterated with castor oil [A] and that adulterated with palm oil [B] with 100% accuracy level. Misclassification may accord if variables

used were not appropriate or the studied oils (authentic and adulterated oils) had very close similarity [22]. This indicated that DA was an effective tools for classification of oils for authentication purposes.

■ CONCLUSION

FTIR spectroscopy in combination with chemometrics of PLS regression and DA using certain wavenumbers region has been successfully used for authentication of patchouli oil from castor oil and palm oil. The developed method was rapid, ease in sample preparation, and not involving excessive solvents and reagents.

■ ACKNOWLEDGMENTS

The authors thank to the Ministry of Research, Technology and Higher Education, Republic Indonesia for partial financial assistance during this study via *Hibah Penelitian Unggulan Perguruan Tinggi* (PUPT) 2017 with contract number 2328/UN1.P.III/DIT-LIT/LT/2017.

■ REFERENCES

- [1] Zhu, B.C.R., Henderson, G., Yu, Y., and Laine, R.A., 2003, Toxicity and repellency of patchouli oil and patchouli alcohol against formosan subterranean termites *Coptotermes formosanus* Shiraki (Isoptera: Rhinotermitidae), *J. Agric. Food Chem.*, 51 (16), 4585–4588.
- [2] Akhila, A., and Tewari, R., 1984, Chemistry of patchouli oil: A review, *Curr. Res. Med. Arom. Plants*, 6, 38–54.
- [3] Su, Z., Liao, J., Liu, Y., Liang, Y., Chen, H., Chen, X., Lai, X., Feng, X., Wu, D., Zheng, Y., Zhang, X., and Li, Y., 2016, Protective effects of patchouli alcohol isolated from *Pogostemon cablin* on lipopolysacchride-induced acute lung injury in mice, *Exp. Ther. Med.*, 11 (2), 674–682.
- [4] Huang, X., Liu, R., and Liu, Lv, Q., 2009, The effect of patchouli alcohol on oscopolamine-induced learninand memory impairment of mice, *Chin. Tradit. Herbal Drugs*, 40 (9), 1431–1433
- [5] Jeong, J.B., Choi, J., Lou, Z., Jiang, X., and Lee, S.H., 2013, Patchouli alcohol, an essential oil of *Pogostemon cablin*, exhibits anti-tumorigenic activity in human colorectal cancer cells, *Int. Immunopharmacol.*, 16 (2), 184–190.
- [6] Li, Y.C., Peng, S.Z., Chen, H.M., Zhang, F.X., Xu, P.P., Xie, J.H., He, J.J., Chen, J.N., Lai, X.P., and Su, Z.R., 2012, Oral administration of patchouli alcohol isolated from *Pogostemonis herba* augments protection against influenza viral infection in mice, *Int. Immunopharmacol.*, 12 (1), 294–301.
- [7] Kocevski, D., Du, M., Kan, J., Jing, C., Lačanin, I., and Pavlović, H., 2013, Antifungal effect of *Allium tuberosum*, *Cinnamomum cassia*, and *Pogostemon cablin* essential oils and their components against population of *Aspergillus* species, *J. Food Sci.*, 78 (5), M731–M737.
- [8] Swamy, M.K., Akhtar, M.S., and Sinniah, U.R., 2016, Antimicrobial properties of plant essential oils against human pathogens and their mode of action: An updated review, *Evid. Based Complementary Altern. Med.*, 2016, 3012462.
- [9] Bae, S.Y., Lee, E.J., Son, R.H., and Lee, Y.H., 2009, The inhibitory effects of *Pogostemon cablin* Bentham extract on melanogenesis, *J. Soc. Cosmet. Sci. Korea*, 35 (1), 33–39.
- [10] Do, T.K.T., Hadji-Minaglou, F., Antoniotti, S., and Fernandez, X., 2015, Authenticity of essential oils, *TrAC, Trends Anal. Chem.*, 66, 146–157.
- [11] Salgueiro, L., Martins, A.P., and Correia, H., 2010, Raw materials: The importance of quality and safety. A review, *Flavour Fragrance J.*, 25, 253–271.
- [12] Goodner, K., and Rouseff, R., 2011, *Practical Analysis of Flavor and Fragrance Materials*, John Wiley & Sons Ltd., Chichester.
- [13] Juliani, H.R., Kapteyn, J., Jones, D., Koroch, A.R., Wang, M., Charles, D., and Simon, J.E., 2006, Application of near-infrared spectroscopy in quality control and determination of adulteration of African essential oils, *Phytochem. Anal.*, 17, 121–128.
- [14] König, W.A., and Hochmuth, D.H., 2004, Enantioselective gas chromatography in flavor and fragrance analysis: Strategies for the identification of known and unknown plant volatiles, *J. Chromatogr. Sci.*, 42 (8), 423–439.

- [15] Schipilliti, L., Tranchida, P.Q., Sciarrone, D., Russo, M., Dugo, P., Dugo, G., and Mondello, L., 2010, Genuineness assessment of mandarin essential oils employing gas chromatography-combustion-isotope ratio MS (GC-C-IRMS), *J. Sep. Sci.*, 33 (4-5), 617–625.
- [16] Rohman, A., and Man, Y.B.C., 2012, The chemometrics approach applied to FTIR spectral data for analysis of rice bran oil in extra virgin olive oil, *Chemom. Intell. Lab. Syst.*, 110 (1), 129–134.
- [17] Gjerstad, G., 1961, Spectrophotometric identification and evaluation of volatile oils, *Planta Med.*, 9 (3), 245–250.
- [18] Elzey, B., Norman, V., Stephenson, J., Pollard, D., and Fakayode, S.O., 2016, Purity analysis of adulterated essential oils by FT-IR spectroscopy and partial-least-squares regression, *Spectroscopy*, 31, 26–37.
- [19] Schulz, H., Quilitzsch, R., and Krüger, H., 2016, Rapid evaluation and quantitative analysis of thyme, origano and chamomile essential oils by ATR-IR and NIR spectroscopy, *J. Mol. Struct.*, 661-662, 299–306.
- [20] Li, S., Zhu, X., Zhang, J., Li, G., Su, D., and Shan, Y., 2012, Authentication of pure camellia oil by using near infrared spectroscopy and pattern recognition techniques, *J. Food Sci.*, 77 (4), C374–C380.
- [21] Manaf, M.A., Man, Y.B.C., Hamid, N.S.A., Ismail, A., and Abidin, S.Z., 2007, Analysis of adulteration of virgin coconut oil by palm kernel olein using Fourier transform infrared spectroscopy, *J. Food Lipids*, 14 (2), 111–121.
- [22] Miller, J.N., and Miller, J.C., 2005, *Statistics and Chemometrics for Analytical Chemistry*, 5th ed., Pearson Education, Essex, England.
- [23] Guillén, M.D., and Cabo, N., 1997, Characterization of edible oils and lard by Fourier transform infrared spectroscopy. Relationships between composition and frequency of concrete bands in the fingerprint region, *J. Am. Oil Chem. Soc.*, 74 (10), 1281–1286.
- [24] Lerma-García, M.J., Ramis-Ramos, G., Herrero-Martínez, J.M., and Simó-Alfonso, E.F., 2010, Authentication of extra virgin olive oils by Fourier-transform infrared spectroscopy, *Food Chem.*, 118 (1), 78–83.

Antibacterial Activity of Benzyl Benzoate and Crotepoxide from *Kaempferia rotunda* L. Rhizome

Hartiwi Diastuti*, Mochammad Chasani, and Suwandri

Department of Chemistry, Universitas Jenderal Soedirman,
Jl. dr. Soeparno 61, Karangwangkal, Purwokerto 53123, Indonesia

* **Corresponding author:**

tel: +62-8170611988

email: hartiwidiastuti@yahoo.com

Received: July 26, 2018

Accepted: September 26, 2018

DOI: 10.22146/ijc.37526

Abstract: Benzyl benzoate and crotepoxide are the major components of *Kaempferia rotunda* L. rhizome. However, the bioactivity study of benzyl benzoate and crotepoxide as the antibacterial activity were still limited. Therefore, the antibacterial activity of benzyl benzoate and crotepoxide against four pathogenic bacteria, i.e., *Escherichia coli* ATCC 25922, *Enterococcus aerogenes* ATCC 13048, *Bacillus cereus* ATCC 6538 and *Staphylococcus aureus* ATCC 11778 were investigated. The isolation steps included the extraction by maceration with acetone, and then the acetone extract was partitioned with n-hexane:methanol (1:1) and ethyl acetate:water (1:1) respectively. The isolation by liquid vacuum chromatography followed by column chromatography was yielded benzyl benzoate from the n-hexane fraction and crotepoxide from ethyl acetate fraction. The molecular structure of isolated compounds was identified based on NMR (1D and 2D) spectroscopic data. The antibacterial activity assay of isolated compounds was carried out using the disc diffusion method. The antibacterial evaluation confirms that the benzyl benzoate and crotepoxide exhibits a medium level activity. Benzyl benzoate showed highest antibacterial activity against *B. cereus* with MIC of 50 µg/mL and inhibitory zone of 5.9 mm, while the crotepoxide showed highest antibacterial activity against *E. aerogenes* with MIC of 100 µg/mL with inhibitory zone 6.1 mm.

Keywords: antibacterial; benzyl benzoate; crotepoxide; *K. rotunda* L.

■ INTRODUCTION

Infectious disease is one of the health problems, especially in developing countries including in Indonesia. Treatment of infectious diseases by bacteria with antibiotics has been carried out, but the ability of antibiotics gradually decreased due to the resistance of microorganism. In addition, the use of synthetic antibiotics often causes adverse effects. It encourages the researchers to get the new safe antibiotics, one of them from medicinal plants.

Kaempferia rotunda (Zingiberaceae) is a medicinal plant in Indonesia; It was known locally name as “*kunci pepet*” or “*kunir putih*”. The rhizome of *K. rotunda* was used for traditional medicine such as treating stomach pain, fever, indigestion, inflammation due to bruises or sprains, carminative and accelerate wound healing [1]. The crude extracts, volatile oils and isolated compounds

from *K. rotunda* rhizome exhibited the essential biological activities. According to the previous report, extract of *K. rotunda* rhizome showed antioxidant activity [2-3], insecticides [4], anti-inflammatory [5], anthelmintic [6], antihyperglycemic and antinociceptive [7], antimicrobial [8-10] and anti-androgenic [11]. Some compounds of the *K. rotunda* rhizome also revealed some biological activities. A 2-hydroxy-4,4',6-trimethoxy chalcone showed antioxidant activity with IC₅₀ of 142 µg/mL [3]. Crotepoxide was the main constituent of *K. rotunda* rhizome useful for antitumor agent [5]. In the ethyl acetate and ethanol extract of *K. rotunda* were contain 33.11 and 42.92% crotepoxide, respectively [11]. Pinostrobin, 5,7-dihydroflavanone, and crotepoxide were exhibited anticancer activity against T470 breast cancer cell with IC₅₀ of 59.8, 122.71 and > 1000 µg/mL, respectively [12]. Meanwhile, benzyl

benzoate showed insecticidal activity on *Spodoptera littoralis* with LC₅₀ of 5.6 µg/mL [4].

The essential oil has an important role in the biological activity of *K. rotunda*. The essential oil of *K. rotunda* rhizome was contained about 75 compounds with two main compounds namely benzyl benzoate (69.7%) and *n*-pentadecane (22.9%) [13]. In different locations, it was also mentioned that of 20 compounds in the volatile oil of *K. rotunda* was contain benzyl benzoate 36.60% and bornyl acetate 30.15% [14]. Furthermore, it was reported that essential oils in *n*-hexane extract of *K. rotunda* rhizome could inhibit the growth of some bacteria [9]. The other plant study reported that *Salvia urmiensis* essential oil contained 60.3% benzyl benzoate showed high activity against *Staphylococcus epidermis* and *Staphylococcus cerevisiae* with minimum inhibitory of 9.3 µg/mL [15]. It showed that benzyl benzoate has potential as an antibacterial agent because it is the main component of *K. rotunda* essential oil.

The previous study of some extracts of *K. rotunda* rhizome suggests that the ethyl acetate and water extracts showed significant antibacterial activity against some pathogenic bacteria, whereas the antibacterial activity of benzyl benzoate and crotepoxide were still limited reported. In this article, we wish to report the isolation of the major component of *K. rotunda* rhizome as well as antibacterial properties.

■ EXPERIMENTAL SECTION

Materials

Rhizome of *K. rotunda* (collected from Purwokerto Indonesia), silica gel plate 60 F₂₅₄ aluminium sheets (Merck), silica gel 60 G (7731, 7734 and 7733, Merck), bacterial strains: *E. coli* ATCC 25922, *E. aerogenes* ATCC 13048, *B. cereus* ATCC 6538 and *S. aureus* ATCC 11778 (supplied by Microbiology Laboratory, Faculty of Medicine Unsoed Purwokerto), Muller Hinton Agar (Oxoid), chloramphenicol (Merck) and dimethyl sulfoxide (Merck).

Instrumentation

¹H and ¹³C-NMR (Nuclear Magnetic Resonance) spectra used Agilent DD2 spectrometer operating at 500

(¹H) and 125 (¹³C) Mhz. Optical rotation was measured by Rudolf Research Analytical Autopol IV Auto Polarimeter.

Procedure

Isolation of benzyl benzoate and crotepoxide from *K. rotunda*

Dried powder of *K. rotunda* rhizome (1 kg) was extracted with acetone at room temperature. The acetone extract of *K. rotunda* rhizome filtered and concentrated using a rotary evaporator. Then the concentrated acetone extract was partitioned with *n*-hexane:methanol (1:1) and the soluble *n*-hexane extract was concentrated with a rotary evaporator. On the other hand, the soluble methanol extract was partitioned with ethyl acetate:water (1:1). Next, the ethyl acetate fraction was concentrated with a rotary evaporator.

The *n*-hexane fraction of *K. rotunda* rhizome (20 g) was fractionated by vacuum column chromatography on silica gel and eluted gradually with *n*-hexane, the mixture of *n*-hexane:chloroform (7:3, 6:4, 5:5, 2:8 and 1:9), chloroform, and ethyl acetate. TLC analysis was carried out to all fractions with eluent *n*-hexane:chloroform (1:1). The fractions having similar spot were collected into 7 sub-fractions: F1 (9.5 g), F2 (1.3 g), F3 (0.6 g), F4 (0.2 g), F5 (0.3 g), F6 (0.3 g) and F7 (0.5 g). Furthermore, F1 which contains the main components of benzyl benzoate was purified by column chromatography using eluent *n*-hexane:chloroform (9:1) to yield a pure benzyl benzoate in the form of colorless oil (543 mg). The ethyl acetate fraction of *K. rotunda* rhizome (6 g) was fractionated by vacuum column chromatography then eluted gradually with *n*-hexane:ethyl acetate (8:2, 7.5:2.5, 7:3 and 0:10) to give 5 sub-fraction: F1' (0.05 g), F2' (0.1 g), F3' (0.3 g), F4' (0.9 g), and F5' (1.3 g). Crotepoxide (colorless needles) was isolated from fraction F5' by column chromatography using eluent *n*-hexane:chloroform:ethyl acetate (5:5:1).

Antibacterial activity assays [16]

Selected bacteria were cultured for 24 h at 37 °C under aerobic conditions on agar media (Mueller Hinton Agar). Afterward, the bacteria were suspended in a 0.9% NaCl solution (w/v). The turbidity of

suspension of bacteria was corrected to the 0.5 Mc Farland standard ($1-2 \times 10^8$ bacterial cells /mL).

Agar plate was inoculated with 200 μ L bacterial suspension. 50 μ L of the samples with concentrations of 10, 50, 100 and 500 μ g/mL were dripped on paper disc on agar media and incubated for 24 h at 37 °C. The presence of clear zones around the paper disc was indicated that the sample has antibacterial activity. The inhibitory zone of the sample was determined by measuring the diameter of the clear zone around the paper disc. The assays were also carried out to the negative control (DMSO 10%) and standard antibiotic chloramphenicol (positive control). The assays were conducted in three repetitions.

■ RESULTS AND DISCUSSION

Identification of Benzyl Benzoate and Crotepoixide from *K. rotunda* Rhizome

Benzyl benzoate (Fig. 1) was obtained as colorless oil. The ¹H-NMR spectrum (500 MHz, CDCl₃) of benzyl benzoate was indicated seven proton signals. They revealed an oxygenated methylene signal at δ 5.39, (2H, s), and six signals of two aromatic proton that represented 10H which are at δ 7.36 (2H, t, J = 7.2 Hz, H-3, H-5), δ 7.41 (2H, t, J = 7.2 Hz, H-3' and H-5'), δ 7.44 (1H, t, J = 7.5 Hz, H-4'), δ 7.47 (2H, d, J = 7.2 Hz, H-2', H-6'), δ 7.58 (1H, t, J = 7.2 Hz, H-4), and δ 8.11 (2H, d, J = 7.5 Hz, H-2, H-6) ppm. Three proton triplet (H-3, H-5, and H-4 or H-3', H-5' and H-4') and two proton doublet (H-2, H-6 or H-2', H-6') could be assigned to phenyl groups which indicates a substituent on an aromatic ring. The ¹³C-NMR spectrum

(125 MHz, CDCl₃) confirmed that there are 14 carbon signals, which indicated the presence of two sp³-carbon of oxygenated methylene (CH₂-O-) at δ 66.69 (C-8) ppm, a sp²-carbon of carbonyl ester group at δ 166.43 (C-7) ppm, two quaternary sp²-carbons at δ 130.15 (C-1) and 136.07 (C-1') ppm, and ten sp²-methines at δ 129.70 (C-2, C-6), δ 128.16 (C-3, C-5), δ 133.02 (C-4), δ 128.37 (C-2', C-6'), δ 128.60 (C-3', C-5') and δ 128.24 (C-4') ppm. The ¹H and ¹³C-NMR spectra data of benzyl benzoate (Table 1) was the newest data from published data [17], where previous data was operating at 300 (¹H) and 75 (¹³C) Mhz.

Crotepoixide (Fig. 1) was obtained as colorless needles (mp 152–154 °C, [α]_D²² +66°). The ¹H NMR (500 MHz, CDCl₃) spectrum showed two signal for two methyl of acetyl groups at δ 1.96 (3H, s, H-11) and δ 2.05 (3H, s, H-12) ppm, five signal of the aromatic ring at δ 7.96 (2H,

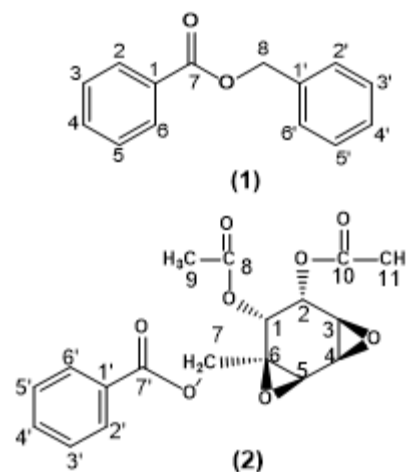


Fig 1. Benzyl benzoate (1) and Crotepoixide (2)

Table 1. HSQC and HMBC spectra of benzyl benzoate

C atom	HSQC		HMBC (¹ H→ ¹³ C)
	δ_c ppm	δ_H (mult, J Hz) ppm	
1	130.15	-	-
2, 6	129.70	8.11 (2H, d, 7,2)	C-1, C-3, C-4, C-5, C-7
3, 5	128.16	7.36 (2H, t, 7,2)	C-2, C-4, C-7
4	133.02	7.58 (1H, t, 7,5)	C-2, C-3, C-5, C-6
7	166.43	-	-
8	66.69	5.39 (2H, s)	C-7, C-1', C-2'
1'	136.07	-	-
2', 6'	128.37	7.47 (2H, d, 7,2)	C-8, C-1', C-3', C-4'
3', 5'	128.60	7.41 (2H, t, 7,2)	C-1', C-2', C-4'
4'	128.24	7.44 (1H, t, 7,5)	C-2', C-3', C-5', C-6'

Table 2. HSQC and HMBC spectra of crotepoxide

C atom	HSQC		HMBC ($^1\text{H} \rightarrow ^{13}\text{C}$)
	δ_{C} ppm	δ_{H} (<i>mult</i> , J Hz) ppm	
1	59.39	-	-
2	69.40	5.64 (1H, <i>d</i> , 9.0)	C-1, C-3
3	70.36	4.91 (1H, <i>d</i> , 9.2)	C-2
4	52.61	3.03 (1H, <i>d</i> , 5.0)	C-3, C-6
5	48.07	3.39 (1H, <i>dd</i> , 5.0 and 2.7)	C-6
6	53.82	3.60 (1H, <i>d</i> , 2.7)	C-5
7	62.40	4.50 (1H, <i>d</i> , 12) 4.17(1H, <i>d</i> , 12)	C-7'
8	169.76	-	-
9	20.65	1.96 (3H, <i>s</i>)	-
10	170.06	-	-
11	20.68	2.05 (3H, <i>s</i>)	C-10
1'	129.08	-	-
2', 6'	129.79	7.96(2H, <i>dd</i>)	C-1', C-3', C-5', C-7'
3', 5'	128.56	7.39 (2H, <i>t</i>)	C-4', C-2', C-6'
4'	133.56	7.53 (1H, <i>t</i>)	C-2', C-3', C-5', C-6'
7'	165.78	-	-

m, H-2', H-6'), δ 7.39 (2H, *m*, H-3', H-5') and δ 7.53 (1H, *m*, H-4') ppm, three signal for oxygenated protons δ 3.39 (1H, *dd*, J = 2.5 and 3.9 Hz, H4), δ 3.08 (1H, *dd*, J = 0.8 and 3.5 Hz, H5) and δ 3.60 (1H, *d*, J = 2.7 Hz, H6) ppm, two signal for oxygenated protons at δ 5.64 (1H, *d*, 9.0 Hz) and δ 4.91 (1H, *d*, 9.0 Hz) ppm, and two signal for AB system at δ 4.50 (1H, J = 12.0 Hz, H-7) and 4.17 (1H, J = 12.0 Hz, H-7) ppm. The ^{13}C -NMR spectra (125 MHz, CDCl_3) of crotepoxide revealed the presence two of methyl of acetyl carbons at δ 20.65 (C-9) and 20.68 (C-11) ppm, six aromatic carbon at δ 129.08 (C-1'), 129.79 (C-2' and C-6'), 128.56 (C-3' and C-5'), and 133.56 (C-4') ppm, a methylene carbon at 62.40 (C-7) ppm, three carbonyl esters at δ 169.76 (C-8), 170.06 (C-10) and 165.78 (C-7') ppm, five methine carbons at δ 60.40 (C-2), 70.36 (C-3), 52.51 (C-4), 43.07 (C-5) and 53.82 (C-6) ppm, and two quaternary carbons at δ 59.39 (C-1) and 129.08 (C-1') ppm. The ^1H and ^{13}C -NMR spectra data of crotepoxide was in agreement with the published data [18].

The one bond correlation between carbon and proton is determined by the 2D (two-dimensional) NMR spectrum of HSQC (Heteronuclear Single Quantum Coherence), whereas the correlation of two or three bonds between carbon and proton is determined by the HMBC

(Heteronuclear Multiple Bond Coherence) spectra. Table 1 and 2 represents the 1D (^1H and ^{13}C) and 2D (HSQC and HMBC) of benzyl benzoate and crotepoxide spectra data. Meanwhile, Fig. 2 describes the correlation of two or three bonds between proton and carbon (HMBC) on the benzyl benzoate and crotepoxide structures.

Antibacterial Activity

Antibacterial activity assays of extract and isolated compounds were conducted on four pathogenic bacteria including two Gram-negative bacteria *E. coli* ATCC 25922

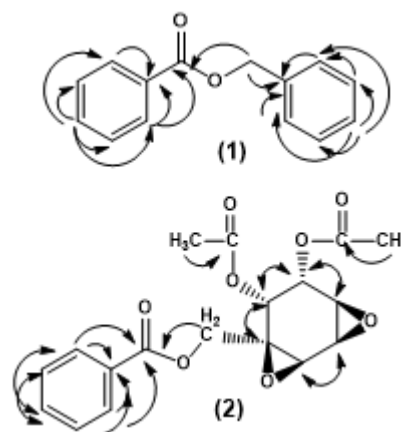
**Fig 2.** HMBC of benzyl benzoate (1) and crotepoxide (2)

Table 3. Antibacterial activity of extract, fraction and isolated compounds of *K. rotunda* rhizome

Sample	Concentration ($\mu\text{g/mL}$)	Zone inhibitory (mm) \pm SD			
		<i>E. coli</i> ATCC 25922	<i>E. aerogenes</i> ATCC 13048	<i>B. cereus</i> ATCC 6538	<i>S. aureus</i> ATCC 11778
Acetone extract	10	-	-	-	3.1 \pm 0.06
	50	3.4 \pm 0.03	-	-	5.4 \pm 0.26
	100	8.0 \pm 0.03	4.3 \pm 0.17	3.6 \pm 0.06	8.1 \pm 0.17
	500	11.7 \pm 0.17	7.9 \pm 0.02	10.1 \pm 0.36	12.1 \pm 0.36
<i>n</i> -Hexane fraction	10	4.2 \pm 0.11	3.0 \pm 0.06	4.1 \pm 0.03	4.0 \pm 0.06
	50	8.2 \pm 0.06	8.1 \pm 0.11	7.9 \pm 0.17	10.0 \pm 0.03
	100	11.1 \pm 0.36	12.2 \pm 0.86	15.9 \pm 0.01	15.2 \pm 0.26
	500	20.2 \pm 0.06	18.9 \pm 0.03	19.8 \pm 0.66	19.5 \pm 0.50
Ethyl acetate fraction	10	-	-	-	-
	50	-	6.9 \pm 0.11	-	-
	100	-	9.5 \pm 0.01	-	2.4 \pm 0.26
	500	5.0 \pm 0.03	11.8 \pm 0.36	3.6 \pm 0.36	4.1 \pm 0.17
Benzyl benzoate	10	-	-	-	-
	50	-	-	5.9 \pm 0.06	3.6 \pm 0.06
	100	5.2 \pm 0.17	4.0 \pm 0.06	8.1 \pm 0.06	6.1 \pm 0.06
	500	7.0 \pm 0.03	8.9 \pm 0.17	9.9 \pm 0.11	9.1 \pm 0.06
Crotopoxide	10	-	-	-	-
	50	-	-	-	-
	100	-	6.1 \pm 0.03	4.2 \pm 0.03	-
	500	-	8.6 \pm 0.36	7.0 \pm 0.11	3.8 \pm 0.06
Chloramphenicol	10	14.2 \pm 0.36	10.9 \pm 0.06	15.0 \pm 0.03	15.0 \pm 0.50
	50	27.0 \pm 0.17	15.2 \pm 0.25	20.0 \pm 0.03	25.7 \pm 0.11
	100	31.9 \pm 0.01	24.0 \pm 0.03	27.0 \pm 0.01	28.2 \pm 0.06
	500	34.7 \pm 0.36	27.3 \pm 0.17	30.7 \pm 0.17	31.9 \pm 0.06

SD= Standard Deviation

and *E. aerogenes* ATCC 13048, and two Gram-positive bacteria *B. cereus* ATCC 6538 and *S. aureus* ATCC. Antibacterial assays were also performed on acetone extract, *n*-hexane and ethyl acetate fractions of *K. rotunda* rhizome.

The results of antibacterial activity assay to acetone extract, *n*-hexane and ethyl acetate fraction, and isolated compounds of *K. rotunda* rhizome was indicated different inhibitory zone to all test bacteria (Table 3). All sample tests showed the lower antibacterial activity than positive control (chloramphenicol). The inhibitory zone level of bacterial growth is classified as follows: weak (< 5 mm), moderate (5–10 mm), strong (11–20 mm) and very strong (> 21 mm) [19].

Acetone extract of *K. rotunda* rhizome showed

moderate activity against *E. coli* and *S. aureus* with an inhibitory zone of 8.0 and 8.1 mm at 100 $\mu\text{g/mL}$ concentrations, and it exhibits high antibacterial activity (11.7 and 12.1 mm) at 500 $\mu\text{g/mL}$. While on *E. aerogenes* and *B. cereus* at 500 $\mu\text{g/mL}$ showed inhibitory zone 7.9 and 10.1 mm, respectively. The *n*-hexane fraction of the *K. rotunda* rhizome showed antibacterial activity against all test bacteria. The *n*-hexane fraction of *K. rotunda* rhizome showed moderate activity at 50 $\mu\text{g/mL}$ with the inhibitory zone 7.9 to 10.0 mm. The intense activity (11.1–20.2 mm) of the *n*-hexane fraction was shown at 100 $\mu\text{g/mL}$ and 500 $\mu\text{g/mL}$. Both acetone extract and *n*-hexane fraction *K. rotunda* rhizome are potential as an antibacterial. The ethyl acetate fraction showed

antibacterial activity against *E. aerogenes* at a minimum concentration of 50 µg/mL with an inhibitory zone of 6.9 mm, however to the other bacteria showed weak activity.

The benzyl benzoate have lower activity than acetone extract and *n*-hexane fraction; it is suggested that the other compounds both in acetone extract and *n*-hexane fraction of *K. rotunda* rhizome have higher antibacterial activity than benzyl benzoate. Synergism is observed when the effect of combined substances is greater. Benzyl benzoate showed moderate antibacterial activity against *B. cereus* at 50–500 µg/mL with an inhibitory zone of 5.9–9.9 mm, against *E. coli* and *S. aureus* at 100–500 µg/mL with an inhibitory zone of 5.2–7.0 and 6.1–9.1 mm respectively, and to *E. aerogenes* at 500 µg/mL with an inhibitory zone of 8.9 mm.

Meanwhile, crotepoixide exhibited moderate antibacterial activity against *E. aerogenes* at 100–500 µg/mL with an inhibitory zone 6.1–8.6 mm and against *B. cereus* at 500 µg/mL with inhibitory zone 7.0 mm, while to other bacteria do not have activity. Its suggested that crotepoixide have lower activity than ethyl acetate fraction, except against *B. cereus*.

Generally, crotepoixide showed lower antibacterial activity than benzyl benzoate. This is possible because both compounds have a different structure, functional groups, and lipophilicity. The lipophilicity of compounds was affected by their ability to penetrate the cell wall of bacteria. The cell wall of bacteria has the lipid layers (lipophiles) that make these bacteria more resistant against some compounds and impermeable with limited diffusion [20]. Crotepoixide has lower lipophilicity than benzyl benzoate; therefore its ability to penetrate the bacteria cell wall was less than benzyl benzoate.

The antibacterial activities of essential oil and their components or some cyclic hydrocarbon compounds have been previously reviewed and the mechanism of action has not been studied in great detail, because most of the cyclic hydrocarbon compounds showed to have no specific cellular targets. Such as typical lipophiles, they pass through the cell wall and cytoplasmic membrane, disrupt the structure of their different layers of polysaccharides,

fatty acid, and phospholipids. They can coagulate the cytoplasm and damage lipids and protein [21].

■ CONCLUSION

The benzyl benzoate and crotepoixide from *K. rotunda* rhizome were successfully isolated. The evaluation of antibacterial activity of benzyl benzoate and crotepoixide against four pathogenic bacteria confirmed that benzyl benzoate and crotepoixide have lower antibacterial activity than acetone extract and *n*-hexane fraction of *K. rotunda* rhizome. The benzyl benzoate was exhibited the highest antibacterial activity with moderate classification against *B. cereus* at a minimum concentration of 50 µg/mL and inhibitory zone 5.9 mm whereas crotepoixide showed the highest activity against *E. aerogenes* at a minimum concentration of 100 µg/mL with inhibitory zone 6.1 mm.

■ REFERENCES

- [1] Kim, T.K., 2016, *Edible Medicinal and Non-Medicinal Plants*, Springer-Cham, Switzerland.
- [2] Desmiaty, Y., Winarti, W., Nursih, A.M., Nisrina, H., and Finotory G., 2018, Antioxidant and antielastase activity of *Kaempferia rotunda* and *Curcuma zedoaria*, *Res. J. Chem. Environ.*, 22 (1), 95–98.
- [3] Lotulung, P.D.N., Minarti, Kardono, L.B.S., and Kawarrishi, K., 2008, Antioxidant compound from the rhizomes of *Kaempferia rotunda*, *Pak. J. Biol. Sci.*, 11 (20), 2447–2450.
- [4] Nugroho, B.W., Schwarz, B., Wray, V., and Proksch, P., 1996, Insecticidal constituents from rhizomes of *Zingiber cassumunar* and *Kaempferia rotunda*, *Phytochemistry*, 41 (1), 129–132.
- [5] Imam, S.A., Rout, S.K., Sutar, N., Sharma U.S., and Sutar, R., 2013, Wound healing activity of *Kaempferia rotunda* Linn leaf extract, *Int. J. Curr. Microbiol. Appl. Sci.*, 2 (12), 74–78.
- [6] Agrawal, S., Bhawsar, A., Choudhary, P., Sing, S., Keskar, N., and Chaturvedi, M., 2011, In-vitro anthelmintic activity of *Kaempferia rotunda*, *Int. J. Pharm. Life Sci.*, 2 (9), 1062–1064.

- [7] Sultana, Z., Imam, K.M.S.U., Azam, F.M.S., Rahman, S., Rahman, S., Islam, F., and Rahmatullah, M., 2012, Evaluation of antihyperglycemic and antinociceptive activities of methanolic extract of *Kaempferia Rotunda* L. (Zingiberaceae) rhizomes, *Adv. Nat. Appl. Sci.*, 6 (8), 1302–1306.
- [8] Kabir, S.R., and Reza, M.A., 2014, Antibacterial activity of *Kaempferia rotunda* rhizome lectin and its induction of apoptosis in Ehrlich ascites carcinoma cells, *Appl. Biochem. Biotechnol.*, 172 (6), 2866–2876.
- [9] Kumar, A., Kumar, S., and Navneet, 2015, Antimicrobial activity and phytochemical analysis of *Kaempferia rotunda* L. rhizomes, *Pharm. Lett.*, 7 (9), 389–395.
- [10] Astutiningsih, C., Octaviani, R., and Suratiningsih, S., 2014, Daya hambat minyak atsiri dan ekstrak limbah sisa destilasi rimpang kunir putih (*Kaempferia rotunda* L.) terhadap pertumbuhan *Candida albicans* ATCC 10231, *J. Pharm. Sci. Community*, 11 (1), 18–22.
- [11] Suphrom, N., Sonyot, W., Insumrong, K., Sawangsup, P., Sutamuang, P., and Ingkaninan, K., 2017, GC-MS analysis and *in vitro* anti-androgenic activity of *Kaempferia rotunda* Linn extract, *Naresuan Univ. J. Sci. Technol.*, 25 (4), 34–43.
- [12] Atun, S., and Arianingrum, R., 2015, Anticancer activity of bioactive compounds from *Kaempferia rotunda* rhizome against human breast cancer, *Int. J. Pharmacogn. Phytochem. Res.*, 7 (2), 262–269.
- [13] Woerdenbag, H.J., Windono, T., Bos, R., Riswan, S., and Quax, W.J., 2004, Composition of the essential oil of *Kaempferia rotunda* L. and *Kaempferia angustifolia* Roscoe rhizomes from Indonesia, *Flavour Fragr. J.*, 19 (2), 145–149.
- [14] Sereena, K., Kumar, U.P., and Shree, A.B.R., 2011, Histochemical and phytochemical markers for the authentication of ayurvedic raw drug hallakam (*Kaempferia rotunda*) and its marketed adulterant, *Int. J. Pharm. Sci. Res.*, 2 (11), 2952–2958.
- [15] Farjam, M.H., 2012, Comparative study of the antimicrobial activity of essential oil and two different extracts from *Salvia urmiensis* Bunge, *Asian Pac. J. Trop. Biomed.*, 2 (3), 2–4.
- [16] Balouiri, M., Sadiki, M., and Ibnsouda, S.K., 2016, Methods for *in vitro* evaluating antimicrobial activity: A review, *J. Pharm. Anal.*, 6 (2), 71–79.
- [17] Sindra, H.C., and de Mattos, M.C.S., 2016, Appel reactions of carboxylic acid with tribromoisocyanuric acid/triphenylphosphine: A mild and acid-free preparation of esters and amides, *J. Braz. Chem. Soc.*, 27 (6), 1129–1136.
- [18] Desta, Z.Y., and Sewald, N., 2018, Isolation of non-cytotoxic crotepoide from the root bark of *Croton macrostachyus* and the reassignment of its structure, *Bull. Chem. Soc. Ethiop.*, 31 (3), 465–469.
- [19] Rumengan, I.F.M., Rumampuk, N.D., Rimper, J., and Losung, F., 2014, Produksi dan uji aktivitas antimikroba senyawa bioaktif yang diekstrak dari rotifer (*Brachionus rotundiformis*) strain lokal, *Jurnal LPPM Bidang Sains dan Teknologi*, 1 (1), 56–70.
- [20] Mangunwardoyo, W., and Deasywaty, U.T., 2012, Antimicrobial and identification of active compound *Curcuma xanthorrhiza* Roxb., *IJBAS-IJENS*, 12 (1), 69–78.
- [21] Tripathi, M., Chawla, P., Uphadyay, R., and Trivedi, S., 2013, Essential oils from family Zingiberaceae for antimicrobial activity - A review, *IJPBS*, 4 (4), 149–162.

Synthesis of Silica-Salen Derivative from Rice Husk Ash and its Use for Extraction of Divalent Metal Ions Co(II), Ni(II) and Cu(II)

Duha Hussien Attol and Hayder Hamied Mihsen*

Department of Chemistry, College of Science, University of Kerbala, Karbala 56001, Iraq

* Corresponding author:

email: hayderalhmedat@gmail.com

Received: September 4, 2018

Accepted: December 29, 2018

DOI: 10.22146/ijc.38558

Abstract: Rice husk ash (RHA) was used to prepare sodium silicate, which in turn was functionalized with 3-(chloropropyl)triethoxysilane employing the sol-gel technique to form RHACCl. Chloro group in RHACCl was replaced with iodo group forming RHACI. Ethylenediamine was immobilized on RHACI in order to prepare it for the reaction with salicylaldehyde to form a silica derivative-salen. FT-IR analysis indicated the presence of secondary amine and $-NH$ and $C=N$ absorption bands. XRD analysis revealed the occurrence of the broad diffused peak with maximum intensity at $22-23^\circ$ (2θ). BET measurements showed also that the surface area of the prepared compound is $274.55\text{ m}^2/\text{g}$. Elemental analysis proved the existence of nitrogen in the structure of the prepared compound. The silica derivative-salen showed high potential for extraction and removal of heavy contaminating metal ions Ni(II), Cu(II), and Co(II) from aqueous solutions. The kinetic study demonstrates that the adsorption of the metal ions follows the pseudo-second order.

Keywords: amorphous silica; salicylaldehyde; surface area; preconcentration process; uptake capacity

■ INTRODUCTION

In recent years there has been considerable interest in developing silica-based porous materials that have large specific surface areas. This is due to widespread applications in white light emission process [1], battery applications [2], antibacterial activity [3-4], heavy metal ions separation and extraction [5-12], and catalysis [13-16]. Rice is one of the silica producing plants, where the major SiO_2 content is observed in its husk, which ranges from 8.7 to 28% depending on several factors including origin, geographic location and climate [2,17]. Rice husk (RH) is the protective coat of rice grains. As reported by Govindarao [18], RH constituents on a dry basis are ash (20%), cellulose (38%), lignin (22%) and organic compounds (20%). Rice husk ash (RHA) ash is silica representing (94%) of the whole [19]. Preconcentration of trace metals employing functionalized silica-gel has received much attention in the last few decades. Preliminary experiments were conducted by Leyden and Lutterll [20] and Leyden et al. [21] using amine, dithiocarbamate, and thioether derivatives for

preconcentration process. Recently, this topic was a subject of extensive research, and a variety of functionalized silica compounds were prepared in order to extract or separate metal ions from aqueous solutions [6,11,22-25].

In this work, silica derivative-salen was synthesized from RH via sol-gel technique and nucleophilic substitution reaction. The resultant material was characterized using FTIR, XRD, CHNS, SEM-EDS, AFM, TGA and BET. The metal uptake capacity of the functionalized silica was investigated using aqueous solutions of Ni(II), Co(II) and Cu(II) metal ions. The effect of several factors on the preconcentration process was examined as well as including time of shaking, the concentration of metal ions, the mass of the ligand and pH of the solution.

■ EXPERIMENTAL SECTION

Materials

Sodium hydroxide (BHD, England 99%), nitric acid (CDH, India 70%), 3-chloropropyltriethoxysilane

(Sigma, Germany 99%), Acetone (Romal 99.7%), ethylenediamine (ALPHA CHEMICA, India 99%), triethylamine (CDH, India 98%), salicylaldehyde (CDH, India 99%), Nickel chloride hexahydrate (BDH, England 96%), Cobalt chloride hexahydrate (BDH, England 97%), Copper chloride dihydrate (BDH, England 97%), Toluene (Merk, KGaA, Germany 99%). All the chemicals were used as received without further purification.

Procedure

Characterization techniques

Functional groups in functionalized silica were determined using a Thermo AVATAR instrument. The spectra were recorded in the range of 4000–400 cm^{-1} . Scanning Electron Microscopy (SEM) analysis of functionalized silica was conducted on a FESEM MIRA III (TESCAN). Samples were dispersed in ethanol for 10 min before analysis. Atomic Force Microscopy (AFM) analysis was conducted on an AFM Angstrom AA-3000.

Thermogravimetric (TG) analysis was performed using a TA Q600 instrument. The sample was heated from 50 to 600 °C at a heating rate of 20 °C min^{-1} under Ar atmosphere. The X-ray Diffraction (XRD) patterns were obtained using Shimadzu X-ray Diffractometer using $\text{CuK}\alpha$, and 2θ between 10 and 80°. Surface area and pore volume of the sample were measured by Brunauer-Emmett-Teller using BEL BELSORP MINI II instrument. Elemental analysis was performed using a Thermo Finnigan FlashEA 1112 instrument.

Extraction and functionalization of silica from RH

Extraction of silica from RH. RH was washed with water then rinsed with distilled water then dried at room temperature for 24 h. Afterward, the sample was stirred with (1.0 M) nitric acid at room temperature for 24 h, then washed with distilled water. Subsequently, the wet material dried at 100 °C for 24 h. To obtain amorphous silica, the sample was calcined at 750 °C for 2 h in a muffle furnace to obtain acid leached RHA [26].

Functionalization of RHA with 3-(chloropropyl) triethoxysilane (CPTES). Functionalization of RHA was done in accordance with the procedure described by Adam et al. [27]. Silica obtained from RHA was stirred

with NaOH in a plastic container at 80 °C for 60 min to convert silica into sodium silicate, then CPTES was added to this solution. Next, the solution was titrated with 3.0 M of nitric acid until the pH of the solution dropped to 3. The obtained gel was aged for 2 days, then centrifuged with water profusely. Finally, the gel was washed with acetone, then dried in at 110 °C for 24 h. The obtained powder was labeled as RHACCl.

Iodide-exchanged polymer

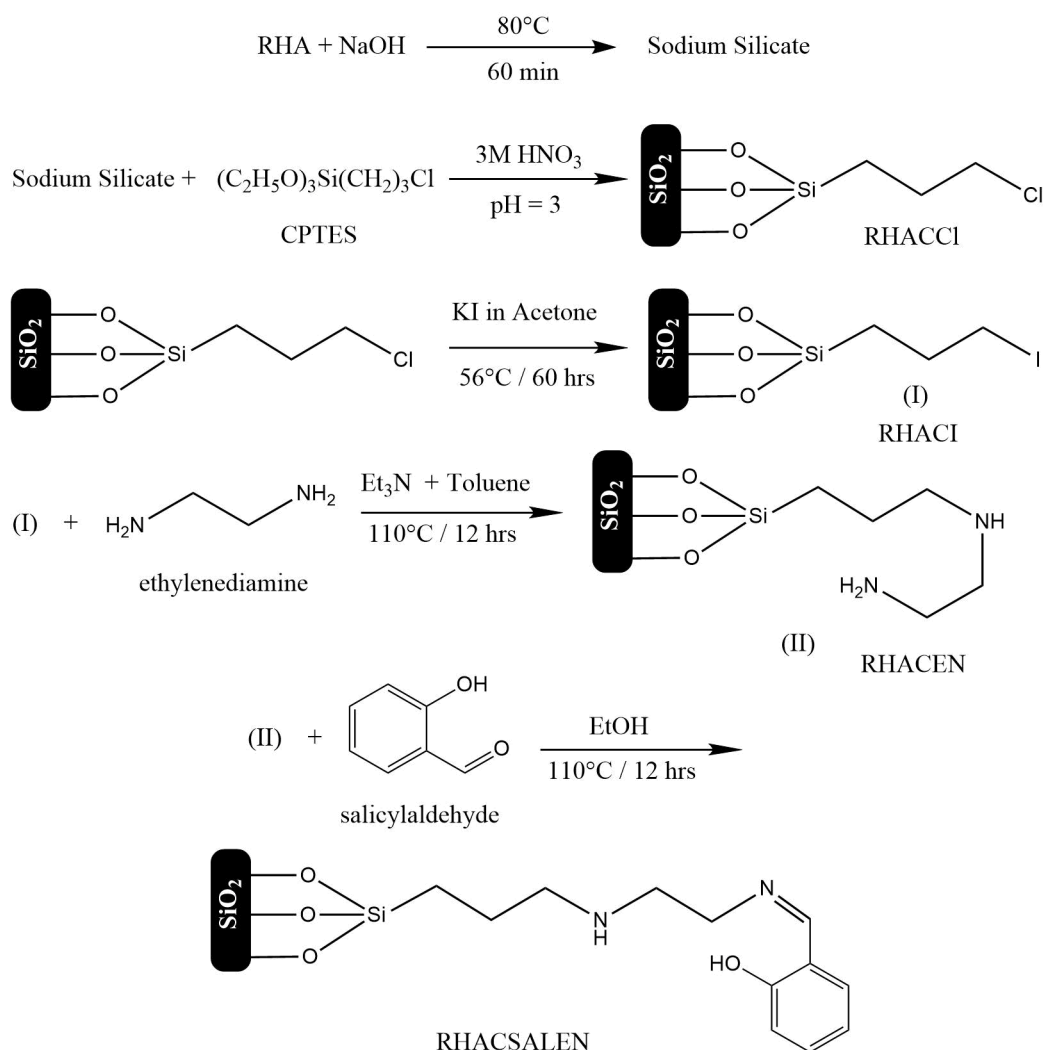
Exchanging chloride ions with iodide ions was carried out in accordance with the procedure described by Ahmed and Parish [28]. RHACCl was suspended within dry acetone containing potassium iodide, and then the mixture was refluxed for 60 h. The obtained solid precipitate was washed with distilled water, methanol and ether and dried at 100 °C. The resultant powder was labeled as RHACI.

Functionalization with ethylenediamine and salicylaldehyde

A mixture of 1.0 g of RHAC-I, 16.6 mmol 0.9 mL of ethylene diamine and 16.6 mmol 2.3 mL of Et_3N was refluxed with 30 mL of toluene at 110 °C in an oil bath for 12 h. The obtained material was filtered and washed with DCM and DMF, then it was dried in an oven. A beige precipitate of ethylene diamine modified silica was formed, labeled RHACEN. 1.0 g of the RHACEN was added to excess mL of salicylaldehyde about 3.0, and the mixture was refluxed in 30 mL of ethanol at 50 °C for 6 h. The products were filtered and washed with an amount of ethanol and acetone. The yellow precipitate was collected and labeled as RHACSALEN. Scheme 1 represents the steps followed in the preparation of RHACSALEN ligand.

Metal uptake experiments

Two hundred and fifty milligrams of RHACSALEN was shaken with 50 mL, 0.1 M of aqueous solution of metal(II) ions (Co(II) , Ni(II) , Cu(II)) using a plastic container. Measurements of the concentration of metal ions were carried out by withdrawing a sample of 0.5 mL from the solution using a filtered syringe. Samples were diluted to the linear range of the calibration curve for



Scheme 1. Synthesis of RHACSALEN ligand

each metal. Metal ion uptake was calculated as mmole of metal per gram of ligand. Time of shaking, the concentration of metal, the mass of the ligand and pH of the solution were examined.

■ RESULTS AND DISCUSSION

FTIR Spectroscopy Analysis

Functionalization of the obtained silica was monitored by comparing FTIR spectra of precursor and products. FTIR spectra of RHA, RHACCL, RHACI, RHACEN are presented in Fig. 1(a-d) and FTIR spectrum of RHACSALEN is presented in Fig. 1(e). The peaks at 1082, 796, and 474 cm^{-1} are present in all spectra and are attributed to the Si–O–Si group [14]. The broadband that

appears between 3200 and 3600 cm^{-1} is attributed to O–H stretching vibration of Si–OH groups as well as absorbed water onto the surface of silica. The appearance of the peak at 2951 cm^{-1} , which is attributed to the stretching of the aliphatic CH_2 group, is a strong evidence of the successful attachment of CPTES to the prepared silica. The peaks at 3523 and 3446 cm^{-1} in Fig. 1(d) are attributed to the symmetric and asymmetric stretching of N–H bond of the primary amine in RHACEN, while the peaks at 3341 and 1663 cm^{-1} are attributed respectively to the stretching and bending of N–H bond in the secondary amine in the same moiety. The appearance of these peaks is a strong evidence of the successful attachment of ethylenediamine group to RHACI.

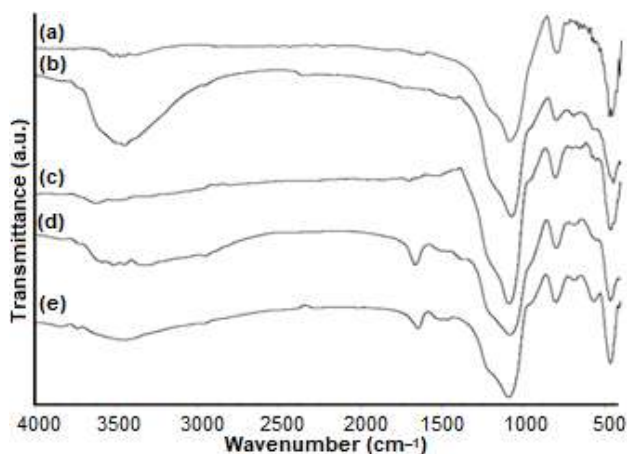


Fig 1. FTIR spectra: (a) RHA, (b) RHACl, (c) RHACI, (d) RHACEN and (e) RHACSALEN

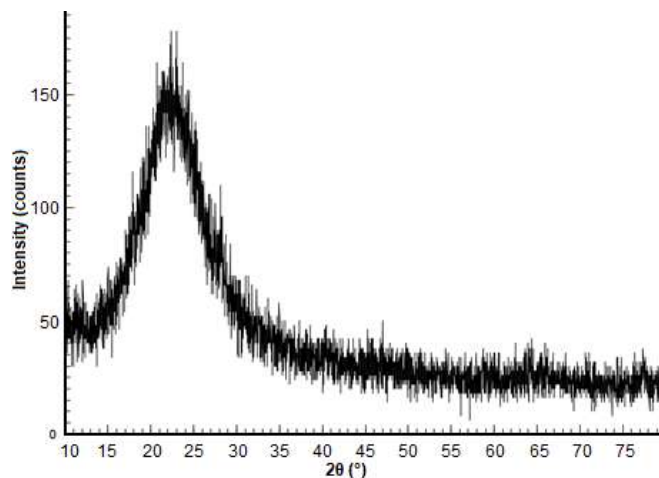


Fig 2. XRD pattern of RHACSALEN

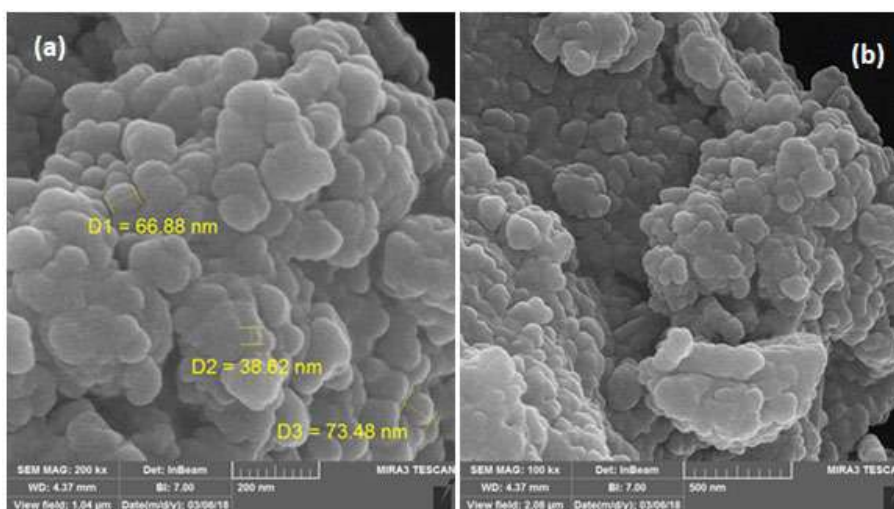


Fig 3. SEM images of the functionalized silica. (a) 200 nm (b) 500 nm

It can be seen from Fig. 1(e) that the peaks attributed to the stretching of the N-H bond of primary amine are absent in this spectrum. In addition, the peak at 1644 cm^{-1} refers to the isomethene group (C=N) [29]. The stretching of aliphatic CH_2 for propyl chain appears at 2955 cm^{-1} . This provides strong evidence that the reaction between RHACEN and salicylaldehyde was successful and the Schiff base was formed.

X-ray Diffraction Pattern

The X-ray diffraction pattern of RHACSALEN is shown in Fig. 2. XRD analysis revealed the occurrence of the broad diffused peak with maximum intensity at $22\text{--}23^\circ$ (2θ), though sharp peaks were absent. This result, which

is in agreement with a strong broad peak of amorphous silica [30], indicates that the amorphous nature of the functionalized silica was analyzed.

Elemental Analysis CHNS

Elemental analysis of RHACSALEN showed an increase in the percentages of C and H compared with RHA and RHACI [14]. Furthermore, the elemental analysis of RHACSALEN indicated the presence of N which provides further confirmation of the successful immobilization of the Schiff base onto RHACI. A similar conclusion was drawn by Adam et al. [27] and Mihsen et al. [14].

SEM-EDS Analysis

SEM images of the functionalized silica are shown in Fig. 3. These images show that the particles of the functionalized silica are granular and irregularly shaped with an average diameter of ca. 60 nm.

Fig. 4 shows the spectrum obtained from EDX analysis. This spectrum showed the presence of nitrogen which can be considered further proof for the successful incorporation of salen complex onto the surface of silica. The average value of the chemical composition obtained from EDX analysis is shown in Table 2.

AFM Analysis

AFM technique was employed to investigate the topography of the prepared ligand surface. The atomic force microscopy (AFM) images and granularity normal distribution of the RHACSALEN are shown in Fig. 5-6. The obtained results revealed that the average roughness of the surface for RHACI was increased upon functionalization process from 6.35 to 11.6 nm. This change may be attributed to the successful modification of the surface of the ligand from RHACI to RHACSALEN. Additionally, AFM results showed that the average diameter of the prepared ligand was 72 nm which is slightly larger than the result obtained via SEM technique.

Thermal Analysis

TGA-DTG analysis was performed to determine the thermal stability of the functionalized silica, and the obtained results are depicted in Fig. 7.

Table 1. Elemental analysis of RHA, RHACI, and RHACSALEN

Sample	C (%)	H (%)	N (%)	S (%)
RHA	1.6	0.84		
RHACI	9.98	1.61	-	-
RHACSALEN	11.57	1.95	1.90	-

Table 2. The average values obtained from EDX analysis of RHACSALEN

Element	W%	A%
C	11.83	19.24
N	0.89	1.25
O	36.52	44.59
Si	48.05	33.42
S	0.21	0.13
Cl	2.49	1.37
I	0.01	0.01
	100	100

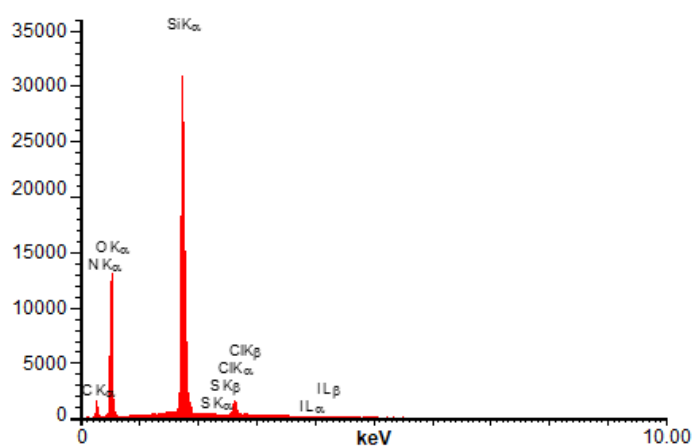


Fig 4. EDX chart for RHACSALEN

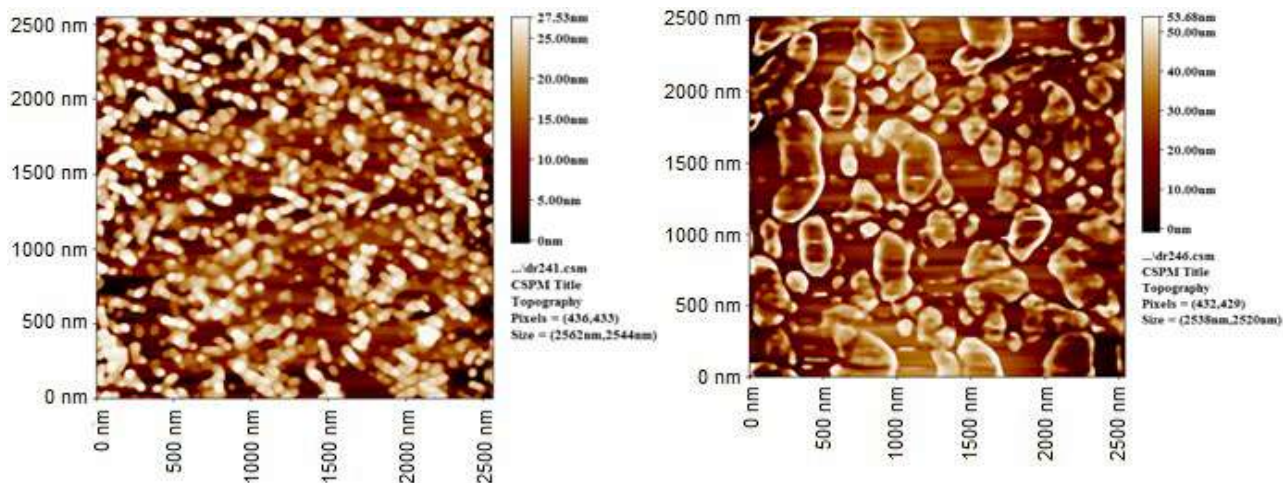


Fig 5. AFM image of RHACI (left); RHACSLAEN (right)

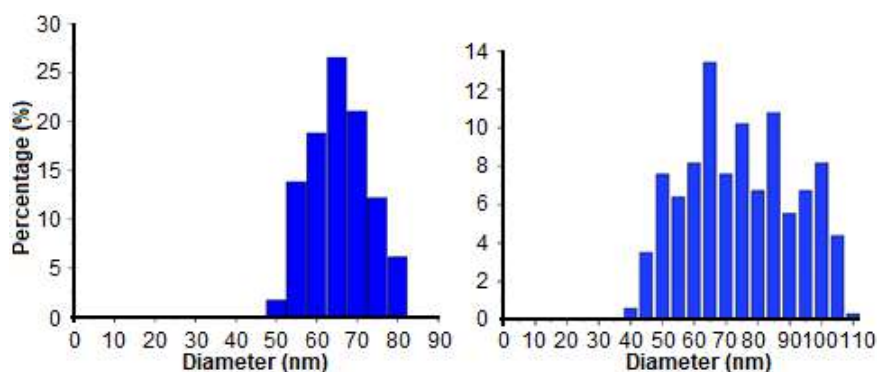


Fig 6. The granularity cumulation distribution of RHACI (left); RHACSLAEN (right)

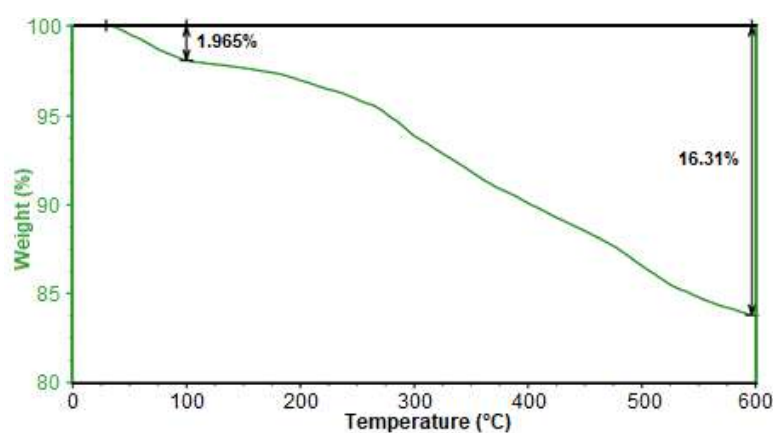


Fig 7. TGA plot of RHACSALEN

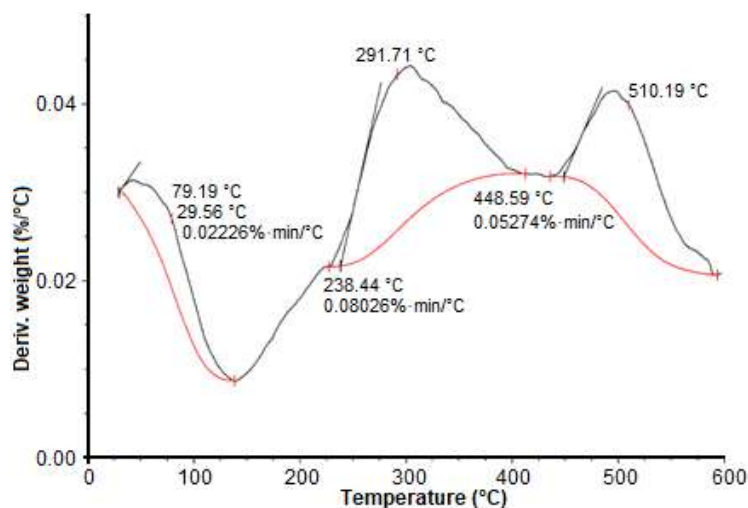


Fig 8. DTG plot of RHACSALEN

The results showed that the functionalized silica exhibited two characteristic weight loss stages. Initially, weight loss occurred between 25 and 120 °C with about 2 wt.% loss. This was attributed to the evaporation of water molecules adsorbed on the surface of silica [14,31]. The second weight loss happened between 250 and 600 °C with

about 16 wt.% loss, which may be ascribed to dihydroxylation and loss of water or alcohol from silica [32-33].

Fig. 8 shows the result of DTG analysis for RHACSALEN. It reveals two major weight loss steps which are in agreement with the results obtained from

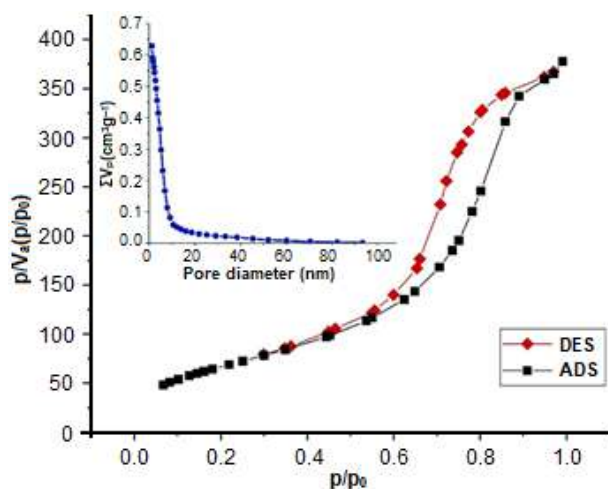


Fig 9. Adsorption/desorption isotherm of the functionalized silica. Inset: The pore size distribution

TGA analysis about the evaporation of water molecules and the dihydroxylation and loss of water and alcohol from silica [34].

Nitrogen Adsorption Desorption Analysis

The surface area of the functionalized silica was investigated employing nitrogen adsorption-desorption. Fig. 9 shows the obtained isotherm. The pore size distribution graph is inset. According to the IUPAC classification of hysteresis loops, this isotherm follows type IV and H2 isotherms [35]. It can be seen in Fig. 9 that N_2 adsorption isotherm of the functionalized silica gave a hysteresis loop observed in the range of p/p_0 values between 0.6 and 0.9, which is associated with capillary condensation, a characteristic of mesoporous materials [11].

A specific area, pore size and pore volume of the functionalized silica was obtained employing BET analysis, and it was found to be equal to $247.55 \text{ m}^2/\text{g}$, $0.582 \text{ cm}^3/\text{g}$, and 9.41 nm respectively.

Metal Uptake Experiments

Effect of shaking time on the metal uptake

In order to determine the effect of shaking time on the metal uptake, 0.25 g of the ligand was shaken with an aqueous solution of divalent metal ions for 24 h . The results, depicted in Fig. 10, shows an increase in the uptake of the metal ions as a function to the time of exposure in a nonlinear fashion. Metal ion uptake

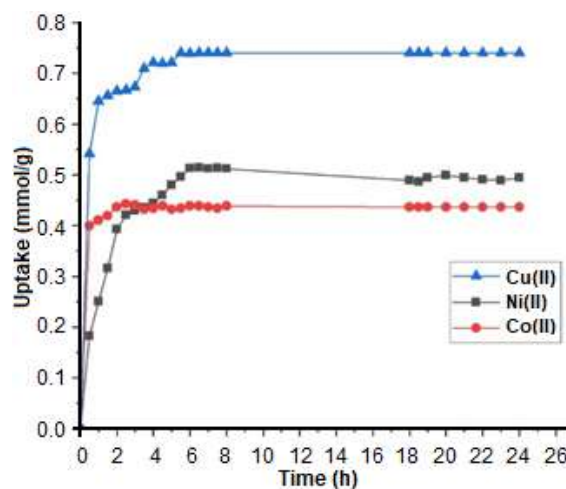


Fig 10. The uptake of Co(II), Ni(II) and Cu(II) ions by RHACSALEN versus time

increased rapidly at the beginning then it became slower as the time progressed, with the exception of the case of Ni(II) ions which showed an increase in metal uptake capacity after reaching its maximum. The increase in metal uptake capacity may be ascribed to diffusion factors, as the already complexed groups prevent metal ions from contacting unreacted ligand groups. These results are in line with other works [12]. Saturation occurred after 3 h in case of cobalt, while in case of nickel and copper saturation occurred after 6 h .

First order (Eq. (1)), second order (Eq. (2)) [25], pseudo-first order (Eq. (3)) and pseudo-second-order (Eq. (4)) [36] were employed to evaluate the experimental data in order to determine the adsorption kinetics.

Kinetic model and parameters for Ni(II), Cu(II) and Co(II) are presented in Table 3.

$$\ln C_e = -k_1 t + \ln C_0 \quad (1)$$

$$\frac{1}{C_e} = k_2 t + \frac{1}{C_0} \quad (2)$$

$$\log \left(1 - \frac{q_t}{q_e} \right) = -\frac{k_3}{2.303} t \quad (3)$$

$$\frac{t}{q_t} = \frac{1}{k_4 q_e^2} + \frac{1}{q_e} t \quad (4)$$

where C_e is the concentration of metal ion at equilibrium (mM), C_0 is the initial concentration of metal ion (mM); q_e and q_t are the amounts of metal ions adsorbed (mol g^{-1}) at equilibrium and at any time t (mmol g^{-1}), respectively;

k_1 , k_2 , k_3 and k_4 are adsorption rate constant of first order (min^{-1}), second order ($\text{mM}^{-1} \text{min}^{-1}$), pseudo-first order (min^{-1}) and pseudo-second-order ($\text{g mmol}^{-1} \text{min}^{-1}$), respectively.

The obtained results show that the pseudo-second-order model has the highest correlation coefficient for Ni(II), Cu(II) and Co(II). Additionally, the value of q_e calculated from the pseudo-second-order as ($21.23 \text{ mmol g}^{-1}$ for Ni(II), $22.13 \text{ mmol g}^{-1}$ for Cu(II), 17.53 for Co(II)) is close to the experimental q_e as ($22.47 \text{ mmol g}^{-1}$ for Ni(II), 23.8 mmol g^{-1} for Cu(II), $18.21 \text{ mmol g}^{-1}$ for Co(II)) in comparison with the experimental q_e obtained from the pseudo-first-order model as ($11.67 \text{ mmol g}^{-1}$ for Ni(II), 7.93 mmol g^{-1} for Cu(II), 8.11 mmol g^{-1} for Co(II)). These results indicate that the applicability of pseudo-second-order model is a better option to describe the adsorption of Ni(II), Cu(II) and Co(II) ions onto RHACSALEN. Consequently, the kinetic does not involve a mass transfer in solution and the adsorption is chemical [25].

Effect of the initial concentration of metal ion solution

The effect of the initial concentration of the metal

ion solution was investigated. 0.25 g of RHACSALEN was shaken for 8 h with three solutions of metal ion where each of the solution has different initial concentration. The results, expressed in Fig. 11(a-c), show

Table 3. Rate constant of Ni(II), Cu(II) and Co(II) adsorption on RHACSALEN and the linear coefficient in various kinetics models

Kinetic model	Rate constant	R ²
Ni(II)		
First order	0.0999 min^{-1}	0.8536
Second order	1.5354 $\text{mM}^{-1} \text{min}^{-1}$	0.9104
Pseudo-first order	0.4629 min^{-1}	0.9434
Pseudo-second order	0.0603 $\text{mM}^{-1} \text{min}^{-1}$	0.9942
Cu(II)		
First order	0.0511 min^{-1}	0.9477
Second order	1.0047 $\text{mM}^{-1} \text{min}^{-1}$	0.9521
Pseudo-first order	0.3977 min^{-1}	0.9220
Pseudo-second order	0.0731 $\text{mM}^{-1} \text{min}^{-1}$	0.9932
Co(II)		
First order	0.0316 min^{-1}	0.9226
Second order	0.5483 $\text{mM}^{-1} \text{min}^{-1}$	0.9230
Pseudo-first order	0.2716 min^{-1}	0.9142
Pseudo-second order	0.579 $\text{mM}^{-1} \text{min}^{-1}$	0.9949

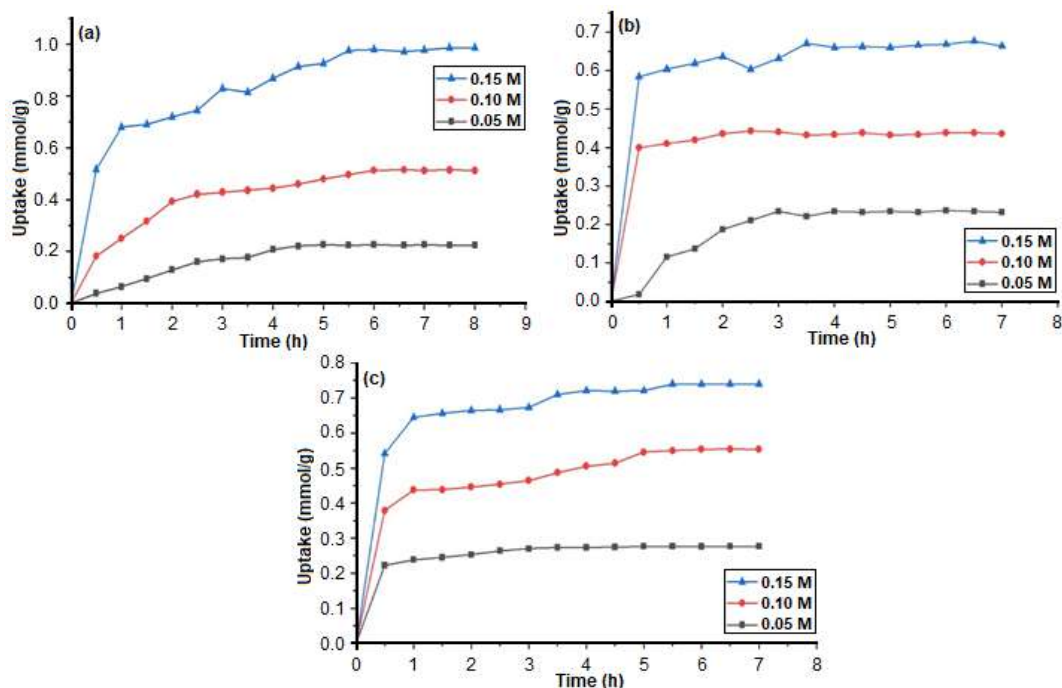


Fig 11. The uptake of (a) Ni(II) ions, (b) Co(II) ions, and (c) Cu(II) ions by RHACSALEN versus different initial concentrations of metal ion solution

Table 4. Langmuir and Freundlich parameters for Ni(II), Cu(II) and Co(II) adsorption

	Langmuir parameters			Freundlich parameters		
	R ²	q _m	b	R ²	K _f	n
Ni(II)	0.932	57.4 mg/g	10.69	0.990	0.293	1.13
Cu(II)	0.863	90.2 mg/g	6.624	0.979	0.247	1.24
Co(II)	0.937	83.72 mg/g	6.299	0.997	0.588	1.0

Table 5. Comparison of maximum capacity q_m (mg/g) for Ni(II), Cu(II) and Cu(II) adsorption by variously reported adsorbents

No	Adsorbent	Metal-ion	q _m (mg/g)	Ref
1	Surface modified Strychnos potatorum seeds	Ni(II)	74.55	[37]
2	Modified magnetic chitosan chelating resin	Ni(II), Cu(II), Co(II)	40.15, 103.16, 53.51	[38]
3	Phosphonate modified silica	Ni(II), Cu(II), Co(II)	12.47, 21.02, 7.43	[39]
4	Xanthate-modified chitosan/poly(N-isopropylacrylamide) composite hydrogel	Ni(II), Cu(II)	71.8, 125.3	[40]
5	Salen-modified silica (RACSALEN)	Ni(II), Cu(II), Co(II)	57.4, 90.2, 83.72	This work

that the uptake capacity increases as the initial concentration of metal ion solution increases. As the initial concentration of the metal ions increased from 0.05 to 0.15 M, the uptake of Ni(II), Cu(II) and Co(II) ions increased from 0.20 to 0.90, 0.20 to 0.65 and 0.23 to 0.70 mmol metal(II)/g ligand respectively.

The obtained data were fitted to Langmuir and Freundlich two-parameters isotherm models. The linear shape of the Langmuir model is described as follows [36]:

$$\frac{C_e}{q_e} = \frac{C_e}{q_m} + \frac{1}{q_m b} \quad (5)$$

where q_e is the equilibrium amount of adsorbate (mg/g), C_e is the equilibrium concentration of adsorbate (mg/L), q_m is the maximum adsorption capacity and b is the Langmuir constant.

Freundlich model is described as follows:

$$\ln q_e = \ln K_f + \frac{1}{n} \ln C_e \quad (6)$$

where q_e is the amount of adsorbate (mg/g), C_e is the equilibrium concentration of adsorbate (mg/L), K_f and $1/n$ are the Freundlich constants.

The relationship between the Langmuir and Freundlich parameters with correlation coefficient was shown in Table 4. R² values suggest that the adsorption isotherm data were best fitted to the Freundlich adsorption isotherm model. These results suggest that the adsorption of Ni(II), Cu(II) and Cu(II) onto RHACSLAEN was in multilayer fashion [37].

The comparison of maximum capacity for Ni(II), Cu(II) and Cu(II) adsorption by variously reported adsorbents is given in Table 5.

Effect of the mass of the functionalized silica

The effect of the mass of the functionalized silica was investigated using three different masses of ligand (100, 150, and 250 mg). Fig. 12(a-c) illustrate the uptake capacity of RHACSALEN for Ni(II), Co(II) and Cu(II) ions respectively. The obtained results showed that the maximum uptake capacity increased as the mass of the ligand increased for both of Ni(II) and Co(II) ions (0.9 and 0.65 mmol metal(II)/g ligand respectively), however in the case of Cu(II) ions the maximum uptake capacity

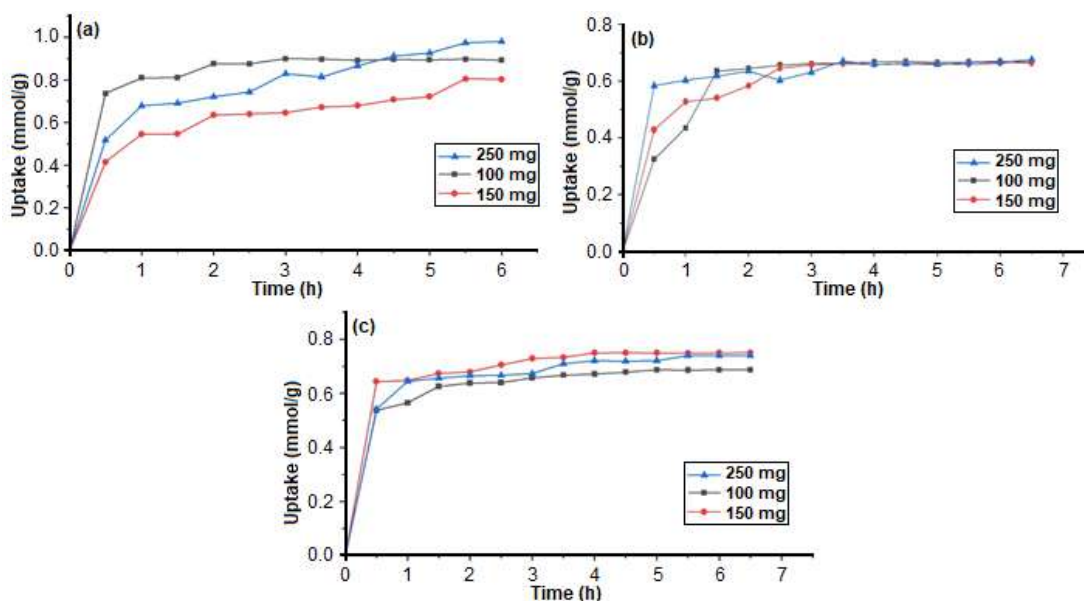


Fig 12. The uptake of (a) Ni(II) ions, (b) Co(II) ions, and (c) Cu(II) ions by RHACSALEN versus different masses of the ligand

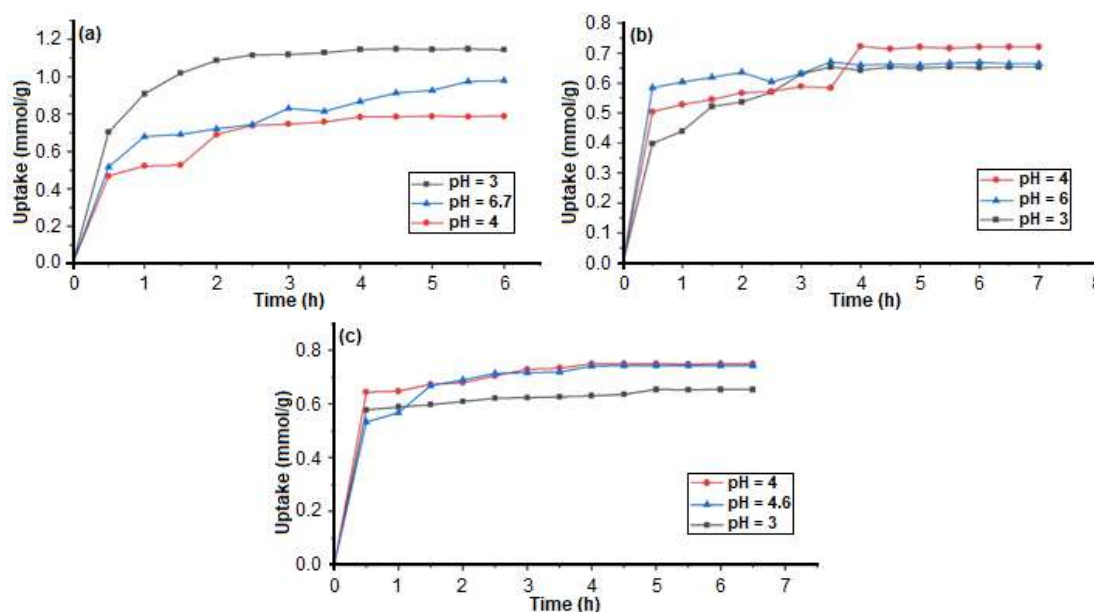


Fig 13. The uptake of (a) Ni(II) ions, (b) Co(II) ions, and (c) Cu(II) ions by RHACSALEN versus different initial pH values of metal ion solution

was very close in both 150 and 250 mg of the ligand. These results can be rationalized on the basis that as the amount of the ligand increases, more ligand site is accessible for complexation with metal ions.

Effect of pH

The effect of pH of the metal ion solution on the preconcentration process was studied by exposing the

functionalized silica to solutions of metal ions at three different pH values. The results, expressed in Fig. 13(a-c), show that metal uptake capacity increased as the pH decreased and reached its maximum at pH = 3 in the case of Ni and pH = 4 in the case of Co and Cu. The decreasing of pH can be due to ionization of hydrogen of the hydroxyl group in salen moiety and coordinate

oxygen atom with metal ions. It was noted that the uptake capacity of the ligand declined as the pH of the solution increased. This behavior is ascribed to the formation of metal hydroxides [9].

■ CONCLUSION

Silica derivative-salen ligand was synthesized and used to extract divalent metal ions (Ni(II), Co(II) and Cu(II)) from aqueous solutions. The techniques of characterization proved the successful synthesis of RHACSALEN. FTIR spectra showed the formation of the C=N bond. Nitrogen adsorption-desorption analysis stated that RHACSLAEN has a high surface area 247.55 m²/g. AFM and SEM analysis showed that the average diameter for the prepared ligand particles ranges between 63 and 72 nm. The prepared ligand is very efficient in the removal of metal ions from aqueous solutions, and such a material can be used in numerous applications not only for separation and removal of contaminants but also many other purposes such as catalysts for most organic reactions.

■ ACKNOWLEDGMENTS

The authors are thankful to the University of Kerbala, Ministry of Higher Education and Scientific Research, Republic of Iraq, for supporting this work.

■ REFERENCES

- [1] Bose, S., Ganayee, M.A., Mondal, B., Baidya, A., Chennu, S., Mohanty, J.S., and Pradeep, T., 2018, Synthesis of silicon nanoparticles from rice husk and their use as sustainable fluorophores for white light emission, *ACS Sustainable Chem. Eng.*, 6 (5), 6203–6210.
- [2] Shen, Y., 2017, Rice husk silica derived nanomaterials for sustainable applications, *Renewable Sustainable Energy Rev.*, 80, 453–466.
- [3] Inba, P.J.K., Annaraj, B., Thalamuthu, S., and Neelakantan, M.A., 2013, Cu(II), Ni(II), and Zn(II) complexes of salan-type ligand containing ester groups: Synthesis, characterization, electrochemical properties, and *in vitro* biological activities, *Bioinorg. Chem. Appl.*, 2013, 439848.
- [4] Tahmasbi, L., Sedaghat, T., Motamedi, H., and Kooti, M., 2018, Mesoporous silica nanoparticles supported copper(II) and nickel(II) Schiff base complexes: Synthesis, characterization, antibacterial activity and enzyme immobilization, *J. Solid State Chem.*, 258, 517–525.
- [5] El-Kurd, H.M., El-Nahhal, I.M., and El-Ashgar, N.M., 2005, Synthesis of new polysiloxane-immobilized ligand system di(amidomethyl)amine tetraacetic acid, *Phosphorus Sulfur Silicon Relat. Elem.*, 180 (7), 1657–1671.
- [6] El-Nahhal, I.M., and El-Ashgar, N.M., 2007, A review on polysiloxane-immobilized ligand systems: Synthesis, characterization and applications, *J. Organomet. Chem.*, 692 (14), 2861–2886.
- [7] El-Ashgar, N.M., El-Nahhal, I.M., Chehimi, M.M., Babonneau, F., and Livage, J., 2010, Extraction of Co, Ni, Cu, Zn and Cd ions using 2-aminophenylaminopropylpolysiloxane, *Environ. Chem. Lett.*, 8 (4), 311–316.
- [8] El-Nahhal, I.M., El-Shetary, B.A., Salib, K.A.R., El-Ashgar, N.M., and El-Hashash, A.M., 2001, Uptake of divalent metal ions (Cu²⁺, Ni²⁺, and Co²⁺) by polysiloxane immobilized triamine-thiol and thiol-acetate ligand system, *Anal. Lett.*, 34 (12), 2189–2202.
- [9] Hao, S., Verlotta, A., Aprea, P., Pepe, F., Caputo, D., and Zhu, W., 2016, Optimal synthesis of amino-functionalized mesoporous silicas for the adsorption of heavy metal ions, *Microporous Mesoporous Mater.*, 236, 250–259.
- [10] Ezzeddine, Z., Batonneau-Gener, I., Pouilloux, Y., Hamad, H., Saad, Z., and Kazpard, V., 2015, Divalent heavy metals adsorption onto different types of EDTA-modified mesoporous materials: Effectiveness and complexation rate, *Microporous Mesoporous Mater.*, 212, 125–136.
- [11] Das, T., Roy, A., Uyama, H., Roy, P., and Nandi, M., 2017, 2-Hydroxy-naphthyl functionalized mesoporous silica for fluorescence sensing and removal of aluminum ions, *Dalton Trans.*, 46 (22), 7317–7326.
- [12] El-Nahhal, I.M., Zaggout, F.R., and El-Ashgar, N.M., 2000, Uptake of divalent metal ions (Cu, Zn

- and Cd) by polysiloxane immobilized monoamine ligand system, *Anal. Lett.*, 33 (10), 2031–2053.
- [13] Chen, L., Li, B.D., Xu, Q.X., and Liu, D.B., 2013, A silica gel supported cobalt(II) Schiff base complex as efficient and recyclable heterogeneous catalyst for the selective aerobic oxidation of alkyl aromatics, *Chin. Chem. Lett.*, 24 (9), 849–852.
- [14] Mihsen, H., and Sobh, H., 2018, Preparation and characterization of thiourea-silica hybrid as heterogenous catalyst, *Asian J. Chem.*, 30 (5), 937–943.
- [15] Das, D.D., and Sayari, A., 2007, Applications of pore-expanded mesoporous silica 6. Novel synthesis of monodispersed supported palladium nanoparticles and their catalytic activity for Suzuki reaction, *J. Catal.*, 246 (1), 60–65.
- [16] Das, D.D., and Sayari, A., 2007, Amine grafted pore-expanded MCM-41 as base catalysts, *Stud. Surf. Sci. Catal.*, 170, 1197–1204.
- [17] Chen, H., Wang, W., Martin, J.C., Oliphant, A.J., Doerr, P.A., Xu, J.F., DeBorn, K.M., Chen, C., and Sun, L., 2013, Extraction of lignocellulose and synthesis of porous silica nanoparticles from rice husks: A comprehensive utilization of rice husk biomass, *ACS Sustainable Chem. Eng.*, 1 (2), 254–259.
- [18] Govindarao, V.M.H., 1980, Utilization of rice husk-a preliminary-analysis, *J. Sci. Ind. Res.*, 39 (9), 495–515.
- [19] Carmona, V.B., Oliveira, R.M., Silva, W.T.L., Mattoso, L.H.C., and Marconcini, J.M., 2013, Nanosilica from rice husk: Extraction and characterization, *Ind. Crops Prod.*, 43 (1), 291–296.
- [20] Leyden, D.E., and Luttrell, G.H., 1975, Preconcentration of trace metals using chelating groups immobilized via silylation, *Anal. Chem.*, 47 (9), 1612–1617.
- [21] Leyden, D.E., Steele, M.L., Jablonski, B.B., and Somoano, R.B., 1978, Structural studies of immobilized ethylenediamine as a preconcentrating agent for molybdate and tungstate, *Anal. Chim. Acta*, 100, 545–554.
- [22] El-Nahhal, I.M., Chehimi, M., and Selmane, M., 2017, Synthesis and structural characterization of G-SBA-IDA, G-SBA-EDTA and G-SBA-DTPA modified mesoporous SBA-15 silica and their application for removal of toxic metal ions pollutants, *Silicon*, 10 (3), 981–993.
- [23] El-Ashgar, N.M., Silmi, M.K., El-Nahhal, I.M., Chehimi, M.M., and Babonneau, F., 2015, Template synthesis of iminodiacetic acid polysiloxane immobilized ligand systems and their metal uptake capacity, *Silicon*, 9 (4), 563–575.
- [24] El-Ashgar, N.M., El-Nahhal, I.M., Chehimi, M.M., Babonneau, F., and Livage, J., 2012, Synthesis of polysiloxane-immobilized monoamine, diamine, and triamine ligand systems in the presence of CTAB and their applications, *Phosphorus Sulfur Silicon Relat. Elem.*, 187 (3), 392–402.
- [25] Hastuti, S., Nuryono, and Kuncaka, A., 2015, L-arginine-modified silica for adsorption of gold(III), *Indones. J. Chem.*, 15 (2), 108–115.
- [26] Ahmed, A.E., and Adam, F., 2007, Indium incorporated silica from rice husk and its catalytic activity, *Microporous Mesoporous Mater.*, 103 (1-3), 284–295.
- [27] Adam, F., Osman, H., and Hello, K.M., 2009, The immobilization of 3-(chloropropyl)triethoxysilane onto silica by a simple one-pot synthesis, *J. Colloid Interface Sci.*, 331 (1), 143–147.
- [28] Ahmed, I., and Parish, R.V., 1993, Insoluble ligands and their applications: IV. Polysiloxane-bis(2-aminoethyl)amine ligands and some derivatives, *J. Organomet. Chem.*, 452 (1-2), 23–28.
- [29] Nandi, M., Roy, P., Uyama, H., and Bhaumik, A., 2011, Functionalized mesoporous silica supported copper(II) and nickel(II) catalysts for liquid phase oxidation of olefins, *Dalton Trans.*, 40 (46), 12510–12518.
- [30] Thuadaj, N., and Nuntiya, A., 2008, Synthesis and characterization of nanosilica from rice husk ash prepared by precipitation method, *J. Nat. Sci.*, 7 (1), 59–65.
- [31] El-Nahhal, I.M., El-Ashgar, N.M., Chehimi, M.M., Bargiela, P., Maquet, J., Babonneau, F., and Livage, J., 2003, Metal uptake by porous iminobis(N-2-aminoethylacetamide)-modified polysiloxane ligand system, *Microporous Mesoporous Mater.*, 65 (2-3), 299–310.

- [32] Hao, S., Zhong, Y., Pepe, F., and Zhu, W., 2012, Adsorption of Pb^{2+} and Cu^{2+} on anionic surfactant-templated amino-functionalized mesoporous silicas, *Chem. Eng. J.*, 189-190, 160–167.
- [33] Harlick, P.J.E., and Sayari, A., 2007, Applications of pore-expanded mesoporous silica. 5. Triamine grafted material with exceptional CO_2 dynamic and equilibrium adsorption performance, *Ind. Eng. Chem. Res.*, 46 (2), 446–458.
- [34] Akl, M.A., Kenawy, I.M.M., and Lasheen, R.R., 2004, Organically modified silica gel and flame atomic absorption spectrometry: Employment for separation and preconcentration of nine trace heavy metals for their determination in natural aqueous systems, *Microchem. J.*, 78 (2), 143–156.
- [35] Thommes, M., 2010, Physical adsorption characterization of nanoporous materials, *Chem. Ing. Tech.*, 82 (7), 1059–1073.
- [36] Samarghandi, M.R., Zarrabi, M., Sepehr, M.N., Panahi, R., and Foroghi, M., 2012, Removal of acid red 14 by pumice stone as a low-cost adsorbent: kinetic and equilibrium study, *Iran. J. Chem. Chem. Eng.*, 31 (3), 19–27.
- [37] Anbalagan, K., Kumar, P.S., Gayatri, K.S., Hameed, S.S., Sindhuja, M., Prabhakaran, C., and Karthikeyan, R., 2015, Removal and recovery of Ni(II) ions from synthetic wastewater using surface modified *Strychnos potatorum* seeds: Experimental optimization and mechanism, *Desalin. Water Treat.*, 53 (1), 171–182.
- [38] Monier, M., Ayad, D.M., Wei, Y., and Sarhan, A.A., 2010, Adsorption of Cu(II), Co(II), and Ni(II) ions by modified magnetic chitosan chelating resin, *J. Hazard. Mater.*, 177 (1-3), 962–970.
- [39] Widjonarko, D.M., Jumina, Kartini, I., and Nuryono, 2014, Phosphonate modified silica for adsorption of Co(II), Ni(II), Cu(II) and Zn(II), *Indones. J. Chem.*, 14 (2), 143–151.
- [40] Wu, S., Wang, F., Yuan, H., Zhang, L., Mao, S., Liu, X., Alharbi, N.S., Rohani, S., and Lu, J., 2018, Fabrication of xanthate-modified chitosan/poly(*N*-isopropylacrylamide) composite hydrogel for the selective adsorption of Cu(II), Pb(II) and Ni(II) metal ions, *Chem. Eng. Res. Des.*, 139, 197–210.

Hydrogen Adsorption Characteristics for Zeolite-Y Templated Carbon

Rika Wijiyanti¹, Triyanda Gunawan¹, Noor Shawal Nasri², Zulhairun Abdul Karim^{3,4}, Ahmad Fauzi Ismail^{3,4}, and Nurul Widiastuti^{1,*}

¹Department of Chemistry, Faculty of Science, Institut Teknologi Sepuluh Nopember, Keputih, Sukolilo, Surabaya 60111, Indonesia

²Sustainable Waste-to-Wealth Program, Resource Sustainability Research Alliance, UTM-MPRC Institute for Oil and Gas, Universiti Teknologi Malaysia, 81310 UTM Johor Bahru, Malaysia

³Advanced Membrane Technology Research Centre (AMTEC), Universiti Teknologi Malaysia, 81310 UTM Skudai, Johor Darul Ta'zim, Malaysia

⁴Department of Energy Engineering, School of Chemical and Energy Engineering, Universiti Teknologi Malaysia, 81310 UTM Johor Bahru, Johor, Malaysia

* **Corresponding author:**

email: nurul_widiastuti@chem.its.ac.id

Received: September 21, 2018

Accepted: January 18, 2019

DOI: 10.22146/ijc.38978

Abstract: The hydrogen adsorption, kinetic and thermodynamic of adsorption onto the zeolite templated carbon (ZTC) were examined at the temperature range of 30-50 °C and ambient pressure. The ZTC was prepared from zeolite-Y template and sucrose carbon precursor by impregnation method and showed its specific surface area of 932 m²/g as well as 0.97 cm³/g for total pore volume. Analysis of physical and chemical characteristics for materials were performed using XRD, SEM, TEM and N₂ isotherm. The results indicated that the ZTC has some ordered network structure of carbon and also exhibits the formation of the carbon layer outside the zeolite micropore. We observed the ZTC for hydrogen adsorption both gravimetric and volumetric method up to 1.72 and 1.16 wt.% at the lowest temperature, respectively. The kinetic process at all studied temperature was best approximated by the pseudo-second-order kinetic model. The aspects of thermodynamic such as heat of adsorption and the entropy change were -14.41 kJ/mol and -40.93 J/K mol, respectively. Both values were negative, indicating an exothermic reaction and low disorder at the hydrogen and ZTC interface when the adsorption process took place. Meanwhile, the enthalpy change value exhibits a characteristic of a physical process. The Gibbs energy change calculated at 30, 40 and 50 °C were -1.99, -1.59 and -1.19 kJ/mol, respectively, indicating a spontaneous adsorption process.

Keywords: zeolite-Y templated carbon; hydrogen adsorption; adsorption kinetics; thermodynamics

■ INTRODUCTION

Hydrogen is a clean alternative fuel as its main product from the burning process is only water. Moreover, hydrogen is the highest element up to 75% from the normal mass of earth, and thus it can be employed as prosperous sources for hydrogen fuel generation [1]. Hydrogen also has almost three times higher of energy content (33 kWh/kg) as compared to the

gasoline (12 kWh/kg) [2]. Therefore, research efforts have been actively pursued to utilize hydrogen for fuel cell vehicles.

In addition to high energy density and its availability, the hydrogen storage system including volume, weight, safety and the reversibility of hydrogen adsorption rate should be concerned [2]. The conventional hydrogen storage systems are compressed hydrogen tank or liquefied hydrogen. However, it has a

safety risk due to high pressure and low temperature system [3]. More recently, the main concern of research has been focused on solid state porous materials to meet the United States Department of Energy (DOE) onboard storage target due to its high densities of both gravimetric and volumetric at lower pressure. The DOE ultimate targets for storage density at or close to ambient condition are 7.6 wt.% (gravimetrically) and 0.07 kg/dm³ (volumetrically), respectively [1-2]. Recently, hydrogen storage system in solid state porous materials, for instance, carbons, zeolites or metal organic frameworks, is attractive because of their advantages such as fast adsorption kinetics, high cyclability, and reversibility of hydrogen uptake and release [4-5].

Among of these porous materials, carbon-based materials received a lot of interest since it has a high gravimetric and volumetric densities, high thermal and good chemical stability [4,6-7]. The amount of hydrogen uptake in carbon materials reached up to 11 wt.% [8]. Hydrogen can be adsorbed reversibly in the carbons by physisorption process at ambient temperature. Based on physisorption, the physical properties including pore size, specific surface area, and micropore volume seriously affect the hydrogen capacity [9-11]. Carbons possess some superiorities such as a large surface area up to 3500 m²/g, lightweight and easy to modify the pore structure [1]. Yet, the main drawback for carbon materials in the storage system is its wide pore size distribution [7,10]. Hence, the pore structure of carbons should be modified in order to enhance adsorption capacities. The templated method could be an excellent way to gain a new carbon porous materials with a large surface area up to 4000 m²/g, and controlled porosity reached 1.6 cm³/g for hydrogen storage purpose. Yang et al. [12] reported that templated carbon exhibited the highest storage capacity than the other materials, such as zeolites, carbon nanotubes, metal organic frameworks, and organic microporous polymer. It is found that a high microporosity and specific surface area of carbons provide a linear relation with hydrogen adsorption capacity [12-13].

The choice of materials such as carbon precursor and the inorganic template is being a major factor contributing to the carbon structure [7,14-15]. The

inorganic templates widely used for templated carbon include zeolite, silica, Metal Organic Framework (MOF) and layered clay. Zeolite and MOF used as template result in microporous carbon with large surface area and well-defined porous structure. However, the synthesis of MOF template needs a lot of time and results in low yield. On the contrary, a silica template is employed to prepare mesoporous carbon. Also, the resulting carbon with low surface area and high graphitization degree are obtained by using a layered clay template. However, a porous material is suited for application in gas adsorption; thus, zeolite exhibits outstanding potential template material to fabricate microporous carbon. There are several studies of templated carbon materials synthesized using various carbon sources or different zeolite type templates. Zeolites have ordered pores and channels; therefore they can be more appropriate to synthesize carbon with micropore structure for hydrogen storage purpose [11,16].

Kyotani et al. [15] synthesized templated carbon via a combination of two methods (furfuryl alcohol by impregnation and propylene via CVD) using a different type of zeolite (zeolite-Y, L, β , mordenite, and ZSM-5) as templates. The regularity of the carbon using zeolite-Y was much better than other zeolites such as superior surface area (2750 m²/g) as well as perfect microporosity (1.5 cm³/g). Templated carbons using different zeolite (13-X and Y) and acetonitrile have also been prepared by Yang et al. [17]. Carbon with zeolite-Y template exhibited 21% larger surface area and 263% higher micropore volume than that of zeolite-13X. As reported by Johnson et al. [18], pyrolytic carbon synthesized in the channel of zeolite-Y was preferable since it has three dimensionally interconnected micropore structure. On the other hand, Yang et al. [17] also prepared carbon material using different carbon sources (acetonitrile or ethylene) and zeolite-Y as hard template. They investigated that carbon with acetonitrile and zeolite-Y had a surface area ranging from 1910 to 1920 m²/g, micropore volume of 0.1 to 0.5 cm³/g and significantly obtained ordered carbon structure. When ethylene was employed as carbon source, the surface area and micropore volume of the ZTC reached to 1300 m²/g and

0.2 cm³/g, respectively, obtained ordered not only carbon but also a high amount of graphitization. It is believed that hydrogen uptake capacity linearly relates to the surface area and microporosity. Therefore, it can be controlled by material selection.

In addition to the porosity of materials, hydrogen uptake in the adsorptive system is directly related to the operation conditions [6]. For hydrogen storage system, carbon materials would be more appropriate when they could adsorb at or near to room condition, as described by the DOE [1]. Several researchers have reported the hydrogen storage capacity of ZTC at a temperature of -196 °C [11-12,17,19]. Hydrogen uptake capacity at ambient temperature (30 °C) has been reported by Nishihara et al. [20] for zeolite templated carbon. They investigated the small amount of hydrogen sorption in the range of 0.41–0.87 wt.% at high pressure of 98 bar. Whereas, the hydrogen uptake capacity on SWNTs at ambient pressure (1 bar) and temperature of < 40 °C was reported by Hirscher et al. [21], and the capacity obtained was 1.8 wt.%. Moreover, the ZTC's performance at or close to room temperature and pressure is still unknown. Therefore, in this work, we examine the hydrogen uptake performance at or close to ambient temperature and pressure.

In addition, to provide an understanding of the adsorption mechanism, the kinetic study of hydrogen adsorption would be necessary [22]. Zamora et al. [22] studied the kinetic hydrogen adsorption on the composite comprising TiNT decorated with Cd₃Fe^{III} by implementing the intra-particle diffusion model. Furthermore, thermodynamic aspects such as enthalpy, entropy, and Gibbs free energy are other main factors to be considered in the adsorption process in order to determine the feasibility of ZTC for H₂ storage purpose. The change of enthalpy provides the information of binding strength between gas molecules and adsorbent and to explain the influence of temperature in the adsorption process [4]. Based on DOE's target, the desired enthalpy value of hydrogen uptake under room conditions is between 15 to 25 kJ mol⁻¹ for reversibly hydrogen storage [23]. However, the standard heat of hydrogen adsorption on carbon (active carbon or carbon

nanotube) is only 6 kJ/mol, and it is too weak to adsorb hydrogen at ambient temperature which was investigated by Myers et al. [23].

The goals of the present work were to report the amount of hydrogen adsorption on templated carbon at or near to room temperature (30, 40 and 50 °C) and ambient pressure by both gravimetric and volumetric methods. Templated carbon was prepared by utilizing zeolite-Y template with sucrose as a carbon precursor by a simple impregnation method. Sucrose is a small organic molecule and contains high carbon yield which is widely used as a precursor to prepare microporous carbon [12,15,23]. Most of the experiment has been conducted on hydrogen storage materials, yet the kinetic and thermodynamic studies are scarce in this field. In this investigation, the kinetic study was analyzed in terms of the pseudo-first and second order as well as the intraparticle diffusion model to provide deeper insight for mechanisms of hydrogen adsorption. The thermodynamic aspects including the heat of adsorption, the Gibbs energy, and the entropy change were also determined in order to evaluate the feasibility of templated carbon as storage system of hydrogen.

■ EXPERIMENTAL SECTION

Materials

The materials used were sodium aluminate powder (NaAlO₂, 95.45%) and sodium silicate (Na₂SiO₃) provided by Sigma Aldrich, sodium hydroxide pellet (NaOH) purchased from Merck, sucrose (C₁₂H₂₂O₁₁ 98% Fluka), sulfuric acid (H₂SO₄ 98% pa), fluoric acid (HF, 48%) provided by Merck, hydrochloric acid (HCl, 37% SAP), deionized water, ultra-high purity N₂ (99.99%) and H₂ gas (99.99%).

Instrumentation

X-Ray Diffraction (XRD) diffractograms were recorded by Expert PAN Analytical using radiation of CuKα (λ = 0.154 nm at 40 kV and 30 mA). To identify the crystal phase and crystallinity of the ZTC, the X-ray diffractograms were determined in the range of 3–50°. Physical properties of the zeolite-Y and ZTC were determined via N₂ sorption at -196 °C using a

Quantachrome Autosorb-1. The powders were degassed at 250 °C in vacuum for overnight prior to the analysis. The Brunauer-Emmett-Teller method at P/P_0 between 0.04 to 0.31 was used to determine the specific surface area. While the total pore volume (V_t) of the sample was estimated from the amount of N_2 adsorbed at P/P_0 0.993, and the micropore volume was calculated using Saito Foley (SF) method. Pore size distribution (PSD) of samples was determined from the N_2 isotherm using Horvath-Kawazoe (HK) theory with the assumption of slit pore shape and Barrett-Joyner-Halenda (BJH) method. The morphology analysis for zeolite-Y and ZTC was performed by scanning electron microscope (SEM, ZEISS EVO MA 10). Transmission Electron Micrographs were collected with H9500 at 200 kV acceleration voltage to identify the structure of samples.

Procedure

Synthesis of zeolite-Y template

Zeolite-Y was synthesized using sodium aluminate (Sigma-Aldrich, 13404-5KG-R), sodium silicate (Sigma-Aldrich, 338443-3L), NaOH (99% pa, Merck, 011-022-00-6) and deionized water as source materials. Zeolite-Y was made through three steps: seed gel, feedstock gel and overall gel [24]. The molar composition of seed gel was

$10.67Na_2O:1Al_2O_3:10SiO_2:180H_2O$ and the molar ratio of feedstock to seed gel was 18:1. The adding of seed gel to feedstock gel formed an overall gel and subsequently subjected to the hydrothermal process at 100 °C for 7 h. The sample obtained was flowed by deionized water to get neutral pH of filtrate and subsequently dried at 110 °C for 12 h. Prior further treatment, the zeolite-Y sample was pretreated at 200 °C for 4 h in flowing nitrogen.

Synthesis of zeolite-Y templated carbon (ZTC)

The ZTC was synthesized from zeolite-Y template and sucrose (98% Fluka) by impregnation method as presented in Fig. 1. The detailed procedure of ZTC synthesis is described as follows:

The sucrose was dissolved in 0.35 M H_2SO_4 at room temperature, then the pretreated zeolite-Y was added to this clear solution. Based on our previous study, the optimum ratio of sucrose to zeolite-Y was 1.25 (wt.%). The solution was stirred for 72 h at ambient temperature and then filtered, followed by carbonization treatment in a tubular furnace under N_2 atmosphere. The carbonization process was conducted to the fixed temperature of 800 °C for 4 h dwelling time by a heating rate of 2 °C/min according to the best result in our preceding study. The resulted of the black composite was

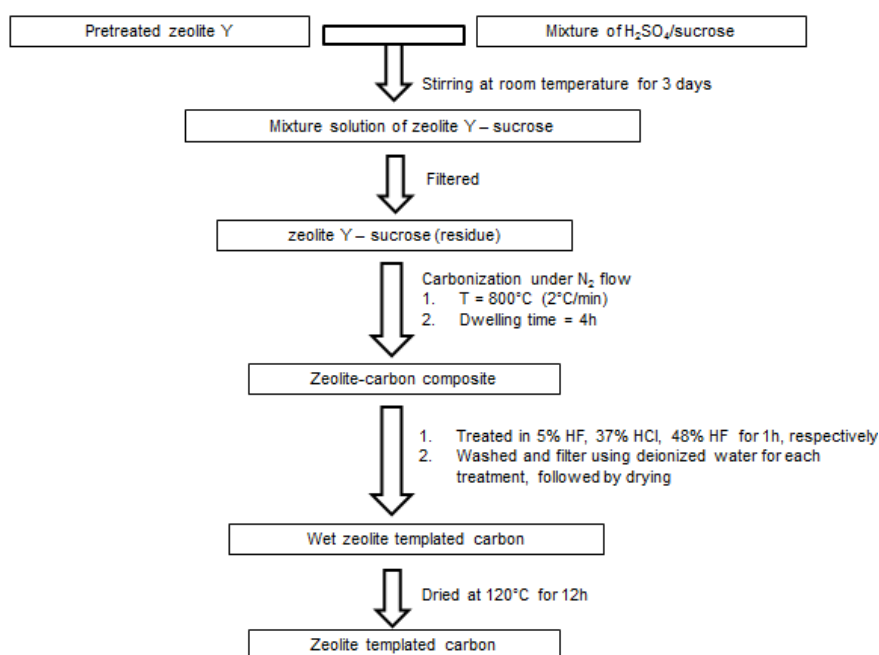


Fig 1. Schematic of preparation procedure of zeolite templated carbon

cooled until room temperature using N₂ stream and then washed by three steps of acid to remove the zeolite-Y template. (1) The composite was treated with 5% HF solution at ambient temperature for 1 h to break the Si-O-Al bond of template. The sample was washed using deionized water insistently to obtain a neutral pH of filtrate and dried at 110 °C for 12 h. (2) Then, the sample was immersed in 37% HCl via reflux at 60 °C for 1 h to remove aluminum of zeolite framework, subsequently filtered and washed by deionized water and followed by drying for 12 h at temperature of 120 °C (3). In addition, the solid sample was soaked in 48% HF solution for 1 h for removal of silica content from zeolite template. The sample was then washed by deionized water to get a neutral pH of filtrate, then a residue of sample known as zeolite templated carbon (ZTC) was dried during 12 h at 120 °C.

Hydrogen adsorption test

The amounts of hydrogen uptake on the ZTC were determined in a custom-fabricated packed-bed adsorption system using volumetric, pressure and temperature measurement in equilibrium conditions by static adsorption procedure adopted from other studies [25-26]. The fixed bed adsorption unit was used at static mode to collect single gas adsorption data presented in Fig. 2. The adsorption apparatus was made using stainless steel tubing and proper Swagelok fittings. The cell was placed in a well-insulated furnace to control the temperature, pressure, and volume in equilibrium state for single gas uptake. The hydrogen sorption capacity was measured at different temperature of 30, 40 and 50 °C. Prior to the adsorption test, the adsorbent was dried in-situ at 105 °C for 1 h. The gas presented in the adsorption cell was purged using a vacuum pump before to start the test. Digital pressure transducer and thermocouple put axially in the middle of the adsorption cell to observe the temperature of cell continuously.

An adsorption cell was filled with 1.5018 g adsorbent. The adsorption was conducted at a temperature of 30, 40 and 50 °C (± 3 °C) using the single sample weight. Prior passing the hydrogen to the adsorption cell, the gas pressure of the loading cell was set at the equilibrium of 2 bar as an initial value, and then gas

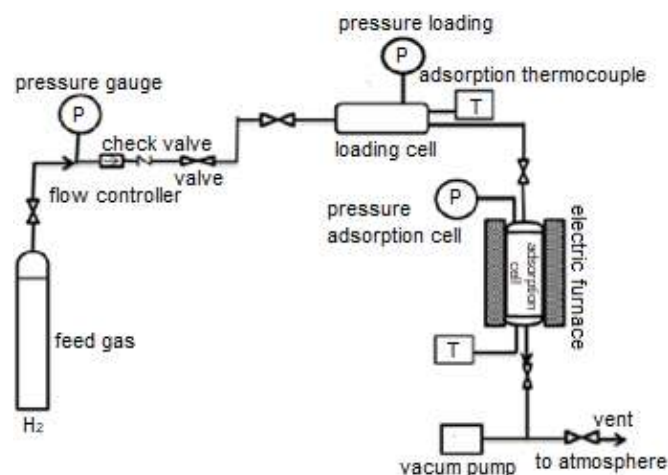


Fig 2. Schematic diagram of the fixed bed volumetric adsorption test rig

was flowed into the adsorption cell by opening the connecting valve at the target temperature. Pressure and temperature measurement of both cells were monitored to obtain the amount of hydrogen adsorbed. The pressure of loading (P_l) and adsorption (P_a) cell measured were recorded until the equilibrium conditions were obtained. Adsorption equilibrium is achieved when the operating conditions (temperature and pressure) were constant. The amount of hydrogen uptake was determined using the mass balance through both cells in terms of temperature and pressure recorded at initial and equilibrium condition, according to the Eq. (1) [26]:

$$q_e = \frac{1}{m} \left[\frac{V_v}{R} \left(\left| \frac{P}{ZT} \right|_i - \left| \frac{P}{ZT} \right|_{eq} \right)_a + \frac{V_l}{R} \left(\left| \frac{P}{ZT} \right|_i - \left| \frac{P}{ZT} \right|_{eq} \right)_l \right] \quad (1)$$

in which the pressure is P, the temperature is T, the gas constant is R, the adsorption cell is a, the adsorption cell volume is V_v, the compressibility factor is Z, the loading cell is l, the loading cell volume is V_l, i and eq represent the initial and equilibrium state, respectively; and the adsorbent mass is m.

The hydrogen sorption was also performed using the gravimetric method (Fig. 3) as follows. Prior to the experiment, the ZTC was dried at 105 °C during 1 h and then degassed by a heating rate of 3 °C/min to 350 °C for 3 h. The pretreated sample (0.3 g) as initial mass was then cooled to the adsorption temperature. The adsorption process was conducted over the temperature

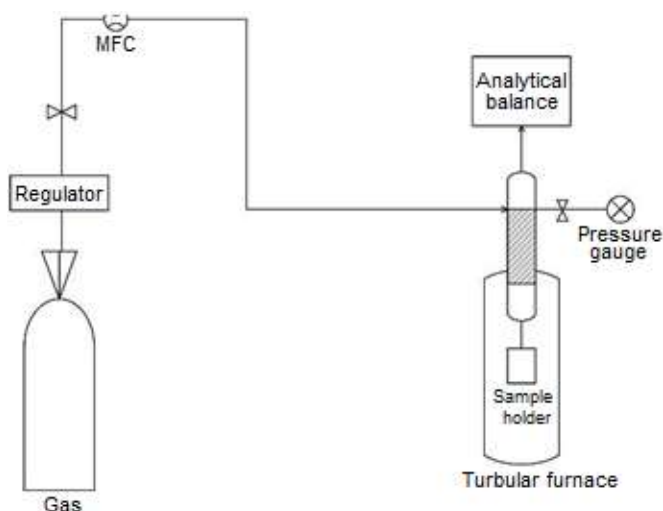


Fig 3. Schematic diagram of gravimetric adsorption test

of 30, 40, 50 °C and ambient pressure. Adsorption measurement was started via initiating the hydrogen flow rate of 20 mL/min, then evaluated within a few minutes to achieve sorption equilibrium of ZTC and recorded as mass at equilibrium state. The capacity of hydrogen uptake was obtained from the mass balance through the adsorption cell, according to the Eq. (2):

$$\%wt = \frac{m_t - m_0}{m_0} \times 100\% \quad (2)$$

where m_t is the mass at t min and m_0 is the initial mass.

Kinetics data analysis

Adsorption kinetic models of the pseudo first order, pseudo-second order, and intraparticle diffusion were determined to investigate of hydrogen sorption mechanism onto ZTC [25,27]. The pseudo first-order model is generally applied for the adsorption process, expressed by Eq. (3).

$$\frac{dq_t}{dt} = k_f (q_e - q_t) \quad (3)$$

where q_t (mmol/g) is the amount of hydrogen adsorbed at time t (min), q_e (mmol/g) is the adsorption capacity at equilibrium state, k_f (min^{-1}) is the rate constant of pseudo-first order. After integrating at boundary conditions $q_t = 0$ at $t = 0$ and $q_t = q_t$ at $t = t$, yields the Eq. (4).

$$\ln(q_e - q_t) = \ln q_e - k_f t \quad (4)$$

The pseudo second-order model is defined in Eq. (5).

$$\frac{dq_t}{dt} = k_s (q_e - q_t)^2 \quad (5)$$

in which k_s ($\text{g mg}^{-1} \text{ min}^{-1}$) is pseudo-second-order rate constant. This can be integrated by using the initial conditions of $q_t = 0$ at $t = 0$ and $q_t = q_t$ at $t = t$ and the equation above is a linear equation:

$$\frac{t}{q_t} = \frac{1}{k_s q_e^2} + \frac{1}{q_e} t \quad (6)$$

A straight line with slope $1/q_e$ will be obtained from a plot between t/q_t and t when adsorption mechanism fits this kinetic model.

The equation of intra-particle diffusion is given as follows:

$$q_t = k_{id} t^{1/2} + C \quad (7)$$

where k_{id} ($\text{mmol g}^{-1} \text{ min}^{-0.5}$) is the rate constant, t is time (min). The values of k_{id} and C can be calculated experimentally through the slope and intercept of q_t versus $t^{1/2}$, respectively. An intercept value of C indicates the thickness of the boundary layer, in which the bigger value of C , the greater effect for the boundary layer.

Thermodynamic study

The adsorption enthalpy (ΔH) and entropy (ΔS_H) change of hydrogen adsorption are calculated from the graph between $\ln P$ versus $1/T$ based on the Van't Hoff equation [22]:

$$\ln P = 2 \left(\frac{\Delta H}{RT} - \frac{\Delta S_H}{R} \right) \quad (8)$$

in which ΔH in kJ mol^{-1} and ΔS_H in $\text{J K}^{-1} \text{ mol}^{-1}$. T is temperature (K), p is pressure at constant equilibrium uptake (bar), and R is the gas constant ($\text{J mol}^{-1} \text{ K}^{-1}$). The slopes of the straight line give the value of $2\Delta H/R$, and the intercepts give the value of $-(2 \Delta S_H/R)$.

The Gibbs energy (ΔG_{ads}) value is commonly calculated by the following equation:

$$\Delta G_{ads} = \Delta H - T\Delta S_H \quad (9)$$

in which ΔG_{ads} in kJ mol^{-1} .

RESULTS AND DISCUSSION

XRD Analysis

The X-ray diffraction patterns of zeolite standard and zeolite-Y obtained are presented in Fig. 4(a) and (b), respectively. It could be seen that the diffraction patterns and intensities for zeolite-Y obtained were similar to the standard data of JCPDS No.: 39-1380. This clearly

indicated that the zeolite-Y prepared using NaOH-NaAlO₂-Na₂SiO₃-H₂O system was successfully formed. These peak patterns have still appeared in the diffraction peaks for composite sample, but these peaks slightly shifted to the higher angle, as shown in Fig. 4(c). The shift of the peaks might be due to the shrinkage of the zeolite framework after carbonization process [28]. Furthermore, these diffraction peak intensities were also decreased as compared to the zeolite-Y, suggesting that the carbon might be in the surface of the template [29].

The peak patterns of the ZTC obtained are demonstrated in Fig. 4(d). This sample exhibited XRD peak around 6.05°, close to those of parent zeolite-Y (~6.14°). This indicated that there was a regular ordering of pore structure for carbon sample, corresponding to the (111) peak of template [11,30]. Furthermore, a broad peak centered around $2\theta = 25^\circ$ was appeared with low relative intensity and also observed in zeolite templated carbon by other studies [12,30]. This peak suggests the formation of amorphous graphitic carbon (002) plane due to the stacking graphene nanosheets outside zeolite micropore. This stacking graphene may be formed due to the presence of carbon deposition in the pore mouth of zeolite upon the carbonization process, therefore, obstructing access of sucrose into the zeolite [11]. It can be concluded that ZTC in this study kept some pore structure ordering of zeolite and also produced the graphitic carbon.

SEM and TEM Observation

The SEM analysis for zeolite-Y and ZTC were presented in Fig. 5(a) and (b), respectively. Zeolite-Y

image as shown in Fig. 5(a) exhibited a clear crystal face from each particle. The shape morphology for zeolite-Y was partially replicated in the ZTC sample (Fig. 5(b)), indicating that the ZTC did not fully retain the morphology of the template. A few aggregates of the amorphous graphitic structure was observed in the ZTC sample, which was in accordance with the XRD result. The particle size of ZTC was up to 500 nm, smaller as compared to the zeolite-Y template due to the particle shrinkage during the carbonization process. The particle shrinkage might be due to the shrinkage of the zeolite template as confirmed by the XRD observation [28].

The TEM images for the zeolite-Y, zeolite-carbon composite and ZTC samples are shown in Fig. 6. The octahedral morphology for zeolite-Y is similar to the

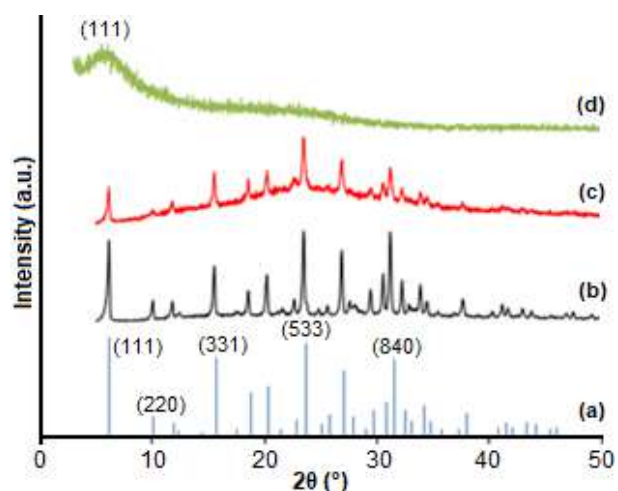


Fig 4. XRD pattern of (a) standard JCPDS No. 39-1380, (b) as-synthesized zeolite-Y, (c) zeolite-carbon composite, and (d) zeolite templated carbon

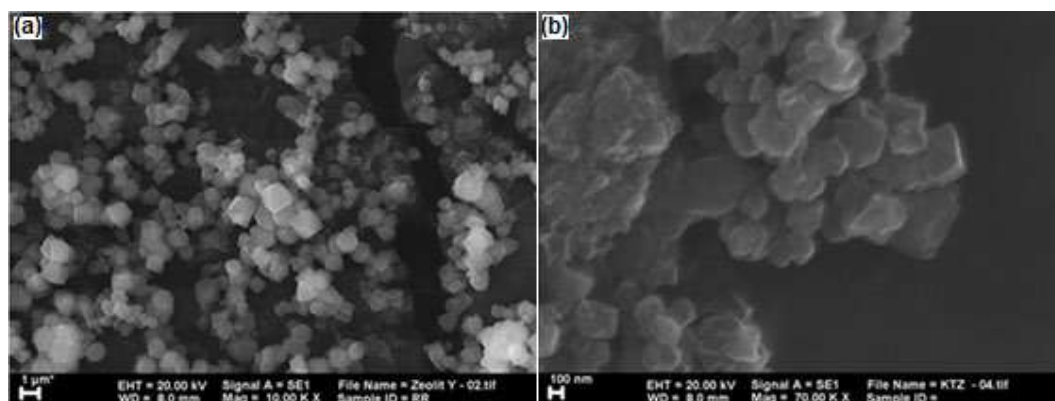


Fig 5. The SEM images of (a) zeolite-Y and (b) ZTC

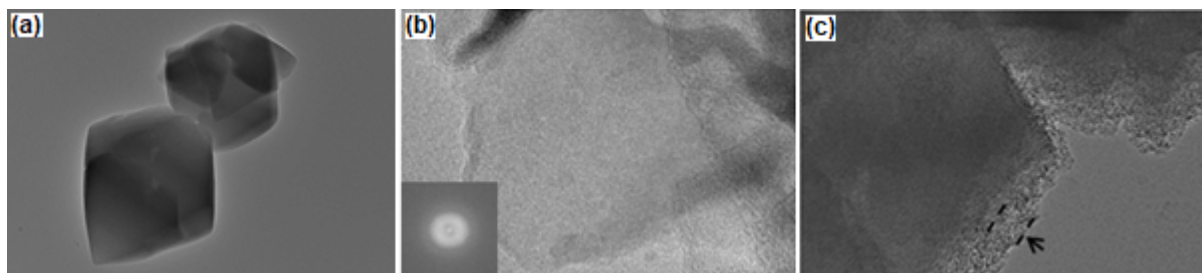


Fig 6. The TEM images of (a) zeolite-Y, (b) ZTC (the inset corresponds to electron diffraction pattern taken from this image), and (c) ZTC (the region indicated by an arrow are the dense amorphous carbon layers deposited in the external surface of zeolite micropore

SEM images in Fig. 5 with the measured particle size up to 1000 nm. However, a diffused ring in the SAED pattern of ZTC (inset of Fig. 6(c)) suggests that the amorphous structure is observed, which is similar to XRD and SEM analysis [31]. The diffraction ring can be attributed as a thin and dense graphitic carbon, indicating carbon (002) layer around the external surface of zeolite-Y particles (Fig. 6(c)) [32-33]. The graphitic shell thickness was ranging from 15–50 nm (black arrow region).

Textural Properties of the Sample

The textural properties of zeolite-Y and ZTC such as BET surface area, micropore, and mesopore volume were obtained using their adsorption isotherm (Fig. 7(a)) and the values were presented in Table 1. As seen from the figure, the adsorption isotherm for the zeolite-Y template was a typical type I isotherm, indicating a microporous material for zeolite sample. On the other hand, the existence of desorption hysteresis in the ZTC

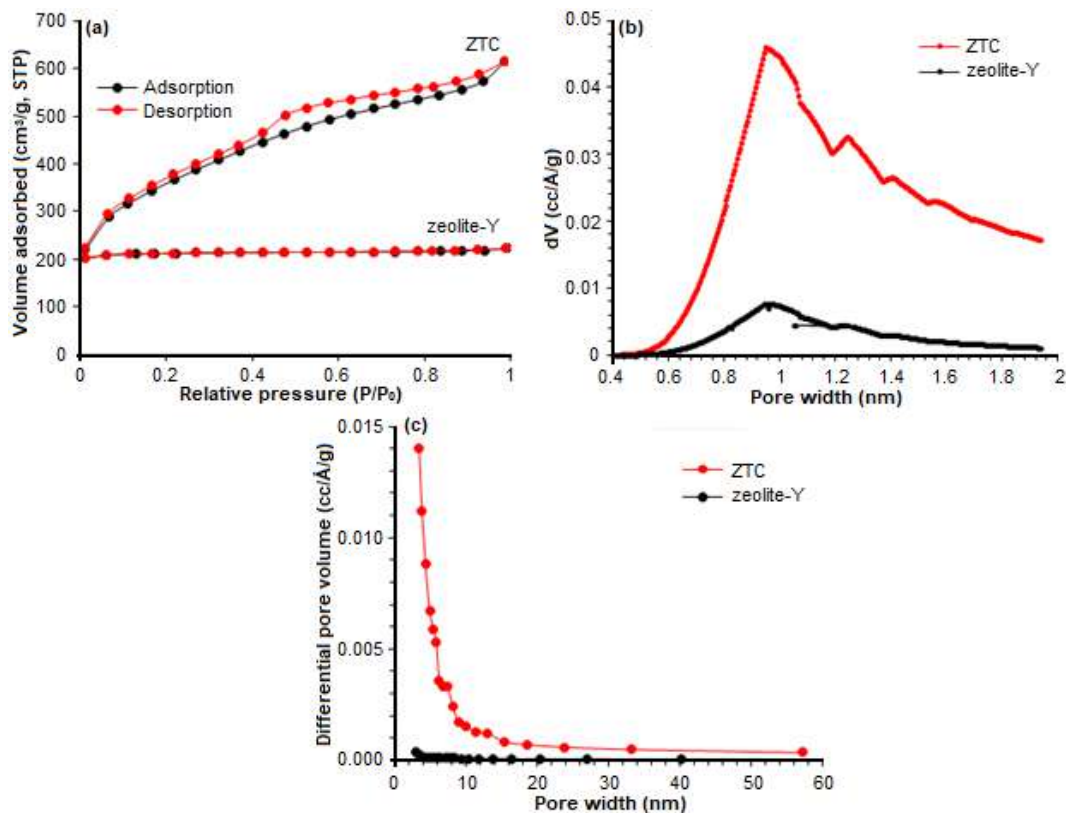


Fig 7. The N₂ adsorption-desorption isotherm on the zeolite-Y template and ZTC at -196 °C (a) PSD analyzed using HK method (b) and BJH method (c) of the prepared zeolite-Y and ZTC

Table 1. Textural properties of the resultant zeolite-Y and ZTC

Sample	BET surface area (m ² /g)	Total pore volume (cm ³ /g)	Micropore volume (cm ³ /g)
Zeolite-Y	686	0.40	0.34
ZTC	932	0.97	0.30

sample suggested the mesopores characteristic. The mesopore structure might be attributed by (1) the unfilled region of carbon due to incomplete filling of sucrose to the template pore channels and/or (2) the shrinkage of zeolite-carbon during the carbonization due to the oxygen rich of sucrose resulting in the large amount of gaseous species such as CO₂ and H₂O [12,33-34]. Furthermore, we have used HK method by assuming slit pore geometry to evaluate micropore size (below 2 nm) distribution and BJH method to analyze the mesopores above 2 nm of the zeolite-Y and ZTC, as shown in Fig. 7(b) and (c). It can be seen that the as-synthesized ZTC exhibits a sharp peak around 0.7–1.5 nm (Fig. 7(b)), indicating the presence of micropores of the ZTC and the size distribution of the ZTC is sharper than the zeolite-Y. In addition, the BJH method (Fig. 7(c)) confirms the presence of mesopores in the ZTC around 3–23 nm. The mesopores were attributed to the amorphous graphitic carbon, covering the ZTC particles. The BET surface area, total pore volume and micropore volume of ZTC in this study were 932 m²/g, 0.97 cm³/g, and 0.3 cm³/g, respectively. Konwar and De [29] also reported the ZTC synthesis materials with zeolite-Y and sucrose, the highest BET surface area, total pore volume, and micropore volume were 1033 m²/g, 0.676 cm³/g, and 0.293 cm³/g, respectively, which were close to the value in this study. However, better properties of sucrose-based carbon via template method using zeolite-Y was achieved from another study [13].

Hydrogen Adsorption Study of ZTC

The process of hydrogen adsorption on carbons is governed by physisorption and preferably occurs at a lower temperature [34-35]. However, it is greatly desirable for adsorbent materials that adsorb hydrogen at or near room temperature for its application to meet the DOE target for the hydrogen storage system.

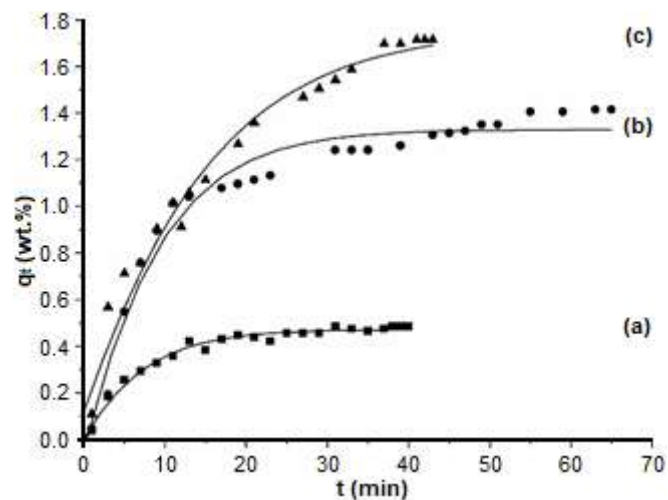


Fig 8. Adsorption capacity with adsorption time at various temperature measured gravimetrically (a) 30, (b) 40 and (d) 50 °C

The hydrogen uptake measured gravimetrically at different temperature of 30, 40 and 50 °C and pressure of 1 bar (Fig. 8) were studied in the present work. Highest hydrogen sorption was obtained at the lowest temperature of 30 °C with 1.72 wt.% storage. It could be occurred since physically adsorption take places in the interaction between hydrogen molecules and carbon material on van der Waals force. At low temperature, the thermal motion energy of hydrogen was in accordance with the van der Waals force, leading to the stronger interaction [36]. The electronegativity between carbon and hydrogen as an atom has a low range, and therefore, the bonding has a weak dipole moment and keep their characteristics when the adsorption process occurs. Comparing the adsorption of ZTC with data available in the previous literature is presented in Table 2. In this study, the hydrogen adsorption capacities were quite low. It could be attributed with a low quantity of micropore volume, resulting to the low interaction energy between pore walls and hydrogen molecules in the narrower pores and less accessible adsorption sites for hydrogen molecules [19].

In order to confirm the hydrogen sorption gravimetrically, adsorption was also conducted using the volumetric determination of the prepared ZTC. The hydrogen uptake capacities performed by the volumetric method were 5.81, 5.68 and 5.64 mmol/g or equal to 1.16,

Table 2. Physical properties and hydrogen adsorption capacity for different carbon-based materials

Carbon source	Zeolite template	Preparation method	Textural properties			Hydrogen uptake (wt.%)	Temperature (°C) and pressure (bar) adsorption	Ref.
			Specific surface area (m ² /g)	Micropore volume (cm ³ /g)	Mesopore volume (cm ³ /g)			
Sucrose	USY zeolite	Carbonization	701-1219	0.30-0.5	0.09-0.61	1.15-1.43 ^a	-196; 1	[19]
Sucrose	NH ₄ Y zeolite	Carbonization	684-1033	0.21-0.29	0.20-0.38	0.25-0.30 ^b	-100; 1	[29]
Furfuryl alcohol	NH ₄ Y zeolite	Carbonization	1886	0.01-0.51	0.07-0.80	0.08-0.29 ^b	-100; 1	[7]
Sucrose	NH ₄ Y zeolite	Carbonization	1500	0.78	0.52	2.4 ^c	-196; 10	[13]
Propylene and butylene	Zeolite-Y	CVD	1040-2470	0.43-1.05	0.27-0.47	0.8-2.0 ^a	-196; 1	[11]
Furfuryl alcohol-acetylene	Zeolite-10X	CVD	1303-3331	0.33-1.00	0.55-0.94	1.09-2.27 ^a	-196; 1	[34]
Sucrose	Zeolite-Y	Carbonization	932	0.30	0.67	0.48-1.72 ^a 1.10-1.14 ^c	30-50; 1 30-50; 2	This study

^aHydrogen uptake is measured via gravimetric adsorption method

^bHydrogen uptake is measured via H₂-TPD method

^cHydrogen uptake is measured via volumetric method

1.14 and 1.12 wt.% at 30, 40 and 50 °C (± 3 °C) and 2 bars, respectively. A slightly different result of the hydrogen adsorption capacity obtained between the two techniques due to a small difference in operating pressure. At low pressure, hydrogen prefers to occupy the position at the adsorbate-pore interaction. Therefore, the density of hydrogen is highest in the smaller pores (micropores) [37]. At a temperature of 30, 40 and 50 °C, this calculated hydrogen adsorption capacity is equal to a volumetric density of 17.43, 17.04 and 16.92 g/L, respectively. Furthermore, the volumetric density values reported in this study were much lower to the ultimate DOE target of 70 g/L. The performance of adsorption can be improved on the control of the surface area and micropore volume via synthesis conditions. Another attempt of improving the hydrogen capacity is chemically surface modification of carbon to enhance the interaction with hydrogen.

Adsorption Kinetics Study

In order to determine the adsorption mechanism, the kinetic study of hydrogen adsorption would be indispensable. Three kinetic models in terms of pseudo-

first and second order, as well as intra particle diffusion model, were tested to fit with experimental data.

Pseudo first order model

This equation is proposed to explain unsteady state adsorption in porous material [38]. The pseudo first order kinetic plots between t and $\ln(q_e - q_t)$ of hydrogen sorption at 30, 40 and 50 °C by ZTC were presented in Fig. 9. The parameter values calculated from fitting the

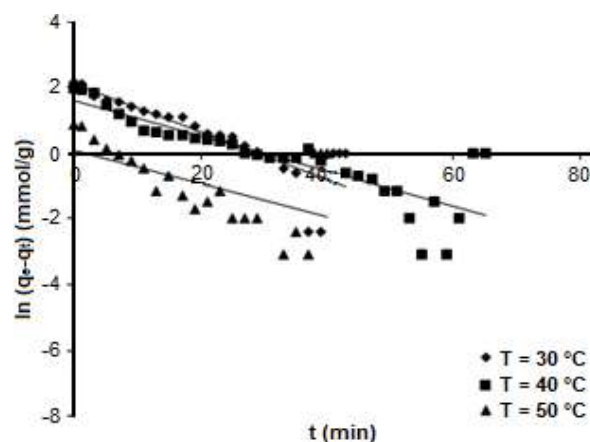


Fig 9. Pseudo first order kinetic plots for hydrogen adsorption onto ZTC at 30, 40, and 50 °C

experimental data are summarized in Table 3. As can be seen, the increasing temperature at constant pressure leads to a lower rate constant k_f value. This showed that a lower temperature leads to a higher amount of hydrogen adsorbed. For all samples, the correlation coefficients (R^2) for this kinetic model were clearly poor. It was also observed that the calculated adsorption capacities (q_e) at three samples deviated to the experimental values in Fig. 8. These indicate that the adsorption mechanism of hydrogen into ZTC could not be characterized by this kinetic model.

Pseudo second-order model

This kinetic model is assumed that linearity exists between adsorption capacity with the presence of active sites in adsorbent [39]. Fig. 10 showed the slope and intercept plots of time t and adsorbed capacity q_t , while the values were presented in Table 3. It showed a higher adsorption rate for a lower temperature and the correlation coefficient (R^2) values calculated were well at the whole condition. The calculated adsorption capacities were also close to the experimental data in Fig. 8. It can be summarized that the hydrogen adsorption process at all studied temperatures were best approximated to this kinetic model.

Intra particle diffusion model

In this study, this model is used to identify diffusion for adsorption process. By plotting of q_t versus $t^{0.5}$ in Fig.

11, the q_e and the rate constant values can be calculated. Such plots showed double linearity region that indicates two steps of the adsorption process. The first step line is attributed to the hydrogen diffusion through an external surface or boundary layer of ZTC, and the other line relates to the internal surface diffusion (micropore or mesopore diffusion). During the adsorption process, hydrogen diffusion was very fast in the early step and subsequently slow diffusion over the internal surface (Fig. 11).

Table 3. Kinetic parameters for hydrogen adsorption at three kinetic models

Kinetic models	Parameters		
Pseudo-first-order			
Temperature (°C)	q_e (mmol/g)	k_f (min ⁻¹)	R^2
30	8.01	0.09	0.72
40	4.86	0.05	0.72
50	2.30	0.05	0.32
Pseudo-second-order			
Temperature (°C)	k_s (mmol/g min)	q_e (mmol/g)	R^2
30	0.97	10.34	0.97
40	0.71	8.45	0.93
50	0.51	2.69	0.98
Intra particle diffusion			
Temperature (°C)	k_{id} (mmol/g min ^{0.5})	R^2	
30	1.20	0.94	
40	0.83	0.86	
50	0.31	0.81	

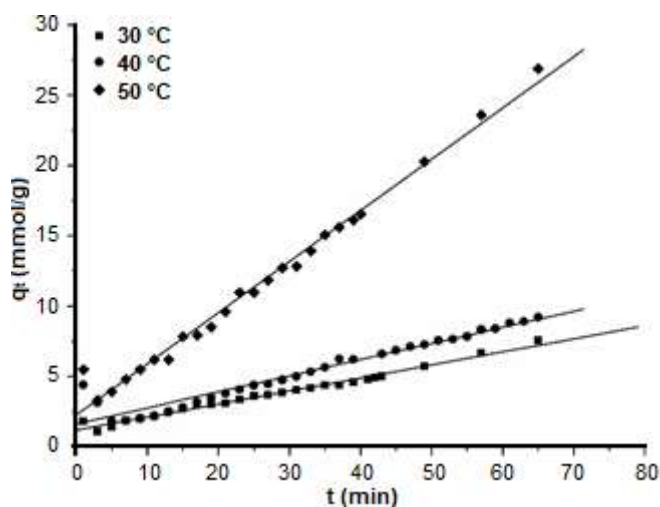


Fig 10. Pseudo second order kinetic plots for hydrogen adsorption by ZTC at 30, 40, and 50 °C

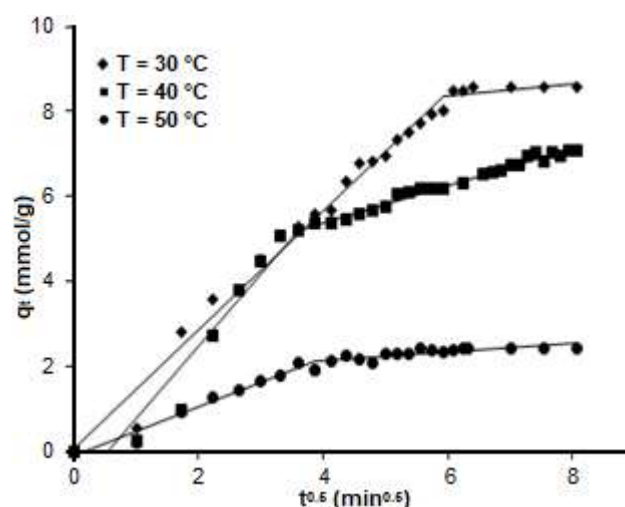
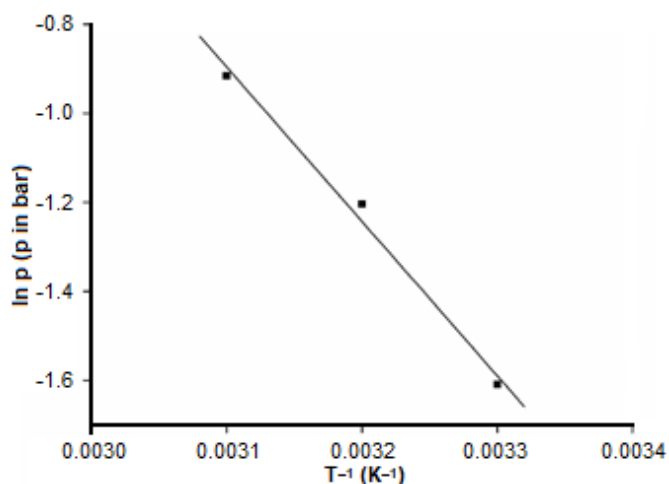


Fig 11. Intraparticle diffusion plots for hydrogen adsorption by ZTC at 30, 40, and 50 °C

Table 4. Thermodynamic parameters for hydrogen adsorption onto zeolite templated carbon

T (°C)	ΔG (kJ mol ⁻¹)	ΔH (kJ mol ⁻¹)	ΔS_H (J K ⁻¹ mol ⁻¹)
30	-1.99		
40	-1.59	-14.41	-40.93
50	-1.19		

**Fig 12.** Enthalpy of adsorption of hydrogen onto the ZTC

Thermodynamic Studies

The thermodynamic aspects (Fig. 12) provide a conceptual insight of the adsorption mechanism of the adsorption process. As presented in Table 4, the ΔG and ΔH values were negative which indicate a spontaneous and exothermic process, respectively [40]. The ΔH value obtained was much smaller than 80 kJ mol⁻¹ (14.41 kJ mol⁻¹), indicating a physical adsorption process of hydrogen into ZTC [22,26]. Such ΔH value was significantly larger than that shown by other studies [12,18]. The material which is able to adsorb the hydrogen at room temperature possess a heat of adsorption change value of 15.1 kJ/mol, which is very close with the value in this study [23]. The small of ΔG value together with the high temperature revealed that the adsorption is more efficient or spontaneous at a lower temperature. Small randomness in the interface of ZTC and hydrogen during the adsorption process was revealed by the negative value of ΔS_H (-40.93 J K⁻¹ mol⁻¹).

CONCLUSION

In summary, a zeolite templated carbon (ZTC) was successfully synthesized via carbonization and

investigated their hydrogen uptake properties. Such material is principally amorphous with a surface area of 932 m²/g, total pore volume of 0.97 cm³/g and exhibits well pore ordering structure derived from the template as well as some graphitic carbon. The ZTC obtained was tested for hydrogen storage at a temperature of 30–50 °C and its capacity was greatly dependent with temperature condition. Greater hydrogen uptake was observed at lower temperature and pressure of 1 bar as high as 1.72 wt.%. This value was close to the calculated adsorption capacity by volumetric method as high as 1.16 wt.% at 2 bar, similar to a volumetric density of 17.43 g H₂/L. The calculated value here was much lower to the ultimate DOE target of 7.5 wt.% and 70 g H₂/L. Therefore, preparing method here should be improved to obtain a significant proportion of micropores or even ultramicropores, which is contributed to higher H₂ uptake. The kinetic models showed that pseudo second order kinetic model best fitted for all adsorption condition. The thermodynamic aspects such as enthalpy and entropy change were 14.41 kJ mol⁻¹ and -40.93 J K⁻¹ mol⁻¹, respectively. A small value of the enthalpy described the physical adsorption process and found to be exothermic as confirmed by a negative sign of the enthalpy. The change of entropy was negative indicating decreasing randomness at the ZTC and hydrogen interface during physisorption process. The process occurred spontaneously as indicated by the negative Gibbs free energy change values. This value decreased by high temperature, indicating less effective of the adsorption process.

According to the results above, it can be said that ZTC is an attractive material for hydrogen storage and deserves further study in order to achieve better performance of adsorption.

ACKNOWLEDGMENTS

The authors are grateful to the Directorate General of Higher Education, Ministry of Research, Technology and Higher Education of Republic of Indonesia for providing financial support under PMDSU scholarship for doctoral degree for Rika Wijiyanti and Triyanda Gunawan, and also the research funding under

“Program Penelitian Magister Doktor Sarjana Unggul (PMDSU)” (No: 135/SP2H/LT/DRPM/IV/2017).

■ REFERENCES

- [1] Xia, Y., Yang, Z., and Zhu, Y., 2013, Porous carbon-based materials for hydrogen storage: Advancement and challenges, *J. Mater. Chem. A*, 1 (33), 9365–9381.
- [2] Hydrogen Storage Technical Team, 2017, *Hydrogen Storage Technical Team Roadmap*, United States Department of Energy.
- [3] Krishna, R., Titus, E., Salimian, M., Okhay, O., Rajendran, S., Rajkumar, A., Sousa, J.M.G., Ferreira, A.L.C., Gil, J.C., and Gracio, J., 2012, “Hydrogen Storage for Energy Application” in *Hydrogen Storage*, Eds., Liu, J., IntechOpen, London, 243–266.
- [4] Tedds, S., Walton, A., Broom, D.P., and Book, D., 2011, Characterisation of porous hydrogen storage materials: Carbons, zeolites, MOFs and PIMs, *Faraday Discuss.*, 151, 75–94.
- [5] Nijkamp, M.G., Raaymakers, J.E.M.J., van Dillen, A.J., and de Jong, K.P., 2001, Hydrogen storage using physisorption—materials demands, *Appl. Phys. A*, 72 (5), 619–623.
- [6] Zubizarreta, L., Arenillas, A., and Pis, J.J., 2009, Carbon materials for H₂ storage, *Int. J. Hydrogen Energy*, 34 (10), 4575–4581.
- [7] Konwar, R.J., and De, M., 2013, Effects of synthesis parameters on zeolite templated carbon for hydrogen storage application, *Microporous Mesoporous Mater.*, 175, 16–24.
- [8] Darkrim, F.L., Malbrunot, P., and Tartaglia, G.P., 2002, Review of hydrogen storage by adsorption in carbon nanotubes, *Int. J. Hydrogen Energy*, 27 (2), 193–202.
- [9] Armandi, M., Bonelli, B., Areán, C.O., and Garrone, E., 2008, Role of microporosity in hydrogen adsorption on templated nanoporous carbons, *Microporous Mesoporous Mater.*, 112 (1-3), 411–418.
- [10] Dong, J., Wang, X., Xu, H., Zhao, Q., and Li, J., 2007, Hydrogen storage in several microporous zeolites, *Int. J. Hydrogen Energy*, 32 (18), 4998–5004.
- [11] Chen, L., Singh, R.K., and Webley, P., 2007, Synthesis, characterization and hydrogen storage properties of microporous carbons templated by cation exchanged forms of zeolite Y with propylene and butylene as carbon precursors, *Microporous Mesoporous Mater.*, 102 (1–3), 159–170.
- [12] Yang, Z., Xia, Y., and Mokaya, R., 2007, Enhanced hydrogen storage capacity of high surface area zeolite-like carbon materials, *J. Am. Chem. Soc.*, 129 (6), 1673–1679.
- [13] Guan, C., Wang, K., Yang, C., and Zhao, X.S., 2009, Characterization of a zeolite-templated carbon for H₂ storage application, *Microporous Mesoporous Mater.*, 118 (1-3), 503–507.
- [14] Song, X.H., Xu, R., and Wang, K., 2013, The structural development of zeolite-templated carbon under pyrolysis, *J. Anal. Appl. Pyrolysis*, 100, 153–157.
- [15] Kyotani, T., Ma, Z., and Tomita, A., 2003, Template synthesis of novel porous carbons using various types of zeolites, *Carbon*, 41 (7), 1451–1459.
- [16] Böhme, K., Einicke, W., and Klepel, O., 2005, Templated synthesis of mesoporous carbon from sucrose—the way from the silica pore filling to the carbon material, *Carbon*, 43 (9), 1918–1925.
- [17] Yang, Z., Xia, Y., Sun, X., and Mokaya, R., 2006, Preparation and hydrogen storage properties of zeolite-templated carbon materials nanocast via chemical vapor deposition: Effect of the zeolite template and nitrogen doping, *J. Phys. Chem. B*, 110 (37), 18424–18431.
- [18] Johnson, S.A., Brigham, E.S., Ollivier, P.J., and Mallouk, T.E., 1997, Effect of micropore topology on the structure and properties of zeolite polymer replicas, *Chem. Mater.*, 9 (11), 2448–2458.
- [19] Cai, J., Yang, M., Xing, Y., and Zhao, X., 2014, Large surface area sucrose-based carbons via template-assisted routes: Preparation, microstructure, and hydrogen adsorption properties, *Colloids Surf., A*, 444, 240–245.
- [20] Nishihara, H., Hou, P.X., Li, L.X., Ito, M., Uchiyama, M., Kaburagi, T., Ikura, A., Katamura, J., Kawarada, T., Mizuuchi, K., and Kyotani, T., 2009, High-pressure hydrogen storage in zeolite-templated carbon, *J. Phys. Chem. C*, 113 (8), 3189–3196.

- [21] Hirscher, M., and Becher, M., 2003, Hydrogen storage in carbon nanotubes, *J. Nanosci. Nanotechnol.*, 3 (1-2), 3–17.
- [22] Zamora, B., Al-Hajjaj, A.A., Shah, A.A., Bavykin, D.V., and Reguera, E., 2013, Kinetic and thermodynamic studies of hydrogen adsorption on titanate nanotubes decorated with a Prussian blue analogue, *Int. J. Hydrogen Energy*, 38 (15), 6406–6416.
- [23] Bhatia, S.K., and Myers, A.L., 2006, Optimum conditions for adsorptive storage, *Langmuir*, 22 (4), 1688–1700.
- [24] Synthesis Commission of the International Zeolite Association, 2016, *Verified Syntheses of Zeolitic Materials*, Eds., Mintova, S., International Zeolite Association.
- [25] Luo, J., Liu, Y., Jiang, C., Chu, W., Jie, W., and Xie, H., 2011, Experimental and modeling study of methane adsorption on activated carbon derived from anthracite, *J. Chem. Eng. Data*, 56 (12), 4919–4926.
- [26] Khalili, S., Ghoreyshi, A.A., and Jahanshahi, M., 2012, Carbon dioxide captured by multi-walled carbon nanotube and activated charcoal: A comparative study, *Chem. Ind. Chem. Eng. Q.*, 19 (1), 153–164.
- [27] Widiastuti, N., Wu, H., Ang, H.M., and Zhang, D., 2011, Removal of ammonium from greywater using natural zeolite, *Desalination*, 277 (1-3), 15–23.
- [28] Su, F., Zhao, X.S., Lv, L., and Zhou, Z., 2004, Synthesis and characterization of microporous carbons templated by ammonium-form zeolite Y, *Carbon*, 42 (14), 2821–2831.
- [29] Konwar, R.J., and De, M., 2015, Development of templated carbon by carbonisation of sucrose-zeolite composite for hydrogen storage, *Int. J. Energy Res.*, 39 (2), 223–233.
- [30] Nishihara, H., and Kyotani, T., 2012, “Zeolite-Templated Carbon – Its Unique Characteristics and Applications” in *Novel Carbon Adsorbents*, Eds., Tascón, J.M.D., Elsevier Ltd, Amsterdam, 295–322.
- [31] Greer, H.F., and Zhou, W., 2011, Electron diffraction and HRTEM imaging of beam-sensitive materials, *Crystallogr. Rev.*, 17 (3), 163–185.
- [32] Choi, S., Kim, H., Lee, S., Wang, Y., Ercan, C., Othman, R., and Choi, M., 2015, Large-scale synthesis of high-quality zeolite-templated carbons without depositing external carbon layers, *Chem. Eng. J.*, 280, 597–605.
- [33] Ma, Z., Kyotani, T., and Tomita, A., 2002, Synthesis methods for preparing microporous carbons with a structural regularity of zeolite Y, *Carbon*, 40 (13), 2367–2374.
- [34] Cai, J., Li, L., Lv, X., Yang, C., and Zhao, X., 2014, Large surface area ordered porous carbons via nanocasting zeolite 10x and high performance for hydrogen storage application, *ACS Appl. Mater. Interfaces*, 6 (1), 167–175.
- [35] Saha, D., Wei, Z., and Deng, S., 2008, Equilibrium, kinetics and enthalpy of hydrogen adsorption in MOF-177, *Int. J. Hydrogen Energy*, 33 (24), 7479–7488.
- [36] Jin, H., Lee, Y.S., and Hong, I., 2007, Hydrogen adsorption characteristics of activated carbon, *Catal. Today*, 120 (3-4), 399–406.
- [37] Bonenfant, D., Kharoune, M., Niquette, P., Mimeault, M., and Hausler, R., 2008, Advances in principal factors influencing carbon dioxide adsorption on zeolites, *Sci. Technol. Adv. Mater.*, 9 (1), 013007.
- [38] Delavar, M., Asghar Ghoreyshi, A., Jahanshahi, M., Khalili, S., and Nabian, N., 2012, Equilibria and kinetics of natural gas adsorption on multi-walled carbon nanotube material, *RSC Adv.*, 2 (10), 4490–4497.
- [39] Ho, Y.S., and McKay, G., 1999, Pseudo-second order model for sorption processes, *Process Biochem.*, 34 (5), 451–465.
- [40] Rodrigues, L.A., and da Silva, M.L.C.P., 2010, Thermodynamic and kinetic investigations of phosphate adsorption onto hydrous niobium oxide prepared by homogeneous solution method, *Desalination*, 263 (1-3), 29–35.

Homology Modeling and Structural Dynamics of the Glucose Oxidase

Farhan Azhwin Maulana¹, Laksmi Ambarsari^{2,*}, and Setyanto Tri Wahyudi³

¹Master of Biochemistry Program, Postgraduate School, Bogor Agricultural University, Kampus IPB Dramaga, Bogor 16680, West Java, Indonesia

²Molecular Biology Division, Department of Biochemistry, Bogor Agricultural University, Kampus IPB Dramaga, Bogor 16680, West Java, Indonesia

³Computational Biophysics and Molecular Modeling Research Group, Department of Biophysics, Bogor Agricultural University, Kampus IPB Dramaga, Bogor 16680, West Java, Indonesia

* **Corresponding author:**

tel: +62-251-8423267

email: laksmi@apps.ipb.ac.id

Received: September 27, 2018

Accepted: December 4, 2018

DOI: 10.22146/ijc.39135

Abstract: Glucose oxidase from *Aspergillus niger* IPBCC.08.610 (GOD_IPBCC) is a locally sourced flavoenzyme from Indonesia that can potentially be developed in a variety of industrial processes. Although this enzyme has a high activity in catalyzing the redox reactions, the use of this enzyme was still limited to be applied as glucose biosensor. Using information from the amino acid sequences, a computational structure of GOD_IPBCC was therefore designed by homology modeling method using two homologous structures of GOD from protein data bank (1CF3 and 5NIT) as the templates. The quality of the resulting structures was evaluated geometrically for selection of the best model, and subsequently, 50 ns of MD simulations were carried out for the selected model as well as the corresponding template. Results obtained from the validation analysis showed that the 1CF3 template-built structure was selected as the best reliable model. The structural comparison exhibited that the best-modeled structure consisted of two functional domains and three catalytic residues similarly to the corresponding experimental structure. The overall dynamic behavior of the 50 ns of the structure was structurally stable and comparable with that of the positive control both from globally and locally observations. Implications of these stable nature within the best-modeled structure unfold the possibilities in search of notable residues and their roles to enhance enzyme thermostability.

Keywords: glucose oxidase; homology modeling; molecular dynamics; three-dimensional structure

■ INTRODUCTION

Glucose oxidase (GOD), or β -D-glucose, oxygen 1-oxidoreductase is a flavoprotein oxidase (EC 1.1.3.4) catalyzing the redox reaction of β -D-glucose and molecular oxygen to generate δ -gluconolactone and hydrogen peroxide, respectively. In the initial step catalysis (reductive-half reaction), GOD uses flavin adenine dinucleotide (FAD) as a redox carrier through a mechanism of hydride abstraction describing the removal of a proton at hydroxyl group in C1 atom of glucose by His516 and thus facilitates hydride transfer from the anomeric carbon to N5-isoalloxazine ring of FAD,

creating negative charge around N1 of the reduced coenzyme. Subsequently, in the oxidative-half reaction, the reduced enzyme was therefore re-oxidized by oxygen via stepwise single-electron transfers [1-2]. GOD has an important application in the fields of chemical, pharmaceutical, and food industries, which reach far beyond its typical use as blood glucose biosensor in preliminary diagnostics. Economically, this versatile enzyme has gained valuable importance [3].

The source of GOD is extracted mainly from *Aspergillus* and *Penicillium* that have been studied in detail, especially for biotechnological applications. The

GOD produced from *Aspergillus* is more stable but less affinity constant for β -D-glucose than from *Penicillium* [3-5]. In Indonesia, GOD had successfully been produced from a strain of *Aspergillus niger* IPBCC.08.610 (GOD_IPBCC). A study regarding the development of this enzyme concluded that at the enzymatic level, the isolated GOD_IPBCC was ideal only to be utilized for blood glucose measurement both in normal and hyperglycemia situations [5]. These conditions pave the path of developing it into a more diverse utilization, such as glucose-based biofuel cells for example by designing the enzyme with modified kinetics parameters such as low-affinity constant value (K_m) for β -D-glucose but large maximum velocity (V_{max}) to boost power output and improved in thermal resistance [6]. Several mutagenesis studies elucidated that a highly-evolved GOD could merely achieve minor enhancement of its kinetic properties (approximately 5 times lower K_m) [2,7-8]. In the present study, we used the three-dimensional structure-based understanding derived from its encoding genes, as an alternative way to provide extensive knowledge regarding the design of this enzyme suitable for biofuel cell, before the protein experiment in the lab. Unfortunately, the experimental structure of GOD_IPBCC has not been determined.

Experimentally, the structure of a protein can be determined by relatively expensive and time-consuming technics such as crystallography and nuclear magnetic resonance spectroscopy. Moreover, these technics also require high protein purity that needs to be solved. As an alternative, in-silico protein prediction has provided advances in knowledge to compute and predict protein structures based on their amino acid sequences. Among the other computational protein prediction methods, the most reliable approach is by using homology modeling, in which a target sequence is modeled using known structures of candidate proteins where the similarity between their sequences are judged to be similar [9-10]. This methods also have the important benefits in the sense of gaining insightful information about the structure-function relationship in GOD, as previously reported [11].

Exploration of conformational dynamics and stability

in proteins can be observed computationally at the atomic level and complements the analysis of experimental structures by also delineating the underlying dynamics of the protein. For example, the observation of residual rigidity located in the active site using atomistic (MD) simulations has often been found to be prominent than for noncatalytic. This preorganized and rigid active site makes the chemical step more efficient, which positively affects enzymatic rates and minimizes the futile enzyme-substrate encounters. This method is also useful in determining how mutations affect the active-site preorganization, leading to an enhancement in their catalytic efficiency [2].

Therefore, the aim of this study was to predict the three-dimensional structure of GOD_IPBCC by a homology modeling procedure based on the most homologous crystal structures of *Aspergillus niger* GOD, deposited in Protein Data Bank (PDB ID 1CF3 [12] and 5NIT [2] with 97 and 96% identity, respectively). The generated models were screened for geometrically favorable structure and reliability. The Molecular dynamics (MD) simulation was employed to the selected model with the positive control in the hope of revealing the importance of certain elements of the GOD_IPBCC structure in the overall enzymatic thermostability.

■ EXPERIMENTAL SECTION

Computational Section

Hardware

The entire simulations were conducted by a single CPU with specifications of a Quad-core 3.4-GHz Intel® i7 processor, RAM of 16 GB, and Ubuntu version 16.04 operating system.

Software

The multiple sequence alignment was performed using Esript program [13]. All structure visualizations were generated by PYMOL version 2.0 [14]. For minimization and MD simulations, both model and template structures were applied to the AMBER system version 16 [15]. The resulting trajectories were analyzed using cpptraj in the AmberTools16 module to generate RMSD and RMSF profiles using the initial structure of each simulation as a reference. The B-Factors analysis of

wild-type GOD (PDB ID 1CF3) was performed using B-Fitter program [16]. The visual molecular dynamics (VMD) [17] was used to produce electrostatic energy and solvent accessible area data. The generated plots except in RMSF were smoothed with moving average method in Microsoft Excel before displayed into the plots.

Procedure

Model construction and evaluation

The protein sequence of the GOD_IPBCC with GB (GenBank) accession number MH593586 was obtained from NCBI (<https://www.ncbi.nlm.nih.gov/>). The amino acid properties of GOD_IPBCC was computed by ProtParam such as molecular weight, aliphatic index, grand average of hydropathy (GRAVY), and instability index [18]. The protein was modeled by SWISS-MODEL [19] using two known crystallographic structures (PDB ID 1CF3 [12] and 5NIT [2]). The evaluation of these structures was performed such as the residual percentage of Ramachandran plot and overall G-factor value using PROCHECK [20]. Another evaluation tools (molProbity and proQ) were also carried out [21]. Moreover, the functional regions of the best protein were then predicted using the Pfam web server [22]. The secondary structural elements (α -helices and β -strands) were analyzed by PDBsum and other components present in the protein tertiary structure [23].

Molecular dynamics simulation

MD simulations of the best model were carried out in apo-monomer form. The preparation step was performed by firstly removing the hydrogen atoms and other organic molecules within the best model and its corresponding template. Subsequently, the new hydrogen atoms were added and the protonation state of the titratable side chain within the proteins was adjusted by the Virginia Tech H++server (<http://biophysics.cs.vt.edu/H++>) [24-25]. These structures were then prepared in an explicit solvent solvated box implementing TIP3P water molecules with the box distance of 16 Å. The sodium ions were added to neutralize the system.

The six series of energy minimizations were run with a total of 60000 steps and 50000 steps for final stage by using constrained steepest descent followed by conjugate

gradient algorithm methods. After which the system was gradually heated from 0 to 300 K with 50 K interval using the implementation of the Langevin dynamics. After the desired temperature was attained, the equilibration phase was performed in a total of 6 stages to ensure the stability of structural properties concerning time. In the initial equilibration, the constraint was first applied in a fixed volume run (NVT) for 50 ps. In the subsequent phase, under constant pressure (NPT), the constraint was then removed slowly for 300 ps in total. This allows the system to obtain a proper density and is likewise to avoid aggregation [26]. The final step of the simulation was a long production run, where the solvated protein was run for 50 ns of simulation in 25 separate stages of 2.0 ns each (2.0-fs timestep). The non-bonded cutoff value used was 10 Å and the long-range electrostatic energy was calculated using the Particle Mesh Ewald (PME) algorithm.

RESULTS AND DISCUSSION

Protein Modeling and Validation

A number of 605 amino acid sequences of the GOD_IPBCC was successfully obtained for further analysis. The physicochemical parameters from ProtParam calculation revealed the majority of its primary structure comprised non-polar residues with rich alanine content and had the monomeric average molecular weight of 63 kDa, whereas the aliphatic index of protein (83.63) showed the protein could withstand for a wide range of temperature. Moreover, this enzyme also had negative GRAVY score (-0.208) which signifies a better interaction with the solvent due to its greater hydrophilicity. These results along with instability index (28.88) rendered information that the properties of the GOD_IPBCC primary structure was categorized good and needed to be discussed even further.

The model of GOD_IPBCC was constructed using two templates that shared over 95% homologous sequences. The first template was a structure of *A. niger* glucose oxidase (PDB ID 1CF3 [12]), whereas the second was the mutant form (PDB ID 5NIT [2]). The final resolution of these structures was resolved at 1.9 and 1.87 Å, respectively. The residual alignment of

GOD_IPBCC with the templates is displayed in Fig. 1. Most of GOD_IPBCC amino acids were homologous (*) with 16 distinct residues found when compared with both 5NIT and 1CF3 experimental structures. Other than that, the first 22 amino acid residues of GOD_IPBCC were

observed as peptide signals and therefore excluded in the three-dimensional structure as depicted in Fig. 2.

The model generated by SWISS-MODEL results in the QMEAN statistical value that provides how native the structure in a global scope [27]. The global QMEAN



Fig 1. Multiple sequence alignment of GOD_IPBCC and the selected templates

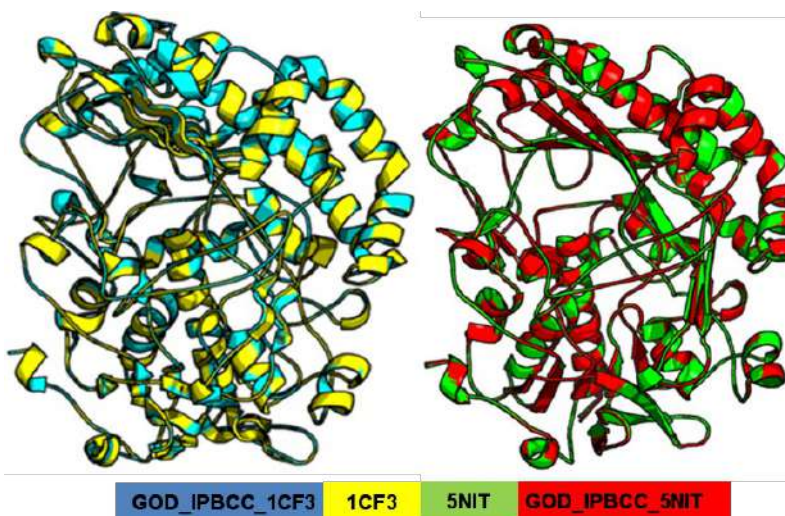


Fig 2. Structural alignment of GOD_IPBCC homology models and corresponding templates in cartoon representation

profile of the 1CF3 template-built model (0.04) rendered a high degree of nativeness compared with the 5NIT template-generated model (-0.48). Nevertheless, the initial constructed protein model from a comparative modeling study does not ensure a valid 3D structure since it contains the possibility of mistakenly folded from the native conformation. Thus, the quality of the computationally determined protein structure needed to be analyzed.

The quality estimation of GOD_IPBCC models was evaluated by PROCHECK consisting of Ramachandran plot and overall G-factor value. As shown in Table 1, the highest percentage of residues (89.4%) were found similar in the favored region for 5NIT experimental structure and GOD_IPBCC_1CF3 protein model, whereas 1CF3 template showed the lowest score (88.4%). The Ramachandran percentage for GOD_IPBCC_5NIT showed one residue less (89.2%) in the favored area compared to the homology model from the 1CF3 crystal structure. None of the residues were located in the outlier region (0%) for all structures. In general, a protein with good backbone dihedral angles (ϕ and ψ) of the amino acid residues are expected to have 90% of the residues in the core or

favored region and also has an overall geometrical factor (G-factor) above -0.5 and vice versa as an indication of having a stereochemical agreement [28-29].

Moreover, the successful attempt in constructing the structure of GOD_IPBCC was indicated when comparing the quality of each model generated by two different templates (1CF3 and 5NIT). The models which were built from both templates respectively were good and reliable since nearly 90% residues fell into the favored regions. However, the overall geometry score (G-factor) found in GOD_IPBCC_1CF3 (-0.08) structure was greater than that of GOD_IPBCC_5NIT (-0.16), indicated the protein is in agreement with defined values.

In addition, the overall molProbity scores for 1CF3 template-built model structure exhibited the lowest (the highest crystallographic resolution) than that of GOD_IPBCC_5NIT and even those two templates (Table 2), whereas results from the proQ (LGscore and Maxsub) showed all input structures were categorized as the very good model. Nonetheless, this validation analysis clearly explained that the modeled structure of GOD_IPBCC_1CF3 was superior in overall quality. As

Table 1. Summary of the protein quality assessed by PROCHECK

Protein	Ramachandran plot (%) ^a		Overall G-factor ^b
	Favored region	Disallowed region	
5NIT	89.4	0.0	-0.08
GOD_IPBCC_5NIT	89.2	0.0	-0.16
1CF3	88.6	0.0	0.09
GOD_IPBCC_1CF3	89.4	0.0	-0.08

^aRamachandran plot consists of the percentage of residues plotted into one internal coordinate (i.e., favored, allowed, generally allowed, and disallowed region)

^bGeometrical factors (G-factors) divided into the quality of covalent and overall dihedral distances. For a reliable model, the score should be greater than -0.5

Table 2. Summary of the protein quality assessed by PROCHECK

Protein	proQ ^a		MolProbity score ^b
	LGscore	Disallowed region	
5NIT	6.834	0.533	1.51
GOD-IPBCC-5NIT	6.815	0.526	1.38
1CF3	7.009	0.546	1.16
GOD-IPBCC-1CF3	6.944	0.531	0.91

^aProQ is calculated based on a number of structural characteristics and optimized to uncover native structures comprising LGscore and Maxsub. A protein with good quality should have LGscore above 5 and Maxsub ranges from 0 to 1, where 0 is insignificant and vice versa

^bMolProbity score incorporates Ramachandran outliers, clashscore, and bad rotamer into a single score, normalized to be on the same scale as X-ray resolution

the best model, further characterization of the secondary structural information was therefore conducted by PDBsum.

Structural Features of the *A. niger* 1CF3 Template-built Structure

Analysis of the GOD_IPBCC_1CF3 secondary structure was found to have 28 α -helices, 23 β -strands, 23 helix-helix interactions, 1 disulfide bridge, 45 beta, and 18 gamma turns, respectively. This results correlated well with the domain features of *A. niger* glucose oxidase crystal structure (PDB ID 1CF3), where consists of two following functional regions; FAD-binding domain and C-terminal domain (substrate binding) as is apparent from Fig. 3(a). These domains are characterized by two separate and distinctive β -sheet systems, one of which is a sandwich form comprising five-stranded sheet incorporated into FAD-binding domain, the other one contains a large antiparallel β -sheet bolstered by four α -helices that subsequently form one side of the active site [30].

Moreover, three catalytic residues Glutamate-410 (E410), Histidine-514 (H514), and Histidine-557 (H557) (equivalent to E412, H516, and H559 respectively in experimental structure) were also positioned in accordance with the same conformation in the 1CF3 experimental structure [12]. The hydrogen bond formed between E412 and H559 in 2.7 Å atomic distance plays a vital role in maintaining the reactivity on the catalytic site. The catalytically important H516 involves as proton acceptor from the anomeric carbon of glucose and has found to be flexible in the wild-type [2]. A single conserved disulfide bridge by Cysteine-162 (C162) and Cysteine-204 (C204) (equivalent to C164 and C206 in the crystal structure) were located in the protein surface area. This region facilitates the path for electron transfer from the flavin oxygen-4 (O4) [12]. In respect to the sulfur atoms in the *A. niger* GOD crystallographic structure, Marín-Navarro et al. [11] elucidated a new sulfur- π interaction formed by residual mutation of threonine to methionine in position 554

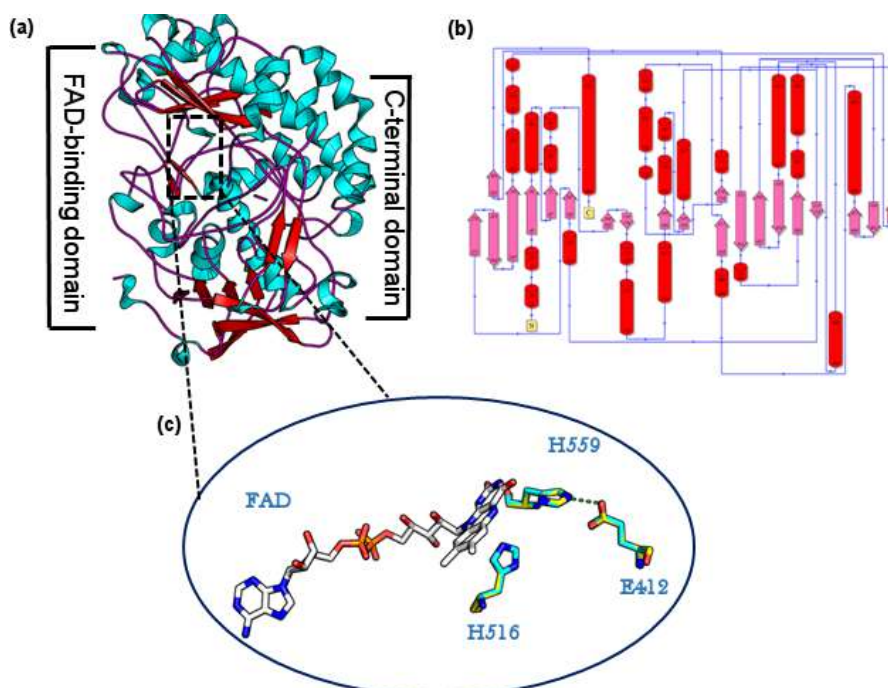


Fig 3. (a) The domain view of the GOD_IPBCC_1CF3 secondary structural model. (b) Topology diagram of the GOD_IPBCC_1CF3 protein with helix, sheet, beta turn, and gamma turn simulated by PDBsum. (c) Stick representation of FAD and three amino acids responsible for catalytic activity of GOD_IPBCC_1CF3 as according to Hecht et al. [30]. The hydrogen bond is shown in green dashed line

(T554M) that has greater thermally stabilization energy (4.2–12.6 kJ/mol) when compared with that of hydrogen bond-associated (1.3–6.3 kJ/mol). On the whole observation, the biochemical characterization within the GOD_IPBCC_1CF3 is correlated well to its experimental structure.

Stabilization of the Structure by MD Simulations

Validation of simulation was performed using comparative analysis of the calculated average B-factor for each residue between the experimental and simulation structure (Fig. 4(a)). The simulation resulted in higher B-factor compared with x-ray but showed a similar trend, indicates the MD performance was reasonably good agreement in total with the crystallographic data.

The 50 ns of simulation was applied to investigate the stability of the positive control (PDB ID 1CF3) and its homology model. The global stability of these structures was monitored by RMSD backbone. The modeled structure was found to be generally stable during the simulation, comparable to RMSD value of 1CF3 template (Fig 4(b)). In the absence of FAD (apo form), this enzyme conformation may result in the inactive form that leads to dissociation of its tertiary structure (less stable) either experimentally or computationally [31]. The overall structural stability of the single monomer of GOD_IPBCC_1CF3 was considered to be good as indicated by C α RMSD < 2 Å.

Furthermore, the residual fluctuation of all systems was analyzed through RMSF calculation (Fig. 5). The greatest fluctuation was found in the C-terminal because this region was unrestrained, whereas the fluctuation around the catalytic residues was relatively high. This might be due to the absence of the substrate that altered all catalytic systems from open to closed conformation and their secondary structure as well, as previously reported [29,31]. The difference in RMSF values between two structures was observed from residue numbers 160 to 162; these residues adopted a turn shape in 1CF3 which fluctuates more in nature than the same residues in its homology model as 3(10)-helical conformation. These results were due to the formation of two additional intermolecular hydrogen bonds between Phenylalanine-158 (F158) and Asparagine-159 (N159) and between Alanine-160 (A160) and Histidine-163 (H163) in GOD_IPBCC_1CF3 which were not found in its template (Fig. 5). These interactions can reversibly switch the two protonation forms of histidine (and pKa value) [32] and are regarded to be important in many biological systems [29,33]. The other natural, flexible residues ranging from the number 257 to 262 formed loops in both 1CF3 and GOD_IPBCC_1CF3 structures were also high in RMSF. These fluctuating regions can be targeted for improved enzyme thermostability [34].

The stability of the protein conformation during MD was determined by calculating its non-bonded energy

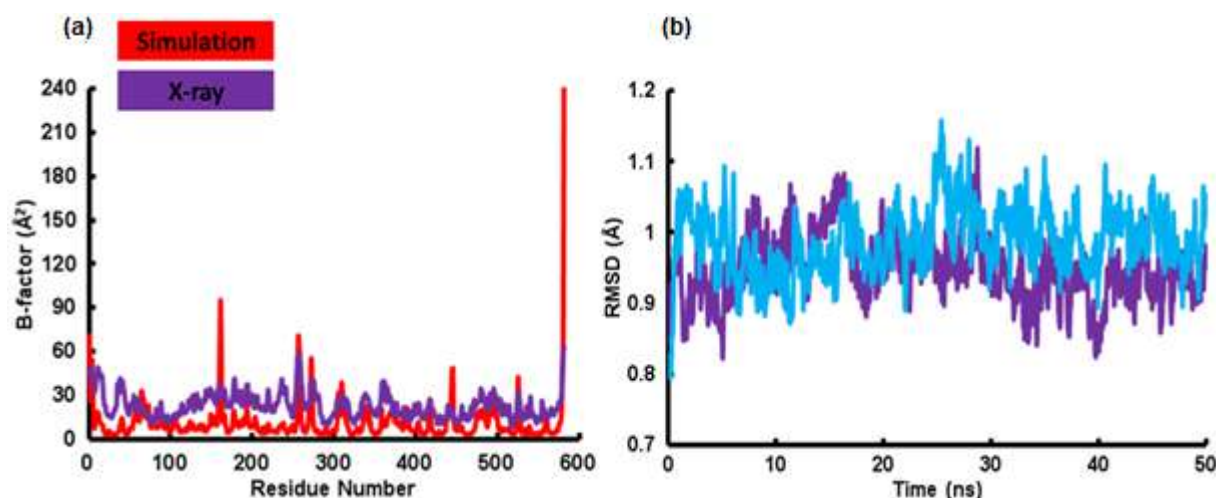


Fig 4. (a) Comparison of amino acid B-factor in GOD. (b) The RMSD trajectory for polypeptide chain backbone throughout 50 ns of simulation

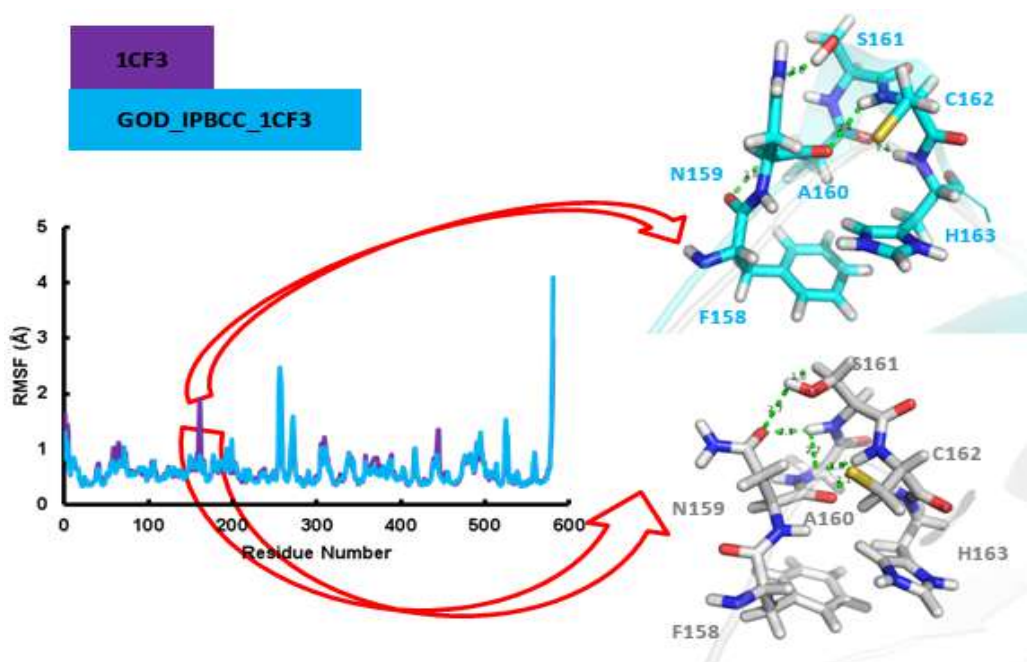


Fig 5. Residual RMSF profile of all systems during 50 ns of simulation. Panel on the right display details of fluctuating residues in the 50 ns structure of GOD_IPBCC_1C3 (blue stick) and 1CF3 (gray stick). The hydrogen bond is represented in green dashed line

which is plotted in Fig. 6(a). These interactions play the ubiquitous role in steering the folding route and modulating stability. The electrostatic strength has two distinctive effects, direct charge-charge interactions, and long-range effects, which together contribute to funneling the binding landscape of predicted structure [33].

In the positive control, the total average of non-bonded energy (coulomb electrostatic and van der Waals) over the course of MD simulation can be observed higher

than GOD_IPBCC_1CF3, the lowest fluctuation was observed at 27 ns (approximately -18700 kcal/mol) in the latter structure. The hydrophobicity content between these structures is not so different since their structural homology is high. However, the 1CF3 template-built structure conformation consistently exposed a decreased total surface area (Fig 6(b)) than that of the template during the first ns of trajectory, meaning the content of hydrophobic and hydrophilic surfaces in the structure

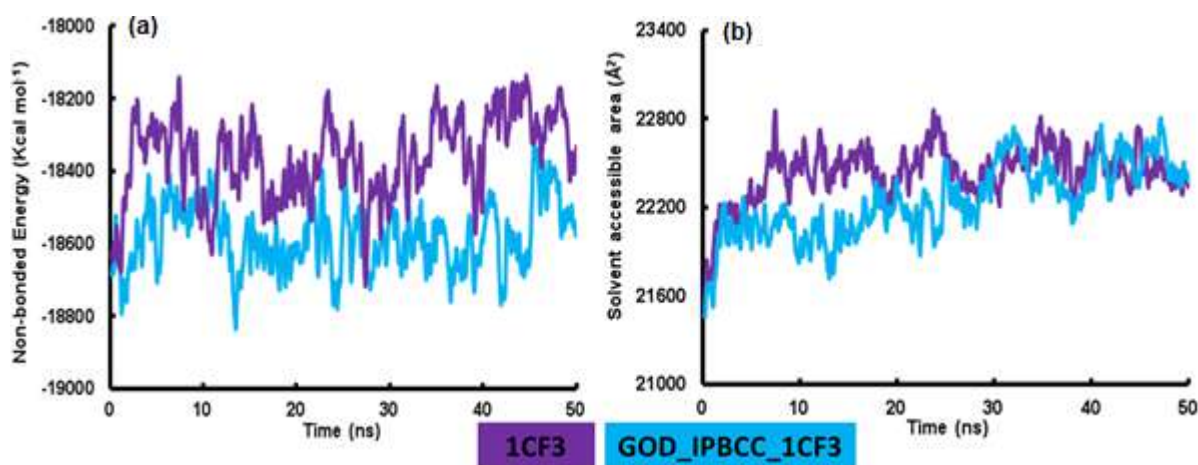


Fig 6. (a) Total non-bonded energy (in kcal/mol) and (b) protein SASA profile during 50 ns of simulation

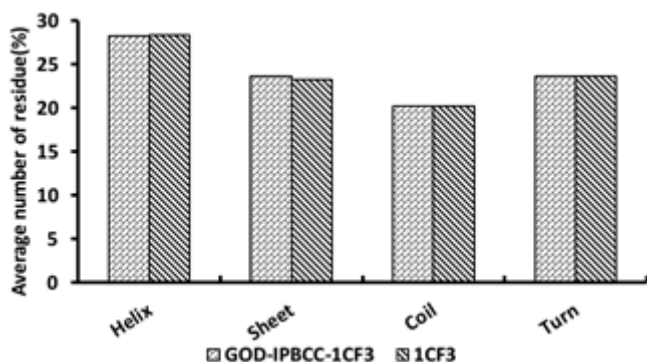


Fig 7. Average number of residual occurrence forming secondary structure during 50 ns of simulation

were in the equilibrium state and finally comparable at the end of simulation to around 22300 Å. Together, these trends imply that the modeled structure is modulated by increasing the non-bonded strength and having a stable hydrophobic context leading to the integrity of the tertiary structure.

An investigation related to a change in secondary structure (SS) is essential for enzymes to carry out their biological activity [31,35]. On overall observation, we found that the percentage of secondary structure for both structures was nearly similar where α -helices occupied the major proportion (approximately 28%) among the other structures (Fig. 7). Interestingly, these structures were constant over the course of a simulation, in agreement with the previously reported simulation of GOD [36]. An experimental study about a slight change in GOD secondary structure upon inactivation has been explained under ambient condition, using analysis of the circular dichroic (CD) spectra at 470 nm confirmed that the loss of its secondary structure is minimal [37].

The MD simulations performed revealed that the 50 ns of trajectory within GOD_IPBCC_1CF3 did not show any peculiar features and could retain its conformation on the basis of analyzed parameters. On the long run, the further computational experiment is necessary to figure out the dynamics of this enzyme together with the substrate docked and performs a potential residual mutation having a significant improvement in terms of the thermostability. Structure prediction along with MD simulation will provide more fruitful information regarding the role of each residue components, especially

around the catalytic site to rationalize the design of an engineered enzyme before conducting the laboratory protein experiment.

■ CONCLUSION

In conclusion, the limited use of GOD_IPBCC as only for biosensor prompted the understanding of the structure-function relationship corresponding to the encoding gene. Since it shared high homology level with the GOD from protein data bank (1CF3 [2] and 5NIT [12]), the structural comparison between the constructed structures resulting from their respective templates showed that the GOD_IPBCC_1CF3 can be considered reliable structure not only due to the in-silico methods but the conserved structural features associated with fungal glucose oxidase enzymes. Molecular dynamics simulations denoted that the overall conformation in 50 ns of trajectory did not undergo any significant conformational changes both from the secondary and tertiary structure and form a well-packed structure. This structure will later be used as an initial structure to investigate the thermostability in more details.

■ ACKNOWLEDGMENTS

The support for this research was provided by University Consortium Thesis Grant (Ref. No. GCS17-2758) in part of the scholarship of Southeast Asian Regional Center for Graduate Study and Research in Agriculture (SEARCA).

■ REFERENCES

- [1] Leskovic, V., Trivić, S., Wohlfahrt, G., Kandrač, J., and Peričin, D., 2005, Glucose oxidase from *Aspergillus niger*: The mechanism of action with molecular oxygen, quinones, and one-electron acceptors, *Int. J. Biochem. Cell Biol.*, 37 (4), 731–750.
- [2] Petrović, D., Frank, D., Kamerlin, S.C.L., Hoffmann, K., and Strodel, B., 2017, Shuffling active site substrate populations affects catalytic activity: The case of glucose oxidase, *ACS Catal.*, 7 (9), 6188–6197.
- [3] Bankar, S.B., Bule, M.V., Singhal, R.S., and Ananthanarayan, L., 2009, Glucose oxidase-An overview, *Biotechnol. Adv.*, 27 (4), 489-501.

- [4] Kiess, M., Hecht, H.J., and Kalisz, H.M., 1998, Glucose oxidase from *Penicillium amagasakiense*. Primary structure and comparison with other glucose-methanol-choline (GMC) oxidoreductases, *Eur. J. Biochem.*, 252 (1), 90–99.
- [5] Rohmayanti, T., Ambarsari, L., and Maddu, A., 2017, Enzymatic activity of glucose oxidase from *Aspergillus niger* IPBCC.08.610 on modified carbon paste electrode as glucose biosensor, *IOP Conf. Ser.: Earth Environ. Sci.*, 58 (1), 12046.
- [6] Zhu, Z., Momeu, C., Zakhartsev, M., and Schwaneberg, U., 2006, Making glucose oxidase fit for biofuel cell applications by directed protein evolution, *Biosens. Bioelectron.*, 21 (11), 2046–2051.
- [7] Holland, J.T., Lau, C., Brozik, S., Atanassov, P., and Banta, S., 2011, Engineering of glucose oxidase for direct electron transfer via site-specific gold nanoparticle conjugation, *J. Am. Chem. Soc.*, 133 (48), 19262–19265.
- [8] Holland, J.T., Harper, J.C., Dolan, P.L., Manginell, M.M., Arango, D.C., Rawlings, J.A., Aplett, C.A., and Brozik, S.M., 2012, Rational redesign of Glucose oxidase for improved catalytic function and stability, *PLoS One*, 7 (6), e37924.
- [9] Altschul, S.F., Boguski, M.S., Gish, W., and Wootton, J.C., 1994, Issues in searching molecular sequence databases, *Nat. Genet.*, 6 (2), 119–129.
- [10] He, Y., Rackovsky, S., Yin, Y., and Scheraga, H.A., 2015, Alternative approach to protein structure prediction based on sequential similarity of physical properties, *Proc. Natl. Acad. Sci. U.S.A.*, 112 (16), 5029–5032.
- [11] Marín-Navarro, J., Roupain, N., Talens-Perales, D., and Polaina, J., 2015, Identification and structural analysis of amino acid substitutions that increase the stability and activity of *Aspergillus niger* glucose oxidase, *PLoS One*, 10 (12), e0144289.
- [12] Wohlfahrt, G., Witt, S., Hendle, J., Schomburg, D., Kalisz, H.M., and Hecht, H.J., 1999, 1.8 and 1.9 Å resolution structures of the *Penicillium amagasakiense* and *Aspergillus niger* glucose oxidases as a basis for modelling substrate complexes, *Acta Crystallogr., Sect. D: Biol. Crystallogr.*, 55 (Pt 5), 969–977.
- [13] Robert, X., and Gouet, P., 2014, Deciphering key features in protein structures with the new ENDscript server, *Nucleic Acids Res.*, 42 (Web Server issue), W320–W324.
- [14] DeLano, W.L., 2002, The PyMOL molecular graphics system, *Proteins*, 30, 442–454.
- [15] Case, D.A., Betz, R.M., Botello-Smith, W., Cerutti, D.S., Cheatham, III, T.E., Darden, T.A., Duke, R.E., Giese, T.J., Gohlke, H., Goetz, A.W., Homeyer, N., Izadi, S., Janowski, P., Kaus, J., Kovalenko, A., Lee, T.S., LeGrand, S., Li, P., Lin, C., Luchko, T., Luo, R., Madej, B., Mermelstein, D., Merz, K.M., Monard, G., Nguyen, H., Nguyen, H.T., Omelyan, I., Onufriev, A., Roe, D.R., Roitberg, A., Sagui, C., Simmerling, C.L., Botello-Smith, W.M., Swails, J., Walker, R.C., Wang, J., Wolf, R.M., Wu, X., Xiao, L., and Kollman P.A., 2016, *AMBER 2016*, University of California, San Francisco.
- [16] Reetz, M.T., Carballeira, J.D., and Vogel, A., 2006, Iterative saturation mutagenesis on the basis of b factors as a strategy for increasing protein thermostability, *Angew. Chem. Int. Ed.*, 45 (46), 7745–7751.
- [17] Humphrey, W., Dalke, A., and Schulten, K., 1996, VMD: Visual molecular dynamics, *J. Mol. Graphics*, 14 (1), 33–38.
- [18] Gasteiger, E., Hoogland, C., Gattiker, A., Duvaud, S., Wilkins, M.R., Appel, R.D., and Bairoch, A., 2005, “Protein Identification and Analysis Tools on the ExPASy Server” in *The Proteomics Protocols Handbook*, Eds., Walker J.M., Humana Press, New York City.
- [19] Biasini, M., Bienert, S., Waterhouse, A., Arnold, K., Studer, G., Schmidt, T., Kiefer, F., Cassarino, T.G., Bertoni, M., Bordoli, L., and Swede, T., 2014, SWISS-MODEL: Modelling protein tertiary and quaternary structure using evolutionary information, *Nucleic Acids Res.*, 42 (Web Server issue), W252–W258.
- [20] Laskowski, R.A., Jabłońska, J., Pravda, L., Vařeková, R.S., and Thornton, J.M., 2018, PDBsum: Structural summaries of PDB entries, *Protein Sci.*, 27 (1), 129–134.

- [21] Chen, V.B., Arendall, W.B., Headd, J.J., Keedy, D.A., Immormino, R.M., Kapral, G.J., Murray, L.W., Richardson, J.S., and Richardson, D.C., 2010, MolProbity: All-atom structure validation for macromolecular crystallography, *Acta Crystallogr., Sect. D: Biol. Crystallogr.*, 66 (Pt 1), 12–21.
- [22] Finn, R.D., Coggill, P., Eberhardt, R.Y., Eddy, S.R., Mistry, J., Mitchell, A.L., Potter, S.C., Punta, M., Qureshi, M., Sangrador-Vegas, A., Salazar, G.A., Tate, J., and Bateman, A., 2016, The Pfam protein families database: Towards a more sustainable future, *Nucleic Acids Res.*, 44 (D1), D279–D285.
- [23] Laskowski, R.A., 2001, PDBsum: Summaries and analyses of PDB structures, *Nucleic Acids Res.*, 29 (1), 221–222.
- [24] Anandakrishnan, R., Aguilar, B., and Onufriev, A.V., 2012, H++ 3.0: Automating pK prediction and the preparation of biomolecular structures for atomistic molecular modeling and simulations, *Nucleic Acids Res.*, 40 (Web Server issue), W537–W541.
- [25] Myers, J., Grothaus, G., Narayanan, S., and Onufriev, A., 2006, A simple clustering algorithm can be accurate enough for use in calculations of pKs in macromolecules, *Proteins*, 63 (4), 928–938.
- [26] Case, D.A., Cheatham, T.E., Darden, T., Gohlke, H., Luo, R., Merz, K.M., Onufriev, A., Simmerling, C., Wang, B., and Woods, R.J., 2005, The Amber biomolecular simulation programs, *J. Comput. Chem.*, 26 (16), 1668–1688.
- [27] Benkert, P., Biasini, M., and Schwede, T., 2011, Toward the estimation of the absolute quality of individual protein structure models, *Bioinformatics*, 27 (3), 343–350.
- [28] Laskowski, R.A., MacArthur, M.W., Moss, D.S., and Thornton, J.M., 1993, PROCHECK: A program to check the stereochemical quality of protein structures, *J. Appl. Crystallogr.*, 26, 283–291.
- [29] Yusuf, M., Baroroh, U., Hasan, K., Rachman, S.D., Ishmayana, S., and Subroto, T., 2017, Computational model of the effect of a surface-binding site on the *Saccharomycopsis fibuligera* R64 α -amylase to the substrate adsorption, *Bioinf. Biol. Insights*, 11, 1177932217738764.
- [30] Hecht, H.J., Kalisz, H.M., Hendle, J., Schmid, R.D., and Schomburg, D., 1993, Crystal structure of glucose oxidase from *Aspergillus niger* refined at 2.3 Å resolution, *J. Mol. Biol.*, 229 (1), 153–172.
- [31] Janati-Fard, F., Housaindokht, M.R., and Monhemi, H., 2016, Investigation of structural stability and enzymatic activity of glucose oxidase and its subunits, *J. Mol. Catal. B: Enzym.*, 134 (Part A), 16–24.
- [32] Liao, S.M., Du, Q.S., Meng, J.Z., Pang, Z.W., and Huang, R.B., 2013, The multiple roles of histidine in protein interactions, *Chem. Cent. J.*, 7 (1), 44.
- [33] Meyer, E.A., Castellano, R.K., and Diederich, F., 2003, Interactions with aromatic rings in chemical and biological recognition, *Angew. Chem. Int. Ed.*, 42 (11), 1210–1250.
- [34] Yu, H., Yan, Y., Zhang, C., and Dalby, P.A., 2017, Two strategies to engineer flexible loops for improved enzyme thermostability, *Sci. Rep.*, 7, 41212.
- [35] Tsai, M.Y., Zheng, W., Balamurugan, D., Schafer, N.P., Kim, B.L., Cheung, M.S., and Wolynes, P.G., 2016, Electrostatics, structure prediction, and the energy landscapes for protein folding and binding, *Protein Sci.*, 25 (1), 255–269.
- [36] Todde, G., Hovmöller, S., Laaksonen, A., and Mocci, F., 2014, Glucose oxidase from *Penicillium amagasakiense*: Characterization of the transition state of its denaturation from molecular dynamics simulations, *Proteins*, 82 (10), 2353–2363.
- [37] Caves, M.S., Derham, B.K., Jezek, J., and Freedman, R.B., 2011, The mechanism of inactivation of glucose oxidase from *Penicillium amagasakiense* under ambient storage conditions, *Enzyme Microb. Technol.*, 49 (1), 79–87.

Structure and Optical Properties of Al-doped ZnO Nanodrums as Anti-Reflection Coating Material in Solar Cells

Putri Luthfiana Sari¹, Hanik Munawaroh^{1,2}, Sayekti Wahyuningsih^{1,*}, and Ari Handono Ramelan¹

¹Inorganic Material Research Group, Faculty of Mathematics and Natural Sciences, Sebelas Maret University, Kentingan Jebres, Surakarta 57126, Indonesia

²Chemistry Program, Graduate School of Sebelas Maret University, Kentingan Jebres, Surakarta 57126, Indonesia

* **Corresponding author:**

tel: +62-81568455281

email: sayekti@mipa.uns.ac.id

Received: September 30, 2018

Accepted: December 14, 2018

DOI: 10.22146/ijc.39260

Abstract: Al-doped ZnO (AZO) nanodrums were synthesized using hydrothermal method at 80 °C for 20 h using precursor $Zn(CH_3COO)_2 \cdot 2H_2O$ and $Al(OH)(CH_3COO)_2$ as a dopant by varying the addition of Al concentrations in the range of 0, 1, 5, 10, 15, and 20 mM. The variation of Al can affect the crystal growths, structure properties, and optical properties of ZnO. Addition of Al can inhibit the crystal growth with the decrease of the crystal size ranging from about 43.46 to 37.21 nm. Morphology of Al variation doped ZnO of Al was studied using a Scanning Electron Microscope (SEM) and Transmission Electron Microscope (TEM) and showed nanodrums morphology. Optical properties of thin film AZO was evaluated using UV-Visible spectrophotometer. The crystallite size of AZO can affect optical properties with the occurrence of blue shift. The transmission spectra showed that AZO has ~85% transparency in the visible spectra with a sharp peak in the UV region. AZO with the addition of 20 mM Al has the largest transmittance and the lowest reflectance. The thin film with transparent properties is a good candidate for application in the dye-sensitized solar cells, such as anti-reflection coating. AZO (20 mM of Al) was prepared as anti-reflection on the DSSCs system. The best efficiency of DSSCs performance was examined by varying the thickness of the layers of AZO and pointed an efficiency improvement up to 18.29 times.

Keywords: Al-doped ZnO; structure properties; optical properties; anti-reflection coating; DSSCs

■ INTRODUCTION

Dye-sensitized solar cells (DSSCs) is a third generation solar cell which was firstly introduced by Grätzel in 1991 [1]. DSSCs have continued to be developed until now. On DSSCs system, abundant sunlight was reflected, so the efficiency is still low. Scattering of photons in the DSSCs system causes the efficiency of solar cells to be less optimum. Therefore, they need an anti-reflecting material which can increase light harvesting from the thin layers [2].

ZnO is a semiconductor material that has many functions in optoelectronic application [3]. ZnO has about 3.37 eV (at 300 K) band gap energy [4]. It is transparent in visible light areas and has good adhesion and hardness properties. ZnO has a refractive index value

of ± 2 which is convenient to index requirement of anti-reflection coating solar cells [5-6]. Improvement of the optical, physical and electrical properties of ZnO can be conducted using the doping method [7] in order to optimize the transmitted light. Doping means adding impurity atoms (dopant) into the semiconductor crystal structure in order to improve the properties of the semiconductor. The metals such as Ga, In, Sn, Mg, B, and Al were commonly used as substituted dopants into the ZnO structure [8].

Aluminum (Al) is a dopant metal that is able to increase the electrical conductivity of ZnO because it has a smaller ionic radius than ZnO, and it is cheaper than other materials [9]. Sengupta et al. reported that aluminum as a ZnO dopant can improve optical

properties and decrease band gap energy of ZnO [10]. Recently, ZnO which is doped with Al metals is known as Al-doped ZnO (AZO).

In this study, we have prepared AZO with a variation of Al concentrations using a simple and low-cost hydrothermal method. The effect of Al dopant on structural and optical properties of AZO was investigated. The best performing of AZO was applied as an anti-reflection to the DSSCs (dye-sensitized solar cells).

■ EXPERIMENTAL SECTION

Materials

The materials used in this research were $\text{Zn}(\text{CH}_3\text{COO})_2 \cdot 2\text{H}_2\text{O}$ (Aldrich), $\text{Al}(\text{OH})(\text{CH}_3\text{COO})_2$ (Aldrich), Polyethylene glycol 1000 ($\text{HO}(\text{C}_2\text{H}_4\text{O})_n\text{H}$) (Merck), Ethanol (Merck), Ammonia (Merck), KI (Merck), I_2 (Merck), Dye Ruthenium N3 (Aldrich), paste of TiO_2 18 NRT (Dyesol), Platinum paste (Dyesol). Distilled water was obtained from *MIPA Terpadu* laboratory.

Instrumentation

The characterization of crystal structure and crystallite size of AZO were done using X-Ray Diffraction (XRD) Bruker type D8 with anode Cu. The Morphology of AZO was analyzed by Scanning Electron Microscopy (SEM) quanta 250 and Transmission Electron Microscope (TEM) JEOL JEM 1400. The optical properties of AZO were characterized by UV-Visible spectrophotometer Lambda 25 Perkin Elmer. The electrical properties and the efficiency of solar cells were characterized using Current-Voltage (IV) meters Keithley 2602 A. Crystallite size of AZO was calculated by Debye-Scherrer in Eq. (1).

$$D(\text{nm}) = \frac{k\lambda}{B \cos \theta} \quad (1)$$

where D = crystallite size (nm), k = constant value (0.9), λ = the X-ray wavelength (0.15406 nm), B = full width at half the maximum (FWHM) in radians and θ is the Bragg's angle (deg).

Procedure

Synthesis of AZO

AZO was synthesized from 0.1 M $\text{Zn}(\text{CH}_3\text{COO})_2 \cdot 2\text{H}_2\text{O}$ and dopant of $\text{Al}(\text{OH})(\text{CH}_3\text{COO})_2$, as precursors. The precursors were dissolved in distilled water. $\text{Al}(\text{OH})(\text{CH}_3\text{COO})_2$ initial concentration was varied as 1, 5, 10, 15, and 20 mM. Polyethylene Glycol (PEG) 1000 0.1 M was then added to the solution. The mixture was stirred for 60 min. Then, the addition of ammonia to the solution was conducted until the pH of the solution became neutral [7]. The solution was put into a Teflon-lined autoclave for being processed hydrothermally at 80 °C for 20 h. The precipitate was washed using ethanol and distilled water and then dried at 60 °C. The obtained AZO powder was calcinated at 600 °C for 2 h.

DSSCs fabrication

The platinum electrode was coated to a conductive thin film, and the working electrode was arranged with a layer of AZO/ TiO_2 /dye. Then, the working electrode was put on the top of the platinum electrode. Both of electrodes were arranged to be sandwich-form-DSSCs. An electrolyte solution was then dropped into the gap of the sandwich. The solar cells performance was characterized using Keithley 2602 A. The efficiency of DSSCs was calculated by Eq. (2).

$$\eta = \frac{P_{\max}}{P_{\text{in}}} \times 100\% = \frac{V_{\text{oc}} \times I_{\text{sc}} \times \text{FF}}{P_{\text{in}}} \times 100\% \quad (2)$$

where η = efficiency of solar cells (%), P_{\max} = the maximum electrical power output (W/m^2), P_{in} = the solar power input (W/m^2), V_{oc} = the open-circuit voltage (V), I_{sc} = the short-circuit current density (A/m^2), FF (fill factor) = index of loss electric generation.

■ RESULTS AND DISCUSSION

Structure Properties of AZO

Structure of AZO was analyzed from the pattern of XRD peaks (Fig. 1). Characterization results from XRD showed the peaks fit ICSD standard No. 67848 with the

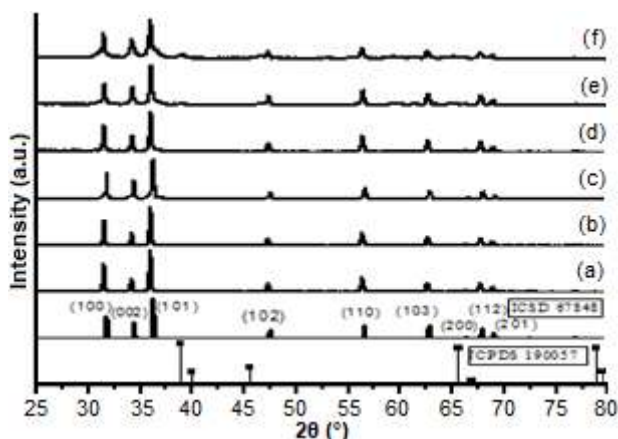


Fig 1. XRD pattern of AZO with Al variation of (a) 0, (b) 1, (c) 5, (d) 10, (e) 15, and (f) 20 mM

hexagonal wurtzite crystal structure. The main peak of AZO showed lattice planes of (100), (002), (101), (102), (110), (103), (200), (112), and (201) of hexagonal wurtzite of ZnO. However, in the AZO with Al variation of 15 and 20 mM, there were peaks that not coincide to the ICSD. Those incompatible peaks were presented at 2θ about 38–39° as the peak of Al according to JCPDS 19-0057. The presence Al peak is due to the addition of a considerable Al concentration of 15 and 20 mM.

The captured peak shift in the plane of (100) (002) and (101) was shown in Fig. 2. The shift of the plane (002) occurred to a larger diffraction angle with increasing of dopant Al, except for the addition of 5 mM Al. Meanwhile, the peak shift of (100) and (101) plane was not significant. The peak shift to larger diffraction angle indicated the inclusion of dopant Al^{3+} ions which have a smaller radius than Zn^{2+} ions into the lattice of ZnO [11-12]. Meanwhile, the shifted peak to a smaller diffraction angle was caused by a tensile voltage that raised distortion in the lattice of ZnO.

The crystallite size was calculated using the Debye-Scherrer equation [13]. The results of the crystallite size showed that the greater of Al concentration was able to decrease the crystallite size (Table 1). AZO crystallite size decreased because the radius of Zn^{2+} ions was greater than Al^{3+} ions ($r_{\text{Al}} = 0.0054$ nm and $r_{\text{Zn}} = 0.074$ nm) and rendered the substitution of Al ions to Zn in the ZnO lattice [14-15]. The substitution caused the cell unit of ZnO to shrink [16].

Morphological appearance of AZO was interpreted by SEM image (Fig. 3). The morphology and particle shape of AZO was nanodrums with the hexagonal cross-sectional shape. The use of Polyethylene glycol 1000 as non-ionic surfactant affected the morphology of AZO at low temperature in the hydrothermal process. This result was similar to the

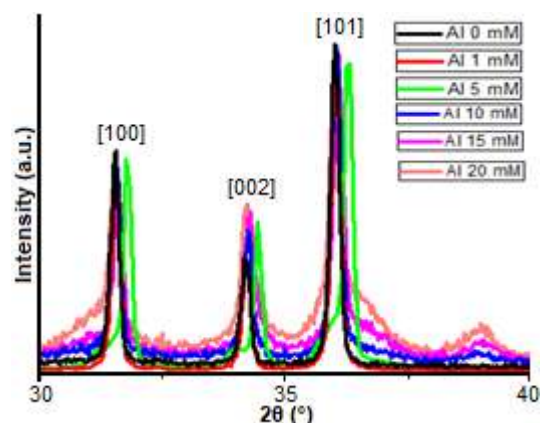


Fig 2. The peak shift of AZO

Table 1. Crystallite size of AZO

Al Concentration (mM)	Crystallite size (D)(nm)
0	43.46
1	43.00
5	42.86
10	41.40
15	40.10
20	37.21

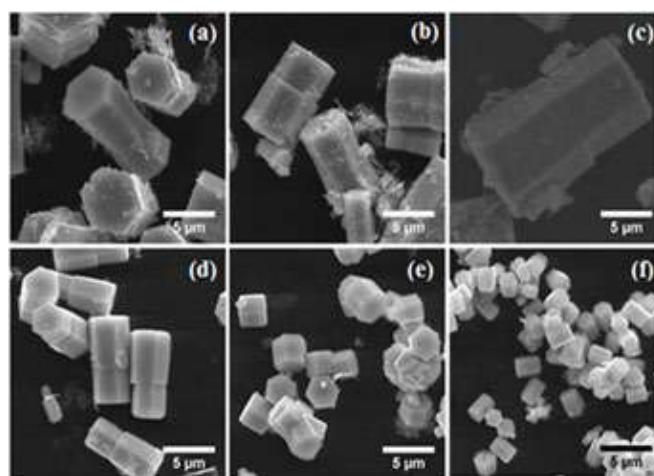
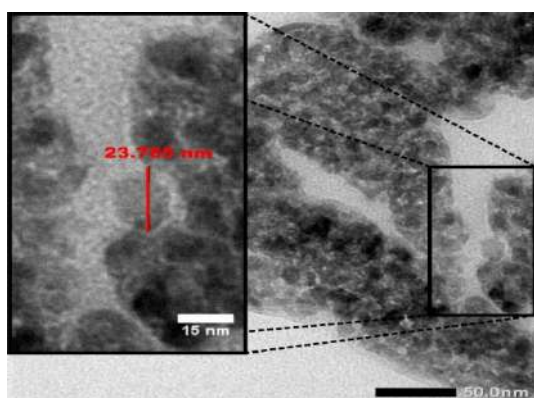


Fig 3. SEM image of AZO with Al variation of (a) 0, (b) 1, (c) 5, (d) 10, (e) 15, and (f) 20 mM

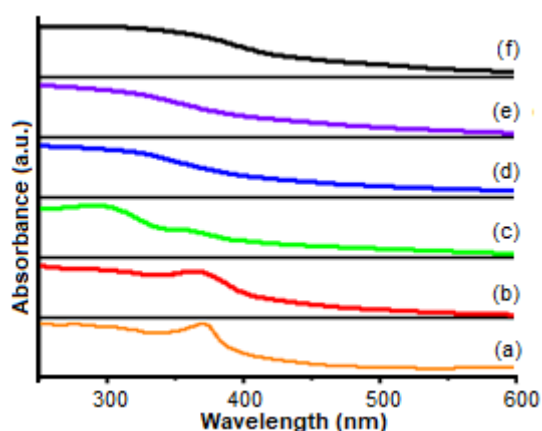
Table 2. The length and diameter of AZO

Al Concentration (mM)	Length (μm)	Diameter (μm)
0	8.36	5.28
1	7.95	4.93
5	16.06	8.53
10	7.24	3.35
15	2.24	3.00
20	2.19	1.59

**Fig 4.** TEM image of AZO with a concentration of 20 mM Al

previous research of Jung and Moo (2014) [17], which stated that the addition of non-ionic surfactants could influence the formation of ZnO nanodrums.

The average particle sizes of AZO seemed to be smaller, but with the addition of Al 5 mM (Fig. 3(c)), the AZO particle size appeared larger. The differences level of polarity (polar face) on the surface of AZO caused greater

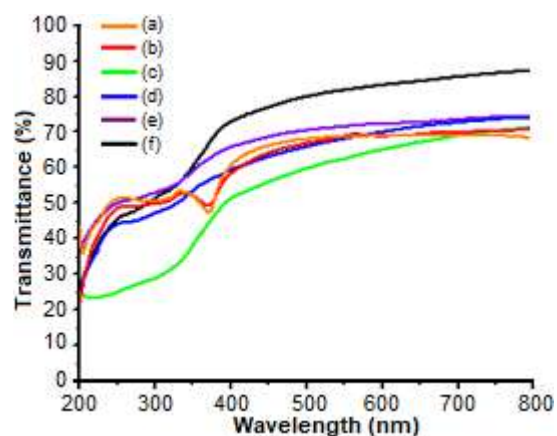
**Fig 5.** Absorbance spectra of AZO with Al variation of (a) 0, (b) 1, (c) 5, (d) 10, (e) 15, and (f) 20 mM

growth of particle sizes. Meanwhile, the addition of 10, 15, and 20 mM Al has contributed to the decrease in length and diameter (Table 2). According to Ridhuan et al. [18], this probably occurred when both polar faces of ZnO crystal contain a high amount of $[\text{Al}(\text{OH})_4]^-$, Al^{3+} was adsorbed to its surface attracting each other and inhibiting the growth of ZnO, and the particle size became smaller. Imaging AZO morphology using TEM (Fig. 4) represented surface of nanodrums clearly. The particle size of AZO (Al 20 mM) is around 23.765 nm. TEM image showed that the ZnO nanodrum was successfully synthesized.

Optical Properties of AZO

Absorbance analysis of AZO (Fig. 5) showed that the addition of Al-dopant stimulated the shifted peak of the AZO to the smaller wavelength (a blue shift phenomenon). The UV-Visible absorption spectra of AZO was in the range 250–369 nm coinciding to a characteristic of absorption spectra for ZnO with hexagonal structures located in the wavelength ranging from 200–400 nm [19].

The transmittance spectra of AZO in Fig. 6 displayed transmittance value in visible light areas in the range 50–90%. The best transmittance value was AZO in addition of 20 mM Al because it has smaller diameter and length. The small particle size enacted the surface area of larger particles to increase the transmitted light [20].

**Fig 6.** Transmittance spectra of AZO with Al variation of (a) 0, (b) 1, (c) 5, (d) 10, (e) 15, and (f) 20 mM

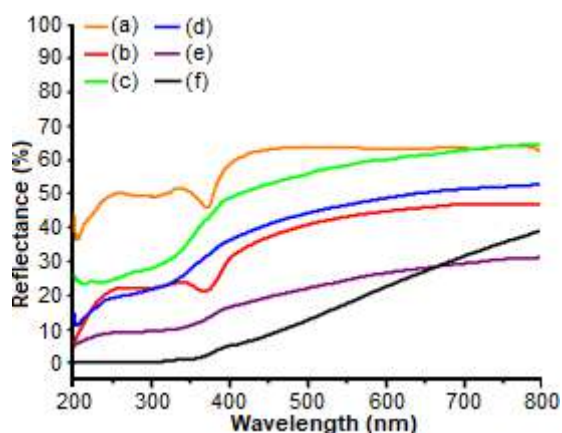


Fig 7. Reflectance spectra of AZO with Al variation of (a) 0, (b) 1, (c) 5, (d) 10, (e) 15, and (f) 20

The addition of Al in the ZnO structure caused a decrease of reflectance value (Fig. 7). The decrease of AZO reflectance was due to differences in light scattering from the effect of different dopants concentrations. The lowest reflectance was obtained in the AZO with the addition of 20 mM Al.

The best optical property was AZO with a concentration of 20 mM Al. Then, the band gap energy of AZO calculated with Kubelka-Munk equation showed that the addition of Al dopant 1, 5, 15, and 20 mM could decrease band gap energy and yield defect in ZnO crystals. The band gap energy of AZO 0 and 20 mM were 3.10 and 3.085 eV, respectively.

AZO Nanodrum as Anti-Reflection Coating on DSSCs

AZO nanodrum with Al concentration of 20 mM are used as anti-reflection since they have a good crystal structure, the lowest reflectance, and the best transmittance among others, whereas ZnO (AZO 0 mM) was used as the control of anti-reflection. Deposition of AZO layer on DSSCs varied in thickness of 1, 2 and 3 layers. The best efficiency of DSSCs performance was achieved by utilizing 1 layer of AZO anti-reflection (Fig. 8), where it improved efficiency up to 18.29 times compared with ZnO (AZO 0 mM).

CONCLUSION

Al-doped ZnO (AZO) nanodrum were successfully synthesized using the hydrothermal method with the

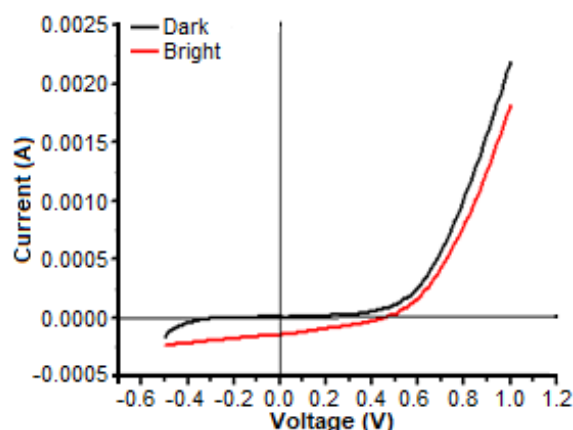


Fig 8. I-V curve of DSSCs with 1 layer of AZO as anti-reflection

addition of varied Al dopant in the range of 0, 1, 5, 10, 15, 20 mM. The variation of Al affected the structure and optical properties of AZO. Increasing concentrations of Al decreased the crystallite size. The optical properties of AZO showed the occurrence of blue shifts in the wavelength 250–369 nm, the decrease of reflectance value and the increase of transmittance value. The addition of 1 layer AZO as an anti-reflection coating on DSSCs provided the best performance as showed by efficiency improvement up to 18.29 times.

ACKNOWLEDGMENTS

The Authors would like to thank Sebelas Maret University for support funding through *Penelitian Mandatory* (Mandatory Research) No. 543/UN27.21/PP/2018.

REFERENCES

- [1] Grätzel, M., 2003, Dye-sensitized solar cells, *J. Photochem. Photobiol., C*, 4 (2), 145–153.
- [2] Wahyuningsih, S., Fadillah, G., Hidayat, R., and Ramelan, A.H., 2016, Thin film ZnO coated on FTO/TiO₂ as an anti-reflection coating for enhancing visible light harvesting in dye sensitized solar cells system, *Procedia Chem.*, 19, 632–637.
- [3] Putri, A.A., Wahyuningsih, T.D., and Kartini, I., 2011, Hydrothermal synthesis of rod and chrysanthemum like nanostructured ZnO, *Indones. J. Chem.*, 11 (2), 131–134.

- [4] Choi, K., Kang, T., and Oh, S.G., 2012, Preparation of disk-shaped ZnO particles using a surfactant and their PL properties, *Mater. Lett.*, 75, 240–243.
- [5] Aslan, M.H., Oral, A.Y., Menşur, E., Gül, A., and Başaran, E., 2004, Preparation of c-axis-oriented zinc-oxide thin films and the study of their microstructure and optical properties, *Sol. Energy Mater. Sol. Cells*, 82 (4), 543–552.
- [6] Vinodkumar, R., Lethy, K.J., Beena, D., Satyanarayana, M., Jayasree, R.S., Ganesan, V., Nayar, V.U., and Pillai, V.P.M., 2009, Effect of thermal annealing on the structural and optical properties of nanostructured zinc oxide thin films prepared by pulsed laser ablation, *Sol. Energy Mater. Sol. Cells*, 93 (1), 74–78.
- [7] Kim, C.E., Moon, P., Kim, S., Myoung, J.M., Jang, H.W., Bang, J., and Yun, I., 2010, Effect of carrier concentration on optical bandgap shift in ZnO:Ga thin films, *Thin Solid Films*, 518 (22), 6304–6307.
- [8] Yun, S., Lee, J., Yang, J., and Lim, S., 2010, Hydrothermal synthesis of Al-doped AZO nanorod arrays on Si substrate, *Physica B*, 405 (1), 413–419.
- [9] Nunes, P., Fortunato, E., Tonello, P., Fernandes, F.B., Vilarinho, P., and Martins, R., 2002, Effect different dopant elements on the properties of ZnO thin films, *Vacuum*, 64 (3-4), 281–285.
- [10] Sengupta, D., Mondal, B., and Mukherjee, K., 2017, Genesis of flake-like morphology and dye-sensitized solar cell performance of AZO particles: A study, *J. Nanopart. Res.*, 19 (3), 100.
- [11] Jeong, C., Kim, H., Chang, D., and Kamisako, K., 2008, Effect on Al₂O₃ doping concentration of RF magnetron sputtered ZnO:Al film for solar cell applications, *Jpn. J. Appl. Phys.*, 47 (7), 5656–5658.
- [12] Zhang, P., Hong, R.Y., Chen, Q., and Feng, W.G., 2014, On the electrical conductivity and photocatalytic activity of aluminium-doped zinc oxide, *Powder Technol.*, 253, 360–367.
- [13] Monshi, A., Foroughi, M.R., and Monshi, M.R., 2012, Modified Scherrer equation to estimate more accurately nano-crystallite size using XRD, *World J. Nano Sci. Eng.*, 2 (3), 154–160.
- [14] Ghazai, A.J., Salman, E.A., and Jabbar, Z.A., 2016, Effect of aluminum doping on zinc oxide thin film properties synthesis by spin coating method, *Am. Sci. Res. J. Eng., Technol., Sci.*, 26 (3), 202–211.
- [15] Sahay, P.P., and Nath, R.K., 2008, Al-doped zinc oxide thin films for liquid petroleum gas (LPG) sensors, *Sens. Actuators, B*, 133 (1), 222–227.
- [16] Shui, A., Wang, S., Wang, H., and Cheng, X., 2009, Preparation and properties for aluminium doped zinc oxide powders with the coprecipitation method, *J. Ceram. Soc. Jpn.*, 117 (5), 703–705.
- [17] Jung, M.H. and Chu, M.J., 2014, Synthesis of hexagonal ZnO nanodisks, nanosheets and nanowires by the ionic effect during the growth of hexagonal ZnO crystals, *J. Mater. Chem. C*, 2 (32), 6675–6682.
- [18] Ridhuan, N.S., Lockman, Z., Aziz, A.A., and Razak, K.A., 2016, Properties of Al-doped ZnO nanorods synthesized using the low-temperature hydrothermal method, *Mater. Sci. Forum*, 846, 459–464.
- [19] Irannejad, A., Janghorban, K., Tan, O.K., Huang, H., Lim, C.K., Tan, P.Y., Fang, X., Chua, C.S., Maleksaeedi, S., Hejazi, S.M.H., Shahjamali, M.M., and Ghaffari, M., 2011, Effect of the TiO₂ shell thickness on the dye-sensitized solar cells with ZnO-TiO₂ core-shell nanorod electrodes, *Electrochim. Acta*, 58, 19–24.
- [20] Hong, C.S., Park, H.H., Moon, J., and Park, H.H., 2006, Effect of metal (Al, Ga, and In)-dopants and/or Ag-nanoparticles on the optical and electrical properties of ZnO thin films, *Thin Solid Films*, 515 (3), 957–960.

New Access to Pyrano[2,3-c]pyrazole-3-carboxylates via Domino Four-Component Reaction and Their Antimicrobial Activity

Muhammad Siddiq Maarop¹, Fatin Nur Ain Abdul Rashid¹, Mohd Fazli Mohammat^{2*}, Zurina Shaameri², Saiful Azmi Johari³, Mazurah Mohamed Isa³, and Anis Low Muhammad Low⁴

¹Department of Chemistry, Faculty of Applied Sciences, Universiti Teknologi MARA, UiTM Shah Alam, 40450 Shah Alam, Selangor, Malaysia

²Organic Chemistry Laboratory, Institute of Science, Universiti Teknologi MARA, Kampus Puncak Alam, 42300 Bandar Puncak Alam, Selangor, Malaysia

³Antimicrobial Laboratory, Anti-Infective Branch, Bioactivity Programme, Natural Products Division, Forest Research Institute Malaysia (FRIM), 52109 Kepong, Selangor, Malaysia

⁴Atta-ur-Rahman Institute (AURINS), Universiti Teknologi MARA, Kampus Puncak Alam, 42300 Bandar Puncak Alam, Selangor, Malaysia

* Corresponding author:

email: mohdfazli@salam.uitm.edu.my

Received: October 10, 2018

Accepted: April 4, 2019

DOI: 10.22146/ijc.39566

Abstract: A library of some novel classes of pyrano[2,3-c]pyrazole-3-carboxylates was synthesized by employing uncatalyzed domino four-component reaction using diethylxaloacetate, hydrazine hydrate, aldehydes and malononitrile in refluxing of ethanol-acetic acid solvent systems. Series of domino reactions involving of pyrazolone formation, Michael addition, and Thorpe-Ziegler cyclization reaction managed to produce the cyclized products from moderate to excellent yield. This protocol provides a reliable, general and salient procedure for the title compound using a one-pot approach. Preliminary biological screening unveiled limited potentials of this class of compounds for antimicrobial lead compound due to its limited solubility properties.

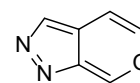
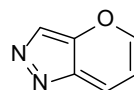
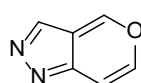
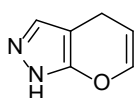
Keywords: four-component reactions; pyrano[2,3-c]pyrazole-3-carboxylate; diethylxaloacetate

■ INTRODUCTION

Isomeric pyranopyrazole structure includes pyrano[2,3-c]pyrazole, pyrano[4,3-c]pyrazole, pyrano[3,2-c]pyrazole and pyrano[3,4-c]pyrazole (Fig. 1). Functionalized pyrano[2,3-c]pyrazoles are the most explored and widely studied and displayed significant roles in pharmaceutical fields. It possesses many interesting biological activities varying from antimicrobial [1], analgesic [2], vasodilator [3], anticancer [4], anti-inflammatory [5], inhibitors of human Chkl

kinase [6], antifungicidal [7] and also as biodegradable agrochemicals [8].

The construction of pyrano[2,3-c]pyrazole structures has been established through different modes of multicomponent reactions (MCRs) either in two-, three- or four-component reactions [9-11]. MCRs are considered convergent one-pot reaction protocol involving two or more of simple yet different starting materials to provide highly complex materials or archetypical molecules with high variability. In addition,



Pyrano[2,3-c]pyrazole Pyrano[4,3-c]pyrazole Pyrano[3,2-c]pyrazole Pyrano[3,4-c]pyrazole

Fig 1. Structures of isomeric pyranopyrazole

MCR approaches also offered multiple advantages including the elimination of complicated purification operations, the use of readily available flexible building blocks as well as solvent and reagent economical purposes [12].

Currently, most MCRs toward constructing the pyranopyrazole ring skeleton involved the reagents of hydrazines, β -ketoesters, aldehydes, and the active methylene nitriles. Interestingly, with regards to our literature searches, there is only a single report that successfully employed diethyl oxaloacetate as the source of the active methylene group. This one-pot reaction was successfully performed by Gein et al. during the synthesis of ethyl 6-amino-4-aryl-5cyano-1,4-dihydropyrano[2,3-c]pyrazole-3-carboxylates, using a four-component two-parallel reaction manner [13]. Previously, diethyl oxalacetate was reported as a non-common source of the active methylene group in most of the MCRs for bearing two active ester groups that prone to undergo different multiple substitution reactions [14].

Initially, replicating four-component two-parallel reaction manner as reported by Gein et al. [13], we managed to synthesize a library of some novel dihydropyrano[2,3-c]pyrazoles-3-carboxylates, but in reasonable yield. Nevertheless, upon changing the original reaction protocol to domino type reaction manner furnished the title compounds and their derivatives from moderate to excellent yields. This library of compounds was then subjected to antimicrobial study as part of our endeavor on the screening of biologically active heterocyclic type compounds [15-18].

■ EXPERIMENTAL SECTION

Materials

All reagents and starting materials were purchased from Sigma-Aldrich Co. and Merck Chemical Co. Thin layer chromatography (TLC) was performed using aluminum precoated sheets (Merck Kieselgel 60 GF₂₅₄, 0.25 mm thick) and was visualized with an ultraviolet lamp (254 and 365 nm). Bacterial species for *in vitro* antibacterial test were *Escherichia coli* (E.C), *Salmonella typhimurium* (S.T), and *Proteus vulgaris* (P.V) as Gram-negative (-ve) and *Staphylococcus aureus* (S.A),

Staphylococcus cohnii (S.C) and *Staphylococcus haemolyticus* (S.H) as Gram-positive.

Instrumentation

Melting points were determined on an automatic FP62 melting point apparatus from Mettler Toledo and are uncorrected. ¹H and ¹³C-NMR spectra were recorded on JOEL NMR Spectrometer instrument operating at 400 MHz at room temperature, in CDCl₃ or DMSO solutions. Chemical shift values are given in δ units (ppm) relative to TMS as an internal standard. IR spectra (4000–400 cm⁻¹) were recorded on Varian Excalibur 3100 FT-IR spectrometer, using ATR. CHNS was performed on Flash Elemental Analyzer 110 series.

The antimicrobial test were performed using Well Diffusion Method, Sample concentration: 5.0 mg/mL (50% DMSO prepared in 2 mL), Incubation temperature: 37 °C, Positive Control: Streptomycin, Chloramphenicol (500 μ g/mL), Negative Control: 50% DMSO.

Procedure

General procedure for the synthesis of pyranopyrazole 5a-5t. (Method A)

To a solution of diethyl oxalacetate sodium salt (5.5 mmol) in 20 mL ethanol, 35% hydrazine solution (5.5 mmol) and 1 mL of acetic acid were added and refluxed for 15 min. Then, carbonyl compound (5 mmol) and malononitrile (5 mmol) were added to the reaction mixture, and the reflux continued for an additional 15 min. The reaction mixture was left to cool, and the resulting solid was filtered off, washed with water.

(5a) Ethyl 6-amino-5-cyano-4-phenyl-1,4-dihydropyrano[2,3-c]pyrazole-3-carboxylate. Following the above mentioned procedure, 5a was isolated as a white solid (82%). m.p 226–227 °C. IR spectrum, ν , cm⁻¹: 3388 (NH₂), 3218 (NH), 2199 (CN), 1716 (COOEt), 1651 (C=C). ¹H-NMR (400 MHz, DMSO): 7.26–7.22 (m, 2H), 7.17–7.13 (m, 1H), 7.06 (m, 2H), 6.99 (s, 2H), 4.71 (s, 1H), 4.06–4.01 (m, 2H), 1.01–0.98 (t, 3H). ¹³C-NMR (100 MHz, DMSO): ¹³C-NMR (100 MHz, DMSO): 160.5 (CNH₂), 158.6 (C=O), 156.1 (CNH), 145.4 (quat. Ar C), 129.5 (C=N), 128.7 (Ar C), 127.8 (ArC), 127.1 (Ar C), 120.8 (CN), 104.1 (quat. C), 61.3 (CH₂), 58.3 (quat.

C), 37.5 (CH), 14.3 (CH₃). Anal. calc. (%) for C₁₆H₁₄N₄O₃, C 61.93, H 4.55 Found: C 62.04; H 4.52.

(5b) Ethyl 6-amino-5-cyano-4-(4-methoxyphenyl)-1,4-dihydropyran[2,3-c]pyrazole-3-carboxylate. Following the above mentioned procedure, 5b was isolated as a white solid (65%), m.p 235–236 °C. IR spectrum, ν , cm⁻¹: 3429 (NH₂), 33180 (NH), 2195 (CN), 1717 (COOEt), 1633 (C=C). ¹H-NMR (400 MHz, DMSO): 7.02–6.97 (m, 2H), 6.95 (s, 2H), 6.81–6.77 (m, 2H), 4.65 (s, 1H), 4.08–4.03 (m, 2H), 3.66 (s, 3H), 1.06–1.03 (t, 3H). ¹³C-NMR (100 MHz, DMSO): 160.4 (CNH₂), 158.7 (C=O), 158.4 (CNH), 137.6 (Ar C), 130.5 (Ar C), 128.8 (Ar C), 127.1 (Ar C), 120.9 (CN), 114.9 (quat. C), 114.1 (quat. C), 104.5 (quat. C), 61.3 (CH₂), 58.6 (quat. C), 55.5 (OCH₃), 36.7 (CH), 14.3 (CH₃). Anal. calc. (%) for C₁₇H₁₆N₄O₄, C 59.99, H 4.74 Found: C 54.59; H 3.51.

(5c) Ethyl 6-amino-5-cyano-4-(4-ethoxyphenyl)-1,4-dihydropyran[2,3-c]pyrazole-3-carboxylate. Following the above mentioned procedure, 5c was isolated as a yellowish solid (60%), m.p 210–211 °C. IR spectrum, ν , cm⁻¹: 3413 (NH₂), 3290 (NH), 2206 (CN), 1740 (COOEt), 1660 (C=C). ¹H-NMR (400 MHz, DMSO): 6.95–6.92 (m, 4H), 6.78–6.76 (m, 2H), 4.64 (s, 1H), 4.05 (m, 2H), 3.91 (m, 2H), 1.25 (t, 3H), 1.04 (t, 3H). ¹³C-NMR (100 MHz, DMSO): 160.4 (CNH₂), 158.7 (C=O), 157.6 (quat. C), 137.4 (quat. Ar C), 129.4 (quat. C), 128.8 (Ar C), 120.9 (CN), 114.5 (Ar C), 104.5 (quat. C), 63.4 (CH₂), 61.3 (CH₂), 58.6 (quat. C), 36.71 (CH), 15.19 (CH₃), 14.3 (CH₃). Anal. calc. (%) for C₁₈H₁₈N₄O₄, C 61.01, H 5.12 Found: C 59.53; H 4.93.

(5d) Ethyl 6-amino-5-cyano-4-(4-ethylphenyl)-1,4-dihydropyran[2,3-c]pyrazole-3-carboxylate. Following the above mentioned procedure, 5d was isolated as a yellowish solid 69%, m.p 212–213 °C. IR spectrum, ν , cm⁻¹: 3433 (NH₂), 3155 (NH), 2194 (CN), 1727 (COOEt), 1631 (C=C). ¹H-NMR (400 MHz, DMSO): 7.08 (dd, 2H), 6.97–6.94 (m, 4H), 4.66 (s, 1H), 4.06–4.01 (m, 2H), 2.51 (m, 2H), 1.65 (t, 3H), 1.02 (t, 3H). ¹³C-NMR (100 MHz, DMSO): 160.5 (CNH₂), 158.7 (C=O), 156.1 (CNH), 142.8 (quat. Ar C), 142.5 (quat. Ar C), 129.4 (quat. C), 128.1 (Ar C), 127.7 (Ar C), 120.9 (CN), 104.3 (quat. C), 61.3 (CH₂), 58.4 (quat. C), 37.1 (CH), 28.1 (CH₂), 16.0 (CH₃), 14.2

(CH₃). Anal. calc. (%) for C₁₈H₁₈N₄O₃, C 63.89, H 5.36 Found: C 64.46, H 5.41.

(5e) Ethyl 6-amino-5-cyano-4-(4-nitrophenyl)-1,4-dihydropyran[2,3-c]pyrazole-3-carboxylate. Following the above mentioned procedure, 5e was isolated as a yellowish solid 75%, m.p 235–237 °C. IR spectrum, ν , cm⁻¹: 3357 (NH₂), 3155 (NH), 2195 (CN), 1723 (COOEt), 1631 (C=C). ¹H-NMR (400 MHz, DMSO): 8.14–8.11 (m, 2H), 7.37–7.33 (m, 2H), 7.15 (s, 2H), 4.92 (s, 1H), 4.05–4.00 (m, 2H), 1.01–0.97 (t, 3H). ¹³C-NMR (100 MHz, DMSO): 160.7 (CNH₂), 158.4 (C=O), 152.7 (CNH), 146.7 (quat. Ar C), 129.5 (quat. C), 129.3 (Ar C), 124.1 (Ar C), 120.4 (CN), 102.7 (quat. C), 61.5 (CH₂), 57.0 (quat. C), 37.1 (CH), 14.3 (CH₃). Anal. calc. (%) for C₁₆H₁₃N₅O₅, C 54.09, H 3.69 Found: C 54.22, H 3.60.

(5f) Ethyl 6-amino-5-cyano-4-(3-nitrophenyl)-1,4-dihydropyran[2,3-c]pyrazole-3-carboxylate. Following the above mentioned procedure, 5f was isolated as a yellowish solid 83%, m.p 224–225 °C. IR spectrum, ν , cm⁻¹: 3432 (NH₂), 3183 (NH), 2189 (CN), 1713 (COOEt), 1635 (C=C). ¹H-NMR (400 MHz, DMSO): 8.07–8.05 (m, 1H), 7.93 (m, 1H), 7.57 (m, 2H), 7.16 (s, 2H), 4.97 (s, 1H), 4.03 (m, 2H), 1.00 (t, 3H). ¹³C-NMR (100 MHz, DMSO): 160.7 (CNH₂), 158.4 (C=O), 155.9 (CNH), 148.1 (quat. Ar C), 147.5 (quat. Ar C), 134.9 (Ar C), 130.5 (Ar C), 129.8 (quat. C), 122.4 (Ar C), 120.5 (CN), 102.8 (quat. C), 61.5 (CH₂), 57.3 (quat. C), 36.9 (CH), 14.2 (CH₃). Anal. calc. (%) for C₁₆H₁₃N₅O₅, C 53.92, H 3.62 Found: C 54.09; H 3.69.

(5g) Ethyl 6-amino-4-(4-bromophenyl)-5-cyano-1,4-dihydropyran[2,3-c]pyrazole-3-carboxylate. Following the above mentioned procedure, 5g was isolated as a white solid 73%, m.p 221–222 °C. IR spectrum, ν , cm⁻¹: 3400 (NH₂), 3174 (NH), 2189 (CN), 1770 (COOEt), 1637 (C=C). ¹H NMR (400 MHz, DMSO): 7.45–7.43 (m, 2H), 7.05 (s, 2H), 7.04–7.01 (m, 2H), 4.73 (s, 1H), 4.07–4.02 (m, 2H), 1.05–1.00 (t, 3H). ¹³C-NMR (100 MHz, DMSO): 160.5 (CNH₂), 158.6 (C=O), 156.0 (CNH), 144.8 (quat. Ar), 131.6 (Ar C), 130.1 (Ar C), 129.6 (quat. C), 120.6 (CN), 103.5 (quat. C), 61.4 (CH₂), 57.8 (quat. C), 36.9 (CH), 14.3 (CH₃). Anal. calc. (%) for C₁₆H₁₃BrN₄O₃, C 49.38, H 3.37 Found: C 48.40, H 3.18.

(5h) Ethyl 6-amino-5-cyano-4-(4-hydroxyphenyl)-1,4-dihydropyrano[2,3-c]pyrazole-3-carboxylate. Following the above mentioned procedure, 5h was isolated as a white solid 57%, m.p 217–218 °C. IR spectrum, ν , cm^{-1} : 3406 (NH_2), 3222 (NH), 2273 (CN), 1731 (COOEt), 1650 ($\text{C}=\text{C}$). $^1\text{H-NMR}$ (400 MHz, DMSO): 9.23 (s, 1H), 6.91 (s, 2H), 6.85–6.82 (s, 2H), 6.63–6.60 (m, 2H), 4.59 (s, 1H), 4.09–4.04 (m, 2H), 1.07–1.03 (t, 3H). $^{13}\text{C-NMR}$ (100 MHz, DMSO): 160.3 (CNH_2), 158.7 ($\text{C}=\text{O}$), 156.4 (CNH), 156.0 (quat. Ar C), 135.9 (quat. Ar C), 129.4 (quat. C), 128.8 (Ar C), 120.9 (CN), 115.4 (Ar C), 104.8 (quat. C), 61.3 (CH_2), 58.8 (quat. C), 36.7 (CH), 14.3 (CH_3). Anal. calc. (%) for $\text{C}_{16}\text{H}_{14}\text{N}_4\text{O}_4$, C 58.89, H 4.32 Found: C 58.91, H 4.31.

(5i) Ethyl 6-amino-4-(3-bromo-4-hydroxyphenyl)-5-cyano-1,4-dihydropyrano[2,3-c]pyrazole-3-carboxylate. Following the above mentioned procedure, 5i was isolated as a white solid 73%, m.p 224–225 °C. IR spectrum, ν , cm^{-1} : 3402 (NH_2), 3320 (NH), 2196 (CN), 1712 (COOEt), 1644 ($\text{C}=\text{C}$). $^1\text{H-NMR}$ (400 MHz, DMSO): 10.12 (s, 1H), 7.15 (m, 1H), 7.00 (s, 2H), 6.85–6.80 (m, 2H), 4.63 (s, 1H), 4.07 (m, 2H), 1.09 (t, 3H). $^{13}\text{C-NMR}$ (100 MHz, DMSO): 160.4 (CNH_2), 158.6 ($\text{C}=\text{O}$), 155.8 (CNH), 153.1 (quat. Ar C), 137.7 (quat. Ar C), 132.1 (Ar C), 129.5 (quat. C), 128.1 (Ar C), 120.8 (CN), 116.7 (quat. Ar C), 109.1 (quat. C), 104.0 (quat. C), 61.4 (CH_2), 58.2 (quat. C), 36.3 (CH), 14.3 (CH_3). Anal. calc. (%) for $\text{C}_{16}\text{H}_{13}\text{BrN}_4\text{O}_4$, C 47.43, H 3.23 Found: C 47.18, H 3.15.

(5j) Ethyl 6-amino-4-(3-chloro-4-hydroxyphenyl)-5-cyano-1,4-dihydropyrano[2,3-c]pyrazole-3-carboxylate. Following the above mentioned procedure, 5j was isolated as a white solid 50%, m.p 228–229 °C. IR spectrum, ν , cm^{-1} : 3406 (NH_2), 3319 (NH), 2202 (CN), 1701 (COOEt), 1649 ($\text{C}=\text{C}$). $^1\text{H-NMR}$ (400 MHz, DMSO): 10.04 (s, 1H), 7.00 (s, 2H), 6.80–6.70 (m, 3H), 4.63 (s, 1H), 4.409–4.07 (m, 2H), 1.08 (t, 3H). $^{13}\text{C-NMR}$ (100 MHz, DMSO): 160.4 (CNH_2), 158.6 ($\text{C}=\text{O}$), 152.1 (CNH), 152.1 (quat. Ar C), 137.4 (quat. Ar C), 129.5 (quat. C), 129.2 (Ar C), 127.4 (Ar C), 120.8 (CN), 119.4 (quat. Ar C), 117.0 (Ar C), 104.0 (quat. C), 61.4 (CH_2), 58.2 (quat. C), 36.4 (CH), 14.3 (CH_3). Anal. calc. (%) for $\text{C}_{16}\text{H}_{13}\text{ClN}_4\text{O}_4$, C 53.27, H 3.63 Found: C 53.02, H 3.57.

(5k) Ethyl 6-amino-5-cyano-4-(4-cyanophenyl)-1,4-dihydropyrano[2,3-c]pyrazole-3-carboxylate. Following the above mentioned procedure, 5k was isolated as a yellowish

solid 74%, m.p 218–219 °C. IR spectrum, ν , cm^{-1} : 3386 (NH_2), 3214 (NH), 2233 (CN), 1713 (COOEt), 1650 ($\text{C}=\text{C}$). $^1\text{H-NMR}$ (400 MHz, DMSO): 7.74–7.72 (m, 2H), 7.28–7.12 (m, 2H), 7.12 (s, 2H), 4.85 (s, 1H), 4.05–4.00 (m, 2H), 0.99 (t, 3H). $^{13}\text{C-NMR}$ (100 MHz, DMSO): 160.6 (CNH_2), 158.4 ($\text{C}=\text{O}$), 156.0 (CNH), 150.7 (quat. Ar C), 132.9 (Ar C), 129.7 (quat. C), 129.0 (Ar C), 120.5 (CN), 119.3 (quat. Ar C), 102.8 (quat. C), 61.4 (CH_2), 57.2 (quat. C), 37.4 (CH), 14.3 (CH_3). Anal. calc. (%) for $\text{C}_{17}\text{H}_{13}\text{N}_5\text{O}_3$, C 60.89, H 3.91 Found: C 62.02, H 3.83.

(5l) Ethyl 6-amino-5-cyano-4-(furan-2-yl)-1,4-dihydropyrano[2,3-c]pyrazole-3-carboxylate. Following the above mentioned procedure, 5l was isolated as a yellowish solid 63%, m.p 216–218 °C. IR spectrum, ν , cm^{-1} : 3404 (NH_2), 3298 (NH), 2192 (CN), 1713 (COOEt), 1644 ($\text{C}=\text{C}$). $^1\text{H-NMR}$ (400 MHz, DMSO): 7.44 (m, 1H), 7.08 (s, 2H), 6.31 (t, 1H), 6.07 (dd, 1H), 4.87 (s, 1H), 4.15–4.11 (m, 2H), 1.13 (t, 3H). $^{13}\text{C-NMR}$ (100 MHz, DMSO): 161.3 (CNH_2), 158.7 ($\text{C}=\text{O}$), 156.0 (CNH), 155.9 (quat. Ar C), 142.4 (Ar C), 129.7 (Ar C), 120.6 (CN), 110.8 (Ar C), 105.9 (quat. C), 61.4 (CH_2), 55.2 (quat. C), 31.2 (CH), 14.3 (CH_3). Anal. calc. (%) for $\text{C}_{14}\text{H}_{12}\text{N}_4\text{O}_4$, C 56.00, H 4.03 Found: C 56.29, H 4.04.

(5m) Ethyl 6-amino-5-cyano-4-(thiophen-2-yl)-1,4-dihydropyrano[2,3-c]pyrazole-3-carboxylate. Following the above mentioned procedure, 5m was isolated as a yellowish solid 65%, m.p 205–207 °C. IR spectrum, ν , cm^{-1} : 3402 (NH_2), 3256 (NH), 2203 (CN), 1729 (COOEt), 1627 ($\text{C}=\text{C}$). $^1\text{H-NMR}$ (400 MHz, DMSO): 7.28 (m, 1H), 7.10 (s, 2H), 6.88–6.86 (m, 2H), 5.08 (s, 1H), 4.16–4.11 (m, 2H), 1.13 (t, 3H). $^{13}\text{C-NMR}$ (100 MHz, DMSO): 160.7 (CNH_2), 158.6 ($\text{C}=\text{O}$), 155.4 (CNH), 141.0 (quat. Ar C), 129.7 (Ar C), 127.1 (Ar C), 124.7 (Ar C), 120.7 (CN), 104.2 (quat. C), 61.5 (CH_2), 58.2 (quat. C), 32.6 (CH), 14.3 (CH_3). Anal. calc. (%) for $\text{C}_{14}\text{H}_{12}\text{N}_4\text{O}_3\text{S}$, C 53.16, H 3.82 Found: C 54.35, H 3.61.

(5n) Ethyl 6-amino-5-cyano-4-ethyl-1,4-dihydropyrano[2,3-c]pyrazole-3-carboxylate. Following the above mentioned procedure, 5n was isolated as a yellowish solid 90%, m.p 180–182 °C. IR spectrum, ν , cm^{-1} : 3421 (NH_2), 3178 (NH), 2192 (CN), 1712 (COOEt), 1633 ($\text{C}=\text{C}$). $^1\text{H-NMR}$ (400 MHz, DMSO): 6.91 (s, 1H), 4.29–4.22 (m, 2H), 3.72 (t, 1H), 1.86–1.79 (s, 1H), 1.69–1.59

(m, 1H), 1.28–1.26 (t, 3H), 0.61–0.58 (t, 3H). ¹³C-NMR (100 MHz, DMSO): 162.2 (CNH₂), 159.0 (C=O), 156.6 (CNH), 121.2 (CN), 103.8 (quat. C), 96.9 (quat. C), 61.6 (CH₂), 54.7 (quat. C), 31.9 (CH), 28.0 (CH₂), 14.5 (CH₃), 8.78 (CH₃). Anal. calc. (%) for C₁₂H₁₄N₄O₃, C 54.96, H 5.38 Found: C 53.85, H 5.57.

(5o) Ethyl 6-amino-5-cyano-4-isopropyl-1,4-dihydro pyrano[2,3-c]pyrazole-3-carboxylate. Following the above mentioned procedure, 5o was isolated as a yellowish solid 91%, m.p 200–201 °C. IR spectrum, ν , cm⁻¹: 3427 (NH₂), 3178 (NH), 2192 (CN), 1712 (COOEt), 1633 (C=C). ¹H-NMR (400 MHz, DMSO): 6.98 (s, 2H), 4.30–4.21 (m, 2H), 3.57 (d, 1H), 2.00–1.97 (m, 1H), 1.25 (t, 3H), 0.93 (t, 3H), 0.57 (t, 3H). ¹³C-NMR (100 MHz, DMSO): 163.5 (CNH₂), 159.1 (C=O), 156.9 (CNH), 128.7 (quat. C), 122.3 (CN), 105.2 (quat. C), 61.5 (CH₂), 51.6 (quat. C), 37.6 (CH), 35.4 (CH), 20.7, 17.1 (CH₃). Anal. calc. (%) for C₁₃H₁₆N₄O₃, C 56.51, H 5.84 Found: C 56.18, H 5.85.

(5p) Ethyl 6-amino-5-cyano-4-heptyl-1,4-dihydropyrano [2,3-c]pyrazole-3-carboxylate. Following the above mentioned procedure, 5p was isolated as a yellowish solid 11%, m.p 204–206 °C. IR spectrum, ν , cm⁻¹: 3427 (NH₂), 3178 (NH), 2192 (CN), 1712 (COOEt), 1633 (C=C). ¹H-NMR (400 MHz, DMSO): 6.88 (s, 2H), 4.32–4.26 (m, 2H), 3.70 (t, 1H), 1.75 (m, 1H), 1.56 (m, 1H), 1.27 (t, 3H), 1.16 (m, 10H), 0.83 (t, 3H). ¹³C-NMR (100 MHz, DMSO): 162.0 (CNH₂), 159.0 (C=O), 156.4 (CNH), 129.0 (quat. C), 121.2 (CN), 104.5 (quat. C), 61.5 (CH₂), 55.2 (quat. C), 35.8 (CH), 31.6 (CH), 31.1 (CH₂), 29.3 (CH₂), 29.0 (CH₂), 24.0 (CH₂), 22.5 (CH₂), 14.5 (CH₃), 14.4 (CH₃). Anal. calc. (%) for C₁₇H₂₄N₄O₃, C 61.43, H 7.28 Found: C 61.44, H 7.22.

(5q) Ethyl 6'-amino-5'-cyano-2-oxo-1'H-spiro[indoline-3,4'-pyrano[2,3-c]pyrazole]-3'-carboxylate. Following the above mentioned procedure, 5q was isolated as a yellowish solid 69%, m.p 270–271 °C. IR spectrum, ν , cm⁻¹: 3371 (NH₂), 3165 (NH), 2187 (CN), 1713 (COOEt), 1648 (C=C). ¹H-NMR (400 MHz, DMSO): 0.86–0.89 (t, 3H), 3.85–3.88 (q, 2H), 6.81–6.92 (m, 3H), 7.13–7.15 (m, 1H), 7.25 (s, 2H), 10.55 (s, 1H). ¹³C-NMR (100 MHz, DMSO): 178.0 (C=O), 161.5 (CNH₂), 158.1 (C=O), 142.6 (CNH), 134.6 (Ar C), 129.0 (Ar C), 124.2 (Ar C), 122.6 (CN), 118.5 (Ar C), 109.8 (quat. C), 100.6 (quat. C), 61.3 (CH₂), 57.3

(quat. C), 48.0 (quat. C), 14.0 (CH₃). Anal. calc. (%) for C₁₇H₁₃N₅O₄, C 58.12, H 3.73 Found: C 57.89, H 3.68.

(5r) Ethyl 6-amino-5-cyano-5'-(4-methoxyphenyl)-1'-methyl-2'-oxo-1H-spiro[pyrano[2,3-c]pyrazole-4,3'-pyrrolidine]-3-carboxylate. Following the above mentioned procedure, 5r was isolated as a yellowish solid 26%, m.p 212–214 °C. IR spectrum, ν , cm⁻¹: 3366 (NH₂), 3193 (NH), 2193 (CN), 1733 (COOEt), 1672 (C=C). ¹H-NMR (400 MHz, DMSO): 1.26–1.30 (t, 3H), 1.96–2.01 (dd, 1H), 2.51 (s, 3H), 2.83–2.86 (dd, 1H), 3.72 (s, 3H), 4.31–4.33 (q, 2H), 4.63–4.67 (t, 1H), 6.89–6.92 (m, 2H), 7.09 (s, 2H), 7.33–7.35 (d, 2H). ¹³C-NMR (100 MHz, DMSO): 173.8 (C=O), 161.0 (CNH₂), 159.4 (quat. Ar C), 158.5 (C=O), 155.6 (quat. C), 133.8 (quat. Ar C), 128.9 (quat. C), 128.0 (Ar C), 120.5 (CN), 114.6 (Ar C), 105.2 (quat. C), 62.0 (CH₂), 61.3 (CH), 60.9 (quat. C), 55.6 (NCH₃), 40.4 (CH₂), 40.2 (quat. C), 29.3 (OCH₃), 14.6 (CH₃). Anal. calc. (%) for C₂₁H₂₁N₅O₅, C 59.57, H 5.00 Found: C 59.72, H 5.20.

(5s) Ethyl 6-amino-5-cyano-2',3',5',6'-tetrahydro-1H-spiro[pyrano[2,3-c]pyrazole-4,4'-thiopyran]-3-carboxylate. Following the above mentioned procedure, 5s was isolated as a yellowish solid 19%, m.p 190–191 °C. ¹H-NMR (400 MHz, DMSO-D₆): δ 6.85 (s, NH₂), 4.31 (q, 2H), 3.48 (td, 2H), 2.69–2.60 (td, 2H), 2.40 (d, 2H), 1.92 (d, 2H), 1.31 (t, 3H); ¹³C-NMR (100 MHz DMSO): 161.5 (CNH₂), 158.7 (C=O), 154.6 (CNH), 129.1 (quat. C), 124.5 (CN), 110.3 (quat. C), 61.9 (CH₂), 59.0 (quat. C), 36.8 (quat. C), 33.2 (2XCH₂), 23.4 (2XCH₂), 14.63 (CH₃). Anal. calc. (%) for C₁₄H₁₆N₄O₃S, C 52.49, H 5.03 Found: C 52.49, H 5.07.

(5t) Ethyl 6'-amino-5'-cyano-1-methyl-1'H-spiro[pipe ridine-4,4'-pyrano[2,3-c]pyrazole]-3'-carboxylate [5t]. Following the above mentioned procedure, 5t was isolated as a yellowish solid 23%, m.p 200–202 °C. ¹H-NMR (400 MHz, DMSO-D₆): δ 6.80 (s, NH₂), 4.30 (q, 2H), 3.45 (td, 2H), 3.01 (s, CH₃), 2.69–2.60 (td, 2H), 2.40 (d, 2H), 1.92 (d, 2H), 1.31 (t, 3H); ¹³C-NMR (100 MHz DMSO): 161.5 (CNH₂), 158.7 (C=O), 154.6 (CNH), 129.1 (quat. C), 124.5 (CN), 110.3 (quat. C), 61.9 (CH₂), 59.0 (quat. C), 36.8 (quat. C), 35.8 (CH₃), 33.2 (2XCH₂), 23.4 (2XCH₂), 14.63 (CH₃).

■ RESULTS AND DISCUSSION

First dihydropyrano[2,3-*c*]pyrazole-3-carboxylate type compounds were successfully reported by Gein et al. via one-pot two-parallel reaction manners [13]. These reactions proceeded by short boiling of aromatic aldehydes and malononitrile to give intermediates of arylidenemalonodinitrile. Subsequent addition of the pre-formed pyrazolone upon reacting hydrazine hydrate, diethyl oxaloacetate, and acetic acid onto the prepared reaction of aromatic aldehydes and malononitrile led to the cyclized products from moderate to excellent yield. Replicating the exact Gein's reaction protocol and using similar of hydrazine hydrate, diethyl oxalacetate, benzaldehyde and malononitrile as our reaction model indeed furnished us the cyclized product **5a** but in a reasonable yield of 35%. Attempts on optimization by changing the reaction solvent from mono- to biphasic solvent systems also led to similar reasonable yields (Table 1, Entries 1-6) [11]. Realizing the complexity of the previous reaction protocol we then subjected our reaction model employing domino fashion type of reaction in acidic ethanolic solution which surprisingly furnished us with the cyclized product **5a** in 82% yield (Table 1, Entry 7) (Scheme 1, Method A). The fact that addition of selected known MCRs catalysts as towards optimization steps do not contribute to much higher yield indicates that this catalyst-free domino type MCRs was already performed optimally (Table 1, Entries 8-11).

To probe the generality of this methodology, this method was then extended using a variety of carbonyl functionalities (aromatic, aliphatic, heteroaromatic and diketo compounds). The details of the reaction protocol and the product structure of dihydropyrano[2,3-*c*]pyrazole-3-carboxylates (**5a-5t**) are depicted in Table 2 (Scheme 1, method A). The nature of the substituents on the aromatic ring of the aldehydes displayed a significant effect on the product yields. Aromatic aldehydes bearing electron-withdrawing groups such as nitro, cyano, and halogens (Table 2, Entries 5-11) undoubtedly contributed to much higher yields (74–83%) of the cyclized products as compared to those with electron-donating groups (60–69%) (Table 2, Entries 2-4). This was due to the induced electrophilicity of the aromatic aldehydes from the electron withdrawing group of compounds **5e-5h**. Likewise, heteroaromatic aldehydes of furan-2-carbaldehyde and thiophene-2-carbaldehyde also readily underwent the same sequence of reactions yielding their respected cyclized products in reasonable of 63 and 65% yields (Table 2, Entries 12-13).

Previously, many aliphatic aldehydes were reported not ready to be used as electrophiles in one-pot reaction procedures due to their tendency to undergo self-condensation or Cannizzaro-type reactions [19]. Nevertheless, via our domino-type reaction method, alkylated-pyranopyrazole-type compounds were successfully synthesized by using propanal and 2-methyl propanol in excellent yields (Table 2, Entries 14-15).

Table 1. Synthesis of **5a** in different solvents and reaction conditions

Entry	Solvent	Time (min)	Catalyst	Yield (%)
1	methanol	90	-	18 ^a
2	water	90	-	-
3	ethanol	90	-	29 ^a
4	ethanol:water (1:1)	90	-	-
5	ethanol:water (9:1)	90	-	18 ^a
6	ethanol:acetic acid	90	-	35 ^a
7	ethanol:acetic acid	30	-	82 ^b
8	ethanol:acetic acid	30	Triethylamine	82 ^b
9	ethanol:acetic acid	30	Potassium carbonate	84 ^b
10	ethanol:acetic acid	30	Ammonium acetate	86 ^b
11	ethanol:acetic acid	30	Piperidine	87 ^b

^a Gein's four-component two-parallel reaction manner, ^b Domino one-pot four-component reaction manners

Table 2. Synthesis of dihydropyrano[2,3-*c*]pyrazole-3-carboxylates (**5a-t**)

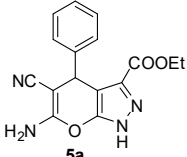
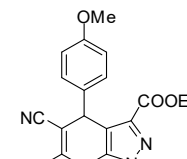
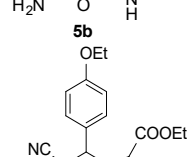
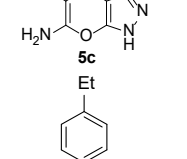
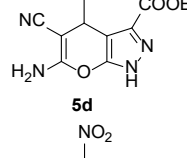
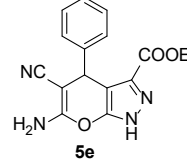
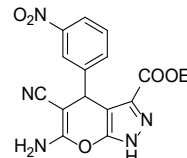
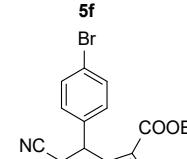
Entry	Product	Time (min)	Yield (%) Method A/B	m.p (°C)
1	 5a	30	35 ^a , 82 ^b	226-227
2	 5b	30	34 ^a , 65 ^b	235-236
3	 5c	30	15 ^a , 60 ^b	210-211
4	 5d	30	69 ^b	212-213
5	 5e	30	33 ^a , 75 ^b	235-237
6	 5f	30	83 ^b	224-225
7	 5g	30	37 ^a , 73 ^b	221-222
8	 5h	30	34 ^a , 57 ^b	217-218

Table 2. Synthesis of dihydropyrano[2,3-c]pyrazole-3-carboxylates (**5a-t**) (*Continued*)

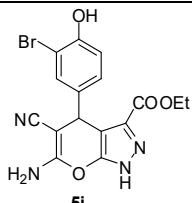
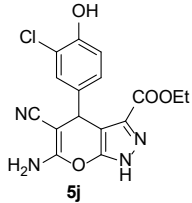
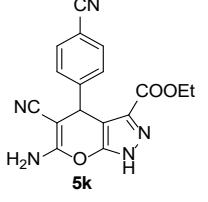
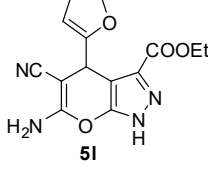
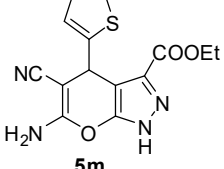
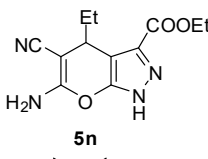
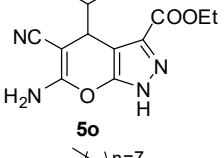
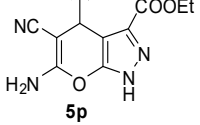
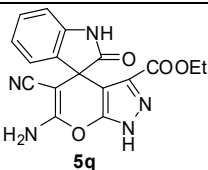
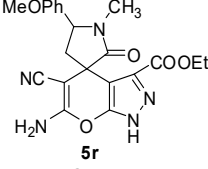
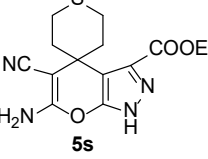
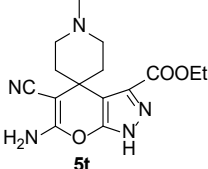
Entry	Product	Time (min)	Yield (%) Method A/B	m.p (°C)
9	 5i	30	73 ^b	224-225
10	 5j	30	50 ^b	228-229
11	 5k	30	10 ^a , 74 ^b	218-219
12	 5l	30	22 ^a , 63 ^b	216-218
13	 5m	30	18 ^a , 65 ^b	205-207
14	 5n	30	90 ^b	180-182
15	 5o	30	5 ^a , 91 ^b	190-192
16	 5p	30	5 ^a , 11 ^b	200-203

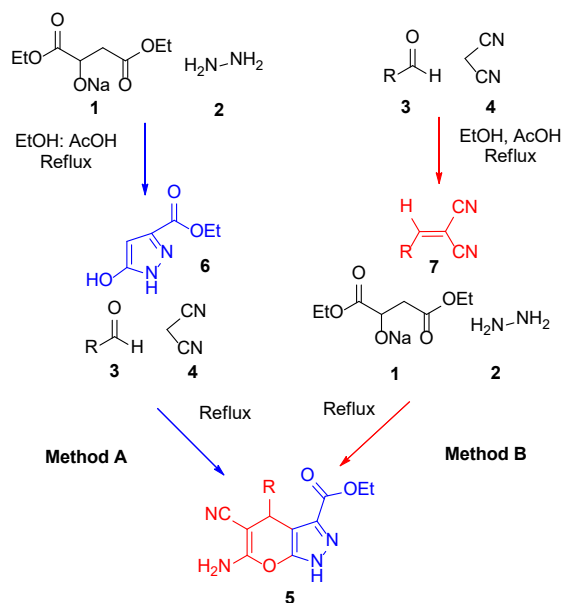
Table 2. Synthesis of dihydropyrano[2,3-*c*]pyrazole-3-carboxylates (**5a-t**) (Continued)

Entry	Product	Time (min)	Yield (%) Method A/B	m.p (°C)
17		30	69 ^b	270-271
18		30	26 ^b	212-214
19		30	19 ^b	190-191
20		30	23 ^b	200-202

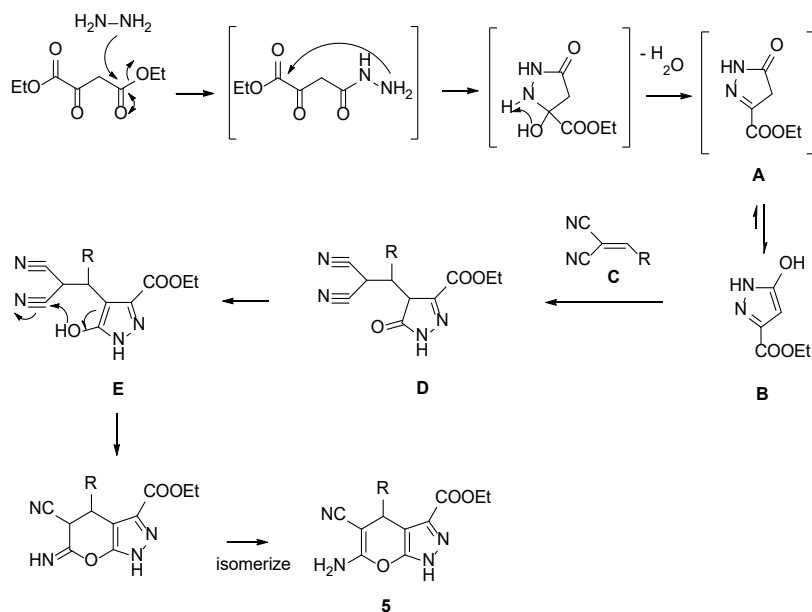
In spite of that, the product yield of an alkylated-pyranopyrazole was observed to decrease significantly upon increasing the aliphatic chain length (Table 2, Entry 16). Further advance of non-optimized MCRs reaction by employing diketone compounds had also successfully furnished us the interesting novel spiropyrano-pyrazole carboxylate type of compounds in reasonable yields (Table 2, Entries 17-20).

In a different mechanistic study, a reverse domino one-pot reaction manner was also performed in which arylidenemalonodinitrile intermediates, **7** were synthesized prior to reacting malononitrile and an aromatic aldehyde. Later hydrazine and diethyl oxaloacetate were added onto the reactions. Interestingly, such reverse domino one-pot reaction manner failed to furnish high yields of the cyclized products (5–37%) as many unwanted side products were observed from the T.L.C (Scheme 1, Method B) (Table 2, Entries 1-3, 5, 7-8, 11-13, 15-16).

Based on the above findings, the best plausible mechanism for the synthesis of (**5**) is proposed (Scheme 2).

**Scheme 1.** Different approaches in synthesizing dihydropyrano[2,3-*c*]pyrazoles (**5**)

Pyrazolone (**A**) was initially formed upon condensation of the diethyl oxaloacetate salt with hydrazine, followed by intramolecular nucleophilic cyclization and elimination



Scheme 2. Plausible mechanism for the synthesis of 5(a-t)

Table 3. Antimicrobial screening results

Compound	Gram -ve			Gram +ve		
	E.C	S.T	P.V	S.A	S.C	S.H
5a	-	-	-	-	-	-
5b	-	-	-	-	-	-
5c	-	-	-	-	-	-
5d	-	-	-	-	-	-
5e	-	-	-	-	-	-
5f	-	-	-	-	-	-
5g	-	-	-	-	-	-
5h	-	-	-	-	-	-
5i	-	-	-	-	-	-
5j	-	-	-	-	-	-
5k	-	-	-	-	-	-
5l	-	-	-	-	-	-
5m	-	-	14.0	-	10.5	17.0
5n	-	-	-	-	-	-
5o	-	-	-	-	-	-
5p	-	-	-	-	-	-
+ve Control	17.0	19.0	16.5	18.0	22.0	19.0
-ve Control	-	-	-	-	-	-

Values are mean inhibition zone (mm); No inhibition (-)

E.C = *Escherichia coli*, S.T = *Salmonella typhimurium*, P.V = *Proteus vulgaris*, S.A = *Staphylococcus aureus*, S.C = *Staphylococcus cohnii* (clinical strain), S.H = *Staphylococcus haemolyticus*.

of water. Pyrazolone (A) then underwent tautomerization to a more active enolicpyrazolone (B) in which subsequent reaction with pre-synthesized aryl/alkylidene

malonodinitriles (C) furnished intermediates (D) via Michael-type reaction. Finally, intermediates (D) isomerized to compounds (E), which then underwent

Thorpe-Ziegler intramolecular cyclization to yield the final products of dihydropyrano[2,3-*c*]pyrazol-3-carboxylates (5). In every step of the synthetic transformation, acetic acid was anticipated to play a significant role in increasing the solubility of the diethyl oxaloacetate sodium salt in ethanol and also as a proton donor.

As for antimicrobial screening, study shows that the presence of thiophene ring in the structure of **5m** enhances its activity against *Proteus vulgaris* (P.V), *Staphylococcus cohnii* (S.C), and *Staphylococcus haemolyticus* (S.H). It was also reasoned that limited solubility for most of the compound also contributed to this low antimicrobial activity properties for other pyrano-pyrazole analogs (Table 3).

■ CONCLUSION

In summary, a salient reaction protocol using domino one-pot, four-component approach towards generating pyranopyrazole-carboxylate type compounds has been developed. This protocol was found applicable for both aromatic and aliphatic aldehydes which make it a useful for the synthesis of a different class of pyranopyrazoles under green catalyst-free MCRs reaction. Nevertheless, biological screening of this spiro-pyranopyrazole type compounds revealed limited potential of these compounds for antimicrobial agents.

■ ACKNOWLEDGMENTS

The authors would like to acknowledge Universiti Teknologi MARA and Malaysian Government (MOHE) for the financial support (600-IRMI/FRGS 5/3 (0071/2016).

■ REFERENCES

- [1] Mistry, P.T., Kamdar, N.R., Haveliwala, D.D., and Patel, S.K., 2012, Synthesis, characterization, and *in-vitro* biological studies of some novel pyran fused pyrimidone derivatives, *J. Heterocycl. Chem.*, 49 (2), 349–357.
- [2] Kuo, S.C., Huang, L.J., and Nakamura, H., 1984, Studies on heterocyclic compounds. 6. Synthesis and analgesic and antiinflammatory activities of 3,4-dimethylpyrano[2,3-*c*]pyrazol-6-one derivatives, *J. Med. Chem.*, 27 (4), 539–544.
- [3] Ahluwalia, V.K., Dahiya, A., and Garg, V., 1997, Reaction of 5-amino-4-formyl-3-methyl(or phenyl)-1-phenyl-1H-pyrazoles with active methylene compounds: Synthesis of fused heterocyclic rings, *Indian J. Chem., Sect B*, 36 (1), 88–90.
- [4] Wang, J.L., Liu, D., Zheng, Z.J., Shan, S., Han, X., Srinivasula, S.M., Croce, C.M., Alnemri, E.S., and Huang, Z., 2009, Structure-based discovery of an organic compound that binds Bcl-2-protein and induces apoptosis of tumor cell, *Proc. Natl. Acad. Sci. U.S.A.*, 97 (13), 7124–7129.
- [5] Mandha, S.R., Siliveri, S., Alla, M., Bommena, V.R., Bommineni, M.R., and Balasubramanian, S., 2012, Eco-friendly synthesis and biological evaluation of substituted pyrano[2,3-*c*]pyrazoles, *Bioorg. Med. Chem. Lett.*, 22 (16), 5272–5278.
- [6] Foloppe, N., Fisher, L.M., Howes, R., Potter, A., Robertson, A.G.S., and Surgenor, A.E., 2006, Identification of chemically diverse Chk1 inhibitors by receptor-based virtual screening, *Bioorg. Med. Chem.*, 14 (14), 4792–4802.
- [7] Ramiz, M.M.M., Hafiz, I.S.A., Rahim, M.A.M.A., and Gaber, H.M., 2012, Pyrazolones as building blocks in heterocyclic synthesis: Synthesis of new pyrazolopyran, pyrazolopyridazine and pyrazole derivatives of expected antifungicidal activity, *J. Chin. Chem. Soc.*, 59 (1), 72–80.
- [8] Kiyani, H., Samimi, H.A., Ghorbani, F., and Esmaili, S., 2013, One-pot, four-component synthesis of pyrano[2,3-*c*]pyrazoles catalyzed by sodium benzoate in aqueous medium, *Curr. Chem. Lett.*, 2 (4), 197–206.
- [9] Otto, S., and Engberts, J.B.F.N., 2000, Diels Alder reactions in water, *Pure Appl. Chem.*, 72 (7), 1365–1372.
- [10] Shestopalov, A.M., Emel'yanova, Y.M., Shestopalov, A.A., Rodinovskaya, L.A., Niazimbetova, Z.I., and Evans, D.H., 2003, Cross-condensation of derivatives of cyanoacetic acid and carbonyl compounds. Part 1: Single-stage synthesis of 1'-substituted 6-amino-spiro-4-(piperidine-4')-2H,4H-pyrano[2,3-*c*]pyrazole-5-carbonitriles, *Tetrahedron*, 59 (38), 7491–7496.

- [11] Zonouz, A.M., Eskandari, I., and Khavasi, H.R., 2012, A green and convenient approach for the synthesis of methyl 6-amino-5-cyano-4-aryl-2,4-dihydropyrano [2,3-*c*]pyrazole-3-carboxylates via a one-pot, multi-component reaction in water, *Tetrahedron Lett.*, 53 (41), 5519–5522.
- [12] Weber, L., 2002, Multi-component reactions and evolutionary chemistry, *Drug Discovery Today*, 7 (2), 143–147.
- [13] Gein, V.L., Zamaraeva, T.M., and Kozulina, I.V., 2014, New synthesis of ethyl 6-amino-4-aryl-5-cyano-1,4-dihydropyrano[2,3-*c*]pyrazole-3-carboxylates, *Russ. J. Org. Chem.*, 50 (5), 691–693.
- [14] Kumler, W.D., Kun, E., and Shoolery, J.N., 1962, The enolization of oxaloacetic acid, diethyl oxaloacetate, and diethyl fluorooxaloacetate as determined by NMR analyses, *J. Org. Chem.*, 27 (4), 1165–1167.
- [15] Mohammad, M.F., Shaameri, Z., and Hamzah, A.S., 2009, Synthesis of 2,3-dioxo-5-(substituted) arylpyrroles and their 2-oxo-5-aryl-3-hydrazone pyrrolidine derivatives, *Molecules*, 14 (1), 250–256.
- [16] Mohammad, M.F., Najim, N., Mansor, N.S., Sarman, S., Shaameri, Z., Zain, M.M., and Hamzah, A.S., 2011, Synthesis and bioactivity of some 2-oxo-5-aryl-3-hydrazone and 2-oxo-5-aryl-4-hydrazone pyrrolidine derivatives, *Arkivoc*, 2011 (9), 429–438.
- [17] Johari, S.A., Mohtar, M., Syed Mohammad, S.A., Mohammad, M.F., Sahdan, R., Mohamed, A., and Mohamad Ridhwan, M.J., 2017, *In vitro* evaluations and *in vivo* toxicity and efficacy studies of MFM501 against MRSA, *Biomed Res. Int.*, 2017, 8032865.
- [18] Johari, S.A., Mohtar, M., Syed Mohammad, S.A., Sahdan, R., Shaameri, Z., Hamzah, A.S., and Mohammad, M.F., 2016, *In vitro* inhibitory and cytotoxic activity of MFM 501, a novel codonopsinine derivative, against methicillin-resistant *Staphylococcus aureus* clinical isolates, *Biomed Res. Int.*, 2015, 823829.
- [19] Khalil, T., Manouchehr, M., Nosrat, O.M., and Elahe, K., 2009, Ruthenium-catalyzed cross aldol reaction with aldehydes and ketones, *Arkivoc*, 2009 (2) 68–75.

Supplementary Data

This supplementary data is a part of paper entitled “*Facile Synthesis, Characterization and in vitro Antibacterial Efficacy of Functionalized 2-Substituted Benzimidazole Motifs*”.

Spectra for Characterization

¹H-NMR Spectra

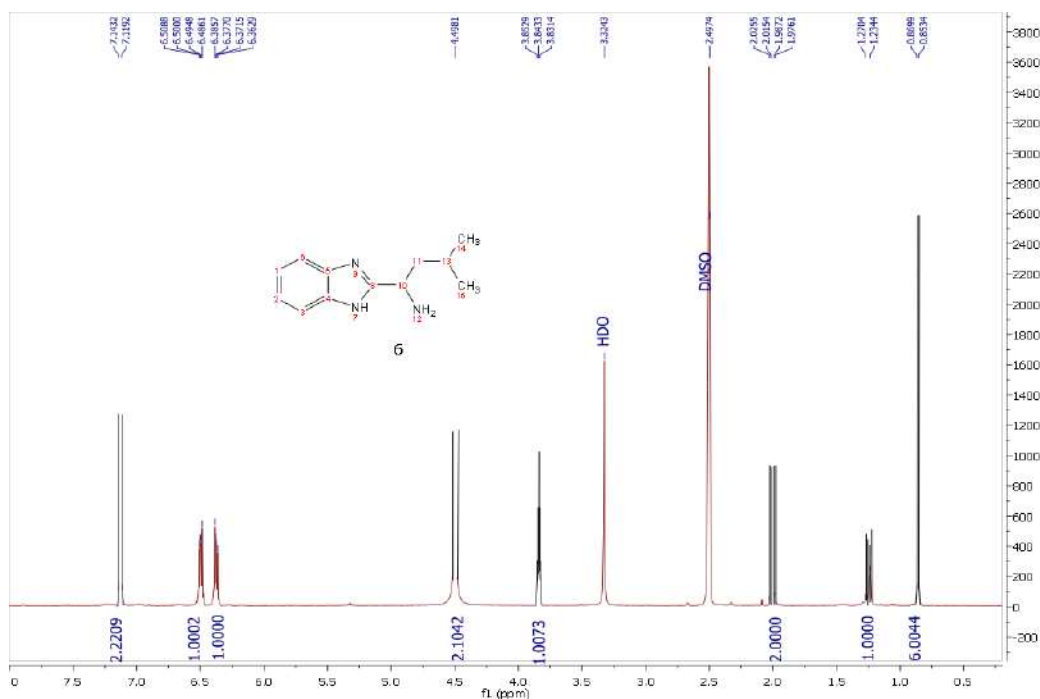


Fig. S1: ¹H-NMR spectrum of 1-(1*H*-benzo[*d*]imidazol-2-yl)-3-methylbutan-1-amine 6

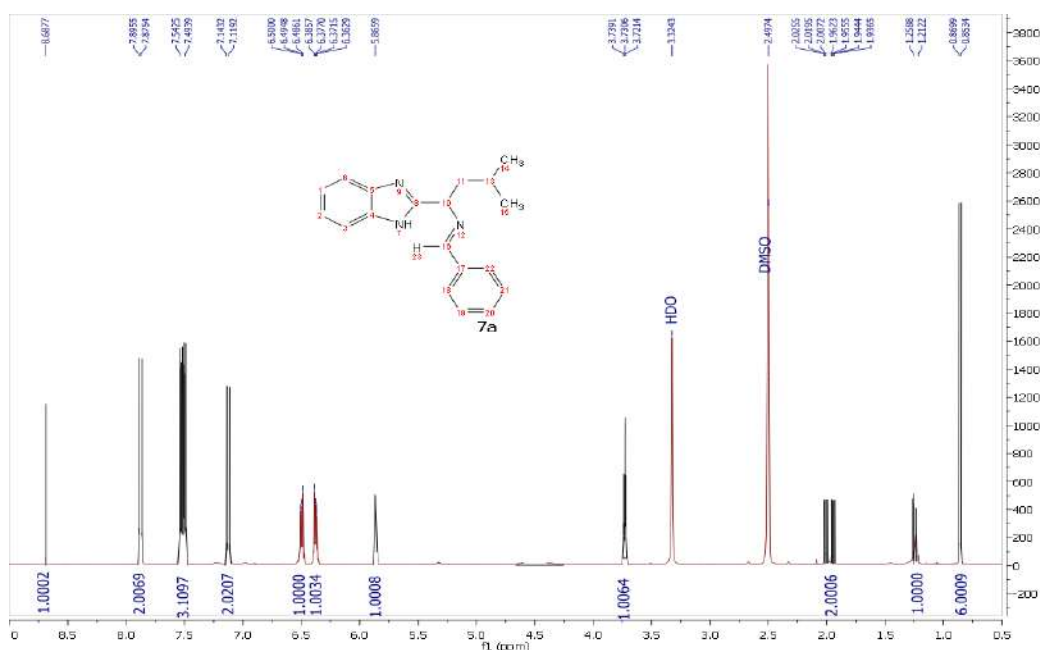


Fig. S2: ¹H-NMR spectrum of 1-(1*H*-benzo[*d*]imidazol-2-yl)-*N*-benzylidene-3-methylbutan-1-amine 7a

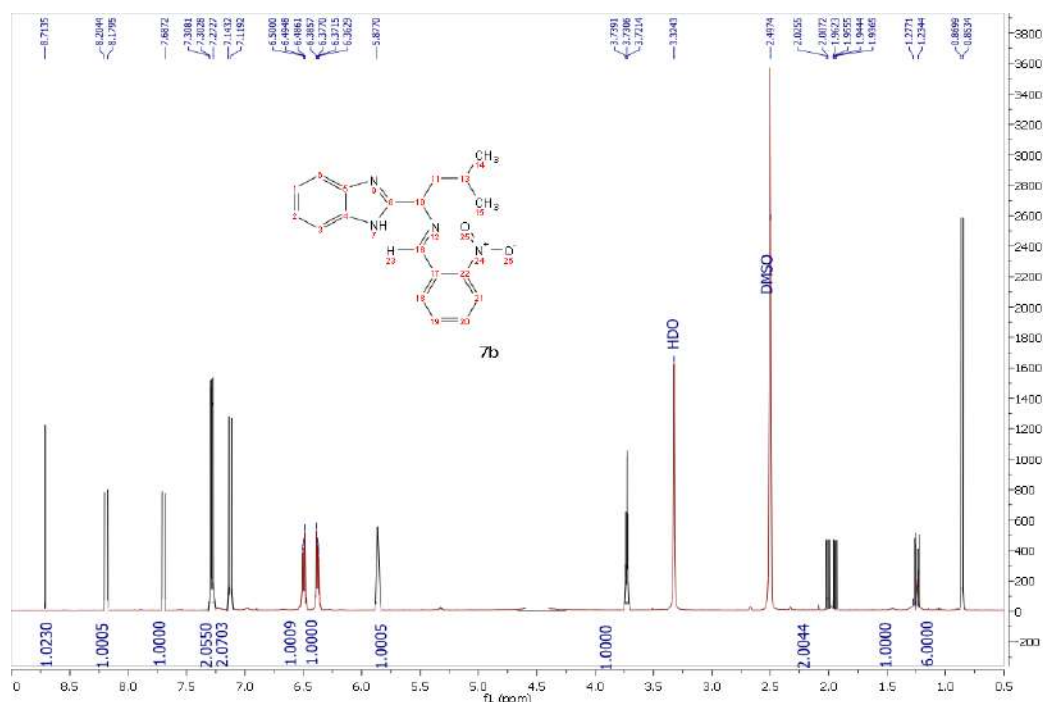


Fig. S3: $^1\text{H-NMR}$ spectrum of 1-(1*H*-benzo[d]imidazol-2-yl)-3-methyl-*N*-(2-nitrobenzylidene)butan-1-amine 7b

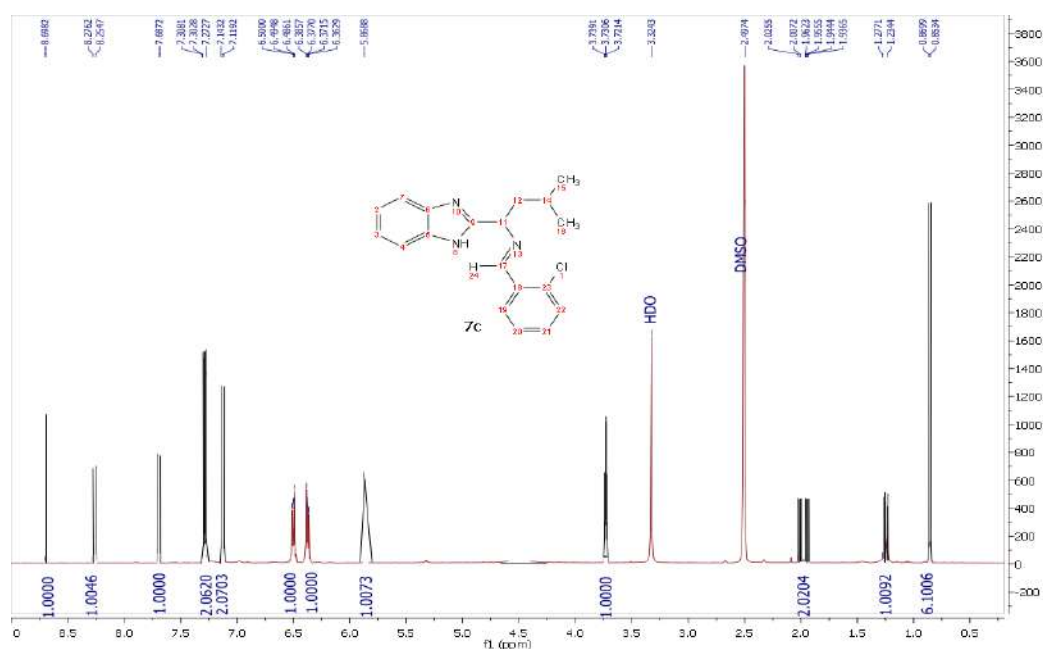


Fig. S4: $^1\text{H-NMR}$ spectrum of 1-(1*H*-benzo[d]imidazol-2-yl)-*N*-benzylidene-3-methylbutan-1-amine 7c

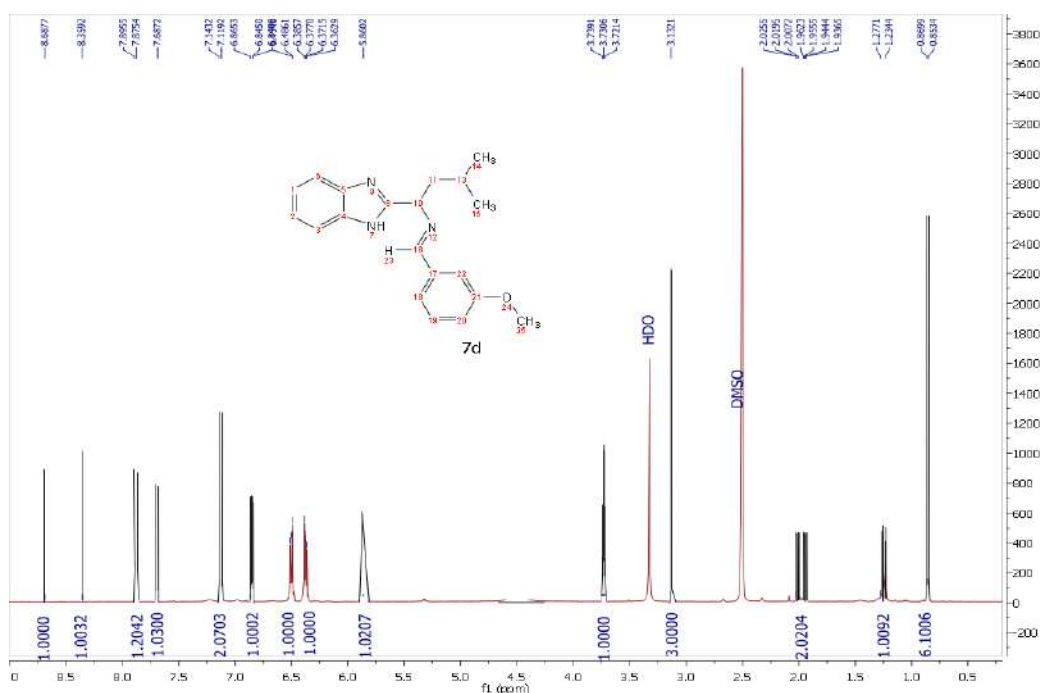


Fig. S5: ¹H-NMR spectrum of 1-(1*H*-benzo[*d*]imidazol-2-yl)-*N*-benzylidene-3-methylbutan-1-amine **7d**

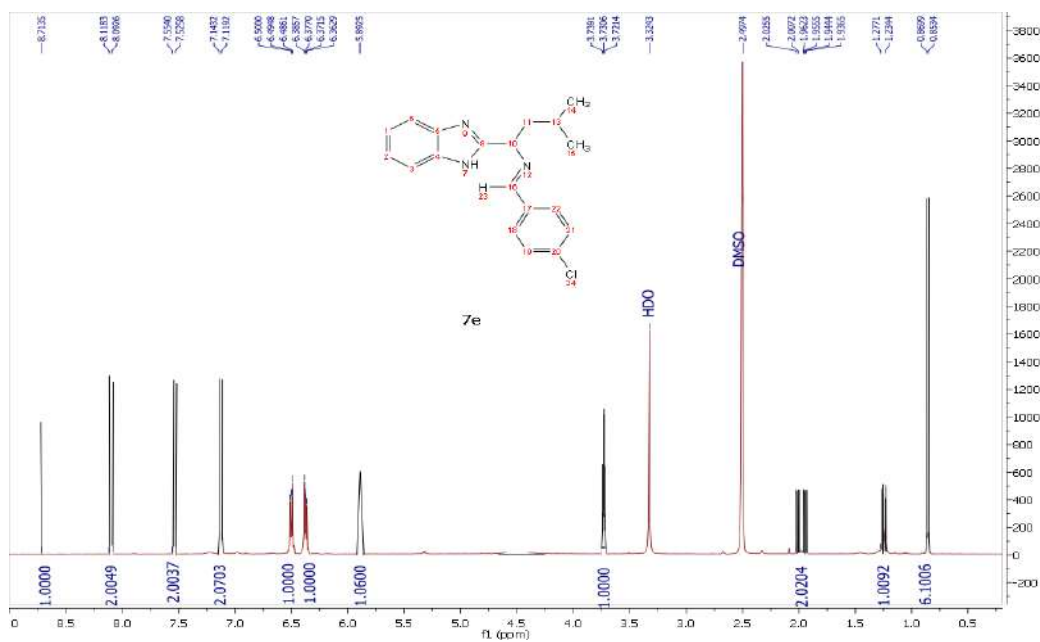


Fig. S6: ¹H-NMR spectrum of 1-(1*H*-benzo[*d*]imidazol-2-yl)-*N*-benzylidene-3-methylbutan-1-amine **7e**

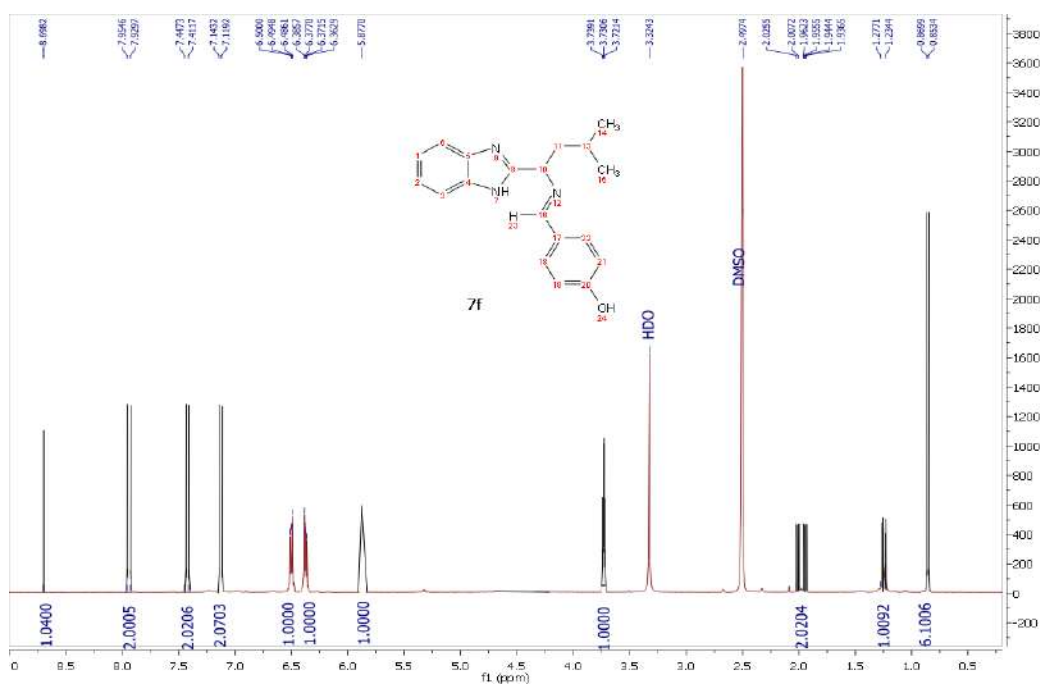


Fig. S7: $^1\text{H-NMR}$ spectrum of 1-(1*H*-benzo[*d*]imidazol-2-yl)-*N*-benzylidene-3-methylbutan-1-amine 7f

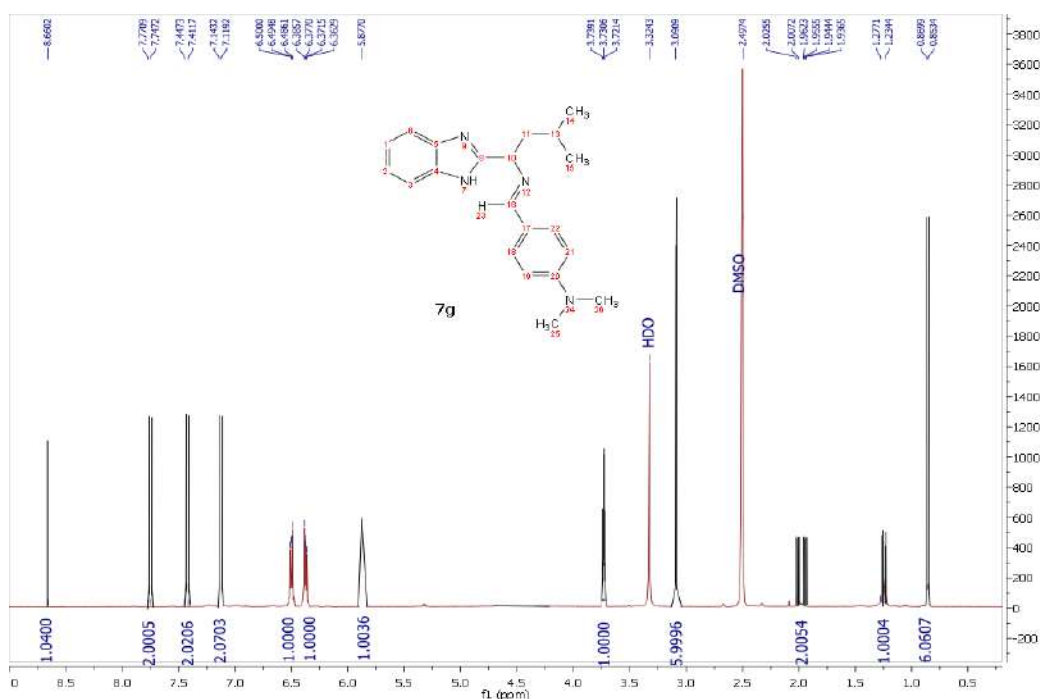


Fig. S8: $^1\text{H-NMR}$ spectrum of 1-(1*H*-benzo[*d*]imidazol-2-yl)-*N*-benzylidene-3-methylbutan-1-amine 7g

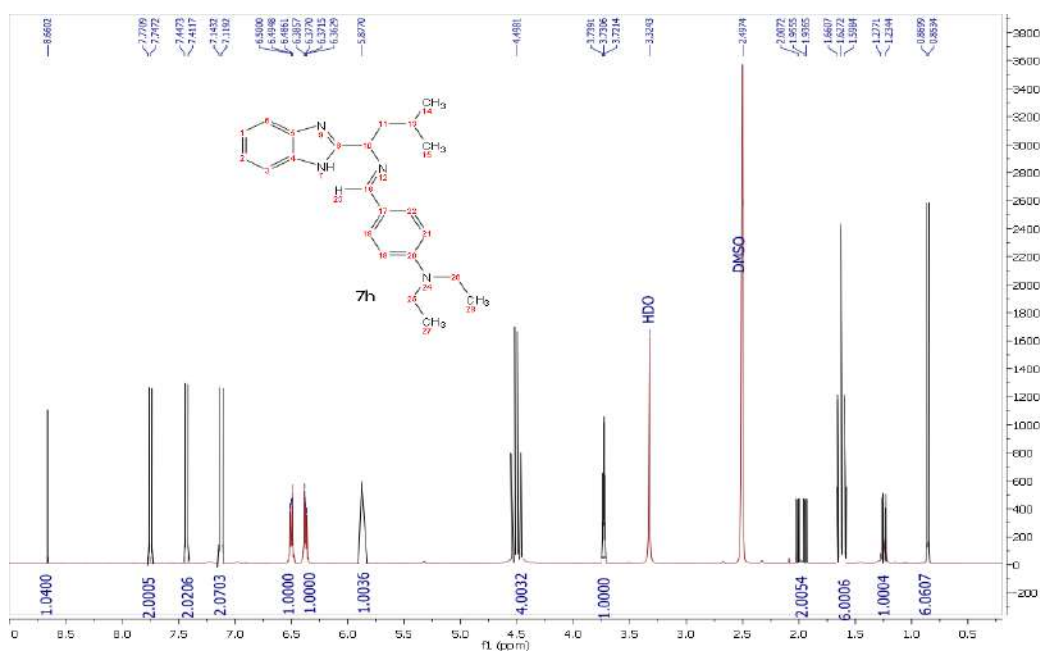


Fig. S9: ¹H-NMR spectrum of 1-(1*H*-benzo[*d*]imidazol-2-yl)-*N*-benzylidene-3-methylbutan-1-amine **7h**

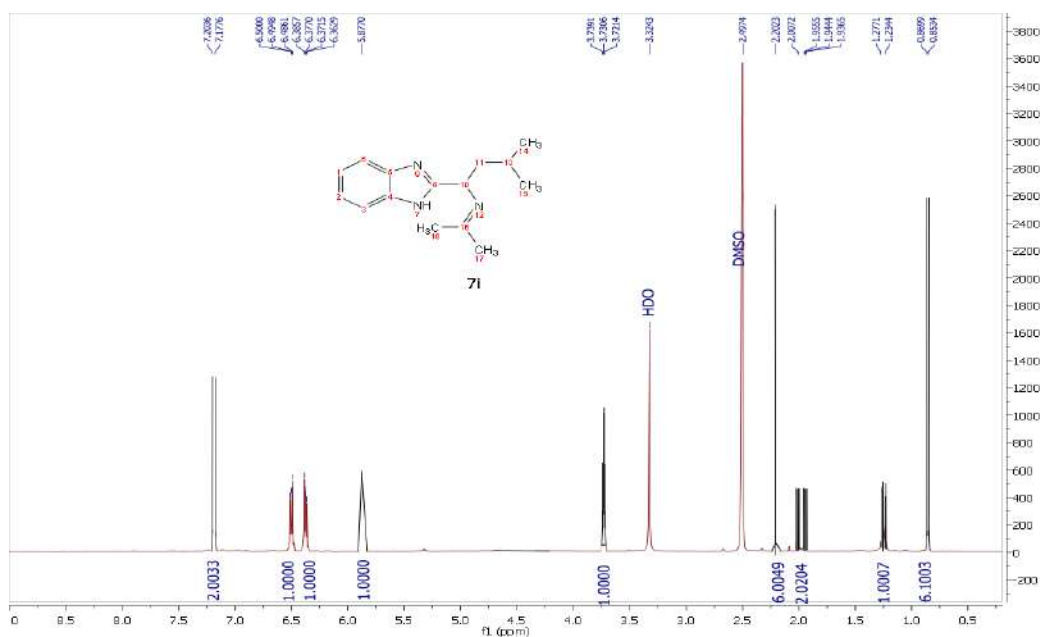


Fig. S10: ¹H-NMR spectrum of 1-(1*H*-benzo[*d*]imidazol-2-yl)-*N*-benzylidene-3-methylbutan-1-amine **7i**

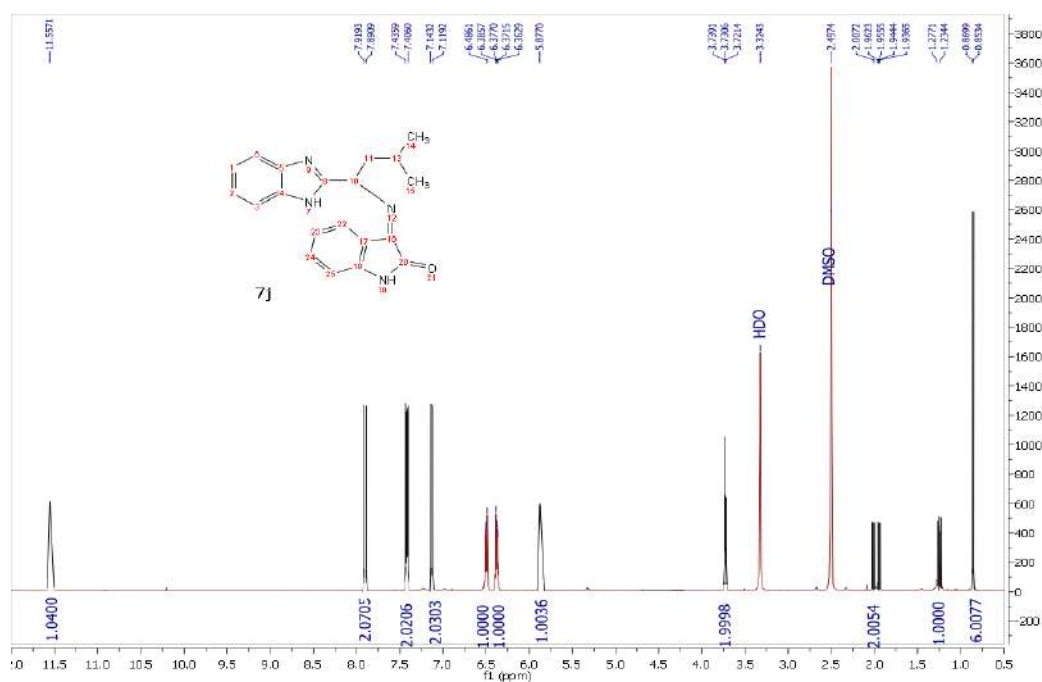


Fig. S11: ¹H-NMR spectrum of 1-(1H-benzo[d]imidazol-2-yl)-N-benzylidene-3-methylbutan-1-amine 7j

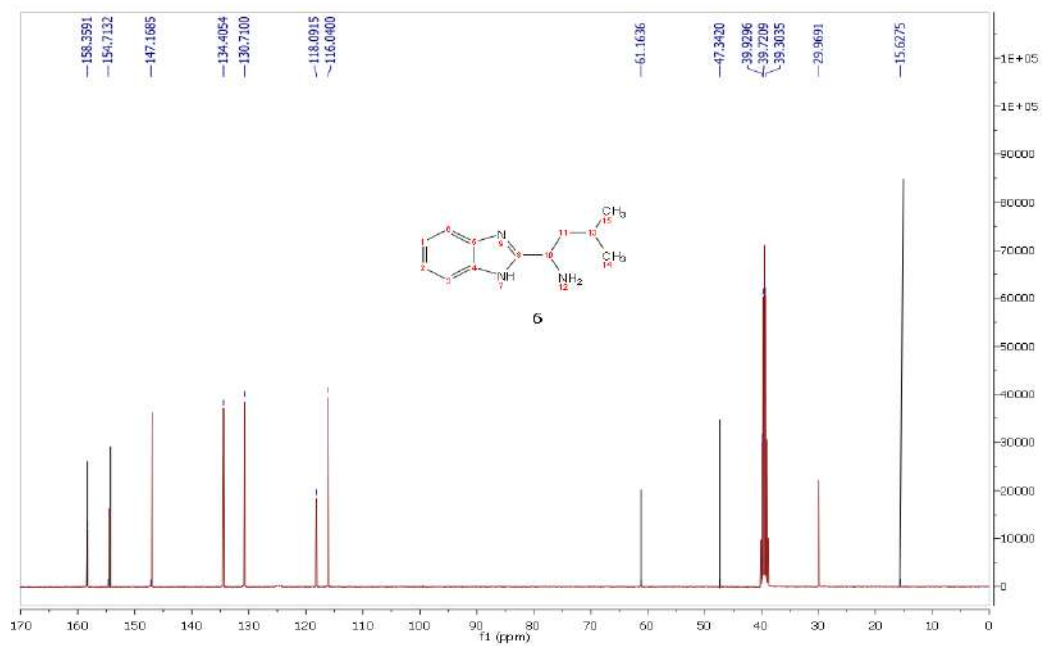
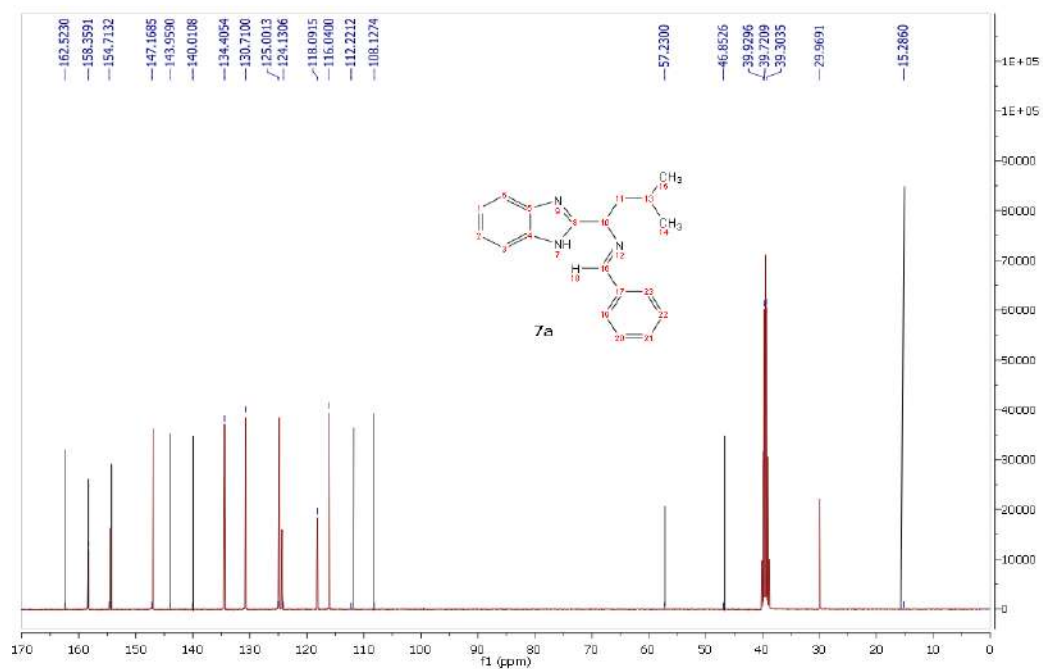
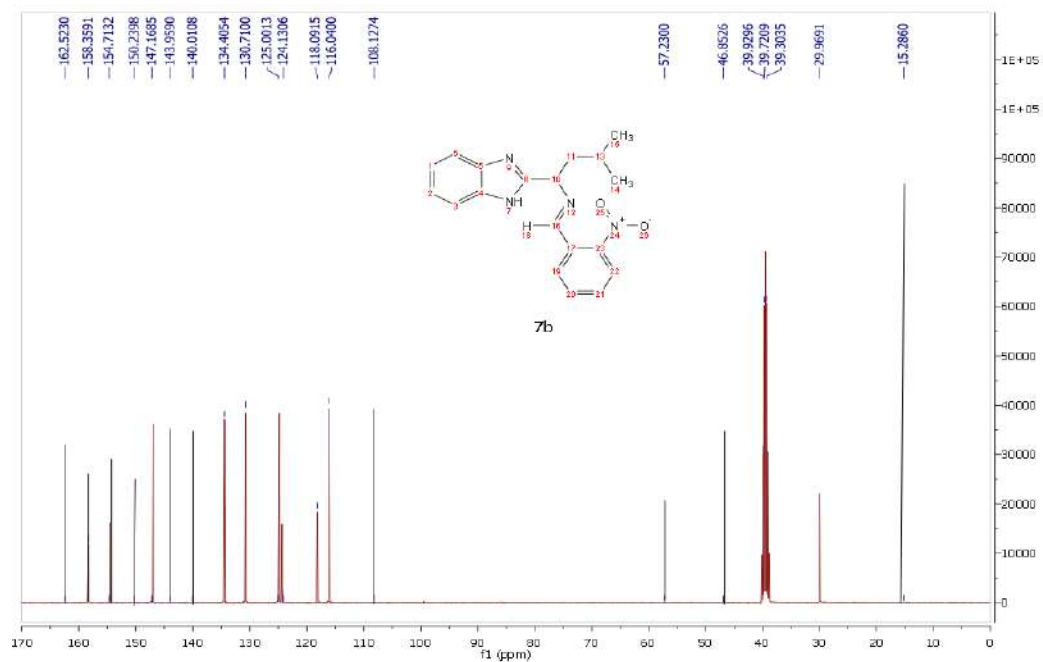
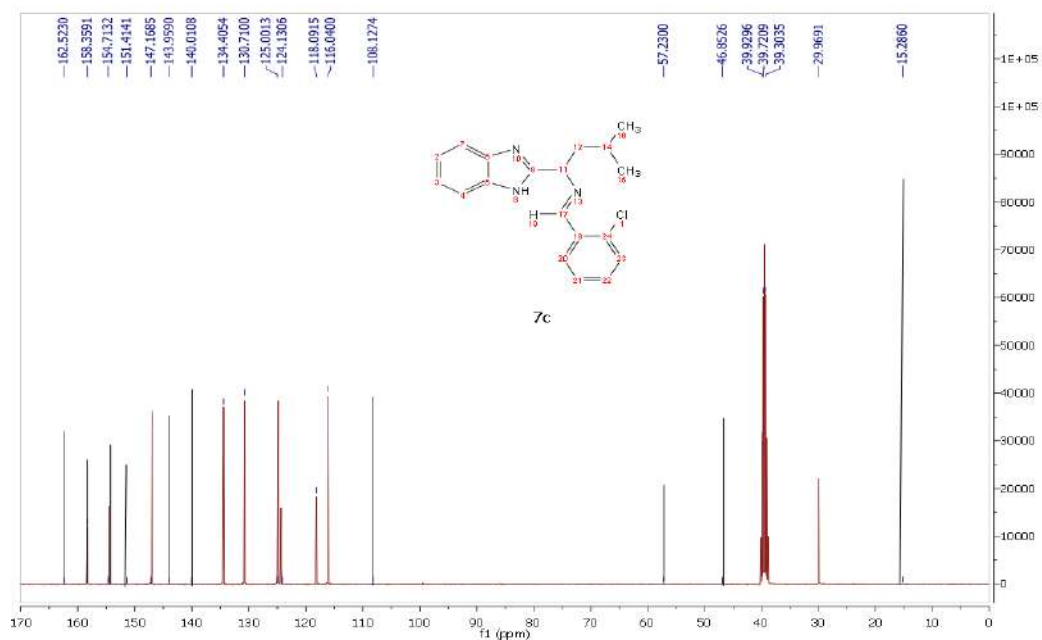
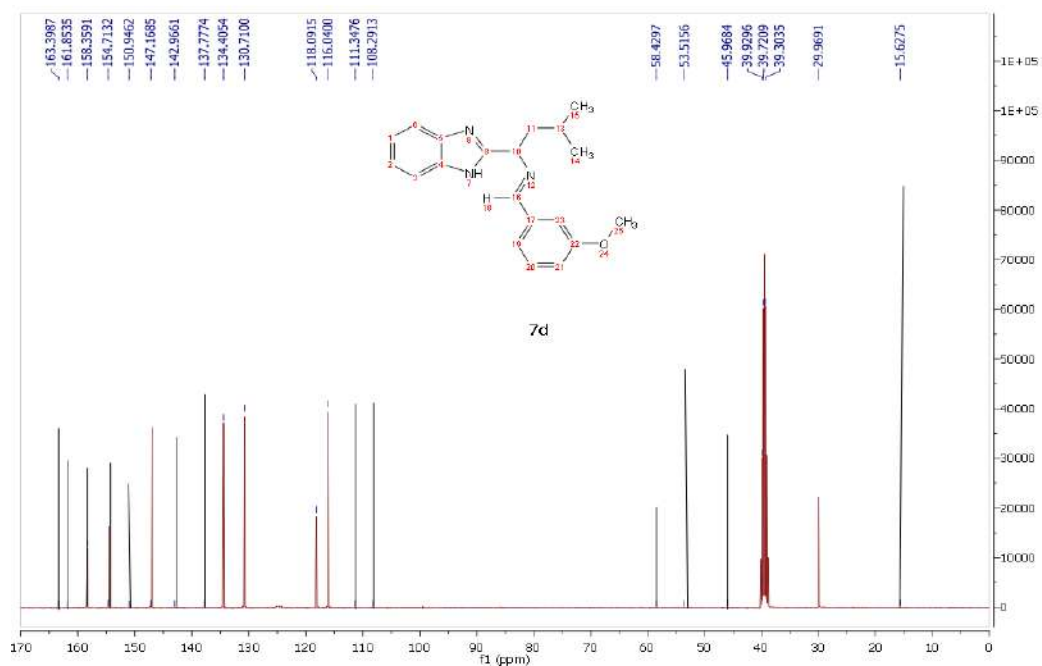
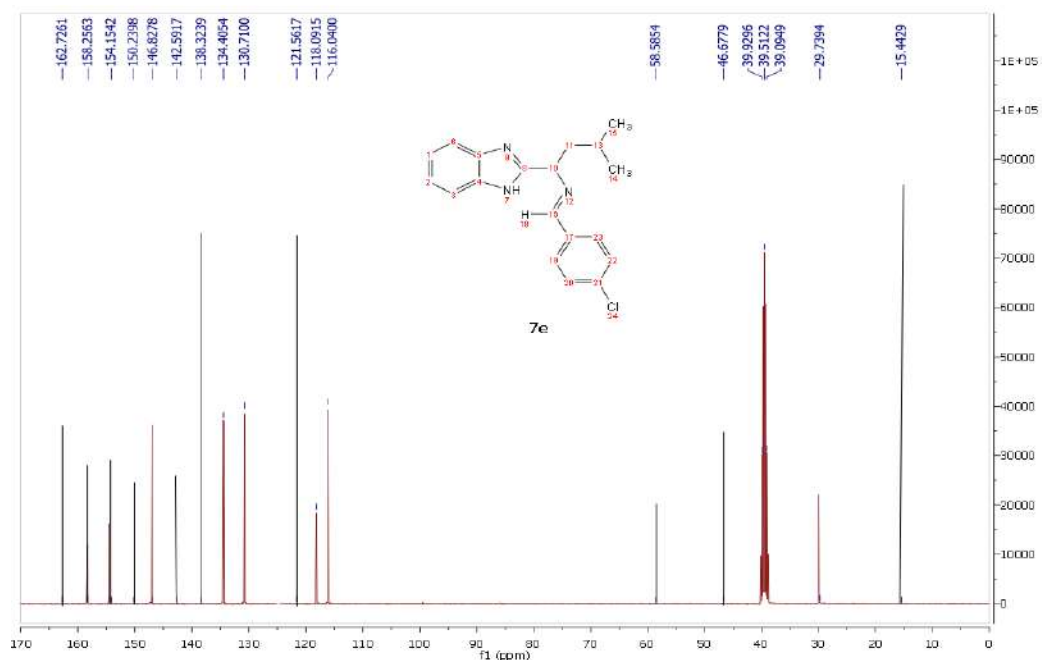
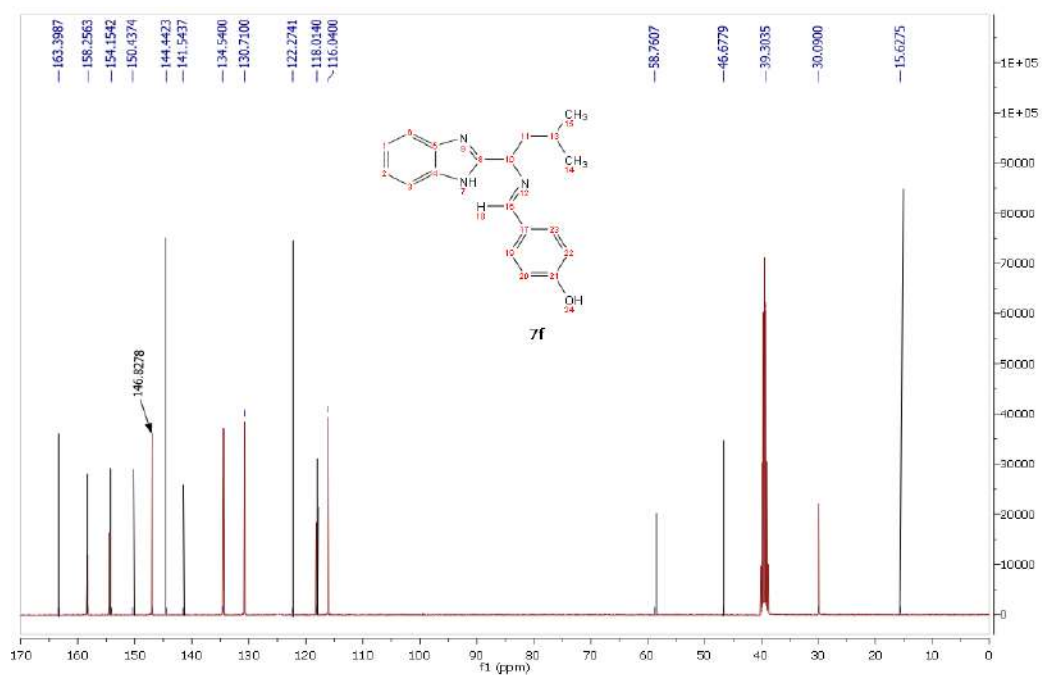
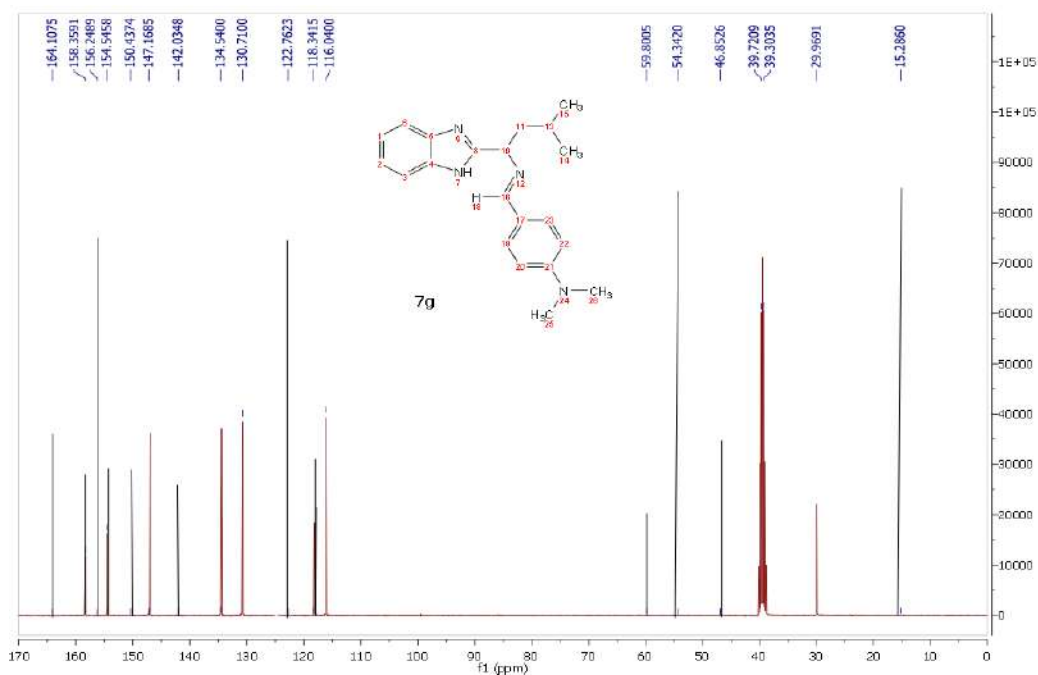
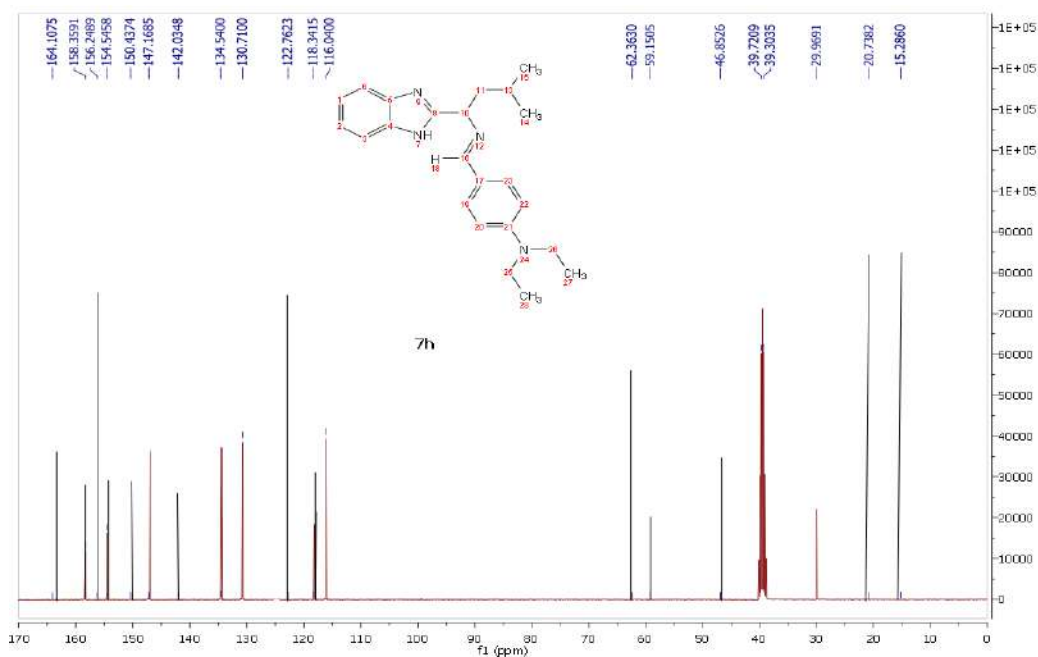


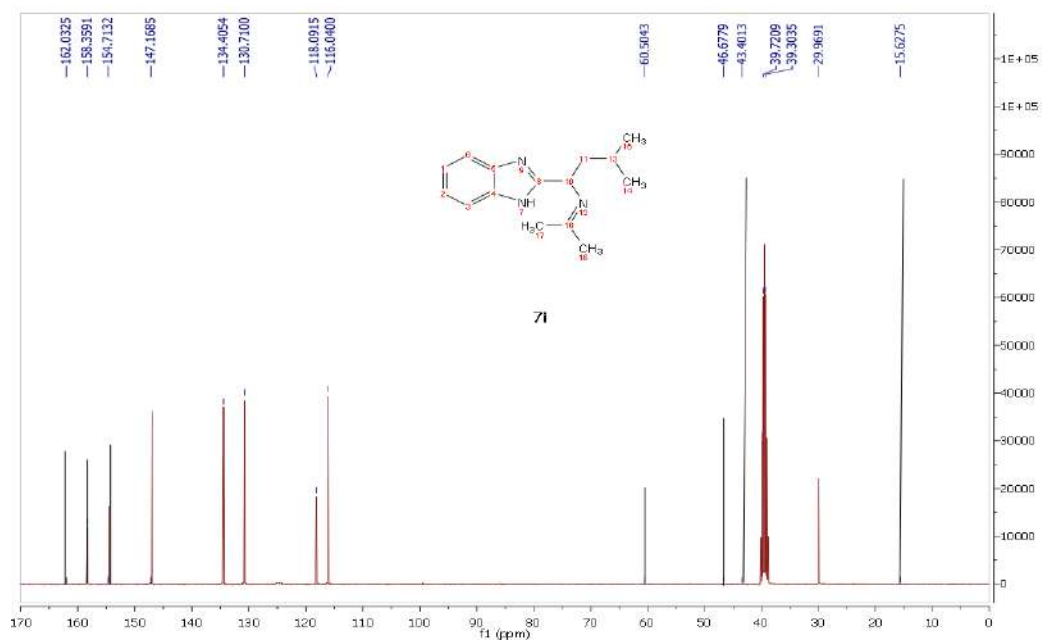
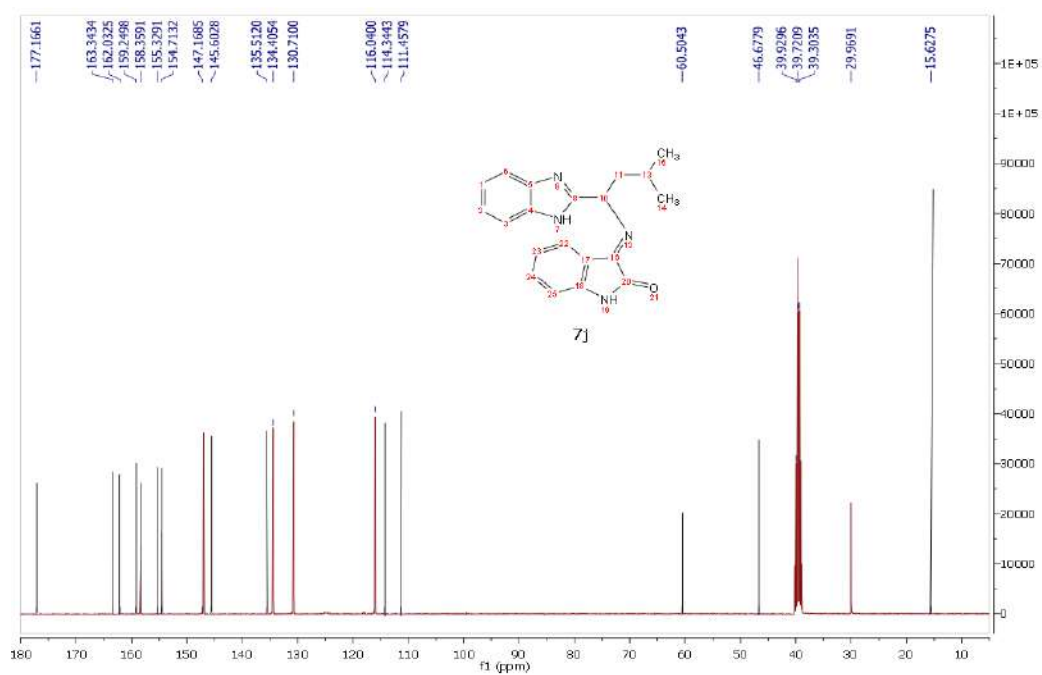
Fig. S12: ¹³C-NMR spectrum of 6

Fig. S13: ^{13}C -NMR spectrum of 7aFig. S14: ^{13}C -NMR spectrum of 7b

Fig. S15: ^{13}C -NMR spectrum of 7cFig. S16: ^{13}C -NMR spectrum of 7d

Fig. S17: ¹³C-NMR spectrum of 7eFig. S18: ¹³C-NMR spectrum of 7f

Fig. S19: ^{13}C -NMR spectrum of 7gFig. S20: ^{13}C -NMR spectrum of 7h

Fig. S21: ^{13}C -NMR spectrum of 7iFig. S22: ^{13}C -NMR spectrum of 7j

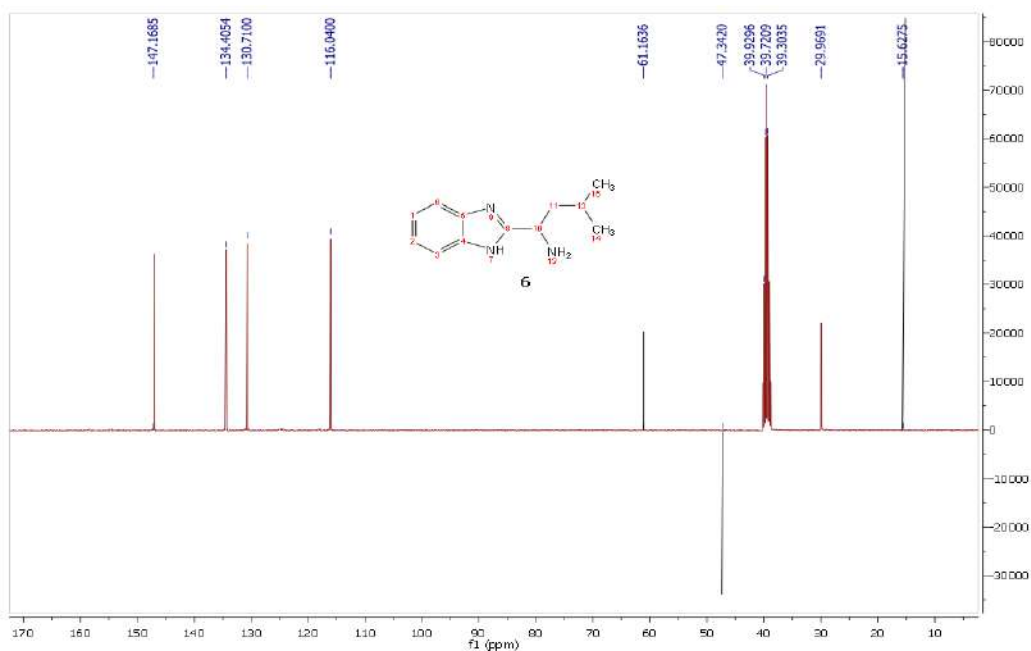


Fig. S23: DEPT 135 NMR spectrum of 6

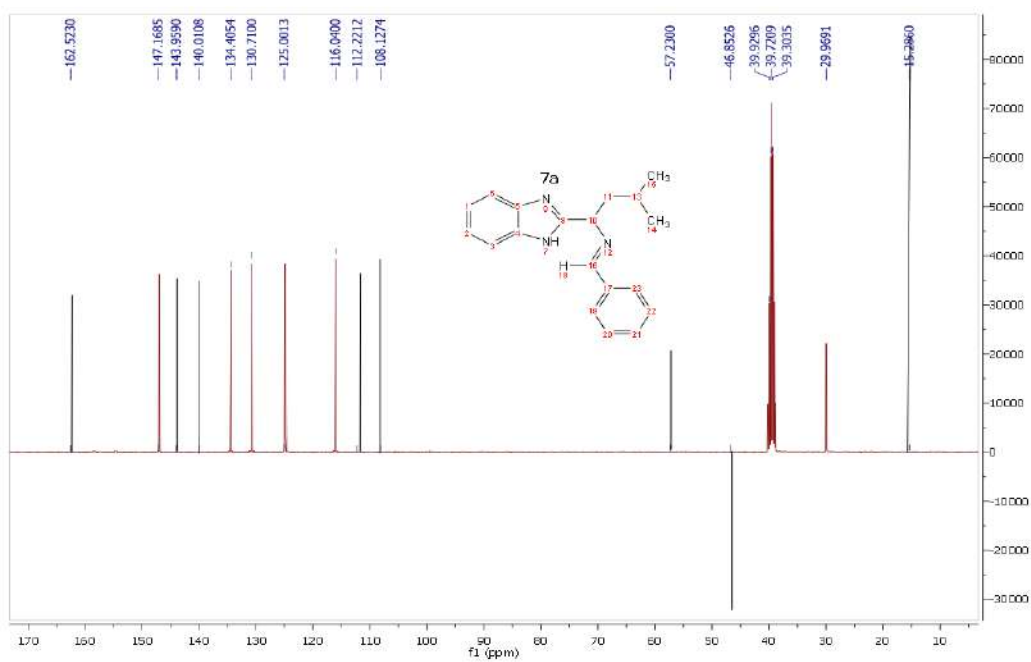


Fig. S24: DEPT 135 NMR spectrum of 7a

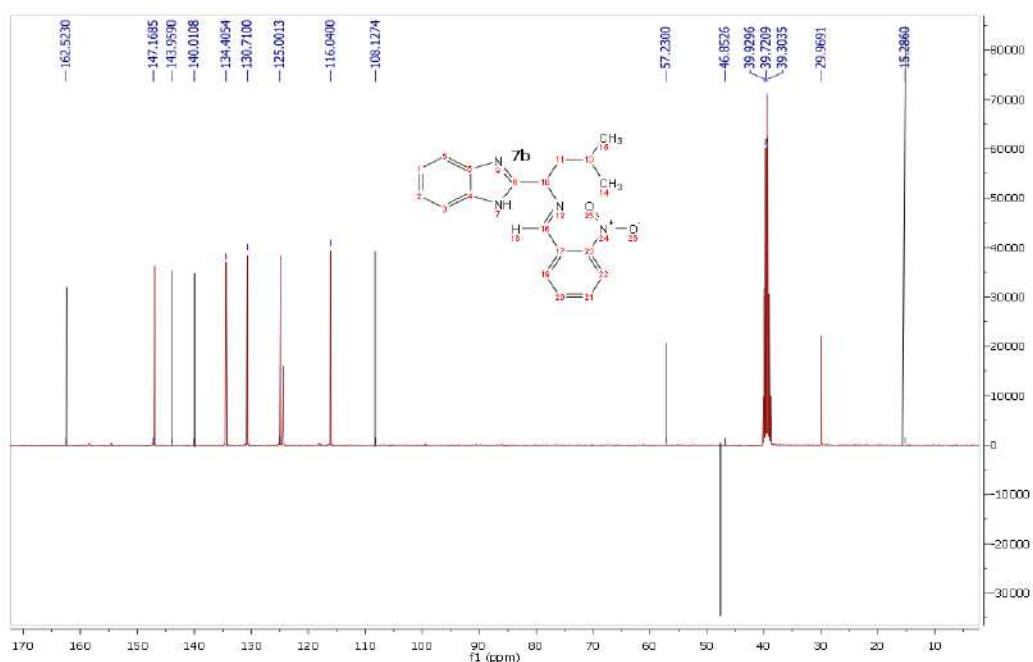


Fig. S25: DEPT 135 NMR spectrum of 7b

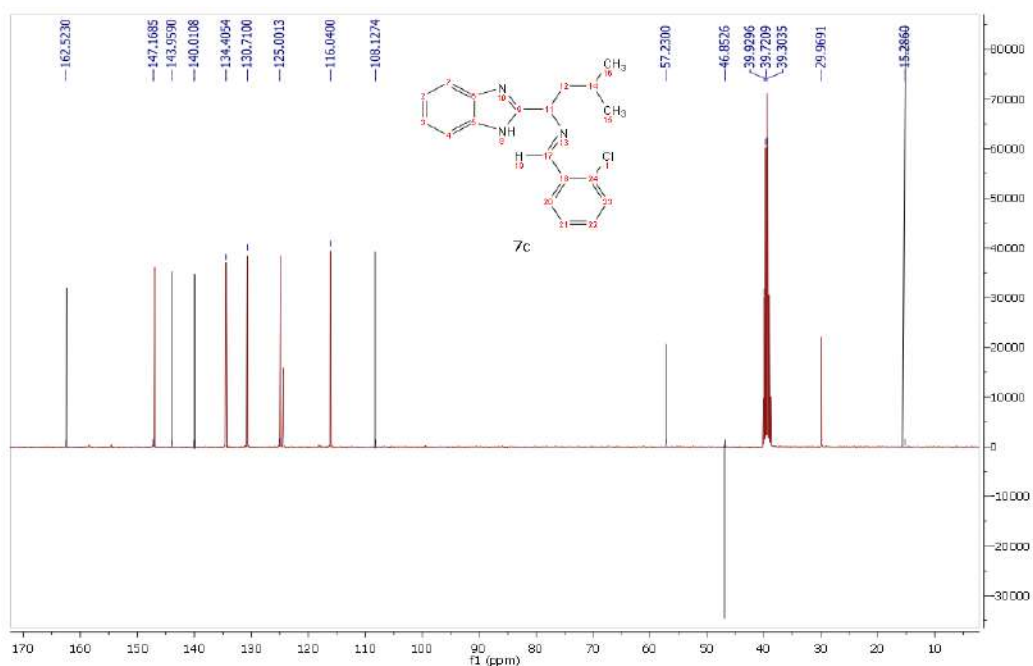


Fig. S26: DEPT 135 NMR spectrum of 7c

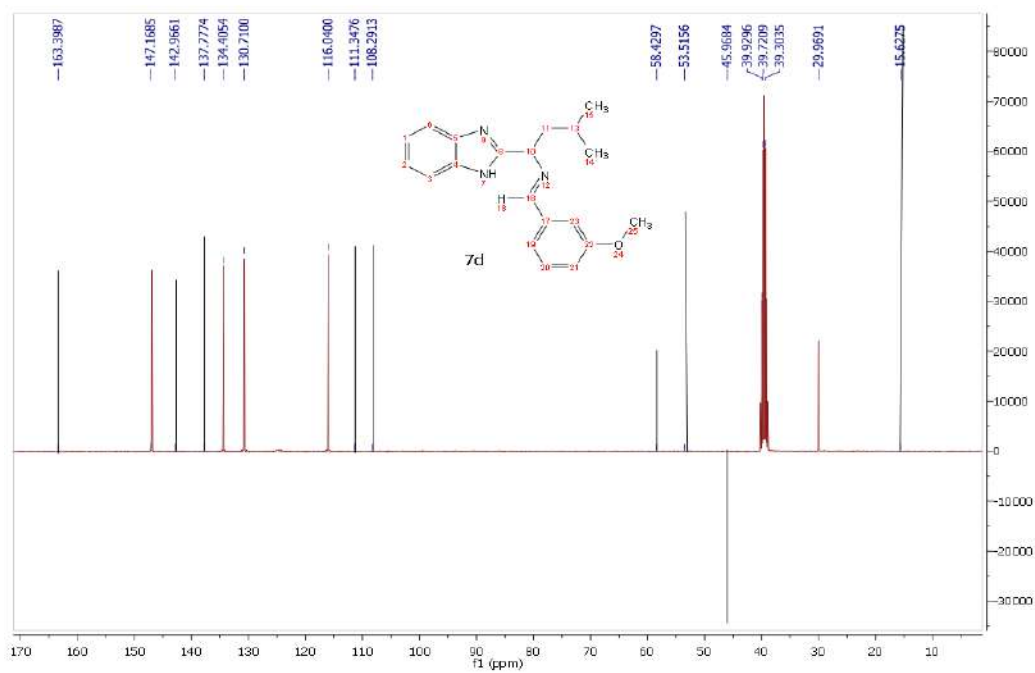


Fig. S27: DEPT 135 NMR spectrum of 7d

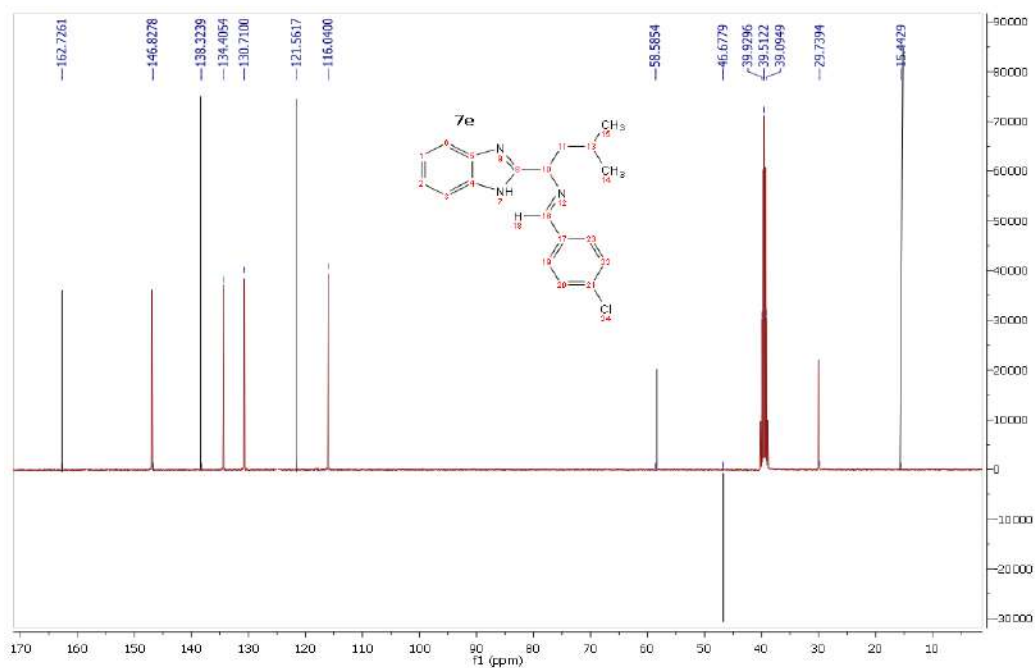


Fig. S28: DEPT 135 NMR spectrum of 7e

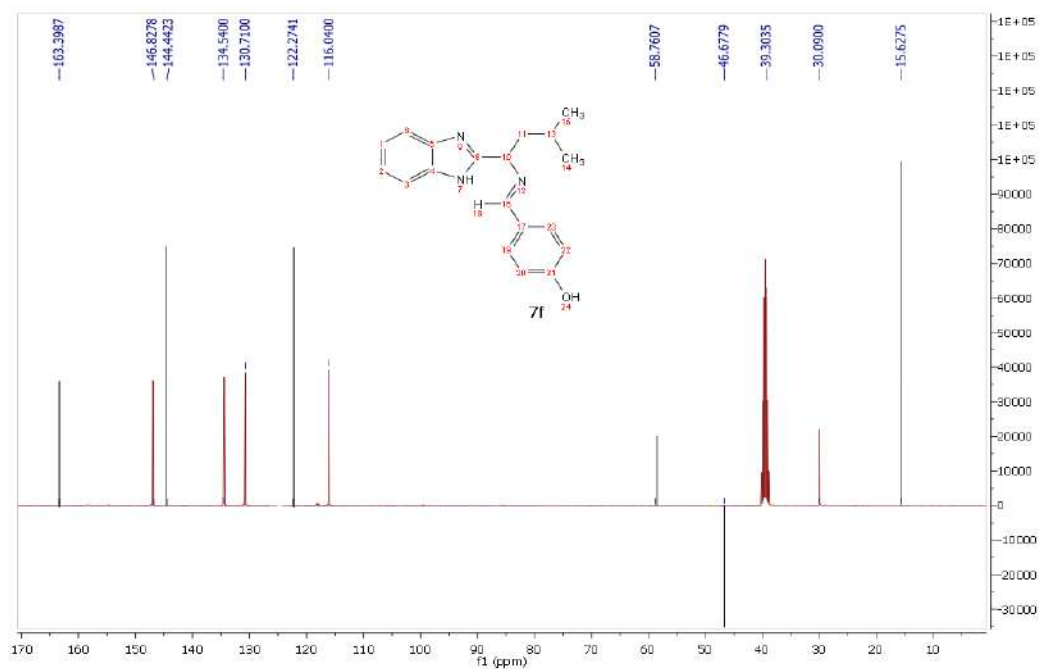


Fig. S29: DEPT 135 NMR spectrum of 7f

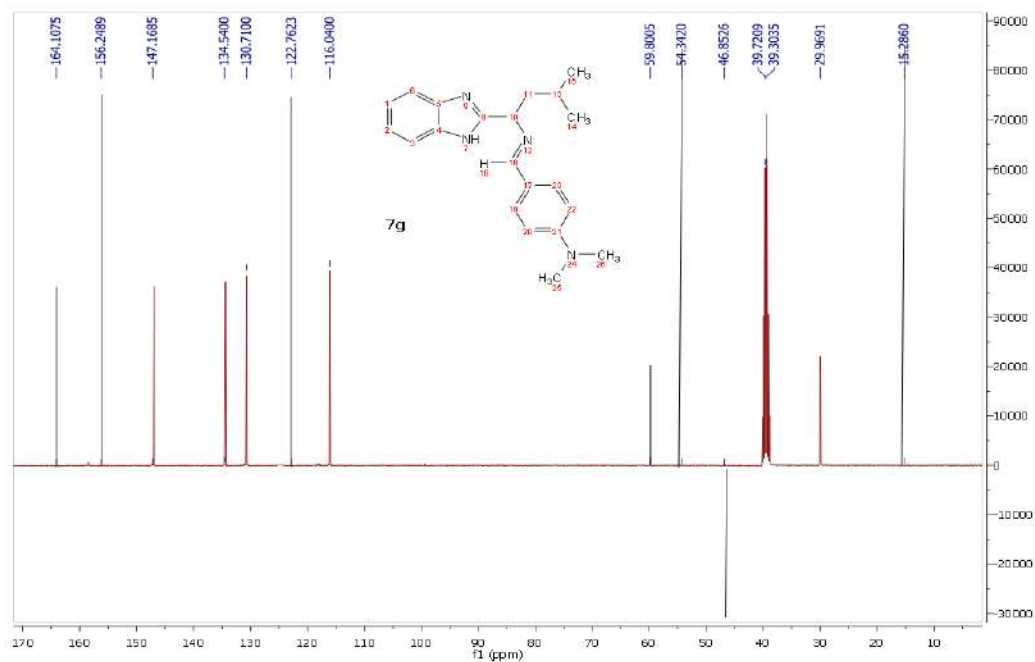


Fig. S30: DEPT 135 NMR spectrum of 7g

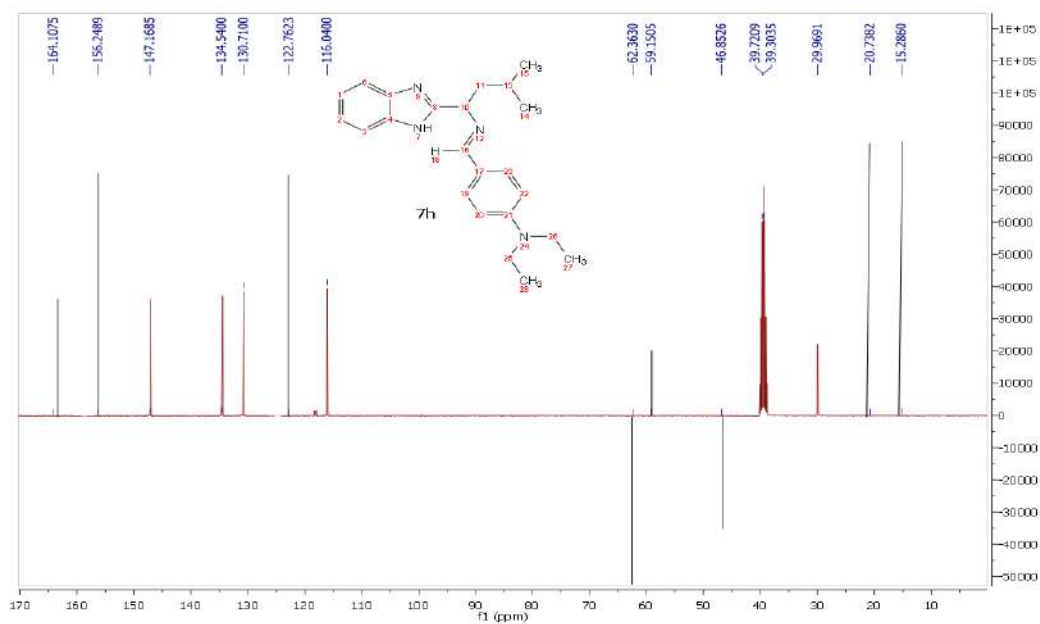


Fig. S31: DEPT 135 NMR spectrum of 7h

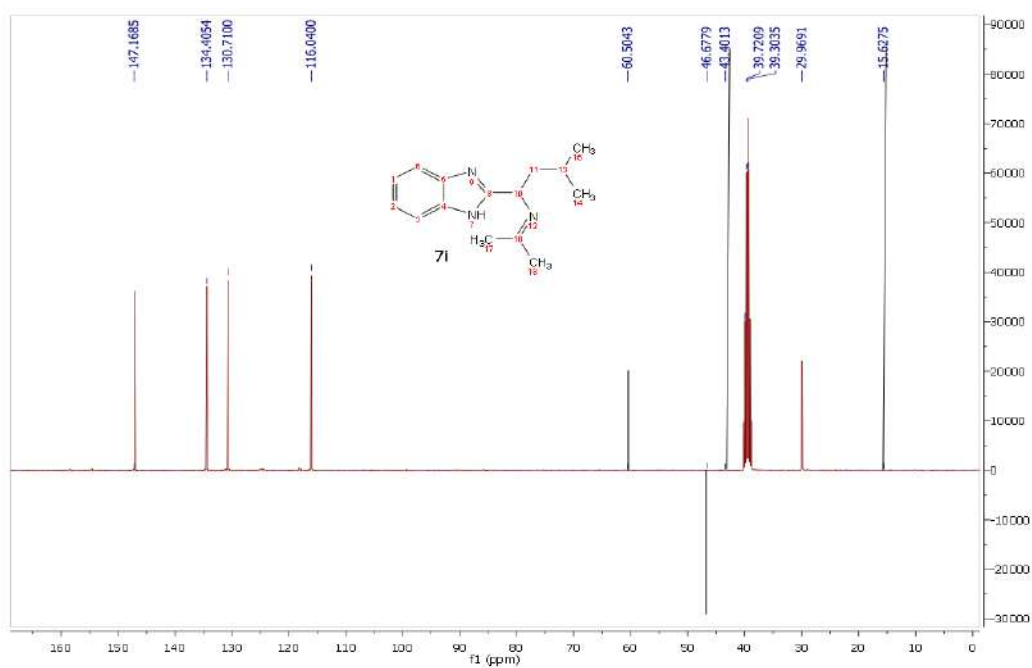


Fig. S32: DEPT 135 NMR spectrum of 7i

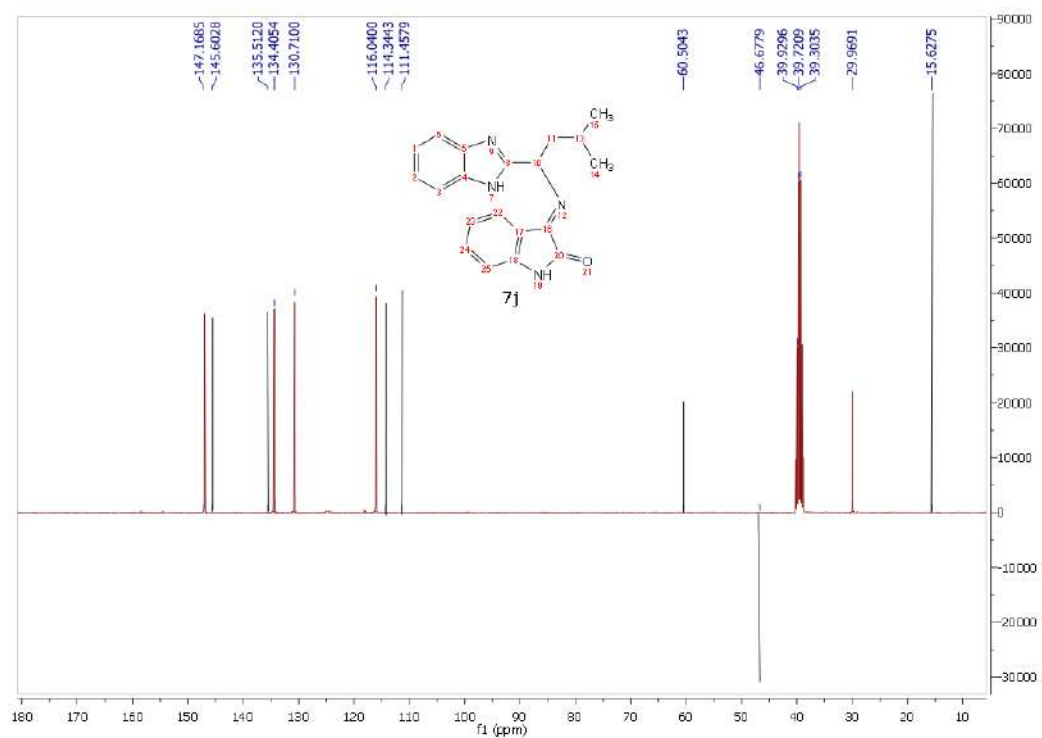


Fig. S33: DEPT 135 NMR spectrum of 7j

Facile Synthesis, Characterization and *in vitro* Antibacterial Efficacy of Functionalized 2-Substituted Benzimidazole Motifs

Olayinka Oyewale Ajani^{1,*}, Olaoluwasubomi Eneyeme Joseph¹, King Tamunodikibugerere Iyaye¹, Natasha October², Damilola Victoria Aderohunmu¹, Shade John Olorunshola³, and Oluwatosin Yemisi Audu²

¹Department of Chemistry, College of Science and Technology, Covenant University, Canaanland, Km 10 Idiroko Road, P.M.B. 1023, Ota, Ogun State, Nigeria

²Department of Chemistry, University of Pretoria, Lynnwood Road, Hatfield, Pretoria, 0002, South Africa

³Department of Biological Science, College of Science and Technology, Covenant University, Canaanland, Km 10 Idiroko Road, P.M.B. 1023, Ota, Ogun State, Nigeria

* **Corresponding author:**

email: ola.ajani@covenantuniversity.edu.ng

Received: November 6, 2018

Accepted: June 28, 2019

DOI: 10.22146/ijc.40448

Abstract: A series of functionalized 2-substituted benzimidazole motifs was designed and successfully synthesized via thermal cyclization of 1,2-diaminobenzene on COOH end of L-leucine to achieve benzimidazole derivatives **6** as the essential precursor. The coupling of the precursor **6** with benzaldehyde derivatives **a-h**, ketone series **i-k**, and aryl sulfonyl chlorides **l-n** led to the formation of the targeted 2-substituted benzimidazole motifs **7a-n** in improved yields. The targeted benzimidazole motifs were structurally authenticated through their spectral data and microanalytical parameters. The targeted final moieties were investigated for potential antimicrobial activity using the agar diffusion method with gentamicin as the clinical standard. All the compounds had a broad spectrum of activity with compound **7k** having the highest remarkable activity with MIC of 0.98 ± 0.02 $\mu\text{g/mL}$ and MBC value of 3.91 ± 0.10 $\mu\text{g/mL}$. These findings suggest that compound **7k** containing camphor might be a good candidate for the design of new antimicrobial small-molecule drugs.

Keywords: benzimidazole; [4+1]-cycloaddition; serial dilution; SAR study; antibacterial

■ INTRODUCTION

Over the years, heterocyclic compounds have been reported to be biomimetically-useful and pharmacophorically-sensitive frameworks with high essentiality in accessing biomolecular drugs and drug-like candidates in drug design [1]. One of the *N*-heterocyclic templates of high diversity in the pharmacological adventure are benzimidazole motifs, and they are known to be unavoidable rubrics in high through screening and identification of valuable lead targets in therapeutic research [2]. They possess observable biochemical interaction with many biomolecules in the body system because of their structural resemblance to some naturally

existing nucleotides [3]. The natural occurrence of benzimidazole was reported in vitamin B₁₂ to contain *N*-ribosyl-dimethyl benzimidazole, which functioned in the form of cobalt metal axial ligand [4]. The methods for the benzimidazoles design and preparation have gained topmost priority in the organic chemists' scale of preference due to the application of these scaffolds in many areas of human endeavors [5].

Although, numerous methods for harnessing benzimidazole derivatives are available in the current literature; nonetheless, the most common and easily adaptable method involves the [4+1]-cycloaddition of *o*-phenylene diamine to alkanolic acids [6], alkanal,

alkanols, and nitriles [7]. It is interesting to note that benzimidazole motifs have contributed immensely as core structures in many macrocyclic moieties with crucial medicinal applications in drug design [8-9]. They are widely available in commercially marketed drugs which include, but not limited to Omeprazole **1**, which is a proton pump inhibitor used as anti-ulcer [10]; Albendazole **2** as anthelmintic [11]; Bendamustine **3** as anticancer [12]; Telmisartan **4** as antihypertensive [13] and Pimozide **5** as antipsychotic agent [14] as shown in Fig. 1. A very recent study showed DNA binding and antiparasitic properties of benzimidazole bichalcophenes [15].

Many methods have been utilized in the preparation of benzimidazole and its functionalized derivatives some of which include reaction of ortho-phenylenediamine (o-PDA) with substituted carboxylic acid using concentrated HCl medium [16]; *p*-toluene sulphonic acid catalyst [17]; reaction of o-PDA with benzaldehyde derivative using Na₂S₂O₅ [18], which release SO₂ gas with pungent smell upon contact with water. Some of these methods involve the tedious work-up procedure and suffer some demerits such as the release of toxic chemicals, harsh reaction conditions, use of expensive reagents, prolonged reaction time, and corrosive nature.

Benzimidazole is a very important biologically active agent in therapeutic medicine because it possesses numerous biological and pharmacological activities. Due to confronting issues such as drug resistance and

consistent increase in the outbreak of new diseases globally [19], there should be an uninterrupted quest for the design and preparation of novel heterocyclic moieties as efficacious antimicrobial drug candidates with the aid of synthetic technique with fast kinetic, eco-friendliness, and cost-effectiveness, which is part of focus of this present study. On this note, it is highly essential and strongly motivational to design and synthesize an array of 2-substituted benzimidazole derivatives with an eco-friendly approach for the possibility of preliminary new drug discovery.

■ EXPERIMENTAL SECTION

Materials

All reagents used were obtained from Sigma-Aldrich Chemicals (St. Louis, Missouri, USA) except ammonium chloride, L-leucine and dichloromethane which were purchased from BDH (Poole, Dorset, England), and concentrated hydrochloric acid and camphor which were obtained from Alfar Aesar (Chao Yang District, Beijing, China).

Instrumentation

Melting points determination was carried out with the Stuart melting point apparatus. Progress was monitored by thin layer chromatographic technique and visualization was done accordingly. Nuclear magnetic resonance (NMR) spectra for ¹H- and ¹³C-NMR analysis

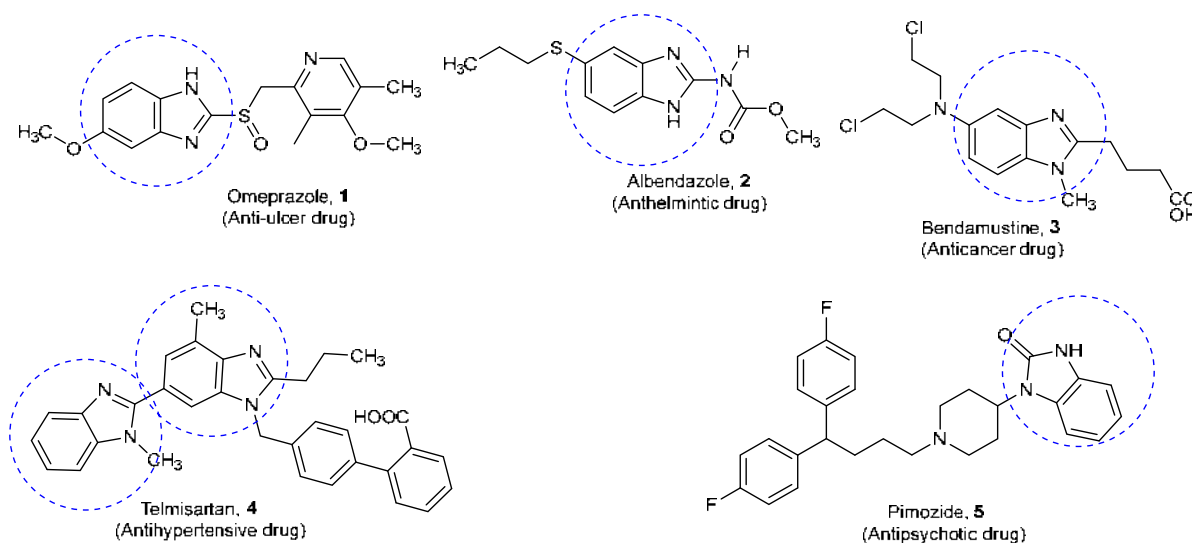


Fig 1. Selected commercially available benzimidazole based drugs

were recorded on Bruker DPX 400 NMR spectrometer at 400 MHz and 100 MHz, respectively, using DMSO- d_6 as the solvent and TMS as the internal standard. DEPT 135 NMR analysis was used for signal assignment to distinguish between methyl (CH_3), methylene (CH_2), and methine (CH) carbon atoms. The Infrared spectra for functional group identification were done with the Bruker FT-IR spectrophotometer; while ultraviolet-visible analysis on the synthesized compounds was carried out in a solution of ethanol ($\text{C}_2\text{H}_5\text{OH}$), using UV-Genesys spectrophotometer. Sample concentration via solvent removal was achieved with IKA[®] RV 10 Rotary evaporator and the vacuum-drying of the sample was done with DHG-9023A. Vacuum Oven. Flash EA 1112 Elemental Analyzer was used for carbon, hydrogen, and nitrogen elemental analyses.

Procedure

Synthesis procedure

Synthesis of 1-(1H-benzo[d]imidazol-2-yl)-3-methylbutan-1-amine (6). According to literature method [20], 15.00 g of o-phenylenediamine (138.00 mmol, 1.00 equiv.) in 80 mL of ethanol was added with ammonium chloride (0.74 g, 13.80 mmol, 10 mol%) as catalyst followed by gradual tipping of L-leucine (18.08 g, 138.00 mmol, 1.00 equiv.). The mixture was then stirred at ambient temperature for 5 min after which it was heated under reflux for 3 h (reaction was monitored with TLC). The resulting substrate was filtered while hot to remove the insoluble impurities. The filtrate obtained was evaporated to dryness at reduced pressure to get a crude compound which was recrystallized from isopropanol to afford **6** as brown solid. Yield: 72.57%. ¹H-NMR (400 MHz, DMSO- d_6) δ_{H} : 7.14-7.12 (d, $J = 9.10$ Hz, 2H, Ar-H), 6.51-6.49 (dd, $J_1 = 3.52$ Hz, $J_2 = 9.10$ Hz, 1H, Ph-H), 6.39-6.36 (dd, $J_1 = 3.44$ Hz, $J_2 = 9.10$ Hz, 1H, Ph-H), 4.50 (d, $J = 4.24$ Hz, 2H, $\text{NH}_2\text{-CH}$), 3.85-3.83 (m, 1H, C-H), 2.30-1.98 (m, 2H, C-H), 1.27-1.23 (m, 1H, C-H), 0.87-0.85 (d, $J = 6.60$ Hz, 6H, $2 \times \text{CH}_3$). ¹³C-NMR (100 MHz, DMSO- d_6) δ_{C} : 158.4, 154.7, 147.2 (CH), 134.4 (CH), 130.7 (CH), 118.1, 116.0 (CH), 61.2 (CH), 47.3 (CH_2), 30.0 (CH), 15.6 ($2 \times \text{CH}_3$). IR (cm^{-1}): 3384 (N-H), 3363 (N-H), 3179, 3037 (C-H aromatic), 2957 (C-H aliphatic), 2865 (C-H aliphatic),

1627 (C=C), 1589 (C=N), 1457 (CH_2 deformation), 1407 (CH_3 deformation), 1294 (C=N bending), 1057 (C-N), 743 (Ar-H). UV-Vis.: λ_{max} (nm)/log ϵ_{max} : 210 (5.40), 236 (5.21), 290 (4.92), 401 (3.90).

(E)-1-(1H-benzo[d]imidazol-2-yl)-N-benzylidene-3-methylbutan-1-amine (7a). Compound **6** (1.00 g, 4.93 mmol, 1.00 equiv.) was dissolved in 10 mL of tetrahydrofuran at room temperature and allowed to stir for 5 min. Benzaldehyde (0.50 mL, 4.93 mmol, 1.00 equiv.) in 5 mL of tetrahydrofuran was added dropwise to the solution of **6** above and refluxed for 3 h. The resulting solution was concentrated under vacuum and the crude product obtained was recrystallized from ethanol to afford **7a** as brown solid. Yield: 61%. ¹H-NMR (400 MHz, DMSO- d_6) δ_{H} : 8.69 (s, 1H, N=CH), 7.90-7.88 (d, $J = 9.10$ Hz, 2H, Ar-H), 7.54-7.49 (m, 3H, Ar-H), 7.14-7.12 (d, $J = 8.04$ Hz, 2H, Ar-H), 6.51-6.49 (dd, $J_1 = 3.52$ Hz, $J_2 = 9.10$ Hz, 1H, Ar-H), 6.39-6.36 (dd, $J_1 = 3.44$ Hz, $J_2 = 9.10$ Hz, 1H, Ar-H), 5.87 (s, 1H, NH), 3.74-3.72 (t, $J = 3.68$ Hz, 1H, CH), 2.02-2.00 (dd, $J_1 = 2.40$ Hz, $J_2 = 10.32$ Hz, 1H, CH_a of CH_2), 1.96-1.94 (dd, $J_1 = 2.74$ Hz, $J_2 = 10.32$ Hz, 1H, CH_b of CH_2), 1.26-1.21 (m, 1H, CH), 0.87-0.85 (d, $J = 6.60$ Hz, 6H, $2 \times \text{CH}_3$). ¹³C-NMR (100 MHz, DMSO- d_6) δ_{C} : 162.5 (CH), 158.3 (C), 154.7 (C), 147.2 (CH), 143.9 (CH), 140.0 (CH), 134.4 (CH), 130.7 (CH), 125.0 (CH), 124.1 (C), 118.1 (C), 116.0 (CH), 112.2 (CH), 108.1 (CH), 57.2 (CH), 46.8 (CH_2), 30.0 (CH), 15.3 ($2 \times \text{CH}_3$). IR (cm^{-1}): 3056 (CH aromatic), 2956 (C-H aliphatic), 2868 (C-H aliphatic), 1610 (C=C), 1579 (C=N), 1444 (CH_2 deformation), 1405 (CH_3 deformation), 1294 (C=N bending), 1070 (C-N), 923 (=C-H bending), 742 (Ar-H). UV-Vis.: λ_{max} (nm)/log ϵ_{max} : 209 (5.25), 293 (4.82).

(E)-1-(1H-benzo[d]imidazol-2-yl)-3-methyl-N-(2-nitrobenzylidene)butan-1-amine (7b). General procedure described for **7a** was used for reaction of **6** (1.00 g, 4.93 mmol) with 2-nitrobenzaldehyde (0.74 g, 4.93 mmol) to produce **7b** as red solid. Yield: 85%. ¹H-NMR (400 MHz, DMSO- d_6) δ_{H} : 8.71 (s, 1H, N=CH), 8.20-8.18 (d, $J = 8.00$ Hz, 1H, Ar-H), 7.69-7.67 (d, $J = 8.02$ Hz, 1H, Ar-H), 7.31-7.27 (m, 2H, Ar-H), 7.14-7.12 (d, $J = 9.10$ Hz, 2H, Ar-H), 6.51-6.49 (dd, $J_1 = 3.52$ Hz, $J_2 = 9.10$ Hz, 1H, Ar-H), 6.39-6.36 (dd, $J_1 = 3.44$ Hz, $J_2 = 9.10$ Hz, 1H, Ar-H),

5.88 (s, 1H, NH), 3.74-3.72 (t, $J = 3.68$ Hz, 1H, CH), 2.02-2.00 (dd, $J_1 = 2.40$ Hz, $J_2 = 10.32$ Hz, 1H, CH_a of CH₂), 1.96-1.94 (dd, $J_1 = 2.74$ Hz, $J_2 = 10.32$ Hz, 1H, CH_b of CH₂), 1.27-1.23 (m, 1H, CH), 0.87-0.85 (d, $J = 6.60$ Hz, 6H, 2 × CH₃). ¹³C-NMR (100 MHz, DMSO-*d*₆) δ_C: 162.5 (CH), 158.3 (C), 154.7 (C), 150.2 (C), 147.2 (CH), 143.9 (CH), 140.0 (CH), 134.4 (CH), 130.7 (CH), 125.0 (CH), 124.1 (C), 118.1 (C), 116.0 (CH), 108.1 (CH), 57.2 (CH), 46.8 (CH₂), 30.0 (CH), 15.3 (2 × CH₃). IR (cm⁻¹): 3058 (C-H aromatic), 2957 (C-H aliphatic), 2869 (C-H aliphatic), 1607 (C=C), 1577 (C=N), 1514 (NO₂ asym.), 1440 (CH₂ deformation), 1406 (CH₃ deformation), 1295 (C=N bending), 1343 (NO₂ sym.), 1078 (C-N), 923 (=C-H bending), 746 (Ar-H). UV-Vis.: λ_{max} (nm)/log ε_{max}: 233 (4.78).

(E)-1-(1H-benzo[d]imidazol-2-yl)-N-(2-chlorobenzylidene)-3-methylbutan-1-amine (7c). General procedure described for **7a** was used for reaction of **6** (1.00 g, 4.93 mmol) with 2-chlorobenzaldehyde (0.55 mL, 4.93 mmol) to produce **7c** as brown solid. Yield: 81%. ¹H-NMR (400 MHz, DMSO-*d*₆) δ_H: 8.70 (s, 1H, N=CH), 8.28-8.25 (d, $J = 8.06$ Hz, 1H, Ar-H), 7.68-7.66 (d, $J = 8.02$ Hz, 1H, Ar-H), 7.27-7.25 (m, 2H, Ar-H), 7.14-7.12 (d, $J = 9.10$ Hz, 2H, Ar-H), 6.51-6.49 (dd, $J_1 = 3.52$ Hz, $J_2 = 9.10$ Hz, 1H, Ar-H), 6.39-6.36 (dd, $J_1 = 3.44$ Hz, $J_2 = 9.10$ Hz, 1H, Ar-H), 5.87 (s, 1H, NH), 3.74-3.72 (t, $J = 3.68$ Hz, 1H, CH), 2.02-2.00 (dd, $J_1 = 2.42$ Hz, $J_2 = 10.32$ Hz, 1H, CH_a of CH₂), 1.96-1.94 (dd, $J_1 = 2.76$ Hz, $J_2 = 10.32$ Hz, 1H, CH_b of CH₂), 1.27-1.23 (m, 1H, CH), 0.87-0.85 (d, $J = 6.62$ Hz, 6H, 2 × CH₃). ¹³C-NMR (100 MHz, DMSO-*d*₆) δ_C: 162.5 (CH), 158.3 (C), 154.7 (C), 151.4 (C), 147.2 (CH), 143.9 (CH), 140.0 (CH), 134.4 (CH), 130.7 (CH), 125.0 (CH), 124.1, 118.1, 116.0 (CH), 108.1 (CH), 57.2 (CH), 46.8 (CH₂), 30.0 (CH), 15.3 (2 × CH₃). IR (cm⁻¹): 3058 (C-H aromatic), 2957 (C-H aliphatic), 2868 (C-H aliphatic), 1607 (C=C), 1573 (C=N), 1440 (CH₂ deformation), 1404 (CH₃ deformation), 1295 (C=N bending), 1051 (C-N), 922 (=C-H), 743 (Ar-H), 668 (C-Cl). UV-Vis.: λ_{max} (nm)/log ε_{max}: 206 (5.27), 281 (4.77).

(E)-1-(1H-benzo[d]imidazol-2-yl)-N-(3-methoxybenzylidene)-3-methylbutan-1-amine (7d). General procedure described for **7a** was used for reaction of **6** (1.00 g, 4.93 mmol) with 3-methoxybenzaldehyde (0.60 mL, 4.93

mmol) to produce **7d** as brown solid. Yield: 71%. ¹H-NMR (400 MHz, DMSO-*d*₆) δ_H: 8.69 (s, 1H, N=CH), 8.36 (s, 1H, Ar-H), 7.89-7.87 (d, $J = 8.12$ Hz, 1H, Ar-H), 7.71-7.69 (d, $J = 8.02$ Hz, 1H, Ar-H), 7.14-7.12 (d, $J = 9.11$ Hz, 2H, Ar-H), 6.86-6.84 (dd, $J_1 = 8.02$ Hz, $J_2 = 8.12$ Hz, 1H, Ar-H), 6.51-6.49 (dd, $J_1 = 3.52$ Hz, $J_2 = 9.10$ Hz, 1H, Ar-H), 6.39-6.36 (dd, $J_1 = 3.44$ Hz, $J_2 = 9.12$ Hz, 1H, Ar-H), 5.86 (s, 1H, NH), 3.74-3.72 (t, $J = 3.68$ Hz, 1H, CH), 3.13 (s, 3H, OCH₃), 2.03-2.00 (dd, $J_1 = 2.42$ Hz, $J_2 = 10.32$ Hz, 1H, CH_a of CH₂), 1.96-1.94 (dd, $J_1 = 2.76$ Hz, $J_2 = 10.32$ Hz, 1H, CH_b of CH₂), 1.27-1.23 (m, 1H, CH), 0.87-0.85 (d, $J = 6.62$ Hz, 6H, 2 × CH₃). ¹³C-NMR (100 MHz, DMSO-*d*₆) δ_C: 163.4 (CH), 161.8 (C), 158.4 (C), 154.7 (C), 150.9 (C), 147.2 (CH), 142.9 (CH), 137.8 (CH), 134.4 (CH), 130.7 (CH), 118.1 (C), 116.0 (CH), 111.3 (CH), 108.3 (CH), 58.4 (CH), 53.5 (OCH₃), 46.0 (CH₂), 30.0 (CH), 15.6 (2 × CH₃). IR (cm⁻¹): 3057 (C-H aromatic), 2956 (C-H aliphatic), 2869 (C-H aliphatic), 1608 (C=C), 1579 (C=N), 1438 (CH₂ deformation), 1406 (CH₃ deformation), 1294 (C=N bending), 1160 (C-O), 1027 (C-N), 924 (=C-H), 743 (Ar-H). UV-Vis.: λ_{max} (nm)/log ε_{max}: 209 (5.25), 245 (4.99), 293 (5.06).

(E)-1-(1H-benzo[d]imidazol-2-yl)-N-(4-chlorobenzylidene)-3-methylbutan-1-amine (7e). General procedure described for **7a** was used for reaction of **6** (1.00 g, 4.93 mmol) with 4-chlorobenzaldehyde (0.69 g, 4.93 mmol) to produce Compound **7e** as black solid. Yield: 79%. ¹H-NMR (400 MHz, DMSO-*d*₆) δ_H: 8.71 (s, 1H, N=CH), 8.12-8.09 (d, $J = 8.14$ Hz, 2H, Ar-H), 7.55-7.53 (d, $J = 8.02$ Hz, 2H, Ar-H), 7.27-7.25 (m, 2H, Ar-H), 7.14-7.12 (d, $J = 9.10$ Hz, 2H, Ar-H), 6.51-6.49 (dd, $J_1 = 3.52$ Hz, $J_2 = 9.10$ Hz, 1H, Ar-H), 6.39-6.36 (dd, $J_1 = 3.44$ Hz, $J_2 = 9.10$ Hz, 1H, Ph-H), 5.89 (s, 1H, NH), 3.74-3.72 (t, $J = 3.68$ Hz, 1H, CH), 2.02-2.00 (dd, $J_1 = 2.42$ Hz, $J_2 = 10.32$ Hz, 1H, CH_a of CH₂), 1.96-1.94 (dd, $J_1 = 2.76$ Hz, $J_2 = 10.32$ Hz, 1H, CH_b of CH₂), 1.27-1.23 (m, 1H, CH), 0.87-0.85 (d, $J = 6.60$ Hz, 6H, 2 × CH₃). ¹³C-NMR (100 MHz, DMSO-*d*₆) δ_C: 162.7 (CH), 158.2 (C), 154.1 (C), 150.2 (C), 146.8 (CH), 142.6 (C), 138.3 (2 × CH), 134.4 (CH), 130.7 (CH), 121.6 (2 × CH), 118.1 (C), 116.0 (CH), 58.6 (CH), 46.7 (CH₂), 29.7 (CH), 15.4 (2 × CH₃). IR (cm⁻¹): 1607 (C=C), 1579 (C=N), 1439 (CH₂ deformation), 1405 (CH₃ deformation), 1295 (C=N bending), 1084 (C-N),

921 (=C-H), 743 (Ar-H), 668 (C-Cl). UV-Vis.: λ_{\max} (nm)/log ϵ_{\max} : 209 (5.28), 296 (5.14).

(E)-4-((1-(1H-benzo[d]imidazol-2-yl)-3-methylbutylimino)methyl)phenol (7f). General procedure described for **7a** was used for reaction of **6** (1.00 g, 4.93 mmol) with 4-hydroxybenzaldehyde (0.60 g, 4.93 mmol) to produce **7f** as red solid. Yield: 99%; $^1\text{H-NMR}$ (400 MHz, DMSO- d_6) δ_{H} : 8.70 (s, 1H, N=CH), 7.95-7.93 (d, $J = 8.00$ Hz, 2H, Ar-H), 7.45-7.42 (d, $J = 8.26$ Hz, 2H, Ar-H), 7.14-7.12 (d, $J = 9.10$ Hz, 2H, Ar-H), 6.51-6.49 (dd, $J_1 = 3.52$ Hz, $J_2 = 9.10$ Hz, 1H, Ar-H), 6.39-6.36 (dd, $J_1 = 3.44$ Hz, $J_2 = 9.10$ Hz, 1H, Ar-H), 5.88 (s, 1H, NH), 3.74-3.72 (t, $J = 3.68$ Hz, 1H, CH), 2.02-2.00 (dd, $J_1 = 2.42$ Hz, $J_2 = 10.32$ Hz, 1H, CH_a of CH₂), 1.96-1.94 (dd, $J_1 = 2.76$ Hz, $J_2 = 10.32$ Hz, 1H, CH_b of CH₂), 1.27-1.23 (m, 1H, CH), 0.87-0.85 (d, $J = 6.60$ Hz, 6H, 2 \times CH₃). $^{13}\text{C-NMR}$ (100 MHz, DMSO- d_6) δ_{C} : 163.4 (CH), 158.3 (C), 154.2 (C), 150.4 (C), 146.8 (CH), 144.4 (2 \times CH), 141.5 (C), 134.5 (CH), 130.7 (CH), 122.3 (2 \times CH), 118.0 (C), 116.0 (CH), 58.8 (CH), 46.7 (CH₂), 30.1 (CH), 15.6 (2 \times CH₃). IR (cm⁻¹): 3380 (OH), 3050 (C-H aromatic), 2956 (C-H aliphatic), 2869 (C-H aliphatic), 1579 (C=N), 1439 (CH₂ deformation), 1405 (CH₃ deformation), 1295 (C=N bending), 1089 (C-N), 922 (=C-H), 743 (Ar-H). UV-Vis.: λ_{\max} (nm)/log ϵ_{\max} : 212 (5.31), 245 (5.21), 293 (5.29).

(E)-4-((1-(1H-benzo[d]imidazol-2-yl)-3-methylbutylimino)methyl)-N,N-dimethyl aniline (7g). General procedure described for **7a** was used for reaction of **6** (1.00 g, 4.93 mmol) with 4-(*N,N*-dimethylamino)benzaldehyde (0.74 g, 4.93 mmol) to produce **7g** as yellow solid. Yield: 80%. $^1\text{H-NMR}$ (400 MHz, DMSO- d_6) δ_{H} : 8.66 (s, 1H, N=CH), 7.77-7.75 (d, $J = 8.08$ Hz, 2H, Ar-H), 7.45-7.41 (d, $J = 8.26$ Hz, 2H, Ar-H), 7.14-7.12 (d, $J = 9.10$ Hz, 2H, Ar-H), 6.51-6.49 (dd, $J_1 = 3.50$ Hz, $J_2 = 9.10$ Hz, 1H, Ar-H), 6.39-6.36 (dd, $J_1 = 3.42$ Hz, $J_2 = 9.10$ Hz, 1H, Ar-H), 5.88 (s, 1H, NH), 3.74-3.72 (t, $J = 3.68$ Hz, 1H, CH), 3.32 (s, 6H, 2 \times CH₃), 2.02-2.00 (dd, $J_1 = 2.42$ Hz, $J_2 = 10.32$ Hz, 1H, CH_a of CH₂), 1.96-1.94 (dd, $J_1 = 2.76$ Hz, $J_2 = 10.32$ Hz, 1H, CH_b of CH₂), 1.27-1.23 (m, 1H, CH), 0.87-0.85 (d, $J = 6.60$ Hz, 6H, 2 \times CH₃). $^{13}\text{C-NMR}$ (100 MHz, DMSO- d_6) δ_{C} : 164.1 (CH), 158.4 (C), 156.2 (2 \times CH), 154.5 (C), 150.4 (C), 147.2 (CH), 142.0 (C), 134.5 (CH), 130.7 (CH), 122.8 (2 \times CH), 118.3 (C), 116.0 (CH), 59.8 (CH), 54.3 (2

\times CH₃), 46.8 (CH₂), 30.0 (CH), 15.3 (2 \times CH₃). IR (cm⁻¹): 3040 (C-H aromatic), 2956 (C-H aliphatic), 2868 (C-H aliphatic), 1607 (C=C), 1578 (C=N), 1439 (CH₂ deformation), 1405 (CH₃ deformation), 1295 (C=N bending), 1063 (C-N), 923 (=C-H), 746 (Ar-H). UV-Vis.: λ_{\max} (nm)/log ϵ_{\max} : 206 (5.10), 260 (4.75), 323 (4.94).

(E)-4-((1-(1H-benzo[d]imidazol-2-yl)-3-methylbutylimino)methyl)-N,N-diethylaniline (7h). General procedure described for **7a** was used for reaction of **6** (1.00 g, 4.93 mmol) with 4-(*N,N*-diethylamino)benzaldehyde (0.87 g, 4.93 mmol) to produce **7h** as orange solid. Yield: 91%. $^1\text{H-NMR}$ (400 MHz, DMSO- d_6) δ_{H} : 8.66 (s, 1H, N=CH), 7.77-7.75 (d, $J = 8.06$ Hz, 2H, Ar-H), 7.45-7.41 (d, $J = 8.24$ Hz, 2H, Ar-H), 7.14-7.12 (d, $J = 9.10$ Hz, 2H, Ar-H), 6.51-6.48 (dd, $J_1 = 3.52$ Hz, $J_2 = 9.10$ Hz, 1H, Ar-H), 6.38-6.36 (dd, $J_1 = 3.44$ Hz, $J_2 = 9.10$ Hz, 1H, Ar-H), 5.88 (s, 1H, NH), 4.53-4.50 (q, $J = 6.70$ Hz, 4H, 2 \times CH₂), 3.74-3.72 (t, $J = 3.68$ Hz, 1H, CH), 2.02-2.00 (dd, $J_1 = 2.42$ Hz, $J_2 = 10.32$ Hz, 1H, CH_a of CH₂), 1.96-1.94 (dd, $J_1 = 2.76$ Hz, $J_2 = 10.32$ Hz, 1H, CH_b of CH₂), 1.66-1.60 (t, $J = 6.70$ Hz, 6H, 2 \times CH₃), 1.27-1.23 (m, 1H, CH), 0.87-0.85 (d, $J = 6.60$ Hz, 6H, 2 \times CH₃); $^{13}\text{C-NMR}$ (100 MHz, DMSO- d_6) δ_{C} : 164.1 (C), 158.3 (C), 156.2 (2 \times CH), 154.5 (C), 150.4 (C), 147.2 (CH), 142.0 (C), 134.5 (CH), 130.7 (CH), 122.8 (2 \times CH), 118.3 (C), 116.0 (CH), 62.4 (2 \times CH₂), 59.2 (CH), 46.9 (CH₂), 30.0 (CH), 20.7 (2 \times CH₃), 15.3 (2 \times CH₃). IR (cm⁻¹): 3058 (C-H aromatic), 2962 (C-H aliphatic), 2929 (C-H aliphatic), 2870 (C-H aliphatic), 1609 (C=C), 1579 (C=N), 1451 (CH₂ deformation), 1405 (CH₃ deformation), 1276 (C=N bending), 1061 (C-N), 924 (=C-H), 744 (Ar-H). UV-Vis.: λ_{\max} (nm)/log ϵ_{\max} : 245 (5.38), 305 (5.38), 545 (-2.48), 578 (2.48).

(E)-1-(1H-benzo[d]imidazol-2-yl)-3-methyl-N-(propan-2-ylidene)butan-1-amine (7i). To a stirred solution of compound **6** (1.00 g, 4.93 mmol) in 10 mL of tetrahydrofuran, was added acetone (1.00 mL, 4.93 mmol) in 5 mL of tetrahydrofuran followed by the addition of two drops of concentrated HCl. The reacting mixture was then refluxed at 85 °C for 4 h as evident by reaction completion through complete consumption of starting material (monitored on TLC, CH₂Cl₂/CH₃OH \rightarrow 9:1, v/v). The resulting solution was cooled and

concentrated to access crude product which was recrystallized from ethanol to afford **7i** as green solid. Yield: 57%. ¹H-NMR (400 MHz, DMSO-*d*₆) δ_H: 7.20-7.18 (d, *J* = 8.00 Hz, 2H, Ar-H), 6.51-6.48 (dd, *J*₁ = 3.52 Hz, *J*₂ = 8.00 Hz, 1H, Ar-H), 6.38-6.36 (dd, *J*₁ = 3.44 Hz, *J*₂ = 8.00 Hz, 1H, Ar-H), 5.88 (s, 1H, NH), 3.74-3.72 (t, *J* = 3.66 Hz, 1H, CH), 2.20 (s, 6H, 2 × CH₃), 2.03-2.00 (dd, *J*₁ = 2.42 Hz, *J*₂ = 10.32 Hz, 1H, CH_a of CH₂), 1.95-1.93 (dd, *J*₁ = 2.76 Hz, *J*₂ = 10.32 Hz, 1H, CH_b of CH₂), 1.28-1.23 (m, 1H, CH), 0.87-0.85 (d, *J* = 6.60 Hz, 6H, 2 × CH₃). ¹³C-NMR (100 MHz, DMSO-*d*₆) δ_C: 162.0 (C), 158.4 (C), 154.5 (C), 147.2 (CH), 134.4 (CH), 130.7 (CH), 118.1 (C), 116.0 (CH), 60.5 (CH), 46.7 (CH₂), 43.4 (2 × CH₃), 30.0 (CH), 15.6 (2 × CH₃). IR (cm⁻¹): 3368 (N-H), 3061 (C-H aromatic), 2956 (C-H aliphatic), 2869 (C-H aliphatic), 1621 (C=C), 1554 (C=N), 1448 (CH₂ deformation), 1414 (CH₃ deformation), 1269 (C=N bending), 1020 (C-N), 926 (=C-H), 728 (Ar-H). UV-Vis.: λ_{max} (nm)/log ε_{max}: 239 (5.47), 269 (5.44), 431 (4.17).

(E)-3-((1-(1H-benzo[d]imidazol-2-yl)-3-methylbutyl)imino)indolin-2-one (7j). General procedure described for **7i** was used for reaction of **6** (1.00 g, 4.93 mmol) with isatin (0.73 g, 4.93 mmol) to produce **7j** as brown solid. Yield: 76%. ¹H-NMR (400 MHz, DMSO-*d*₆) δ_H: 11.56 (s, 1H, NH of amide), 7.92-7.89 (d, *J* = 8.96 Hz, 2H, Ar-H), 7.44-7.41 (m, 2H, Ar-H), 7.14-7.12 (d, *J* = 9.12 Hz, 2H, Ar-H), 6.51-6.48 (dd, *J*₁ = 3.52 Hz, *J*₂ = 9.12 Hz, 1H, Ar-H), 6.38-6.36 (dd, *J*₁ = 3.44 Hz, *J*₂ = 9.12 Hz, 1H, Ar-H), 5.88 (s, 1H, NH), 3.74-3.72 (t, *J* = 3.66 Hz, 1H, CH), 2.03-2.00 (dd, *J*₁ = 2.42 Hz, *J*₂ = 10.32 Hz, 1H, CH_a of CH₂), 1.95-1.93 (dd, *J*₁ = 2.76 Hz, *J*₂ = 10.32 Hz, 1H, CH_b of CH₂), 1.28-1.23 (m, 1H, CH), 0.87-0.85 (d, *J* = 6.60 Hz, 6H, 2 × CH₃). ¹³C-NMR (100 MHz, DMSO-*d*₆) δ_C: 177.2 (C=O), 163.3 (C), 162.0 (C), 159.2 (C), 158.4 (C), 155.3 (C), 154.7 (C), 147.2 (CH), 145.6 (CH), 135.5 (CH), 134.4 (CH), 130.7 (CH), 116.0 (CH), 114.3 (CH), 111.5 (CH), 60.5 (CH), 46.7 (CH₂), 30.0 (CH), 15.6 (2 × CH₃). IR (cm⁻¹): 3396 (N-H), 3057 (C-H aromatic), 2926 (C-H aliphatic), 2869 (C-H aliphatic), 1612 (C=C), 1580 (C=N), 1454 (CH₂ deformation), 1404 (CH₃ deformation), 1274 (C=N bending), 1031 (C-N), 924 (=C-H), 745 (Ar-H). UV-Vis.: λ_{max} (nm)/log ε_{max}: 209 (5.36), 278 (4.92), 353 (4.49).

(E)-1-(1H-benzo[d]imidazol-2-yl)-3-methyl-N-(1,7,7-trimethylbicyclo[2.2.1]heptan-2-ylidene) butan-1-amine (7k). General procedure described for **7i** was used for reaction of **6** (1.00 g, 4.93 mmol) with camphor (0.75 g, 4.93 mmol) to produce **7k** as red solid. Yield: 80%. ¹H-NMR (400 MHz, DMSO-*d*₆) δ_H: 7.24-7.22 (d, *J* = 8.00 Hz, 2H, Ar-H), 6.51-6.49 (dd, *J*₁ = 3.50 Hz, *J*₂ = 8.00 Hz, 1H, Ar-H), 6.39-6.36 (dd, *J*₁ = 3.46 Hz, *J*₂ = 9.10 Hz, 1H, Ar-H), 5.86 (s, 1H, NH), 3.74-3.72 (t, *J* = 3.68 Hz, 1H, CH), 2.02-2.00 (dd, *J*₁ = 2.40 Hz, *J*₂ = 10.32 Hz, 1H, CH_a of CH₂), 1.96-1.94 (dd, *J*₁ = 2.74 Hz, *J*₂ = 10.32 Hz, 1H, CH_b of CH₂), 1.65 (s, 1H, CH), 1.30-1.27 (m, 1H, CH), 1.20 (s, 2H, CH₂), 1.18-1.15 (m, 4H), 1.10 (s, 3H, CH₃), 0.99 (s, 6H, 2 × CH₃), 0.87-0.85 (d, *J* = 6.60 Hz, 6H, 2 × CH₃). ¹³C-NMR (100 MHz, DMSO-*d*₆) δ_C: 149.3 (C), 147.2 (CH), 134.4 (CH), 130.7 (CH), 128.1 (C), 124.5 (C), 118.5 (C), 116.2 (CH), 60.0 (CH), 46.4 (CH₂), 29.3 (CH), 27.8 (CH₂), 27.4 (CH₂), 26.9 (CH₂), 15.7 (2 × CH₃), 15.0 (2 × CH₃), 11.7 (CH₃). IR (cm⁻¹): 3058 (C-H aromatic), 2957 (C-H aliphatic), 2870 (C-H aliphatic), 1607 (C=C), 1578 (C=N), 1454 (CH₂ deformation), 1406 (CH₃ deformation), 1275 (C=N bending), 1046 (C-N), 923 (=C-H), 745 (Ar-H). UV-Vis.: λ_{max} (nm)/log ε_{max}: 209 (5.36), 254 (5.19), 437 (4.71).

(E)-N-(1-(1H-benzo[d]imidazol-2-yl)-3-methylbutyl) benzenesulfonamide (7l). Precursor **6** (5.08 g, 25.00 mmol) was transferred to Na₂CO₃ (5.57 g, 52.5 mmol) in H₂O (30.00 mL) with continuous stirring at 0 °C in ice-bath followed by addition of benzenesulfonyl chloride derivatives (3.83 g, 30.00 mmol) batch-wise for 1 h and the stirring continued at ambient condition for 5 h after which the reaction was terminated. The worked-up was done cautiously by adding 20% aq. HCl until complete neutralization was achieved. The collected crude product was purified by column chromatography on Merck silica gel F (Mesh 200-300) using CHCl₃/CH₃OH, (9:1, v/v) as eluting solvent to afford the benzimidazole-based sulfonamide, motifs **7l** as green solid. Yield: 84%. ¹H-NMR (400 MHz, DMSO-*d*₆) δ_H: 11.01 (s, 1H, NH), 7.94-7.92 (d, *J* = 8.08 Hz, 2H, Ar-H), 7.61-7.54 (m, 3H, Ar-H), 7.14-7.12 (d, *J* = 9.10 Hz, 2H, Ar-H), 6.51-6.49 (dd, *J*₁ = 3.52 Hz, *J*₂ = 9.10 Hz, 1H, Ar-H), 6.39-6.36 (dd, *J*₁ = 3.44 Hz, *J*₂ = 9.10 Hz, 1H, Ar-H), 5.87 (s, 1H, NH), 3.78-3.76 (t, *J*

= 3.70 Hz, 1H, CH), 2.02-2.00 (dd, $J_1 = 3.70$ Hz, $J_2 = 10.32$ Hz, 1H, CH_a of CH₂), 1.96-1.94 (dd, $J_1 = 2.74$ Hz, $J_2 = 10.32$ Hz, 1H, CH_b of CH₂), 1.26-1.21 (m, 1H, CH), 0.87-0.85 (d, $J = 6.60$ Hz, 6H, 2 × CH₃). ¹³C-NMR (100 MHz, DMSO-*d*₆) δ_C: 159.2 (C), 158.3 (C), 155.6 (C), 147.8 (CH), 143.7 (CH), 140.2 (CH), 130.7 (CH), 125.7 (CH), 124.1 (C), 118.1 (C), 116.5 (CH), 113.9 (CH), 110.1 (CH), 59.4 (CH), 46.9 (CH₂), 30.0 (CH), 15.3 (2 × CH₃). IR (cm⁻¹): 3385 (N-H), 3208 (N-H), 1620 (C=C), 1595 (C=N), 1460 (CH₂ deformation), 1405 (CH₃ deformation), 1275 (C=N bending), 1213 (SO₂), 1147 (SO₂), 1032 (C-N), 916 (=C-H), 751 (Ar-H). UV-Vis.: λ_{max} (nm)/log ε_{max}: 206 (5.26), 227 (5.16), 293 (4.25), 452 (3.53).

(E)-N-(1-(1H-benzo[d]imidazol-2-yl)-3-methylbutyl)-2-methylbenzenesulfonamide (7m). General procedure described for **7l** was used for reaction of **6** (1.00 g, 4.93 mmol) with *o*-toluenesulfonyl chloride (0.71 mL, 4.93 mmol) to produce **7m** as red solid. Yield: 91%. ¹H-NMR (400 MHz, DMSO-*d*₆) δ_H: 11.00 (s, 1H, NH), 7.92-7.90 (d, $J = 7.98$ Hz, 1H, Ar-H), 7.44-7.42 (d, $J = 7.84$ Hz, 1H, Ar-H), 7.21-7.18 (m, 2H, Ar-H), 7.14-7.12 (d, $J = 8.00$ Hz, 2H, Ar-H), 6.51-6.49 (dd, $J_1 = 3.52$ Hz, $J_2 = 8.00$ Hz, 1H, Ar-H), 6.39-6.36 (dd, $J_1 = 3.44$ Hz, $J_2 = 8.00$ Hz, 1H, Ar-H), 5.87 (s, 1H, NH), 3.78-3.76 (t, $J = 3.70$ Hz, 1H, CH), 2.39 (s, 3H, CH₃), 2.02-2.00 (dd, $J_1 = 3.70$ Hz, $J_2 = 10.32$ Hz, 1H, CH_a of CH₂), 1.96-1.94 (dd, $J_1 = 2.74$ Hz, $J_2 = 10.32$ Hz, 1H, CH_b of CH₂), 1.26-1.21 (m, 1H, CH), 0.87-0.85 (d, $J = 6.60$ Hz, 6H, 2 × CH₃). ¹³C-NMR (100 MHz, DMSO-*d*₆) δ_C: 151.2 (C), 147.8 (CH), 143.7 (CH), 140.2 (CH), 139.2 (C), 132.6 (CH), 130.7 (C), 125.9 (CH), 124.1 (CH), 118.1 (C), 116.3 (CH), 113.8 (CH), 110.9 (C), 59.4 (CH), 46.9 (CH₂), 30.0 (CH), 22.7 (CH₃), 15.3 (2 × CH₃). IR (cm⁻¹): 3384 (N-H), 3208 (N-H), 1621 (C=C), 1596 (C=N), 1461 (CH₂ deformation), 1406 (CH₃ deformation), 1275 (C=N bending), 1214 (SO₂), 1146 (SO₂), 1032 (C-N), 915 (=C-H), 750 (Ar-H). UV-Vis.: λ_{max} (nm)/log ε_{max}: 200 (5.21), 269 (5.05), 455 (4.83), 578 (3.43).

(E)-N-(1-(1H-benzo[d]imidazol-2-yl)-3-methylbutyl)-4-methylbenzenesulfonamide (7n). General procedure described for **7l** was used for reaction of **6** (1.00 g, 4.93 mmol) with *p*-toluenesulfonyl chloride (0.94 g, 4.93 mmol) to produce **7n** as yellow solid. Yield: 90%. ¹H-NMR (400 MHz, DMSO-*d*₆) δ_H: 11.03 (s, 1H, NH), 7.87-

7.85 (d, $J = 8.18$ Hz, 1H, Ar-H), 7.40-7.38 (d, $J = 8.22$ Hz, 1H, Ar-H), 7.14-7.12 (d, $J = 8.00$ Hz, 2H, Ar-H), 6.51-6.49 (dd, $J_1 = 3.52$ Hz, $J_2 = 8.00$ Hz, 1H, Ar-H), 6.39-6.36 (dd, $J_1 = 3.44$ Hz, $J_2 = 8.00$ Hz, 1H, Ar-H), 5.87 (s, 1H, NH), 3.78-3.76 (t, $J = 3.70$ Hz, 1H, CH), 2.36 (s, 3H, CH₃), 2.02-2.00 (dd, $J_1 = 3.70$ Hz, $J_2 = 10.32$ Hz, 1H, CH_a of CH₂), 1.96-1.94 (dd, $J_1 = 2.74$ Hz, $J_2 = 10.32$ Hz, 1H, CH_b of CH₂), 1.26-1.21 (m, 1H, CH), 0.87-0.85 (d, $J = 6.60$ Hz, 6H, 2 × CH₃). ¹³C-NMR (100 MHz, DMSO-*d*₆) δ_C: 151.4 (C), 147.2 (CH), 145.1 (2 × CH), 140.2 (C), 135.2 (CH), 130.7 (C), 125.9 (2 × CH), 124.1 (C), 118.1 (C), 116.3 (CH), 113.1 (CH), 59.4 (CH), 46.9 (CH₂), 30.0 (CH), 22.7 (CH₃), 15.3 (2 × CH₃). IR (cm⁻¹): 3384 (N-H), 3209 (N-H), 1621 (C=C), 1596 (C=N), 1462 (CH₂ deformation), 1407 (CH₃ deformation), 1275 (C=N bending), 1214 (SO₂), 1146 (SO₂), 1032 (C-N), 916 (=C-H), 751 (Ar-H). UV-Vis.: λ_{max} (nm)/log ε_{max}: 206 (5.23), 257 (5.06), 437 (4.66).

Antibacterial activity assay

The targeted functionalized benzimidazole motifs' antibacterial potential was evaluated using the agar diffusion method [20], while the minimum inhibitory concentration (MIC) and minimum bactericidal concentration (MBC) testing were determined using serial dilution technique [21] with respect to four targeted organisms as shown in Supplementary materials.

RESULTS AND DISCUSSION

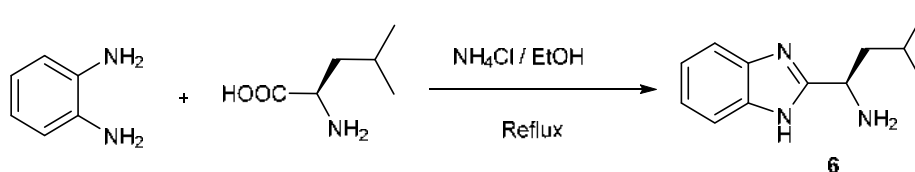
Chemistry

Benzimidazole is a benzo-fused imidazole known to be highly versatile heterocyclic compounds in therapeutic medicine, agrochemicals, and catalysis study. In furtherance of our quest to design and evaluate the biological activity of benzimidazole motifs [2,20], we have herein synthesized novel functionalized benzimidazole scaffolds so as to unveil the antibacterial potential for probable future drug discovery. First, condensation reaction of *o*-phenylenediamine (*o*-PDA) on the COOH functionality of cheap and readily available amino acid, L-leucine was carried out in ethanol solvent using the catalytic amount of ammonium chloride (NH₄Cl) as an eco-friendly medium, as shown in Scheme 1, which was according to our recently reported procedure [20].

Some commonly used catalysts and the medium used for condensation of *o*-PDA in the synthesis of benzimidazole led to the tedious work-up procedure and suffered some setbacks such as the release of toxic chemicals, harsh reaction conditions, use of expensive reagents, prolonged reaction time, and corrosive nature [16-18]. Thus, we have adopted the use of NH_4Cl as an environmentally

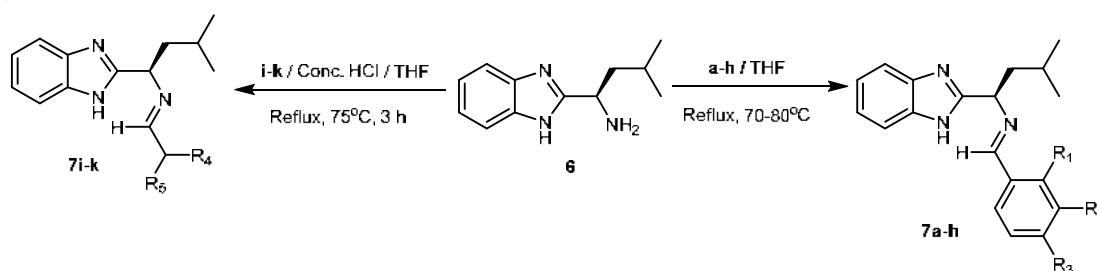
friendly and cost-effective catalyst to achieve some functionalized benzimidazole with bioactive efficacy in this present study. It was worked-up as described in the experimental section to furnish **6** in a 73% yield.

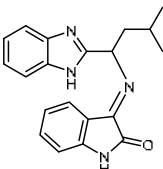
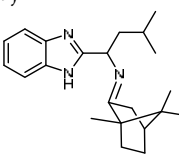
Compound **6** was then utilized as an essential building block by coupling it with eight benzaldehyde derivatives **a-h** in the presence of tetrahydrofuran (THF)



Scheme 1. Synthesis of 1-(1*H*-benzo[*d*]imidazol-2-yl)-3-methylbutan-1-amine, **6**

Table 1. Synthesis of 1-(1*H*-benzo[*d*]imidazol-2-yl)-*N*-(substituted-benzylidene/ketolidene)-3-methylbutan-1-amine, **7a-k**



Entry	R ₁	R ₂	R ₃	R ₄	R ₅	Product	Yield [%]	Elemental Analysis % Calcd. (Found)		
								C	H	N
1	H	H	H	-	-	7a	61	78.32(78.50)	7.26(7.46)	14.42(14.22)
2	NO ₂	H	H	-	-	7b	85	67.84(67.04)	5.99(6.18)	16.66(16.80)
3	Cl	H	H	-	-	7c	81	70.04(69.88)	6.19(6.40)	12.90(12.77)
4	H	OCH ₃	H	-	-	7d	71	74.74(74.82)	7.21(7.39)	13.07(12.96)
5	H	H	Cl	-	-	7e	79	70.04(70.22)	6.19(6.41)	12.90(12.73)
6	H	H	OH	-	-	7f	99	74.24(74.39)	6.89(7.08)	13.67(13.86)
7	H	H	NMe ₂	-	-	7g	80	75.41(75.66)	7.84(7.67)	16.75(16.92)
8	H	H	NEt ₂	-	-	7h	91	76.20(76.14)	8.34(8.14)	15.46(15.71)
9	-	-	-	CH ₃	CH ₃	7i	57	74.03(74.22)	8.70(8.53)	17.27(17.50)
10	-	-	-	-	-		76	72.27(72.45)	6.06(5.88)	16.86(16.89)
11	-	-	-	-	-		80	78.29(78.50)	9.26(9.37)	12.45(12.67)

Me = (CH₃); Et = (CH₂CH₃), Calcd. = Calculated

for the preparation of 1-(1*H*-benzo[*d*]imidazol-2-yl)-*N*-(*s*-benzylidene)-3methylbutan-1-amine, **7a-h**, as shown in Table 1. The reaction of precursor **6** with three distinct ketones **i-k** at a refluxing temperature of 75 °C in ethanol and concentrated HCl catalyst furnished **7i-k** as shown in Table 1. Finally, the coupling of **6** with three derivatives of aryl sulfonyl chlorides **l-n** in sodium carbonate basified medium at 0 °C to stirring at room temperature furnished **7l-n**, as shown in Scheme 2.

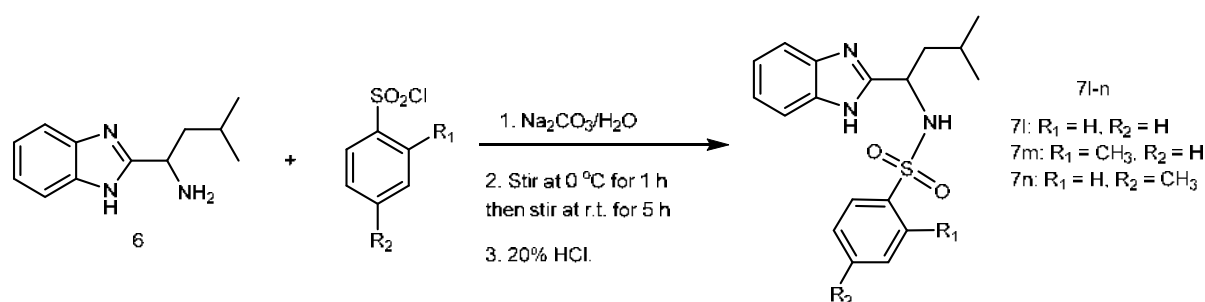
The spectroscopic characterization of the compounds was carried out for structural elucidation of the targeted compounds. The spectroscopic methods used involved ¹H-NMR, ¹³C-NMR, FT-IR, and UV-Vis. spectrophotometric analyses. The series of products was represented by **7a** for a concise spectral discussion. The azomethine proton being the most downfield signal in **7a** resonated as a 1H singlet at 8.59 ppm. The most deshielded aromatic proton was that of 2H doublet of the benzenoid nucleus portion of benzimidazole and they appeared at 7.90-7.88 ppm with a *J* value of 9.10 Hz, while their two neighboring protons on the same benzenoid nucleus resonated as 1H doublets of doublet at 6.51-6.49 ppm (*J*₁ = 3.52 Hz, *J*₂ = 9.10 Hz), and 1H doublets of doublet at 6.39-6.36 ppm (*J*₁ = 3.44 Hz, *J*₂ = 9.10 Hz). The five aromatic protons on the benzylidene portion resonated as a 3H multiplet at 7.54-7.49 ppm and a 2H doublet at 7.14-7.12 ppm with a *J* value of 8.04 Hz. The 1H singlet at 5.87 ppm depicted the presence of NH of benzimidazole.

Other signals in the ¹H-NMR spectrum of **7a** appeared more up-field because they were aliphatic protons which included 1H triplet at 3.74-3.72 ppm, followed by two germinal protons seen as 1H (CH_a of CH₂)

doublets of a doublet at 2.02-2.00 ppm and 1H (CH_b of CH₂) which resonated as doublets of a doublet at 1.96-1.94 ppm. There was 1H multiplet of CH of aliphatic at 1.26-1.21 ppm. The most shielded signal was that of two chemically equivalent methyl groups, which resonated as a 6H doublet at 0.87-0.85 ppm with a *J* value of 6.60 Hz. The first evidence for completion of the reaction was the presence of NH₂ as a doublet at 4.50 ppm in the ¹H-NMR spectral data of precursor **6** which completely disappeared from this region in the spectrum of **7a** but reappeared at a more downfield region as 1H azomethine (C=N-H) singlet at 8.69 ppm in the spectrum of **7a**.

The ¹³C-NMR spectrum of **7a** revealed it to contain nineteen carbon atoms with chemical shift values varied from 162.5 ppm to 15.3 ppm. This showed the presence of twelve CH carbons (162.5-30.0 ppm) and two chemically equivalent CH₃ carbon atoms (15.3 ppm) as positive signals, while the only negative signal at 46.8 ppm revealed that there was only one CH₂ carbon atom in the structure of **7a**. This showed that the remaining four carbon atoms (158.3, 154.7, 124.1, 118.0 ppm) were quaternary in nature.

The IR spectrum of **7a** showed the presence of CH aromatic, CH aliphatic, C=C, C=N as stretching vibrational bands which appeared at 3056, 2956, 1610, and 1579 cm⁻¹, respectively, which agreed with an earlier report with different scaffold but similar functionality [21]. The assignable bending vibrational bands and fingerprint region in agreement with the structure of **7a** were that 1294 cm⁻¹ for C=N, 1070 cm⁻¹ for C-N, 923 cm⁻¹ for =C-H and 742 cm⁻¹ for Ar-H. The UV-vis chart of **7a** unveiled its first peak at λ_{max} = 209 nm (log ε_{max} = 5.25)



Scheme 2. Synthesis of *N*-(1-(1*H*-benzo[*d*]imidazol-2-yl)-3-methylbutyl)-*s*-methylbenzene sulfonamide, **7l-n**

which depicted $\pi \rightarrow \pi^*$ transition traceable to C=C of the phenyl ring. The second signal found at $\lambda_{\max} = 293$ nm ($\log \epsilon_{\max} = 4.82$) was a bathochromic shift ascribable to the extensive conjugation and presence of C=N of imino functionality which originated from $n \rightarrow \pi^*$ transition exhibited by this auxochrome [22].

The physicochemical properties of the precursor **6** and the targeted products **7a-n** were reported to include molecular formula, molecular weight, melting point, % yields, and C, H, N analysis (Experimental). All the products had % yields ranging from 56.58% for **7i** to 99.00% for **7f**. The result of elemental analytical determination for C, H, N showed great correlation and concordance between percentage calculated and percentage observed with the difference of not more than ± 0.25 in all the synthesized benzimidazole motifs.

Biological Properties

The *in vitro* antibacterial properties of the designed motifs were carried out on four bacterial isolates comprising of *Staphylococcus aureus*, *Bacillus cereus*, *Escherichia coli*, and *Pseudomonas aeruginosa*. The screening was done alongside that of a typical clinical

standard antibiotic (Gentamicin). The rationale beneath the choice of Gentamicin as a clinical reference drug was because of the mode of action, which entails the inhibition of protein synthesis [23].

The growth of *S. aureus* was inhibited by all the synthesized compounds with Z.O.I. ranging from 18.00 ± 0.06 mm for benzimidazole motif **7a** to 31.00 ± 0.09 mm for compound **7i**, whereas the Z.O.I. of Gentamicin against *S. aureus* was 20.00 ± 0.08 mm (Table 2). The other gram-positive organism used was *Bacillus cereus*, and it has been reported to be the causative agent for highly devastating non-gastrointestinal-tract infections. It has also been tagged with most of the food poisoning cases and secretion of tissue-destructive exoenzymes [24].

However, it is very interesting to note that, out of the four bacteria, *B. cereus* had the highest susceptibility to the efficiency of the synthesized targeted compounds with zones of inhibition ranging from 35.00 ± 0.09 mm for compound **7g** to 43.00 ± 0.12 mm for compound **7j**, and these Z.O.I. were twice as large as Z.O.I. from Gentamicin standard (20.00 ± 0.08 mm). It was discovered that *E. coli* was resistant to three compounds

Table 2. Result of general sensitivity testing on bacteria with zones of inhibition in (mm)

Comp. No	<i>S. aureus</i> (G ⁺)	<i>B. cereus</i> (G ⁺)	<i>E. coli</i> (G ⁻)	<i>P. aeruginosa</i> (G ⁻)
6	25.00 ± 0.08	40.00 ± 0.12	22.00 ± 0.12	20.00 ± 0.09
7a	18.00 ± 0.06	38.00 ± 0.10	21.00 ± 0.09	20.00 ± 0.09
7b	20.00 ± 0.10	38.00 ± 0.09	20.00 ± 0.09	25.00 ± 0.08
7c	20.00 ± 0.07	37.00 ± 0.09	22.00 ± 0.09	25.00 ± 0.08
7d	30.00 ± 0.10	40.00 ± 0.10	R	20.00 ± 0.08
7e	25.00 ± 0.10	37.00 ± 0.09	31.00 ± 0.11	30.00 ± 0.10
7f	23.00 ± 0.10	40.00 ± 0.15	R	30.00 ± 0.08
7g	28.00 ± 0.09	35.00 ± 0.09	24.00 ± 0.09	26.00 ± 0.10
7h	29.00 ± 0.08	36.00 ± 0.09	22.00 ± 0.08	23.00 ± 0.08
7i	31.00 ± 0.09	37.00 ± 0.09	21.00 ± 0.09	22.00 ± 0.08
7j	30.00 ± 0.09	43.00 ± 0.12	30.00 ± 0.08	26.00 ± 0.08
7k	30.00 ± 0.10	42.00 ± 0.13	30.00 ± 0.10	26.00 ± 0.08
7l	25.00 ± 0.10	36.00 ± 0.10	R	30.00 ± 0.10
7m	30.00 ± 0.10	40.00 ± 0.13	29.00 ± 0.09	28.00 ± 0.08
7n	23.00 ± 0.09	40.00 ± 0.12	28.00 ± 0.08	30.00 ± 0.09
Gtm	25.00 ± 0.09	20.00 ± 0.08	25.00 ± 0.09	26.00 ± 0.08

S. aureus = *Staphylococcus aureus* (G⁺), *B. cereus* = *Bacillus cereus* (G⁺), *E. coli* = *Escherichia coli* (G⁻), *P. aeruginosa* = *Pseudomonas aeruginosa* (G⁻), Gtm. = Gentamicin. G⁺ = Gram positive, G⁻ = Gram negative. Z.O.I. = Zone of Inhibition. R = Resistant.

7d, **7f** and **7l**, which is probably due to antagonistic effect of OCH_3 and OH as the EDG at meta and para positions respectively, but susceptible to the rest of the compounds including the precursor **6** with zones of inhibition varying from 20.00 ± 0.09 mm for compound **7b** to 31.00 ± 0.11 mm for compound **7e** (Table 2).

Lastly, *in vitro* screening against *P. aeruginosa*, revealed that all the compounds were active on this organism with the zones of inhibition ranging from 20.00 ± 0.09 mm for compounds **6**, **7a**, and **7d** to 30.00 ± 0.09 mm for compounds **7e**, **7f**, **7l**, and **7n**, whereas Z.O.I. of Gentamicin against this organism was 26.00 ± 0.09 mm. *Pseudomonas aeruginosa* is an opportunistic organism with low permeability and is responsible for infectious diseases in people experiencing altered immune systems, some of which are burned, HIV, nosocomial and

neutropenic conditions [25]. Despite virulent possession in *P. aeruginosa* and its resistance to many antimicrobial drugs, it is quite interesting that this organism was susceptible to all the benzimidazole motifs designed herein and most of their Z.O.I. were higher than that of Gentamicin standard antibiotic used.

In addition, the activity index in this study was measured using the comparative study of inhibition zones of the synthesized compounds to that of Gentamicin upon all the organisms used (Fig. 2(a-d)). The activity index (A.I.) of the synthesized compounds against the growth of *S. aureus* was presented in Fig. 2(a). It was discovered therein that 47% of the benzimidazole products (**7d**, **7g-k**, **7m**) were more selective than Gentamicin against *S. aureus*; 20% of the benzimidazoles (**6**, **7e**, **7l**) had similar A.I. as Gentamicin,

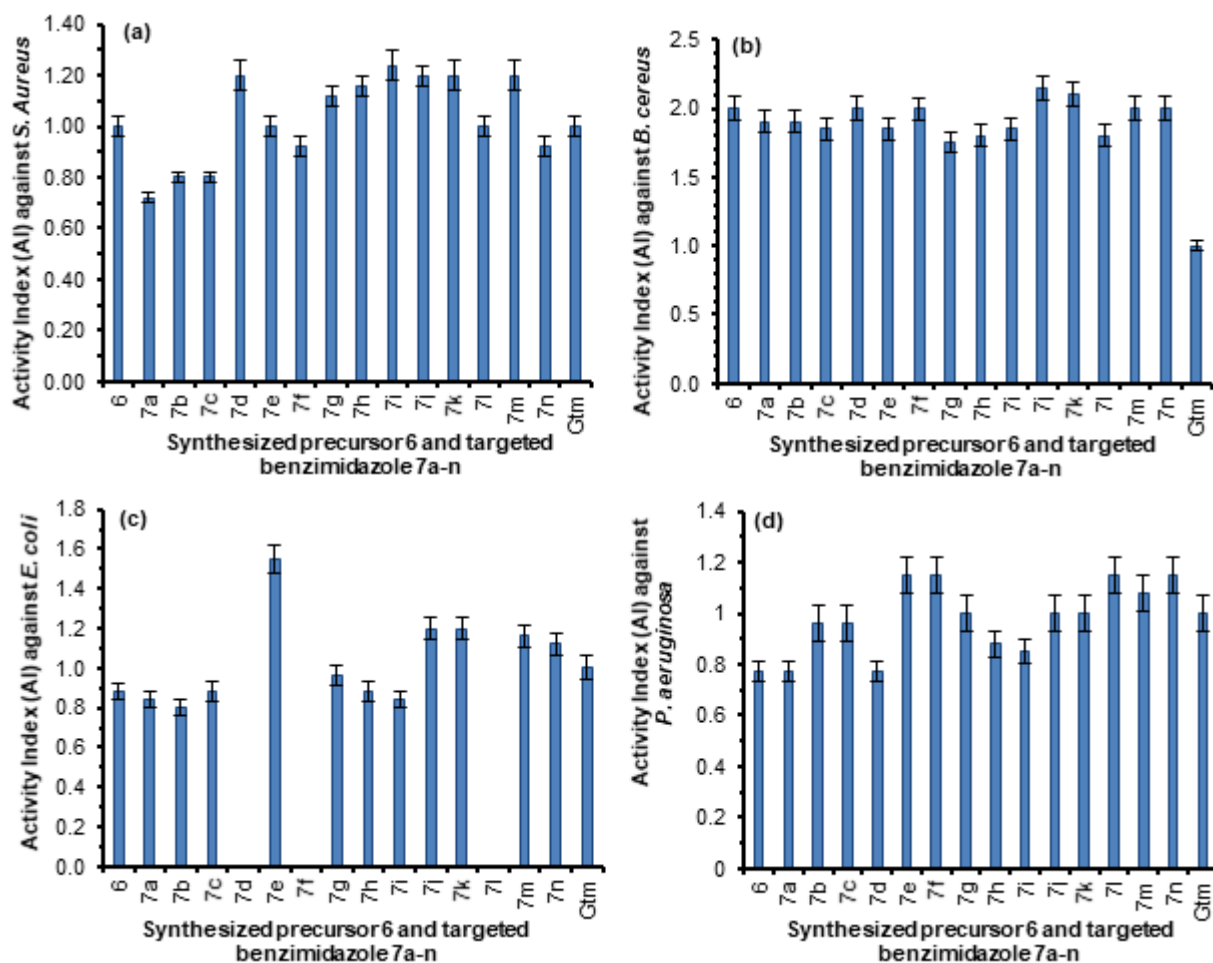


Fig 2. Activity index of the precursor 6 and targeted benzimidazole motifs **7a-n** as compared to Gentamicin clinical standard against (a) *Staphylococcus aureus*, (b) *Bacillus cereus*, (c) *Escherichia coli*, (d) *Pseudomonas aeruginosa*

while the remaining 33% (**7a**, **7b**, **7c**, **7f**, **7n**) were less active than Gentamicin against *S. aureus*. The activity index against the *B. cereus* showed that all the compounds (100%) were more selective than the Gentamicin (Fig. 2(b)), which buttressed the fact that synthesized compounds **7a-n** had impressive growth inhibitory activity against *B. cereus*. Activity index investigation against gram-negative *E. coli* unveiled that 33% of the compounds (**7e**, **7j**, **7k**, **7m**, **7n**) were more selective than Gentamicin, while the rest of the benzimidazoles were less active than Gentamicin apart from 20% of them (**7d**, **7f**, **7l**) where resistance was observed (Fig. 2(c)). Activity index against *P. aeruginosa* showed that 33% of the compounds (**7e**, **7f**, **7l-n**) were more active than Gentamicin (Fig. 2(d)); 20% of the benzimidazole motifs (**7g**, **7j**, **7k**) possessed the same activity as Gentamicin while the remaining 47% of the compounds (**6**, **7a-d**, **7h**, **7i**) were less active than gentamicin against *P. aeruginosa*.

Owing to the broad spectrum of activity, a further effort was made to determine the MIC values using serial dilution technique [21]. The result of the MIC of the precursor **6** and final benzimidazoles **7a-n** against the organisms varied from 0.98 ± 0.02 to 62.50 ± 0.59 $\mu\text{g/mL}$

(Table 3). The MIC values of the screened motifs against *S. aureus* ranged from 0.98 ± 0.02 to 62.50 ± 0.57 $\mu\text{g/mL}$ with compounds **7k** (MIC = 0.98 ± 0.02 $\mu\text{g/mL}$) being the most active. For activity on *B. cereus*, the MIC values varied from 1.95 ± 0.05 to 3.91 ± 0.08 $\mu\text{g/mL}$ with all the screened compounds being strongly active at 1.95 ± 0.05 $\mu\text{g/mL}$ except **7a**, **7d**, **7i** (MIC = 3.91 ± 0.08 $\mu\text{g/mL}$) and **7e** (15.63 ± 0.14 $\mu\text{g/mL}$). It was fascinating to note that among the four organisms, the best activity of the compounds was experienced on the *B. cereus*.

The screening against *E. coli* showed resistance to the compounds of **7d**, **7f**, and **7l**, while motifs **7e** and **7k** (MIC = 1.95 ± 0.05 $\mu\text{g/mL}$) possessed the highest activity against *E. coli*. The MIC values of the screened compounds against *P. aeruginosa* ranged from 3.91 ± 0.07 to 62.50 ± 0.59 $\mu\text{g/mL}$ with compound **7k** and **7n** (MIC = 3.91 ± 0.07 $\mu\text{g/mL}$) being the most active on *P. aeruginosa*. The concise report from the MIC screened clearly identify benzimidazole motif **7k** to be the most outstanding molecular target among the series of compound **7a-n**; therefore, can be a hit for the new antimicrobial drug as compared to the positive control used herein. The efficiency of the precursor **6** and final products **7a-n** was

Table 3. Minimum inhibitory concentration (MIC) of **6** and final products **7a-n** ($\mu\text{g/mL}$)

Comp. No	<i>S. aureus</i>	<i>B. cereus</i>	<i>E. coli</i>	<i>P. aeruginosa</i>
6	1.95 ± 0.05	1.95 ± 0.04	15.63 ± 0.15	31.25 ± 0.29
7a	7.81 ± 0.09	3.91 ± 0.07	15.63 ± 0.14	15.63 ± 0.14
7b	31.25 ± 0.29	1.95 ± 0.05	31.25 ± 0.28	15.63 ± 0.15
7c	7.81 ± 0.09	1.95 ± 0.04	15.63 ± 0.14	15.63 ± 0.14
7d	62.50 ± 0.57	3.91 ± 0.08	N.D.	62.50 ± 0.57
7e	15.63 ± 0.14	15.63 ± 0.14	1.95 ± 0.05	31.25 ± 0.29
7f	1.95 ± 0.05	1.95 ± 0.05	N.D.	15.63 ± 0.14
7g	1.95 ± 0.05	1.95 ± 0.05	7.81 ± 0.09	62.50 ± 0.59
7h	1.95 ± 0.04	1.95 ± 0.05	7.81 ± 0.09	62.50 ± 0.59
7i	3.91 ± 0.07	3.91 ± 0.08	31.25 ± 0.29	31.25 ± 0.28
7j	1.95 ± 0.04	1.95 ± 0.04	7.81 ± 0.09	62.50 ± 0.59
7k	0.98 ± 0.02	1.95 ± 0.05	1.95 ± 0.05	3.91 ± 0.07
7l	7.81 ± 0.09	1.95 ± 0.04	N.D.	15.63 ± 0.15
7m	7.81 ± 0.09	1.95 ± 0.04	15.63 ± 0.15	15.63 ± 0.1
7n	7.81 ± 0.09	1.95 ± 0.05	31.25 ± 0.29	3.91 ± 0.07

S. aureus = *Staphylococcus aureus* (G⁺), *B. lichenformis* = *Bacillus lichenformis* (G⁺). *P. vulgaris* = *Proteus vulgaris* (G⁻). *P. aeruginosa* = *Pseudomonas aeruginosa* (G⁻), Gtm. = Gentamicin. G⁺ = Gram positive, G⁻ = Gram negative, MIC = Minimum Inhibitory Concentration ($\mu\text{g/mL}$). N.D. = Not Determined

lowest against *P. aeruginosa* with very big MIC values of 15.63 to 62.50 $\mu\text{g/mL}$ except for **7k** and **7n** (MIC = 3.91 $\mu\text{g/mL}$). This might be due to the presence of ABC transporters in the hardy cell wall of *P. aeruginosa*, which utilized the porins and efflux pumps to pump out some solution of synthesized compounds herein, immediately after the administration and before the effective distribution of the solution of these compounds **7a-n** takes place [23].

The minimum bactericidal concentration (MBC) test was carried out according to a known procedure [20], and the result was shown in Fig. 3. The MBC in all titled compounds **6**, **7a-n** were observed to be two-fold higher than the MIC against *S. aureus* and *B. cereus* and their MBC varied from 1.95 ± 0.04 to 125 ± 1.20 $\mu\text{g/mL}$, which was an indication that the final benzimidazole products had better potency as compared with the precursor **6**. Against gram-negative *E. coli*, the MBC of all the compounds were two-fold higher than MIC except for precursor **6** wherein MBC (62.50 ± 0.59 $\mu\text{g/mL}$) was four-fold higher than MIC (15.63 ± 0.15 $\mu\text{g/mL}$). The bioactivity of all the compounds was least against *P. aeruginosa* since MBC of three compounds **6**, **7i** (125 ± 1.20 $\mu\text{g/mL}$) and **7c** (62.5 ± 0.59 $\mu\text{g/mL}$) were four-fold higher than their MIC which was 31.25 ± 0.29 $\mu\text{g/mL}$ and 15.63 ± 0.14 $\mu\text{g/mL}$ respectively.

Structure Activity Relationship (SAR) Study

In order to optimize the inhibitory potential of molecules and to understand which residues and

positions that are important for the activity [2,9,20], series of targeted 2-substituted benzimidazole motifs **7a-n** were herein evaluated for SAR study. Thus, SAR pattern identification is a crucial endeavor to harness a better comprehension of the trend of activities of biomolecules based on the pattern of substitution at the side chain to the structurally related pharmacophoric template portion [20]. The series of structurally related benzimidazole derivatives synthesized herein were evaluated for the SAR study to ascertain the effect of substitution pattern and nature of the substituent on the degree of bioactivity (Fig. 4). The choice of *S. aureus* as an organism for SAR discussion was due to its virulent and stubborn nature, difficulty to treat as well as the regular trend in the pattern of bioactivity observed as the moieties' positions are altered on the ring.

Considering the significance of substituents on the activity of the benzylidene side chain of benzimidazoles **7a-h** based on the MIC values, the order of activity against the growth of *S. aureus* was $7f \approx 7g \approx 7h > 7a \approx 7c > 7e > 7b > 7d$. The clear observation of this trend showed that the presence of electron donating group (EDG: -OH, -N(CH₃)₂ and -N(CH₂CH₃)₂) at the para-position of the benzylidene side chain of **7f**, **7g**, and **7h**, led to an increase in the antibacterial activity. This showed that the availability of EDGs on the para-position of benzylidene was an essential criterion for activity enhancement. On the contrary, there was no significant

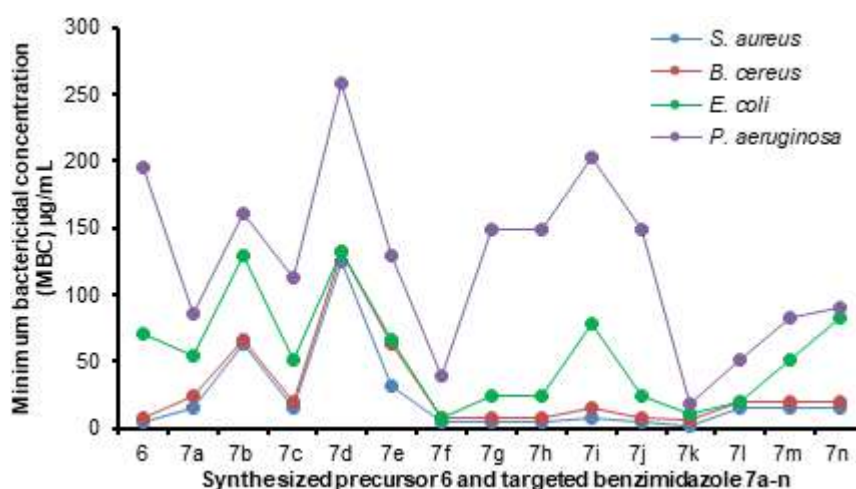


Fig 3. Minimum bactericidal concentration (MBC) result of synthesized benzimidazoles

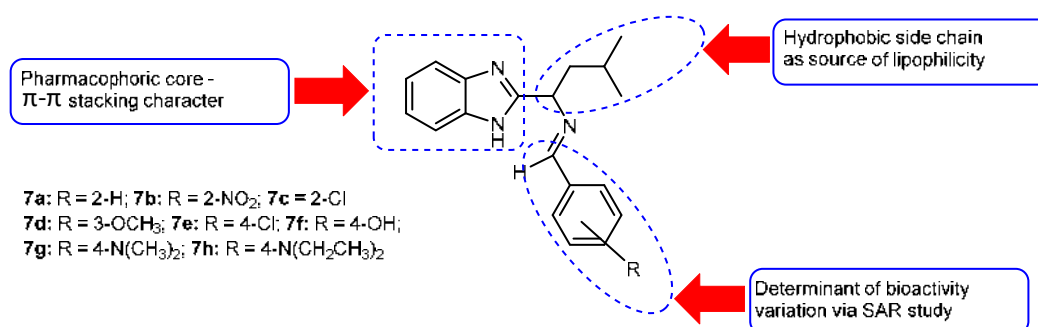


Fig 4. Structural moieties responsible for SAR study in the molecular template

bioactivity contribution to the availability of EWG (Cl, NO₂) at the ortho- or/and para-position led to the loss of antibacterial activity against *S. aureus*. This might be due to the fact that the depletion of electron density at the site of reaction led to the binding affinity reduction.

Considering the series of benzimidazole motifs **7i-k**, which had imine obtained from condensation from ketone, the order of antibacterial activity against *S. aureus* is **7k** > **7j** > **7i**. The highest activity was noticed in **7k** wherein the imine side chain was formed from a bicyclic ketone (camphor), which constituted the steric effect followed by **7j**, which contained bicyclic heterocyclic ketone (isatin). Meanwhile, the lowest activity among the three was from **7i** which was derived from straight chain, ketone acetone.

Thus, the bicyclic ring system of the imino arms contributed a significant function in the boosting of activity, which rendered **7k** to be the most active among **7i-k**. The π - π stacking character in the benzimidazole core also worked synergistically for the improvement of the antibacterial activity [20,26]. According to the activity behavioral pattern of the series of sulfonamido-based benzimidazole motifs **7l-n** against *S. aureus*, the order of activity includes **7l** \approx **7m** \approx **7n**. Since **7m** with ortho-substitution (2-CH₃) and **7n** with para-substitution (4-CH₃) had the same bioactivity with **7l** that had no substituent on its benzene nucleus, then the presence of methyl substituent on the benzene ring of sulfonamido portion played no significant role in activity change whether positive or negative against *S. aureus*. Benzylidene portion of benzimidazole series **7a-h** and bicyclic core orientation, as well as π - π stacking character in benzimidazole series **7i-k**, were accountable for

diversity in bioactivity. Finally, no bioactive significant role could be ascribable to substitution on the series of benzimidazole with sulfonamide side group in **7l-n**.

CONCLUSION

In conclusion, NH₄Cl catalyzed approach was successfully utilized as an environmentally benign technique for the synthesis of novel benzimidazole precursor **6** in good yield. In this present study, the 2-functionalized derivatives of benzimidazole **7a-n** were successfully synthesized. Compound **7k** containing camphor (bulky group) was the most effective antibacterial agent. Thus, there is a need for further studies in order to appreciate the therapeutic efficacy displayed by this series of titled 2-substituted benzimidazole motifs.

ACKNOWLEDGMENTS

The World Academy of Sciences (TWAS) is gratefully acknowledged by OOA for the sponsorship of this project under the TWAS Research Grant for Individual in Basic Science Programme (Grant No. 14-069 RG/CHE/AF/AC_1). Covenant University is gratefully acknowledged for her support.

REFERENCES

- [1] Polshettiwar, V., and Varma, R. S., 2008, Greener and expeditious synthesis of bioactive heterocycles using microwave irradiation, *Pure Appl. Chem.*, 80 (4), 777-790.
- [2] Ajani, O.O., Aderohunmu, D.V., Ikpo, C.O., Adedapo, A.E., and Olanrewaju, I.O., 2016, Functionalized benzimidazole scaffolds: Privileged

- heterocycle for drug design in therapeutic medicine, *Arch. Pharm.*, 349 (7), 475–506.
- [3] Srivastava, S., Pandeya, S.N., Yadav, M.K., and Singh, B.K., 2013, Synthesis and analgesic activity of novel derivatives of 1,2-substituted benzimidazoles, *J. Chem.*, 2013, 694295.
- [4] Salahuddin, Salahuddin, Shaharyar, M., and Mazumder, A., 2017, Benzimidazoles: A biologically active compounds, *Arabian J. Chem.*, 10 (Suppl. 1), S157–S173.
- [5] Alaqeel, S.I., 2017, Synthetic approaches to benzimidazoles from *o*-phenylenediamine: A literature review, *J. Saudi Chem. Soc.*, 21 (2), 229–237.
- [6] Ajani, O.O., Ezeoke, E.K., Edobor-Osoh, A., and Ajani, A.O., 2013, Facile synthesis and characterization of new 2,3-disubstituted benzimidazole derivatives, *Int. Res. J. Pure Appl. Chem.*, 3 (1), 10–21.
- [7] Rithe, S.R., Jagtap, R.S., and Ubarhande, S.S., 2015, One pot synthesis of substituted benzimidazole derivatives and their characterization, *Rasayan J. Chem.*, 8 (2), 213–217.
- [8] Patil, S.A., Patil, S.A., and Patil, R., 2017, Medicinal applications of (benz)imidazole- and indole-based macrocycles, *Chem. Biol. Drug Des.*, 89 (4), 639–649.
- [9] Maruthamuthu, Rajam, S., Stella, P.C.R., Dileepan, A.G.B., and Ranjith, R., 2016, The chemistry and biological significance of imidazole, benzimidazole, benzoxazole, tetrazole and quinazolinone nucleus, *J. Chem. Pharm. Res.*, 8 (5), 505–526.
- [10] Chang, Y.S., 2012, Hypersensitivity reactions to proton pump inhibitors, *Curr. Opin. Allergy Clin. Immunol.*, 12 (4), 348–353.
- [11] Ali, M.S., Saeed, K., Rashid, I., Ijaz, M., Akbar, H., Rashid, M., and Ashraf, K., 2018, Anthelmintic drugs: Their efficacy and cost-effectiveness in different parity cattle, *J. Parasitol.*, 104 (1), 79–85.
- [12] Iwamoto, K., Uehara, Y., Inoue, Y., Taguchi, K., Muraoka, D., Ogo, N., Matsuno, K., and Asai, A., 2017, Inhibition of STAT3 by anticancer drug bendamustine, *PLoS One*, 12 (1), 1–18.
- [13] Zhang, P., Wang, H., Sun, L., Zhang, J., Xi, Y., Wu, Y., Yan, L.L., Li, X., and Sun, N., 2017, Telmisartan and hydrochlorothiazide antihypertensive treatment in high sodium intake population: A randomized double-blind trial, *J. Hypertens.*, 35 (10), 2077–2085.
- [14] Lieberman, L.A., and Higgins, D.E., 2009, A small-molecule screen identifies the antipsychotic drug pimozide as an inhibitor of *Listeria monocytogenes* infection, *Antimicrob. Agents Chemother.*, 53 (2), 756–764.
- [15] Farahat, A.A., Ismail, M.A., Kumar, A., Wenzler, T., Brun, R., Paul, A., Wilson, W.D., and Boykin, D.W., 2018, Indole and benzimidazole bichalcophenes: Synthesis, DNA binding and antiparasitic activity, *Eur. J. Med. Chem.*, 143, 1590–1596.
- [16] Anand, K., and Wakode, S., 2018, Synthesis, characterization and biological evaluation of benzimidazole derivatives, *Int. J. Pharm. Sci. Res.*, 9 (2), 617–624.
- [17] Kadhim, A.J., and Kazim, A.C., 2018, Synthesis and characterization of benzimidazole by using *O*-phenylenediamine with different aldehydes and carboxylic acids in the presence of ρ -tsOh as a catalyst, *Orient. J. Chem.*, 34 (4), 2131–2136.
- [18] Çevik, U.A., Nurlpelin, S.B., Mina, A.C., Yusuf, Ö., and Özlem, A., 2018, Synthesis and evaluation of new benzimidazole derivatives with hydrazone moiety as anticancer agents, *Turk. J. Biochem.*, 43 (2), 151–158.
- [19] Gupta, P.D., and Birdi, T.J., 2017, Development of botanicals to combat antibiotic resistance, *J. Ayurveda Integr. Med.*, 8 (4), 266–275.
- [20] Ajani, O.O., Tolu-Bolaji, O.O., Olorunshola, S.J., Zhao, Y., and Aderohunmu, D.V., 2017, Structure-based design of functionalized 2-substituted and 1,2-disubstituted benzimidazole derivatives and their *in vitro* antibacterial efficacy, *J. Adv. Res.*, 8 (6), 703–712.
- [21] Ajani, O.O., Obafemi, C.A., Nwinyi, O.C., and Akinpelu, D.A., 2010, Microwave assisted synthesis and antimicrobial activity of 2-quinoxalinone-3-hydrazone derivatives, *Bioorg. Med. Chem.*, 18 (1), 214–221.
- [22] Komurcu, S.G., Rollas, S., Ulgen, M., Gorrod, J.W., and Cevikbas, A., 1995, Evaluation of some arylhydrazones of *p*-aminobenzoic acid hydrazide

- as antimicrobial agents and their in vitro hepatic microsomal metabolism, *Boll. Chim. Farm.*, 135 (7), 375–379.
- [23] Prescott, L.M., Harley, J.P., and Klein, D.A., 2005, *Microbiology*, 6th Ed., McGraw-Hill, Inc., New York.
- [24] Bottone, E.J., 2010, *Bacillus cereus*, a volatile human pathogen, *Clin. Microbiol. Rev.*, 23 (2), 382–398.
- [25] Arhin, A., and Boucher, C., 2010, The outer membrane protein OprQ and adherence of *Pseudomonas aeruginosa* to human fibronectin, *Microbiology*, 156 (5), 1415–1423.
- [26] Ren, Y., Zhang, L., Zhou, C.H., and Geng, R.X., 2014, Recent development of benzotriazole-based medicinal drugs, *Med. Chem.*, 4 (9), 640–662.

Thermal and Structure Analysis Based on Exfoliation of Clay in Thermosensitive Polymer by *in-situ* Polymerization

Marwah Noori Mohammed, Kamal Bin Yusoh*, and Jun Haslinda Binti Haji Shariffuddin

Faculty of Chemical and Natural Resources Engineering, Universiti Malaysia Pahang,
Lebuhraya Tun Razak 26300, Gambang, Pahang, Malaysia

* **Corresponding author:**

tel: +60199339541

email: kamal@ump.edu.my

Received: August 3, 2018

Accepted: December 16, 2018

DOI: 10.22146/ijc.40872

Abstract: Poly(*N*-vinylcaprolactam) (PNVCL) offers superior characteristics as a thermoresponsive polymer for various potential applications. An attractive procedure, namely *in-situ* polymerization, was used to prepare NVCL/clay nanocomposite in different clay ratios. Organo-modified clay as C20 and B30 were employed in a range between 1–5% based on weight. Thermogravimetric analysis (TGA) and Fourier transform infrared spectroscopy (FTIR) were used to study thermal decomposition and to assess bond conversion during polymerization of the nanocomposite. This research was conducted to study PNVCL characteristics with the addition of clay as a nanocomposite. The stretch mode of the carboxylic group (C=O) and (C=C) was present in the band range about $\sim 1635\text{ cm}^{-1}$ for the C20, but it was ranging between $1640\text{ to }1664\text{ cm}^{-1}$ for the B30 of the nanocomposite. It was observed that the decomposition was different for each type of organoclay and the temperature peaked at 30 to 800 °C, to measure the degradation points at 5, 10, and 50%. Comparison results for FTIR and TGA showed that the best nanocomposite was found in the C20 (3%) case.

Keywords: polymer; clay; nanocomposite; thermoresponsive; polymerization; thermal

■ INTRODUCTION

In general, the term stimuli-responsive polymer can be described as the chemical or physical changes of polymer responses to a small external variation in environmental conditions [1-2]. Electric or magnetic scope, mechanical stress, and temperature are physical stimuli that critically affect and mutate molecular interactions. While the change in interaction at the molecular level between polymer chains is a chemical stimulus, which includes ionic factors, chemical agents and pH [3]. Research by the pharmaceutical and biological fields showed that, between all stimuli-responsive polymers, temperature responsive polymers have the most significant attention because most of the diseases that appear due to a change in temperature are vital physiological factors in the body [4-6]. Furthermore, an attractive development was also shown for various applications, such as bioseparation platforms [7], tissue engineering [8], artificial muscles [9-10], environmental issues [11] and sensors [12-13].

Poly(*N*-isopropylacrylamide) (PNIPAM) and poly(*N*-vinylcaprolactam) (PNVCL) are the most popular thermoresponsive polymers due to their lower critical solution temperature (LCST) which is about 33 °C [14-16]. PNVCL is reported to have characteristics such as biotoxicity, biocompatibility, and solubility unlike PNIPAM [17]. The actual interest from the comparison is that PNVCL is more promising for bioanalytical and biomedical applications [18]. When utilized in medical or bio-related applications, the important factors for PNVCL are biocompatibility, macro-porosity, thermal and mechanical properties [19]. For instance, the mechanical characteristics enhancement produces PNVCL that is robust enough for scaffolds of tissue engineering and artificial cartilage [20-21] also, the macrospore structure is able to provide spaces for cell culture [22]. Therefore, it is a great technological significance when the mechanical, macro-porosity and other properties of the PNVCL are developed.

Table 1. Chemicals and materials utilized for the synthesis process

Chemicals	Formula	Purity	Phase	Source
Monomer	C ₈ H ₁₃ NO	98%	S	Aldrich
Initiator	(CH ₃) ₂ C(CN)N=NC(CH ₃) ₂ CN	98%	L	Aldrich
Hexane	C ₆ H ₁₄	99%	L	Aldrich
Diethyl ether	(CH ₃ CH ₂) ₂ O	99.7%	L	Aldrich
Cloisite C20, B30	Material		S powder	Chemical lab
distilled water	H ₂ O	99%	L	Chemical lab
Ammonium hydroxide	NH ₄ OH		L	Merck

It is known that monomer *N*-vinyl caprolactam (NVCL) has poor solubility in aqueous solution; therefore, polymerization usually happens in alcohol/water mixed solution, and small chemical molecules are used for cross-linking [23]. In this scope, Makhaeva et al. [24] synthesized PNVCL, and it was found to have a good thermo-sensitivity and polymerization occurred via methylene bisacrylamide (BIS) as chemical cross-linker in ethyl/water mixed solution. Commonly, PNVCL is chemically cross-linked by BIS characteristic with poor mechanical properties due to variation in reactivity among the cross-linker and the monomer [25].

Imaz and Forcada, Kloxin et al. [4,26] attempted to advance PNVCL mechanical properties by using other cross-linkers such as poly(ethylene glycol) diacrylate (PEGDA) and ethylene glycol dimethacrylate (EGDMA) to produce homogeneous polymeric networks. Schweikl et al. [27] also recently approved the cytotoxicity of both organic chemical cross-linkers. For physical cross-linkers, Loos et al. [28] used silica particles to prepare PNVCL by interacting with the hydrogen bonds between the PVCL carbonyl functions and silica particles in a sol-gel process. However, PNVCL preparation modality cannot stimulate macro-porosity in a polymeric matrix; therefore, silica cross-linked PNVCL nanocomposite has limited applications [29]. Substantially, the fabrication and enhancement of PNVCL properties are still challenging. As mentioned before, the drawback in the previous studies were poor mechanical properties and cytotoxicity for most of the chemical cross-linkers. Therefore, in this work, a novel thermoresponsive polymer PNVCL/clay nanocomposite was prepared by using *in-situ*

polymerization depending on clay nanosheets safety as approved by the cytotoxicity test [30-31].

■ EXPERIMENTAL SECTION

Materials

N-vinyl caprolactam (VCL) was purchased from Sigma Aldrich with a molecular weight of 139.19 g mol⁻¹, while, α,α'-Azobisisobutyronitrile, AIBN (Sigma Aldrich) was used as an initiator. Cloisite C20 and B30 bought from Sigma Aldrich and Hexane (Merck) were used as a solvent. The chemicals and materials employed for synthesis the nanocomposite are represented in Table 1.

Procedure

Preparation of PNVCL/clay nanocomposite

PNVCL/clay nanocomposite investigated in this study was prepared by free-radical polymerization by using clay nanosheets as cross-linking agents. Two kinds of organoclays including C20 (Cloisite®20A, dimethyl dehydrogenated tallow quaternary ammonium (2M2HT)-MMT) and B30 (Cloisite®30B, methyl tallow bis-2-hydroxyethyl quaternary ammonium (MT2EtOH)-MMT). Before synthesis, the clay (C20 or B30) was dried overnight at 70 °C in a ventilated oven to intercalate the clay layers. A magnetic stirrer linked to a condenser was fixed, then the flask was vacuumed. A typical preparation procedure of PNVCL/clay nanocomposite gel can be described as follows: the desired amount of clay (1–5%) was put in a 100 mL three-neck flask mixed with 5 g of NVCL and 30 mL of hexane at 50 °C for 1 h. To start polymerization, the solution was heated at 60 °C then 1 mL of AIBN was dissolved in a 10 mL of hexane and injected into the

solution by using a syringe. After a wash with methanol and water (1:1) to remove the unreacted chemicals, the PNVCL/clay nanocomposite was dried in the vacuum oven to obtain a yellowish gel.

Characterization

To identify the bonding structure between the clay particles (C20 and B30) and monomer in the *in-situ* polymerization, FTIR spectrometer was utilized [32]. Nicolet (Avatar 370 DTGS) was used with a resolution of 4 cm^{-1} from 4000 to 400 cm^{-1} . To increase the signal to noise ratio, each spectrum was taken as an average of 64 scans. TGA measures the amount and rate of change in the weight of a material as a function of temperature or time [5,21,33]. The technique can characterize materials that exhibit weight loss or gain due to decomposition, oxidation or dehydration. Samples curves were plotted with the mass change expressed in percent versus temperature or time. Each sample weighted 10 mg and was heated from 30 to $800\text{ }^{\circ}\text{C}$ at $5\text{ }^{\circ}\text{C}/\text{min}$ under nitrogen.

RESULTS AND DISCUSSION

PNVCL/clay nanocomposite and NVCL were analyzed by using FTIR to detect if polymerization had occurred. From the NVCL monomer spectrum, amide group ($\text{C}=\text{O}$) at 1624 cm^{-1} was detected and $\text{C}-\text{C}$ observed at 1430 cm^{-1} was presented to the aliphatic group in the caprolactam ring. Moreover, a further characteristic of $\text{C}=\text{C}$ peak appeared at 1648 cm^{-1} and $\text{C}-\text{H}$ stretching

band was observed at 3108 cm^{-1} in correspondence with studies by Lee et al. and Halligan et al. [8,34].

To ensure polymerization was achieved, i.e., $\text{C}-\text{H}$ and $\text{C}=\text{C}$ bands disappeared in the vinyl group of the NVCL monomer; NVCL/C20 (3%) case was investigated. Fig. 1(a) exhibits the NVCL/C20 spectra new peaks that were not typically associated with PNVCL from the literature as the clay was affected. The $\text{C}-\text{H}$ stretch bond peaks in the range of $2852\text{--}2936\text{ cm}^{-1}$ corresponded to hydroxyl ($\text{C}-\text{H}$) group present on the composite surface [35]. The band, centered at $\sim 1635\text{ cm}^{-1}$, represents the stretch mode of the carboxylic group ($\text{C}=\text{O}$) [36]. The presence of the above-mentioned carbonyl group indicates that organoclays are chemically linked to the polymer through hydrogen bonding, thereby, forming the polymer/clay nanocomposite. The interaction increases with the increase in the ratio of C20 in NVCL, thus, confirming NVCL/C20 polymerization within the organically modified galleries of Cloisite C20 (Fig. 1(b)).

The vibrations related to hydrogen bonding were observed at a range of $1542\text{--}1686\text{ cm}^{-1}$, found more intense with the increasing percentage of organoclay in the nanocomposites matrix (PNVCL - C20), as compared to neat PNVCL [37]. Furthermore, nanoclay (Cloisite C20) has OH groups on its surface and according to the hypothesis of Ross et al. they might interact with $-\text{NCO}$ groups of the isocyanate [38].

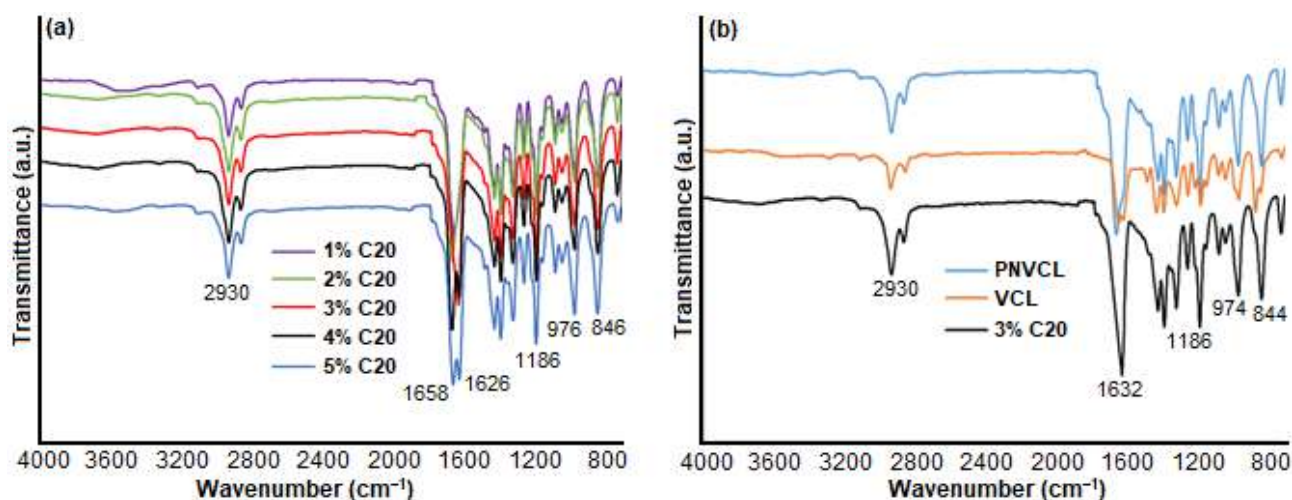


Fig 1. FTIR spectra of: (a) NVCL/C20 (1–5%), (b) PNVCL, NVCL, and NVCL/C20 (3%)

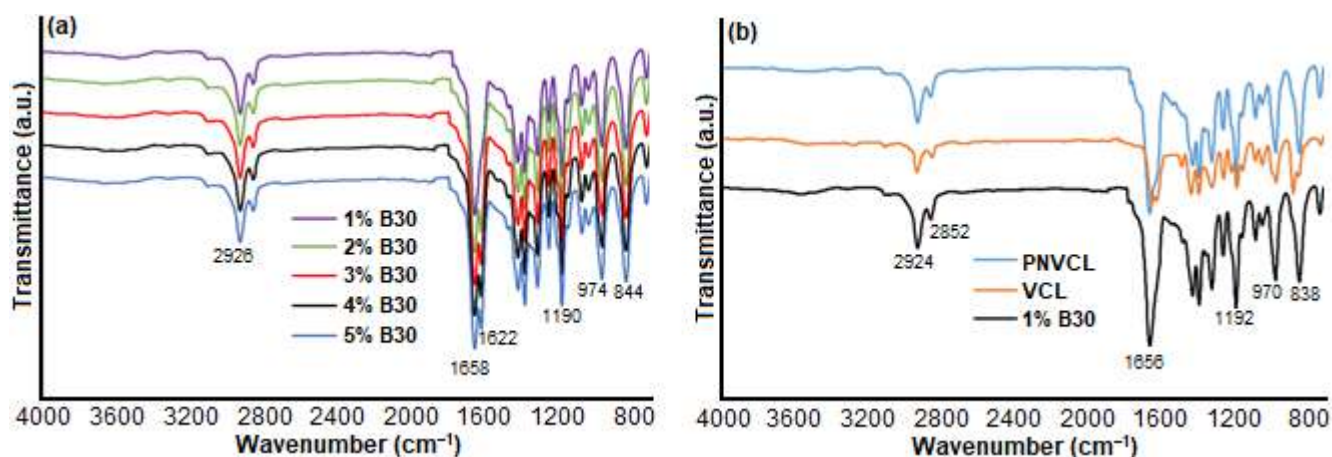


Fig 2. FTIR spectra of: (a) NVCL/B30 (1–5%), (b) PNVCL, VCL, and NVCL/B30 (1%)

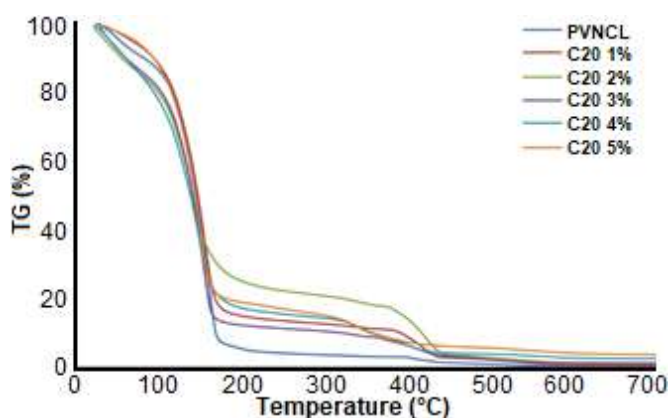


Fig 3. TGA derivative curves for PNVCL and NVCL/C20 (1–5%) nanocomposite

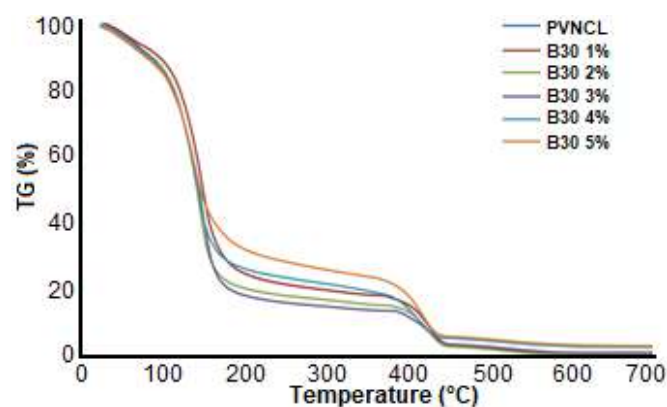


Fig 4. TGA derivative curves for PNVCL and NVCL/B30(1–5%) nanocomposite

B30 effect on the nanocomposite surface based on the FTIR measurements in five ratios are shown in Fig. 2(a). It is clear that the B30 is present in the nanocomposite produced in this study. The C-H stretch band peaks in the range of 2832–2942 cm⁻¹ corresponded to hydroxyl (C-H) group present on the composite surface. The stretch mode of the carboxylic group (C=O) and (C=C) was present in the band range between 1640 to 1664 cm⁻¹ [39]. Fig. 2(b) shows the C=O peak shifting from 1640 cm⁻¹ of NVCL to 1656 cm⁻¹ of NVCL/B30, representing clay intercalation in the nanocomposite. The vibration bands observed for different PNVCL-clays ratios at about wavenumber 1000 to 1100 cm⁻¹ as shown in Fig. 2(a) were due to Si-O stretching and this results corresponding with the study by Sarkar et al. [40].

Results of the TGA weight loss profile of the polymer/clay nanocomposite dried powder samples are shown in Fig. 3 and 4. Organo-modified C20 and B30 were used in this study as a clay. Weight loss occurred when the sample was heated from 30 to 800 °C. The curves in the figures designate the percentage of weight loss with the effect of temperature increase. It can be observed that the weight loss behavior for all samples was huge. Three regions were selected in the TGA pattern for all samples in Fig. 3 and 4. In the first region, the degradation of the mass was very sharp at the temperature range between 100 to 170 °C as shown in Fig. 3 but in Fig. 4 was ranging from 90 to 150 °C. This is due to the loss of the weakly bound OH group and physically adsorbed water from the samples [41].

Table 2. TGA data for PNVCL and nanocomposites under nitrogen flow

Sample	Temperature/°C at mass loss			Residue % at	
	5%	10%	50%	500 °C	600 °C
PNVCL	53.24	81.01	147.14	1.16	0.43
NVCL + 1% (C20)	66.95	93.87	147.80	2.37	0.90
NVCL + 2% (C20)	37.54	56.84	141.88	3.06	1.47
NVCL + 3% (C20)	42.93	61.88	141.94	2.44	1.60
NVCL + 4% (C20)	42.01	60.54	139.08	4.09	2.96
NVCL + 5% (C20)	71.18	94.21	144.72	5.84	4.31
NVCL + 1% (B30)	60.38	92.52	148.66	2.62	0.62
NVCL + 2% (B30)	58.06	86.58	141.57	2.17	0.58
NVCL + 3% (B30)	59.49	82.83	143.97	2.95	1.24
NVCL + 4% (B30)	59.05	86.08	143.19	4.77	3.11
NVCL + 5% (B30)	56.93	82.40	146.16	5.28	3.56

Meanwhile, the degradation of the total weight of the samples ranged from 60 to 95% as shown in Fig. 3, as well as the degradation, was ranging from 56 to 80% as shown in Fig. 4. This behavior appeared in all clay types (C20 and B30). In the second region, the gradual change of weight at a temperature between 170 to 450 °C for C20 and 156 to 400 °C for B30 corresponded to the removal of organic clay residues, interlayer anions and further polymerization of the monomer network [42-43]. The third region showed the lowest weight loss at a temperature above 500 °C due to the strongly bound interlayer anions and removal of the OH group from the sample for both clay types (C20 and B30) as shown in Fig. 3 and 4. The thermograms in Fig. 3 and 4 show that, after an initial loss of 20% of the original weight, there is an almost total rapid degradation of the pure PNVCL and the nanocomposites in the range from 170 to 450 °C. For the decomposition of the nanocomposites around 15–30% is left, probably corresponding to the remaining clay and polymer ashes [42].

Comparison of weight loss through TGA for all nanocomposite samples obtained from polymer/clay polymerization is shown in Table 2. Temperature at weight loss 10 and 50%, and residue at 500 and 600 °C are also presented in Table 2. It can be clearly observed that the percentage of residue increases with the increase in clay ratio from 1 to 5% in the nanocomposite. When the temperature increased to 600 °C, the polymer residue was 0.425%. On the other hand, when C20 clay was used, the

nanocomposite residue ranged from 0.9 to 4.31% based on the increase in clay ratio. The nanocomposite residue increased from 0.618 to 3.560% with the increase of B30 ratio at a temperature of 600 °C. This is ascribed to the continued elimination of strongly bound anions and a small contribution of the OH group.

■ CONCLUSION

In summary, a novel biocompatible thermoresponsive PNVCL-Clay nanocomposite was fabricated, and the successful polymerization conformed to the data via FTIR and TGA. This study allows a much greater understanding of the C20 and B30 intercalation based on the polymer systems that were influenced by the weight ratio. On the basis of the FTIR spectrometer; the shifting of the PNVCL/C20 characteristics and PNVCL/B30 peaks, it can be concluded that the C20 layers intercalation had taken place at NVCL interior more than that of B30. FTIR results confirmed the inclusion of clay in the polymer matrix. Mainly, intercalated composites were obtained. Furthermore, when C20 was used, the NVCL/C20 nanocomposite residue ranged from 0.9 to 4.31% based on the increase in clay ratio per weight. Besides that, the NVCL/B30 residue at a temperature of 600 °C also increased from 0.62 to 3.56% with the increase in ratio. The nanocomposites exhibited improvement in thermal stability as determined by TGA, mainly due to its intercalated structure. TGA data showed that the with

higher clay loadings the depolymerization stage becomes less important, suggesting that the clay affects the mechanism of thermal degradation.

■ ACKNOWLEDGMENTS

The authors would like to be obliged to Universiti Malaysia Pahang for providing laboratory facilities and financial assistance under FRGS research grant (RDU160149) and the internal research funding (RDU150398).

■ REFERENCES

- [1] Strachota, B., Matějka, L., Zhigunov, A., Konefał, R., Spěváček, J., Dybal, J., and Puffr, R., 2015, Poly(*N*-isopropylacrylamide)-clay based hydrogels controlled by the initiating conditions: evolution of structure and gel formation, *Soft Matter*, 11 (48), 9291–9306.
- [2] Francis, R., Gopalan, G.P., Sivadas, A., and Joy, N., 2016, “Properties of Stimuli-Responsive Polymers” in *Biomedical Applications of Polymeric Materials and Composites*, Eds. Francis, R., and Kumar, D.S., Wiley-VCH Verlag GmbH & Co. KGaA, Kottayam, Kerala, India, 187–231.
- [3] Karakasyan, C., Mathos, J., Lack, S., Davy, J., Marquis, M., and Renard, D., 2015, Microfluidics-assisted generation of stimuli-responsive hydrogels based on alginates incorporated with thermo-responsive and amphiphilic polymers as novel biomaterials, *Colloids Surf., B*, 135, 619–629.
- [4] Imaz, A., and Forcada, J., 2010, *N*-vinylcaprolactam-based microgels for biomedical applications, *J. Polym. Sci., Part A: Polym. Chem.*, 48 (5), 1173–1181.
- [5] Mohammed, M.N., Yusoh, K.B., and Shariffuddin, J.H.B.H., 2018, Poly(*N*-vinyl caprolactam) thermo-responsive polymer in novel drug delivery systems: A review, *Mater. Express*, 8 (1), 21–34.
- [6] Wu, W., and Zhou, S., 2013, “Responsive Polymer-Inorganic Hybrid Nanogels for Optical Sensing, Imaging, and Drug Delivery” in *Nanomaterials in Drug Delivery, Imaging, and Tissue Engineering*, Eds. Tiwari, A., and Tiwari, A., Wiley, Hoboken, New Jersey, 263–314.
- [7] Nagase, K., Kobayashi, J., and Okano, T., 2009, Temperature-responsive intelligent interfaces for biomolecular separation and cell sheet engineering, *J. R. Soc. Interface*, 6 (Suppl 3), S293–S309.
- [8] Lee, B., Jiao, A., Yu, S., You, J.B., Kim, D.H., and Im, S.G., 2013, Initiated chemical vapor deposition of thermo-responsive poly(*N*-vinylcaprolactam) thin films for cell sheet engineering, *Acta Biomater.*, 9 (8), 7691–7698.
- [9] Seliktar, D., 2012, Designing cell-compatible hydrogels for biomedical applications, *Science*, 336 (6085), 1124–1128.
- [10] Malhotra, A., Mcinnis, M., Anderson, J., and Zhai, L., 2013, “Stimuli-Responsive Conjugated Polymers: From Electronic Noses to Artificial Muscles” in *Intelligent Stimuli-Responsive Materials*, Eds. Li, Q., Wiley, Hoboken, New Jersey, 423–470.
- [11] Sanna, R., Fortunati, E., Alzari, V., Nuvoli, D., Terenzi, A., Casula, M.F., Kenny, J.M., and Mariani, A., 2013, Poly(*N*-vinylcaprolactam) nanocomposites containing nanocrystalline cellulose: A green approach to thermo-responsive hydrogels, *Cellulose*, 20 (5), 2393–2402.
- [12] Sorber, J., Steiner, G., Schulz, V., Guenther, M., Gerlach, G., Salzer, R., and Arndt, K.F., 2008, Hydrogel-based piezoresistive pH sensors: Investigations using FT-IR attenuated total reflection spectroscopic imaging, *Anal. Chem.*, 80 (8), 2957–2962.
- [13] Granados-Focil, S., 2015, “Stimuli-Responsive Polymers as Active Layers for Sensors” in *Functional Polymer Coatings: Principles, Methods, and Applications*, Eds. Wu, L., and Baghdachi, J., John Wiley & Sons, Inc., Hoboken, New Jersey, 163–196.
- [14] Lau, A.C.W., and Wu, C., 1999, Thermally sensitive and biocompatible poly(*N*-vinylcaprolactam): Synthesis and characterization of high molar mass linear chains, *Macromolecules*, 32 (3), 581–584.
- [15] Maeda, Y., Nakamura, T., and Ikeda, I., 2002, Hydration and phase behavior of poly(*N*-

- vinylcaprolactam) and poly(*N*-vinylpyrrolidone) in water, *Macromolecules*, 35 (1), 217–222.
- [16] Beija, M., Marty, J.D., and Destarac, M., 2011, Thermoresponsive poly(*N*-vinyl caprolactam)-coated gold nanoparticles: Sharp reversible response and easy tenability, *Chem. Commun.*, 47 (10), 2826–2828.
- [17] Cortez-Lemus, N.A., and Licea-Claverie, A., 2016, Poly(*N*-vinylcaprolactam), a comprehensive review on a thermoresponsive polymer becoming popular, *Prog. Polym. Sci.*, 53, 1–51.
- [18] Liu, J., Debuigne, A., Detrembleur, C., and Jérôme, C., 2014, Poly(*N*-vinylcaprolactam): A thermoresponsive macromolecule with promising future in biomedical field, *Adv. Healthcare Mater.*, 3 (12), 1941–1968.
- [19] Imran, A.B., Esaki, K., Gotoh, H., Seki, T., Ito, K., Sakai, Y., and Takeoka, Y., 2014, Extremely stretchable thermosensitive hydrogels by introducing slide-ring polyrotaxane cross-linkers and ionic groups into the polymer network, *Nat. Commun.*, 5, 1–8.
- [20] Sun, J.Y., Zhao, X., Illeperuma, W.R., Chaudhuri, O., Oh, K.H., Mooney, D.J., Vlassak, J.J., and Suo, Z., 2012, Highly stretchable and tough hydrogels, *Nature*, 489 (7414), 133–136.
- [21] Mohammed, M.N., Yusoh, K.B., and Shariffuddin, J.H.B.H., 2016, Methodized depiction of design of experiment for parameters optimization in synthesis of poly(*N*-vinylcaprolactam) thermoresponsive polymers, *Mater. Res. Express*, 3 (12), 125302.
- [22] Murphy, C.M., Haugh, M.G., and O'Brien, F.J., 2010, The effect of mean pore size on cell attachment, proliferation and migration in collagen-glycosaminoglycan scaffolds for bone tissue engineering, *Biomaterials*, 31 (3), 461–466.
- [23] Rao, K.M., Rao, K.S.V.K., and Ha, C.S., 2016, Stimuli responsive poly(vinyl caprolactam) gels for biomedical applications, *Gels*, 2 (1), 6.
- [24] Makhaeva, E.E., Thanh, L.T.M., Starodoubtsev, S.G., and Khokhlov, A.R., 1996, Thermoshrinkage behavior of poly(vinylcaprolactam) gels in aqueous solution, *Macromol. Chem. Phys.*, 197 (6), 1973–1982.
- [25] Belyaev, A.K., Irschik, H., and Krommer, M., 2016, *Mechanics and Model-based Control of Advanced Engineering Systems*, Springer-Verlag Wien, New Delhi, India, 76.
- [26] Kloxin, A.M., Kloxin, C.J., Bowman, C.N., and Anseth, K.S., 2010, Mechanical properties of cellularly responsive hydrogels and their experimental determination, *Adv. Mater.*, 22 (31), 3484–3494.
- [27] Schweikl, H., Hiller, K.A., Bolay, C., Kreissl, M., Kreismann, W., Nusser, A., Steinhauser, S., Wieczorek, J., Vasold, R., and Schmalz, G., 2005, Cytotoxic and mutagenic effects of dental composite materials, *Biomaterials*, 26 (14), 1713–1719.
- [28] Loos, W., Verbrugghe, S., Goethals, E.J., Du Prez, F.E., Bakeeva, I.V., and Zubov, V.P., 2003, Thermoresponsive organic/inorganic hybrid hydrogels based on poly(*N*-vinylcaprolactam), *Macromol. Chem. Phys.*, 204 (1), 98–103.
- [29] Gomes, M.E., Holtorf, H.L., Reis, R.L., and Mikos, A.G., 2006, Influence of the porosity of starch-based fiber mesh scaffolds on the proliferation and osteogenic differentiation of bone marrow stromal cells cultured in a flow perfusion bioreactor, *Tissue Eng.*, 12 (4), 801–809.
- [30] Gürses, A., 2015, *Introduction to Polymer–Clay Nanocomposites*, CRC Press, Taylor & Francis Group, U.S, 105.
- [31] Alcántara, A.C.S., Darder, M., Aranda, P., Ayral, A., and Ruiz-Hitzky, E., 2016, Bionanocomposites based on polysaccharides and fibrous clays for packaging applications, *J. Appl. Polym. Sci.*, 133 (2), 42362.
- [32] Zhang, T., Yuan, Y., Cui, X., Yin, H., Gu, J., Huang, H., and Shu, J., 2018, Impact of side-chain length on the phase structures of P3ATs and P3AT: PCBM films as revealed by SSNMR and FTIR, *J. Polym. Sci., Part B: Polym. Phys.*, 56 (9), 751–761.
- [33] Lyon, R.E., Safronava, N., and Crowley, S., 2018, Thermal analysis of polymer ignition, *Fire Mater.*, 42 (6), 668–679.
- [34] Halligan, S.C., Dalton, M.B., Murray, K.A., Dong, Y., Wang, W., Lyons, J.G., and Geever, L.M., 2017,

- Synthesis, characterisation and phase transition behaviour of temperature-responsive physically crosslinked poly(*N*-vinylcaprolactam) based polymers for biomedical applications, *Mater. Sci. Eng., C*, 79, 130–139.
- [35] Dimitriou, A., Hale, M.D., and Spear, M.J., 2018, The effect of pH on surface activation of wood polymer composites (WPCs) with hydrogen peroxide for improved adhesion, *Int. J. Adhes. Adhes.*, 85, 44–57.
- [36] Subramani, S., Choi, S.W., Lee, J.Y., and Kim, J.H., 2007, Aqueous dispersion of novel silylated (polyurethane-acrylic hybrid/clay) nanocomposite, *Polymer*, 48 (16), 4691–4703.
- [37] Zhang, J., Wu, Q., Li, M.C., Song, K., Sun, X., Lee, S.Y., and Lei, T., 2017, Thermoresponsive copolymer poly(*N*-vinylcaprolactam) grafted cellulose nanocrystals: Synthesis, structure, and properties, *ACS Sustainable Chem.*, 5 (8), 7439–7447.
- [38] Ross, P., Escobar, G., Sevilla, G., and Quagliano, J., 2017, Micro and nanocomposites of polybutadienebased polyurethane liners with mineral fillers and nanoclay: Thermal and mechanical properties, *Open Chem.*, 15 (1), 46–52.
- [39] Kalaivasan, N., and Syed Shafi, S., 2017, Enhancement of corrosion protection effect in mechanochemically synthesized Polyaniline/MMT clay nanocomposites, *Arabian J. Chem.*, 10 (Suppl. 1), S127–S133.
- [40] Sarkar, S., Datta, S.C., and Biswas, D.R., 2014, Synthesis and characterization of nanoclay–polymer composites from soil clay with respect to their water-holding capacities and nutrient-release behaviour, *J. Appl. Polym. Sci.*, 131 (6), 39951.
- [41] Gun'ko, V.M., Savina, I.N., and Mikhalovsky, S.V., 2017, Properties of water bound in hydrogels, *Gels*, 3 (4), 37.
- [42] Fecchio, B.D., Valandro, S.R., Neumann, M.G., and Cavalheiro, C., 2016, Thermal decomposition of polymer/montmorillonite nanocomposites synthesized in situ on a clay surface, *J. Braz. Chem. Soc.*, 27 (2), 278–284.
- [43] Shahabadi, S.I.S., and Garmabi, H., 2014, Qualitative assessment of nanoclay dispersion using thermogravimetric analysis: A response surface study, *J. Thermoplast. Compos. Mater.*, 27 (4), 498–517.

Formulation of Emulsified Modification Bitumen from Industrial Wastes

Mohd Najib Razali*, Syarifah Nur Ezatie Mohd Isa, Noor Adilah Md Salehan, Musfamikri Musa, Mohd Aizudin Abd Aziz, Abdurahman Hamid Nour, and Rosli Mohd Yunus

Faculty of Chemical and Natural Resources Engineering, Universiti Malaysia Pahang, Lebuhraya Tun Razak 26300, Gambang, Pahang, Malaysia

* **Corresponding author:**

tel: +6012-3530738

email: najibrazali@ump.edu.my

Received: August 3, 2018

Accepted: December 14, 2018

DOI: 10.22146/ijc.40888

Abstract: The aim of this research was to characterize and analyze the formulation of emulsified modification bitumen (EMB) as well as the industrial wastes used in the formulation. Bitumen being a non-renewable product with severe environmental issues arising lately led to the use of industrial wastes such as plastic and recycled base oil in this research. Physical characteristic studies were performed to analyze the decomposition temperature, boiling point, flash point, density, moisture content, element content in waste plastics, and flowability of bitumen emulsion. Eight ratios of modified bitumen were formulated and compared with the industrial grade bitumen. The modified bitumen with a penetration value of 103 mm and softening value at 49 °C was chosen for the emulsification process where three emulsifiers were added into the mixture of bitumen and water. These samples were compared with the industrial bitumen emulsion. From the analysis, the formulated emulsion was obtained from a mixture consists of 20% bitumen, 7% polymer, and 73% recycled base oil.

Keywords: bitumen; non-renewable; Emulsified Modified Bitumen (EMB); polyethylene; recycled base oil

■ INTRODUCTION

Bitumen is a thermoplastic material widely used in roofing, waterproofing products, and road construction applications [1]. The current world bitumen consumption is estimated to be 102 million tons per year of which 85% is used as a binder for pavements, 10% for roofing applications, and the rest is used for other purposes [2]. Bitumen emulsion, on the other hand, is a mixture of bitumen, water, and emulsifier which was used to provide breaking of bitumen into smaller particles, allowing the dispersion of bitumen suspended in the liquid [3]. It is widely used in various surface treatment applications, including micro surfacing, slurry seal, and chip seals. These are recognized to be the most promising techniques among various preventive pavement maintenance treatments [4]. The global market size for bitumen is expected to surpass USD150 million by 2024 [5].

In Malaysia, the urge to solve the environmental issue is getting crucial. Rapid urbanization, industrialization, and increasing population have worsened

the situation. In 2003, the average amount of MSW generated in Malaysia was 0.5–0.8 kg/person/day and it has increased to 1.7 kg/person/day in major cities [6]. A survey made by Kathirvale et al. [6] concluded that plastic is the second biggest contributor to wastes generated in Kuala Lumpur at around 11–26% after food and organic waste at 30–54%. Moreover, Environmental Protection Expenditure (EPE) 2014 was reported to the tune of RM2.244 billion with the manufacturing sector being the highest contributor to this EPE at RM1.619 billion [7]. Wastes such as polyethylene and recycled base oil can be used to formulate modified bitumen and essentially with the help of suitable emulsifier, can produce emulsified modification bitumen (EMB). The formulated EMB will be used for insulation and coating of a building.

The EMB formulated from wastes will help to decrease many environmentally threatening aspects such as lowering the energy consumption and level of CO₂ emission to the environment during construction works [8]. Besides, bitumen emulsion presents a much

lower viscosity and can be applied at a temperature as low as 80 °C. A conventional binder is sprayed at 160–200 °C so there is a much more additional risk of fire and explosion [9]. Since the beginning of the evolution in recycling technology, many studies involving EMB formulations and applications have been conducted and published. However, not much waste was used and limited in terms of its application. Carrera et al. [9] stated that using recycled polyethylene by up to 5 wt.% improved the bitumen performance at high service temperatures of 60 °C. Carrera et al. [10] claimed that a higher content of polymer of 4 wt.% enhanced the resistance to permanent deformation at approximately 60 °C compared with the standard nonmodified bituminous emulsions. Cai et al. [11] reported the use of nonrecycled styrene–butadiene–styrene (SBS) at 3–5 wt.% by dissolving it first in toluene. Some properties improved such as thermal stability, adhesion property with aggregates, and better crack resistance compared with those of pure bitumen emulsion. The past research has been focusing on using one type of waste only and particularly for surface dressing application on road constructions. Besides, in this past few years, fungal and mold growth in the operation theatre in hospitals has become a major problem in the health sector [12]. It is produced when the vapor from the air conditioner units turns to liquid, and this wet condition leads to the growth of fungi on the wall. These pathogens can enter human bodies via inhalation, ingestion, and skin contact [13]. It can be life-threatening as it may affect the respiratory system of patients and contaminate the facilities used to treat the patients. So, it is important to produce waterproofing surface dressing known as EMB that can be used both for road construction and building surface dressing to prevent fungi contamination in health sector along with the aim to reduce wastes in Malaysia.

■ EXPERIMENTAL SECTION

Materials

The bitumen grade 80/100 supplied by industry has been used to mix with waste materials. Industrial bitumen emulsion used to compare between formulated bitumen emulsions was obtained from Selangor. High density

polyethylene and polystyrene wastes having a melting point in the range of 125–148 °C and moisture content range from 0.27 to 0.78% were from landfills. Three types of recycled base oil collected from Kemaman, Banting and Kuantan and the waste sludge collected in Kemaman.

Procedure

The modified bitumen was prepared by using an IKA C-MAG HS 7 mechanical stirrer consisting of a three blade stirrer. This device was operated at 500 rpm for 3 h at a blending temperature of 180 °C. Then, HDPE polymer, recycled base oil, and bitumen were added at 80, 60, 40, and 20 wt.%. Next, bitumen emulsion was prepared by using the same device. Three different types of chemical emulsifier were then mixed with the modified bitumen at an operating temperature of 70 °C.

Sample analysis such as TGA was performed to determine the decompose temperature and the composition in a sample. This analysis measures the weight loss percentage of a test sample while heated at increasing 10 °C/min until approximately 900 °C under inert gas. 2.5 mg pf test specimen is weighed and the loss in weight over specific temperature ranges provides an indication to the composition of the sample. This test was carried out using TA Instruments TGA Q-500.

Moisture content was performed using A&D MS-70 moisture analyzer by calculating the loss of weight on drying process employed to extract and measure the moisture in each sample. The sample is placed on a weighing pan located in the drying chamber then the drying chamber is closed. A standard drying temperature at 130 °C is entered. The instrument calculates the moisture content by comparing the initial weight of the sample to the weight after complete drying. The average complete time is below 5 min for solid sample and 1 h for sludge and emulsion.

X-ray Fluorescence (XRF) Spectrometry was carried out to determine the elemental composition of a sample. Each element present in one sample will produce a set of characteristic fluorescent X-rays when it was excited by an external energy source which in turn categorizes the energy by its element. First the sample is filled in the specimen cup. The analysis is started after

standard data is collected. The X radiation illuminates and excites the sample which in turn emits X-rays along with spectrum of wavelengths characteristic to atoms present in the sample. It is conducted using SEA XRF-2000R.

Penetration test was conducted using an automatic penetrometer to determine the bitumen grade. The apparatus used include penetrometer with a needle, timer, sample container, and thermometer. The melted sample was poured into the metal container and allowed to air cool for 45 min. Then the sample was placed in the water bath at 25 °C for about 1 h. After that, the needle was assembled at the penetrator and was positioned until the tip contacts with the surface of the sample. The needle holder was then released for 5 sec. The reading shows the depth of the needle penetrating the sample indicating its grade.

Softening point test is used to measure the softening point of a bitumen sample including shouldered ring, ball cantering guide, ring holder and assembly, beaker, thermometer, and hotplate. The heated sample was poured into two shouldered rings and allow to a cool in ambient temperature for at least 30 min. Then the rings were put in a water bath for 1 h at 25 °C and once cooled, the sample was immersed in the bath and placed in a freezer at 15 °C for 45 min. After that, the apparatus with rings, ball, and thermometer in the bath was assembled. While the bath was heated from below by a hotplate, the temperature of the bath was recorded every minute until the sample softens and slightly touches the bottom of the ring apparatus.

Parallel plate geometry in dynamic shear rheometer TA Instruments Ares-G2 was used with a 5 mm diameter mold and 1 mm binder gap. Temperature sweep testing was performed in oscillatory mode at a fixed frequency of

1.6 Hz and at temperatures varying from 30–78 °C. From these, complex modulus (G^*) was determined. In temperature sweep testing the amplitude and frequency were kept constant while manipulating the temperature. First, the sample was heated and poured on the test plates. The initial, final temperature and ramp of the 5s are entered. Then the test is started after the desired initial temperature is achieved at +0.1 °C.

■ RESULTS AND DISCUSSION

Raw Material Characterization

Table 1 summarizes all analysis involved in which melting point value was obtained from differential scanning calorimeter and residue of plastic was by thermogravimetric analysis. In order to formulate bitumen, the oil needs to have a high flash point as this experiment is conducted at a maximum temperature of 180 °C; and the oil was used as the medium for the polymer to melt [14]. Base oil 3 is chosen because it has a stable supplier besides of its high temperature. Also, to compare in term of density, a highly dense base oil 3 is chosen as it easily tolerates with the polymer in the mixture. Amongst the three polymeric material, High Density Polyethylene (HDPE) 1 sample has the least moisture content of 0.266% followed by HDPE 2 sample at 0.389% and polystyrene sample at 0.757%. Furthermore, the melting point of each sample needs to be determined so that the method developed for this work will ensure all material used is melted accordingly based on the temperature. To compare the material in term of residue, HDPE 1 has the least residue of 0.1026% while HDPE 2 has the highest residue at 2.606%. It is easier for

Table 1. Summary of analysis done on different raw materials

Sample	Flash Point (°C)	Density (kg/m ³)	Moisture Content (%)	Melting Point (%)	Residue (mg)
Base oil 1	132.5	0.9304	1.019	-	-
Base oil 2	20.0	0.8070	0.504	-	-
Base oil 3	65.0	0.8720	0.311	-	-
Sludge	145.5	1.1831	14.479	-	-
HDPE 1	-	-	0.266	125.72	0.1026
HDPE 2	-	-	0.389	123.75	2.6060
Polystyrene	-	-	0.757	147.79	0.1200

a material containing less amount of filler to undergo depolymerization process while being heated and mixed with the bitumen. So, base oil 3 and HDPE 1 was chosen as the raw materials for bitumen formulation.

X-Ray Fluorescence (XRF)

Elements such as chromium, calcium, tin, and sulfur are added to the polymers as fillers, stabilizers and pigments. These elements are used in order to improve the durability and flexibility of polymer but often it does not chemically bond with molecules of plastic rather than only to create a suspension in plastic thus may dislodge from plastic matrix over time [15]. Table 2 depicts the highest element in HDPE 1, HDPE 2 and polystyrene are Ti at 88.46%, P at 44.16% and Ca at 59.71% respectively. The same elements exist in the three plastics are C, P, S, Ca and Fe in which HDPE 2 contained the highest concentration of P whereas polystyrene contained the highest amount of Ca. Besides that, polystyrene has four extra elements namely K, Cu, Mo, and Al. It is because polystyrene is a different type of plastic compared to HDPE 1 and HDPE 2 as both of it came from the same polymer group. The extra elements exist in polystyrene compared to the other two plastics may be caused by their different applications. Roads and Maritime Services [16] and Munera and Ossa [17] stated that polymer-modified bitumen grades only consist of elastomeric and

plastomeric plastics such as rubber, polyethylene, styrene-butadiene-styrene, and ethylene vinyl acetate. The extra elements exist in polystyrene are expected to not contribute positive influence in bitumen properties.

Characterization Formulation of Modified Bitumen

Table 3 shows eight modified bitumen formulation in different ratios of bitumen, HDPE and recycled base oil. The samples were then analyzed using standard bitumen test which is penetration and softening point test also thermogravimetric analysis following American Standard for Testing and Materials (ASTM) to compare the formulated bitumen with industrial grade bitumen.

Penetration Test (ASTM D5)

Bitumen grade is classified based on its penetration value. This value will determine its suitability for every application. In road construction, lower penetration grades were chosen in high temperature regions to prevent grease softening while higher penetration grades were used in colder regions to limit the cracking deformation [18]. For bitumen emulsion purposes, the grade of bitumen will affect its setting time when applied on a surface. The rapid setting is used for surface dressing, the medium setting is used for patch repairs work, and slow setting type of emulsion is used during

Table 2. XRF measurements for elements of three plastics (as percentage)

No	Elements	Concentration (%)		
		HDPE 1	HDPE 2	Polystyrene
1	C	0.879	0.114	1.18
2	P	4.74	44.16	13.87
3	S	2.34	7.16	2.25
4	Ca	1.32	20.29	59.71
5	Fe	0.37	2.88	5.82
6	Cl	-	5.61	2.59
7	Ti	88.46	-	1.09
8	Si	2.16	-	9.30
9	Zn	0.41	-	1.05
10	Pd	-	1.71	-
11	K	-	-	0.98
12	Cu	-	-	0.57
13	Mo	-	-	0.37
14	Al	-	-	2.42

Table 3. The ratio of modified bitumen formulation (of 220 g)

Ratio weight (wt.%)	8:0.7:1.3	8:0.5:1.5	6:0.7:3.8	6:0.5:3.5	4:0.7:5.3	4:0.5:5.5	2:0.7:7.3	2:0.5:7.5
Sample code	A	B	C	D	E	F	G	H
Bitumen	176.0	176.0	132.0	132.0	88.0	88.0	44.0	44.0
HDPE	15.4	11.0	33.0	22.0	15.4	11.0	15.4	11.0
Recycled base oil	28.6	33.0	55.0	66.0	116.6	121.0	160.6	165.0

rainy season. Based on the result shown in Fig. 1, the lowest and the hardest grade of bitumen was at ratio 8:0.7:1.3 (A) which contained 80 wt.% in bitumen, 7 wt.% in HDPE and 13 wt.% in recycled base oil whereas the highest and the softest grade of bitumen was at ratio 2:0.5:7.5 (H) containing the least amount of bitumen at 20 wt.%. From Fig. 1, the closest penetration value is obtained from sample G by the difference of 18 mm. This shows the recycled base oil and bitumen contained completely influence the grade of bitumen.

Softening Point Test (ASTM D36)

This softening value shows the temperature of the bitumen attaining a particular degree of softening point under the test specifications [19]. The softening point also indicates the grade of bitumen with a higher softening point is suitable for high temperature application. From Fig. 2, a lower content of bitumen gave a low softening point. It shows the sample ratio at 2:0.5:7.5 (H) was the softest compared to others thus higher in temperature susceptibility. Out of all the samples, the sample by ratio 8:0.7:1.3 (A) attained the highest softening point meaning it is suitable in a warmer climate; it will not flow during service. This can be related by the least amount of recycled base oil since it was used as the medium to melt the polymer. From Fig. 2, modified bitumen G has the closest softening value to the industrial grade with a difference of 0.9 °C.

Thermogravimetric Analysis (TGA)

Thermogravimetric analysis was carried out to determine a thermal characteristic of materials such as thermal stability, degradation temperature, and residue left at the end of the analysis. Table 4 shows TGA results obtained at a heating rate of 10 °C/min for pure bitumen and different ratios of bitumen, HDPE and recycled base oil. According to the result, pure bitumen has the highest

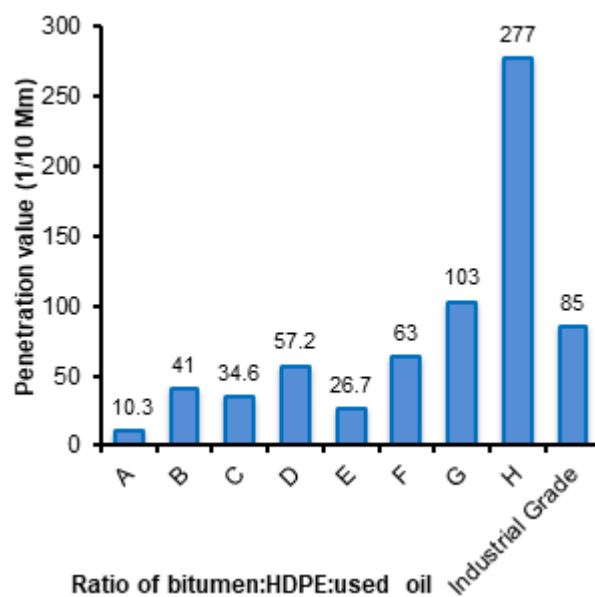


Fig 1. Penetration value against eight modified bitumen samples

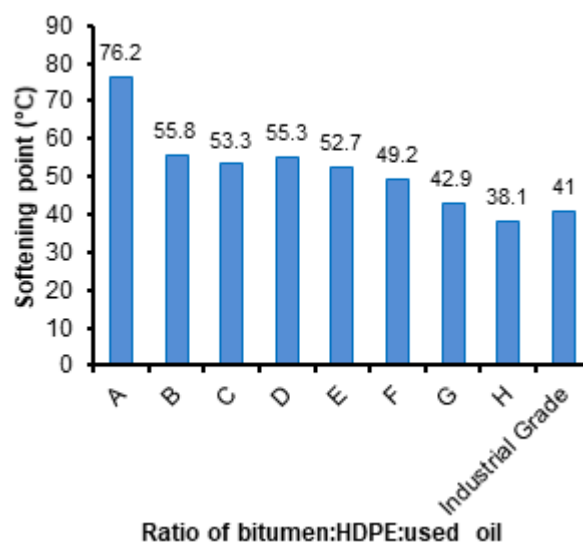


Fig 2. Graph of softening value against eight modified bitumen samples

thermal stability at 896.0 °C while modified bitumens are in the range of 895.8 to 893.3 °C. Also, the residue

Table 3. Thermogravimetric analysis result

No	Sample	Weight change and temperature subjected to sample	Decompose temperature (°C)
1	A	40.9% drop from 100 to 350 °C 47.6% drop from 350 to 500 °C 8.9% drop from 500 to 700 °C Residue is 0.27 mg	895.8
2	B	23.6% drop from 100 to 380 °C 47.6% drop from 400 to 520 °C Residue is 1.38 mg	893.3
3	C	54.1% drop from 100 to 400 °C 37.0% drop from 400 to 480 °C Residue is 0.091 mg	893.5
4	D	39.9% drop from 100 to 380 °C 45.4% drop from 380 to 520 °C Residue is 0.606 mg	893.6
5	E	53.9% drop from 100 to 400 °C 34.5% drop from 400 to 500 °C Residue is 0.090 mg	894.2
6	F	33.9% drop from 100 to 380 °C 32.9% drop from 380 to 520 °C Residue is 0.201 mg	894.2
7	G	79.8% drop from 100 to 400 °C 15.9% drop from 400 to 500 °C Residue is 0.087 mg	894.0
8	H	57.2% drop from 100 to 400 °C 30.0% drop from 400 to 520 °C Residue is 0.244 mg	893.9
9	Industrial grade	32.29% drop from 100 to 350 °C 38.05% drop from 350 to 500 °C 29.36% drop from 500 to 600 °C Residue is 0.013 mg	896.03

content of pure bitumen at the end of analysis is 0.013 mg which is less than modified bitumen that has residue in the range of 1.38–0.087 mg. Lower residue content indicates material possess lower evaporation and higher stability against heat. The closest modified bitumen that has approximately the same final residue are the samples with a ratio (C) 6:0.7:3.8, (E) 4:0.7:5.3 and (G) 2:0.7:7.3. Farahani [20] reported the use of the polymer in bitumen to increase its stability against heat meaning polymer modified bitumen should have less residue content about 0.62 mg lesser than pure bitumen. So in this case, the recycled base oil affects the result by at least 0.074 mg higher than pure bitumen. Thus, it is shown that the degradation temperature and residue of all modified bitumen did not deviate much from pure bitumen.

Characterization Formulation of Emulsified Modification Bitumen

One ratio of modified bitumen among the eight total formulations was chosen based on the penetration and softening point value. The best ratio of formulation which resembles the industrial grade bitumen is 2:0.7:7.3 (bitumen:HDPE:used oil). This ratio was then emulsified by using three different emulsifiers and undergoes moisture content, rheology analysis and comparison with industrial grade bitumen emulsion in order to decide which formulation is the best.

Moisture Content Test

Moisture content is one of the analyses needed to be performed on the bitumen emulsion product as one

of the quality control measures. Table 5 shows the result of moisture content in comparison with the industrial bitumen emulsion obtained from Selangor. There are three different emulsifiers used in this experiment. The only difference of BE 1, BE 2 and BE 3 was the emulsifier used to mix it with water. Initially, the same polymer modified bitumen with a penetration value of 103 mm was used during the emulsification process. So from Table 5, BE 1 has the lowest content of moisture whereas BE 3 contains the highest amount of moisture. The closest amount of moisture content with the industrial grade is BE 2 at approximately 51.12%. The moisture content is related to its viscosity where low moisture content indicates a higher viscosity. In all applications, the viscosity of the emulsion is important, because too viscous emulsions will be less pumpable and too much fluid the emulsions may not form thick films especially in road applications [21].

Rheology

Fig. 3 shows isochronal plots of complex modulus (G^*) versus temperature at 10 Hz loading application on samples of bitumen emulsion containing different ratios of polymer and recycled base oil. These samples are emulsified by using three different emulsifiers which are two anionic and one cationic emulsifier. It can be seen from Fig. 4 that amongst three bitumen emulsions, BE3 is much comparable to industrial grade bitumen emulsion which results in increased stiffness value. Normally at low service temperatures, G^* value will have small increases causing the slope of the complex modulus isochrones to decrease, and at high service temperature, G^* will be incrementally larger [4]. So by comparing both curves (BE3 and industrial grade bitumen emulsion), it shows BE3 is having some improvements in temperature susceptibility thus indicate it could perform better at average service temperatures while showing a shoulder at 100 °C.

Table 5. Moisture content value in bitumen emulsion (%)

Sample	Moisture Content (%)
Industrial BE	43.37
BE 1	31.03
BE 2	51.12
BE 3	55.85

Note: BE: Bitumen emulsion

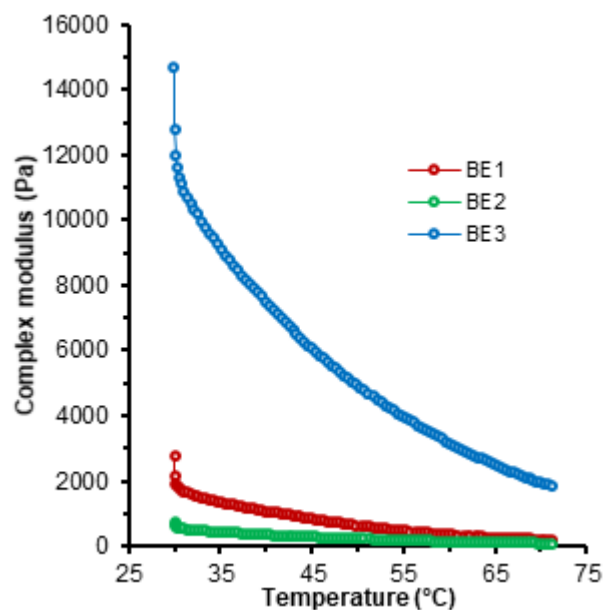


Fig 3. Graph of complex modulus (Pa) against temperature (°C)

CONCLUSION

From several analyses done to the industrial wastes from bitumen conventional analysis on penetration and softening tests, it was found that modified bitumen formulation with a ratio of 2:0.7:7.3 resembles an industrial bitumen but with higher penetration value at 103 mm and softening point of 0.9 °C higher than that of the industrial bitumen. It shows that the modified bitumen has a higher ability in terms of temperature susceptibility. The moisture content analysis done on the bitumen emulsion showed that the amount of moisture content in BE2 was 7.75% higher than the industrial bitumen emulsion. Higher moisture content results in an easier pumping during its application. From the TGA result, the recycled base oil in the formulation gave some effects to the thermal stability of the modified bitumen since it gave lesser residue content of approximately 0.62 mg as polymer will yield higher stability against heat. In the rheology test, BE3 showed higher temperature susceptibility, indicating that it could perform better for its application. In short, emulsified modification bitumen was comparable and had almost similar characteristics with the industrial emulsion.

■ ACKNOWLEDGMENTS

The authors wish to express their gratitude and appreciation for the financial support from the Ministry of Higher Education (MOHE), Malaysia for the Fundamental Research Grant Scheme (FRGS KPT – RDU160129, Reference Number: FRGS/1/2016/TK02/U MP/03/2 entitled Rheological and Structural Characterization of Emulsified Modification Bitumen Synthesized from Industrial Wastes) and the Universiti Malaysia Pahang for the Internal Grant (RDU160324). The support from the Faculty of Chemical and Natural Resources Engineering and Universiti Malaysia Pahang, Malaysia are also acknowledged.

■ REFERENCES

- [1] McNally, T., 2011, *Polymer Modified Bitumen: Properties and Characterization*, Woodhead Publishing, Philadelphia, USA, 1.
- [2] Asphalt Institute and Eurobitume, 2011, *The Bitumen Industry – A Global Perspective: Production, Chemistry, Use, Specification and Occupational Exposure.*, Lexington, Kentucky, USA, 6.
- [3] Arab, D., Kantzas, A., and Bryant, S.L., 2018, Nanoparticle stabilized oil in water emulsions, *J. Pet. Sci. Eng.*, 163, 217–242.
- [4] Khadivar, A., and Kavussi, A., 2013, Rheological characteristics of SBR and NR polymer modified bitumen emulsions at average pavement temperatures, *Constr. Build. Mater.*, 47, 1099–1105.
- [5] Global Market Insights, 2017, *Bitumen emulsifiers market*, <https://www.gminsights.com>, accessed on September 7, 2018.
- [6] Kathirvale, S., Yunus, M.N.M., Sopian, K., and Samsuddin, A.H., 2004, Energy potential from municipal solid waste in Malaysia, *Renewable Energy*, 29 (4), 559–567.
- [7] Department of Statistics Malaysia, 2016, *Department of Statistics Malaysia Press Release Report on Survey of Manufacturing Industries 2015*, <https://www.dosm.gov.my/>, accessed on February 2, 2017.
- [8] Yaacob, H., Hainin, M.R., Aziz, M.M.A., Warid, N.M., Chang, F.L., Ismail, C.R., and Hassan N.A., 2013, Bitumen emulsion in Malaysia-a conceptual, *Jurnal Teknologi*, 65 (3), 97–104.
- [9] Carrera, V., Cuadri, A.A., García-Morales, M., and Partal, P., 2015, The development of polyurethane modified bitumen emulsions for cold mix applications, *Mater. Struct.*, 48 (10), 3407–3414.
- [10] Carrera, V., Partal, P., García-Morales, M., Gallegos, C., and Páez, A., 2009, Influence of bitumen colloidal nature on the design of isocyanate-based bituminous products with enhanced rheological properties, *Ind. Eng. Chem. Res.*, 48 (18), 8464–8470.
- [11] Cai, H.M., Wang, T., Zhang, J.Y., and Zhang, Y.Z., 2017, Preparation of an SBS latex-Modified bitumen emulsion and performance assessment, *Pet. Sci. Technol.*, 28 (10), 987–996.
- [12] Perdelli, F., Cristina, M.L., Sartini, M., Spagnolo, A.M., Dallera, M., Ottria, G., Lombardi, R., Grimaldi, M., and Orlando, P., 2006, Fungal contamination in hospital environments, *Infect. Control Hosp. Epidemiol.*, 27 (1), 44–47.
- [13] Saadoun, I., Tayyar, I.A.A., and Elnasser, Z., 2008, Concentrations of airborne fungal contamination in the medical surgery operation theaters of different hospitals in northern Jordan, *Jordan J. Biol. Sci.*, 1 (4), 181–184.
- [14] Razali, M.N., Isa, S.N.E., Salehan, N.A.M, Musa, M., Aziz, M.A.A., Nour, A.H., and Yunus, R.M., 2018, Characterization of industrial wastes as raw materials for emulsified modified bitumen formulation, *IOP Conf. Ser. Mater. Sci. Eng.*, 342, 012072.
- [15] Piorek, S., 2004, Feasibility of Analysis and Screening of Plastics for Heavy Metals with Portable X-Ray Fluorescence Analyzer with Miniature X-Ray Tube, *Global Plastics Environmental Conference 2004: GPEC 2004*, Marriott Renaissance Center, Detroit, MI, February 18-19, 2004.
- [16] Roads and Maritime Services (RMS), 2010, *Guide to selection of polymer modified binder*, <http://www.rms.nsw.gov.au>, accessed on September 7, 2018.

- [17] Munera, J.C., and Ossa, E.A., 2014, Polymer modified bitumen: Optimization and selection, *Mater. Des.*, 62, 91–97.
- [18] Razali, M.N., Aziz, M.A.A., Jamin, N.F.M., and Salehan, N.A.M, 2018, Modification of bitumen using polyacrylic wig waste, *AIP Conf. Proc.*, 1930 (1), 020051.
- [19] Mathew, T.V., and Rao, K.V.K., 2006, Introduction to Transportation Engineering, *NPTEL Web Course*, Civil Engineering Department, Indian Institute of Technology Bombay, India.
- [20] Farahani, H.Z., Palassi, M., and Galooyak, S.S, 2017, Thermal analysis of bitumen modified with LDPE and CR, *Pet. Sci. Technol.*, 35 (15), 1570–1575.
- [21] Lesueur, D, 2003, The rheological properties of bitumen emulsions. Part I–Theoretical relationships between efflux time and rheological behaviour, *Road Mater. Pavement Des.*, 4 (2), 151–168.

Chemical Reduction Behavior of Zirconia Doped to Nickel at Different Temperature in Carbon Monoxide Atmosphere

Norliza Dzakaria^{1,2,*}, Maratun Najihah Abu Tahari¹, Fairous Salleh¹, Alinda Samsuri³, Masitah Abdul Halim Azizi⁴, Tengku Shafazila Tengku Saharuddin⁵, Muhammad Rahimi Yusop¹, Wan Nor Roslam Wan Isahak⁴, Mohamed Wahab Mohamed Hisham¹, and Mohd Ambar Yarmo¹

¹Catalyst Research Group, School of Chemical Sciences and Food Technology, Faculty of Science and Technology, Universiti Kebangsaan Malaysia, 43600 UKM Bangi, Selangor Darul Ehsan, Malaysia

²School of Chemistry and Environment, Faculty of Applied Sciences, Universiti Teknologi MARA, Cawangan Negeri Sembilan, Kampus Kuala Pilah, Pekan Parit Tinggi, 72000 Kuala Pilah, Negeri Sembilan, Malaysia

³Department of Chemistry, Centre for Defence Foundation Studies, Universiti Pertahanan Nasional Malaysia, Kem Sungai Besi, 57000 Kuala Lumpur, Malaysia

⁴Department of Chemical and Process Engineering, Faculty of Engineering and Built Environment, Universiti Kebangsaan Malaysia, 43600 UKM Bangi, Selangor Darul Ehsan, Malaysia

⁵Faculty of Science and Technology, Universiti Sains Islam Malaysia, Bandar Baru Nilai, 71800, Nilai, Negeri Sembilan, Malaysia

* **Corresponding author:**

tel: +6019-7691734

email: norlizardzakaria75@gmail.com

Received: August 3, 2018

Accepted: December 11, 2018

DOI: 10.22146/ijc.40891

Abstract: The reduction behavior of nickel oxide (NiO) and zirconia (Zr) doped NiO (Zr/NiO) was investigated using temperature programmed reduction (TPR) using carbon monoxide (CO) as a reductant and then characterized using X-ray diffraction (XRD), nitrogen absorption isotherm using BET technique and FESEM-EDX. The reduction characteristics of NiO to Ni were examined up to temperature 700 °C and continued with isothermal reduction by 40 vol. % CO in nitrogen. The studies show that the TPR profile of doped NiO slightly shifts to a higher temperature as compared to the undoped NiO which begins at 387 °C and maximum at 461 °C. The interaction between ZrO₂ with Ni leads to this slightly increase by 21 to 56 °C of the reduction temperature. Analysis using XRD confirmed, the increasing percentage of Zr from 5 to 15% speed up the reducibility of NiO to Ni at temperature 550 °C. At this temperature, undoped NiO and 5% Zr/NiO still show some crystallinity present of NiO, but 15% Zr/NiO shows no NiO in crystalline form. Based on the results of physical properties, the surface area for 5% Zr/NiO and 15% Zr/NiO was slightly increased from 6.6 to 16.7 m²/g compared to undoped NiO and for FESEM-EDX, the particles size also increased after doped with Zr on to NiO where 5% Zr/NiO particles were 110 ± 5 nm and 15% Zr/NiO 140 ± 2 nm. This confirmed that the addition of Zr to NiO has a remarkable chemical effect on complete reduction NiO to Ni at low reduction temperature (550 °C). This might be due to the formation of intermetallic between Zr/NiO which have new chemical and physical properties.

Keywords: nickel; carbon monoxide; zirconia; reduction; temperature programmed reduction

■ INTRODUCTION

Nickel oxide has been used as a well-established catalyst due to its surface oxidation properties [1]. It is known that catalysis is a surface effect in which the

catalyst needs to provide the highest possible active surface area [2]. The reduction of metallic oxides to metal has been extensively studied as it represents a class of heterogeneous reactions which are of considerable

technological and commercial important [3]. Reduction of nickel oxide by hydrogen was studied by several researchers [4-7]. On the other hand, the study in the reduction of nickel oxide using carbon monoxide is limited due to the high possibility of carbide forming that may cause the reaction to be disturbed or retarded. Doping methods have been extensively utilized to modify the electronic structures of nanoparticles to achieve new or improved catalytic, electro-optical, magnetic, chemical, and physical properties [8-9]. The reduction of undoped and doped NiO catalysts has been studied extensively and plays an important role in many catalytic reactions [10].

Moreover, the addition of Zr to NiO enhances the catalytic activity and stability of NiO by improving oxygen storage capacity, reducibility, and resistance to sintering effect. ZrO₂ is an attractive material for catalysis known for its unique reducing, oxidizing, acidic and basic properties [11]. The reducing properties of ZrO₂ play an important role in the support effects [12]. The purpose of the present work is to enhance the reduction behavior by studying the influence of different concentrations of zirconia doping agents and their reduction behavior at different temperatures.

■ EXPERIMENTAL SECTION

Materials

Nickel oxide (99%) was obtained from Acros Organics, zirconyl chloride octahydrate (98%), Cl₂OZr·8H₂O from Acros Organics and ethanol, C₂H₆O (99.5%) from System[®] are pure and used as supplied. Gas mixture CO/N₂ (40% CO) was obtained from MOX.

Instrumentation

Temperature programmed reduction (TPR) measurements were collected by using Micromeritics Autochem 2920 Chemisorption Analyzer fed with 40% CO in N₂ at the flow rate of 20 mL min⁻¹ (STP) as reducing gas. Fifty milligrams of sample was heated up to three different maximum temperature 350, 450, and 550 °C, at a rate of 10 °C/min. The carbon monoxide consumption was monitored using a thermal conductivity detector (TCD). Phase characterization was carried out by X-ray

diffraction (XRD) model Bruker AXS D8 Advance type with X-ray radiation source of Cu Kα (40 kV, 40 mA) to record the 2θ diffraction angle from 10–80° (λ = 0.154 nm) to observe the crystallinity lattice structures of the catalyst samples. In order to identify the crystalline phase composition, the diffraction patterns obtained were matched with standard diffraction (JCPDS) files. In addition, FESEM images were obtained with Zeiss Merlin operating at 20 kV for morphological investigation of the catalysts. A ZEISS MERLIN Compact microscope equipped with a field emission gun and EDX probe was employed. Physical surface analysis of nitrogen adsorption at 77 K (liquid nitrogen) was conducted using a Micromeritics ASAP 2020 instrument to obtain the isotherm of each sample. The Brunauer–Emmett–Teller (BET) formula to get surface area technique was used to calculate the surface area, pore volume, and pore size [14]. The calcined samples of undoped NiO, 5% Zr/NiO and 15% Zr/NiO amounting to 100–300 mg were degassed at 300 °C for 4 h prior to the BET surface area analyses.

Catalyst Preparation

Two different concentrations of Zr doped nickel oxide: 5 and 15% w/w were prepared through the impregnation method. The impregnation method was prepared by using zirconyl chloride octahydrate (Cl₂OZr·8H₂O) and nickel oxide (NiO) powder. The amount of zirconia added was 5 and 15 w/w % of total metal cations. The compounds were dissolved in water followed by adding ethanol at 40 °C with stirring for 4 h which produced a viscous mixture. The solution was evaporated to dry while stirring for 4 h. It was then dried at 120 °C overnight followed by calcination in the air at 400 °C for 4 h [13]. The NiO samples with Zr were denoted as 5% Zr/NiO and 15% Zr/NiO while sample without Zr was denoted as NiO.

■ RESULTS AND DISCUSSION

Thermochemistry

The reduction reaction of nickel oxide using carbon monoxide environment follows the chemical equation NiO(s) + CO(g) → Ni(s) + CO₂ (g) and the

reduction of zirconia oxide by carbon monoxide follows the chemical equation $\text{ZrO}_2(\text{s}) + 2\text{CO}(\text{g}) \rightarrow \text{Zr}(\text{s}) + 2\text{CO}_2(\text{g})$. The thermodynamic quantities for NiO and ZrO_2 reduction by carbon monoxide are shown in Table 1. The Gibbs free energy change (ΔG_r) showed that the reduction of NiO to Ni is favorable and it occurred spontaneously at $\Delta G_r = -48 \text{ kJ}\cdot\text{mol}^{-1}$. The calculated ΔG_r became very negative from -48 to -50 $\text{kJ}\cdot\text{mol}^{-1}$ when the temperature increased from 350 to 550 °C. This showed that the reaction might occur more spontaneously at a higher temperature. Unlike the reduction of NiO to Ni, the reduction of ZrO_2 to Zr is not favorable which might due to the value of $\Delta G_r = +524 \text{ kJ}\cdot\text{mol}^{-1}$ which is positive. The calculated ΔG_r became less positive as the temperature increased, but it is still very positive to induce the reaction. The combination of NiO and ZrO_2 increased the reduction temperature due to the difficulty of zirconia oxide to reduce.

Adsorption Isotherm of N_2

The BET specific areas, average pore size and average pore volume of undoped ZrO_2 and NiO and doped NiO with 5 and 15 mol % Zr samples are summarized in Table 2. The isotherm of the samples is shown in Fig. 1. The catalysts showed type IV isotherm, which is typical for mesoporous materials (1.5–100 nm pore diameter) [14]. Table 2 shows that the BET surface area of NiO and ZrO_2 are 4.6 and 39.0 m^2/g , respectively, while BET surface area of doped NiO with 5 and 15% Zr

are 11.2 and 21.3 m^2/g , respectively. The catalysts have a low surface area due to high crystallinity. It was found that the surface area increased with increased loading of Zr to NiO which is in agreement with Salleh et al. [13] as ZrO_2 has higher BET surface areas than NiO. This suggested that there are more active sites that might be attributed to the higher temperature reduction of NiO after doping. Moreover, Wang et al. [15] suggested in their report that the specific surface area for metal oxide is one of the important factors in a chemical reaction. NiO surface coordination sites were exposed to the reduction gas when a specific surface area is higher. Thus, higher specific surface area provided the best result in reducibility of the nickel oxide. The addition

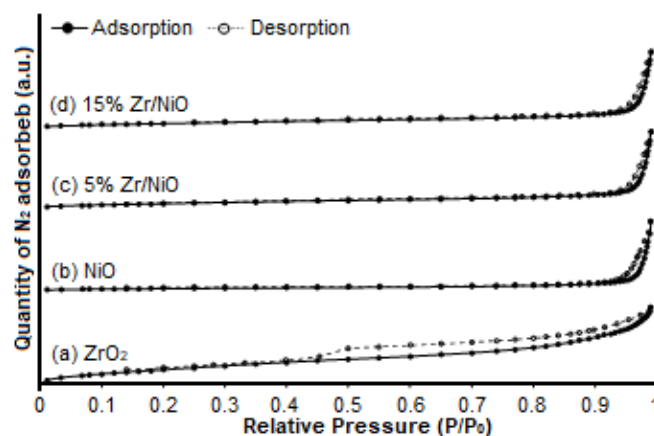


Fig 1. Nitrogen adsorption-desorption isotherms plot of undoped ZrO_2 and NiO and doped NiO with 5 and 15 mol % Zr catalyst

Table 1. Thermodynamic calculation for formation of nickel and zirconium

Reaction	Enthalpy, ΔH_r $\text{kJ}\cdot\text{mol}^{-1}$	Entropy, ΔS_r $\text{kJ}\cdot\text{mol}^{-1} \text{K}^{-1}$	ΔG_r 350 °C $\text{kJ}\cdot\text{mol}^{-1}$	ΔG_r 450 °C $\text{kJ}\cdot\text{mol}^{-1}$	ΔG_r 550 °C $\text{kJ}\cdot\text{mol}^{-1}$
Nickel oxide reduction	-43	+8	-48	-49	-50
Zirconia reduction	+535	+17	+524	+523	+521

Table 2. BET analysis of undoped ZrO_2 and NiO and doped NiO with 5 and 15 mol % Zr

Catalyst	BET surface area (m^2/g)	Average pore size (nm)	Average pore volume (cm^3/g)
ZrO_2	39.0	5.90	0.062
NiO	4.6	40.6	0.047
5% Zr/NiO	11.2	17.5	0.054
15% Zr/NiO	21.3	8.1	0.050

of Zr to NiO significantly increased the BET surface area of NiO due to the formation of new external pore on the NiO surface. In addition, the average pore size of undoped NiO was 40.6 nm, and the pore sizes of doped NiO with 5 and 15% Zr were decreased to 17.5 and 8.1 nm, respectively. The pore volume of undoped NiO was 0.047 cm³/g and decreased from 0.054 to 0.050 cm³/g when the concentration of Zr was increased from 5 to 15%. In this case, it is more likely that the Zr atoms had occupied the NiO mesopores which resulted in the average pore volume reduced when the concentration of Zr was increased.

Catalyst Characterization by TPR

The TPR patterns of non-isothermal 40% CO reductant for ZrO₂, NiO, 5% Zr/NiO and 15% Zr/NiO are shown in Fig. 2. The overall reactions involved a reaction between two different percentage of in mol of Zr/NiO, NiO, and ZrO₂ with carbon monoxide as reductant gas in a gas-solid reaction. The TPR profiles of ZrO₂ showed no peak. Meanwhile, NiO obviously showed one sharp peak that which indicates the reduction of ZrO₂ does not occur below 700 °C. The reduction process uses a one-step reduction profile, temperature region around 387 °C represents the reduction of NiO → Ni. Whereas, for 5% Zr/NiO, the reduction temperature shifted slightly to the right at around 406 °C. While 15% Zr/NiO, the reduction temperature shifted to a higher temperature at around

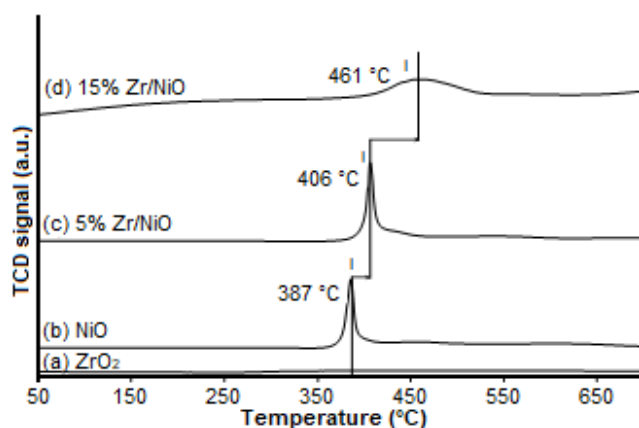


Fig 2. TPR profile of (a) undoped ZrO₂; (b) undoped NiO; (c) 5% Zr/NiO, and (d) 15% Zr/NiO samples (obtained after reduction at 400 °C for 4 h) under 40 vol.% CO at 40–700 °C

461 °C. There is a trace of NiO and Ni observed in the XRD analysis throughout the reduction process at the specified temperature; the peaks are attributed to state that the reduction process is incomplete. Furthermore, the addition of Zr element to NiO would delay the reduction process to a higher temperature and complete at above 550 °C.

Crystallinity Analysis using XRD

The XRD patterns of undoped ZrO₂ and NiO and doped NiO with 5 and 15 mol % Zr obtained after calcination at 400 °C for 4 h are shown in Fig. 3. The diffractogram of these samples was identical to the ZrO₂ phase (zirconia oxide, JCPDS 37-1484) and cubic NiO phase (nickel oxide, JCPDS 00-047-1049). The 2θ values revealed that the contribution of NiO main peaks was at 37.2, 43.4, 62.9, 75.5, and 79.5°. Furthermore, the diffractogram of 5 and 15% Zr/NiO showed no additional peak which suggested that the Zr particles loaded on the NiO are well dispersed. In addition, there is a reduction in the crystallinity of the prepared 5% Zr/NiO and 15% Zr/NiO when it is loaded with Zr, which is corresponded to the smaller NiO peaks intensity. This is due to the surface of NiO was covered or well dispersed by Zr atoms which are in amorphous form. No Zr peak was detected in the diffractogram due to Zr is in a highly amorphous form or well dispersed on the surface. Zr is in nanoparticles form that can be detected

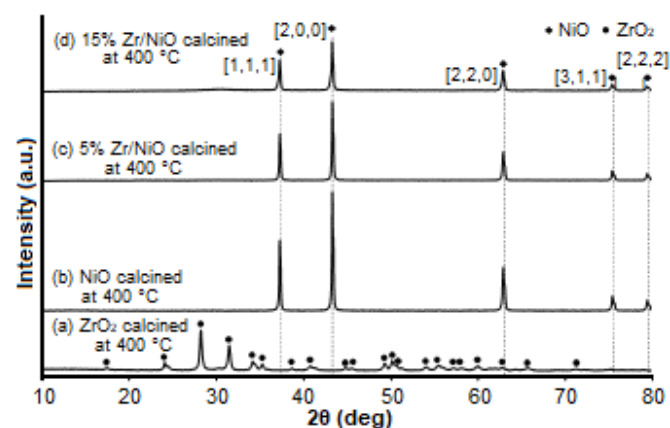


Fig 3. XRD patterns of (a) undoped ZrO₂; (b) undoped NiO; (c) 5% Zr/NiO and (d) 15% Zr/NiO samples obtained after calcination at 400 °C for 4 h

in the range of $0.1\text{--}1.0^\circ$ for wide scan in XRD analysis [16].

In order to investigate the role of Zr in the reduction process of NiO in CO atmospheres, all samples were collected at various reduction temperatures, i.e.: (i) 350, (ii) 450, and (iii) 550 °C for comparison purposes. The characterization using XRD as shown in Fig. 4 at different percent Zr element does give influence on the reduction of NiO in CO atmosphere. The reduction of undoped NiO and doped NiO with 5 and 15 mol % Zr were found to have different results. The diffractogram patterns for these samples at 350 °C showed strong peaks of crystallite cubic phase NiO [1,1,1], NiO [2,0,0], NiO [2,2,0], NiO [3,1,1] and NiO [2,2,2] (JCPDS 00-047-1049). All samples showed the formation of crystallite cubic phase NiO and Ni⁰ [1,1,1], Ni⁰ [2,0,0], Ni⁰ [2,2,0] (JCPDS 01-071-4654) as the temperature is approaching 450 °C. This suggested that the reduction process was initiated. However, as the temperature reached to 550 °C, 15% Zr/NiO sample showed only metallic Ni peaks which implied that the reduction process was completed. This result is contrary to the results of undoped NiO and 5% Zr/NiO samples in which these samples still consists of remaining crystalline phases of NiO. It suggested that there was a change in the properties of solid surface that particularly generates new active sites and promotes a strong modification to the behavior of the catalyst. In addition, the nature of the sample itself is also important, which in this case, the involvement of zirconia element in the structure of nickel oxide may contribute to the enhancement of reducibility process.

The additional Zr does give some advantages as illustrated in Fig. 5. From the illustration, the addition of 15% Zr to NiO completed the reduction of NiO → Ni at 550 °C but for undoped NiO, there was still a residue of NiO which was not reduced to Ni. In addition, based on the observations, we can anticipate that the catalyst has encountered some physical and chemical changes as shown in Fig. 6 with different temperatures for three samples producing different percentages of NiO reduction.

Surface Morphology by FESEM-EDX

Catalyst morphology was investigated by using

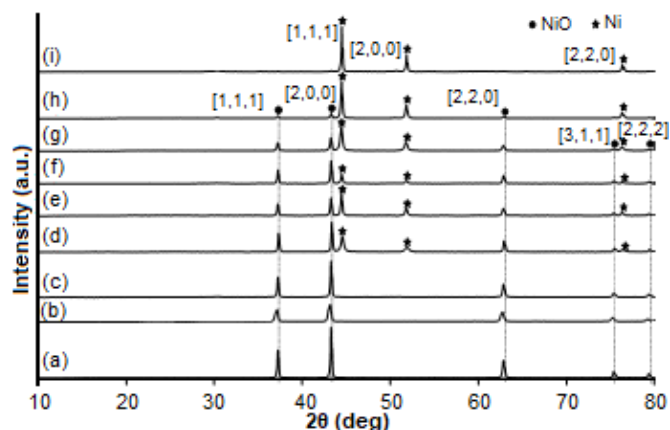


Fig 4. XRD patterns of non-isothermal reduction of undoped NiO and doped NiO with 5 and 15 mol % Zr catalyst using 40% CO in N₂. Note: (a) NiO after reduction 350 °C; (b) 5% Zr/NiO after reduction 350 °C; (c) 15% Zr/NiO after reduction 350 °C; (d) NiO after reduction 450 °C; (e) 5% Zr/NiO after reduction 450 °C; (f) 15% Zr/NiO after reduction 450 °C; (g) NiO after reduction 550 °C; (h) 5% Zr/NiO after reduction 550 °C; (i) 15% Zr/NiO after reduction 550 °C samples with 40 vol.% CO in nitrogen

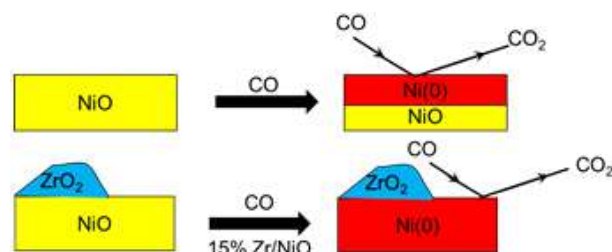


Fig 5. Proposed schematic sketch of CO interaction with undoped NiO and 15% Zr/NiO during reduction process in CO atmosphere

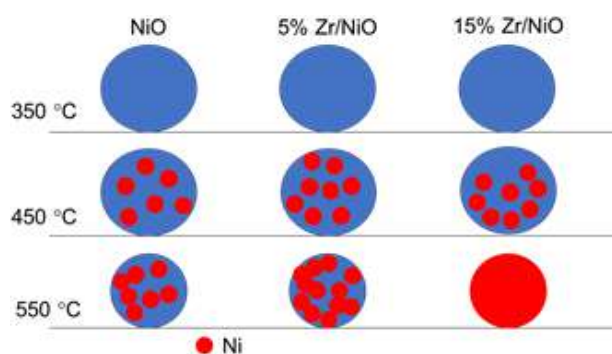


Fig 6. Graphical assumption of reduction for undoped NiO and doped NiO with 5 and 15 mol % Zr in CO atmosphere

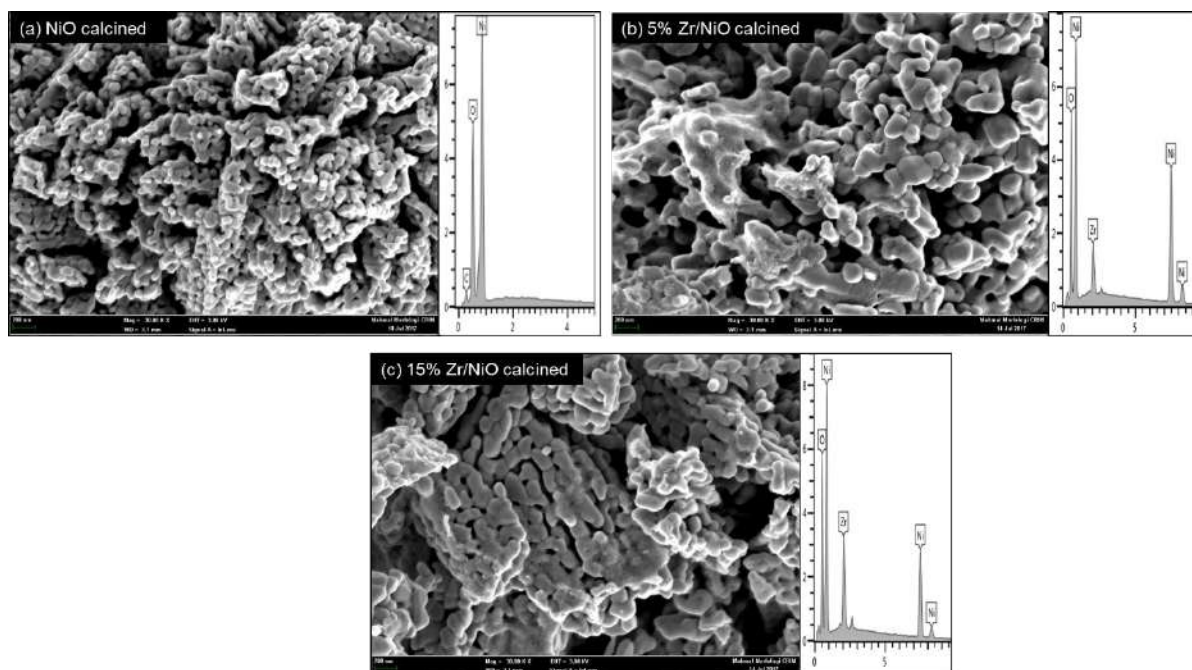


Fig 7. FESEM images of zirconia doped nickel oxide (a) Undoped NiO; (b) Doped NiO with 5 mol % Zr; (c) Doped NiO with 15% Zr (Magnification: 30K x) after calcined at 400 °C for 4 h

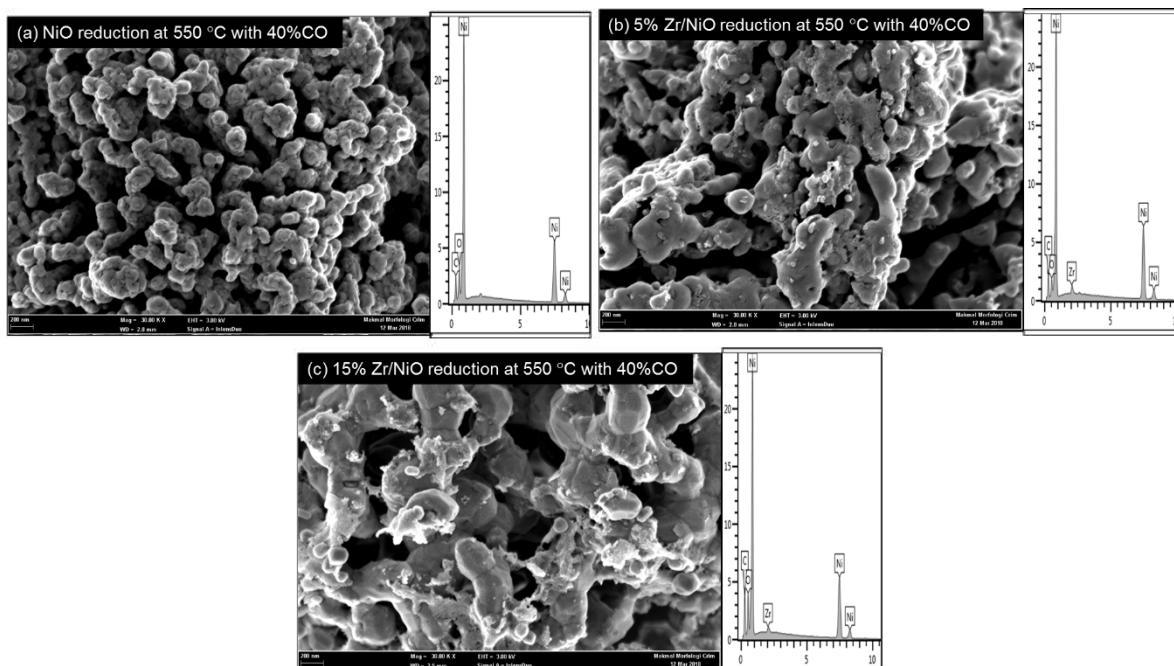


Fig 8. FESEM images of zirconia doped nickel oxide (a) Undoped NiO; (b) Doped NiO with 5 mol % Zr; (c) Doped NiO with 15 mol % Zr (Magnification: 30K x) after reduction with 40% CO in nitrogen

FESEM and the results are shown in Fig. 7. The NiO catalyst was observed as a rod structure. The addition of Zr to NiO altered the morphology significantly. The morphology of NiO catalysts was influenced by the Zr.

Doped NiO with 5 and 15 mol % Zr catalysts exhibited irregular shape and non-uniform particle size distribution. The structure and morphology of the catalyst were influenced by doped metal oxide [17].

Compare to undoped NiO, the particle size is smaller than doped NiO with 5 and 15 mol % Zr. The average sizes of the undoped NiO and doped NiO with 5 and 15 mol % Zr were measured by using the Scion image program averaged over 100 particles. The average sizes of the undoped NiO were found to be 45 ± 5 nm, while doped NiO with 5 mol % Zr particles 110 ± 5 nm and doped NiO with 15 mol % Zr/NiO 140 ± 2 nm. These numbers showed that there is a change in the particle size due to the loading of big particles such as Zr. As an exhibit in Fig. 8, it is observed that at reduction temperature of 550 °C, the particle size of undoped NiO and doped NiO with 5 mol % Zr remain the same. Meanwhile, the doped NiO with 15 mol % Zr particle size was increased due to the formation of Ni metal. This result showed the formation of metallic Ni after reduction of doped NiO with 15 mol % Zr with CO contributed in the formation of agglomeration of particle surfaces which is in agreement with Zielinska et al. [18] report. Furthermore, the agglomeration will increase the availability of the surface area and thus influences the rate of the reduction process.

■ CONCLUSION

Analysis by TPR showed the addition of Zr has a remarkable influence on the reduction process where the peak is shifted to the right from lower to higher temperature (387 to 461 °C). Zr dopant enhances the reduction process with the reduction completed at temperature 550 °C with only metallic phase detected by XRD compared to undoped NiO and doped NiO with 5 mol % Zr which has residue NiO detected. This is due to the catalytic effect of doped NiO with 15 mol % Zr. Therefore, Zr species played an important role in enhancing the reduction of NiO by completing the reduction at temperature 550 °C, due to Zr particles were fully dispersed on the NiO surface. Moreover, the addition of Zr to NiO provides higher surface area, and for FESEM the particles size become larger as with the increase of Zr concentration.

■ ACKNOWLEDGMENTS

The author wishes to thank the Ministry of Higher Education (MOHE), research grants ST-2018-005

(MTJA) and Centre of Research and Innovation Management CRIM-UKM for instrumentation facilities.

■ REFERENCES

- [1] Rahim, M.A.A., Hameed, R.M.A., and Khalil, M.W., 2004, Nickel as a catalyst for the electro-oxidation of methanol in alkaline medium, *J. Power Sources*, 134 (2), 160–169.
- [2] Antolini, E., 2003, Formation of carbon-supported PtM alloys for low temperature fuel cells: A review, *Mater. Chem. Phys.*, 78 (3), 563–573.
- [3] Ostyn, K.M., and Carter, C.B., 1982, On the reduction of nickel oxide, *Surf. Sci.*, 121 (3), 360–374.
- [4] Syed-Hassan, S.S.A., and Li, C.Z., 2011, NiO reduction with hydrogen and light hydrocarbons: Contrast between SiO₂-supported and unsupported NiO nanoparticles, *Appl. Catal., A*, 398 (1-2), 187–194.
- [5] Chatterjee, R., Banerjee, S., Banerjee, S., and Ghosh, D., 2012, Reduction of nickel oxide powder and pellet by hydrogen, *Trans. Indian Inst. Met.*, 65 (3), 265–273.
- [6] Jeangros, Q., Hansen, T.W., Wagner, J.B., Damsgaard, C.D., Dunin-Borkowski, R.E., Hébert, C., Van Herle, J., and Hessler-Wyser, A., 2013, Reduction of nickel oxide particles by hydrogen studied in an environmental TEM, *J. Mater. Sci.*, 48 (7), 2893–2907.
- [7] Manukyan, K.V., Avetisyan, A.G., Shuck, C.E., Chatilyan, H.A., Rouvimov, S., Kharatyan, S.L., and Mukasyan, A.S., 2015, Nickel oxide reduction by hydrogen: Kinetics and structural transformations, *J. Phys. Chem. C*, 119 (28), 16131–16138.
- [8] Liao, L., Mai, H.X., Yuan, Q., Lu, H.B., Li, J.C., Liu, C., Yan, C.H., Shen, Z.X., and Yu, T., 2008, Single CeO₂ nanowire gas sensor supported with Pt nanocrystals: Gas sensitivity, surface bond states, and chemical mechanism, *J. Phys. Chem. C*, 112 (24), 9061–9065.
- [9] Koao, L.F., Swart, H.C., and Dejene, F.B., 2010, Effects of aluminum co-doping on

- photoluminescence properties of Ce³⁺-doped SiO₂ glasses, *J. Rare Earths*, 28 (Suppl. 1), 206–210.
- [10] Laosiripojana, N., Sutthisripok, W., and Assabumrungrat, S., 2005, Synthesis gas production from dry reforming of methane over CeO₂ doped Ni/Al₂O₃: Influence of the doping ceria on the resistance toward carbon formation, *Chem. Eng. J.*, 112 (1-3), 13–22.
- [11] Mekhemer, G.A.H., 1998, Characterization of phosphated zirconia by XRD, Raman and IR spectroscopy, *Colloids Surf., A*, 141 (2), 227–235.
- [12] Tanabe, K., 1985, Surface and catalytic properties of ZrO₂, *Mater. Chem. Phys.*, 13 (3), 347–364.
- [13] Salleh, F., Saharuddin, T.S.T., Samsuri, A., Othaman, R., and Yarmo, M.A., 2015, Effect of zirconia and nickel doping on the reduction behavior of tungsten oxide in carbon monoxide atmosphere, *Int. J. Chem. Eng. Appl.*, 6 (6), 389–394.
- [14] Brunauer, S., Emmett, P.H., and Teller, E., 1938, Adsorption of gases in multimolecular layers, *J. Am. Chem. Soc.*, 60 (2), 309–319.
- [15] Wang, C., Yin, L., Zhang, L., Xiang, D., and Gao, R., 2010, Metal oxide gas sensors: sensitivity and influencing factors, *Sensors*, 10, 2088–2106.
- [16] Pradhan, D., 2009, Unusual Phase Transformation Behavior of Amorphous Zirconia, *Thesis*, Department of Ceramic Engineering, National Institute of Technology Rourkela, India.
- [17] Namratha, K., and Byrappa, K., 2012, Novel solution routes of synthesis of metal oxide and hybrid metal oxide nanocrystals, *Prog. Cryst. Growth Charact. Mater.*, 58 (1), 14–42.
- [18] Zielińska, K., Stankiewicz, A., and Szczygieł, I., 2012, Electroless deposition of Ni-P-nano-ZrO₂ composite coatings in the presence of various types of surfactants, *J. Colloid Interface Sci.*, 377 (1), 362–367.

Removal of Methylene Blue from Aqueous Solution by Using Electrical Arc Furnace (EAF) Slag

Suhanna Natalya Mohd Suhaimy* and Luqman Chuah Abdullah

Department of Chemical and Environmental Engineering, Universiti Putra Malaysia, 43400 UPM Serdang, Malaysia

* **Corresponding author:**

tel: +60-012-3202690

email: suhanna1285@gmail.com

Received: August 3, 2018

Accepted: December 14, 2018

DOI: 10.22146/ijc.40910

Abstract: In recent years, environmental protection has gained a major concern. In line with the rapid growth of various industries, high amount of effluent has been generated and discharged to the environment. One of the concerns is the presence of synthetic dye in the wastewater stream, as it may endanger human and aquatic life. In this experiment, the Electrical Arc Furnace (EAF) slag has been used as an adsorbent to remove methylene blue from the aqueous solution. Batch experiments have been conducted, and the effects of initial dye concentration, pH, adsorbent dosage and temperature were studied respectively. Chemical treatment has been performed to modify the adsorbent. The results reveal that treated EAF Slag has higher efficiency in removing methylene blue compared to raw EAF slag. More pores have been exposed, and impurities on the adsorbent's surface have been removed, to enhance better removal efficiency. The maximum adsorption capacity for treated EAF is 14.2029 mg/g and for raw EAF Slag is 9.615 mg/g. The maximum removal percentage for treated EAF Slag is 71.01%, whereas raw EAF shows 37.19% removal at pH 10. Both raw EAF Slag and treated EAF slag fits the data for the Langmuir isotherm model which obeys the monolayer adsorption process.

Keywords: adsorption; Electrical Arc Furnace (EAF) slag; batch experiment

■ INTRODUCTION

Wastewater can be defined as any water that leaves from houses and industries through the main drain pipe which is contaminated by chemical residues through human activities. The wastewater must be treated in order to remove the dyes before releasing it to the environment [1]. The release of industrial wastewater has a significant negative impact on the ecosystems which could harm the environment and hydrosphere organisms [2].

Methylene blue or known as methylthionium chloride is a dark green crystalline powder. It is a basic synthetic dye which commonly used to impart color for cotton, wool, and silk, for an attractive finishing [3]. The overexposure to methylene blue may cause the following effects: dizziness, nausea, and abdominal pain.

The textile manufacturing process is one of a water-intensive process which discharges a huge amount of wastewater. Approximately 200 L of water is required to produce 1 kg of textile [4]. Wastewater from the textile industries is contaminated with other chemical

substances such as soap of metals, hydrogen peroxide, acids and alkali [5]. High pH and temperature may poses threats to the aquatic life, eventually will lead to the species distinction. Carcinogens compounds from textile wastewater can cause damage to human living tissues through metabolism disruption and eventually lead to cancer [6]. The presence of dyes will limit the light penetration in water, which will cause retardation of the photosynthesis process and eventually will disrupt the food chain of the aquatic life [7].

The application of EAF slag as an adsorbent in this experimental work has double benefits, transforming the waste product generated from the Electric Arc Furnace operation, which can be used in wastewater treatment as well as reducing the amount of EAF slag to be disposed to the municipal landfill. In steel production industries, iron ore as the primary raw material are melted at high temperature, in the equipment known as electric arc furnace. There are two possible expected products generated which are carbons steel or ferrous

steel, which later will be used in various applications. At the same time, the undesirable product from the process is a substance called Electric Arc Furnace Slag has been generated. An adsorbent can be considered as a low cost adsorbent if its presence in abundance in nature, requires less processing or it is a waste materials, which is the by-product from other industries [8]. Generally, it is composed of impure components such as metal oxide and lime [9]. It has been fully utilized and widely used in the field of agriculture as a fertilizer and also a field of civil as road construction material [10]. Slag has been an alternative compound, apart from granular activated carbon in wastewater treatment due to its sportive characteristics [11]. Apart from having a high melting point and its porous structure, slag can be chemically treated to modify the surface charge to adsorb the desired adsorbate on its active sites [12].

The application of slag as an adsorbent has been conducted, and it was found that 80.03 mg/g of reactive dyes have been removed by using the surface modified EAF slag [9]. Steel slag is capable to remove Manganese ions, positively charged ions, with the removal percentage of more than 95% in batch experimental adsorption process [13]. Thus, it has shown that the EAF slag is a potential adsorbent for the real application. Adsorption is an effective method for water decontamination process [14]. In addition, the adsorption method is known to be low cost operating process, as well as an easy operation method compared to other wastewater treatment methods [15].

■ EXPERIMENTAL SECTION

Materials Preparation

The EAF slag was obtained from a local steel manufacturing company located in Peninsular of Malaysia. The slag was sieved using a mechanical sieve shaker, followed by washing thoroughly with distilled water to remove the debris trapped on the surface of the EAF slag particles. 600-micron slag particles were used in this study. It was then dried in the oven for 24 h at 90 °C.

The treated slag was prepared by adding the EAF slag into 1 M of hydrochloric acid. The solution was allowed for mixing for 2 h. The treated EAF slag was then washed with distilled water to remove the acid residue and

dried in the oven for 24 h at 90 °C. Hydrochloric acid is used to activate EAF, and it is expected to improve uptake of dye by EAF through altering of physical properties which leads to increase in surface porosity and surface area of the treated EAF slag [16].

All the chemicals and reagents used in this experimental work were analytical grade, from Merck.

Procedure

The methylene blue stock solution with a concentration of 1000 ppm was prepared by adding an accurate amount of methylene blue powder with distilled water. Few series of dilution were performed to prepare a different concentration of the dye solution which was used to develop the calibration curve.

To determine the effect of pH, adsorbent dosage and initial concentration, batch adsorption experiment are carried out by adding raw EAF slag and treated EAF slag into the dye solution. A series of dye solution was prepared with the pH of the solution ranging pH 2 to 10, adsorbent dosage ranging from 0.1 to 0.5 g and a concentration ranging from 60 to 180 ppm.

Raw EAF slag (0.5 g) and treated EAF slag (0.5 g) were mixed with 100 ppm of methylene blue dye solution in a series of conical flasks for 2 h at 150 rpm. The pHs of the solution was adjusted by using 0.1 M hydrochloric solution and 0.1 M sodium hydroxide solution. The solution was then filtered, and the concentrations were determined using the UV-spectrophotometer.

Characterization of adsorbent

The surface morphology of raw EAF slag and treated EAF slag were observed using a Scanning Electron Microscope (SEM Hitachi, Japan). The elemental composition on both samples was analyzed using Energy Dispersive X-ray Spectroscopy (EDX) using the same instrument.

The specific surface area and single point pore volume were analyzed using a Surface Area Analyser (Micromeritics, USA) by applying Brunauer Emmet and Teller (BET) test method. The surface area was determined by physical adsorption of a gas on the surface of the adsorbent and by calculating the amount

of adsorbate gas corresponding to a monomolecular layer on the surface.

Removal efficiency, adsorption capacity, and adsorption isotherm

The removal percentage (%) is calculated by using Eq. 1 and the amount of adsorbate adsorbed per unit mass of adsorbent is calculated using Eq. 2 [13].

$$\frac{C_0 - C_e}{C_0} \times 100 \quad (1)$$

$$\frac{C_0 - C_t}{m} \times V \quad (2)$$

C_0 and C_e are the initial and final concentration of the Methylene blue solution in mg/L. C_t is the concentration of contact time. V is the volume of the dye solution in L whereby m is the mass (dosage) of adsorbent used in the experimental work.

Equilibrium data were analyzed using the Freundlich isotherm model and Langmuir isotherm model for both samples. The Freundlich isotherm model is given in Eq. 3, whereby k and n are the Freundlich constant which can be obtained from the graph plot [13].

$$\log q_e = \log k_f + \frac{1}{n} \log C_e \quad (3)$$

The Langmuir isotherm model is given in Eq. 4, whereby b and q_m are the Langmuir constant which can be obtained from the graph plot [13].

$$\frac{c_e}{q_e} = \frac{1}{bq_m} + \frac{c_e}{q_m} \quad (4)$$

RESULTS AND DISCUSSION

Characterization of Raw EAF Slag and Treated EAF Slag

The surface morphology of both raw EAF slag and

treated EAF slag were examined using a Scanning Electron Microscope (SEM). The results reveal that the pores on the surface are more significant after the treatment process as shown in Fig. 1(b), as the flocs-like impurities as shown in Fig. 1(a) has been removed and exposing the coarser surface. The presence of pores on the surface of the EAF slag confirmed its porosity. The removal of those impurities has exposed more pores on the adsorbent's surface, which eventually increased the efficient removal of the adsorbate.

The samples were further analyzed using the Energy Dispersive X-ray (EDX) spectroscopy. The results revealed that the elemental composition in weight percentage (wt.%) has a significant difference in the elements, before and after the chemical treatment. The results for the chemical characterization are shown in Table 1.

From the data tabulated in Table 1, the existing elements in the EAF slag were C, Mg, Al, Si, S, Ca, Mn and Fe. Treatment with acid has removed 13.4% of silicon and 29.38% of calcium, as shown in Table 1.

Table 1. Elements present in raw EAF slag and treated EAF slag

Element	Composition (wt.%)	
	Raw EAF slag	Treated EAF slag
C	11.63	31.65
Mg	3.19	2.61
Al	9.28	6.77
Si	19.03	5.99
S	0.66	0.00
Ca	35.49	6.11
Mn	3.58	3.49
Fe	17.14	43.39

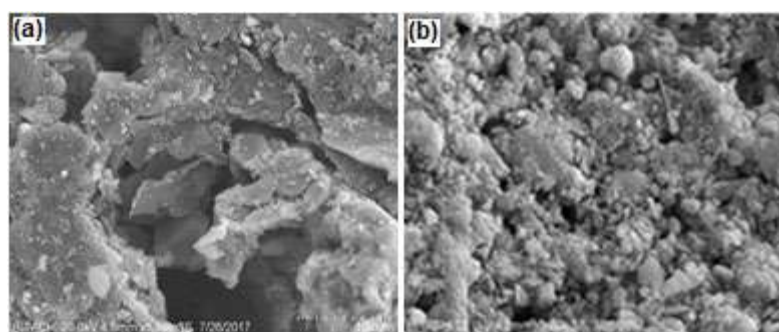


Fig 1. Surface morphology of (a) raw EAF slag and (b) treated EAF slag

Hence, the flocs-like impurities as observed in Fig. 1(a), were mainly composed of silicon and calcium as the major component. After treatment, the composition of carbon and iron were dominant. The composition of carbon has increased by 20.02% whereby the composition of iron has increased by 26.25%. EAF slag typically contains more than 25% of iron oxide [17]. More pores will be available for adsorption to occur when the impurities have been removed after the treatment process.

As the pores were observed from the Scanning Electron Microscope (SEM), further analysis to evaluate the particle size, specific surface area, and pore diameter has been conducted. The Brunauer Emmet and Teller (BET) test has been performed, and the results are shown in Table 2.

The data shown in Table 2 reveals that the surface area and pore volume of treated EAF slag was higher compared to raw EAF slag. Particle size, pore diameter, and specific surface area are the main factors affecting the adsorption capacity of the adsorbent [16].

Adsorption Study

Effect of pH

The pH of dye solution is one of the significant factors affecting the uptake of methylene blue by both raw EAF slag and treated EAF slag. pH is an important factor for dye adsorption, which it directly affects the dissociative and adsorptive ability of the dye onto the surface of the adsorbent [20]. Based on Fig. 2, both raw EAF slag and

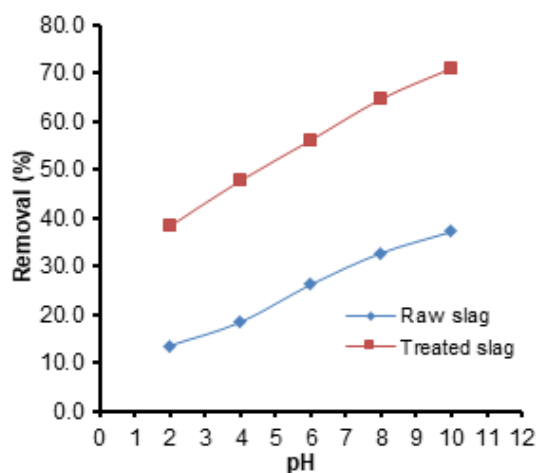


Fig 2. Removal percentage of methylene blue dye against pH of dye solution

treated EAF slag showed the maximum removal at pH 10, which are 37.19% and 71.01%, respectively. At pH 10, the adsorption capacity demonstrates by the raw EAF slag is 7.44 mg/g and it has shown a significant increase for treated EAF slag which is 14.21 mg/g.

In the lower pH solution, the presence of H^+ ions will compete with methylene blue, which is a cationic dye to occupy the adsorption site, which will eventually reduce the dye uptake [13]. As the pH of the solution increase, the removal of methylene blue increased due to the electrostatic attraction forces between the adsorbent and the dye, as it will attach to the vacant binding sites on the adsorbent.

Effect of adsorbent dosage

The removal percentage of methylene blue dye and adsorption capacity by both raw EAF slag and treated EAF slag increases when the amount of adsorbent increase due to the availability of surface area for the adsorption site [10]. In this batch adsorption study, the adsorbent dosages varied from 0.1 to 0.5 g. As shown in Fig. 3, treated EAF slag showed higher removal percentage

Table 2. Surface area and pore volume data

Parameter	Raw EAF slag	Treated EAF slag
BET Surface Area (m ² /g)	1.38000	1.477100
Single Point Pore Volume (m ³ /g)	0.05498	0.054860

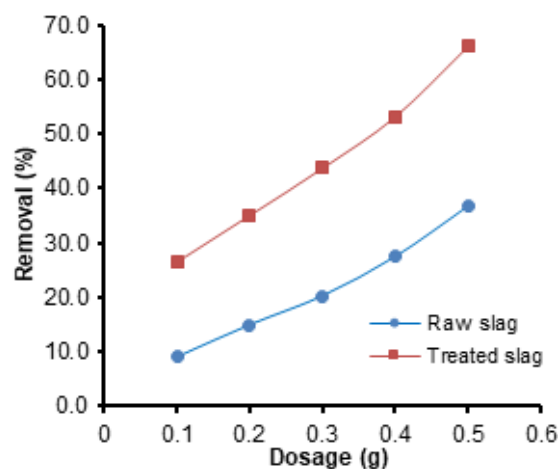


Fig 3. Removal percentage of methylene blue dye against adsorbent dosage

compared to raw EAF slag at a fixed adsorbent dosage. The highest dye uptake is 66.01% by using the treated EAF slag which is 29.26% higher compared to the removal percentage by using the raw EAF slag. The adsorption capacity increases from 7.35 to 13.203 mg/g, by using the treated EAF slag.

Effect of initial concentration

The results represented in Fig. 4 reveals that the removal percentage of both raw EAF slag and treated EAF slag is inversely proportional to the initial concentration of the dye solution. At lower concentration, the dye can be easily occupied onto the adsorption sites. Increasing the concentration will result in decreasing the dye uptake due to the limited active sites on the adsorbent's surface, lowering the adsorption process to take place [19]. At a fixed value of initial concentration, treated EAF slag demonstrates higher removal efficiency compared to raw EAF slag. Raw EAF slag demonstrates the highest removal of 49.24% at 60 ppm, with the adsorption capacity of 5.909 mg/g. Treated EAF slag demonstrate the highest removal

of 80.12% at 60 ppm, with the adsorption capacity of 9.615 mg/g.

Adsorption isotherm

Based on the Freundlich isotherm model as shown in Fig. 5, the linear coefficient for raw EAF slag is 0.9872

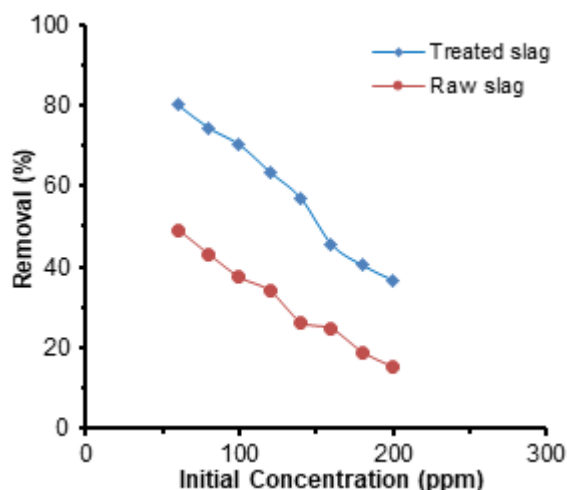


Fig 4. Removal percentage of methylene blue dye against initial concentration

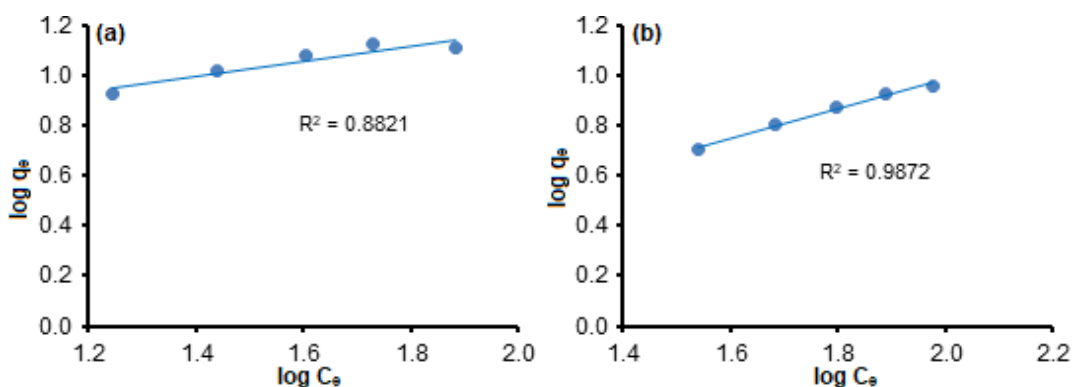


Fig 5. Freundlich isotherm model for (a) raw EAF slag and (b) treated EAF slag

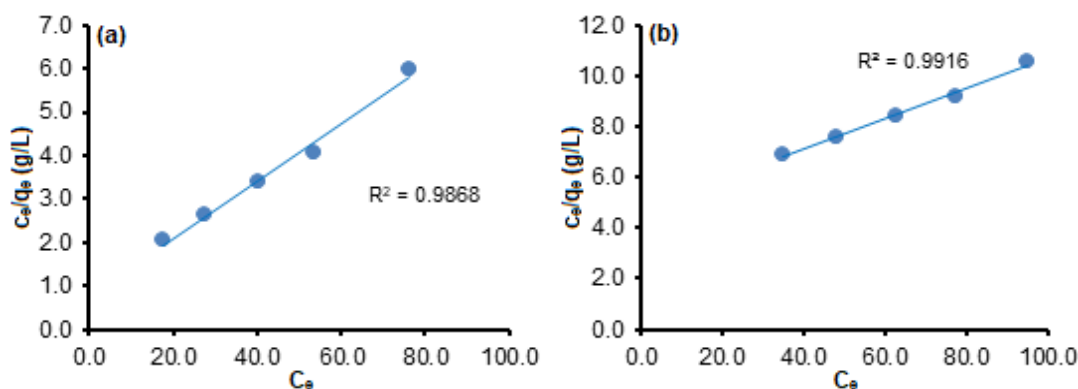


Fig 6. Langmuir isotherm model for (a) raw EAF slag and (b) treated EAF slag

and treated EAF slag is 0.8821. As for the Langmuir isotherm model shown in Fig. 6, the linear coefficient for raw EAF slag is 0.9916 and treated EAF slag is 0.9868. Based on the results, it reveals that both raw EAF slag and treated EAF slag fits the data for the Langmuir isotherm model compared to the Freundlich isotherm model. It may be due to the homogeneous distribution of active sites on the surface of the EAF slag surface, as the Langmuir equation assumed that the surface is homogeneous [20].

■ CONCLUSION

Treated EAF slag improved the methylene blue removal efficiency, as more surface area has increased after the treatment process, as shown in the BET test results. As the impurities have been removed through the chemical treatment process, more adsorption sites were exposed to the adsorption process to occur and increase the dye removal efficiency. The results reveal that treated EAF slag has higher removal efficiency compared to raw EAF slag. The maximum removal percentage for treated EAF slag is 71.01%, whereas raw EAF shows 37.19% removal at pH 10. Both raw EAF slag and treated EAF slag fits the data for the Langmuir isotherm model which obeys the monolayer adsorption process.

■ REFERENCES

- [1] Chiou, M.S., and Li, H.Y., 2003, Adsorption behavior of reactive dye in aqueous solution on chemical cross-linked chitosan beads, *Chemosphere*, 50 (8), 1095–1105.
- [2] Walsh, G.E., Bahner, L.H., and Horning, W.B., 1980, Toxicity of textile mill effluents to freshwater and estuarine algae, crustaceans and fishes, *J. Environ. Pollut. A*, 21 (3), 169–179.
- [3] Khanday, W.A., Marrakchi, F., Asif, M., and Hameed, B.H., 2017, Mesoporous zeolite-activated carbon composite from oil palm ash as an effective adsorbent for methylene blue, *J. Taiwan Inst. Chem. Eng.*, 70, 32–41.
- [4] Ghaly, A.E., Ananthashankar, R., Alhattab, M., and Ramakrishnan, V.V., 2014, Production, characterization and treatment of textile effluents: A critical review, *J. Chem. Eng. Process Technol.*, 5 (1), 1000182.
- [5] Holkar, C.R., Jadhav, A.J., Pinjari, D.V., Mahamuni, N.M., and Pandit, A.B., 2016, A critical review on textile wastewater treatments: Possible approaches, *J. Environ. Manage.*, 182, 351–366.
- [6] Akarslan, F., and Demiralay, H., 2015, Effects of textile materials harmful to human health, *Acta Phys. Pol. A*, 128 (2B), B407.
- [7] Garg, V.K., Amita, M., Kumar, R., and Gupta, R., 2004, Basic dye (methylene blue) removal from simulated wastewater by adsorption using Indian rosewood sawdust: A timber industrial waste, *Dyes Pigm.*, 63 (3), 243–250.
- [8] Bailey, S.E., Olin, T.J., Bricka, R.M., and Adrian, D.D., 1999, A review of potentially low-cost sorbents for heavy metals, *Water Res.*, 33 (11), 2469–2479.
- [9] Xue, Y., Hou, H., and Zhu, S., 2009, Adsorption removal of reactive dyes from aqueous solution by modified basic oxygen furnace slag: isotherm and kinetic study, *Chem. Eng. Sci.*, 147 (2-3), 272–279.
- [10] Majid, Z.A., Hong, F.W., Rosmi, M.S., Ismail, N., Suriani, A.B., Dalila, A.R., and Rusop, M., 2014, Removal of reactive dyes from aqueous solution by modified electric arc furnace slag, *Adv. Mater. Res.*, 832, 804–809.
- [11] Lim, J.W., Chew, L.H., Thomas, S.Y.C., Tezara, C., and Yazdi, M.H., 2016, Overview of steel slag application and utilization, *MATEC Web Conf.*, 74, 00026.
- [12] Duan, J., and Su, B., 2014, Removal characteristics of Cd(II) from acidic aqueous solution by modified steel-making slag, *J. Chem. Eng.*, 246, 160–167.
- [13] Zahar, M.S.M., Kusin, M.F., and Muhammad, S.N., 2015, Adsorption of manganese in aqueous solution by steel slag, *Procedia Environ. Sci.*, 30, 145–150.
- [14] Dąbrowski, A., 2001, Adsorption – from theory to practice, *Adv. Colloid Interface Sci.*, 93 (1-3), 135–224.
- [15] Geetha, K., and Velmani, N., 2015, Diverse technology and methods for dye treatment: A review, *Asian J. Chem.*, 27 (4), 1177–1184.

- [16] Gharsalli, A., Bagane, M., Porte, C., Havet, J.L., and Ammar, S., 2017, Response surface optimization and modeling of ammonium chloride activation process of bentonite, *Courrier du Savoir*, 22, 61–68.
- [17] Liang, H., Zhou, S., Chen, Y., Zhou, F., and Yan, C., 2015, Diatomic coated with Fe_2O_3 as an efficient heterogeneous catalyst for degradation of organic pollutants, *J. Taiwan Inst. Chem. Eng.*, 49, 105–112.
- [18] Mittal, A., Kaur, D., Malviya, A., Mittal, J., and Gupta, V.K., 2009, Adsorption studies on the removal of coloring agent phenol red from wastewater using waste materials as adsorbents, *J. Colloid Interface Sci.*, 337 (2), 345–354.
- [19] Wang, F.Y., Wang, H., and Ma, J.W., 2010, Adsorption of cadmium(II) ions from aqueous solution by a new low-cost adsorbent–bamboo charcoal, *J. Hazard. Mater.*, 177 (1-3), 300–306.
- [20] Foo, K.Y., and Hameed, B.H., 2014, Insight into the modelling of adsorption isotherm systems, *Chem. Eng. J.*, 156 (1), 2–10.

Application of Functionalized Multi-Walled Carbon Nanotubes for Growth Enhancement of Mustard Seed Germination

Agus Subagio^{1*}, Erma Prihastanti², and Ngadiwiyan³

¹Department of Physics, Faculty of Science and Mathematics, Universitas Diponegoro, Jl. Prof. Sudarto, S.H. Tembalang, Semarang 50275, Indonesia

²Department of Biology, Faculty of Science and Mathematics, Universitas Diponegoro, Jl. Prof. Sudarto, S.H. Tembalang, Semarang 50275, Indonesia

³Department of Chemistry, Faculty of Science and Mathematics, Universitas Diponegoro, Jl. Prof. Sudarto, S.H. Tembalang, Semarang 50275, Indonesia

* **Corresponding author:**

tel: +62-81548404171

email: agussubagio@fisika.undip.ac.id

Received: November 26, 2018

Accepted: April 6, 2019

DOI: 10.22146/ijc.41340

Abstract: Multi-walled carbon nanotubes (MWCNTs) are one of the nanomaterials that can be applied to agriculture. This work investigates the beneficial effects of MWCNT function on mustard plants. In this study, the material of MWCNTs is functionalized with nitric acid to attach the carboxylic group onto the tube wall. The functionalized MWCNTs were characterized by SEM, TEM, XRD, and FTIR. The MWCNT diameter produced ranges from 20 to 50 nm and the inner diameter is 5 to 10 nm at the pyrolysis temperature of 900 °C. It was found that crystallites of the MWCNTs have (002) and (100) directions. There is a weak peak in MWCNTs prior to the functionalization process due to the presence of metal carbide (Fe₃C), which serves as an active catalyst. FTIR results clearly indicate the presence of hydroxyl and carboxylic groups. These functionalized MWCNTs were dispersed into distilled water with various concentrations at 25, 50 and 75 µg/mL. By utilizing an immersion time of 24 h, mustard (*Brassica juncea*) seeds were soaked in each functionalized and non-functionalized MWCNT solution. Functionalized MWCNT solution at a concentration of 50 µg/mL was found to affect the growth of mustard seeds more significantly.

Keywords: multi-walled carbon nanotubes; functionalization; mustard; seed; germination

■ INTRODUCTION

Currently, the application of nanotechnology in agriculture is important. Various problems related to agriculture have been solved by utilizing nanotechnology. Such technology has supported modern agriculture in terms of providing, for example, pesticide sensor technology as well as both pesticide and fertilizer delivery systems [1]. Nanoparticles can reduce the loss rate of fertilizer nutrients into the soil by leaching and/or leaking and can extend the effective duration of the nutrient supply of fertilizers into soil [2]. Nano-sized material of mineral micronutrients may improve solubility and dispersion of insoluble nutrients in the soil, reduce soil

absorptional fixation, and increase bioavailability. Nanometer-sized fertilizers have been used to increase yields [3]. The use of nano silica fertilizer to improve the yield of rice and horticulture can be implemented by spraying onto the leaves through the mouth of the leaf. Nanosilica particles enter the mouth of a micrometer-sized leaf with relative ease [4].

Several nanoparticles with different characteristics have recently gained interest because of the possibility of their application in the treatment of plant growth [5]. Nanoparticles of varying composition, size, concentration, and other physical/chemical properties have been reported to provide positive or negative effects, particularly with respect to influencing growth

and development of various plant species. Multi-Walled Carbon Nanotubes (MWCNTs) is a nanomaterial with new interest for many scientists in terms of agricultural applications as a biosensor, fertilizer, catalyst, and pesticide adsorbent [6-12]. Penetrating MWCNTs in seed as well as the root system significantly affects their biological activity by enhancing the amount of water present inside the seed during the germination period [13]. However, it is necessary to optimize the diameter size of MWCNTs to allow them to enter into the seed and root walls. There are several methods used for the production of MWCNTs including arc discharge, laser ablation, chemical vapor deposition and spray pyrolysis [14-19]. One of the easier methods used to produce MWCNTs by adjusting its diameter is spray pyrolysis. The length and diameter of MWCNTs can be determined by growth temperature, which is a crucial consideration for MWCNT applications.

MWCNTs produced by several methods of growth as mentioned above have hydrophobic properties meaning that it is difficult to disperse them, particularly in water. This fundamental issue becomes a technical barrier to its wider application. To overcome this problem, the functionalization of MWCNTs or SWCNTs needs to be done through the reflux process, which increases its biocompatibility capabilities, particularly in terms of adsorption ability, electrostatic interactions, and covalent bonds by the presence of carboxylic groups on the walls [20-21]. However, the reflux process carried out using nitric, sulfuric, and peroxide acids or a combination of them causes significant damage to MWCNT bonds if it is not optimally controlled [22-24]. Therefore, the acid concentration and duration of the reflux process are still a substantial challenge to be addressed by future research.

Biological and bioactive species such as proteins, carbohydrates, and nucleic acids can be conjugated with MWCNTs [5]. MWCNTs can be applied as a nutrient transfer path within the plant tissue. Soaking plant germination seeds in carbon nanotube material which has been dispersed in aquadest assists the growth process [25]. However, issues arise if the MWCNT concentration is excessive, and it is thus necessary to optimize the concentration of carbon nanotubes in various types of

plants. Khodakovskaya et al. [20] reported the increasing tomato seed germination through better moisture permeation using carbon nanotube material. MWCNTs function as providing new pores to allow water to permeate by penetrating the seed layer and acting as a part to channel water.

The use of MWCNTs as a pore medium for water canals is interesting because excessive MWCNT use also causes toxicity to plants [26]. Srivastava and Rao [13] explored the potential influence of 0–50 µg/mL of MWCNT on different seeds at varying concentrations on wheat, maize, peanut, and garlic. MWCNTs at low doses were able to increase water absorption and have an impact on the faster germination process and hence shorten germination time.

In this study, the influence of functionalized MWCNT material for the treatment of mustard plants by soaking mustard seeds in a functionalized MWCNT solution at various concentrations was analyzed. The growth temperature of MWCNTs, the process of functionalized MWCNTs, their characterization using X-ray diffraction (XRD), Fourier transform infrared spectrometry (FTIR), scanning electron microscopy (SEM), transmission electron microscopy (TEM) were also studied. The mustard plants were soaked in nanotubes, and their impact was then investigated by observing the growth of the plants and analyze differences in root and cell sizes. Based on this research, particular characteristics of MWCNTs will be obtained, especially the dimension and composition of the functionalized MWCNTs for treatment of mustard plant growth.

■ EXPERIMENTAL SECTION

Materials

Materials used in this study were benzene (CAS 71-43-2, 109646 - Merck Millipore) as a carbon precursor for MWCNT, ferrocene (Aldrich-F408; Ferrocene 0.98; CAS No.: 102-54-5) as a precursor for Fe catalyst, argon gas, nitric acid solution, and distilled water.

Instrumentation

A spray pyrolysis system was used to make the MWCNT material. The morphology images of the

functionalized MWCNTs were obtained using SEM (JEOL JSM-6390A) equipped with an Energy Dispersive X-ray (EDX) system which permits sub-micrometer elemental identification and compositional analysis. The structures of the functionalization of MWCNTs were obtained using XRD (Phillip analytical X-Ray B.V) with CuK α radiation ($\lambda = 1.5418 \text{ \AA}$) at 40 KV. TEM images were obtained on a JEOL 2011. The functionalized groups present in the MWCNTs were obtained using FTIR (Thermo Scientific Nicolet IS 10).

Procedure

MWCNT material was produced using a spray pyrolysis method (Fig. 1) at varying temperatures (800, 900, 1,000 °C). The source of the material used for making the MWCNTs was benzene and ferrocene. The optimal parameter of benzene as a carbon source and ferrocene as a catalyst was 3 g of ferrocene and 50 mL of benzene. The solution of ferrocene in benzene was introduced into the quartz reactor. MWCNTs produced from this method were still relatively difficult to disperse, and there were still residual Fe impurities from ferrocene. To resolve these issues, the work was directed towards developing methods to modify surface properties of MWCNTs with functionalization. This work was carried out using a reflux process with a nitric acid solution for 3 h to attach the carboxylic group to the tube wall. The MWCNT was washed with nitric acid only using MWCNT grown at the optimum temperature of 900 °C. Another effect of this reflux process is that the MWCNT wall will be damaged and lead to the attachment of the carboxylic group on the outer tube wall. For the application of the seed germination method, functionalized MWCNTs were dispersed into distilled water at various concentrations (0,

25, 50, and 75 $\mu\text{g/mL}$). By utilizing an immersion time of 24 h, the mustard (*Brassica juncea*) seeds were soaked in each functionalized MWCNT solution. Monitoring of seed growth of mustard seeds was performed, and growth of roots and stems was recorded.

RESULTS AND DISCUSSION

Temperature determines the pyrolysis process of hydrocarbon compounds and catalyst into its constituent carbon elements. Using varying temperatures affects the diameter and length of MWCNTs. It was found that lower temperatures of 800 °C will produce shorter MWCNTs, which were larger in diameter compared to when using higher temperatures. Low temperatures not only produce shorter MWCNTs but also bend the resulting MWCNTs (Fig. 2(a)). If the temperature is increased to 900 and 1,000 °C, the pyrolysis process takes place more rapidly and effectively, leading to MWCNT tubes being formed that are longer (Fig. 2(b) and 2(c)). At these temperatures, the

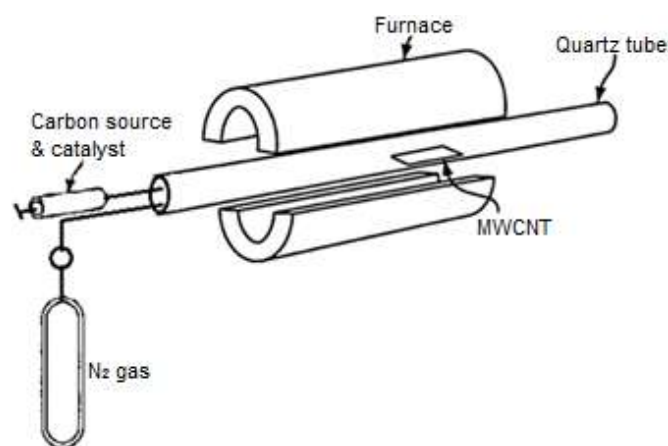


Fig 1. Schematic representation of spray pyrolysis method

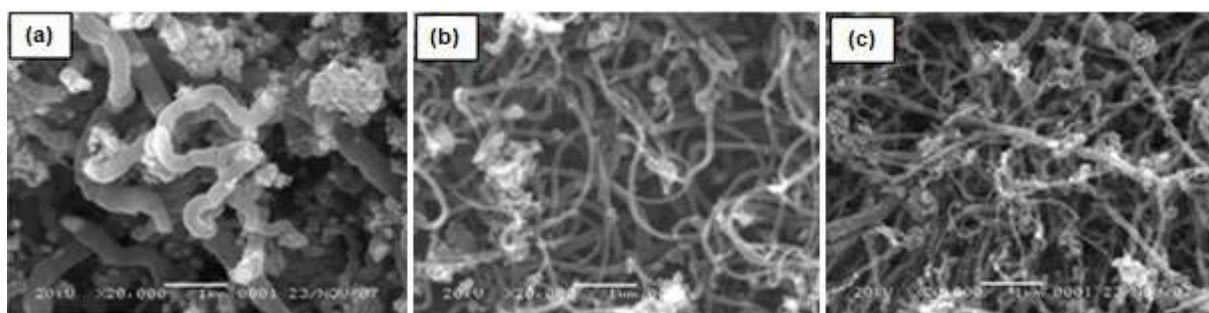


Fig 2. SEM images of MWCNTs with varying temperatures of growth: (a) 800, (b) 900 and (c) 1,000 °C

source will split into more constituent carbons, a process which causes increasing diffusion of carbons on the surface of the catalyst metal [19]. Therefore, more MWCNTs form and their diameters will be smaller. MWCNTs produced at a growth temperature of 1,000 °C are slightly damaged; other studies have also determined that structural graphite cannot be formed at such temperatures [5].

The reflux process, as shown in Fig. 3, illustrates that nitric acid treatment releases Fe particles and attaches COOH groups to the walls of the MWCNT tubes. The reflux process leads to defects in the MWCNT wall due to the presence of nitric acid. These intrinsic defects are supplemented by oxidative damage to the nanotube framework. In particular, the treatment of MWCNTs with strong acids such as HNO₃, H₂SO₄ or a mixture of them will tend to open these tubes that serve to tether many different types of chemical moieties onto the ends and defect sites of the tubes. MWCNTs functionalized using this method have an advantage in that they are soluble in various organic solvents due to possessing many functional groups such as carboxylic (COOH) ones derived from the reflux process with nitric acid [27-28]. The longer reflux process tends to produce increased Fe particle content derived from ferrocene catalysts and a decreasing Fe particle content between the before and after the reflux process, as explained from the EDX characterization.

Fig. 4 provides SEM images of MWCNT material before and after purification. It can be seen that many

material morphologies are not patterned (amorphous) and white spots are present. Clearly, these white lumps and spots are not a representation of MWCNTs, but rather other materials which are by-products or waste materials from the process of MWCNT synthesis, namely amorphous carbon. The red circle insert is part of amorphous carbon. Removal of Fe impurities and amorphous carbon can be done through a reflux process with several acid solutions. The use of strong acids to reflux MWCNT materials such as hydrochloric acid (HCl), nitric acid (HNO₃) and sulfuric acid (H₂SO₄) is particularly effective in reducing Fe particles and amorphous carbon. In this research, HNO₃ was used to reflux MWCNT.

Fig. 5 demonstrates that MWCNT material that has been refluxed has tube ends not covered by Fe impurities. During spray pyrolysis, Fe particles typically

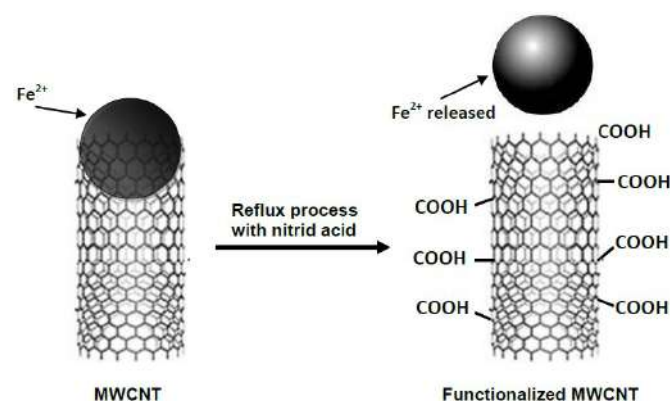


Fig 3. Illustration of MWCNT reflux process — from MWCNTs to functionalized MWCNTs

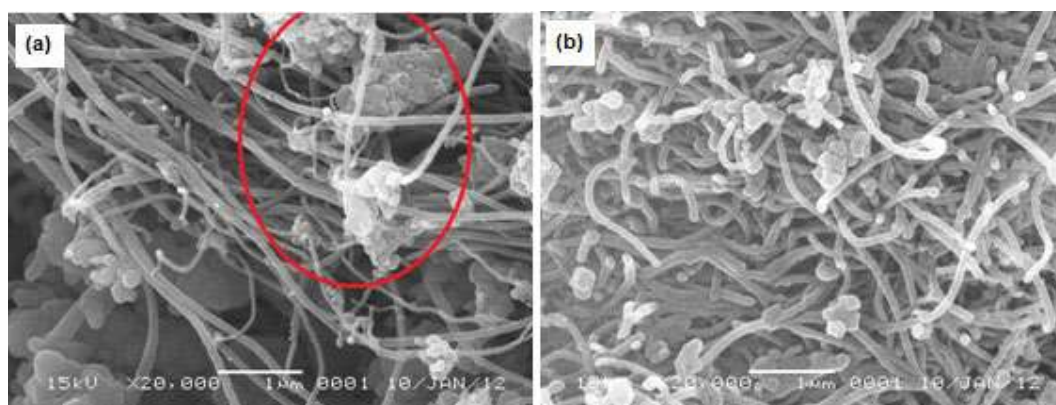


Fig 4. SEM images of MWCNT with temperature of growth of 900 °C (a) without reflux process and (b) with reflux process following spray pyrolysis. The red circle insert is part of amorphous carbon

move and act as the head followed by the tail in the form of carbon bonds so that the position of Fe particles is at the end of the tube. The reflux process is intended to release Fe particles from the end of tubes. Furthermore, for MWCNTs that have been purified, the morphological form appears more orderly and uniform; the morphology that is not patterned disappears completely, with only a few white spots remaining. As reported by Edward et al. the purification of carbon nanotubes using acids can reduce Fe attached to the end of the MWCNT surface [29]. In addition, purification with acid is also able to reduce amorphous carbon which is not shaped as nanotubes [30].

The diameter of MWCNTs produced by spray pyrolysis ranges from 20 to 50 nm. There are several walls forming a tube with an inner diameter of 5 to 10 nm, as shown by TEM characterization in Fig. 6(a). The MWCNT production using a ferrocene catalyst on the spray pyrolysis method will leave Fe as an impurity at the end of the tube (Fig. 6(b)). Therefore, the purification process of MWCNT from Fe catalyst residue needs to be carried out using a reflux treatment.

Table 1 shows the results of the EDX analysis of MWCNT treatment with and without reflux. It can be seen that reflux treatment will reduce the atomic percentage of Fe compared to without reflux. The mechanism of Fe reduction has been explained previously.

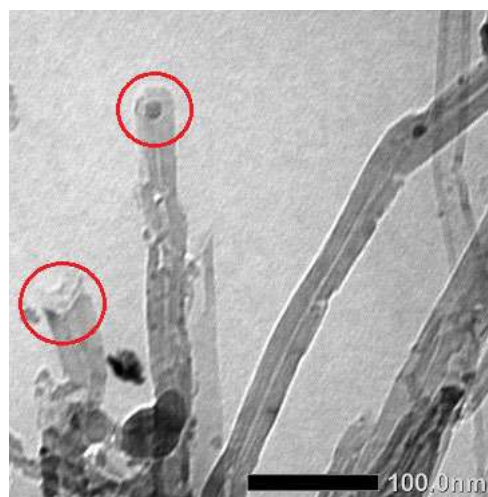


Fig 5. TEM image of MWCNT material which was refluxed. The insert red circle shows that the Fe particle has escaped from the end of tube after reflux process

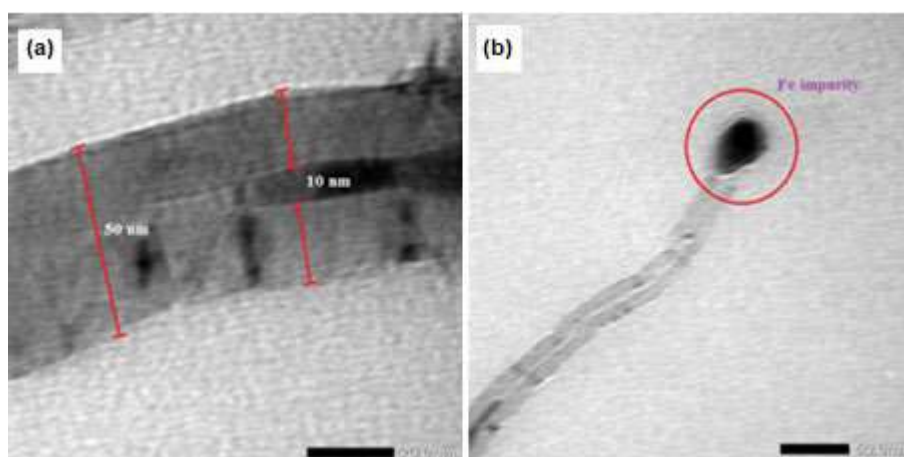


Fig 6. TEM image of (a) inner and outer diameter of MWCNT tube and (b) the presence of Fe impurities at the end of the MWCNT tube EDX was used to identify the quantitative amounts of different elements present in MWCNTs

Table 1. Results of EDX analysis of MWCNT treatment with and without reflux

No	Sample	Chemical composition in atomic %	
		C	Fe
1	MWCNT without reflux	96.40	3.60
2	MWCNT reflux	99.64	0.36

Fig. 7(a) and 7(b) illustrate XRD analysis of MWCNTs before and after the functionalization process, respectively. There are two graphite crystal orientations at 2 theta angles of 26.4 and 43.7° corresponding to the main plane of (002) and the additional plane of (100) [31]. The results also show that the peaks of CNT (002) are in symmetry, indicating good crystallite dimensions and in agreement with Das et al. [32]. MWCNT has different chiralities, consisting of different layers and shows the same peak diffraction pattern (002) with a graphite sheet. In addition, the honeycomb lattice structure of a single graphene cell caused the peak family (hk0) to be related to the (100) plane. The peak (hk0) is generated because of the curved nature of nanotubes [33]. The small peak at 37.4° in the MWCNTs prior to functionalization suggests the presence of Fe₃C in the sample. The metal carbide acts as an active catalyst in the formation of tubular structures of graphitic carbon and indicates the impurity of the sample [19].

FTIR is generally used to investigate the functionalization of MWCNTs, particularly for assaying the existence of groups attached to MWCNT tube walls. The level of functionalization would change MWCNTs properties and lead to them dissolving in water if it were used for appropriate applications. In this research, FTIR analysis was carried out to determine the functional groups present in both non-functionalized and functionalized MWCNTs. The resulting MWCNTs typically contain C-H, C=C, and C-O groups due to the spray pyrolysis process [24,31]. The reaction between

benzene and ferrocene as a catalyst at high temperatures produces carbide bonds. The carbides formed will tend to bind themselves in chains or rings, not only with one bond (C-C) but also as double bonds (C=C).

Fig. 8(a) presents spectra of functionalized MWCNTs, comprising C-O groups at the wave number of 1,027 cm⁻¹, the wide transmission band at 3,450 cm⁻¹ indicates the presence of O-H groups [17]. Wave numbers of 2,350 cm⁻¹ are characteristic of C=C groups [34]. The weak peak at around 2,850 cm⁻¹ is assigned to vibration modes of C-H or C-H₂ while the wave number of 1,720 cm⁻¹ is attributed to C=O stretching vibrations in carboxyl groups [35]. Fig. 8(b) shows the spectra of non-functionalized MWCNTs. The band at wave number 1,157 cm⁻¹ is the absorption of C-O groups, while the wave number of 2,850 cm⁻¹ is associated with the vibration modes of C-H or C-H₂. Wave numbers of 2,350 cm⁻¹ are characteristic of the C=C group due to the integrity of the hexagonal MWCNT structure.

In the case of functionalized MWCNTs, the characteristic O-H band appeared significantly broad and with higher intensity. This higher intensity is attributed to the increase in the number of hydroxyl groups on the MWCNT surface after functionalization. Decreasing the absorbance of C=C at 2,350 cm⁻¹ indicates oxidation of carbon with the emergence of a peak at 1,645 cm⁻¹ as carbonyl (C=O) stretching vibration of carboxyl groups, indicating the expansion of carboxylation on the surfaces of functionalized MWCNTs. The FTIR results

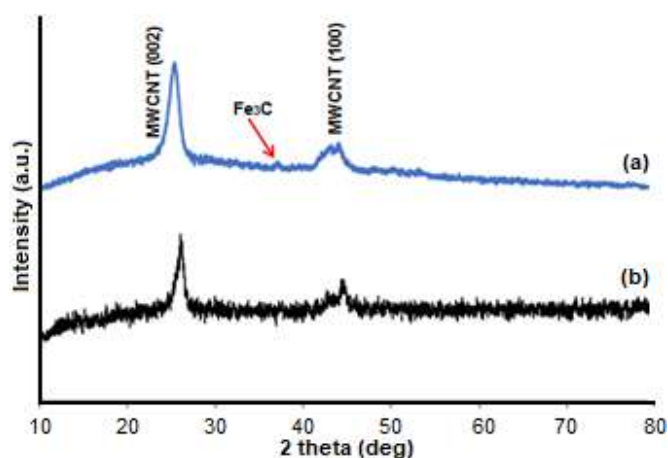


Fig 7. X-ray diffraction pattern of MWCNTs (a) before and (b) after functionalization

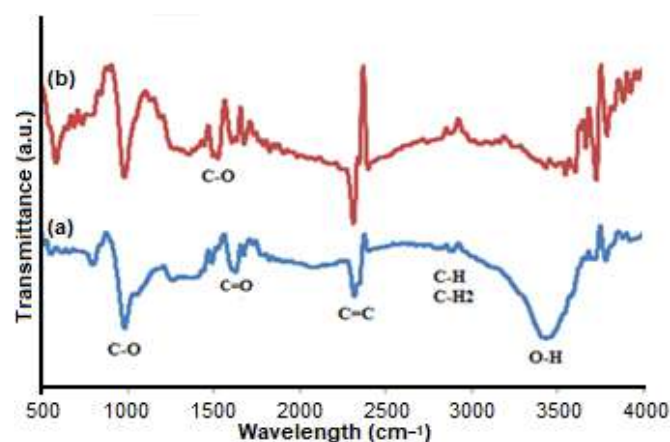


Fig 8. FTIR spectra of (a) functionalized and (b) non-functionalized MWCNTs

clearly demonstrate that the hydrophilic groups such as hydroxyl and carboxylic have been introduced onto the treated MWCNT surfaces. Thus, the functionalization of MWCNTs by the change in properties from hydrophobic to hydrophilic with the emergence of hydroxyl and carboxylic groups on its surface can be utilized as a nutrient transfer path within the plant tissue.

Fig. 9 illustrates non-functionalized and functionalized MWCNT solutions at several concentrations used for immersion of mustard seeds. Non-functionalized MWCNT cannot be dissolved in water and tend to float on the surface. At the functionalized MWCNT solution with a concentration of 25 $\mu\text{g/mL}$, the solution still appears clear because several MWCNTs are still dissolved, while at concentrations of 50 and 75 $\mu\text{g/mL}$, it appears black due to the presence of more MWCNT material. This result shows that the functionalization process of MWCNTs has been able to help the dispersion process in water because

there is a carboxylic group on the surface of MWCNTs which will increase the surface energy and reduce chemical affinity with dispersing media [36]. Surface functionalization can be developed to improve their dispersion, stability, and biocompatibility by introducing carboxylic groups.

Observations on the growth of germination of mustard plants are shown in Fig. 10. A significant positive effect on root and stem growth was seen to be very different between seeds treated by immersion in non-functionalized MWCNT solution of (a) 50 $\mu\text{g/mL}$ and functionalized MWCNT solutions with different concentration of (b) 25 $\mu\text{g/mL}$, (c) 50 $\mu\text{g/mL}$ and (d) 75 $\mu\text{g/mL}$. The functionalized MWCNT solution of 50 $\mu\text{g/mL}$ has an effect on maximum growth compared to concentrations of 25 $\mu\text{g/mL}$ and 75 $\mu\text{g/mL}$. This result demonstrates that a concentration of 50 $\mu\text{g/mL}$ is the

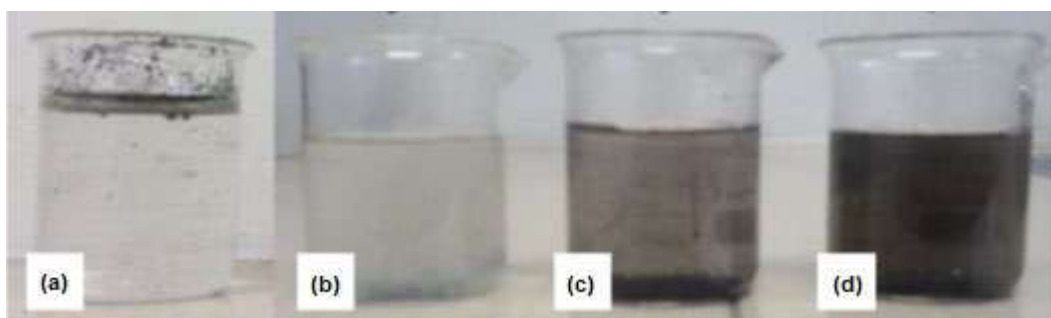


Fig 9. Photos of non-functionalized MWCNT solution of (a) 50 $\mu\text{g/mL}$ and functionalized MWCNT solutions with different concentration of (b) 25 $\mu\text{g/mL}$, (c) 50 $\mu\text{g/mL}$ and (d) 75 $\mu\text{g/mL}$

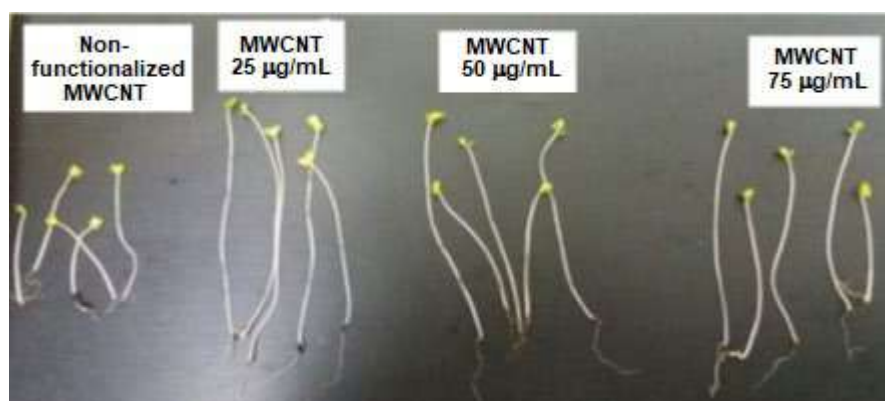


Fig 10. Photos of the effect of soaking mustard seeds for five days in non-functionalized MWCNTs solution of (a) 50 $\mu\text{g/mL}$ and functionalized MWCNTs solutions with different concentration of (b) 25 $\mu\text{g/mL}$, (c) 50 $\mu\text{g/mL}$ and (d) 75 $\mu\text{g/mL}$

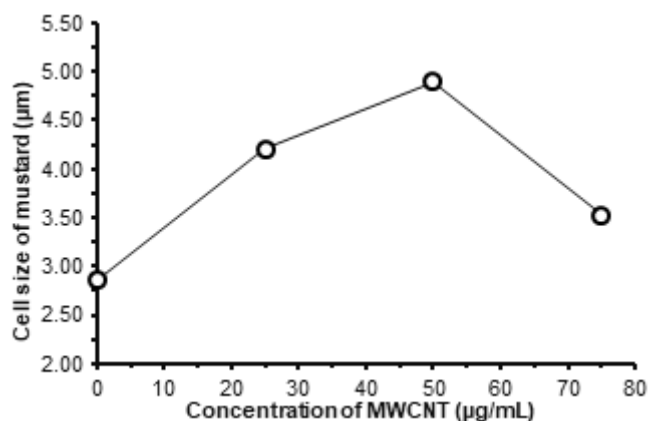


Fig 11. Effect of functionalized MWCNTs on mustard cell growth

optimum concentration where MWCNT material can enter the cell wall of mustard seeds and root systems and significantly affect their biological activity by increasing the amount of water that penetrates inside the seed during the germination period [13]. At the functionalized MWCNT solution of 75 µg/mL, aggregation of MWCNT within the roots can occur, potentially causing negative effects such as inducing nanotoxicity, inhibiting nutrient transport, and affecting plant growth [37].

Differences in the size of mustard plant cells were observed due to immersion treatment in functionalized MWCNTs (Fig. 11). Mustard plants soaked in the functionalized MWCNT solution of 50 µg/mL had a larger cell size than those soaked in concentrations of 25 µg/mL, 75 µg/mL, and control. The optimum concentration at 50 µg/mL gives the opportunity to transfer water into the wall of mustard seeds at a higher rate than other concentrations. However, the excess of MWCNTs in plants is still a question for researchers.

■ CONCLUSION

This work has demonstrated that the process of MWCNT functionalization can be successfully carried out to activate MWCNT walls in the presence of carboxylic groups. Functionalized MWCNT solutions at a concentration of 50 µg/mL led to the highest mustard seed growth rates. These functionalized MWCNTs enter the germination wall and allow the water absorption required for mustard germination to be more effective.

■ ACKNOWLEDGMENTS

The authors gratefully acknowledge Ministry of Research, Technology and Higher Education of the Republic of Indonesia (National Strategic Research Grant 2015-2017, 007/SP2H/LT/DRPM/V/2017) for financial support.

■ REFERENCES

- [1] Veronica, N., Guru, T., Thatikunta, R., and Reddy, S.N., 2015, Role of nano fertilizers in agricultural farming, *Int. J. Environ. Sci. Technol.*, 1 (1), 1–3.
- [2] Kottegoda, N., Munaweera, I., Madusanka, N., and Karunaratne, V., 2011, A green slow-release fertilizer composition based on urea-modified hydroxyapatite nanoparticles encapsulated wood, *Curr. Sci.*, 101 (1), 73–78.
- [3] Manjunatha, S.B., Biradar, D.P., and Aladakatti, Y.R., 2016, Nanotechnology and its applications in agriculture: A review, *J. Farm Sci.*, 29 (1), 1–13.
- [4] Subagio, A., Prihastanti, E., Ngadiwiyan, Rowi, K., and Gufron, A., 2015, Fabrication of NanoChiSil for Application of Fertilizer, *Proceeding of the 5th International Seminar on New Paradigm and Innovation on Natural Sciences and Its Application (5th ISNPINSA)*, 7-8 October 2015, Semarang, Indonesia, 113–116.
- [5] Aguilar-Elguezabal, A., Antunez, W., Alonso, G., Espinosa, F., and Miki-Yoshida, M., 2006, Study of carbon nanotubes synthesis by spray pyrolysis and model of growth, *Diamond Relat. Mater.*, 15 (9), 1329–1335.
- [6] Mukesh, T., and Jha, A.K., 2017, A review on: carbon nanotubes are vital for plant growth, *Am. J. Agric. For.*, 5 (5-1), 1–9.
- [7] Tiwari, D.K., Dasgupta-Schubert, N., Cendejas, L.M.V., Villegas, J., Montoya, L.C., and García, S.E.B., 2014, Interfacing carbon nanotubes (CNT) with plants: Enhancement growth, water and ionic nutrient uptake in maize (*Zea mays*) and implications for nanoagriculture, *Appl. Nanosci.*, 4 (5), 577–591.
- [8] Rameshaiah, G.N., Pallavi, J., and Shabnam, S.,

- 2015, Nano fertilizers and nano sensors – an attempt for developing smart agriculture, *Int. J. Eng. Res. Gen. Sci.*, 3 (1), 314–320.
- [9] Yatim, N.M., Shaaban, A., Dimin, M.F., and Yusof, F., 2015, Statistical evaluation of the production of urea fertilizer-multiwalled carbon nanotubes using Plackett Burman experimental design, *Procedia Soc. Behav. Sci.*, 195, 315–323.
- [10] Tonucci, M.C., Gurgel, L.V.A., and de Aquino, S.F., 2015, Activated carbons from agricultural byproducts (pine tree and coconut shell), coal, and carbon nanotubes as adsorbents for removal of sulfamethoxazole from spiked aqueous solutions: Kinetic and thermodynamic studies, *Ind. Crops Prod.*, 74, 111–121.
- [11] Park, S., and Ahn, Y.J., 2016, Multi-walled carbon nanotubes and silver nanoparticles differentially affect seed germination, chlorophyll content, and hydrogen peroxide accumulation in carrot (*Daucus carota* L.), *Biocatal. Agric. Biotechnol.*, 8, 257–262.
- [12] Shen, X., Li, S., Zhang, H., Chen, W., Yang, Y., Li, J., Tao, S., and Wang, X., 2018, Effect of multiwalled carbon nanotubes on uptake of pyrene by cucumber (*Cucumis sativus* L.): Mechanistic perspectives, *NanoImpact*, 10, 168–176.
- [13] Srivastava, A., and Rao, D.P., 2014, Enhancement of seed germination and plant growth of wheat, maize, peanut and garlic using multiwalled carbon nanotubes, *Eur. Chem. Bull.*, 3 (5), 502–504.
- [14] Sharma, R., Sharma, A.K., and Sharma, V., 2015, Synthesis of carbon nanotubes by arc-discharge and chemical vapor deposition method with analysis of its morphology, dispersion and functionalization characteristics, *Cogent Eng.*, 2 (1), 1094017.
- [15] Kumar, M., and Ando, Y., 2010, Chemical vapor deposition of carbon nanotubes: A review on growth mechanism and mass production, *J. Nanosci. Nanotechnol.*, 10, 3739–3758.
- [16] Arora, N., and Sharma, N.N., 2014, Arc discharge synthesis of carbon nanotubes: Comprehensive review, *Diamond and Relat. Mater.*, 50, 135–150.
- [17] Chrzanowska, J., Hoffman, J., Małolepszy, A., Mazurkiewicz, M., Kowalewski, T.A., Szymanski, Z., and Stobinski, L., 2015, Synthesis of carbon nanotubes by the laser ablation method: Effect of laser wavelength, *Phys. Status Solidi B*, 252 (8), 1860–1867.
- [18] Vilatela, J.J., Rabanal, M.E., Cervantes-Sodi, F., García-Ruiz, M., Jiménez-Rodríguez, J.A., Reiband, G., and Terrones, M., 2015, A spray pyrolysis method to grow carbon nanotubes on carbon fibres, steel and ceramic bricks, *J. Nanosci. Nanotechnol.*, 15 (4), 2858–2864.
- [19] Annu, A., Bhattacharya, B., Singh, P.K., Shukla, P.K., and Rhee, H.W., 2017, Carbon nanotube using spray pyrolysis: Recent scenario, *J. Alloys Compd.*, 691, 970–982.
- [20] Khodakovskaya, M.V., Dervishi, E., Mahmood, M., Xu, Y., Li, Z., Watanabe, F., and Biris, A.S., 2009, Carbon nanotubes are able to penetrate plant seed coat and dramatically affect seed germination and plant growth, *ACS Nano*, 3 (10), 3221–3227.
- [21] Tripathi, S., Sonkar, S.K., and Sarkar, S., 2011, Growth stimulation of gram (*Cicer arietinum*) plant by water soluble carbon nanotubes, *Nanoscale*, 3 (3), 1176–1181.
- [22] Ahmed, D.S., Haider, A.J., and Mohammad, M.R., 2013, Comparison of Functionalization of multiwalled carbon nanotubes treated by oil olive and nitric acid and their characterization, *Energy Procedia*, 36, 1111–1118.
- [23] Takada, T., Santida, D., and Abe, S., 2010, Suitable conditions for sidewall carboxylation of multiwalled carbon nanotubes, *Nano Biomed.*, 2 (2), 147–152.
- [24] Jun, L.Y., Mubarak, N.M., Yon, L.S., Bing, C.H., Khalid, M., and Abdullah, C., 2018, Comparative study of acid functionalization of carbon nanotube via ultrasonic and reflux mechanism, *J. Environ. Chem. Eng.*, 6 (5), 5889–5896.
- [25] Khodakovskaya, M.V., de Silva, K., Biris, A.S., Dervishi, E., and Villagarcia, H., 2012, Carbon nanotubes induce growth enhancement of tobacco cells, *ACS Nano*, 6 (3), 2128–2135.
- [26] Begum, P., Ikhtiari, R., and Fugetsu, B., Matsuoka, M., Akasaka, T., and Watari, F., 2012, Phytotoxicity

- of multi-walled carbon nanotubes assessed by selected plant species in the seedling stage, *Appl. Surf. Sci.*, 262, 120–124.
- [27] Jeon, I.Y., Chang, D.W., Kumar, N.A., and Baek, J.B., 2011, “Functionalization of Carbon Nanotubes” in *Carbon Nanotubes-Polymer Nanocomposites*, Eds. Yellampalli, S., IntechOpen, London.
- [28] Hamilton, R.F., Wu, Z., Mitra, S., and Holian, A., 2018, The effects of varying degree of MWCNT carboxylation on bioactivity in various in vivo and in vitro exposure models, *Int. J. Mol. Sci.*, 19 (2), 354.
- [29] Edward, E.R., Antunes, E.F., Botelho, E.C., Baldan, M.R., and Corat, E.J., 2011, Evaluation of residual iron in carbon nanotubes purified by acid treatments, *Appl. Surf. Sci.*, 258 (2), 641–648.
- [30] Stancu, M., Ruxanda, G., Ciuparu, D., and Dinescu, A., 2011, Purification of multiwall carbon nanotubes obtained by AC arc discharge method, *Optoelectron. Adv. Mater. Rapid Commun.*, 5 (8), 846–850.
- [31] Pisal, S.H., Harale, N.S., Bhat, T.S., Deshmukh, H.P., and Patil, P.S., 2014, Functionalized multi-walled carbon nanotubes for nitrogen sensor, *IOSR J. Appl. Chem.*, 7 (11), 49–52.
- [32] Das, R., Abd Hamid, S.B., Ali, M.E., Ramakrishna, S., and Yongzhi, W., 2015, Carbon nanotubes characterization by X-ray powder diffraction – A review, *Curr. Nanosci.*, 11 (1), 23–35.
- [33] Lambin, P., Loiseau, A., Culot, C., and Biro, L.P., 2002, Structure of carbon nanotubes probed by local and global probes, *Carbon*, 40 (10), 1635–1648.
- [34] Wulandari, S.A., Arifin, Widiyandari, H., and Subagio, A., 2018, Synthesis and characterization carboxyl functionalized multi-walled carbon nanotubes (MWCNT-COOH) and NH₂ functionalized multi-walled carbon nanotubes (MWCNT-NH₂), *J. Phys. Conf. Ser.*, 1025, 012005.
- [35] Cui, H., Yan, X., Monasterio, M., and Xing, F., 2017, Effects of various surfactants on the dispersion of MWCNTs-OH in aqueous solution, *Nanomaterials*, 7 (9), 262.
- [36] Lee, J., Kim, M., Hong, C.K., and Shim, S.E., 2007, Measurement of the dispersion stability of pristine and surface-modified multiwalled carbon nanotubes in various nonpolar and polar solvents, *Meas. Sci. Technol.*, 18 (12), 3707–3712.
- [37] Chen, G., Qiu, J., Liu, Y., Jiang, R., Cai, S., Liu, Y., Zhu, F., Zeng, F., Luan, T., and Ouyang, G., 2015, Carbon nanotubes act as contaminant carriers and translocate within plants, *Sci. Rep.*, 5, 15682.

Adsorption Study of Rhodamine B and Methylene Blue Dyes with ZSM-5 Directly Synthesized from Bangka Kaolin without Organic Template

Ani Iryani^{1,2}, Hadi Nur³, Mardi Santoso², and Djoko Hartanto^{2,*}

¹Department of Chemistry, Faculty of Mathematics and Natural Sciences, Universitas Pakuan, Jl. Pakuan, Tegallega, Bogor 16143, Indonesia

²Department of Chemistry, Faculty of Sciences, Institut Teknologi Sepuluh Nopember, Keputih, Surabaya 60111, Indonesia

³Ibnu Sina Institute for Scientific and Industrial Research, Universiti Teknologi Malaysia, Johor, Malaysia

* Corresponding author:

email: djokohar@its.ac.id

Received: November 27, 2018

Accepted: March 8, 2019

DOI: 10.22146/ijc.41369

Abstract: Rhodamine B (RB) and Methylene Blue (MB) dyes adsorption using adsorbent ZSM-5 synthesized from Bangka kaolin were investigated in this study. The effects of the initial concentration, contact time, and temperature on the adsorption process were also analyzed. The effect of the initial concentration and contact time played an important role in the adsorption process; however, the effect differs significantly in both dyes. The temperature plays little role in the dye adsorption process. The results showed that the adsorption process occurred in ZSM-5 adhere to Langmuir isothermal adsorption model showing that the adsorption process occurred to be monolayer. Based on the kinetics studies, the pseudo-first-order kinetic model represents the adsorption kinetics that occurs for both dyes onto the synthesized ZSM-5. Thermodynamic parameters namely Gibbs free energy (ΔG°), standard entropy changes (ΔS°) and standard enthalpy (ΔH°) reveal that the adsorption process onto ZSM-5 for both dyes was spontaneous and exothermic.

Keywords: Bangka kaolin; dyes; isotherm adsorption; kinetics; thermodynamics; ZSM-5

■ INTRODUCTION

The presence of dye effluent on the environment has become a major world problem due to their damaging effects on aquatic life and ecosystem [1]. Discharge of dye effluent also has a great health threat to all forms of life as a dye is either toxic or mutagenic and also carcinogenic compounds [2]. On water bodies, dye effluent leads the changes in water color, which reduce light penetration and inhibit photosynthesis of aqueous organism and flora. Moreover, the dye is not only highly soluble and stable in water, but also not easily degraded in the aqueous system that makes removal efforts complicated and arduous [3]. Rhodamine B (RB) and Methylene Blue (MB) are two cationic dyes that commonly used as dyes in the textile industry for cotton, leather, and wool coloration. These dyes come from thiazine and xanthate class, respectively, which also used in the cosmetics and pharmaceutical industry [4-5]. RB and MB are known to

be carcinogenic, mutagenic, and poisonous to animal and human life. Also, it is nonbiodegradable and persists into the environment at high concentration [6-7]. Thus, the treatment of colored effluents before discharge as wastewater become a major concern.

Several processes had been developed by experts to solve this problem such as sonochemical degradation [8], photochemistry [9], electrochemistry [10], membrane separation [11], adsorption [12] oxidation or ozonation [13]. From the mentioned methods, the adsorption process has attracted the attention of researchers because of its advantages in terms of flexibility, cost, and simplicity. The adsorption process was proven as an effective method to remove metal ions in water. Interestingly, the adsorption process is also commercially efficient, versatile and feasible to remove textile dyes from wastewater [14].

Several studies have been performed on dyes

adsorption to investigate the factors that affect adsorption performance including isotherm models, kinetics, and thermodynamic studies. Many adsorbents were studied on their performance to remove dyes from wastewater, including bamboo dust, coconut shell, bagasse, and activated carbon [15]. However, the high cost of treatment and activation limit the usage of these adsorbents. This is the reason why researchers have to study the feasibility of using cheap and commercially available materials with large pore-space and special surface property such as clay-based material like MCM-41 and zeolites [16]. Zeolites are a series of microporous aluminosilicate crystal with interconnected pores and channels in size range from 0.3 to 1 nm. Their three-dimensional framework facilitates the adsorption of an organic molecule into its channel [17].

ZSM-5 is a type of zeolite that very potential to be developed as an adsorbent for an organic molecule. This material is usually prepared using an organic template or well known as organic structure-directing agent (OSDA) template to alter the formation of pores in their particles. However, the usage of OSDA templates, for example tetrapropylammonium [18], cetyl trimethylammonium bromide (CTAB) [19], organosilane compounds [14,18] or carboxymethyl cellulose (CMC) [20], during the ZSM-5 synthesis implies the increase in the production costs and air pollution due to thermal decomposition of this OSDA. Moreover, a tedious step must be employed to prepare ZSM-5 from this method [21]. In addition, the ZSM-5 is usually synthesized using fine chemicals such as sodium aluminate (NaAlO_2) as an alumina source and Ludox or TEOS as a silica source. In this works, kaolin Bangka was used as an alumina source. Kaolin is an aluminosilicate clay mineral that consists of alumina and silica with a ratio of 1:1. The relatively high alumina content in kaolin Bangka can reduce the use of expensive and less environmentally-friendly chemicals [22]. Thus, it is expected to reduce the production cost as well as the environmental impact of ZSM-5 synthesis.

The adsorption of RB and MB, indeed, have been reported by several researchers. Damiyine et al. reported the usage of clay to adsorb RB, and the result suggested that the adsorption process preferably at higher pH with

the adsorption capacity of the material reached 89.28 mg/g of RB [23]. Turning to MB, Ngapa et al. reported adsorption of MB using natural zeolite (Mordenite) from Ende [24]. It was found that the modification of natural zeolites could significantly increase the adsorption of MB. The unmodified natural zeolite could only adsorb as much as 16–17 mg/g of MB, and this number increase twofold (reaching 36–37 mg/g) after modification using the hydrothermal process [24]. Vezentsev et al. also reported adsorption of MB using bentonite clay and hydroxyapatite, and it was found that bentonite clay could adsorb MB significantly higher than hydroxyapatite. The adsorption using Bentonite was 175.4 mg/g, 17.8 times higher than hydroxyapatite ones. [25]. Lately, Santosa et al. adsorb MB using peat soil humin. They revealed that this material could adsorb the MB up to 60.77 mg/g. Despite these reports, the adsorption of this dye should still be improved to reach the practical application [26]. In this case, the adsorption process using ZSM-5 synthesized of kaolin Bangka as starting material and without organic template has not been reported yet. The usage of different starting material and different synthesis route compare to conventional ZSM-5 synthesis could lead to the formation of a specific characteristic of the yielded ZSM-5 powders. Therefore, the adsorption of RB and MB dyes on ZSM-5 synthesized using kaolin Bangka and without organic template was investigated in this study to understand the effectiveness of this ZSM-5 and its characteristic in adsorption of both dyes. The characteristics of the ZSM-5 were characterized by Fourier transform infrared spectroscopy (FTIR), X-ray diffraction (XRD), N_2 -sorption (BET and BJH methods), and scanning electron microscopy (SEM). Then, the ability of ZSM-5 as adsorbents to adsorb RB and MB dyes from aqueous media was evaluated.

■ EXPERIMENTAL SECTION

Materials

ZSM-5, in this work, was synthesized from Bangka kaolin without pre-treatment nor without using organic (OSDA) template. The synthesis process was adopted from previous work taking the Si/Al molar ratio of 60

[27]. Two types of dyes materials were used as adsorbate in this experiment which are RB and MB. RB has a chemical formula of $C_{28}H_{31}ClN_2O_3$ and molecular weight of 479.02 g/mol, melting point 210–211 °C and λ_{max} 355 and 543 nm, whereas MB has a chemical formula of $C_{16}H_{18}ClN_3S$ and molecular weight of 319.85 g/mol, a melting point between 100–110 °C and λ_{max} 665 nm.

Procedure

Synthesis procedure

ZSM-5 was synthesized from kaolin directly without the addition of organic (OSDA) template. The synthesis was started by dividing 16.59 g of aqua DI into two parts. Then, 0.8 g of NaOH was dissolved into the first half of the aqua DI followed by addition 0.93 g of kaolin under constant stirring. Subsequently, 22.58 g of Ludox was added to the mixture step by step. The second half of water was added to the mixture to give a final ratio of $10Na_2O:120SiO_2:2Al_2O_3:1800H_2O$. This mixture was then aged at room temperature for 12 h. The silicalite-1 seed was then added to the mixture and continued by constant stirring for 30 min. The mixture was then moved into stainless-steel Teflon autoclave for a hydrothermal process. The hydrothermal process was performed under a closed condition at 448 K for 24 h. The resulted powders were separated by centrifugation (5000 rpm) and washed with aqua DI until reaching neutral pH and were then dried at 373 K for 12 h. This process produced Na-ZSM-5. The resulted powders were calcined at 773 K under air atmosphere. After calcination, 1 g of Na-ZSM-5 was placed into 20 mL ammonium chloride solution 0.6 M. The mixture was then stirred for 1 h. The powders were then filtered and were washed using aqua DI to reach neutral pH (pH = 6–7). The resulted powders were dried and were calcined at 773 K for 6 h. This process resulted in H-ZSM-5 or mentioned as ZSM-5.

Characterization of ZSM-5

The synthesized ZSM-5 was characterized using X-ray diffraction (XRD) by powder technique and with CuK α irradiation ($\lambda = 1.54 \text{ \AA}$) at 2θ range of 5–40°. The textural properties of the sample were characterized by Nitrogen adsorption at 77 K on Micromeritics ASAP 2020 instrument. Prior to sorption measurements, the samples

are placed into the U-shaped tube at 400 °C for 8 h for degassing. The determination of the total surface area was based on the Brunauer–Emmett–Teller (BET) adsorption isotherm model. Meanwhile, the Barrett–Joyner–Halenda (BJH) is used to calculate the pore size distribution and the pore volume. Scanning electron microscopy (SEM) was conducted to examine the particle morphology of the zeolite particles. This analysis was conducted using a Zeiss EVO MA at 20 kV. The infrared Spectroscopy was carried out using Fourier Transform Infrared (FTIR) Shimadzu Spectrum One 8400S to analyze function group of the synthesized material.

Adsorption procedure

Adsorption of RB and MB dyes were conducted by the batch method. The experiment procedure conducted on a container that filled with 50 mL dyes solution (both RB and MB) with variation concentration of 50, 100, 150, 200 and 250 mg/L for each dye. The initial pH of the solution is 7, and the amount of adsorbent (ZSM-5) is 0.05 g. The tube was then stirred at a determined temperature until equilibrium is reached. Upon equilibrium, the solution then filtered through 0.1 μm of membrane filter (Millipore, Japan) and the absorption were measured at maximum absorbance of dyes with UV-Visible Spectrophotometer (Thermo GeneSYS 10S) to determine the residual of dye concentration. The adsorption capacity was calculated by Eq. (1):

$$Q_e = \frac{(C_o - C_e)}{m} \times V \quad (1)$$

where Q_e is the adsorption capacity per unit of adsorbent (mg/g), C_o is the initial dye concentration (mg/L), C_e is the residual dye concentration (mg/L), V is the volume of the solution (L) and m is the weight of the adsorbent (g).

The results of this study were analyzed using the isotherm adsorption model of Langmuir, Freundlich, Temkin, and Dubinin-Radushkevich (DR) [28–29]. Calculation of the isotherm adsorption model is taken from data obtained between contact time 0–180 min. The sample solution was taken every 10 min along contact time and directly analyzed with UV-Visible spectrophotometer. This analysis is carried out with dye

(adsorbate) concentration of 50, 100, 150, 200 and 250 mg/L. The variation temperature applied are 303, 313, and 323 K.

RESULTS AND DISCUSSION

ZSM-5 was successfully synthesized from Bangka kaolin using silicalite-1 seeds and without an organic template. For this synthesis process, the molar ratio of reactants is determined based on the previous study reported by Prasetyoko et al. who synthesized ZSM-5 with a molar ratio of $10\text{Na}_2\text{O}:120\text{SiO}_2:2\text{Al}_2\text{O}_3:1800\text{H}_2\text{O}$ [30]. However, this study uses kaolin Bangka as a source of alumina and silica.

Characterization of ZSM-5

Fig. 1 illustrated the powder XRD diffractogram of Bangka kaolin and synthesized ZSM-5. The comparison of the diffractogram shows that the specific peak of kaolin did not appear in the diffractogram of synthesized ZSM-5. These results point out that kaolin phase was fully transformed into ZSM-5 after synthesis process. The main peaks of Synthesized ZSM-5 at $2\theta = 7.9, 8.9, 23.2,$ and 24.5° are identical with reference of ZSM-5, which mean that pure ZSM-5 was obtained without impurities [30]. High intensity shows that the ZSM-5 was synthesized with good crystallinity.

The FTIR spectra of kaolin and synthesized ZSM-5 can be seen in Fig. 2. The spectra show that there is great difference between Bangka kaolin and Synthesized ZSM-5, which suggest that the kaolin bond was disconnected and transformed into novel ZSM-5 bond by synthesis process. The characteristic peak of ZSM-5 at 1221 and 1102 cm^{-1} represent the asymmetric stretching vibration of TOT bond; peak at 796 cm^{-1} displays symmetric stretching vibration of T-O-T bond; 546 cm^{-1} shows the framework vibration of pentacyclic ring that is characteristic vibration of the MFI-type structure and peak at 450 cm^{-1} is a result of the bending vibration of TOT, where T is Si or Al atoms [31-32].

The SEM micrograph of the synthesized ZSM-5 is presented in Fig. 3. The morphology of ZSM-5 reveals the typical smooth and fine hexagonal structure with a size of about $9.6\text{--}3.3\text{ }\mu\text{m}$. However, there is some part that exhibits irregularly layered and cracked structure with a rectangular

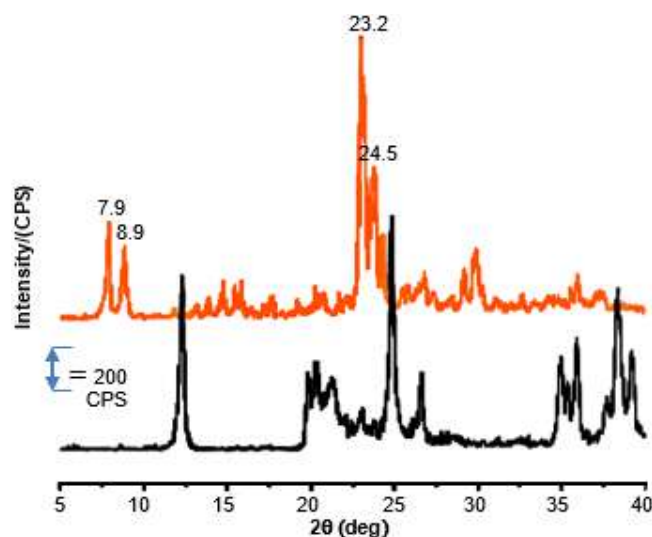


Fig 1. Diffractogram XRD of (a) Bangka kaolin and (b) synthesized ZSM-5

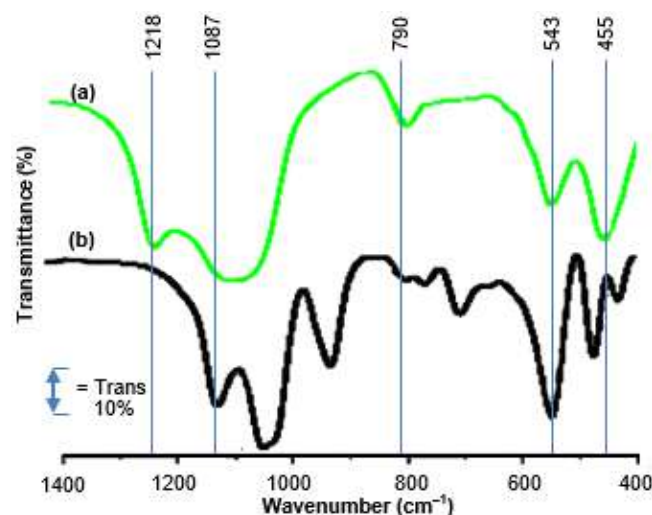


Fig 2. Infrared spectra of (a) Bangka kaolin and (b) synthesized ZSM-5



Fig 3. Micrograph SEM of synthesized ZSM-5

shape in size of about 9.6–3.8 μm .

The textural properties of synthesized ZSM-5 were evaluated by nitrogen physisorption and can be seen in Fig. 4. The N_2 Sorption of ZSM-5 shows the significant increase of adsorption in two steps, as can be seen in the relative pressure (P/P_0) < 0.02 and (P/P_0) > 0.95 . The first increase at (P/P_0) < 0.02 indicates the filling of the micropore exists in the ZSM-5 surface. In contrast, the increase in a higher pressure at (P/P_0) > 0.95 indicates the presence of interparticle void caused by aggregation of primary crystal.

The ZSM-5 also shows the hysteresis loop at $\sim 0.5 < P/P_0 < 0.9$, which indicates the presence of mesopore. The relatively large hysteresis indicates the existence of interconnected open mesopore to the external surface of ZSM-5. This interconnected mesopore could improve the molecular transport due to the reducing of diffusion length to the micropore. The surface area of the sample is found to be about $333 \text{ m}^2/\text{g}$ based on BET calculation. Meanwhile, the pore diameter of ZSM-5 calculated using the BJH method was found to be 5.72 \AA and $24\text{-}26 \text{ \AA}$ [33-34].

Batch adsorption studies of RB and MB in aqueous media was performed to examine the adsorption performance of ZSM-5 from Bangka kaolin. The effect of initial concentration, contact time, and the temperature are explained detail in the following discussion.

Effect of Initial Concentration and Contact Time

The initial concentration of dye and contact time are

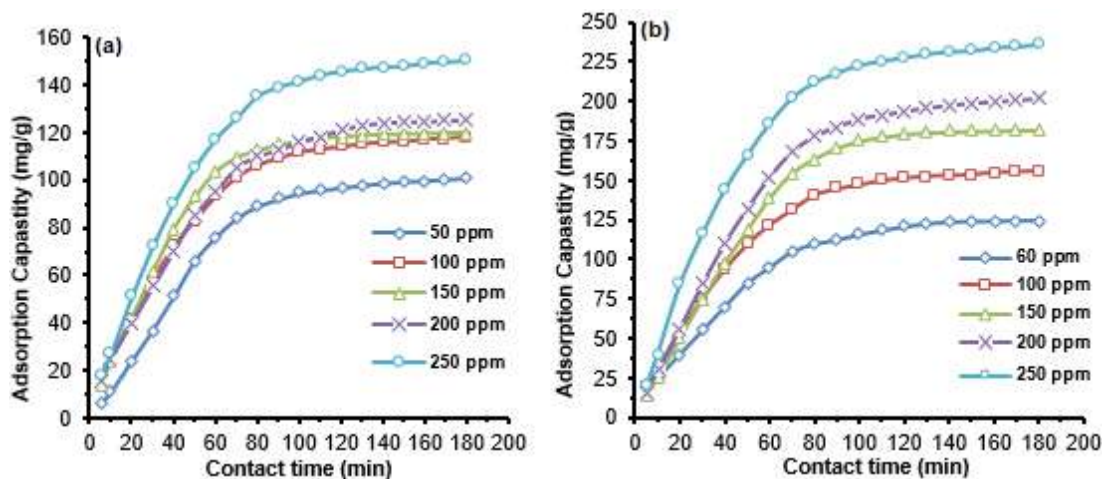


Fig 5. Effect of initial dyes concentration and contact time on adsorption of (a) RB and (b) MB

two important factors influencing the adsorption process, since initial concentration can affect the driving force of dye molecules to overcome limited mass transport between solid-liquid phase boundaries. Contact time also a crucial factor in revealing equilibrium adsorption point of dye molecules [16]. The effect of initial dyes concentration and contact time on the adsorption capacity of RB and MB by ZSM-5 is illustrated in Fig. 5. The curve in Fig. 5 shows that the adsorption capacity of the ZSM-5 synthesized from

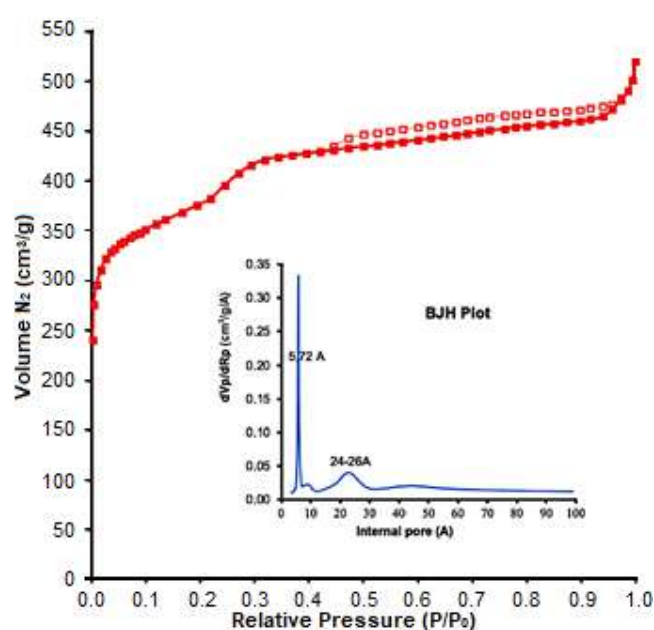


Fig 4. Nitrogen sorption equilibrium at 77 K of Synthesized ZSM-5 from Bangka kaolin adsorption studies

Bangka kaolin increased along with the increase of initial concentrations. This result suggests that the removal of dyes depends on initial dyes concentration [18].

In general, the adsorption capacity of the ZSM-5 rises rapidly in the early time of the adsorption process, and it remains stable above 100 and 80 min of contact time, for both dyes. This phenomenon suggests that the adsorption has reached the equilibrium [14,16,18]. Apparently, the adsorption behavior for both dye solutions of RB and MB is not the same. The adsorption of RB is more irregular than the MB one. This is likely due to adsorption that takes place on the adsorbent ZSM-5 is less moderate on RB adsorbate than MB dye, which appears more regular and systematically. Of course, this is concerned with the structural difference of the 2 dyes, where MB molecule with a dimension of $5.9 \text{ \AA} \times 13.8 \text{ \AA}$ is smaller and straight whereas RB molecule with a dimension of $9.8 \text{ \AA} \times 15.0 \text{ \AA}$ are bulkier and would occupy larger areas [35-36]. This property leads to more irregular adsorption behavior of RB dyes due to similarity pore of ZSM-5 ($24\text{--}26 \text{ \AA}$) with RB molecule dimension.

Temperature Effect

The effect of temperature on the adsorption of RB and MB dyes summarized Fig. 6. Based on those results, both dyes are rapidly adsorbed in the low temperature and decreased with increasing temperature. The increasing temperature can affect kinetics energy of adsorbate, which reduces the interactions between adsorbent-adsorbate. Although there is some difference among both dyes, MB dye is decreased more rapidly than RB. This fact correlated with the molecular size of MB that contributes to this phenomenon.

Adsorption Isotherm

Adsorption isotherm was calculated to understand the adsorption behavior of RB and MB dyes onto ZSM-5 from Bangka kaolin. By this analysis, the interaction between adsorbate and adsorbent could be examined. The analysis is carried out by fitting with four types of isotherm model, i.e., Langmuir, Freundlich, Temkin, and Dubinin-Radushkevich. The Langmuir model assumes that the adsorption occurs on a specified surface of homogeneous adsorbents. This adsorption could only form

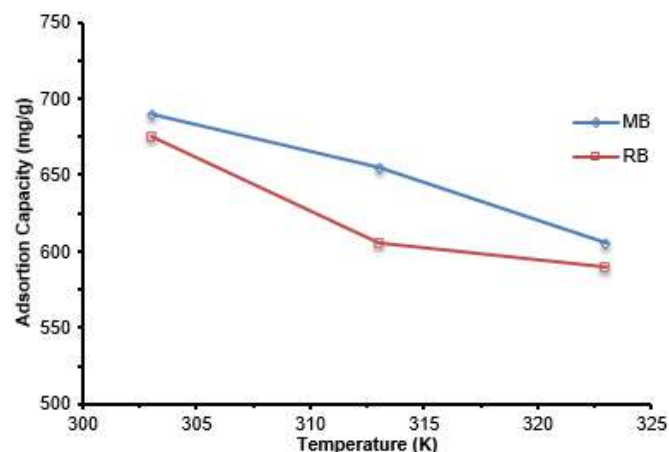


Fig 6. Effect of temperature on adsorption capacity

one layer of adsorbate in the surface of the adsorbent, meaning that each part of the surface in adsorbent could only hold one molecule or atom. This Langmuir model is presented in Eq. (2):

$$\frac{C_e}{q_e} = \frac{1}{q_m b} + \frac{C_e}{q_m} \quad (2)$$

where C_e (mg L^{-1}) is the equilibrium concentration, q_e (mg g^{-1}) is the amount of adsorbed adsorbate per unit mass of adsorbent, and q_m is the adsorption capacity, and b is the rate of adsorption [37-40]. The Freundlich isotherm is used to represent the non-ideal heterogeneous behavior of the adsorption process. This model is presented in Eq. (3):

$$\ln q_e = \ln k_f + \frac{1}{n} \ln C_e \quad (3)$$

where k_f is the Freundlich constant ($\text{mg g}^{-1} (\text{mg L}^{-1})^n$), and $1/n$ is the heterogeneity factor ranged from 0 to 1 which is a characteristic of surface heterogeneity, becoming more homogeneous as its close to unity [37-40].

The Temkin isotherm assumes that the adsorption heat of the adsorbate constantly decreases with adsorbent layer coverage rather than logarithmic due to the interaction of adsorbate and adsorbent. This model is presented in Eq. (4):

$$q_e = B \ln A + B \ln C_e \quad (4)$$

where B is the constant related to the heat of sorption, and A (L mg^{-1}) is the Temkin equilibrium isotherm constant [38-40]. The Dubinin-Radushkevich isotherm model can be used to examine the porosity in relation to

the free energy, E , and the characteristics of the adsorption process. This model is more general than the Langmuir model because it does not assume a homogeneous surface or constant adsorption potential. This isothermal equation is expressed in Eq. (5):

$$\ln q_e = \ln q_{\max} - \beta \varepsilon^2 \quad (5)$$

where q_e and q_{\max} are defined above, b is the activity coefficient related to mean adsorption energy ($\text{mol}^2 \text{kJ}^{-2}$), and e is the Polanyi potential [38-39]. The calculation of all model is compiled in Table 1.

Based on the important parameter mentioned in Table 1, the correlation coefficient (R^2) was used to determine the most suitable model for the adsorption of RB and MB dye onto ZSM-5. The results show that the Langmuir model possesses higher approximation to the value of one rather than the other models. The detailed trend is as follow: Langmuir > Freundlich > Temkin > Dubinin-Radushkevich. This result suggests that the adsorption process of both dyes into adsorbents can be described better using the Langmuir model, which consider the adsorption to be monolayer rather than multi-layer adsorption [16,18]. This Langmuir adsorption is in good accordance with the isothermal adsorption type reported by several researchers. Vezensev et al. [25] reported in his findings that the adsorption of MB in bentonite-like clay and hydroxyapatite also followed the Langmuir model. The more recent findings reported by

Santosa et al. [26] also shows the same result. So did the result reported by Ding et al. [12]. This similarity is quite reasonable since the adsorbent material possessing active functional groups in its surface, such as activated carbon, zeolite material as well as pit soil humin could bind the dye molecules via those functional groups [26].

Another crucial finding based on this calculated provided in Table 1 is the adsorption capacity of the ZSM-5. The Q_m values, which represents the maximum adsorption capacity for RB and MB, are 97.08 and 128.21 mg/g, respectively. This MB adsorption capacity is quite higher than other reported adsorbent materials such as hydroxyapatite with an adsorption capacity of 9.88 mg/g [25], mordenite (37.362 mg/g) [41], but it is lower than bentonite (136.98 mg/g) [25]. Turning to the rhodamine B, the adsorption capacity in this works is higher than mordenite (3.61 mg/g) [23], montmorillonite (42.19 mg/g) [42] and bentonite (98.62 mg/g). However, the adsorption capacity of ZSM-5 in this works is much lower than activated carbon that has adsorption capacity up to 478.50 mg/g [12]. The difference in adsorption capacity is reasonable as the certain parameter in the adsorption process could influence the adsorbent performance. However, in adsorbent with the Langmuir model, it seems that the pore diameter and the functional groups that exist in the surface of the adsorbent play an important role in determining the adsorption capacity [12,26].

Table 1. Parameters of several adsorption isotherm models for the adsorption of RB and MB on ZSM-5

Mathematical Methods	Parameters	RB	MB
Langmuir Isotherm	R^2	0.9962	0.993
	K_L	0.007	0.009
	Q_m (mg/g)	128.21	97.08
Freundlich Isotherm	R^2	0.978	0.949
	K_f	4.6×10^6	13.6×10^4
	N	0.54	0.48
Temkin		0.0033	0.0036
	B (mol/KJ)	-776.02	-788.91
D-R		0.975	0.933
	q_m (mg/g)	161.95	137.15
	B	0.0032	0.0035
	E (KJ/mol)	12.500	11.952
	R^2	0.9228	0.855

Kinetic and Thermodynamic Studies

The kinetics profile of RB and MB dyes adsorption on ZSM-5 adsorbent were conducted by batch method at an initial dye concentration of 50 mg L⁻¹. The procedure of kinetics studies was similar to equilibration experiments with several preset intervals of sampling time. Three different kinetic models were used to investigate the kinetics studies, namely pseudo-first-order, pseudo-second-order, and intraparticle diffusion models [38,43-45]. The results are shown in Table 2. Based on the obtained coefficient of correlation from the adsorption of RB and MB dye onto ZSM-5, the pseudo-first-order model kinetics are more adequate than those obtained from the pseudo-second-order model. It can

also be concluded that adsorption of RB and MB dye onto ZSM-5 has physically occurred because the pseudo-first-order-reaction was driven by one variable that is correlated with our result that the adsorption capacity depends on the concentration of adsorbate. The higher concentration of adsorbate increases the adsorption kinetics. Based on the intra-particle diffusion model, it seems that the intraparticle diffusion is not the rate limiting step as the straight line did not pass through the origin (C value not equal to zero). This implies that other factor also plays a crucial role in adsorption such as film diffusion, adsorption of adsorbate on the interior surface of adsorbents or their combination [12,45]. The plot of the intra-particle kinetics model is shown in Fig. 7.

Table 2. Kinetic and thermodynamic parameters for the adsorption of RB and MB on ZSM-5

Mathematical Methods	Parameters	RB	MB
Pseudo-First-order kinetics	R ²	0.9983	0.9952
	K ₁	0.0309	0.0274
	Q _e (mg/g)	789.66	977.01
Pseudo-Second-order kinetics	R ²	0.9762	0.9364
	K ₂	2.244 × 10 ⁻⁵	7.199 × 10 ⁻⁶
	Q _e (mg/g)	909.09	1250
Intra-particle diffusion	R ²	0.9024	0.9590
	k _{id} (g/mg/min ^{1/2})	58.668	69.085
	C (mg/g)	24.706	101.84
Thermodynamic study	R ²	0.9648	0.8894
	ΔH° (J/mol)	-188.201	-161.414
	ΔS° (J/mol K)	0.5940	0.517
	-ΔG° × 10 ² kJ/mol		
	303K (kJ/mol)	-8.234	4.859
	313K (kJ/mol)	-2.294	-0.307
	323K (kJ/mol)	-3.645	-5.474031754

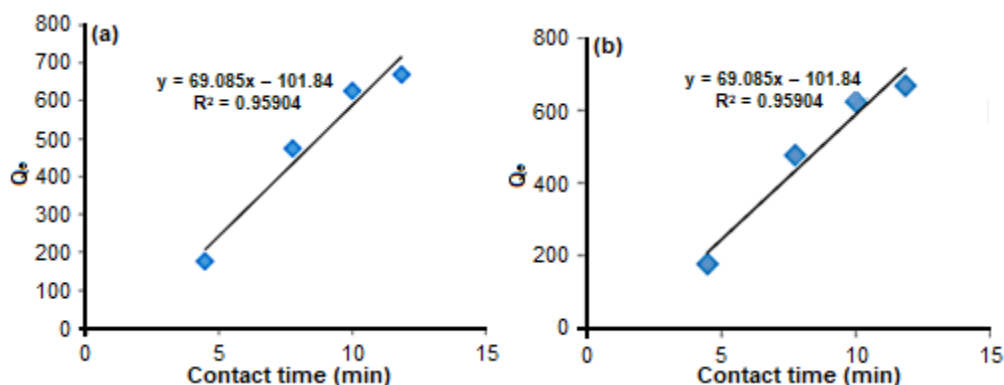


Fig 7. The kinetic plot of intra-particle diffusion model on (a) RB and (b) MB

The effect of temperature in the adsorption process could be studied by analyzing the thermodynamic parameters. These thermodynamic parameters are presented in Table 2. The data shows that the adsorption of RB and MB is an exothermic reaction indicated by the negative value of ΔH° . In the same way, the value of ΔG° is also found as a negative value indicating that this adsorption process could occur spontaneously in nature. This happened in all studied temperatures. However, those values are varied. The higher negative value of ΔG° indicates the energetically preferred process. Also, it seems that the ΔG° decrease in line with the increase of temperature, suggesting that at a higher temperature, the driving force become lessen, thus lowering the adsorption uptake.

■ CONCLUSION

In this paper, the ability of ZSM-5 from Bangka kaolin as an efficient adsorbent for RB and MB removal had been demonstrated. The fitting of the isothermal adsorption model revealed that the adsorption process follows the Langmuir model. The kinetic study revealed that the adsorption of both RB and MB follow the pseudo-first model indicating the intraparticle diffusion is not only the rate-limiting step but also is influenced by another factor such as film diffusion, adsorption of adsorbate on the interior surface of adsorbents. In addition, the thermodynamic studies indicate that all the adsorption process could occur spontaneously and exothermic. These findings confirm that ZSM-5 synthesized from Bangka kaolin could be promising as an adsorbent for RB and MB removal.

■ ACKNOWLEDGMENTS

The authors acknowledge the Ministry of Research, Technology and Higher Education (KEMENRISTEKDIKTI) for financial support for this work through Acceleration of International Publication Program (P3I) grant.

■ REFERENCES

- [1] Rafatullah, M., Sulaiman, O., Hashim, R., and Ahmad, A., 2010, Adsorption of methylene blue on low-cost adsorbents: A review, *J. Hazard. Mater.*, 177 (1-3), 70–80.
- [2] Ip, A.W.M., Barford, J.P., and McKay, G., 2009, Reactive Black dye adsorption/desorption onto different adsorbents: Effect of salt, surface chemistry, pore size and surface area, *J. Colloid Interface Sci.*, 337 (1), 32–38.
- [3] Cardoso, N.F., Pinto, R.B., Lima, E.C., Calvete, T., Amavisca, C.V., Royer, B., Cunha, M.L., Fernandes, T.H.M., and Pinto, I.S., 2011, Removal of remazol black B textile dye from aqueous solution by adsorption, *Desalination*, 269 (1-3), 92–103.
- [4] Gupta, V.K., Suhas, Ali, I., and Saini, V.K., 2004, Removal of rhodamine B, fast green, and methylene blue from wastewater using red mud, an aluminum industry waste, *Ind. Eng. Chem. Res.*, 43 (7), 1740–1747.
- [5] Rochkind, M., Pasternak, S., and Paz, Y., 2014, Using dyes for evaluating photocatalytic properties: a critical review, *Molecules*, 20 (1), 88–110.
- [6] Inyinbor, A.A., Adekola, F.A., and Olatunji, G.A., 2015, Adsorption of Rhodamine B dye from aqueous solution on *Irvingia gabonensis* biomass: Kinetics and thermodynamics studies, *S. Afr. J. Chem.*, 68, 115–125.
- [7] Gillman, P.K., 2011, CNS toxicity involving methylene blue: The exemplar for understanding and predicting drug interactions that precipitate serotonin toxicity, *J. Psychopharmacol.*, 25 (3), 429–436.
- [8] Abbasi, M., and Asl, N.R., 2008, Sonochemical degradation of Basic Blue 41 dye assisted by nanoTiO₂ and H₂O₂, *J. Hazard. Mater.*, 153 (3), 942–947.
- [9] Gupta, V.K., Jain, R., Mittal, A., Mathur, M., and Sikarwar, S., 2007, Photochemical degradation of the hazardous dye Safranin-T using TiO₂ catalyst, *J. Colloid Interface Sci.*, 309 (2), 464–469.
- [10] Fan, L., Zhou, Y., Yang, W., Chen, G., and Yang, F., 2008, Electrochemical degradation of aqueous solution of Amaranth azo dye on ACF under potentiostatic model, *Dyes Pigm.*, 76 (2), 440–446.

- [11] Sachdeva, S., and Kumar, A., 2009, Preparation of nanoporous composite carbon membrane for separation of rhodamine B dye, *J. Membr. Sci.*, 329 (1-2), 2–10.
- [12] Ding, L., Zou, B., Gao, W., Liu, Q., Wang, Z., Guo, Y., Wang, X., and Liu, Y., 2014, Adsorption of Rhodamine-B from aqueous solution using treated rice husk-based activated carbon, *Colloids Surf., A*, 446, 1–7.
- [13] Malik, P., and Saha, S., 2003, Oxidation of direct dyes with hydrogen peroxide using ferrous ion as catalyst, *Sep. Purif. Technol.*, 31 (3), 241–250.
- [14] Brião, G.V., Jahn, S.L., Foletto, E.L., and Dotto, G.L., 2017, Adsorption of crystal violet dye onto a mesoporous ZSM-5 zeolite synthesized using chitin as template, *J. Colloid Interface Sci.*, 508, 313–322.
- [15] Heibati, B., Rodriguez-Couto, S., Amrane, A., Rafatullah, M., Hawari, A., and Al-Ghouti, M.A., 2014, Uptake of Reactive Black 5 by pumice and walnut activated carbon: Chemistry and adsorption mechanisms, *J. Ind. Eng. Chem.*, 20 (5), 2939–2947.
- [16] Hamed, A.K., Dewayanto, N., Du, D., Ab Rahim, M.H., and Nordin, M.R., 2016, Novel modified ZSM-5 as an efficient adsorbent for methylene blue removal, *J. Environ. Chem. Eng.*, 4 (3), 2607–2616.
- [17] Lamia, M., Fatiha, D., Boucekara, B., and Ayada, D., 2016, Adsorption of methyl green onto zeolite ZSM-5(pyrr.) in aqueous solution, *Orient. J. Chem.*, 32 (1), 171–180.
- [18] Nejad-Darzi, S.K.H., Samadi-Maybodi, A., and Ghobakhluo, M., 2013, Synthesis and characterization of modified ZSM-5 nanozeolite and their applications in adsorption of Acridine orange dye from aqueous solution, *J. Porous Mater.*, 20 (4), 909–916.
- [19] Jin, H., Ansari, M.B., Jeong, E.Y., and Park, S.E., 2012, Effect of mesoporosity on selective benzylation of aromatics with benzyl alcohol over mesoporous ZSM-5, *J. Catal.*, 291, 55–62.
- [20] Sabarish, R., and Unnikrishnan, G., 2017, Synthesis, characterization and catalytic activity of hierarchical ZSM-5 templated by carboxymethyl cellulose, *Powder Technol.*, 320, 412–419.
- [21] Yue, Y., Gu, L., Zhou, Y., Liu, H., Yuan, P., Zhu, H., Bai, Z., and Bao, X., 2017, Template-free synthesis and catalytic applications of microporous and hierarchical ZSM-5 zeolites from natural aluminosilicate minerals, *Ind. Eng. Chem. Res.*, 56 (36), 10069–10077.
- [22] Holmes, S.M., Khoo, S.H., and Kovo, A.S., 2011, The direct conversion of impure natural kaolin into pure zeolite catalysts, *Green Chem.*, 13 (5), 1152–1154.
- [23] Damiyine, B., Guenbour, A., and Boussen, R., 2017, Rhodamine B adsorption on natural and modified Moroccan clay with cetyltrimethylammonium bromide: Kinetics, equilibrium and thermodynamics, *J. Mater. Environ. Sci.*, 12 (3), 860–871.
- [24] Ngapa, Y.D., Sugiarti, S., and Abidin, Z., 2018, Hydrothermal transformation of natural zeolite from Ende-NTT and its application as adsorbent of cationic dye, *Indones. J. Chem.*, 16 (2), 138–143.
- [25] Vezentsev, A.I., Thuy, D.M., Goldovskaya-Peristaya, L.F., and Glukhareva, N.A., 2018, Adsorption of methylene blue on the composite sorbent based on bentonite-like clay and hydroxyapatite, *Indones. J. Chem.*, 18 (4), 733–741.
- [26] Santosa, S.J., Kunarti, E.S., Aprilita, N.H., Wulandari, B., and Bawani, D.N., 2019, Sorption mechanism and performance of peat soil humin for methylene blue and *p*-nitrophenol, *Indones. J. Chem.*, 19 (1), 198–210.
- [27] Hartanto, D., Yuan, L.S., Sari, S.M., Sugiarto, D., Murwani, I.K., Ersam, T., Prasetyoko, D., and Nur, H., 2016, Can kaolin function as source of alumina in the synthesis of ZSM-5 without an organic template using a seeding technique?, *Malays. J. Fundam. Appl. Sci.*, 12, 85–90.
- [28] Vijayaraghavan, K., Padmesh, T., Palanivelu, K., and Velan, M., 2006, Biosorption of nickel(II) ions onto *Sargassum wightii*: Application of two-parameter and three-parameter isotherm models, *J. Hazard. Mater.*, 133 (1-3), 304–308.
- [29] Hamdaoui, O., and Naffrechoux, E., 2007, Modeling of adsorption isotherms of phenol and

- chlorophenols onto granular activated carbon Part I. Two-parameter models and equations allowing determination of thermodynamic parameters, *J. Hazard. Mater.*, 147 (1-2), 381–394.
- [30] Prasetyoko, D., Ayunanda, N., Fansuri, H., Hartanto, D., and Ramli, Z., 2012, Phase transformation of rice husk ash in the synthesis of ZSM-5 without organic template, *J. Math. Fundam. Sci.*, 44 (3), 250–262.
- [31] Mohamed, R.M., Fouad, O.A., Ismail, A.A., and Ibrahim, I.A., 2005, Influence of crystallization times on the synthesis of nanosized ZSM-5, *Mater. Lett.*, 59 (27), 3441–3444.
- [32] Armaroli, T., Simon, L.J., Digne, M., Montanari, T., Bevilacqua, M., Valtchev, V., Patarin, J., and Busca, G., 2006, Effects of crystal size and Si/Al ratio on the surface properties of H-ZSM-5 zeolites, *Appl. Catal., A*, 306, 78–84.
- [33] Cychosz, K.A., and Thommes, M., 2018, Progress in the physisorption characterization of nanoporous gas storage materials, *Engineering*, 4 (4), 559–566.
- [34] Wang, T., Lu, X., and Yan, Y., 2010, Synthesis, characterization and crystallization mechanism of SAPOs from natural kaolinite, *Microporous Mesoporous Mater.*, 136 (1-3), 138–147.
- [35] Canning, J., Huyang, G., Ma, M., Beavis, A., Bishop, D., Cook, K., McDonagh, A., Shi, D., Peng, G.D., and Crossley, M., 2014, Percolation diffusion into self-assembled mesoporous silica microfibrils, *Nanomaterials*, 4, 157–174.
- [36] Chen, C., Chen, Y., Lu, Z., Qian, M., Xie, H., and Tay, F.R., 2017, The effects of water on degradation of the zirconia-resin bond, *J. Dent.*, 64, 23–29.
- [37] Eren, Z., and Acar, F.N., 2006, Adsorption of Reactive Black 5 from an aqueous solution: Equilibrium and kinetic studies, *Desalination*, 194 (1-3), 1–10.
- [38] Dada, A.O., Olalekan, A.P., Olatunya, A.M., and Dada, O., 2012, Langmuir, Freundlich, Temkin and Dubinin–Radushkevich isotherms studies of equilibrium sorption of Zn²⁺ onto phosphoric acid modified rice husk, *IOSR J. Appl. Chem.*, 3 (1), 38–45.
- [39] Foo, K.Y., and Hameed, B.H., 2010, Insights into the modeling of adsorption isotherm systems, *Chem. Eng. J.*, 156 (1), 2–10.
- [40] Allen, S.J., Mckay, G., and Porter, J.F., 2004, Adsorption isotherm models for basic dye adsorption by peat in single and binary component systems, *J. Colloid Interface Sci.*, 280 (2), 322–333.
- [41] Esmaili, S., Zanjanchi, M.A., Golmojdeh, H., and Mizani, F., 2018, Increasing the adsorption capability of mordenite and Y zeolites via post-synthesis chemical/physical treatments in order to remove cationic dyes from polluted water, *Water Environ. J.*, 0, 1–18.
- [42] Selvam, P.P., Preethi, S., Basakaralingam, P., Thinakaran, N., Sivasamy, A., and Sivanesan, S., 2008, Removal of rhodamine B from aqueous solution by adsorption onto sodium montmorillonite, *J. Hazard. Mater.*, 155 (1-2), 39–44.
- [43] Largitte, L., and Pasquier, R., 2016, A review of the kinetics adsorption models and their application to the adsorption of lead by an activated carbon, *Chem. Eng. Res. Des.*, 109, 495–504.
- [44] Ip, A.W.M., Barford, J.P., and McKay, G., 2010, A comparative study on the kinetics and mechanisms of removal of Reactive Black 5 by adsorption onto activated carbons and bone char, *Chem. Eng. J.*, 157 (2-3), 434–442.
- [45] Qiu, H., Lv, L., Pan, B., Zhang, Q., Zhang, W., and Zhang, Q., 2009, Critical review in adsorption kinetic models, *J. Zhejiang Univ. Sci. A*, 10 (5), 716–724.

Multivariate Statistical Analysis Applied to Water Quality of a Tropical Coastal Lagoon, Cartagena, Colombian Caribbean

Ildefonso Baldiris-Navarro¹, Juan Carlos Acosta-Jimenez², Ángel Darío González-Delgado^{3,*}, Álvaro Realpe-Jiménez³, and Juan Gabriel Fajardo-Cuadro⁴

¹SENA CINAFLUP– Cartagena, Cr. A Mamonal #15, Cartagena de Indias, Colombia

²Fundacion Universitaria Tecnológico Comfenalco, Cra. 44 #30a-91, 130015, Cartagena de Indias, Colombia

³University of Cartagena, Avenida del Consulado, Cll. 30 # 48-152, 130015, Cartagena de Indias, Colombia

⁴Universidad Tecnológica de Bolívar, Cra.21 #25-92 Manga, 130001, Cartagena de Indias, Colombia

* **Corresponding author:**

tel: +57-3164942938

email: agonzalezd1@unicartagena.edu.co

Received: January 26, 2019

Accepted: July 1, 2019

DOI: 10.22146/ijc.43035

Abstract: Coastal lagoons are one of the most threatened ecosystems in the world, because of population growth, habitat destruction, pollution, wastewater, overexploitation and invasive species which are the main causes of their degradation. The objective of this paper was to evaluate the water quality behavior in a stressed coastal lagoon in Cartagena, Colombian Caribbean. Environmental data was analyzed using hypothesis testing, confidence intervals, and also Principal components analysis (PCA). The study was focused on water parameters such as dissolved oxygen (DO), biochemical oxygen demand (BOD₅), chemical oxygen demand (COD), salinity, pH, total dissolved solids, total coliforms (TC), Fecal coliforms (FC), ammonium (NH₄⁺) and total phosphorus (TP). The analysis was conducted in line with the Colombian national water standard. Results showed that BOD₅, COD, phosphorus, and coliforms are out of the limits permitted for these variables in Colombia and are reaching levels that may be a threat to human health. Principal components analysis detected five components that explained 79.4% of the variance of data and showed that anthropogenic and temporal factors might be affecting the variation of the parameters.

Keywords: coastal lagoon; water quality; statistics; multivariable analysis; Colombia

■ INTRODUCTION

Worldwide, coastal areas are densely populated ecosystems of high ecological, economic, and social importance. Coastal lagoons, in particular, play an important role as productive ecosystems, species-rich habitats, and areas for storm protection and tourism. The main services provided by coastal systems include food provisioning (mainly fish and shellfish), freshwater storage, hydrological balance, climate regulation, flood protection, water purification, oxygen production, fertility, recreation, and ecotourism [1-2]. Nowadays, coastal lagoons are one of the most threatened ecosystems in the world, because of population growth, habitat destruction, pollution, wastewater, overexploitation and invasive species which are the main causes of their degradation [3].

Coastal lagoons are particular ecosystems where many interests may conflict, from fisheries to tourism, and from aquaculture to harbor facilities or urban development. In developing countries, water-related tourism is an increasing source of incomes. Clean water contributes to the recreation and tourism industry; that is why quality water availability is often considered the main limiting factor for developing tourism [4]. In the touristic city of Cartagena, which is visited by millions of tourists every year, there is an inner water body named Cabrero lagoon, which is highly impacted by subnormal population growth and other human activities. People living near the lagoon are extremely poor, and they found a place to live in the shores of it. This unauthorized urbanization of the lagoon has been

bringing untreated wastewater that is discharged without any treatment directly into the lagoon. Solid wastes and fecal matter are also a problem for the ecosystem because people throw them into the water, leading to serious issues on lagoon health [5].

Descriptive statistics (mean, SD, among others) and some graphical tools may give a simple assessment of water behavior. Inferential statistics have tools like hypothesis testing and confidence intervals that may help to assess the performance of a water body in a period [6]. The problem of evaluating water quality becomes more and more complicated as we increase the number of measured variables; then the use of both multivariate techniques and data reduction are almost mandatory to achieve satisfactory results. Multivariate analysis techniques such as principal components analysis (PCA) may be used to analyze large databases without losing valuable information [7] and allow monitoring of all the variables and their relations simultaneously. PCA techniques have been widely used to evaluate water quality, identify the latent sources that influence surface water, and offer a valuable tool for reliable management of water resources as well as effective solutions to pollution in the last decade [6,8].

Mitra et al. assessed the water quality in Hooghly River Estuary, India, using PCA and cluster analysis [9]. Taoufik et al. studied the variation of water quality in the River Wadi El Bey for two years using PCA and cluster analysis [10]. Hajigholizadeh and Melesse [11] used cluster analysis and discriminant analysis to study southern Florida water quality, analyzing a 15-year database and over 35,000 observations to assess the state of water pollution and its time-space variation. Tosic et al. [12] used basic descriptive statistics to explain the temporal variation of water quality and sediments in the Bay of Cartagena. Yoon et al. [13] studied the temporal and spatial variation in Chilika lagoon using PCA and data collected from 1999 to 2009. Jung et al. [14] analyzed the behavior of water quality in the Nakdong River basin by principal component analysis and cluster analysis. Through principal component analysis and cluster analysis, Jiang et al. [15] studied the distribution of arsenic and other compounds in groundwater in Mongolia.

Marinovic and Ruzdjak [16] by PCA and CA analyses determined a baseline of water quality of the Sava River in Croatia after the war in this country.

The aim of this research was to analyze the temporal variability and the fulfillment of the Colombian environmental law of marine water quality in Cabrero lagoon using a data set of 9 years (2008–2017) which contains parameters such as: pH, salinity, dissolved oxygen (DO), total suspended solids (TSS), total coliform (TC), fecal coliforms (FC), total phosphorus (TP), ammonium (NH_4^+), biochemical oxygen demand (BOD5) and chemical oxygen demand (COD), in order to provide better tools for the environmental management of this marine resource.

■ EXPERIMENTAL SECTION

Study Area

Cabrero lagoon located at coordinates $10^\circ 25' 52.8''$ N $75^\circ 32' 27''$ W, has an approximate length of 1.38 km, a water area of about 26 hectares and an average depth of 2.3 m. This Cartagena's inner lagoon is connected to different highly polluted water bodies through channels, which are also connected to the Caribbean Sea. In this lagoon, the mangrove ecosystem is constituted by *Rhizophora mangle* L., *Avicennia germinans* L., *Laguncularia racemosa* L., and *Conocarpus erectus*. The study area is characterized by exhibiting two climatic periods; one of rainfall between April and November, and the other period is dry and goes from December to April [17].

Analytical Procedures

In situ studied parameters were dissolved oxygen (SM 4500-O G), pH (SM 4500-H+) and salinity (SM-2520-B), measures were done with the help of a portable water analysis kit (multi-parameter - Hach 5465011 SensIon). Parameters of biological oxygen demand was performed by Winkler method (SM 4500-O G), chemical oxygen demand (COD) by closed reflux, and total phosphorus by ascorbic method (SM 4500-P B, E). In addition, ammonium (SM 4500-NH3 B, C), total coliforms (SM 9222B), fecal coliforms and total suspended solids (SM 2540D) were analyzed in the

laboratory following the standard methods for water and wastewater analysis. Data were then compared to the threshold values of the water quality law (decree 1594-1984) adopted by the government of Colombia [18-19].

Data Analysis

In order to evaluate the compliance of the Colombian environmental law in Cabrero lagoon, confidences intervals, and hypothesis testing were conducted toward the physicochemical and microbiological data gathered from 2000 to 2017. Non-parametric Wilcoxon signed-rank test was used to detect possible differences between the medians of water quality variables during dry and rainy periods. Principal components analysis was applied to obtain composite variables, which was expected to identify factors affecting water quality and latent pollution sources.

Hypothesis testing and confidence interval

A statistical hypothesis is a statement about the parameters of one or more populations; it involves measuring the strength of evidence provided by sample data. In particular, hypothesis testing involves formulating opposing statements- the null and alternative hypothesis- about the population parameter of interest. The goal of hypothesis testing is to decide whether or not to support the original claim, based on whether we reject the null hypothesis. To do so, a sample statistic is measured or observed, and a decision is made to reject or fail to reject the null Hypothesis based on the extremity of the sample statistic. This decision is based on the probability, called the *p*-value, of observing the sample statistic, under the assumption that the null hypothesis is true. If the *p*-value is smaller than 0.05, then we reject the null hypothesis. Hypothesis testing is an effective tool to compare the mean of a population to a specified value. In this research hypothesis testing will be used to evaluate the accomplishment of the Colombian water law (see Table 1).

A confidence interval gives an estimated range of values which is likely to include an unknown population parameter. The estimated range is calculated from a given set of sample data. The interval has an associated confidence level that quantifies the level of confidence that the parameter lies in the interval [20-21].

Wilcoxon signed-rank test

Wilcoxon signed-rank test is a nonparametric test procedure used for the analysis of matched-pair data or the one-sample problem. For a matched-pair setting, this procedure is used to evaluate the hypothesis that the probability distribution of the first sample is equal to the probability distribution of the second sample [22]. In this research, such a test will be used to compare the two different weather seasons (Dry-Wet) during the monitoring program (see Table 2).

Principal component analysis

The principal component analysis is a multivariate analysis technique that can be used to find new variables represented by a linear combination of variables having correlations via the variance-covariance matrix of several multivariate variables. The principal components (PC) are orthogonal variables obtained by multiplying the original correlated variables with the eigenvector. Principal components may be written as:

$$z_{ij} = a_{i1}x_{1j} + a_{i2}x_{2j} + \dots + a_{im}x_{mj}$$

where *z* is the component score, *a* is the component loading, *x* is the variable value, *i* is the component number, *j* is the sample number and *m* is the total number of variables. Based on the loading coefficient and correlation

Table 1. Hypothesis testing for Colombian water law

Null Hypothesis	Alternative Hypothesis
$H_0 : \mu_{DO} \leq 4$	$H_1 : \mu_{DO} > 4$
$H_0 : \mu_{BOD_5} \geq 3$	$H_1 : \mu_{BOD_5} < 3$
$H_0 : \mu_{COD} \geq 1000$	$H_1 : \mu_{COD} < 1000$
$H_0 : \mu_{NH_4^+} \geq 1$	$H_1 : \mu_{NH_4^+} < 1$
$H_0 : \mu_{TP} \geq 0.003$	$H_1 : \mu_{TP} < 0.003$
$H_0 : \mu_{TSS} \geq 90$	$H_1 : \mu_{TSS} < 90$
$H_0 : \mu_{pH} \leq 6.5$	$H_1 : \mu_{pH} > 6.5$
$H_0 : \mu_{TC} \geq 5000$	$H_1 : \mu_{TC} < 5000$
$H_0 : \mu_{FC} \geq 1000$	$H_1 : \mu_{FC} < 1000$
$H_0 : \mu_{Sal} \leq 33$	$H_1 : \mu_{Sal} > 33$

Table 2. Hypothesis testing for dry-wet season comparison

Null Hypothesis	Alternative Hypothesis
$H_0 : \theta_{Dry} = \theta_{Wet}$	$H_1 : \theta_{Dry} \neq \theta_{wet}$

value with the PC. It explains most of the total variations with some important principal components. The new axes lie along the directions of maximum variance. PCA provides an objective way of finding indices of this type so that the variation in the data might be accounted for as concisely as possible [23-24].

■ RESULTS AND DISCUSSION

Statistical Resume

A summary of the mean value and standard deviation of 10 measured variables in the lagoon water samples and the recommended value allowed by Colombian law for secondary contact is provided in Table 3.

Hypothesis tests showed that the oxygen values were above 5.70 mg/L, which complies to the Colombian law with a confidence interval of 5.70–6.50 mg/L. OD may present high values, probably due to the presence of algae in the water, which during the photosynthesis process, consume carbon dioxide and produce oxygen. For BOD5 there was not enough information to conclude that the mean was lower than 3, in fact, 90% of the time the value of this parameter was between [4.47–5.62 mg/L] which means that wastewater and solid wastes are deteriorating the quality of water in terms of organic material in the lagoon water [25]. The values for COD are high with values above the norm; this is possible due to the addition of chlorine from the sea because the lagoon is connected to it through different channels and also probably due to the chemicals coming from solid waste and anthropogenic activities like car wash services near the zone. Ammonium

showed a confidence interval of 0.39–0.57 mg/L complying with environmental law. With a confidence of 90%, the mean value for phosphorus was in the range 0.16–0.21 mg/L. This parameter is out of the acceptable interval; this level indicates that water is near eutrophication which may be a threat for any species living in this habitat and may cause a bloom of different algae [26-27]. This is possible maybe due to the poor disposal of wastewater, water with soup or other kind of chemicals. Total suspended solid showed improvements because in the first years of the monitoring, the values were out of range, but lately, they became under control. In addition, pH showed good behavior with a confidence interval of 7.79–7.92, which complies with the law limits. Total and fecal coliforms are totally out of control in the Cabrero lagoon; this is evident due to the high number of outliers presented in the data above the threshold for this parameter. Total coliforms presented a confidence interval of 5509–29288 MPV, and fecal coliforms 1975.8–22648 MPV. These values represent a real threat for flora and fauna and the community around this lagoon, and the local government should take measures immediately in order to low these levels. Salinity varied from 26.1 to 27.5 possibly due to the entrance of freshwater from the communities around the lagoon. Results are depicted in Fig. 1.

Temporal Variation in Water Quality

Non-parametric Wilcoxon signed-rank test was performed in order to assess differences in the behavior

Table 3. Summary of descriptive statistics for water quality in Cabrero lagoon

Parameter	Mean	SD	Min	Max	Guide level*
DO	6.11	1.82	1.02	9.04	> 4
BOD5	5.10	5.62	1	13.58	< 3
COD	1014	379.5	261	2019	< 1000
NH ₄ ⁺	0.49	0.42	0.07	1.65	< 1
TP	0.19	0.12	0.02	0.92	< 0.003
TSS	48.82	54.53	7	289	< 90
pH	7.85	0.304	7.17	8.64	6.5–8.5
TC (mpv)	17398	54633	1.8	33× 10 ⁴	< 5000
FC (mpv)	12312	47496	1.8	33× 10 ⁴	< 1000
Sal (%o)	27.79	7.81	9.2	37.3	33–36

*Levels according to Colombian water law

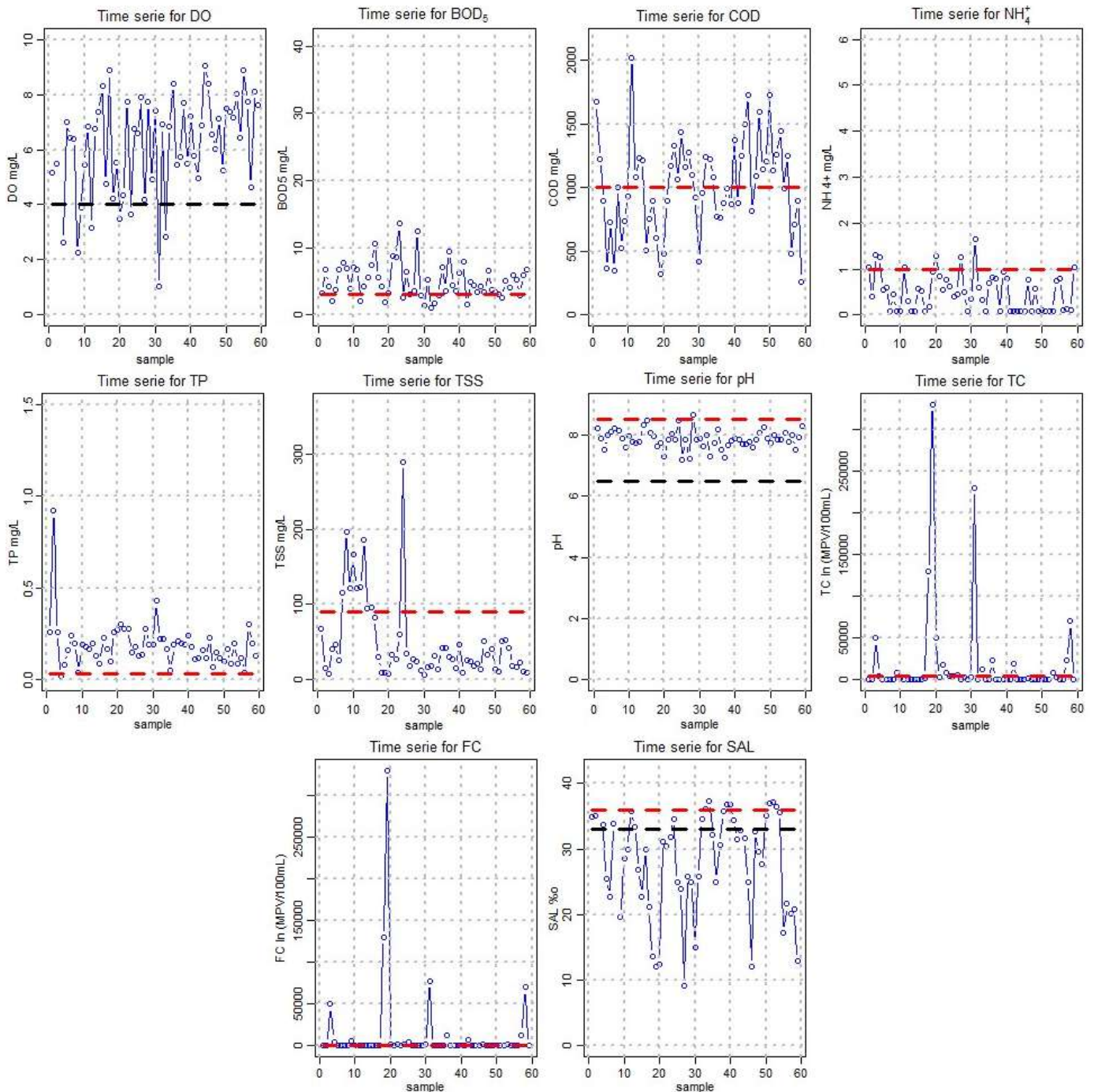


Fig 1. Time series for water quality parameters in Cabrera lagoon

of water quality in the dry and rainy season. As shown in Fig. 2, dissolved oxygen values were higher during the rainy season probably caused by the addition of freshwater. BOD5 presented a wider range during the dry season, possibly caused by the dilution of organic matter in the rainy season.

Values were above the threshold values during both seasons. COD presented no statistical difference between the dry and rainy season. Ammonium parameter was affected by the season ($p < 0.05$). During dry season the values were higher and exceeding the limits according to Colombian laws. Total phosphorus

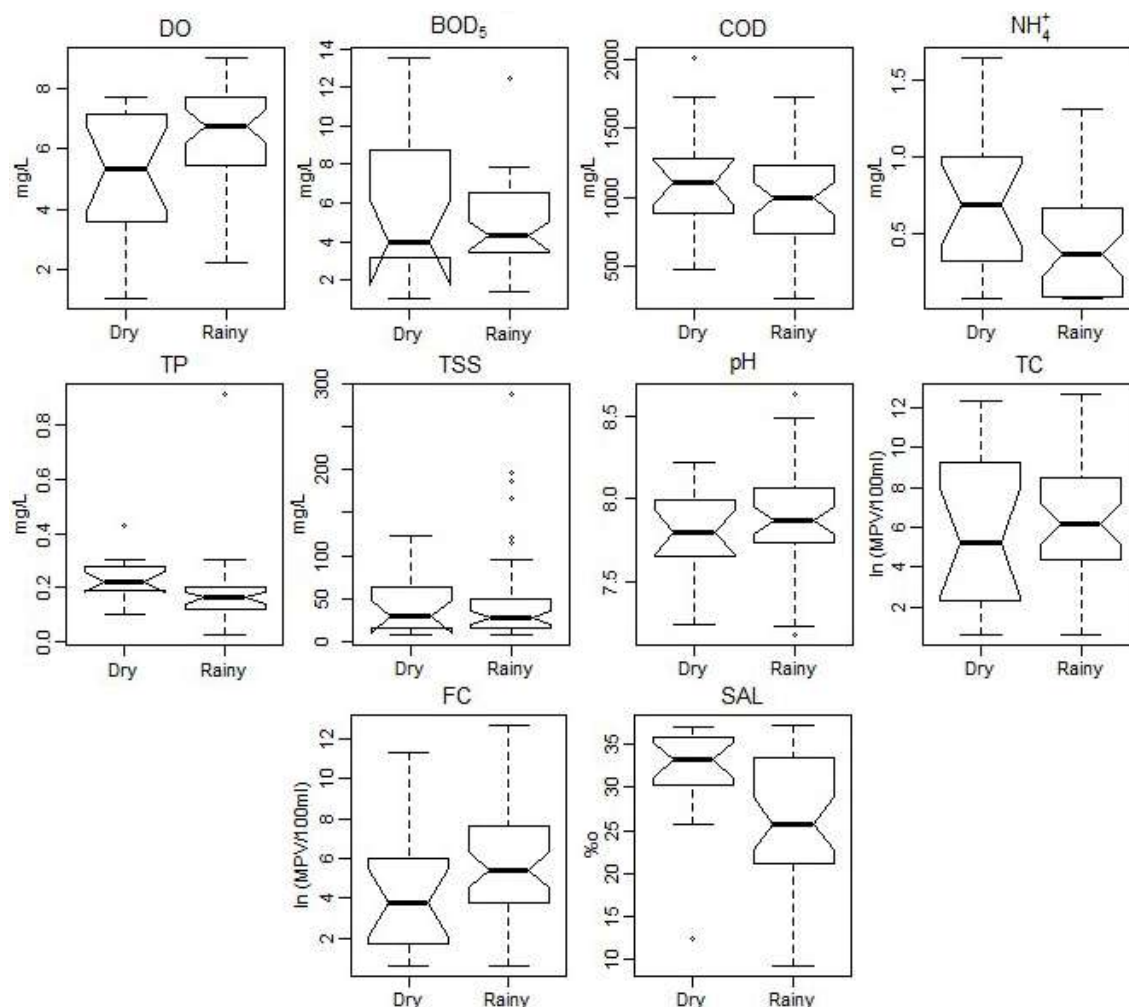


Fig 2. Temporal variation of water quality parameters

also presented statistical differences depending on the season ($p < 0.05$). In both seasons, values were outside of the allowed limits, especially during the dry season where the values were higher than in the rainy season.

Correlation between the seasons and suspended solids may also be explained in terms of the increased quantity of eroded material and urban run-off expected while raining; this is the reason for multiple outliers in the data. Comparing seasonal behavior for total coliforms, there is no significant difference between the seasons, but the values in both seasons are outside of the Colombian law limits. For fecal coliform, results showed that during the rainy season, values were higher, however there was no significant differences between the seasons. The non-significant correlation of total and fecal coliforms with seasons indicates the contribution of anthropogenic

sources in the catchment areas. Salinity, as expected, presented a statistical difference between the dry and rainy season, which is caused by the entrance of freshwater during the rainy season. According to Fig. 2, levels of contaminants are out of limits no matter the season. The values reached by these parameters suggest the need for alternatives to reduce contaminants in aquatic ecosystems. It is also important to educate communities nearby the lagoon about the environmental impacts of throwing garbage and developing social projects around ecotourism activities.

Principal Components Analysis

The purpose of this analysis is to obtain a reduced number of linear combinations of the 10 variables that explain 79.4% of the total variance in the data set. In this

Table 4. Loadings of experimental variables on significant components for all lagoon water samples

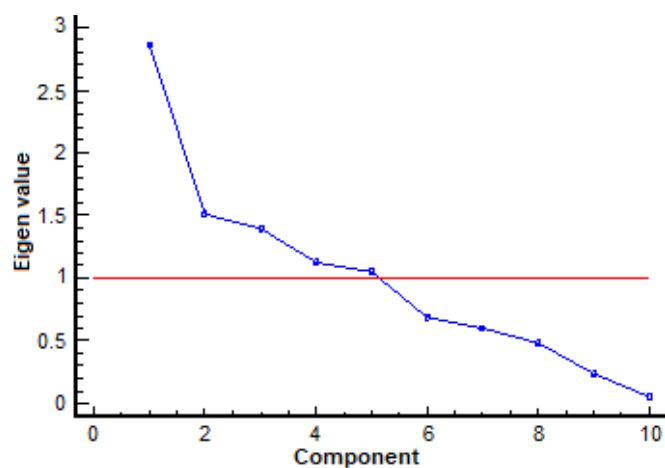
Parameters	PC1	PC2	PC3	PC4	PC5
DO (mg/L)	0.289	-0.479	0.032	-0.468	0.147
BOD ₅ (mg/L)	0.116	0.167	0.631	-0.289	-0.135
COD (mg/L)	0.296	0.340	-0.302	-0.251	0.421
NH ₄ ⁺ (mg/L)	-0.299	0.281	0.268	0.101	-0.320
TP (mg/L)	-0.126	0.538	0.210	-0.388	0.126
TSS (mg/L)	0.194	0.096	0.250	0.676	0.332
pH	0.236	-0.271	0.561	0.029	0.289
TC (MPV)	-0.517	-0.024	0.036	-0.062	0.297
FC (MPV)	-0.481	-0.149	0.021	-0.079	0.371
Sal (g/kg)	0.340	0.387	-0.113	0.049	0.492

case, 5 components were extracted since 5 components had eigenvalues greater than or equal to 1.0.

An eigenvalue gives a measure of the significance of the factor; the factors with the highest eigenvalue are the most significant. The scree plot (see Fig. 3) was used to identify the number of Principal Components graphically.

The loading of five retained components is presented in Table 4. PC1 explains 28.56% of the variance and is highly contributed to the microbiological variables (total and fecal coliforms), this fecal factor represents the bacteriological pollution, essentially, originated from the domestic waste and poor disposal of human excrement. PC2 explains 15.15% of the variance and includes DO and TP. This factor mainly indicate the point sources of pollution by nutrients from domestic sewage. PC3 (13.89% of variance) is positively contributed by BOD and pH; it represents the variability of chemical and biological sources of discharge. PC4 (11.3% of variance) is positively contributed by TSS, and negatively by DO; it represents pollution generated by eroded material and urban run-off. Finally, PC5, which explains 10.46% of the variance is positively contributed by COD and salinity and indicates the variability of different natural and anthropogenic ions entering the lagoon.

With these results (see Table 4) and in order to use Cabrero lagoon as an ecotourist attraction for its natural beauty, local authorities should carry out pollution prevention strategies focus on the reduction or elimination of waste from the source. This effort should involve the community living around the channel. Prevention is widely regarded as the most effective way to protect the environment.

**Fig 3.** Scree plot for Principal Components Analysis in Cabrero lagoon

CONCLUSION

In this study, surface water quality data for 10 parameters collected from 2008 to 2017 were analyzed using inferential statistics and multivariable statistical techniques. Most of the studied parameters presented many outliers which produced a non-normal distribution of data. Due to the high amount of data, hypothesis testing could be performed without any normalization technique. Microbiological and biochemical parameters were above the threshold values and reached dangerous levels. According to analysis results, Cabrero lagoon is presenting eutrophication problems in the dry and rainy season that may be caused by wastewater. The eutrophication leads to the high concentration of oxygen in the water due to the presence of algae that consume CO₂, nitrogen and phosphorus during daylight in order to perform the

photosynthesis process. The principal component analysis determined a reduced number of components that explained over 79% of the data set variance. Components obtained from PCA indicate that the parameters responsible for water quality variations are mainly related to anthropogenic and seasonal factors. Finally, this analysis showed the usefulness of inferential and multivariate statistical techniques serving as an exceptional exploratory tool in analysis and interpretation of complex data set on water quality, identification of pollution sources/factors and understanding temporal variations in water quality for effective management of the lagoon water quality.

■ ACKNOWLEDGMENTS

The authors would like to thank Fundacion Universitaria Tecnológico Comfenalco, University of Cartagena and SENA for financially supporting this research.

■ REFERENCES

- [1] Newton, A., Brito, A.C., Icely J.D., Derolez V., Clara, I., Angus, S., Schernewski, G., Inácio, M., Lillebø, A.I., Sousa, A.I., Béjaoui, B., Solidoro, C., Tosic, M., Cañedo-Argüelles, M., Yamamuro, M., Reizopoulou, S., Tseng, H.C., Canu, D., Roselli, L., Maanan, M., Cristina, S., Ruiz-Fernández, A.C., de Lima, R.F., Kjerfve, B., Rubio-Cisneros, N., Pérez-Ruzafa, A., Marcos, C., Pastres, R., Pranovi, F., Snoussi, M., Turpie, J., Tuchkovenko, Y., Dyack, B., Brookes, J., Povilanskas, R., and Khokhlov, V., 2018, Assessing, quantifying and valuing the ecosystem services of coastal lagoons, *J. Nat. Conserv.*, 44, 50–65.
- [2] Alves, J.P.H., Fonseca, L.C., Chielle, R.S.A., and Macedo, L.C.B, 2018, Monitoring water quality of the Sergipe River basin: An evaluation using multivariate data analysis, *Rev. Bras. Recur. Hídricos.*, 23, e27.
- [3] Anteneh, Y., Zeleke, G., and Gebremariam, E., 2018, Assessment of surface water quality in Legedadie and Dire catchments, Central Ethiopia, using multivariate statistical analysis, *Acta Ecol. Sin.*, 38 (2), 81–95.
- [4] Pérez-Ruzafa, A., Marcos, C., and Pérez-Ruzafa, I.M., 2011, Mediterranean coastal lagoons in an ecosystem and aquatic resources management context, *Phys. Chem. Earth*, 36 (5-6), 160–166.
- [5] Alvarez-Vázquez, A., and Olivella-Beltran, R., 2018, Hydraulic simulation of water bodies between the Cabrero's lagoon and the gates of Chambacú of the city of Cartagena - Colombia, *Thesis*, University of Cartagena, Colombia.
- [6] Baldiris-Navarro, I., Sanchez-Aponte, J., Gonzalez-Delgado, A., Acosta-Jiménez, J.C., and Jiménez, A.R., 2018, Multivariable statistical evaluation of water quality in Juan Polo coastal lagoon (Colombian Caribbean), *Contemp. Eng. Sci.*, 11 (27), 1339–1348.
- [7] Azhar, S.C., Aris, A.Z., Yusoff, M.K., Ramli, M.F., and Juahir, H., 2015, Classification of river water quality using multivariate analysis, *Procedia Environ. Sci.*, 30, 79–84.
- [8] Alberto, W.D., del Pilar, D.M., Valeria, A.M., Fabiana, P.S., Cecilia, H.A., and de los Ángeles, B.M., 2001, Pattern recognition techniques for the evaluation of spatial and temporal variations in water quality. A case study: Suquia River Basin (Córdoba-Argentina), *Water Res.*, 35 (12), 2881–2894.
- [9] Mitra, S., Ghosh, S., Satpathy, K.K., Bhattacharya, B.D., Sarkar, S.K., Mishra, P., and Raja, P., 2018, Water quality assessment of the ecologically stressed Hooghly River Estuary, India: A multivariate approach, *Mar. Pollut. Bull.*, 126, 592–599.
- [10] Taoufik, G., Khouni, I., and Ghrabi, A., 2017, Assessment of physico-chemical and microbiological surface water quality using multivariate statistical techniques: A case study of the Wadi El-Bey River, Tunisia, *Arabian J. Geosci.*, 10, 181.
- [11] Hajigholizadeh, M., and Melesse, A.M., 2017, Assortment and spatiotemporal analysis of surface water quality using cluster and discriminant analyses, *Catena*, 151, 247–258.
- [12] Tosic, M., Restrepo, J.D., Lonin, S., Izquierdo, A., and Martins, F., 2019, Water and sediment quality in Cartagena Bay, Colombia: Seasonal variability and potential impacts of pollution, *Estuarine Coastal Shelf Sci.*, 216, 187–203.
- [13] Yoon, J.Y., Bhatta, K., Rastogi, G., Muduli, P.R., Do, Y., Kim, D.K., Pattnaik, A.K., and Joo, G.J., 2016, Application of multivariate analysis to determine spatial and temporal changes in water quality after

- new channel construction in the Chilika Lagoon, *Ecol. Eng.*, 90, 314–319.
- [14] Jung, K.Y., Lee, K.L., Im, T.H., Lee, I.J., Kim, S., Han, K.Y., and Ahn, J.M., 2016, Evaluation of water quality for the Nakdong River watershed using multivariate analysis, *Environ. Technol. Innovation*, 5, 67–82.
- [15] Jiang, Y., Guo, H., Jia, Y., Cao, Y., and Hu, C., 2015, Principal component analysis and hierarchical cluster analyses of arsenic groundwater geochemistry in the Hetao basin, Inner Mongolia, *Geochemistry*, 75 (2), 197–205.
- [16] Ruždjak, A.M., and Ruždjak, D., 2015, Evaluation of river water quality variations using multivariate statistical techniques: Sava River (Croatia): A case study, *Environ. Monit. Assess.*, 187, 215.
- [17] DIMAR, 2017, *Weather conditions in Cartagena de Indias*, Centro de Investigaciones Oceanograficas e Hidrograficas, <https://www.cioh.org.co/meteorologia/Climatologia/Climatologia%20Cartagena.pdf>, accessed on 10 January 2019.
- [18] Baird, R., Eaton, A.D., and Rice, E.W., 2017, *Standard Methods for the Examination of Water and Wastewater*, 23rd Ed., American Public Health Association, American Water Works Association, Water Environment Federation.
- [19] Acosta, J.C., Baldiris, I., and Pacheco, H.P., 2015, Análisis de la variación en la calidad del agua en la bahía de Barbacoas-Cartagena durante el periodo 2001–2014, *Rev. Ingeniería Innovación*, 3 (1), 7–17.
- [20] Montgomery, D.C., Runger, G.C., and Hubele, N.F., 2010, *Engineering Statistics*, 5th Ed., John Wiley & Sons, New York.
- [21] Navarro, I.B., and Aponte, J.H.S., 2017, Application of multivariate statistical methods to water quality assessment in Arroyo Plata, Colombian Caribbean, *Teknos Revista Científica*, 17, 11–21.
- [22] Woolson, R.F., 2008, “Wilcoxon signed-rank test” in *Wiley Encyclopedia of Clinical Trials*, Eds. D’Agostino, R.B., Sullivan, L., and Massaro, J., John Wiley & Sons, 1–3.
- [23] Razmkhah, H., Abrishamchi, A., and Torkian, A., 2010, Evaluation of spatial and temporal variation in water quality by pattern recognition techniques: A case study on Jajrood River (Tehran, Iran), *J. Environ. Manage.*, 91 (4), 852–860.
- [24] Kaveh, A.R., Shahedi, K., Roshan, M.H., and Ghorbani, J., 2015, Assessment of spatio-temporal variations of surface water quality and prioritization of pollution Sources (Case study: Talar Watershed, Mazandaran province), *Environ. Resour. Res.*, 3, 27–45.
- [25] Barakat, A., El Baghdadi, M., Rais, J., Aghezzaf, B., and Slassi, M., 2016, Assessment of spatial and seasonal water quality variation of Oum Er Rbia River (Morocco) using multivariate statistical techniques, *Int. Soil Water Conserv. Res.*, 4 (4), 284–292.
- [26] Ménesguen, A., and Lacroix, G., 2018, Modelling the marine eutrophication: A review, *Sci. Total Environ.*, 636, 339–354.
- [27] Cutrim, M.V.J., Ferreira, F.S., dos Santos, A.K.D., Cavalcanti, L.F., Araújo B.O., de Azevedo-Cutrim, A.C.G., Furtado, J.A., and Oliveira, A.L.L., 2019, Trophic state of an urban coastal lagoon (northern Brazil), seasonal variation of the phytoplankton community and environmental variables, *Estuarine Coastal Shelf Sci.*, 216, 98–109.

Assessment of the Level and Health Risk of Fluoride and Heavy Metals in Commercial Toothpastes in Bangladesh

Chanchal Chayan Paul¹, Md. Abu Shamim Khan², Probir Kumar Sarkar¹, Abdul Hakim², Md. Waliullah², and Bablu Hira Mandal^{3,*}

¹Department of Chemical Engineering, Jashore University of Science and Technology, Jashore-7408, Bangladesh

²Environmental Laboratory, Asia Arsenic Network, Jashore, Bangladesh

³Department of Chemistry, Jashore University of Science and Technology, Jashore-7408, Bangladesh

* **Corresponding author:**

tel: +880-1711013881

email: bhiramandal@gmail.com

Received: February 10, 2019

Accepted: August 1, 2019

DOI: 10.22146/ijc.43266

Abstract: Toothpaste is one of the daily essentials, and good quality control practices over it are very important to protect the oral public health from adverse effects. The current study aimed to assess the concentration of fluoride and heavy metals, physicochemical properties in ten different toothpaste samples in Bangladesh, followed by related health risk analysis. pH, moisture content, F⁻, As, Cu, Pb contents were measured by membrane electrode, thermogravimetric, SPADNS, HG-AAS, flame-AAS methods, respectively. The results were compared to the specification of the packet and Bangladesh Standard and Testing Institute (BSTI) standard. The physicochemical properties well-matched the formulation standard values. The moisture content was 27.18 ± 2.20 to 52.10 ± 5.01%, with 50% of the samples in permissible limit but the pH of all the samples (6.40-8.60) was within the standard limit. Available F⁻, Cu, Pb, and As content ranged from 803–1617, 2.78–13.10, 0.27–2.12, and 0.027–0.637 mg/Kg, respectively. F⁻ content in 80% toothpaste did not meet the packet specification and was higher than BSTI standard, though heavy metals were within the BSTI limit. Hazard quotient (HQ) and HI (Hazard Index) analysis revealed that toothpaste safe from heavy metal related to health risk.

Keywords: toothpaste; fluoride; heavy metals; health risk

■ INTRODUCTION

Toothpaste is absolutely necessary for our daily oral hygiene routine. It is used for cleaning and polishing the surface of teeth to remove dental plaque formed on teeth and gums as well as it prevents from the most common oral disease like dental cavities and periodontal usually caused by bacteria in the mouth [1]. Principal ingredients in toothpaste formulations are polishing agents, binding agents, foaming agents, flavoring agents, humectants, and water [2]. In modern toothpaste, sodium fluoride or monofluorophosphate is added as anticaries agents because fluoride is widely believed to prevent dental decays [3]. However, various studies have shown that excessive fluoride (F⁻) intake causes fluorosis, cancer, arthritis and it has also been linked to symptoms of stomach pain and indigestion [4-7]. It is an additional source to other

different means (polluted air, water, and the food chain) of entering excessive amounts of fluoride in the form of various compounds into the human body [8]. There are several previous reports which claimed questionable anti-caries effectiveness of commercial toothpaste as a result of lack of free available fluoride or inhomogeneity in total and free fluoride concentrations of toothpaste [9-10]. Thus, research and monitoring of the fluoride contents in commercial toothpaste in many parts of the world have got interested [11-18]. In addition to fluoride content, physicochemical and microbial properties of the toothpaste are also very important for oral health [19-20].

On the other hand, heavy metals are regarded as micropollutants since their excess presence has an adverse effect both on health and the environment.

However, their occurrence in nature is not harmful to our environment as they are present only in very small amounts [21-22]. They have gained significant importance due to their persistence, high toxicity, and bioaccumulation properties. Heavy metals like lead, arsenic, copper, cadmium, mercury have been proved to have a negative impact on human health and their chronic toxicity to humans is associated with many chronic diseases like mental disorders, hypertension, pneumonia, gastrointestinal disorders, vascular disease, coronary heart disease, myocardial infarction, central nervous functions, kidney disorder and cancer [23-24]. They can be exposed through direct and indirect sources like drinking water [5,22], food [25-26], air [27-28], soil [29-30] and body care products [6,31-33]. Besides the reports on the evaluation of the possible contact and adverse health effects of the heavy metals from traditionally regulated sources, the exposure to metal toxins from toothpaste and mouthwashes have also gained importance in the recent years [6-7,10-12,18-21,34]. However, the investigation on toothpaste or oral care products remained comparatively ignored and needs more study especially in developing countries like Bangladesh.

As far as we know, there are still no evaluation reports on the toothpaste and mouthwashes available in the markets of Bangladesh. Therefore, we have aimed to assess some physicochemical properties, concentrations of fluoride ion, and heavy metals (Cu, As, and Pb) in different commercial kinds of toothpaste available in the local markets in Bangladesh and the related potential health risk. Eventually, this study will help to find an idea

about these products, which will help to build up awareness of good quality control over the toothpaste to protect public oral health.

■ EXPERIMENTAL SECTION

Materials

All reagents were of analytical grade like Nitric acid (Merck, Germany), Hydrochloric acid (Merck, Germany), Sodium Borohydride (Organic, Belgium), Potassium Iodide (Kanto, Japan), while deionized water used for the preparation of all solutions were stored in polyethylene bottles. SPADNS reagent, fluoride, metals, and buffer standards were purchased from HACH, USA.

Instrumentation

The electric oven (Digi system, Taiwan) was used for drying. pH was measured with HACH sensION 156 Multi-Parameter Meter, USA, while fluoride was determined with DR/2010 Spectrophotometer, HACH, USA. Heavy metals were estimated with an atomic absorption spectrophotometer (AA-6200, Shimadzu, Japan).

Procedure

Sample collection

A total of 10 widely used toothpaste samples of different brands were collected from local markets of the Jashore city in Bangladesh and labeled TP-1 to TP-10. Among these samples five (TP-1-5) were general, one medicated (TP-6), two herbal (TP-7 and 8), and two were baby toothpaste (TP-9 and 10) (Table1). The samples

Table 1. List of toothpaste samples along with their category, chemical formulation, and color

Sample ID.	Brand name	Category	Chemical formulation	Color
TP-1	Pepsodent	General	Cream	White
TP-2	Close up	General	Gel	Green
TP-3	White plus	General	Cream	White
TP-4	Fresh gel	General	Gel	Green
TP-5	Colgate active salt	General	Cream	Blue
TP-6	Medi plus	Medicated	Cream	White
TP-7	Pepsodent herbal	Herbal	Cream	Light Green
TP-8	Colgate herbal	Herbal	Cream	White
TP-9	Meril baby	Baby	Gel	Red
TP-10	Kodomo	Baby	Cream	White

were properly checked for their physical appearance, name of the manufacturer, batch number, and manufacturing date, expiry date, manufacturing license number, testing board seal, and dental foundation seal at the time of purchase.

Sample preparation

Ten grams of raw samples were oven-dried at 105 °C until a constant weight was obtained on cooling in a desiccator. Toothpaste samples (1 g each) were soaked in a 250 mL glass beaker with 100 mL water for 24 h. The mixture was filtered into the 100 mL volumetric flask through Whatman-1 filter paper, the residue was washed thoroughly, and the filtrate was made up to volume with deionized water [35-36].

The homogeneity test

To test the homogeneity of the toothpaste samples, the normal force was applied at the crimped end of the tube at room temperature, and the nature extrusion of paste from the collapsible tube was observed [36-37].

Determination of gritty matter

A small amount of each toothpaste sample was rubbed with a finger for about 15 to 20 cm long on a butter paper. The number and intensity of scratches that appeared on the butter paper were judged for the presence of solid particles [36-37].

Determination of fineness

The toothpaste samples were checked on two standard sieves of 150 and 75 microns. For this, 50 mL of water was added into 10 g of toothpaste in a 100 mL beaker. The mixture was stirred occasionally for 30 min until the toothpaste was completely dispersed and was passed through sieves. Then the sieve was washed with running tap water until all the soluble matters passed through the sieves. The residue retained on sieves was collected and dried in an oven at 105 °C. The dried residue was weighed, and the fineness was calculated with the Eq. (1) [37]:

$$\% \text{ Mass} = \frac{M_1}{M} \times 100 \quad (1)$$

where, M_1 = Mass of residue retained on the sieve (g); M = Mass of material taken for the test (g).

Determination of spreadability

A dry and clean glass plate (10 cm × 10 cm) was taken, and 1 g of sample was kept at the center of the plate. Another glass plate was carefully placed over it. To avoid the sliding of the plate's 2 Kg weight was placed above the glass plates at the center and allowed for 30 min. The diameter of the spreading paste was measured in centimeters [36].

Determination of foaming power

In a typical process, 5 g of toothpaste sample was taken in a glass beaker (100 mL), and 10 mL of water was added into it, which was kept for 30 min for complete dispersion. The volume was adjusted to 50 mL by adding sufficient water. The mixture was then transferred to a 250 mL measuring cylinder. It was ensured that no residue was left in the beaker, no foam was formed, and no lump paste was transferred during the transfer of slurry into a measuring cylinder. A uniform suspension was also confirmed at a temperature of 30 °C. The stoppered cylinder was given 12 complete shakes and was allowed to stand for 5 min. The volume of foam with water and water only were recorded. Foaming power was calculated using the Eq. (2) [36].

$$\text{Foaming power} = V_1 - V_2 \quad (2)$$

where, V_1 = Volume of foam with water (mL); V_2 = Volume of water only (mL).

Moisture content estimation

For moisture content analysis, 10 g of sample was taken in a pre-weighted glass dish and put it in an electric oven to dry it at 105 °C for 24 h. The dried sample was taken in desiccators for cooling, and the weight of the dried sample was taken by the electric balance. Moisture contents were calculated from the differences between the weight of the raw wet sample and the oven-dried sample using the Eq. (3) [35-36].

$$\% \text{ moisture} = \frac{(w_1 - w_2) \times 100}{w_1} \quad (3)$$

where, w_1 = weight toothpaste (g); w_2 = weight of raw dried toothpaste (g).

pH measurement

pH was measured by the membrane electrode

method in 1% (w/v) aqueous suspension of each toothpaste and de-ionized water with a pH meter [35-36].

Fluoride estimation

In this process, 10 mL of sample was taken in a test tube, and 2.00 mL of SPADNS reagent was added into it for color development. The pink color was developed and absorbance was measured by UV-VIS spectrophotometer (HACH, DR/2010, USA) at 570 nm [35-36]. Before measurement, the UV-Vis spectrophotometer was calibrated by the fluoride ion reference solution.

Heavy metals estimation

The heavy metals in toothpaste were analyzed by atomic absorption spectrophotometer using flame-AAS method for copper and lead, and HG-AAS methods for As [36-38]. In brief, 5g of dried toothpaste sample was digested with concentrated nitric acid and 30% hydrogen peroxide at 95 °C following USEPA guidelines [38]. A solution of 100 mL was prepared with necessary dilution with dilute nitric acid and distilled water. The metal content by mass of sample (mg/Kg) was calculated automatically by the instrument and manually with the Eq. (4).

$$\text{Metal concentration (mg / Kg)} = \frac{(A - B)C}{D} \quad (4)$$

where, A = concentration of metal in sample, as determined by AAS; B = concentration of the metal found in blank (mg/L); C = volume of extract (mL); D = weight of sample (Kg).

Data analysis

The experimental data were analyzed with SPSS software. Daily intake of fluoride and heavy metals (Cu, Pb, and As), Hazard Quotients (HQ) and Hazard Index(HI) were calculated using the Eq. (5-7) [37-38].

$$\text{Daily Intake, DI (mg / Kg / day)} = \frac{C_i \times D_{\text{intake}}}{B_{\text{weight}}} \quad (5)$$

where, C_i = Concentration of 'i' in sample taken for analysis (in mg/Kg); D_{intake} = the daily intake of toothpaste (0.264 g/person/day); B_{weight} = the body weight (60 Kg in this study).

$$\text{Hazard Quotient, HQ} = \frac{\text{DI}}{R_f D} \quad (6)$$

where, DI = Daily intake (mg/Kg/day); $R_f D$ = Oral Reference Dose (mg/Kg/day); Oral Reference Dose (mg/Kg/day) for F, Cu, Pb and As are 6.0×10^{-2} , 4.0×10^{-2} , 4.0×10^{-3} , 3.0×10^{-4} .

$$\text{Hazard Index, Hi} = \sum_i^4 \text{HQ}_i \quad (7)$$

where, HI = Hazard Index; HQ_i = Hazard Quotient.

RESULTS AND DISCUSSION

Ten most widely used toothpaste samples were analyzed following standard methods [36]. From the results of physical parameters (Table 2), all the kinds of toothpaste were found to be homogeneous, i.e., they released from the collapsible tube in the form of a homogeneous mass at room temperature, indicating no toothpaste solidified out of the tube and too thin to be

Table 2. Physical parameters study data

Sample ID	Spreadability (cm)	Gritty Matter	Foaming Power (mL)	Homogeneity	Fineness	
					150-micron sieve	75-micron sieve
TP-1	7.75	Absent	65	Homogeneous	0.30	1.38
TP-2	6.50	Absent	53	Homogeneous	0.23	1.22
TP-3	7.91	Absent	54	Homogeneous	0.21	1.14
TP-4	7.45	Few granular	58	Homogeneous	0.35	1.65
TP-5	7.34	Few granular	70	Homogeneous	0.26	1.32
TP-6	9.33	Absent	55	Homogeneous	0.18	1.07
TP-7	7.38	Absent	72	Homogeneous	0.22	1.12
TP-8	6.95	Absent	74	Homogeneous	0.31	1.43
TP-9	8.25	Absent	51	Homogeneous	0.11	0.85
TP-10	7.89	Absent	52	Homogeneous	0.16	0.96

held in the tube. The samples were also free from hard and sharp-edged abrasive particles, i.e., the ingredients added to these toothpastes were grounded properly and uniformly mixed. So, the toothpaste samples are safe for the gums and enamel since the regular use of toothpaste with gritty matters may wear off the teeth in the long run. According to the BSTI standard, the maximum particles retained on the sieve is 0.5% by mass for 150 microns and 2.0% by mass for 75 microns [36]. The fineness of the toothpastes varied from 0.11–0.35% (w/w) and 0.85–1.85% (w/w) for 150 and 75-micron sieve, respectively (Table 2), which satisfied the BSTI standards. It is also inferred that there were no coarse particles in the toothpaste which may cause scratching on the enamel surface.

The spreadability of the samples (6.50–9.33 cm) was within the standard value (maximum 8.5 cm) except sample no. TP-6 (Table 2) [36]. Thus, there was no difficulty in the filling and extrusion of toothpaste from the tubes. In the case of the foam formation, all the toothpastes revealed the standard foam formation (minimum 50 mL), ranged from 51–74 mL, and indicated sufficient cleansing action in terms of the foam formation property.

The obtained results for moisture contents, pH values, fluoride, and heavy metals content (Table 3) were compared with the specification of the packets and BSTI standard [36]. Moisture content prevents toothpaste from hardening on exposure to air during storage and

preservation. The average moisture content found in toothpaste samples was 35.26%, which matched with standard values (35%). However, 50% of the samples had higher values and the rest 50% had below the standard value. Maximum and minimum moisture contents observed were $52.10 \pm 5.01\%$ and $27.18 \pm 2.20\%$ in TP-10 and TP-4, which were specialized for children and gel type toothpaste, respectively (Table 3). The pH value indicates the inorganic constituents in toothpaste. Acidic pH encourages the growth of mouth bacteria that causes dental caries [4]. The average pH of toothpaste samples was detected 7.52 which is within BSTI standard (6.50 to 10.50). The maximum and minimum pH was found 8.60 ± 0.40 and 6.40 ± 0.28 in TP-6 and TP-4. Fifty percent of the samples were nearly neutral pH, and 50% of the samples were slightly alkaline. Thus the toothpaste having alkaline pH value contain inorganic ingredients like calcium carbonate and phosphate, and the neutral values are silica-based [10].

Fluoride is believed to prevent tooth decay and most of the dental diseases [3]. So, the fluoride level determines the activity, potency, and commercial acceptability of toothpaste [36,39]. The average fluoride concentration in the samples was 1251.03 mg/Kg, which is greater than the maximum recommended value (1000 mg/Kg) [37]. Only one sample (TP-1) contained the tolerable fluoride concentration and another one (TP-10) sample below the

Table 3. Moisture content, pH, F⁻, Cu, Pb and As content

Sample ID	Moisture content (%)	pH	Conc. of F ⁻ (mg/Kg)	Conc. of Heavy Metals (mg/Kg)		
				Cu	Pb	As
TP-1	36.51 ± 5.22	8.15 ± 0.32	1000.12 ± 52.09	4.64 ± 0.78	0.88 ± 0.09	0.044 ± 0.02
TP-2	32.08 ± 3.51	7.12 ± 0.13	1351.21 ± 24.69	4.26 ± 0.59	0.77 ± 0.10	0.085 ± 0.03
TP-3	28.16 ± 4.62	8.33 ± 0.21	1169.02 ± 40.12	2.78 ± 0.48	0.27 ± 0.03	0.027 ± 0.01
TP-4	27.18 ± 2.20	6.40 ± 0.28	1427.65 ± 33.12	5.63 ± 1.02	1.34 ± 0.12	0.224 ± 0.08
TP-5	39.80 ± 4.10	6.93 ± 0.15	1617.33 ± 51.20	5.38 ± 0.96	1.27 ± 0.15	0.153 ± 0.05
TP-6	36.05 ± 4.25	8.60 ± 0.40	1298.18 ± 46.23	13.10 ± 1.68	2.12 ± 0.26	0.637 ± 0.12
TP-7	37.56 ± 3.82	8.23 ± 0.28	1446.51 ± 36.21	5.02 ± 1.12	1.23 ± 0.22	0.098 ± 0.04
TP-8	32.63 ± 2.69	8.38 ± 0.35	1355.12 ± 25.32	4.49 ± 0.51	0.34 ± 0.01	0.183 ± 0.07
TP-9	30.54 ± 2.58	6.42 ± 0.46	1042.08 ± 41.25	4.37 ± 0.39	0.98 ± 0.10	0.042 ± 0.01
TP-10	52.10 ± 5.01	6.60 ± 0.52	803.08 ± 20.13	3.71 ± 0.88	0.57 ± 0.06	0.076 ± 0.03
Maximum	52.10	8.60	1617.33	13.10	2.12	0.64
Minimum	27.18	6.40	803.08	2.78	0.27	0.03
Average	35.26	7.52	1251.03	5.34	0.98	0.16

“±” indicates SD, n = 3

permissible range, while 80% of the samples exceeded the BSTI level. The highest concentration of fluoride ion, 1617 ± 51.20 mg/Kg, was detected in sample TP-5, which is a medicated toothpaste. The least concentration, 803 ± 20.13 mg/Kg, was in the sample TP-10 which was the special toothpaste for children (Table 3). Two pediatric types of toothpaste (TP-9 and TP-10) contained 1042 ± 41.25 mg/Kg and 803.08 ± 20.13 mg/Kg fluoride ion, respectively. However, the recommended permissible limit for fluoride in pediatric toothpaste is 425–625 mg/Kg, and for adults is 825–1250 mg/Kg [36,40-41]. Hence, both of the baby toothpaste contained excess fluoride concentration, and 70% of the adult toothpaste samples contained higher fluoride, which can be a threat to oral health [6-7].

Fluoride toothpaste is recommended to be more effective in preventing tooth decay at higher fluoride concentrations. Nevertheless, excess fluoride ion (> 1000 mg/Kg) could cause tooth enamel decay, skeletal fluorosis, abdominal pain, excessive saliva, nausea, vomiting, seizures and muscle spasms, death due to respiratory paralysis [10-12,40-41]. In addition, being an endocrine disrupter higher fluoride concentration can affect the bones, brain, thyroid gland, pineal gland, and even the blood sugar levels [7,40]. Therefore, the high fluoride concentrations measured in the adult toothpaste pose a serious health concern. However, if fluoride is ingested during the development of the tooth, it resists the attacks of acids on the enamel in the future [41]. Hence, the concentration of fluoride in the pediatric toothpaste (TP-9 and 10) may be beneficial to children. It is interesting to observe that some of the toothpaste did not mention the maximum fluoride content on the packet level. This means the fluoride concentration has not been properly checked for those samples.

On the other hand, the samples having packet leveling, simply mentioned the maximum fluoride content 1000 mg/Kg instead of the exact concentration. Unfortunately, almost none of them meet their demand rather contained excess fluoride. As a result, the use of these kinds of toothpaste may create a threat to public health.

Heavy metals are considered as mere contaminants for toothpaste as their roles are not clearly defined in the

toothpaste formulation. However, their presence in the toothpaste may be accounted for abrasives, materials used from the plant sources [42-43], accidental cross-contamination during processing, and the deliberate introduction of metals as therapeutic ingredients for more efficacy [43]. Consequently, these metals may become harmful when they are ingested above the tolerance level, and daily use may have a significant adverse health effect.

Table 3 represents the concentration of arsenic, copper, and lead in different toothpaste samples. The average concentration of arsenic, copper, and lead was 0.16, 5.34 and 0.98 mg/Kg, respectively, which are within the permissible range for toothpaste. However, the average concentration of As exceeded the threshold value (max 0.05 mg/Kg) for drinking water [40]. The maximum concentration of arsenic, copper, and lead was found 0.637 ± 0.12 , 13.10 ± 1.68 , and 2.12 ± 0.26 mg/Kg in TP-06, which are higher than USEPA standard as well as BSTI [36,39]. The higher level may be due to the coloring active salt contents in creamy toothpaste. On the other hand, the minimum concentration of arsenic, copper, and lead was detected 0.27 ± 0.01 , 2.78 ± 0.48 and 0.27 ± 0.03 mg/Kg in TP-03, a white creamy toothpaste, which satisfies the USEPA standard [38-39]. It is surprising to note that the presence of these heavy metals in the specification on the labeling of the packets was not mentioned in any of the samples. This should be mentioned since the excess presence of these heavy metals may be toxic to human health [36].

The Pearson correlation indicates positive correlation among the metals present in the toothpaste samples, having R^2 value for Pb and As, Pb and Cu, and Cu and As are 0.5990, 0.7537, and 0.9345, respectively (Fig. 1-3). So, these metals might have been incorporated in toothpaste from the same sources.

Table 4 shows the acceptable upper limit (UP) of Pb, Cu, As, and F^- [40] whereas, Fig. 4 and 5 represent the fluoride, and the metals intake through the daily intake of toothpaste. It is seen that in 90% of toothpaste samples, the daily intake of fluoride is greater than the tolerable upper limit of daily intake (UL). However, the value is very high in the baby toothpaste (TP-9 and 10), which may cause fluorosis in the long run [38].

Since these metals are considered as potentially carcinogenic substances [39-40], the potential health risk from fluoride, Cu, Pd, and As, was assessed with the related parameter, Hazard quotient (HQ) and Hazard Index (HI) (Table 5). Hazard quotient was estimated using oral

Table 4. Tolerable Upper Limit (UL) for investigated element [40]

Element	UL (mg/day)
Pb	0.240
Cu	10.00
As	0.01
F ⁻	4.00, 1.00-2.20*

*Children (4-14 years)

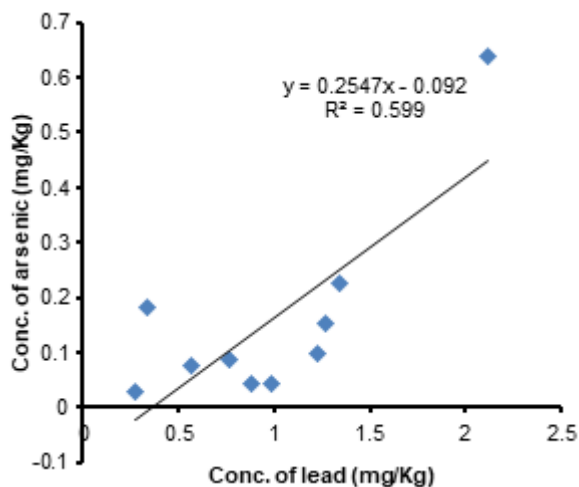


Fig 1. Correlation chart of Pb and As

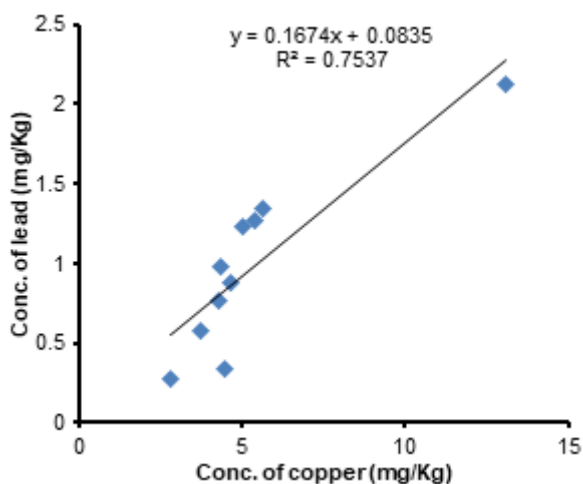


Fig 2. Correlation chart of Cu and Pb

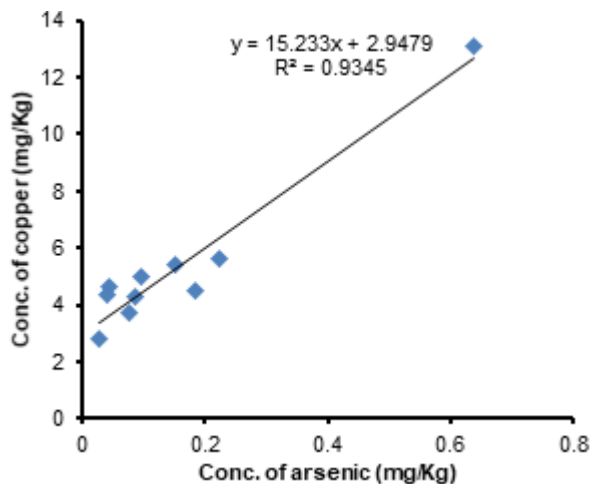


Fig 3. Correlation chart of Cu and As

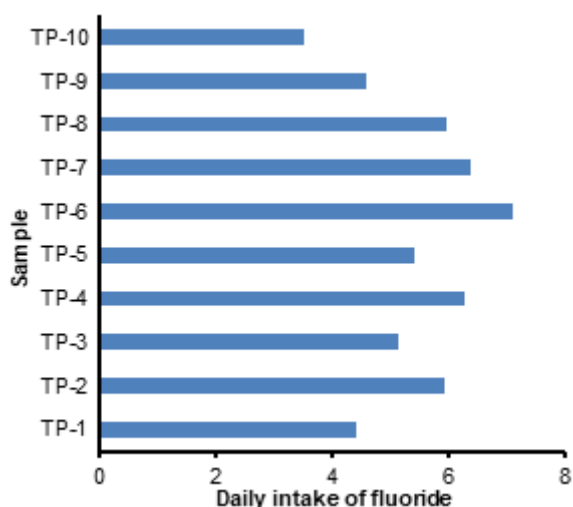


Fig 4. Daily intake of fluoride

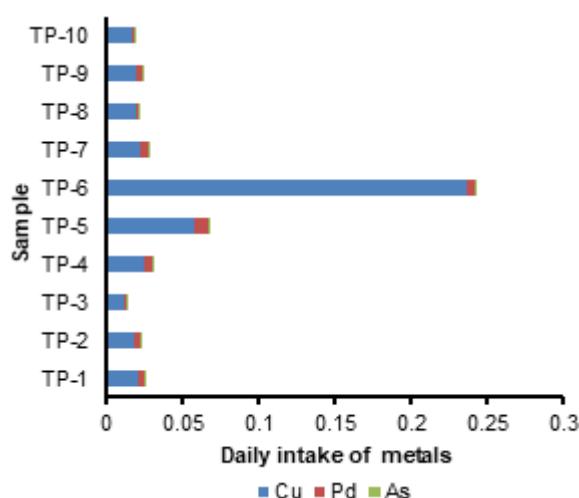


Fig 5. Daily intake of Cu, Pb and As

Table 5. Hazard Quotient (HQ) of fluoride, copper, lead, and arsenic

Sample ID	HQ				HI
	Cu($\times 10^{-3}$)	Pb($\times 10^{-3}$)	As($\times 10^{-4}$)	F ⁻	
TP-01	0.51	0.968	0.633	0.733	> 1
TP-02	0.46	0.85	1.246	0.099	> 1
TP-03	0.305	0.297	0.25	0.0857	> 1
TP-04	0.619	1.474	0.2797	0.1046	> 1
TP-05	0.5918	1.397	1.683	0.1186	> 1
TP-06	1.436	2.332	9.342	0.0889	> 1
TP-07	0.52	1.353	1.078	0.106	> 1
TP-08	0.493	0.374	2.13	0.0994	> 1
TP-09	0.48	1.078	0.462	0.0764	> 1
TP-10	0.408	0.627	0.836	0.0588	> 1
Average value	0.58	1.08	1.79	0.16	

Reference Dose (mg/Kg/day) 6.0×10^{-2} , 4.0×10^{-2} , 4.0×10^{-3} , 3.0×10^{-4} for individual F⁻, Cu, Pb and As respectively [39].

According to the WHO and USEPA, HQ and HI value should be less than one for health safety [39-40]. Average HQ of arsenic, copper, lead, and fluoride was calculated 1.79×10^{-4} , 0.58×10^{-3} , 1.08×10^{-3} , and 0.16, respectively, i.e., all values were below one. Hazard Index (HI) was also found less than one. So, it revealed that metal contents in the toothpaste were safe from the risk of cancer [38]. Although this study suggests no potential health risk from these heavy metals, it must be kept in mind that these small quantities will be added to the potentially toxic metals ingested into the human body from other sources such as water, beverage, and foods, and consequently their cumulative effect may get detrimental. This can also be conceivable from the Pearson correlation which indicated the strong positive correlation (R^2 value ranged from 0.599 to 0.9345) among these three metals.

■ CONCLUSION

Toothpaste samples exhibited good physicochemical properties except for moisture content. Fluoride content in most of the brands was higher than the standard, revealing the potential health risk, although the heavy metal related health risk is negligible. Some brands available in the market neither satisfied nor had a clear specification, which shows the availability of low-quality toothpaste in the market of Bangladesh. Substandard

toothpaste causes not only a waste of money but is responsible for health hazards. So, the respective regulatory authorities should take proper measures to prevent the manufacture and marketing of low standard toothpaste in any situation in order to protect public oral health. The testing authority should also strengthen their monitoring and establish more effective analytical measures to analyze the marketed toothpaste to ensure safe public oral hygiene health. Moreover, for oral hygiene, pH, moisture content, fluoride content and heavy metal contents in the toothpaste should be clearly specified on the packet or tube.

■ ACKNOWLEDGMENTS

The authors gratefully acknowledge the support of the Department of Chemical Engineering, Jashore University of Science and Technology, Jashore and Asia Arsenic Network (AAN), Krishnabati, Pulerhat, Jashore, Bangladesh for their kind cooperation and permission to use their laboratory for the analysis to carry out this study. The authors are also thankful to Dr. Anjon Kumar Mondal, Manager, API Production, Beximco Chemical Division, Tongi, Gazipur, Bangladesh, for his critical suggestions in preparing this manuscript.

■ REFERENCES

- [1] Burt, B.A., 1998, Prevention policies in the light of the changed distribution of dental caries, *Acta Odontol. Scand.*, 56 (3), 179-186.

- [2] Safra, J.E., Constantine, S.Y., and Goulk, J.E., 1998, *The New Encyclopedia Britannica*, 15th Ed., Encyclopedia Britannica, Inc., London UK, 2, 356; 7, 678; 10, 931; 14, 547; 17, 293, 259; 20, 513; 25, 55-56, 61, 68; 26, 846; 28, 307.
- [3] Ivanova, M., and Christova, R., 1995, Potentiometric determination of fluorine in dentifrices of high ionic level, *Anal. Lab.*, 4, 47–50.
- [4] Carton, R.J., 2006, Review of the 2006 United States National Research Council report: Fluoride in drinking water, *Fluoride*, 39 (3), 163–172.
- [5] Konieczka, P., Zygmunt, B., and Namieśnik, J., 2000, Effect of fluorine content in drinking water in ricity on its concentration in urine of pre-school children, *Toxicol. Environ. Chem.*, 74 (2), 125–130.
- [6] Odukudu, F.B., Ayenimo, J.G., Adekunle, A.S., Yusuff, A.M., and Mamba, B.B., 2014, Safety evaluation of heavy metal exposure from consumers, *Int. J. Consum. Stud.*, 38 (1), 25–34.
- [7] Sainio, E.L., and Kanerva, L., 1995, Contact allergens in toothpaste and a review of their hypersensitivity, *Contact Dermatitis*, 33 (2), 100–105.
- [8] Waldbolt, G.L., 1998, The preskeletal phase of chronic fluoride intoxication, *Fluoride*, 31 (1), 13–20.
- [9] Jordan, R.A., Markovich, L., Gaengler, P., and Zimmer, S., 2011, Total and free fluoride concentrations of African dentifrices marketed in West Africa, *Oral Health Prev. Dent.*, 9 (1), 53–58.
- [10] Oyewale, A.O., 2005, Estimation of essential inorganic constituents of commercial toothpaste, *J. Sci. Ind. Res.*, 64 (2), 101–107.
- [11] Ideriah, T.J.K., Obunwo, C.C., and Eretoru, T.D., 2016, Assessment of fluoride and heavy metals concentrations in toothpastes marketed in Port Harcourt Nigeria, *Int. J. Adv. Innovative Res.*, 5 (5), 28–34.
- [12] Teki, K., and Bhat, R., 2013, Estimation of the components in oral care products available in Indian market – Part II: Toothpaste, *Int. J. Pharm. Chem. Sci.*, 2 (2), 705–712.
- [13] Benzian, H., Holmgren, C., Buijs, M., van Loveren, C., van der Weijden, F., and van Palenstein Helderma, W., 2012, Total and free available fluoride in toothpastes in Brunei, Cambodia, Laos, the Netherlands and Suriname, *Int. Dent. J.*, 62 (4), 213–221.
- [14] de Freitas, J.F., 1984, Fluoride stability in toothpastes, *Aust. Dent. J.*, 29 (1), 30–35.
- [15] Hashizume, L.N., de Oliveira Lima, Y.B., Kawaguchi, Y., and Cury, J.A., 2003, Fluoride availability and stability of Japanese dentifrices, *J. Oral Sci.*, 45 (4), 193–199.
- [16] Thakkar, V.P., Rao, A., Rajesh, G., Shenoy, R., and Pai, M., 2015, Fluoride content and labeling of toothpastes marketed in India, *Community Dent. Health*, 32 (3), 170–173.
- [17] Ko, H.Y., Kang, S.M., Kwon, H.K., and Kim, B.I., 2015, Evaluation of fluoride bioavailability in toothpastes, *J. Korean Acad. Oral Health*, 39 (2), 81–87.
- [18] Krishna, D.G., Al-Amri, S.H., Al-Mamari, F.S., Al-Sidairi, A.S., and Devi, C.K., 2015, Estimation of the essential inorganic constituents of various commercial toothpastes, *Int. J. Inorg. Bioinorg. Chem.*, 5 (1), 14–15.
- [19] Anju, T., and Aiswarya, K., 2016, Formulation and antimicrobial evaluation of toothpastes containing arginine and proline, *Int. J. Adv. Pharm., Biol. Chem.*, 5 (2), 143–147.
- [20] Prasanna, S.G.V., Abllasha, R., and Gopinath, 2016, In vitro comparison of antimicrobial efficacy of different toothpaste, *J. Pharm. Sci. Res.*, 8 (10), 1195–1198.
- [21] Rao, R.N., and Rao, T.N., 2014, Determination heavy metals in toothpastes containing tin as an ingredient, *Indian J. Chem. Tehnol.*, 21 (4), 238–243.
- [22] Mohod, C.V., and Dhote, J., 2013, Review of heavy metals in drinking water and their effect on human health, *Int. J. Innovative Res., Sci. Eng. Technol.*, 2 (7), 2992–2996.
- [23] Kawata, K., Yokoo, H., Shimazaki, R., and Okabe, S., 2007, Classification of heavy metal toxicity by human DNA microarray analysis, *Environ. Sci. Technol.*, 41 (10), 3769–3774.
- [24] Järup, L., 2003, Hazards of heavy metal contamination, *Br. Med. Bull.*, 68 (1), 167–182.

- [25] Chien, L.C., Hung, T.C., Choang, K.Y., Yeh, C.Y., Meng, P.J., Shieh, M.J., and Han, B.C., 2002, Daily intake TBT, Cu, Zn, Cd and As for fisherman in Taiwan, *Sci. Total Environ.*, 285 (1-3), 177–185.
- [26] Food and Nutrition Board, 2004, *Dietary reference intakes (DRIs): Recommended intakes for individuals*, Institute of Medicine, US National Academies, Washington DC, United States.
- [27] Gharaibeh, A.A., El-Rjoob, A.O., and Harb, M.K., 2010, Determination of selected heavy metals in air samples from the northern part of Jordan, *Environ. Monit. Assess.*, 160 (1-4), 425–429.
- [28] Pandey, J., Pandey, R., and Shubhashish, K., 2009, Air-borne heavy metal contamination to dietary vegetables: A case study from India, *Bull. Environ. Contam. Toxicol.*, 83 (6), 931–936.
- [29] Fernandes, C., Fontainhas-Fernandes, A., Cabral, D., and Salgado, M.A., 2008, Heavy metals in water, sediment and tissues of *Liza saliens* from Esmoriz-Paramos lagoon, Portugal, *Environ. Monit. Assess.*, 136 (1-3), 267–275.
- [30] Aguilar, C.A., Montalvo, C., Rodriguez, L., Ceron, J.G., and Ceron, R.M., 2012, American oyster (*Crassostrea virginica*) and sediments as a coastal zone pollution monitor by heavy metal, *Int. J. Environ. Sci. Technol.*, 9 (4), 579–586.
- [31] Salve, K.S., and Sonwane, N.S., 2015, Detection of heavy metals in cosmetics, *World J. Pharm. Res.*, 4 (4), 1368–1372.
- [32] Ayenimo, J.G., Yusuf, A.M., Adekunle, A.S., and Makinde, O.W., 2010, Heavy metal exposure from personal care products, *Bull. Environ. Contam. Toxicol.*, 84 (1), 8–14.
- [33] Bocca, B., Pino, A., Alimonti, A., and Forte, G., 2014, Toxic metals contained in cosmetics: A status report, *Regul. Toxicol. Pharmacol.*, 68 (3), 447–467.
- [34] Orisakwe, O.E., Okolo, K.O., Igweze, Z.N., Ajaezi, G.C., and Udowelle, N.A., 2016, Potential hazards of toxic metals found in toothpastes commonly used in Nigeria, *Rocz. Panstw. Zakl. Hig.*, 67 (2), 197–204.
- [35] American Public Health Association, 2005, *Standard Methods for the Examination Water and Wastewater*, 21st Ed., Eds. Eaton, A.D., Clesceri, L.S., Franson, M.A.H., Rice, E.W., and Greenberg, A.E., American Public Health Association, Washington DC, United States.
- [36] Bangladesh Standard and Testing Institution (BSTI), 2001, *Bangladesh Standard Specification for Tooth-paste*, 1st revision, Bangladesh Standard and Testing Institution (BSTI), Dhaka, Bangladesh.
- [37] Akelesh, T., Kumar, R.S., Jothi, R., Rajan, V., Arulraj, P., and Venkatnarayanan, R., 2010, Evaluation of standards of some selected cosmetic preparations, *Asian J. Pharm. Res. Health Care*, 2 (4), 302–306.
- [38] United States Environmental Protection Agency (USEPA), 2007, *Integrated risk information system-database*, U.S. Environmental Protection Agency, Washington DC, United States.
- [39] United States Environmental Protection Agency (USEPA), Office of Water Regulations and Standards, 1989, *Assessing human health risks from chemically contaminated fish and shellfish: A guidance manual*, U.S. Environmental Protection Agency, Washington DC, United States.
- [40] WHO, 2010, *Preventing disease through healthy environments – Inadequate or excess fluoride: A major public health concern*, World Health Organization, Geneva.
- [41] Petersen, P.E., and Lennon M.A., 2004, Effective use of fluorides for the prevention of dental caries in the 21st century: The WHO approach, *Community Dent. Oral Epidemiol.*, 32 (5), 319–321.
- [42] Abou-Arab, A.A., and Abou Donia, M.A., 2000, Heavy metals in Egyptian spices and medicinal plants and the effect of processing on their leaves, *J. Agric. Food Chem.*, 48 (6), 2300–2304.
- [43] Wu, J., Zou, Y., Zhan, X., Lu, G., and Lai, F., 2008, Survey of heavy metal pollution in four Chinese crude drugs and their cultivated soils, *Bull. Environ. Contam. Toxicol.*, 81 (6), 571–573.

Synthesis, Spectroscopic and Computational Studies of Some Metals Chelates with Chromene-2-one and Pyrazine-Based Ligands

Taghreed Mohy Al-Deen Musa¹, Mahmoud Najim Abid Al-Jibouri^{1*},
Bayader Fadhil Abbas¹, and Nahid Hasani²

¹Department of Chemistry, College of Science, Mustansiriyah University, Baghdad, Iraq

²Department of Inorganic Chemistry, Faculty of Chemistry, University of Mazandaran, Babolsar, Iran

* **Corresponding author:**

email:

mahmoud_inor71@uomustansiriyah.edu.iq

Received: February 7, 2019

Accepted: July 18, 2019

DOI: 10.22146/ijc.43857

Abstract: The present paper deals with the synthesis of cobalt(II), nickel(II), copper(II) and cadmium(II) complexes with two bidentate ligands, L¹ (3-(quinoxaline-2-yl)-coumarin) and L² (2-methylene-2H-chromene-3-(methyl carbonimidic)thioanhydride). The L¹ ligand was prepared by treating ω-bromo-3-acetylcoumarin with 1,2-phenylenediamine whereas the ligand L² was prepared through substitution reaction of ω-bromo-3-acetylcoumarin with potassium thiocyanate in ethanol medium. The confirmation of the structures for L¹ and L² were done by (C.H.N.S.) elemental analysis, FT-IR, NMR and mass spectra. The metal complexes of cobalt(II), nickel(II), copper(II) and cadmium(II), with L¹ and L², were prepared and isolated in the solid state and then characterized by (C.H.N.M) elemental analysis, proton and carbon-13 NMR, FT-IR and mass spectra. Furthermore, the thermal analysis (TG-DSC) for some complexes assisted us in the elucidation of the suggested structures of complexes and confirmed their thermal stability. The results obtained from elemental analysis, magnetic susceptibility and thermal analysis confirmed that all metal complexes were formed in 2:1 molar ratio of ligand to metal with octahedral structures except cadmium(II) complexes which were in a tetrahedron geometry with 1:1 mole ratio. The complexes are found to be soluble in DMF and DMSO. The results obtained from TG-DSC analysis revealed that the metal complexes were thermally stable with point decomposition over 350 °C. The DFT/TDDFT calculations were carried out to provide the electronic structures and spectra of the compounds.

Keywords: transition metal complexes of pyrazine ligands; theoretical studies of metal complexes

■ INTRODUCTION

The metal complexes possessing chromen-2-one and pyrazine rings have gained attention in the field of the pharmaceutical industry [1-3]. It is well-known from literature, the transition elements complexes with bidentate Lewis bases of coumarin have known during the last decades as antitumor agents [4-5]. As well as the semicarbazone of pyrazine derivatives with their metal chelate have adopted as active materials in the treatment of rare diseases [6-7]. The coordination chemistry of coumarin ligand has great interesting in the field of colorimetric determination of

trace amounts of heavy metals [8]. The antimicrobial activity of coumarin nucleus and antioxidant activity [9] has a great important effect like antibacterial, anti-thrombotic and Esculetin, a coumarin compound can inhibit the growth of human leukemia [10]. As it has been investigated in the literature, the biological activity of some chromene derivatives are significantly enhanced by binding to metal ions [11-12]. In continuation with the description of new metal complexes of quinoxaline and coumarin ligands, we report the synthesis, characterization and thermal study of some first-row transition metal

complexes with two ligands derived from 3-bromoacetyl-coumarin-2-one. The gaining comprehensive insight into the properties and chemical behavior of the transition metal complexes, the quantum chemical calculations using density functional theory (DFT) and time-dependent density functional theory (TDDFT) have been carried out to authenticate the plausible geometry of the titled compounds. Here in, the electronic structures, also electronic excitations together with the nature of the frontier orbital are interpreted by theoretical calculations.

■ EXPERIMENTAL SECTION

Materials

All chemicals were of reagent grade, and solvents were dried and distilled before use according to the standard procedures. 3-Acetylcoumar-2-one was purchased from Sigma-Aldrich company and other starting materials like potassium thiocyanate and 1,2-phenylenediamine were supported from laboratories of the Chemistry Department, College of Science, Mustansiriya University. The hydrated chlorides $\text{CoCl}_2 \cdot 6\text{H}_2\text{O}$, $\text{NiCl}_2 \cdot 6\text{H}_2\text{O}$, $\text{CuCl}_2 \cdot 2\text{H}_2\text{O}$ and $\text{CdCl}_2 \cdot 2\text{H}_2\text{O}$ and were purchased from Alfa company, and were used without further purification as received. The measurements of molar conductivity were made on a Hanna conductivity bridge with a cell constant 1.0 cm^{-1} . The magnetic susceptibility measurements were made on Gouy's balance at room temperature using $\text{Hg}[\text{Co}(\text{SCN})_4]$ as calibrating on Sherwood magnetic balance. The FT-IR spectra were recorded in a KBr and CsI matrix using a Shimadzu FTIR spectrometer model 983. The electronic spectra in the range (200–1000 nm) were done for all complexes and the

free ligands complexes in DMF and ethanol solutions were scanned on Carry 2390 Instrument. TG and DSC (Differential Scanning Colorimetric) thermograms in different ranges were carried out at (R.T) heating rate = $10 \text{ }^\circ\text{C}/\text{min}$ (Linseis STA PT-1000) were run on service laboratories of Ibn-Haithum college of education, University of Baghdad. The metal contents of the complexes were determined by flame atomic absorption spectroscopy on A Spect LS/FL 1.3.0.0 model. The magnetic susceptibility of the solid complexes was measured according to Faraday's method using auto Magnetic susceptibility Balance Sherwood Scientific. The mass spectra were performed using the instrument: GC MS-QP 2010 VLTRA, University of Mustansiriya.

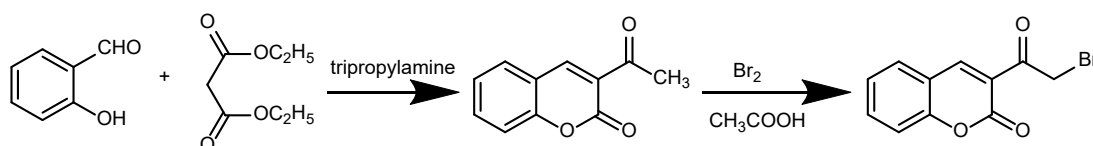
Procedure

Synthesis of ω -bromo-3-acetylcoumarin

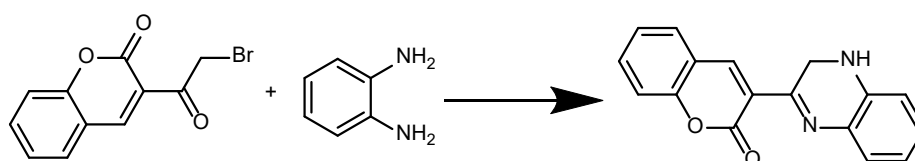
The preparation of bromo-3-acetylcoumarin was carried out according to the method described in the literature [12], (Scheme 1).

Synthesis of L^1 ligand

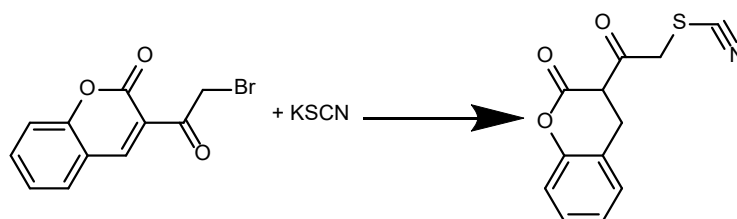
A solution of (5 mmol) ω -bromo-3-acetylcoumarin and (5 mmol) 1,2-phenylenediamine in absolute methanol (20 mL) was refluxed for 4 h. The solid obtained was filtered, washed with ethanol and dried under vacuum. The crude product was recrystallized from ethanol/benzene mixture to give compound 11 as pale brown crystals, (Scheme 2). Chem. Anal. Calc. for $\text{C}_{17}\text{H}_{12}\text{O}_2\text{N}_2$, L^1 (MW: 276.29): C, 73.90; H, 4.38; N, 10.14. Found: C, 73.09; H, 4.23; N, 10.19. Yield 77%, decomposition point: (148–150 $^\circ\text{C}$). IR ν (KBr disc)/ cm^{-1} : 3088, 3455, 3292, 1649, 1622, 1580, 1554.



Scheme 1. Synthesis of ω -bromo-3-acetylcoumarin



Scheme 2. Synthesis of $[L^1]$

Scheme 3. Synthesis of L²

Synthesis of L² ligand

A solution of compound (2) (10 mmol) in methanol (40 mL) was refluxed with potassium thiocyanate (10 mmol) for 3 h. The solid formed on cooling filtered off, washed with ethanol and dried under vacuum. The product was then recrystallized from acetic acid to afford brown needles, (Scheme 3). Chem. Anal. Calc. for C₁₂H₇O₃NS, L²; (MW: 245.25): C, 58.77; H, 2.88; N, 5.71; S, 13.07. Found: C, 58.18; H, 2.52; N, 5.98; S, 13.54. Yield 90%, Decomposition point: (138–140 °C). IR ν (KBr disc)/cm⁻¹: 3117, 3354, 1649, 1606, 1556.

Synthesis of the metal complexes

[Co(L¹)₂Cl₂]H₂O. [C₃₄H₂₆O₅N₄Cl₂Co]; (Mwt: 698.42): C, 58.47; H, 3.46; N, 8.02; Cl, 10.15; Co, 8.44%. Found: C, 58.02; H, 3.16; N, 8.27; Cl, 9.22; Co, 8.17%. M.P: (182–184 °C). IR ν (KBr disc)/cm⁻¹: 3650, 3023, 2933, 1649, 1593–1559, 424–472. Λ_m/Ω⁻¹ cm² mol⁻¹ (in DMF22). Color: brown.

[Ni(L¹)₂Cl₂]H₂O. [C₃₄H₂₆O₅N₄Cl₂Ni]; (Mwt.: 700.19): C, 58.49; H, 3.46; N, 8.79; Cl, 10.16; Ni, 8.02%. Found: C, 58.17; H, 3.12; N, 8.92; Cl, 9.96; Ni, 7.89%. M.P: (161–163 °C). IR ν (KBr disc)/cm⁻¹: 3440, 3088, 2987, 1664–1651, 1622, 1554, 542, 455. Λ_m/Ω⁻¹ cm² mol⁻¹ (in DMF16). Color: brown.

[Cu(L¹)₂Cl₂]H₂O. [C₃₄H₂₆O₅N₄Cl₂Cu]; (Mwt: 705.05): C, 64.40; H, 4.13; N, 8.84; Cu, 10.02%. Found: C, 64.11; H, 3.98; N, 8.90; Cu, 9.95%. M.P: (198–200 °C). IR ν (KBr disc)/cm⁻¹: 3200–3600, 3012, 2901, 1645, 1622, 1624, 1585, 1566, 1533, 511–559, 434–489. Λ_m/Ω⁻¹ cm² mol⁻¹ (in DMF31). Color: purple.

[Cd(L¹)₂]Cl₂·H₂O. [C₃₄H₂₆O₅N₄Cl₂Cd]; (Mwt: 753.91): C, 64.40; H, 4.13; N, 8.84; Cd, 10.02%. Found: C, 64.11; H, 3.98; N, 8.90; Cd, 9.95%. M.P: (195–197 °C). IR ν (KBr disc)/cm⁻¹: 3043, 2926, 1656, 1611, 1599, 1579, 546, 434. Λ_m/Ω⁻¹ cm² mol⁻¹ (in DMF 90). Color: purple.

[Co(L²)₂Cl₂]. [C₂₄H₁₄O₆N₂S₂Cl₂Co]; (Mwt: 620.35): C, 46.47; H, 2.27; N, 4.52; S, 10.34; Cl, 11.43; Co, 9.47%. Found: C, 46.09; H, 2.11; N, 4.63; S, 10.22; Cl, 11.09; Co, 9.13%. M.P: (200–202 °C). IR ν (KBr disc)/cm⁻¹: 3089, 1606, 1550, 754, 620. Λ_m/Ω⁻¹ cm² mol⁻¹ (in DMF 22). Color: Green.

[Ni(L²)₂Cl₂]2H₂O. [C₂₄H₁₈O₈N₂S₂Cl₂Ni]; (Mwt: 656.14): C43.93; H, 2.77; N, 4.27; S, 9.77; Cl, 10.81; Ni, 8.95%. Found: C, 43.12; H, 2.09; N, 4.50; S, 9.22; Cl, 10.51; Ni, 8.21%. M.P: (> 300 decomposition). IR ν (KBr disc)/cm⁻¹: 3340, 3302, 3120, 1714, 1630, 1606, 1558, 1292, 1249, 624, 752. Λ_m/Ω⁻¹ cm² mol⁻¹ (in DMF 14). Color: Dark green.

[Cu(L²)₂Cl₂]. [C₂₄H₁₄O₆N₂S₂Cl₂Cu]; (Mwt: 624.96): C, 46.12; H, 2.26; N, 4.48; S, 10.26; Cl, 11.35; Cu, 10.17%. Found: C, 45.91; H, 2.19; N, 4.66; S, 10.01; Cl, 11.12; Cu, 9.98%. M.P: (190–192 °C). IR ν (KBr disc)/cm⁻¹: 3148, 1728, 1718, 1635, 1606, 1560, 1244, 1166, 622, 758. Λ_m/Ω⁻¹ cm² mol⁻¹ (in DMF 19). Color: Silver.

[Cd(L²)₂]Cl₂. [C₂₄H₁₄O₆N₂S₂Cl₂Cd]; (Mwt: 673.82): C, 46.64; H, 2.80; N, 3.89; S, 8.89; Cl, 10.52; Cd, 15.59%. Found: C, 46.13; H, 2.43; N, 3.98; S, 8.67; Cl, 10.21; Cd, 15.33%. M.P: (260–262 °C). IR ν (KBr disc)/cm⁻¹: 3128, 1728, 1606, 1590, 1367, 1290, 725, 634. Λ_m/Ω⁻¹ cm² mol⁻¹ (in DMF 120). Color: Grey.

DFT procedure

The electronic structures of the two series of Schiff base ligands, L¹ and L², and their metal complexes including Co(II), Ni(II), Cu(II) and Cd(II) have been optimized by density functional calculations (DFT) without any symmetry constraints, employing the Gaussian 09-package [13]. Frequency calculations were performed on all the optimized geometries to ensure the correct local minima. All the calculations were carried out in the framework of the Becke three-parameter

hybrid exchange and Lee–Yang–Parr correlation functional (B3LYP) together with a split-valence Pople basis set plus polarization and diffuse functions, 6-31+G(d,p) for H, C, N, O, Cl and S atoms and a double- ζ quality LANL2DZ basis set for metal atoms [14]. All the “inner electrons” of metal ions were replaced and described with a scalar relativistic electron core potential (ECP). Time-dependent density functional theory (TD-DFT) calculations were performed to obtain the UV-Vis spectra and characterization of the frontier orbital, at B3LYP/6-31+G (d,p) level with the polarized continuum model (CPCM) in DMF solvent [15].

RESULTS AND DISCUSSION

Analysis and Physical Measurements

All the complexes are sparingly soluble in common organic solvents but highly soluble in DMF and DMSO. The analytical data indicate that the complexes are mononuclear with a 2:1 molar ratio of ligand to the metal ion. The molar conductance in DMF for all complexes are in agreement of their structures with no remarkable conductivity due to absence of chloride counter ions while the cadmium(II) complexes were electrolyte in 2:1 ratio due to the motion of positively ionic complex and chloride counterion [16], and the complexes have the

formula $[M(L^1)_2Cl_2] \cdot H_2O$ where $M = Co(II), Ni(II), [Cu(L^1)_2Cl_2]$ and $[Cd(L^2)_2]Cl_2 \cdot 2H_2O$.

Mass Spectra

Fig. 1 clearly exhibits the molecular ion peak $m/e = 188$ which agree well with the formula $C_{11}H_8O_3$ [16]. As well as the bromination of 3-acetyl coumarin (A) by Br_2 in chloroform solution leads to A2 derivative which its mass spectra in Fig. 2 displays a base peak at 267 that is consistent with $C_{10}H_7O_3Br$. However, the other peaks at 186 and 88 are extremely attributed to $M-Br^+$ ion. The ring closure of 1,2-phenylenediamine with A2 derivative, Scheme 3 results in ligand L^1 which shows molecular ion $m/e = 274$ at relative intensity 100% then supports the proposed structure of the L^1 ligand. On the other hand, the Fig. 3 represents the mass spectra of L^2 ligand which shows absorptions at 245, 244, 192, 160, 128 and 81 that are assigned to $C_{12}H_7NSO_3$ and fragments of $M-SCN$, $M-CH_2SCN$ and the base peak of $C_5H_5O^+$ respectively [17], Fig. 3.

NMR Spectra

The 1H -NMR spectra of the L^1 ligand in d_6 -DMSO solvent. Fig. 4 shows multiple signals at 6.5-7.90 ppm, corresponding to the eight protons aromatic ring protons

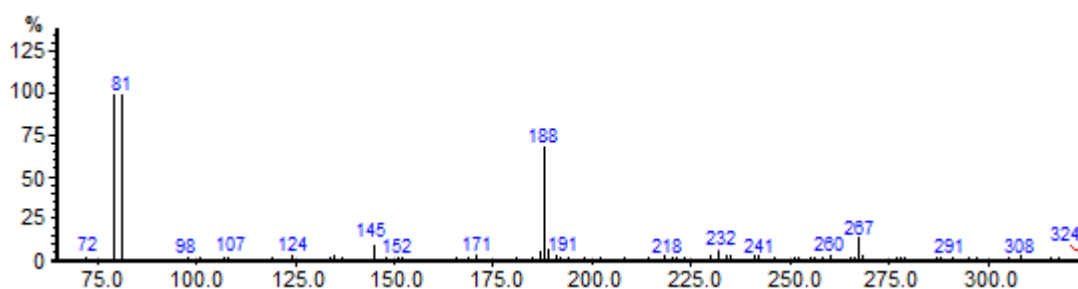


Fig 1. Mass of ω-bromo-3-acetylcoumarin

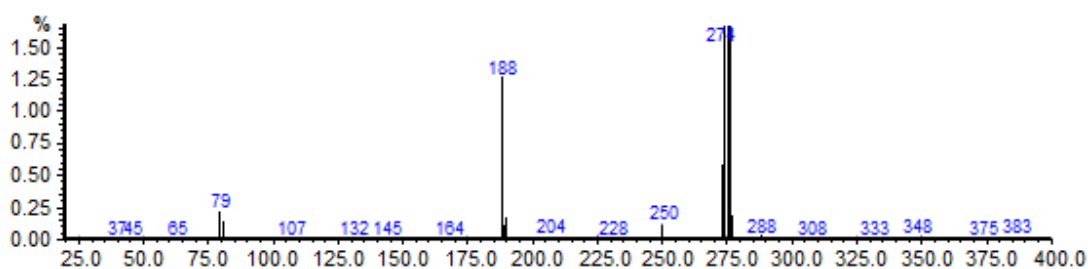


Fig 2. Mass of L^1

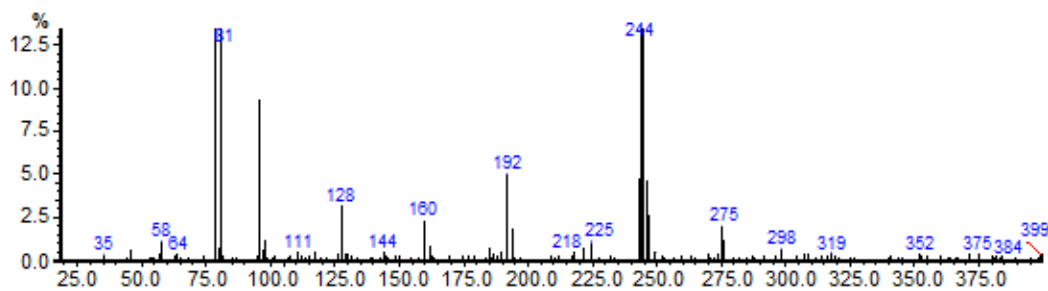


Fig 3. Mass of 3-(2-thiocyanatoacetyl)-2H-chromen-2-one L²

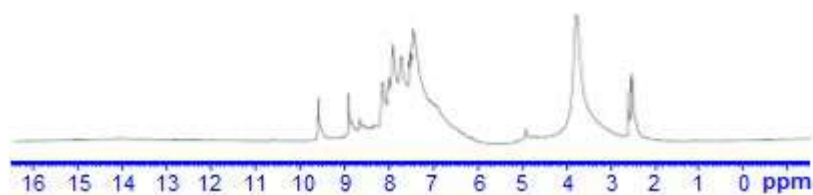


Fig 4. H-NMR spectra of L¹ in *d*₆-DMSO solvent

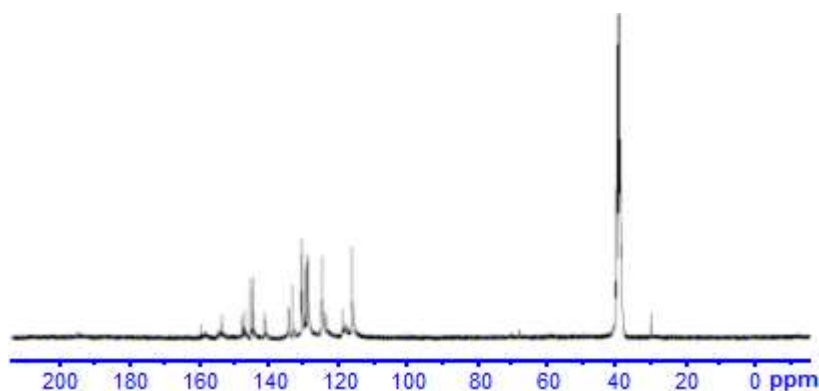


Fig 5. ¹³C-NMR spectra of L¹ in *d*₆-DMSO solvent

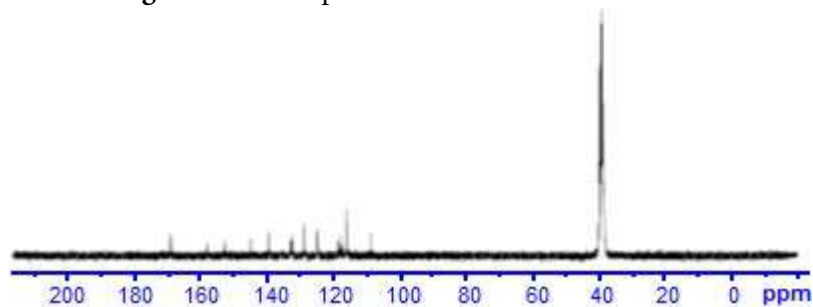


Fig 6. ¹³C-NMR spectra of L² in *d*₆-DMSO solvent

of the phenyl and pyrazine moieties [18]. The singlet at 4.60 ppm was attributed to the two protons of the $-\text{CH}_2-\text{Br}$ group [10]. The signal of the $-\text{NH}$ proton in the quinoxaline moiety was observed at 9.55 ppm, and the singlet peak at 8.77 ppm is attributed to $\text{H}-\text{C}=\text{C}-$ in position 4 of the coumarin ring. As well as the Fig. 5 shows the ¹³C-NMR of L¹ in *d*₆-DMSO which displays resonance peaks related to aromatic $-\text{C}=\text{C}-$ in the regions (113-125)

ppm and 127-131 ppm are assigned to $-\text{C}=\text{O}$, $-\text{C}=\text{N}$ - and $-\text{C}-\text{N}$ moieties respectively. The Fig. 5-6 show the ¹H and ¹³C-NMR spectra of L² in *d*₆-DMSO where the absorptions in the region 6.2-7.80 ppm are ascribed to Ar-H protons and the chemical shift at (8.04-8.70) ppm are assigned to protons of the annulated coumarin ring [12-16]. The singlet peak at (11.40-11.50) ppm may be attributed to $\text{H}-\text{C}=\text{C}$ of the coumarin ring in C₄

position. However, the weak peak at 4.10 ppm could be assigned to $\text{CH}_2\text{-Br}$ due to the effect of electron-withdrawing effect of bromine and thiocyanato groups on the deshielding of aliphatic protons toward the weak magnetic field [11,19].

FT-IR Spectra

The appearance of medium absorptions around $(780\text{-}870)\text{ cm}^{-1}$ in the IR-spectrum of ω -bromo-3-acetylcoumarin confirms the bromination on methyl group of the starting material [16-20]. As well as the strong absorptions in the IR spectrum of L^1 around 2962, 1710, and 1630 cm^{-1} could be attributed to aliphatic $\text{-CH}_2\text{-}$, -C=O of pyran ring and -C=C- moiety respectively [12]. Furthermore, the IR spectrum of ligand L^1 exhibited medium band at 1630 cm^{-1} assigned to -C=N- of quinoxaline moiety then support the ring closure up on condensation with 1,2-phenylenediamine [13]. However, the L^2 ligand displayed distinct bands around 1450-1590, 2230-2130 and 1735 cm^{-1} assigned to -C=N- , -S-C=N- and -C=O respectively then confirms the proceeding the nucleophilic substitution of -SCN on the carbon atom bearing -Br moiety [11,17]. The comparison of the positions of these bands with those observed in the infrared spectra of its Ni(II), Co(II), Cu(II) and Cd(II) complexes indicated that the band at $1670\text{-}1705\text{ cm}^{-1}$ showed a marked shift, this discussed that carbonyl group shared in the chelation toward metal ions under study, whereas the broad bands around $(3328\text{-}3306)\text{ cm}^{-1}$ may be resulted from stretching vibration of coordinated water molecules in the structures of metal complexes [17]. This fact suggests the coordination of L^2 through the nitrogen -S-CN and oxygen of -C=O together and tending to form stable complexes. The observed medium intensity band at 912 cm^{-1} in the free L^2 ligand assigned to the rocking of $\delta(\text{CSC})$ moiety with lowering in their energies in all IR spectra of metal complexes to a range $890\text{-}910\text{ cm}^{-1}$ confirming the participation of nitrogen atom in bonding with the empty orbitals of the metal ion [1,12]. On the other hand, the new absorptions in the regions 400-470 and $490\text{-}5440\text{ cm}^{-1}$ are ascribed to M-O and M-N bonds [21-22].

Magnetic Measurements

The magnetic susceptibilities of the complexes, recorded at room temperature show low magnetic moments indicating the presence of a spin-exchange interactions between the metal ions. The values obtained of copper(II) complexes lie in the 1.73-1.85 BM range and corresponds to one unpaired electron. As well as the orbital contributions of cobalt(II) and nickel(II) complexes in the ranges 4.8-4.9 and 2.88-3.22 BM respectively indicating the high spin octahedral structures around Co(II) and Ni(II) ions [23]. The expected enhancement in the values of magnetic moments for cobalt(II) complexes are reasoned from the orbital contribution in the t_{2g} level [23] then supports the octahedral environment around the Co(II) ion, Table 1.

Electronic Spectral Studies

The ligands L^1 and L^2 exhibited similar spectral features in the UV-Vis region with bands around 255-310 and 330-366 nm, respectively. These absorptions are assigned to a ligand transition ($n\text{-}\pi^*$) and ($\pi\text{-}\pi^*$). The green solutions of cobalt(II) complexes exhibited weak peaks around 600-800 nm and 677-800 nm assigning to spin-allowed transitions ${}^4\text{T}_{1g} \rightarrow {}^4\text{T}_{2g}$, ${}^4\text{T}_{1g} \rightarrow {}^4\text{A}_{2g}$ respectively, then confirms the octahedral geometry of CoL complexes. As well as the nickel(II) complexes in DMF solutions displayed spin-allowed transitions at 488-722 nm and 477-766 nm respectively. Furthermore, the copper(II) complexes showed separated low-energy absorptions around 550-760 nm and 390-588 nm which attributed to ${}^2\text{B}_{1g} \rightarrow {}^2\text{B}_{2g}$ and ${}^2\text{B}_{1g} \rightarrow {}^2\text{E}_g$ transitions revealing the formation of distorted octahedral around Cu(II) ion [22-23]. However, the cadmium(II) complexes formed with L^1 showed only absorptions in the 250-350 nm indicating the charge transfer and the aromatic bands of the coumarin ring [23-25].

Thermal Analysis

The thermal degradation of Co(II), Cu(II) and Cd(II) complexes was studied using TG-DSC analysis, Table 2. The data from the thermogravimetric analysis clearly indicated that the decomposition of the complexes

Table 1. The electronic spectra and molar conductance of the prepared complexes

Compound	UV-visible λ (nm)	Tentative assignment	μ (B.M.)	Geometry	ϵ L.mole ⁻¹ .cm ⁻¹
L ¹	310	n \rightarrow π^*	-	-	7400
	255	$\pi \rightarrow \pi^*$			20000
[Co(L ¹) ₂ Cl ₂].2H ₂ O	340	LMCT	4.80	Octahedral	30000
	600	⁴ T _{1g} \rightarrow ⁴ T _{2g} (F)			1000
	800	⁴ T _{1g} \rightarrow ⁴ A _{2g} (F)			700
[Ni(L ¹) ₂ Cl ₂].H ₂ O	300	LMCT	2.88	Octahedral	18700
	488	³ A _{2g} \rightarrow ³ T _{2g} (F)			766
	722	³ A _{12g} \rightarrow ³ T _{1g} (F)			17900
[Cu(L ¹) ₂ Cl ₂]	249	LMCT	1.73	Octahedral	26100
	550	² A _{1g} \rightarrow ² B _{1g}			650
	760	² A _{1g} \rightarrow ² B _{2g}			1010
[Cd(L ¹) ₂]Cl ₂	319	n \rightarrow π^*	0.0	Tetrahedral	9570
	350	LMCT			13950
	389				24000
L ²	366	n \rightarrow π^*	-		10300
	330	LMCT			21200
[Co(L ²) ₂ Cl ₂].H ₂ O	290	$\pi \rightarrow \pi^*$	4.90	Octahedral	30000
	677	⁴ T _{1g} \rightarrow ⁴ T _{2g} (F)			1220
	800	⁴ T _{1g} \rightarrow ⁴ A _{2g} (F)			1010
[Ni(L ²) ₂ Cl ₂]	233	$\pi \rightarrow \pi^*$	3.22	Octahedral	27000
	477	³ A _{2g} \rightarrow ³ T _{2g} (F)			1033
	766	³ A _{12g} \rightarrow ³ T _{1g} (F)			944
[Cu(L ²) ₂ Cl ₂].2H ₂ O	306	n \rightarrow π^*	1.85	Octahedral	15500
	390	LMCT			31000
	588	² E _g \rightarrow ² T _{2g}			1300
[Cd(L ²) ₂]Cl ₂	290	n \rightarrow π^*	0.00	Tetrahedral	29400
	377	LMCT			23899

ϵ : molar extinction coefficients of the prepared compounds

Table 2. TG-DTA of Co(II), Cu(II) and Cd(II) complexes with the L¹ ligand

Compound	Decomposition step	Temperature range (°C)	Removes species	Weight loss % (Calc.)	Weight Loss % Found
[Co(L ¹) ₂ Cl ₂].2H ₂ O	1 st	147-181	2H ₂ O	2.64	2.04
	2 nd	181-247	Cl	5.4	4.4
	3 rd	247-352	(C ₂ H ₆ N ₂ Cl)	16.72	16.63
[Cu(L ¹) ₂ Cl ₂]	1 st	45-63.63	-2Cl	3.3	3.16
	2 nd	63-116.84	-C ₂ H ₆ N ₂ Cl	7.2	6.95
	3 rd	116-261	-C ₈ H ₁₀	14.04	13.75
	4 th	261.8-368	-C ₄ H ₂ O ₂	19.27	18.58
Cd[L ¹]Cl ₂	1 st	45-119	2Cl	2.44	2.37
	2 nd	119-222	-C ₂ H ₃ N	10.7	11.9
	3 rd	222-351	-C ₂ H ₂ N	18.57	17.1
			C ₂ H ₆ N ₂		

proceeds in three or four steps. The hydrated water molecules were lost between 50-63.63 °C in all complexes, Fig. 8-11. The CuL^1 complex with L^1 ligand showed exothermic peaks over temperatures (122 °C) as indicated

by DSC analysis. The corresponding values of the entropy of activation ΔS^* , wherein range -0.547 to $-0.480 \text{ J mole}^{-1}$. The negative values of ΔH^* means that the decomposition processes are endothermic, Fig. 7-8.

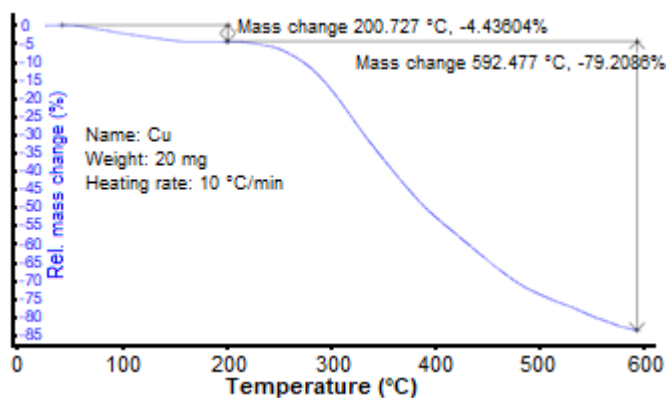


Fig 7. TG analysis of Cu(II) complex with L^1 ligand

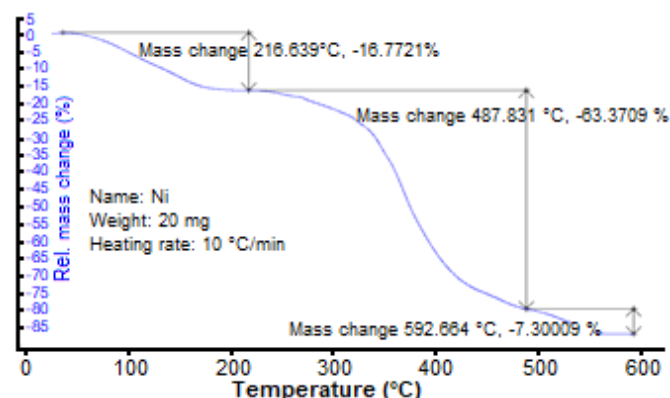


Fig 8. TG analysis of $[\text{Ni}(\text{L}^1)_2\text{Cl}_2]$ complex

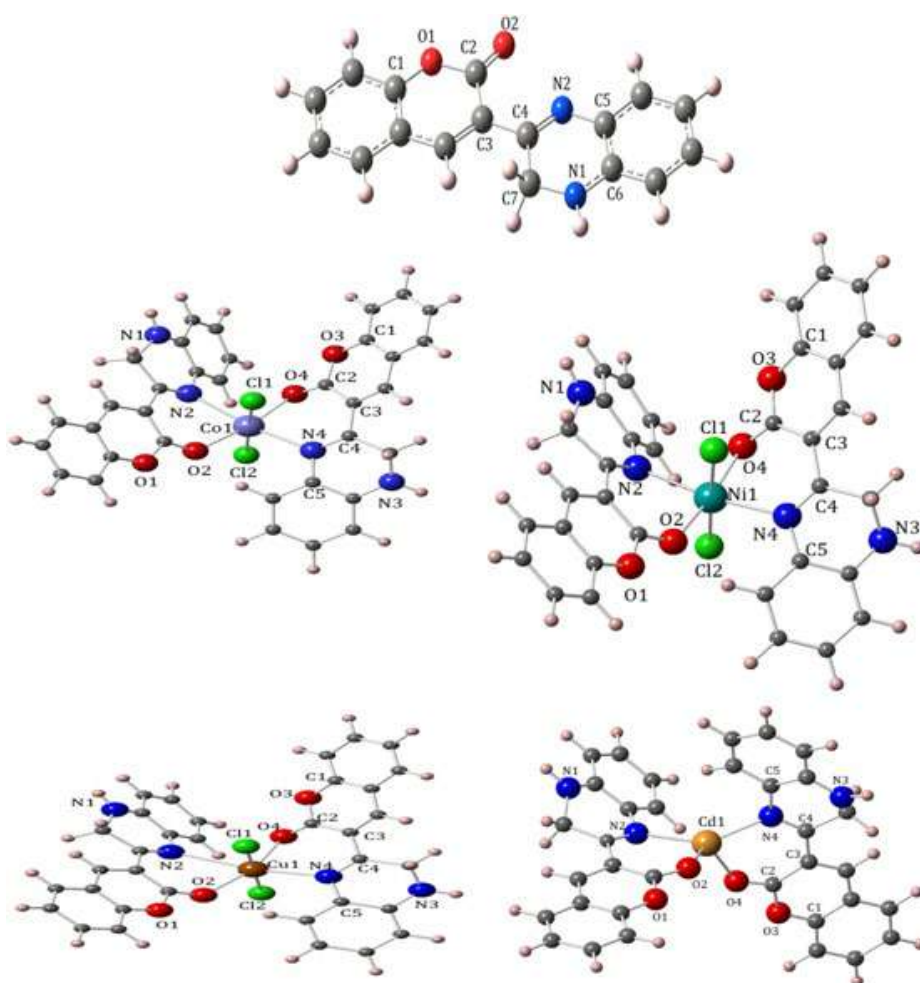


Fig 9. The optimized structures of L^1 series

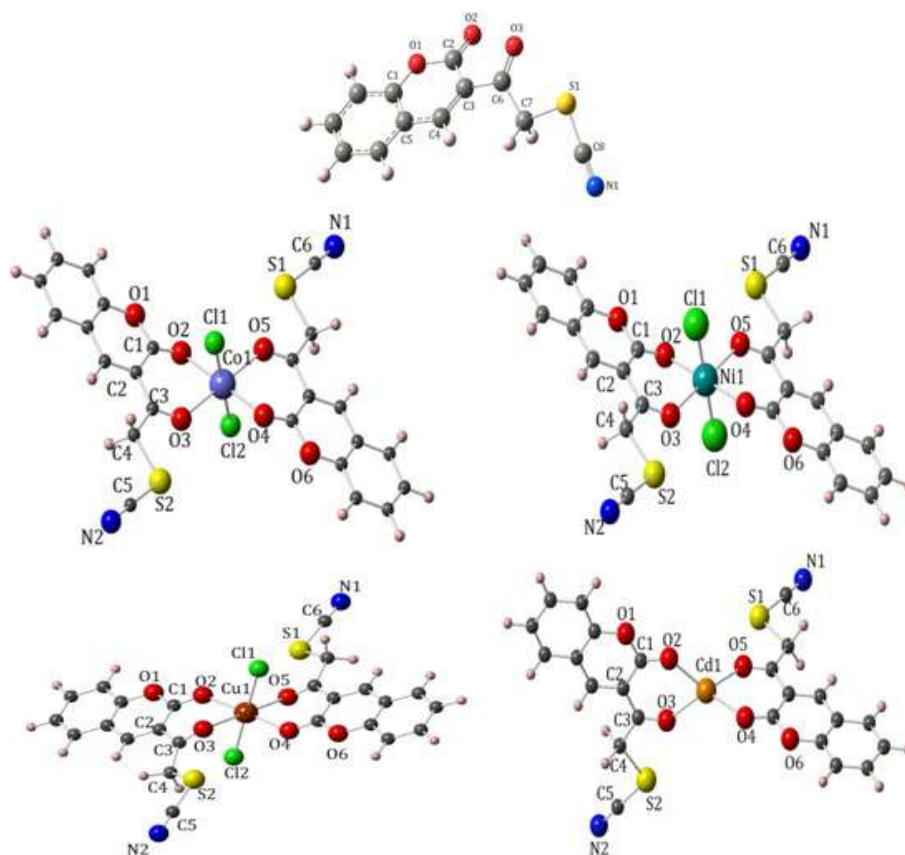


Fig 10. The optimized structures of L^2 series

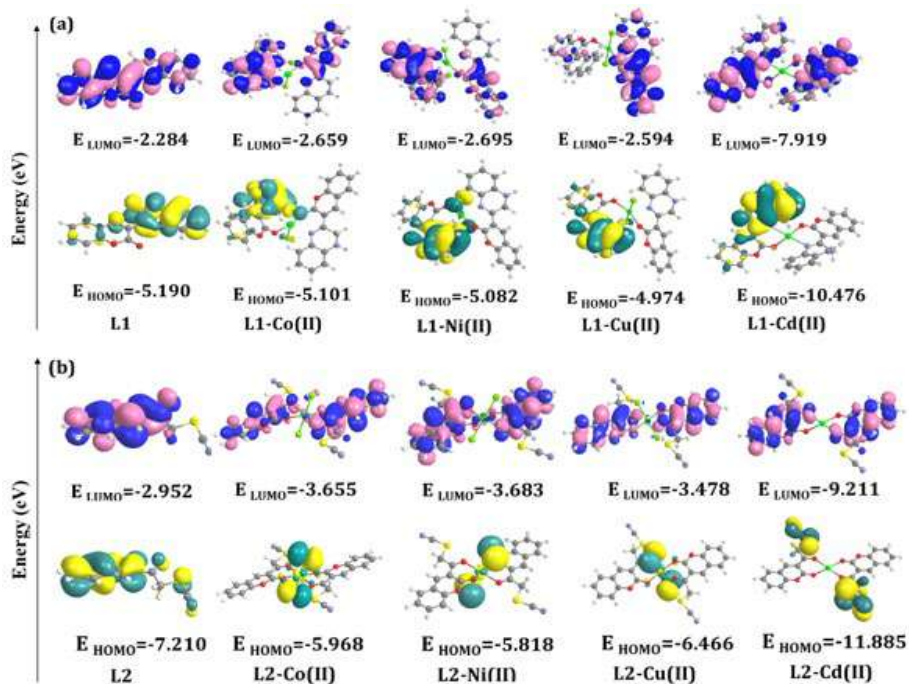


Fig 11. Surface plot of the frontier orbitals (α MOs) of the optimized Schiff base (a) L^1 and (b) L^2 and the related metal complexes along with their energies. The yellow and pink colors exhibit a positive charge and the green and blue colors show the negative charge

Theoretical Studies

Structural optimization

To establish the electronic structures of the L^1 and L^2 Schiff base ligands and the corresponding metal complexes with Co(II), Ni(II), Cu(II) and Cd(II) ions DFT computations were employed in the ground state. The geometric structures of the isolated ligands (L^1 and L^2) together with their complexes were fully optimized using B3LYP functional. Due to the conjoint of the electronic spectra and magnetic susceptibility measurements, a plausible octahedral geometries suggested for the cobalt(II), Nickel(II) and copper(II) complexes while the cadmium(II) complexes adopt a tetrahedral geometry. The optimized structures of the titled compounds of L^1 and L^2 series were depicted in Fig. 11 and 12, respectively. The optimized geometric parameters are given in Table 3. Both L^1 and L^2 ligands behave as a bidentate ligand so far the coordination in L^1 is achieved through the phenoxo O(2), the imine N(2), while in L^2 is occurred via both phenoxo O(2) and O(3) atoms. So, the best possible structures of Co(II), Ni(II), Cu(II) complexes of both Schiff bases have resulted in a distorted octahedral coordination sphere in which two chlorine atoms were coordinated in the axial position of the complexes. On the other hand, the cadmium(II) complexes have a different geometry than the other metal ions with a tetrahedral geometry, coordinating the phenoxo O(2) and O(4) and the imine N(2) and N(4) atoms relevant to L^1 and also phenoxo O(2,4) and carbonyl O(3,5) atoms in L^2 analogue, Fig. 9-10.

TD-DFT calculations

In order to get deep insights into the electronic transitions and the compositions of the molecular orbitals (MOs), TD-DFT calculations on the optimized geometries were employed by the PCM method, taken in DMSO solution [15]. A contour plot of selected molecular orbital with its density value $0.02 e \text{ Bohr}^{-3}$ are given in Fig. 11. TD-DFT results showed that upon coordination of both Schiff base ligands to metal ions the energy differences of the frontier molecular orbital HOMO-LUMO considerably decrease so that energy gap in Cu(II) complex of both L^1 and L^2 ligands is lower than those for

other compounds. The analysis of the MO compositions revealed that the contributions of metal ions in the higher HOMO levels and lower LUMO levels in L^1 complexes are very negligible, while these contributions are increased in lower HOMO levels (H-4, 14% Co, 13% Ni, 5% Cu and H-10 3% Cd). Also, the compositions in the higher LUMO levels were obtained (L+12, 75% Co, 75% Ni, 72% Cu and L+14, 50% Cd) along with reduced contribution (~18%) of π ligand L^1 . In addition, in L^2 complexes the major contributions for L+14 are (62% Co, 59% Ni, 62% Cu and 45% Cd) and those for H-11 are taken (23% Co, 19% Ni, 19% Cu and 3% Cd) along with reduced contribution of the L^2 ligand fragment about 80% for lower HOMO levels and 36% for the lower LUMO levels. From theoretical findings, it is clear that the most electron density is localized over the almost whole Schiff base and chlorine ligands and metal ions have insignificant participated in major HOMO and LUMO orbital.

The electronic transitions of the titled compounds are carried out using TDDFT/CPCM calculations in DMSO solvent in order to find out more details of the absorption bands about the compounds of this study. The results of TDDFT computations together with the experimental measurements of the metal complexes of both L^1 and L^2 ligand are tabulated in Table 4 and Table 5, respectively. The calculated singlet-singlet transitions obtained from TDDFT are a reasonable agreement with the experimental ones. Fig. 12 and 13 show the TD-DFT spectra and molecular orbital diagram together with major electronic excited states of the compounds, respectively. The results reveal that the experimental peaks at around 800 nm for CoL^1 and CoL^2 (assigned to ${}^4T_{1g} \rightarrow {}^4A_{2g}(F)$) are not resolved theoretically. A similar observation has been encountered in case of complex NiL^2 where the experimental peak at 766 nm (assigned to ${}^3A_{2g} \rightarrow {}^3T_{1g}(F)$) are not observed in theoretical one which those may be attributed to asymmetry forbidden transition in TD-DFT computations [26]. However, there may be an experimental peak due to vibronic couplings in this case.

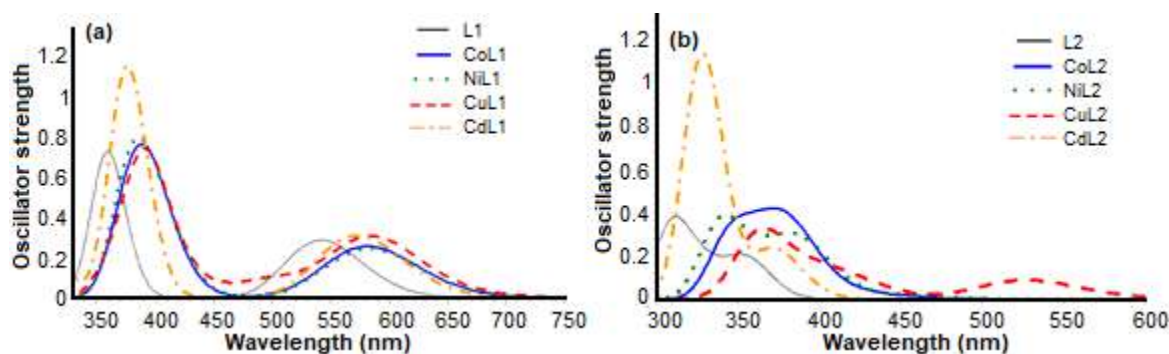
The other low energy peak at 568.9 nm of complex CdL^1 cannot be identified from its experimental spectra.

Table 3. The electronic transition calculated by TDDFT/CPCM method of L¹ and its metal complexes

	Bond length (Å)		Bond angle (°)		Bond length (Å)		Bond angle (°)	
L¹	C(1)-O(1)	1.36	O(3)-C(2)-O(4)	115.1	C(1)-O(1)	1.36	C(7)-S(1)	1.848
	C(2)-O(1)	1.41	C(4)-N(4)-C(5)	121	C(2)-O(1)	1.4	C(8)-S(1)	1.705
	C(2)-O(2)	1.2			C(2)-O(2)	1.2	C(8)-N(1)	1.167
	C(6)-N(1)	1.37			C(6)-N(1)	1.37	S(1)-C(8)-N(1)	177.9
	C(7)-N(1)	1.45			C(2)-C(3)	1.48	C(7)-S(1)-C(8)	96.81
	C(4)-N(2)	1.29			C(3)-C(4)	1.36	C(6)-C(7)-S(1)	108
	C(5)-N(2)	1.39			C(4)-C5)	1.44	O(1)-C(2)-O(2)	117.6
	C(2)-C(3)	1.49			C(1)-C(5)	1.41	O(3)-C(2)-C(3)	122.2
CoL¹	Co(1)-Cl(1)	2.52	N(2)-Co(1)-N(4)	168.8	Co(1)-Cl(1)	2.41	C(5)-S(2)	1.76
	Co(1)-Cl(2)	2.4	O(2)-Co(1)-O(4)	169.2	Co(1)-Cl(2)	2.41	C(5)-N(2)	1.769
	Co(1)-O(2)	2.11	Cl(1)-Co(1)-Cl(2)	173.9	Co(1)-O(2)	2.15	Cl(1)-Co(1)-O(5)	94.2
	Co(1)-O(4)	2.12	O(3)-C(2)-O(4)	115.3	Co(1)-O(4)	2.15	Cl(1)-Co(1)-O(2)	87.01
	Co(1)-N(2)	2.32	C(4)-N(4)-C(5)	119.5	Co(1)-O(3)	2.16	Cl(2)-Co(1)-O(3)	94.23
	Co(1)-N(4)	2.36			Co(1)-O(5)	2.16	Cl(2)-Co(1)-O(4)	87.02
	C(1)-O(3)	1.24			C(1)-O(1)	1.4	O(2)-Co(1)-O(3)	80.14
	C(2)-O(4)	1.39			C(2)-O(2)	1.23	O(5)-Co(1)-O(4)	80.14
NiL¹	C(2)-C(3)	1.46			C(2)-C(3)	1.48	C(4)-S(2)-C(5)	95.43
	C(4)-N(2)	1.31			C(3)-O(3)	1.25	S(2)-C(5)-N(2)	178.3
	C(5)-N(2)	1.42			C(4)-S(2)	1.91		
	Ni(1)-Cl(1)	2.53	N(2)-Ni(1)-N(4)	170.6	Ni(1)-Cl(1)	2.43	C(5)-S(2)	1.76
	Ni(1)-Cl(2)	2.41	O(2)-Ni(1)-O(4)	171.5	Ni(1)-Cl(2)	2.43	C(5)-N(2)	1.177
	Ni(1)-O(2)	2.06	Cl(1)-Ni(1)-Cl(2)	176.2	Ni(1)-O(2)	2.09	Cl(1)-Ni(1)-O(5)	94.16
	Ni(1)-O(4)	2.07	O(3)-C(2)-O(4)	115.4	Ni(1)-O(4)	2.09	Cl(1)-Ni(1)-O(2)	86.9
	Ni(1)-N(2)	2.28	C(4)-N(4)-C(5)	119.4	Ni(1)-O(3)	2.09	Cl(2)-Ni(1)-O(3)	86.89
NiL²	Ni(1)-N(4)	2.26			Ni(1)-O(5)	2.09	Cl(2)-Ni(1)-O(4)	94.15
	C(2)-O(3)	1.39			C(1)-O(1)	1.4	O(2)-Ni(1)-O(3)	83.82
	C(2)-O(4)	1.24			C(2)-O(2)	1.24	O(5)-Ni(1)-O(4)	83.81
	C(2)-C(3)	1.46			C(2)-C(3)	1.25	C(4)-S(2)-C(5)	95.97
	C(4)-N(4)	1.31			C(3)-O(3)	1.48	S(2)-C(5)-N(2)	178.4
	C(5)-N(4)	1.42			C(4)-S(2)	1.91		
	Cu(1)-Cl(1)	2.41	N(2)-Cu(1)-N(4)	168.6	Cu(1)-Cl(1)	2.37	C(5)-S(2)	1.76
	Cu(1)-Cl(2)	2.35	O(2)-Cu(1)-O(4)	161.9	Cu(1)-Cl(2)	2.37	C(5)-N(2)	1.177
CuL¹	Cu(1)-O(2)	2.14	Cl(1)-Cu(1)-Cl(2)	177.4	Cu(1)-O(2)	2.05	Cl(1)-Cu(1)-O(5)	95.74
	Cu(1)-O(4)	2.18	O(3)-C(2)-O(4)	115.5	Cu(1)-O(4)	2.05	Cl(1)-Cu(1)-O(2)	88.38
	Cu(1)-N(2)	2.59	C(4)-N(4)-C(5)	120.2	Cu(1)-O(3)	2.42	Cl(2)-Cu(1)-O(3)	88.4
	Cu(1)-N(4)	2.27			Cu(1)-O(5)	2.42	Cl(2)-Cu(1)-O(4)	95.74
	C(2)-O(3)	1.4			C(1)-O(1)	1.4	O(2)-Cu(1)-O(3)	77.12
	C(2)-O(4)	1.24			C(2)-O(2)	1.24	O(5)-Cu(1)-O(4)	77.12
	C(2)-C(3)	1.47			C(2)-C(3)	1.24	C(4)-S(2)-C(5)	95.37
	C(4)-N(4)	1.31			C(3)-O(3)	1.49	S(2)-C(5)-N(2)	178.2
CdL¹	C(5)-N(4)	1.42			C(4)-S(2)	1.91		
	Cd(1)-O(2)	2.18	N(2)-Cd(1)-N(4)	145.2	Cd(1)-O(2)	2.17	O(2)-Cd(1)-O(5)	126.6
	Cd(1)-O(4)	2.18	O(2)-Cd(1)-O(4)	113.9	Cd(1)-O(3)	2.21	O(3)-Cd(1)-O(4)	126.7
	Cd(1)-N(2)	2.29	O(3)-C(2)-O(4)	113.9	Cd(1)-O(4)	2.17	O(2)-Cd(1)-O(3)	78.27
	Cd(1)-N(4)	2.29	C(4)-N(4)-C(5)	121.2	Cd(1)-O(5)	2.21	C(4)-S(2)-C(5)	95.66
	C(2)-O(3)	1.37			C(1)-O(1)	1.37	S(2)-C(5)-N(2)	178.9
	C(2)-O(4)	1.26			C(1)-O(2)	1.26		
	C(2)-C(3)	1.46			C(2)-C(3)	1.46		
CdL²	C(4)-N(4)	1.32			C(3)-C(4)	1.51		
	C(5)-N(4)	1.42			C(4)-S(2)	1.91		

Table 4. The electronic transition calculated by TDDFT/CPCM method of L¹ and its metal complexes

Compound	Excited state	λ_{cal} (nm),(eV)	Oscillator strength (f)	Key transition	λ_{exp} (nm), ϵ L.mole ⁻¹ .cm ⁻¹	Character
L ¹	S3	359.4, 3.4496	0.7037	H-2→LUMO (%68)	310 (7400)	n → π*
	S6	292.1, 4.2436	0.1663	H-4→LUMO (%64)	255 (20000)	π → π*
	S12	255.7, 4.8488	0.1938	H-1→L+1 (%57)		
	S8	594.28, 2.0863	0.1187	HOMO (β)→LUMO (β) (%69)	340 (30000)	LMCT
CoL ¹	S9	576.4, 2.1508	0.1026	H-1 (β)→L+1 (β) (%60)	600 (1000)	⁴ T _{1g} → ⁴ T _{2g} (F)
	S21	415.0, 2.9875	0.0921	H-2 (α)→LUMO (α) (%67)	800 (700)	⁴ T _{1g} → ⁴ A _{2g} (F)
	S32	390.8, 3.1721	0.088	H-3 (α)→L+1 (α) (%66)		
	S37	381.2, 3.2524	0.1239	H-5 (β)→LUMO (β) (%60)		
NiL ¹	S6	596.5, 2.0783	0.1244	HOMO (α)→LUMO (α) (%69)	300 (17700)	LMCT
	S7	574.9, 2.1564	0.0994	H-1 (β)→LUMO (β) (%54)	410 (766)	¹ A _{1g} → ¹ B _{1g}
	S23	416.3, 2.9780	0.0684	H-2 (α)→LUMO (α) (%72)	422 (790)	¹ A _{1g} → ¹ B _{2g}
	S23	411.1, 3.0155	0.0327	H-2 (β)→LUMO (β) (%87)		
	S30	397.7, 3.1169	0.0631	H-3 (β)→L+1 (β) (%66)		
	S36	386.9, 3.2045	0.0763	HOMO (β)→L+4 (β) (%60)		
	S38	382.5, 3.2412	0.0935	H-6 (β)→LUMO (β) (%34)		
	S42	376.5, 3.2931	0.1279	H-4 (α)→L+2 (α) (%60)		
CuL ¹	S5	885.3, 1.4005	0.0007	H-6 (β)→LUMO (β) (%44)	249 (26100)	LMCT
	S13	591.1, 2.0973	0.1081	HOMO (β)→L+2 (β) (%65)	550 (650)	² A _{1g} → ² B _{1g}
	S14	583.9, 2.1233	0.1707	H-1 (β)→L+3 (β) (%59)	760 (1010)	² A _{1g} → ² B _{2g}
	S27	438.6, 2.8264	0.0272	H-10 (β)→LUMO (β) (%46)		
	S29	426.9, 2.9041	0.0309	H-10 (β)→LUMO (β) (%55)		
	S34	398.8, 3.1088	0.1639	H-2 (α)→LUMO (α) (%63)		
CdL ¹	S50	359.3, 3.4499	0.127	H-5 (α)→L+1 (α) (%47)		
	S2	568.9, 2.1790	0.1464	H-1 →LUMO (%69)	319 (9570)	n → π*
	S5	386.4, 3.2082	0.0277	H-1 →L+2 (%59)	350 (13950)	LMCT
	S7	376.6, 3.2918	0.6494	H-3 →LUMO (%45)	389 (24000)	LMCT
	S9	373.2, 3.3217	0.1599	H-2 →LUMO (%48)		
S17	308.2, 4.0222	0.2879	H-7 →LUMO (%51)			

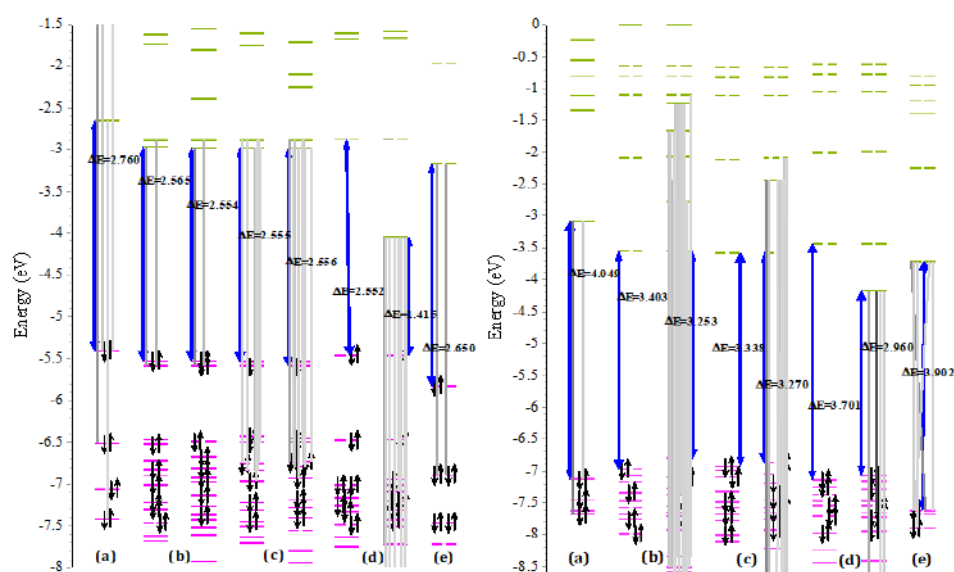
**Fig 12.** TDDFT calculations of UV-Vis spectra of the metal complexes of (a) L¹ and (b) L²

As shown in Fig. 13 the HOMOs are of π orbital localized on the different fragments of both L¹ and L². On the other hand, The LUMOs have localized more on

π^* orbital of the ligands and metal ions orbital play an insignificant role in the HOMOs and LUMOs. So, both these transitions are intra-ligand $\pi \rightarrow \pi^*$ in nature, Fig. 12 [27].

Table 5. The electronic transition calculated by TDDFT/CPCM method of L² Schiff base and its metal complexes

Compound	Excited state	λ_{cal} (nm),(eV)	Oscillator strength (f)	Key transition	λ_{exp} (nm), $\epsilon L.mole^{-1}.cm^{-1}$	Character
L ²	S2	354.7, 3.4949	0.1637	HOMO→LUMO (%62)	366 (10300)	$n \rightarrow \pi^*$
	S3	327.8, 3.7821	0.1394	H-1→LUMO (%65)	330 (21200)	LMCT
	S4	309.1, 4.0108	0.3363	H-2→LUMO (%66)		
	S9	471.5, 2.6295	0.0015	HOMO (β)→LUMO (β) (%100)	290 (30000)	$\pi \rightarrow \pi^*$
CoL ²	S11	449.9, 2.7558	0.0013	H-1 (α)→LUMO (α) (%97)	677 (1220)	$^4T_{1g} \rightarrow ^4T_{2g}(F)$
	S19	423.0, 2.9308	0.0091	H-1 (β)→L+1 (β) (%93)	800 (1010)	$^4T_{1g} \rightarrow ^4A_{2g}(F)$
	S29	388.9, 3.1875	0.1486	H-4 (β)→L+1 (β) (%78)		
	S33	374.9, 3.3070	0.2096	H-5 (β)→L+1 (β) (%73)		
	S49	344.9, 3.5945	0.272	H-4 (β)→L+2 (β) (%56)		
NiL ²	S10	460.4, 2.6927	0.0031	H-1(β)→LUMO (β) (%83)	233 (27000)	$\pi \rightarrow \pi^*$
	S16	446.3, 2.7777	0.0095	H-1 (α)→LUMO (α) (%81)	477 (1033)	$^3A_{12g} \rightarrow ^3T_{2g}(F)$
	S30	394.5, 3.1422	0.1814	H-4 (β)→L+1 (β) (%83)	766 (944)	$^3A_{12g} \rightarrow ^3T_{1g}(F)$
	S32	375.6, 3.3007	0.1191	HOMO (β)→L+4 (β) (%60)		
	S33	367.2, 3.3758	0.0405	H-7 (α)→L+1 (α) (%57)		
	S46	344.0, 3.6032	0.146	H-6 (β)→L+1 (β) (%51)		
	S49	336.4, 3.6848	0.1909	H-7 (β)→LUMO (β) (%53)		
	S5	648.1, 1.9128	0.0036	H-6 (β)→LUMO (β) (%44)	306 (15500)	$n \rightarrow \pi^*$
CuL ²	S8	527.2, 2.3518	0.0879	HOMO (β)→L+2 (β) (%65)	390 (31000)	LMCT
	S16	421.3, 2.9424	0.0485	H-1 (β)→L+3 (β) (%59)	588 (1300)	$^2E_g \rightarrow ^2T_{2g}$
	S32	400.4, 3.0961	0.0066	H-10 (β)→LUMO (β) (%46)		
	S28	386.6, 3.2070	0.0233	H-10 (β)→LUMO (β) (%55)		
	S39	366.0, 3.3874	0.0598	H-2 (α)→LUMO (α) (%63)		
	S44	354.6, 3.4957	0.0534	H-5 (α)→L+1 (α) (%47)		
CdL ²	S48	349.8, 3.5437	0.023	H-4 (α)→L+2 (α) (%52)		
	S2	372.7, 3.3261	0.0914	HOMO →L+2 (%61)	290 (29400)	$n \rightarrow \pi^*$
	S9	328.7, 3.7714	0.8854	H-4 →L+1 (%48)	377 (23890)	LMCT
	S12	325.4, 3.8100	0.2257	H-3 →L+2 (%47)		
	S21	253.1, 4.8968	0.4177	H-1 →L+4 (%31)		
S25	245.9, 5.0402	0.0636	H-3 →L+3 (%48)			

**Fig 13.** The molecular orbital diagram together with electronically excited states of (a) Schiff base L¹ and L², (b) CoL, (c) NiL, (d) CuL and (e) CdL in both α and β spin states

■ CONCLUSION

According to the results obtained from elemental analysis, spectral, magnetic susceptibility measurements and the TG-DSC analyses, the octahedral geometry around cobalt, nickel, and copper(II) ions. As well as the vibration absorptions obtained from experimental FT-IR were in well-agreement of their theoretical obtained from DFT calculations then support the bidentate behaviors of the two Lewis bases L^1 and L^2 . The optimized structures of all the synthesized complexes were shown in Fig. 11 and 12 and it is obvious that all complexes were octahedral except cadmium(II) which were tetrahedral and the TD-DFT results investigate the experimental data related to spectral analyses.

■ ACKNOWLEDGMENTS

We are so thankful for the members of chemistry department laboratories at Mustansiriyah University for carrying out the analysis of IR, UV and MS spectra. As well as we appreciate the facilities of Al-Bait University, Amman, Jordan for measuring of NMR spectra.

■ REFERENCES

- [1] Abdel-Shafi, A.A., Khalil, M.M.H., Abdalla, H.H., and Ramadan, R.M., 2002, Ruthenium, osmium and rhodium-2,3-bis(2'-pyridyl)quinoxaline complexes, *Transition Met. Chem.*, 27 (1), 69–74.
- [2] AL-Hashime, S.M., Sarhan, B.M., and Alazawi, S.A.S., 2007, Synthesis and studies of some mixed-ligand metal complexes containing benzotriazole with some other ligands, *J. Al-Nahrain Univ.*, 10 (2), 82–88.
- [3] Al-Jibouri, M.N., 2014, Template synthesis, characterization and antimicrobial study of new metal complexes from 2,6-diaminopyridine and 1,4-dihydroquinoxalin-2,3-dione, *Eur. Chem. Bull.*, 3 (4), 384–389.
- [4] Appendino, G., Mercalli, E., Fuzzati, N., Arnoldi, L., Stavri, M., Gibbons, S., Ballero, M., and Maxia, A., 2004, Antimycobacterial coumarins from the Sardinian giant fennel (*Ferulacommunis*), *J. Nat. Prod.*, 67 (12), 2108–2110.
- [5] Badawy, M.A., Mohamed, G.G., Omar, M.M., Nassar, M.M., and Kamel, A.B., 2010, Synthesis, spectroscopic and thermal characterization of quinoxaline metal complexes, *Eur. J. Chem.*, 1 (4), 282–288.
- [6] Bejaoui, L., Rohlicek, J., and Hassen, R.B., 2018, New cobalt(II) complexes of '3-acetyl-4-hydroxy-2H-chromene-2-one': Crystal structure and Hirshfeld surface analysis, fluorescence behaviour and antioxidant activity, *J. Mol. Struct.*, 1173, 574–582.
- [7] Cotton, F.A., Wilkinson, G., Murillo, C.A., and Bochmann, M., 1999, *Advanced Inorganic Chemistry*, 6th Ed., John Wiley & Sons, Inc., New York, USA.
- [8] Creaven, B.S., Egan, D.A., Kavanagh, K., McCann, M., Noble, A., Thati, B., and Walsh, M., 2006, Synthesis, characterization and antimicrobial activity of a series of substituted coumarin-3-carboxylatosilver(I) complexes, *Inorg. Chim. Acta*, 359 (12), 3976–3984.
- [9] Devienne, K.F., Raddi, M., Coelho, R.G., and Vilegas, W., 2005, Structure–antimicrobial activity of some natural isocoumarins and their analogues, *Phytomedicine*, 12 (5), 378–381.
- [10] Emmanuel-Giota, A.A., Fylaktakidou, K.C., Litinas, K.E., Nicolaidis, D.N., and Hadjipavlou-Litina, D.J., 2001, Synthesis and biological evaluation of several 3-(coumarin-4-yl)tetrahydroisoxazole and 3-(coumarin-4-yl)dihydropyrazole derivatives, *J. Heterocycl. Chem.*, 38 (3), 717–722.
- [11] Grazul, M., and Budzisz, E., 2009, Biological activity of metal ions complexes of chromones, coumarins and flavones, *Coord. Chem. Rev.*, 253 (21-22), 2588–2598.
- [12] Geary, W.J., 1971, The use of conductivity measurements in organic solvents for the characterisation of coordination compounds, *Coord. Chem. Rev.*, 7 (1), 81–122.
- [13] Frisch, M.J., Trucks, G.W., Schlegel, H.B., Scuseria, G.E., Robb, M.A., Cheeseman, J.R., Scalmani, G., Barone, V., Mennucci, B., Petersson, G.A., Nakatsuji, H., Caricato, M., Li, X., Hratchian, H.P., Izmaylov, A.F., Bloino, J., Zheng, G., Sonnenberg, J.L., Hada, M., Ehara, M., Toyota, K., Fukuda, R.,

- Hasegawa, J., Ishida, M., Nakajima, T., Honda, Y., Kitao, O., Nakai, H., Vreven, T., Montgomery, Jr., J.A., Peralta, J.E., Ogliaro, F., Bearpark, M., Heyd, J.J., Brothers, E., Kudin, K.N., Staroverov, V.N., Kobayashi, R., Normand, J., Raghavachari, K., Rendell, A., Burant, J.C., Iyengar, S.S., Tomasi, J., Cossi, M., Rega, N., Millam, J.M., Klene, M., Knox, J.E., Cross, J.B., Bakken, V., Adamo, C., Jaramillo, J., Gomperts, R., Stratmann, R.E., Yazyev, O., Austin, A.J., Cammi, R., Pomelli, C., Ochterski, J.W., Martin, R.L., Morokuma, K., Zakrzewski, V.G., Voth, G.A., Salvador, P., Dannenberg, J.J., Dapprich, S., Daniels, A.D., Farkas, O., Foresman, J.B., Ortiz, J.V., Cioslowski, J., and Fox, D.J., 2009, *Gaussian 09, Revision A.1*, Gaussian, Inc., Wallingford CT.
- [14] Lee, C., Yang, W., and Parr, R.G., 1988, Development of the Colle-Salvetti correlation-energy formula into a functional of the electron density, *Phys. Rev. B: Condens. Matter*, 37, 785–789.
- [15] Tomasi, J., Mennucci, B., and Cammi, R., 2005, Quantum mechanical continuum solvation models, *Chem. Rev.*, 105 (8), 2999–3094.
- [16] Brown D.J., Ellman J.A., and Taylor, E.C., 2004, *Quinoxalines, Supplement 2-Chemistry of Heterocyclic Compounds: A Series of Monographs*, 1st Ed., Wiley-Interscience, New York.
- [17] Kostova, I., Bhatia, S., Grigorov, P., Balkansky, S., Parmar, V.S., Prasad, A.K., and Saso, L., 2011, Coumarins as antioxidants, *Curr. Med. Chem.*, 18 (25), 3929–3951.
- [18] Kulkarni, N.V., Kurdekar, G.S., Budagumpi, S., and Revankar, V.K., 2010, Spectroscopy, structure, and electrochemistry of transition metal complexes having $[M_2N_2OS_2]$ coordination sphere, *J. Coord. Chem.*, 63 (18), 3301–3312.
- [19] Liu, F., Martin-Mingot, A., Lecornué, F., Jouannetaud, M.P., Maresca, A., Thibaudeau, S., and Supuran, C.T., 2012, Carbonic anhydrases inhibitory effects of new benzenesulfonamides synthesized by using superacid chemistry, *J. Enzyme Inhib. Med. Chem.*, 27 (6), 886–891.
- [20] Cotton, F.A., Wilkinson, G., Murillo, C.A., and Bochmann, M., 1999, *Advanced Inorganic Chemistry*, 6th Ed., John Wiley & Sons, Inc., New York.
- [21] Morse, G.E., Paton, A.S., Lough, A., and Bender, T.P., 2010, Chloro boron subphthalocyanine and its derivatives: dyes, pigments or somewhere in between?, *Dalton Trans.*, 39 (16), 3915–3922.
- [22] Shaker, S.A., Khaledi, H., and Ali, H.M., 2011, Spectroscopic investigations and physico-chemical characterization of newly synthesized mixed-ligand complexes of 2-methylbenzimidazole with metal ions, *Chem. Pap.*, 65 (3), 299–307.
- [23] Silverstein, R.M., and Bassler, G.C., 1962, Spectrometric identification of organic compounds, *J. Chem. Educ.*, 39 (11), 546.
- [24] Wang, C.J., Hsieh, Y.J., Chu, C.Y., Lin, Y.L., and Tseng, T.H., 2002, Inhibition of cell cycle progression in human leukemia HL-60 cells by esculetin, *Cancer Lett.*, 183 (2), 163–168.
- [25] Wright, J.S., Johnson, E.R., and DiLabio, G.A., 2001, Predicting the activity of phenolic antioxidants: Theoretical method, analysis of substituent effects, and application to major families of antioxidants, *J. Am. Chem. Soc.*, 123 (6), 1173–1183.
- [26] Shaffer, C.J., Martens, J., Marek, A., Oomens, J., and Tureček, F., 2016, Photoleucine survives backbone cleavage by electron transfer dissociation. A near-UV photodissociation and infrared multiphoton dissociation action spectroscopy study, *J. Am. Soc. Mass. Spectrom.*, 27 (7), 1176–1185.
- [27] Manna, S., Mistri, S., Bhunia, A., Paul, A., Zangrando, E., and Manna, S.C., 2017, Manganese(IV) complex with a polydentate Schiff base ligand: Synthesis, crystal structure, TDDFT calculation, electronic absorption and EPR spectral study, *J. Coord. Chem.*, 70 (2), 296–313.

Synthesis, Structural and Optical Characterization of Titanium Dioxide Doped by (Ce, Yb) Dedicated to Photonic Conversion

Zobair El Afia^{1,2,*}, Mohamed Youssef Messous², Mohammed Cherkaoui¹, and Mounia Tahri³

¹Laboratory of Materials, Electrochemistry, and Environment, Faculty of Sciences, University Ibn Tofail, 14000 Kenitra, Morocco

²Material Sciences Unit USM/DERS, National Center for Energy, Sciences and Nuclear Techniques-CNESTEN, B.P 1382 R.P 10001 Rabat, Morocco

³National Center for Energy, Sciences and Nuclear Techniques-CNESTEN-B.P 1382 R.P 10001 Rabat, Morocco

* **Corresponding author:**

email: zobair.elafia@gmail.com

Received: March 4, 2019

Accepted: September 4, 2019

DOI: 10.22146/ijc.43947

Abstract: The synthesis of TiO₂ co-doped by (Ce, Yb) rare earth couple has been realized. This couple of rare earth can convert a high-energy photon to two low energy photons to enhance the energy efficiency of silicon solar cells. The undoped, 2% Ce doped- and (2% Ce, 4% Yb) Codoped- Titanium oxide were prepared by the co-precipitation method. The Infrared spectroscopy FTIR-ATR analysis indicates a continuous visible absorption in the 750–400 cm⁻¹ region, confirming the formation of a titanium-oxygen bond. The X-Ray Diffraction characterization showed the dominance of the rutile crystalline phase with the presence of anatase one and the calculated crystallite size is between 7 to 13 nm. The X-Ray Fluorescence confirms the insertion of the dopants while the Inductively Coupled Plasma Mass Spectrometry ICP-MS showed the ratio 2 between Ce and Yb concentration. The thermogravimetric analysis indicated that Ce/Yb doped titanium was thermally stable. The absorption in the UV-visible (200 and 1000 nm) has been improved proportionally with the dopants.

Keywords: titanium dioxide; co-precipitation; rutile; anatase; photonic conversion

■ INTRODUCTION

Photovoltaic energy is one of the most important renewable energies, but this energy source has an efficiency limitation problem due to silicon used as a material for photon-electricity conversion. Recently, the Quantum Cutting process through which one high energy photon is converted into two near infrared ones attracted considerable attention. It can be adopted to minimize the energy loss by the thermalization of the charge carriers caused by the absorption of high-energy photons. Until here, some work has been done by combining Ytterbium (Yb) with other rare earth elements. In this paper, the preparation of Titanium dioxide, known as Titania, TiO₂, doped with the couple (Ce, Yb) was presented. It belongs to transparent semiconducting oxides (TCOs) class materials, which are simultaneously optically transparent

and electrically conductive. Titanium dioxide has great potential for a lot of applications such as photocatalytic treatment in wastewater, transparent devices in electronics and probes or light detectors and telecommunication transmitter devices [1-5].

There are different methods for the TiO₂ nanopowders preparation like thermal (ethanol thermal, hydrothermal and solvothermal) [6-12], dip coating [13], spin coating [14], electrochemical [15-17], chemical solvent [18], RF sputtering [19] and sol-gel [20-25]. The sol-gel process is one of the most successful techniques for preparing nanocrystalline TiO₂ due to its flexibility in fabrication, low cost, and low processing temperature. Due to the low absorption efficiency of commercial Silica-based cells, which are around 15%, titanium was used to improve the performance of these cells [26].

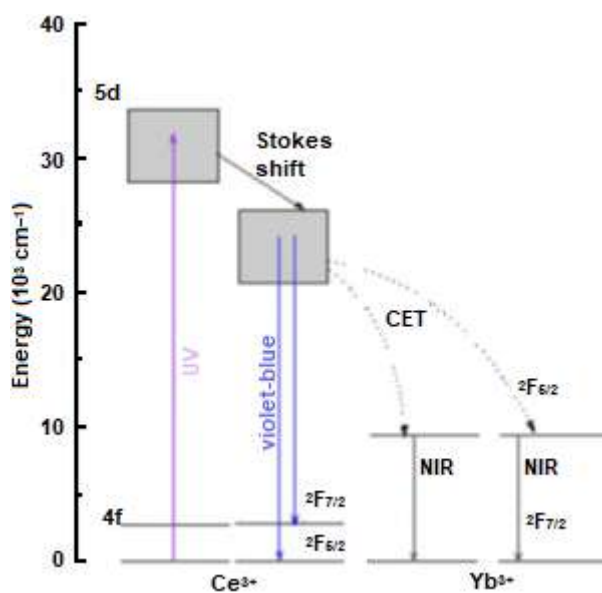


Fig 1. Schematic energy-level diagram of Ce/Yb cooperative energy transfer process from Ce^{3+} to Yb^{3+}

The synthesis of undoped and doped TiO_2 with Cerium and Ytterbium has been done by the co-precipitation method. This couple known for their exceptional optical properties attributed to down conversion [27-32], one ultraviolet/visible photon converted into two near infrared photons, which get absorbed by Si solar cells [33]. Indeed, the charge transfer (CT) follows the UV excitation of Ce^{3+} , from $\text{Ce}^{3+}:5d^1$ to $\text{Yb}^{3+}:^2F_{5/2}$ [34-37]. The NIR emission (976 nm and 1028 nm) occurs through the transition $\text{Yb}^{3+}:^2F_{5/2}$ to $\text{Yb}^{3+}:^2F_{7/2}$ Fig. 1 [38].

■ EXPERIMENTAL SECTION

Materials

The undoped and doped titanium dioxide, TiO_2 , was prepared using titanium trichloride solution 15% TiCl_3 (purity $\geq 99.95\%$), $\text{CeCl}_3 \cdot 7\text{H}_2\text{O}$ (99.9%) and $\text{YbCl}_3 \cdot 6\text{H}_2\text{O}$ (99.9%) precursors from Sigma-Aldrich. Fourier Transformed Infrared by Attenuated Total Reflection (ATR-FTIR) spectra was recorded in the $400\text{--}4000\text{ cm}^{-1}$ range on Perkin-Elmer spectrometer UATR two. Powder X-Ray diffraction (XRD) data was carried out with a D2-Phaser Diffractometer from Bruker. S2 Picofox-Bruker based on total reflection X-Ray Fluorescence (TXRF) used to provide a qualitative composition analysis when the

Inductively Coupled Plasma Mass Spectrometry ICP-MS exploited for quantitative one. For the thermogravimetric analysis, LABSYS EVO TGA was used in order to measure the amount of change in material as a function of increasing temperature.

Procedure

Undoped and doped TiO_2 preparation

For the preparation of undoped TiO_2 , 10 mL of titanium chloride was added in Erlenmeyer flask to 40 mL of distilled water. For the second sample TiO_2 (2% Ce) and the third TiO_2 (2% Ce, 4% Yb), 20 mg of CeCl_3 and (20 mg of CeCl_3 + 125 mg of YbCl_3) were added with TiCl_3 , respectively. The mixtures were prepared in an ice bath because the reaction was exothermic. The solutions were heated on a hot plate at $90\text{ }^\circ\text{C}$. The precipitates obtained dried at $110\text{ }^\circ\text{C}$ in an oven for 24 h.

■ RESULTS AND DISCUSSION

X-Ray Diffraction Analysis (XRD)

The XRD diffraction spectrum for synthesis materials is illustrated in Fig. 2. The exhibited diffraction peaks for undoped titanium dioxide at 2θ values 25.05° , 47.5° , and 62.43° are attributed to anatase phase corresponding to crystal plans (101), (200), (204). Rutile peaks are found at 26.81° , 35.67° , 40.65° , 43.53° , 53.7° , and 56° corresponding to crystal plans (110), (101), (200), (210) and (022). For the Cerium doped titanium, Fig. 2 showed the anatase peaks at 2θ value 24.92° , 47.44° , and 62.43° . The rutile peaks appeared at $2\theta = 26.9^\circ$, 35.6° , 40.69° , 43.44° , 53.69° , and 56° . For the third sample, the spectrum showed anatase peaks at $2\theta = 25.23^\circ$, 47.77° , and 62.49° , while the peaks at 26.96° , 35.65° , 40.93° , 43.5° , 53.87° , and 56° are attributed to rutile phase [39-40]. The additional intense peak at 31.2° in all samples is assigned to the reflection on (121) for the Brookite phase [36]. Average particle size D was estimated by using the Scherrer equation (Eq. (1)) [41], the results are presented in Table 1. The lattice parameters a , c and V for the undoped and doped titanium dioxide were calculated from the position (110) peak using the formulas in (Eq. (2)) [42]. Table 2 summarize all the calculated parameters. The introduction of Cerium and

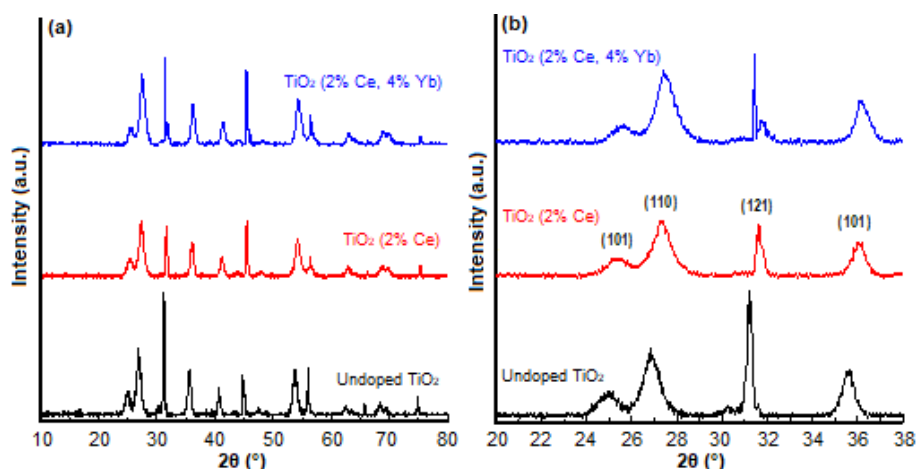


Fig 2. XRD of undoped and doped TiO₂: (a) total spectrum and (b) restricted spectrum

Table 1. Size crystallite D for the undoped TiO₂

Hkl	2θ (°)	Size (Å)
(101)	25.05	77.19
(103)	35.50	123.34
(121)	31.20	131.61

Table 2. Lattice parameters a, c, and V for different samples in plan (110)

	D (Å)	a (Å)	c (Å)	c/a	V (Å ³)
TiO ₂	88.39	3.85	6.68	1.73	86.10
TiO ₂ :2% Ce	76.75	3.84	6.65	1.73	85.26
TiO ₂ :2% Ce;4% Yb	79.22	3.83	6.64	1.73	84.70

Ytterbium atoms into TiO₂ shifted the position of the peak of TiO₂ (Fig. 2), reduced the grains size, and slightly decreased the lattice parameters Table 2.

$$D = \frac{K\lambda}{\beta \cos\theta} \quad (1)$$

$$a = \frac{\lambda}{\sqrt{3} \sin\theta} \quad \text{and} \quad c = \frac{\lambda}{\sin\theta} \quad (2)$$

where λ is the wavelength incident X-ray (= 1.549 Å); K: shape factor (= 0.9); β : Full-width at half maximum (FWHM) of the peak in the XRD patterns; θ : diffraction angle.

X-Ray Fluorescence Spectroscopy (XRF)

To study the elemental composition of TiO₂, qualitative analysis was performed by X-Ray Fluorescence (XRF) Spectroscopy analysis. The spectrum obtained is shown in Fig. 3. XRF pattern shows peaks at 4.51 keV and 4.93 keV corresponding to Ti, which is the major element present in the powder. The spectra corresponding to the doped TiO₂ shows Cerium at (4.80 keV; 5.26 keV; 5.61 keV; 6 keV and 6.30 keV) and Ytterbium at (7.18 keV and 8.40 keV) suggesting that

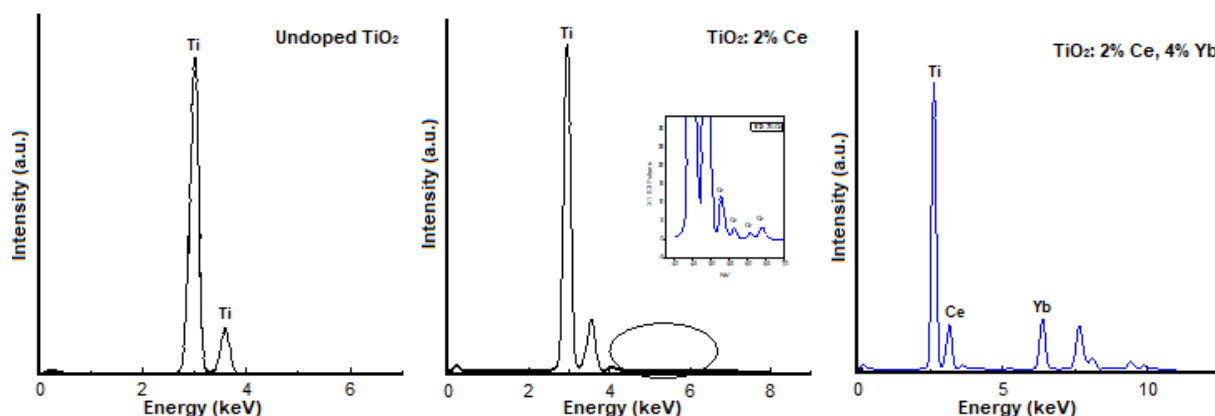


Fig 3. X-Ray fluorescence spectra of: undoped TiO₂; TiO₂ (2% Ce); TiO₂ (2% Ce, 4% Yb)

they were incorporated into the TiO_2 lattice. However, along with these elements, some impurities traces in the form of chlorine was observed.

Fourier Transform Infrared Spectroscopy (ATR-FTIR)

Fourier transform infrared spectroscopy was usually employed as an analytical technique to identify organic (in some cases inorganic) material. Fig. 4 shows the FTIR spectra for doped and undoped TiO_2 . Water and alcohol content is marked as a broad peak in the region $3100\text{--}3500\text{ cm}^{-1}$ and the narrow peak at $1620\text{--}1640\text{ cm}^{-1}$.

The continuous absorption visible in all the samples in the region $750\text{--}400\text{ cm}^{-1}$ are caused by the strong stretching vibrations of Ti-O and Ti-O-Ti bonds [43-44].

Inductively Coupled Plasma Mass spectroscopy ICP-MS

The concentrations obtained for sample (TiO_2 : 2% Ce, 4% Yb) by ICP-MS technique are $39.89 \pm 0.23\text{ mg/g}$ of ^{47}Ti , $4.20 \pm 0.06\text{ mg/g}$ of ^{140}Ce and $8.74 \pm 0.21\text{ mg/g}$ of ^{172}Yb . These data show a ratio of 2 between the concentrations of Ce and Yb and coincide with the quantity of the used precursors.

Thermogravimetric Analysis

The as-synthesized powder was measured for its thermal properties from room temperature to $900\text{ }^\circ\text{C}$. The TG analysis in Fig. 5 presents a weight loss of 8.5% between 25 to $198\text{ }^\circ\text{C}$, 4.5% in the range $198\text{--}600\text{ }^\circ\text{C}$ and

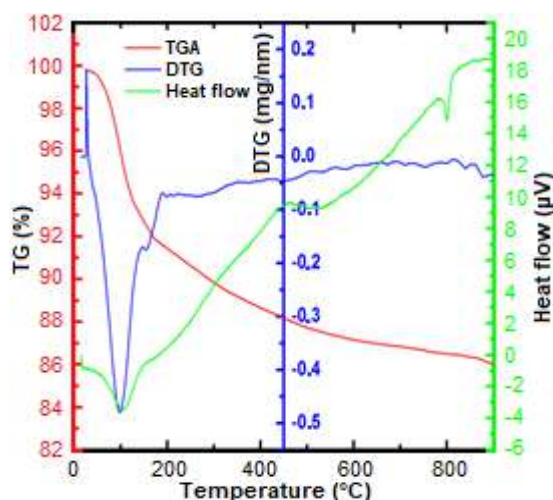


Fig 5. TGA/DTG curve of TiO_2 (2% Ce, 4% Yb)

non-appreciable loss is observed beyond $600\text{ }^\circ\text{C}$ for (Ce, Yb) doped TiO_2 and an essentially constant mass (87% sample) has been found indicating the thermal stability of the sample. The mass loss until $198\text{ }^\circ\text{C}$ attributed to complete dehydration of the powders. The DSC curve showed a broad peak around $799\text{ }^\circ\text{C}$ which can be assigned anatase to rutile transformation [45].

UV-Vis Absorption

Fig. 6 shows the absorbance of the TiO_2 recorded between 200 and 1000 nm at room temperature. This absorbance is improved proportionally with the insertion of the dopants used; therefore, even small proportions of

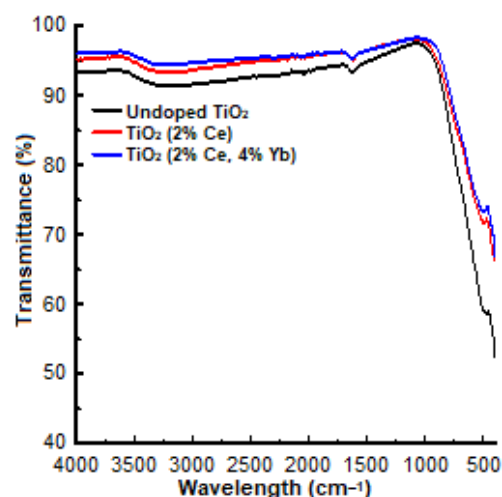


Fig 4. ATR-FTIR spectra of undoped TiO_2 ; TiO_2 (2% Ce) and TiO_2 (2% Ce, 4% Yb)

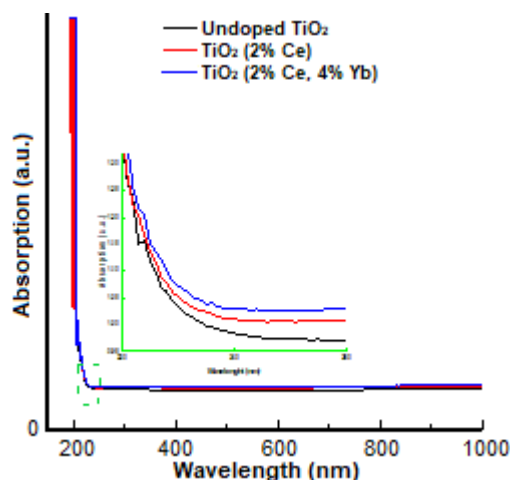


Fig 6. Absorption spectrum of undoped TiO_2 ; TiO_2 (2% Ce) and TiO_2 (2% Ce, 4% Yb)

the rare earth cerium and ytterbium enhance the optical properties of the TiO₂ remarkably.

■ CONCLUSION

The nano-powder titanium dioxide was synthesized by a simple co-precipitation method with an average crystalline size of 77 to 131 Å. The structure deduced from the XRD analysis shows that the nanoparticles are crystallized in the structures of rutile, which is the most dominant phase, also the presence of anatase and brookite phases. However, the introduction of the dopants decreases the size and lattice parameters of TiO₂ slightly. The elemental analysis by RFX shows the incorporation of Cerium and Ytterbium ions into the matrix, while the thermogravimetric analysis shows the transformation of the anatase structure into a rutile structure happened at high temperature between 700 and 800 °C and proved the thermal stability of the materials. Finally, the optical study by the UV-visible showed that the doping with the Ce and Yb rare earth increases the absorption of TiO₂ slightly, which allows it to be used for down-conversion in photovoltaic cells.

■ REFERENCES

- [1] Haider, A.J., AL-Anbari, R.H., Kadhim, G.R., and Salame, C.T., 2017, Exploring potential environmental applications of TiO₂ nanoparticles, *Energy Procedia*, 119, 332–345.
- [2] Gupta, K.K., Jassal, M., and Agrawal, A.K., 2008, Sol-gel derived titanium dioxide finishing of cotton fabric for self cleaning, *Indian J. Fibre Text. Res.*, 33, 443–450.
- [3] Afuyoni, M., Nashed, G., and Nasser, I.M., 2011, TiO₂ doped with SnO₂ and studying its structural and electrical properties, *Energy Procedia.*, 6, 11–20.
- [4] Ray, S., and Lalman, J.A., 2016, Fabrication and characterization of an immobilized titanium dioxide (TiO₂) nanofiber photocatalyst, *Mater. Today-Proc.*, 3 (6), 1582–1591.
- [5] Banfield, J.R., and Zhang, H., 2001, Nanoparticles in the environment, *Rev. Mineral. Geochem.*, 44 (1), 1–58.
- [6] Feng, X., Wang, Q., Wang, G., and Qui, F., 2006, Preparation of nano-TiO₂ by ethanol-thermal method and its catalytic performance for synthesis of dibutyl carbonate by transesterification, *Chin. J. Catal.*, 27 (3), 195–196.
- [7] Askari, M.B., Banizi, Z.T., Soltani, S., and Seifi, M., 2018, Comparison of optical properties and photocatalytic behavior of TiO₂/MWCNT, CdS/MWCNT and TiO₂/CdS/MWCNT nanocomposites, *Optik*, 157, 230–239.
- [8] Wang, F., Shi, Z., Gong, F., Jiu, J., and Adachi, M., 2007, Morphology control of anatase TiO₂ by surfactant-assisted hydrothermal method, *Chin. J. Chem. Eng.*, 15 (5), 754–759.
- [9] Peng, F., Cai, L., Huang, L., Yu, H., and Wang, H., 2008, Preparation of nitrogen-doped titanium dioxide with visible-light photocatalytic activity using a facile hydrothermal method, *J. Phys. Chem. Solids*, 69 (7), 1657–1664.
- [10] Li, G., Chen, L., Dimitrijevic, N.M., and Gray, K.A., 2008, Visible light photocatalytic properties of anion-doped TiO₂ materials prepared from a molecular titanium precursor, *Chem. Phys. Lett.*, 451 (1-3), 75–79.
- [11] Zhao, X., Liu, M., and Zhu, Y., 2007, Fabrication of porous TiO₂ film via hydrothermal method and its photocatalytic performances, *Thin Solid Films*, 515 (18), 7127–7134.
- [12] Askari, M.B., Banizi, Z.T., Seifi, M., Dehaghi, S.B., and Veisi, P., 2017, Synthesis of TiO₂ nanoparticles and decorated multi-wall carbon nanotube (MWCNT) with anatase TiO₂ nanoparticles and study of optical properties and structural characterization of TiO₂/MWCNT nanocomposite, *Optik*, 149, 447–454.
- [13] Salehi, A., Mashhadi, H.A., Abravi, M.S., and Jafarian, H.R., 2015, An ultrasound assisted method on the formation of nanocrystalline fluorohydroxyapatite coatings on titanium scaffold by dip coating process, *Procedia Mater. Sci.*, 11, 137–141.

- [14] Mahadik, S.A., Pedraza, F., and Mahadik, S.S., 2016, Comparative studies on water repellent coatings prepared by spin coating and spray coating methods, *Prog. Org. Coat.*, 104, 217–222.
- [15] Karuppuchamy, S., Suzuki, N., Ito, S., and Endo, T., 2009, A novel one-step electrochemical method to obtain crystalline titanium dioxide films at low temperature, *Curr. Appl. Phys.*, 9 (1), 243–248.
- [16] Song, W., Wu, X., Qin, W., and Jiang, Z., 2007, TiO₂ films prepared by micro-plasma oxidation method for dye-sensitized solar cell, *Electrochim. Acta*, 53 (4), 1883–1889.
- [17] Anicai, L., Petica, A., Patroi, D., Marinescu, V., Prioteasa, P., and Costovici, S., 2015, Electrochemical synthesis of nanosized TiO₂ nanopowder involving choline chloride based ionic liquids, *Mater. Sci. Eng., B*, 199, 87–95.
- [18] Kim, B.H., Lee, J.Y., Choa, Y.H., Higuchi, M., and Mizutani, N., 2004, Preparation of TiO₂ thin film by liquid sprayed mist CVD method, *Mater. Sci. Eng., B*, 107 (3), 289–294.
- [19] Chernozem, R.V., Surmeneva, M.A., Krause, B., Baumbach, T., Ignatov, V.P., Tyurin, A.I., Loza, K., Epple, M., and Surmenev, R.A., 2017, Hybrid biocomposites based on titania nanotubes and a hydroxyapatite coating deposited by RF-magnetron sputtering: Surface topography, structure, and mechanical properties, *Appl. Surf. Sci.*, 426, 229–237.
- [20] Akpan, U.G., and Hameed, B.H., 2010, The advancements in sol-gel method of doped-TiO₂ photocatalysts, *Appl. Catal., A*, 375 (1), 1–11.
- [21] Crișan, M., Brăileanu, A., Răileanu, M., Zaharescu, M., Crișan, D., Drăgan, N., Anastasescu, M., Ianculescu, A., Nițoi, I., Marinescu, V.E., and Hodoroagea, S.M., 2008, Sol-gel S-doped TiO₂ materials for environmental protection, *J. Non-Cryst. Solids*, 354 (2-9), 705–711.
- [22] Shi, J.W., Zheng, J.T., Hu, Y., and Zhao, Y.C., 2007, Influence of Fe³⁺ and Ho³⁺ co-doping on the photocatalytic activity of TiO₂, *Mater. Chem. Phys.*, 106 (2-3), 247–249.
- [23] Saif, M., and Abdel-Mottaleb, M.S.A., 2007, Titanium dioxide nanomaterial doped with trivalent lanthanide ions of Tb, Eu and Sm: Preparation, characterization and potential applications, *Inorg. Chim. Acta*, 360 (9), 2863–2874.
- [24] Fan, X., Chen, X., Zhu, S., Li, Z., Yu, T., Ye, J., and Zou, Z., 2008, The structural, physical and photocatalytic properties of the mesoporous Cr-doped TiO₂, *J. Mol. Catal. A: Chem.*, 284 (1-2), 155–160.
- [25] Essalhi, Z., Hartiti, B., Lfakir, A., Siadat, M., and Thevenin, P., 2016, Optical properties of TiO₂ thin films prepared by sol gel method, *J. Mater. Environ. Sci.*, 7 (4), 1328–1333.
- [26] Zhang, H., Chen, J., and Guo, H., 2011, Efficient near-infrared quantum cutting by Ce³⁺-Yb³⁺ couple in GdBO₃ phosphors, *J. Rare Earths*, 29 (9), 822–825.
- [27] Reszczyńska, J., Esteban, D.A., Gazda, M., and Zaleska, A., 2014, Pr-doped TiO₂. The effect of metal content on photocatalytic activity, *Physicochem. Probl. Miner. Process.*, 50 (2), 515–524.
- [28] Kim, H.S., Li, Y.B., and Lee, S.W., 2006, Nd³⁺-doped TiO₂ nanoparticles prepared by sol-hydrothermal process, *Mater. Sci. Forum*, 510-511, 122–125.
- [29] Li, W., Wang, Y., Lin, H., Shah, S.I., Huang, C.P., Doren, D.J., Rykov, S.A., Chen, J.G., and Barteau, M.A., 2003, Band gap tailoring of Nd³⁺-doped TiO₂ nanoparticles, *Appl. Phys. Lett.*, 83 (20), 4143–4145.
- [30] Antić, Ž., Krsmanović, R.M., Nikolić, M.G., Marinović-Cincović, M., Mitrić, M., Polizzi, S., and Dramićanin, M.D., 2012, Multisite luminescence of rare earth doped TiO₂ anatase nanoparticles, *Mater. Chem. Phys.*, 135 (2-3), 1064–1069.
- [31] Chen, X., and Luo, W., 2010, Optical spectroscopy of rare earth ion-doped TiO₂ nanophosphors, *J. Nanosci. Nanotechnol.*, 10 (3), 1482–1494.
- [32] Mulwa, W.M., Ouma, C.N.M., Onani, M.O., and Dejene, F.B., 2016, Energetic, electronic and optical properties of lanthanide doped TiO₂: An ab initio LDA+U study, *J. Solid State Chem.*, 237, 129–137.
- [33] Qianqian, D., Feng, Q., Dan, W., Wei, X., Jianmin, C., Zhiguo, Z., and Wenwu, C., 2011, Quantum

- cutting mechanism in Tb^{3+} - Yb^{3+} co-doped oxyfluoride glass, *J. Appl. Phys.*, 110 (11), 113503.
- [34] Du, J., Wu, Q., Zhong, S., Gu, X., Liu, J., Guo, H., Zhang, W., Peng, H., and Zou, J., 2015, Effect of hydroxyl groups on hydrophilic and photocatalytic activities of rare earth doped titanium dioxide thin films, *J. Rare Earths*, 33 (2), 148–153.
- [35] Heng, C.L., Wang, T., Su, W.Y., Wu, H.C., Yin, P.G., and Finstad, T.G., 2016, Down-conversion luminescence from (Ce, Yb) co-doped oxygen-rich silicon oxides, *J. Appl. Phys.*, 119 (12), 123105.
- [36] van der Kolk, E., Ten Kate, O.M., Wiegman, J.W., Biner, D., and Krämer, K.W., 2011, Enhanced 1G_4 emission in $NaLaF_4: Pr^{3+}, Yb^{3+}$ and charge transfer in $NaLaF_4: Ce^{3+}, Yb^{3+}$ studied by Fourier transform luminescence spectroscopy, *Opt. Mater.*, 33 (7), 1024–1027.
- [37] Liu, Z., Li, J., Yang, L., Chen, Q., Chu, Y., and Dai, N., 2014, Efficient near infrared quantum cutting in Ce^{3+} - Yb^{3+} codoped glass for solar photovoltaic, *Sol. Energy Mater. Sol. Cells*, 122, 46–50.
- [38] Chen, D., Wang, Y., Yu, Y., Huang, P., and Weng, F., 2008, Quantum cutting down conversion by cooperative energy transfer from Ce^{3+} to Yb^{3+} in borate glasses, *J. Appl. Phys.*, 104 (11), 116105.
- [39] Haque, F.Z., Nandanwar, R., and Singh, P., 2017, Evaluating photodegradation properties of anatase and rutile TiO_2 nanoparticles for organic compounds, *Optik*, 128, 191–200.
- [40] Li, W., Liang, R., Hu, A., Huang, Z., and Zhou, Y.N., 2014, Generation of oxygen vacancies in visible light activated one-dimensional iodine TiO_2 photocatalysts, *RSC Adv.*, 4 (70), 36959–36966.
- [41] Binas, V.D., Sambani, K., Maggos, T., Katsanaki, A., and Kiriakidis, G., 2012, Synthesis and photocatalytic activity of Mn-doped TiO_2 nanostructured powders under UV and visible light, *Appl. Catal., B*, 113–114, 79–86.
- [42] Meddouri, M., Hammiche, L., Slimi, O., Djouadi, D., and Chelouche, A., 2016, Effect of cerium on structural and optical properties of ZnO aerogel synthesized in supercritical methanol, *Mater. Sci. Poland*, 34 (3), 659–664.
- [43] Tong, T., Zhang, J., Tian, B., Chen, E., and He, D., 2008, Preparation and characterization of anatase TiO_2 microspheres with porous frameworks via controlled hydrolysis of titanium alkoxide followed by hydrothermal treatment, *Mater. Lett.*, 62 (17–18), 2970–2972.
- [44] Zhou, L., Deng, J., Zhao, Y., Liu, W., An, L., and Chen, F., 2009, Preparation and characterization of N-I co-doped nanocrystal anatase TiO_2 with enhanced photocatalytic activity under visible-light irradiation, *Mater. Chem. Phys.*, 117 (2–3), 522–529.
- [45] Yodyingyong, S., Sae-Kung, C., Panijpan, B., Triampo, W., and Bull, D.T., 2011, Physicochemical properties of nanoparticles titania from alcohol burner calcinations, *Bull. Chem. Soc. Ethiop.*, 25 (2), 263–272.

Antibacterial Activity of Silver Nanoparticles Capped by *p*-Aminobenzoic Acid on *Escherichia coli* and *Staphylococcus aureus*

Dian Susanthi, Sri Juari Santosa*, and Eko Sri Kunarti

Department of Chemistry, Faculty of Mathematics and Natural Sciences, Universitas Gadjah Mada, Sekip Utara BLS 21, Bulaksumur, Yogyakarta 55281, Indonesia

* Corresponding author:

email: sjuari@ugm.ac.id

Received: April 1, 2019

Accepted: September 12, 2019

DOI: 10.22146/ijc.44652

Abstract: This paper describes the antibacterial performance of silver nanoparticles (AgNPs) which have been synthesized by using *p*-aminobenzoic acid as a reducing and stabilizing agent simultaneously. The silver nitrate with various concentrations was reacted with pH 11-adjusted *p*-aminobenzoic acid with a concentration of 5×10^{-3} mol L⁻¹ for 30 min in a boiling water bath. The synthesized AgNPs were characterized by UV-Vis spectrophotometry, Transmission Electron Microscope (TEM), and Particle Size Analyzer (PSA). The antibacterial performance of the synthesized AgNPs was evaluated by agar well diffusion method on *Escherichia coli* and *Staphylococcus aureus*. The higher silver nitrate concentration, the bigger the nanoparticle size, the wider particle size distribution, and the higher number of AgNPs formed. AgNPs synthesized from higher silver nitrate concentration had higher antibacterial activity. It is an indication that the antibacterial activity of AgNPs is mainly controlled by the silver ion concentration which influences the AgNPs particle size and the existence of silver ion in the AgNPs colloidal solution.

Keywords: antibacterial activity; *p*-aminobenzoic acid; silver nanoparticles

■ INTRODUCTION

Silver has been known as an antibacterial agent for centuries. The advances in science and technology have been enabling the transformation of the bulk form of silver to become silver nanoparticles (AgNPs). Silver nanoparticles are preferable to be used as an antibacterial agent than silver in bulk form because they have a larger surface area to contact with bacteria [1]. Furthermore, AgNPs are also more desirable than using silver ions as antibacterial agents. The reason is that silver ions are relatively reactive and their binding with another ion may induce precipitation (for example, AgCl) and their interaction with protein (for example, albumin) can decrease their antibacterial efficacy and limit their applications [2-3].

In this research, *p*-aminobenzoic acid was used as a reducing and stabilizing agent in AgNPs synthesis. This synthesis has some advantages in the environmental perspective. First, it only uses one chemical reagent which can act simultaneously as reducing and stabilizing agents. Second, it provides a less toxic route of AgNPs synthesis

because *p*-aminobenzoic acid is non-toxic and has been widely used in sunscreen and pharmaceutical products [4]. Third, this synthesis uses water as a solvent which is more environmental friendly than other solvents that have been used for AgNPs syntheses, such as ethylene glycol [5] and methanol [6]. Those three reasons make this synthesis fulfill the green chemistry principles which should be a concern in nanoparticle synthesis [7].

The study of AgNPs antibacterial activity on *Escherichia coli* (gram-negative bacteria) and *Staphylococcus aureus* (gram-positive bacteria) has been performed previously. AgNPs which were synthesized by NaBH₄ with size of about 13 nm had an excellent bactericidal performance on both bacteria [8]. However, this synthesis is less environmentally friendly because NaBH₄ is a hazardous material. AgNPs which were synthesized by chitosan had good antibacterial activity on *Escherichia coli* and *Staphylococcus aureus* [9]. Nevertheless, this synthesis took about 8 h. AgNPs which were biosynthesized using *Garciana mangostana* leaf extract as a reducing agent was found to be highly

effective against *Escherichia coli* and *Staphylococcus aureus* [10]. However, the effect of silver nitrate concentration and AgNPs particle size difference had not been explained yet.

The synthesis of AgNPs using *p*-aminobenzoic acid as a reducing and stabilizing agent was found to be environmentally friendly because of the use of a non-toxic chemical as a reducing and stabilizing agent and because the reaction happened in a short time. The synthesized AgNPs also had excellent stability for more than 16 weeks [11]. In this study, the antibacterial activity of AgNPs which were synthesized using *p*-aminobenzoic acid was evaluated. The concentration of silver nitrate was varied in order to study the effect of silver nitrate concentration on the particle size and antibacterial activity of the synthesized AgNPs. The synthesized AgNPs were characterized by UV-Vis spectrophotometry, Transmission Electron Microscope (TEM), and Particle Size Analyzer (PSA). The antibacterial performance was evaluated by in vitro agar well diffusion method against two bacteria, namely *Escherichia coli* (gram-negative bacteria) and *Staphylococcus aureus* (gram-positive bacteria).

■ EXPERIMENTAL SECTION

Materials

The materials used in this research were silver nitrate (Merck) as precursor of AgNPs, *p*-aminobenzoic acid (Sigma Aldrich) as reducing and stabilizing agents, sodium hydroxide (Merck) as pH adjuster, Mueller-Hinton Agar (Merck), Brain Heart Infusion Broth (Merck), and gentamicin sulfate as positive control in antibacterial activity evaluation. All reagents were used as received without further purification.

Instrumentation

The characterization of AgNPs was performed by using UV-Vis Spectrophotometer (Shimadzu UV-Pharma Spec), TEM (JEOL JEM-1400), and PSA (Nanoparticle Analyzer Horiba SZ-100). The inhibition zone in antibacterial activity assay was observed using Darkfield Quebec Colony Counter.

Procedure

Synthesis of silver nanoparticles

The synthesis of AgNPs was performed according to the previous study [11] with some modification. Briefly, *p*-aminobenzoic acid ($M_r = 137.14 \text{ g mol}^{-1}$) was weighed and dissolved in distilled water. After dissolved completely, the pH of the solution was adjusted to 11 by adding sodium hydroxide and an amount of distilled water was added to the solution in order to make a solution that has a concentration of $10 \times 10^{-3} \text{ mol L}^{-1}$. The pH meter was calibrated with pH buffer of 4.01, 7.00, and 9.21 right before use. The pH-conditioned *p*-aminobenzoic acid solution was then poured to a reaction tube and added by silver nitrate solution ($M_r = 170 \text{ g mol}^{-1}$) with various concentrations (0.2, 0.6, 1.0, 2.0, and $3.0 \times 10^{-3} \text{ mol L}^{-1}$). The volume ratio of the reagent is 1:1 so the final concentration of reagents in the mixture are $5 \times 10^{-3} \text{ mol L}^{-1}$ for *p*-aminobenzoic acid and 0.1, 0.3, 0.5, 1.0, and $1.5 \times 10^{-3} \text{ mol L}^{-1}$ for silver nitrate. The solution was homogenized by shaking it several times and placed in a boiling water bath for 30 min. When the solution turned yellow, it meant that the AgNPs had been formed. After the synthesis was finished, the tube was cooled in tap water and the solution was moved to a storage bottle.

Characterization of silver nanoparticles

The synthesized AgNPs were analyzed by UV-Vis Spectrophotometry in order to monitor their surface plasmon resonance (SPR) absorbance. The resulted AgNPs were poured into a quartz cuvette with 1 cm optical path length and scanned at 200–800 nm wavelength. The scanning speed was fast with the wavelength interval of 1 nm. The SPR absorbance was shown by the absorbance peak in wavelength around 400 nm [12-13].

The shape of the synthesized AgNPs was analyzed by TEM. The AgNPs colloid was immersed by a copper grid and dried at room temperature. The image was taken by using 120 kV accelerating voltage. The size of the AgNPs was measured by using PSA based on dynamic light scattering principle.

Evaluation of the antibacterial performance of silver nanoparticles

The antibacterial performance of the synthesized AgNPs was evaluated by in vitro agar well diffusion method [14-15] with some modification against *Escherichia coli* (gram-negative bacteria) and *Staphylococcus aureus* (gram-positive bacteria). The culture media was made by dissolving Brain Heart Infusion Broth in water, heated, and boiled for 1 min in order to make sure it has been dissolved completely. The solution was then poured in a reaction tube and sterilized by autoclave with a pressure of 15 psi and a temperature of 121 °C for 15 min. The sterilized media was then inoculated by adding the bacteria and stored in the temperature of 37 °C. The Mueller-Hinton Agar was dissolved in water by heating and boiling it for one minute in order to dissolve the medium completely. It was sterilized using autoclave with the same condition as culture media sterilization and cooled in room temperature. The sterilized agar solution was then poured into sterile petri dishes with uniform depth and allowed to cool in room temperature. The plates were stored at 2–8 °C. The surface of the agar was inoculated entirely using a sterile swab which was stepped in the prepared bacteria suspension. A ring with a diameter of 6 mm was placed on the inoculated agar in order to form a well with a certain distance to the other wells. Each plate contained seven wells. Each well was injected by 50 µL solution of

synthesized AgNPs as the sample, *p*-aminobenzoic acid as the negative control, and gentamicin 0.2 g L⁻¹ as the positive control. The plates were then incubated at 37 °C for 24 h. After incubation, the inhibition zone diameter was measured by a ruler in mm unit. The obtained value was reduced by a correction factor of 6 mm as the well diameter. All tests were performed in duplicate.

RESULTS AND DISCUSSION

Synthesis and Characterization of Silver Nanoparticles

The AgNPs formation was indicated by the change of solution color from transparent to yellow and confirmed by their SPR absorbance. The SPR absorbance of AgNPs can be measured by UV-Vis Spectrophotometer based on many previous studies [16-21]. Synthesis of AgNPs was performed by reacting 5 × 10⁻³ mol L⁻¹ *p*-aminobenzoic acid and silver nitrate at various concentrations, ranging from 0 to 1.5 × 10⁻³ mol L⁻¹. The synthesis was performed in the optimum condition based on the previous study [11]. The pH was 11 because the reaction can only take place in this condition. The reaction time was 30 min because longer reaction time did not give any significant increase on SPR absorbance.

The UV-Vis absorbance spectra of the synthesized AgNPs is shown in Fig. 1. The higher silver nitrate concentration will increase the SPR absorbance of the synthesized AgNPs. SPR absorbance values were 0.17, 181,

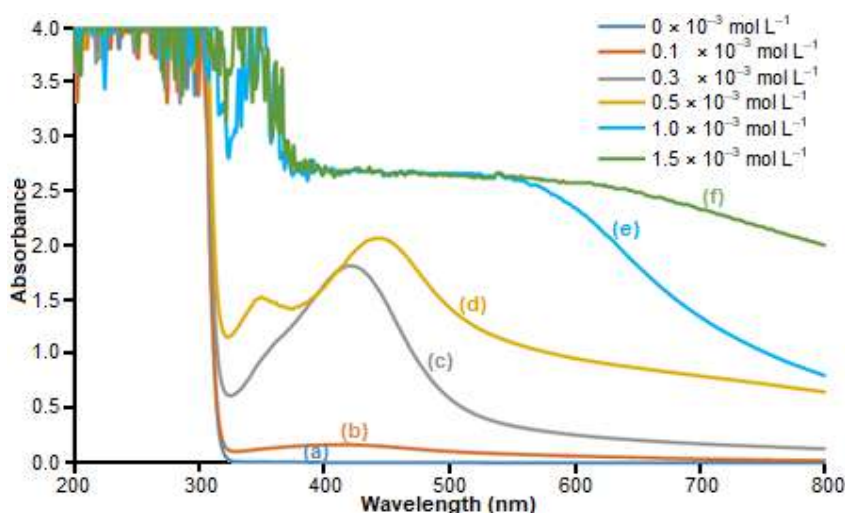


Fig 1. The UV-Vis absorbance spectra of silver nanoparticles synthesized from 5 × 10⁻³ mol L⁻¹ *p*-aminobenzoic acid and silver nitrate 0 (a), 0.1 (b), 0.3 (c), 0.5 (d), 1.0 (e) and 1.5 (f) × 10⁻³ mol L⁻¹

and 2.066 for AgNPs synthesized from silver nitrate with a concentration of 0.1, 0.3, and 0.5×10^{-3} mol L⁻¹, respectively. The SPR absorbance for the AgNPs which were synthesized from silver nitrate with the concentration of 1.0 and 1.5×10^{-3} mol L⁻¹ could not be determined because they were too high to be measured by the instrument. The higher SPR absorbance indicates the higher number of the synthesized AgNPs in the solution [22]. The concentration of the AgNPs was calculated based on the SPR absorbance referring to Paramelle et al. [21]. The molar concentrations of AgNPs were 21, 30, 40, 49, and 51×10^{-12} mol L⁻¹ with yield percentage of 31, 49, 64, 44 and 33% for AgNPs synthesized from silver nitrate with concentration of 0.1, 0.3, 0.5, 1.0, and 1.5×10^{-3} mol L⁻¹, respectively. The AgNPs molar concentrations were increased with the silver nitrate concentration increment even though the yield percentage did not give the same pattern. It means that the higher silver nitrate concentration used in the synthesis will give a higher number of synthesized AgNPs. The same result was also published by previous studies where higher silver nitrate concentration would produce more AgNPs [19,23-25].

Besides SPR absorbance, SPR wavelength of the synthesized AgNPs was also observed. The higher SPR wavelength indicates the bigger particle size [5]. This phenomenon was also reported in AgNPs which were synthesized using sodium citrate [26], AgNPs-chitosan nanocomposites [19], AgNPs synthesized using guar gum [27] and citrate capped AgNPs [21]. In this study, AgNPs

which were synthesized from higher silver nitrate concentrations had higher SPR wavelengths. They were 406, 420, and 444 nm for AgNPs which were synthesized from silver nitrate at the concentration of 0.1, 0.3, and 0.5×10^{-3} mol L⁻¹, respectively. This indicated that the AgNPs size increased along with the increase of silver nitrate concentration. The SPR absorbance band also became more extensive, which means that the particle size distribution also became broader along with the increase of silver nitrate concentration.

Further characterizations were performed in order to support the UV-Vis spectrophotometry results for AgNPs which were synthesized from lowest and highest silver nitrate concentrations. The AgNPs characterization was performed by TEM to observe the AgNPs morphology and PSA to measure the AgNPs diameter based on dynamic light scattering principle. The characterization result of the synthesized AgNPs can be seen in Fig. 2 and 3. TEM result showed that AgNPs which were originated from 0.1×10^{-3} mol L⁻¹ silver nitrate had a uniform spherical shape with an average size of 35.9 nm and a polydispersity index of 0.277. While AgNPs which were originated from 1.5×10^{-3} mol L⁻¹ silver nitrate had a spherical but not uniform shape with an average size of 113.0 nm and a polydispersity index of 0.283. These results were in agreement with the UV-Vis spectrophotometry result where higher silver nitrate concentration resulted in bigger size of AgNPs and broader particle size distribution.

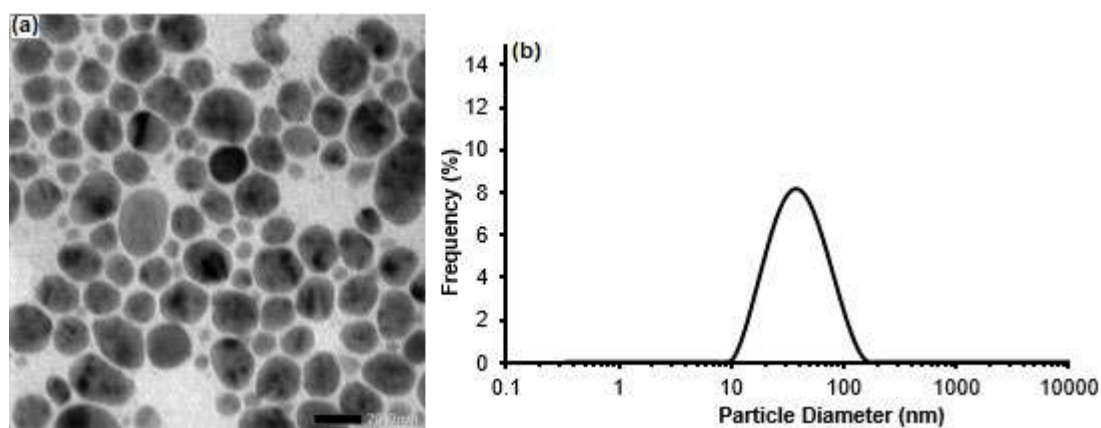


Fig 2. TEM image of silver nanoparticles synthesized from 0.1×10^{-3} mol L⁻¹ AgNO₃ and 5×10^{-3} mol L⁻¹ *p*-aminobenzoic acid with a magnitude of 150000× (a) and particle size distribution from PSA analysis (b)

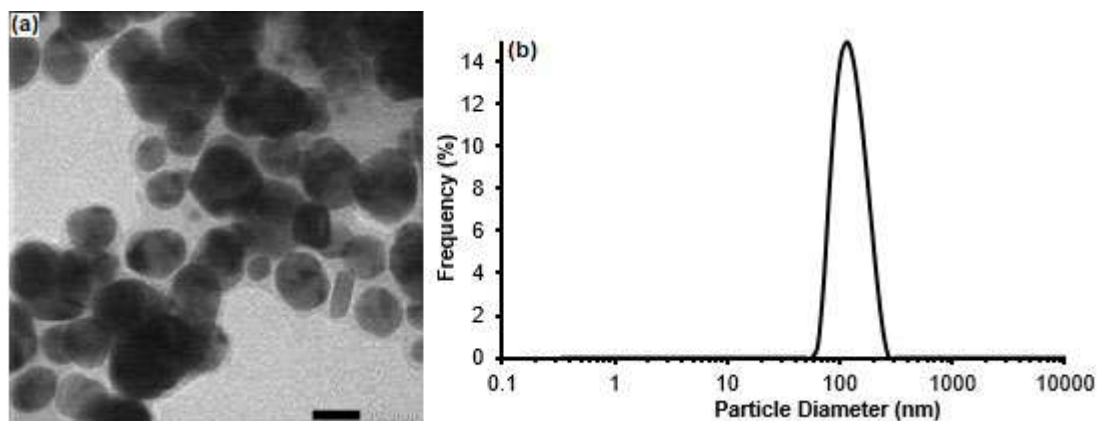


Fig 3. TEM image of silver nanoparticles synthesized from $1.5 \times 10^{-3} \text{ mol L}^{-1} \text{ AgNO}_3$ and $5 \times 10^{-3} \text{ mol L}^{-1} p\text{-aminobenzoic acid}$ with a magnitude of $150000\times$ (a) and particle size distribution from PSA analysis (b)

The nanoparticle formation consists of three different processes; they are the reducing process, the particle growth, and the stabilizing process [28]. In this research, the reducing agent also acts as a stabilizing agent. In the appropriate reactant mole ratio, the reducing agent will reduce silver ion to become silver nanoparticle and stabilize it before it grows to become a bigger particle. The higher silver nitrate concentration will decrease the mole ratio of reactant. It means that the same amount of reducing agent molecules should react with more silver ions. In this condition, the reducing agent will be difficult to stabilize the formed silver nanoparticles. Thus, nanoparticles can grow to bigger particles. This phenomenon also has been reported in the synthesis of AgNPs by chitosan [29].

Antibacterial Activity of Silver Nanoparticles

Antibacterial activity of the synthesized AgNPs was evaluated by agar well diffusion method against two bacteria, namely *Escherichia coli* (gram-negative bacteria) and *Staphylococcus aureus* (gram-positive bacteria). The result is shown in Table 1. Gentamicin was used as a positive control corresponding to the previous study [8] because it has been widely used as a commercial antibiotic for *Escherichia coli* and *Staphylococcus aureus* [15]. Inhibition zones which were formed by AgNPs synthesized using higher silver nitrate concentration were bigger than inhibition zones which were formed by AgNPs synthesized using smaller silver nitrate concentration. Although the particles size was greater,

Table 1. The antimicrobial activity test result of silver nanoparticles (mean \pm standard deviation)

Sample	<i>Escherichia coli</i>		<i>Staphylococcus aureus</i>	
	mm	%	mm	%
Gentamicin 0.2 g L^{-1} (positive control)	14.0 ± 0	100 ± 0	18.8 ± 0	100 ± 0
<i>p</i> -aminobenzoic acid $5 \times 10^{-3} \text{ mol L}^{-1}$ (negative control)	0.0 ± 0	0.0 ± 0	0.0 ± 0	0.0 ± 0
AgNPs synthesized from AgNO_3 $0.1 \times 10^{-3} \text{ mol L}^{-1}$ and <i>p</i> -aminobenzoic acid $5 \times 10^{-3} \text{ mol L}^{-1}$	0.0 ± 0	0.0 ± 0	0.0 ± 0	0.0 ± 0
AgNPs synthesized from AgNO_3 $0.3 \times 10^{-3} \text{ mol L}^{-1}$ and <i>p</i> -aminobenzoic acid $5 \times 10^{-3} \text{ mol L}^{-1}$	0.0 ± 0	0.0 ± 0	0.0 ± 0	0.0 ± 0
AgNPs synthesized from AgNO_3 $0.5 \times 10^{-3} \text{ mol L}^{-1}$ and <i>p</i> -aminobenzoic acid $5 \times 10^{-3} \text{ mol L}^{-1}$	1.0 ± 0	7.1 ± 0	0.0 ± 0	0.0 ± 0
AgNPs synthesized from AgNO_3 $1.0 \times 10^{-3} \text{ mol L}^{-1}$ and <i>p</i> -aminobenzoic acid $5 \times 10^{-3} \text{ mol L}^{-1}$	2.0 ± 0	14.3 ± 0	3.8 ± 1.1	19.7 ± 5.6
AgNPs synthesized from AgNO_3 $1.5 \times 10^{-3} \text{ mol L}^{-1}$ and <i>p</i> -aminobenzoic acid $5 \times 10^{-3} \text{ mol L}^{-1}$	4.5 ± 0	32.1 ± 0	6.3 ± 0.4	32.9 ± 1.9

AgNPs which were synthesized from higher silver nitrate concentration gave higher antibacterial activity. This may indicate that the silver ion is the main actor in the bactericidal mechanism of AgNPs rather than the AgNPs themselves. Silver nanoparticles may act as a reservoir of silver ions which would interact with the bacteria by attacking their membrane, attacking the respiratory chain in their mitochondria, creating free radicals and induce oxidative stress and leading to cell death [1,3,30].

In the previous study, smaller AgNPs would give higher antibacterial activity because smaller AgNPs size has a higher surface area which can increase the contact site with the bacteria [31]. However, the result in this study was different. The higher antibacterial activity came from larger AgNPs which were synthesized from higher silver nitrate concentration. This indicates that the silver nitrate concentrations which were used in the synthesis process had significant roles in the antibacterial activity of AgNPs because it influences the AgNPs particle size and the existence of silver ions in the AgNPs colloidal solution.

The synthesized AgNPs had antimicrobial activity against both gram-negative and gram-positive bacteria. The inhibition zone diameter induced by the synthesized AgNPs against *Escherichia coli* bacteria was relatively smaller than the inhibition zone diameter against *Staphylococcus aureus* bacteria. This may be caused by the different membrane composition of those bacteria. *Staphylococcus aureus* as a gram-positive bacteria have a cell wall which is entirely composed by peptidoglycan layer. This layer is composed of networks of plenty of pores. These pores enable foreign molecules to come into the cell. On the other hand, *Escherichia coli* as a negative-gram bacteria have a thin membrane of peptidoglycan and an outer membrane, which consists of lipopolysaccharide, lipoprotein, and phospholipids. This outer membrane is a potential barrier against foreign molecules [32-33].

Compared to the previous study, a similar result was obtained from AgNPs which were synthesized using *Garciana mangostana* leaf extract as a reducing agent. The inhibition zones were 20 mm for *Staphylococcus aureus* and 15 mm for *Escherichia coli*. Furthermore, the antibacterial activity of AgNPs in this study was not as

good as AgNPs-chitosan, AgNPs-cellulose, AgNPs-microcrystalline cellulose, or AgNPs-carboxymethyl cellulose which have inhibition zones ranged from 15–22 mm on *Staphylococcus aureus* and 13–20 mm on *Escherichia coli* [33]. The lower antibacterial activity of AgNPs can happen because this research used a threefold lower concentration of silver nitrate in AgNPs synthesis. Besides that, the high antibacterial activity may come from the initial antibacterial property of carboxymethyl cellulose and chitosan. However, the AgNPs should be synthesized first using glucose as a reducing agent and then impregnated to chitosan, cellulose, microcrystalline cellulose and carboxymethyl cellulose. This process took more than 6 h, a very long time compared to the AgNPs synthesis in the present study.

■ CONCLUSION

The antibacterial activity of AgNPs which were synthesized from silver nitrate and *p*-aminobenzoic acid has been evaluated against *Escherichia coli* and *Staphylococcus aureus* bacteria. Higher silver nitrate concentration gave bigger AgNPs size, wider particle size distribution, and a higher number of the formed AgNPs. Conversely, smaller silver nitrate concentration gave smaller AgNPs size, narrower particle size distribution, and a smaller number of the formed AgNPs. Nevertheless, AgNPs which were synthesized from more silver nitrate concentration had higher antibacterial activity. It is an indication that the antibacterial activity of AgNPs is mainly controlled by the silver ion concentration which influences the AgNPs particle size and the existence of silver ions in the AgNPs colloidal solution.

■ REFERENCES

- [1] Abbasi, E., Milani, M., Aval, S.F., Kouhi, M., Akbarzadeh, A., Nasrabadi, H.T., Nikasa, P., Joo, S.W., Hanifehpour, Y., Nejati-Koshki, K., and Samiei, M., 2016, Silver nanoparticles: Synthesis methods, bio-applications and properties, *Crit. Rev. Microbiol.*, 42 (2), 173–180.
- [2] Kędziora, A., Speruda, M., Krzyżewska, E., Rybka, J., Łukowiak, A., and Bugła-Płoskońska, G., 2018, Similarities and differences between silver ions and

- silver in nanoforms as antibacterial agents, *Int. J. Mol. Sci.*, 19 (2), 444.
- [3] Marambio-Jones, C., and Hoek, E.M.V., 2010, A review of the antibacterial effects of silver nanomaterials and potential implications for human health and the environment, *J. Nanopart. Res.*, 12 (5), 1531–1551.
- [4] Zhou, L., Ji, Y., Zeng, C., Zhang, Y., Wang, Z., and Yang, X., 2013, Aquatic photodegradation of sunscreen agent *p*-aminobenzoic acid in the presence of dissolved organic matter, *Water Res.*, 47 (1), 153–162.
- [5] Copley, C.M., Skrabalak, S.E., Campbell, D.J., and Xia, Y., 2009, Shape-controlled synthesis of silver nanoparticles for plasmonic and sensing applications, *Plasmonics*, 4 (2), 171–179.
- [6] Bhatte, K.D., Tambade, P.J., Dhake, K.P., and Bhanage, B.M., 2010, Silver nanoparticles as an efficient, heterogeneous and recyclable catalyst for synthesis of β -enamiones, *Catal. Commun.*, 11 (15), 1233–1237.
- [7] Duan, H., Wang, D., and Li, Y., 2015, Green chemistry for nanoparticle synthesis, *Chem. Soc. Rev.*, 44 (16), 5778–5792.
- [8] Kim, J.S., Kuk, E., Yu, K.N., Kim, J.H., Park, S.J., Lee, H.J., Kim, S.H., Park, Y.K., Park, Y.H., Hwang, C.Y., Kim, Y.K., Lee, Y.S., Jeong, D.H., and Cho, M.H., 2007, Antimicrobial effects of silver nanoparticles, *Nanomed. Nanotechnol. Biol. Med.*, 3 (1), 95–101.
- [9] Kumar-Krishnan, S., Prokhorov, E., Hernández-Iturriaga, M., Mota-Morales, J.D., Vázquez-Lepe, M., Kovalenko, Y., Sanchez, I.C., and Luna-Bárcenas, G., 2015, Chitosan/silver nanocomposites: Synergistic antibacterial action of silver nanoparticles and silver ions, *Eur. Polym. J.*, 67, 242–251.
- [10] Veerasamy, R., Xin, T.Z., Gunasagaran, S., Xiang, T.F.W., Yang, E.F.C., Jeyakumar, N., and Dhanaraj, S.A., 2011, Biosynthesis of silver nanoparticles using mangosteen leaf extract and evaluation of their antimicrobial activities, *J. Saudi Chem. Soc.*, 15 (2), 113–120.
- [11] Susanthi, D., Santosa, S.J., and Kunarti, E.S., 2018, The synthesis and stability study of silver nanoparticles prepared using *p*-aminobenzoic acid as reducing and stabilizing agent, *Indones. J. Chem.*, 18 (3), 421–427.
- [12] Roto, R., Marcelina, M., Aprilita, N.H., Mudasir, M., Natsir, T.A., and Mellisani, B., 2017, Investigation on the effect of addition of Fe^{3+} ion into the colloidal AgNPs in PVA solution and understanding its reaction mechanism, *Indones. J. Chem.*, 17 (3), 439–445.
- [13] Roto, R., Rasydta, H.P., Suratman, A., and Aprilita, N.H., 2018, Effect of reducing agents on physical and chemical properties of silver nanoparticles, *Indones. J. Chem.*, 18 (4), 614–620.
- [14] Wanger, A., 2007, “Disk diffusion tests and gradient methodologies” in *Antimicrobial Susceptibility Testing Protocols*, 1st Ed., Eds. Schwalbe, R., Steele-Moore, L., and Goodwin, A.C., CRC Press, Boca Raton, 53–73.
- [15] CLSI, 2016, *Performance standards for antimicrobial susceptibility testing*, CLSI supplement M100S, 26th Ed., Clinical and Laboratory Standards Institute, Wayne, Philadelphia, USA.
- [16] Vasileva, P., Donkova, B., Karadjova, I., and Dushkin, C., 2011, Synthesis of starch-stabilized silver nanoparticles and their application as a surface plasmon resonance-based sensor of hydrogen peroxide, *Colloids Surf., A*, 382 (1-3), 203–210.
- [17] Chhatre, A., Solasa, P., Sakle, S., Thaokar, R., and Mehra, A., 2012, Color and surface plasmon effects in nanoparticle systems: Case of silver nanoparticles prepared by microemulsion route, *Colloids Surf., A*, 404, 83–92.
- [18] Ratnarathorn, N., Chailapakul, O., Henry, C.S., and Dungchai, W., 2012, Simple silver nanoparticle colorimetric sensing for copper by paper-based devices, *Talanta*, 99, 552–557.
- [19] Susilowati, E., Triyono, Santosa, S.J., and Kartini, I., 2015, Synthesis of silver-chitosan nanocomposites colloidal by glucose as reducing agent, *Indones. J. Chem.*, 15 (1), 29–35.
- [20] Daniel, S.C.G.K., Julius, L.A.N., and Gorthi, S.S., 2017, Instantaneous detection of melamine by interference biosynthesis of silver nanoparticles, *Sens. Actuators, B*, 238, 641–650.
- [21] Paramelle, D., Sadovoy, A., Gorelik, S., Free, P., Hopley, J., and Fernig, D.G., 2014, A rapid method

- to estimate the concentration of citrate capped silver nanoparticles from UV-visible light spectra, *Analyst*, 139 (19), 4855–4861.
- [22] Chen, K., Shen, Z., Luo, J., Wang, X., and Sun, R., 2015, Quaternized chitosan/silver nanoparticles composite as a SERS substrate for detecting tricyclazole and Sudan I, *Appl. Surf. Sci.*, 351, 466–473.
- [23] Hebeish, A.A., El-Rafie, M.H., Abdel-Mohdy, F.A., Abdel-Halim, E.S., and Emam, H.E., 2010, Carboxymethyl cellulose for green synthesis and stabilization of silver nanoparticles, *Carbohydr. Polym.*, 82 (3), 933–941.
- [24] Gusrizal, G., Santosa, S.J., Kunarti, E.S., and Rusdiarso, B., 2016, Dual function of *p*-hydroxybenzoic acid as reducing and capping agent in rapid and simple formation of stable silver nanoparticles, *Int. J. ChemTech Res.*, 9 (9), 472–482.
- [25] Song, K.C., Lee, S.M., Park, T.S., and Lee, B.S., 2009, Preparation of colloidal silver nanoparticles by chemical reduction method, *Korean J. Chem. Eng.*, 26 (1), 153–155.
- [26] Šileikaite, A., Puišo, J., Prosyčėvas, I., and Tamulevičius, S., 2009, Investigation of silver nanoparticles formation kinetics during reduction of silver nitrate with sodium citrate, *Mater. Sci.*, 15 (1), 21–27.
- [27] Pandey, S., Goswami, G.K., and Nanda, K.K., 2012, Green synthesis of biopolymer–silver nanoparticle nanocomposite: An optical sensor for ammonia detection, *Int. J. Biol. Macromol.*, 51 (4), 583–589.
- [28] Mittal, A.K., Chisti, Y., and Banerjee, U.C., 2013, Synthesis of metallic nanoparticles using plant extracts, *Biotechnol. Adv.*, 31 (2), 346–356.
- [29] Tran, H.V., Tran, L.D., Ba, C.T., Vu, H.D., Nguyen, T.N., Pham, D.G., and Nguyen, P.X., 2010, Synthesis, characterization, antibacterial and antiproliferative activities of monodisperse chitosan-based silver nanoparticles, *Colloids Surf., A*, 360 (1-3), 32–40.
- [30] Prabhu, S., and Poulouse, E.K., 2012, Silver nanoparticles: Mechanism of antimicrobial action, synthesis, medical applications, and toxicity effects, *Int. Nano Lett.*, 2, 32.
- [31] Guzman, M.G., Dille, J., and Godet, S., 2009, Synthesis of silver nanoparticles by chemical reduction method and their antibacterial activity, *Int. J. Chem. Biomol. Eng.*, 2 (3), 104–111.
- [32] Wang, W., Hong, M.C., Luo, J., Jiang, F., Han, L., Lin, Z., and Cao, R., 2004, Syntheses and characterizations of six hydrogen-bonded silver(I) complexes from assembly of silver(I) nitrate and aminobenzoic acid, *Inorg. Chim. Acta*, 357, 103–114.
- [33] Hassabo, A.G., Nada, A.A., Ibrahim, H.M., and Abou-Zeid, N.Y., 2015, Impregnation of silver nanoparticles into polysaccharide substrates and their properties, *Carbohydr. Polym.*, 122, 343–350.

The Performance of a Fixed-Bed Anaerobic Bioreactor Using Sulfate-Reducing Bacterial Consortium from Sikidang Crater Sediments

Andriyanto^{1,2}, Wahyu Wilopo³, and Endah Retnaningrum^{2,*}

¹Study Program of Biology Education, STKIP YPM Bangko, Jl. Jenderal Sudirman Km. 02 Bangko, Jambi 37311, Indonesia

²Faculty of Biology, Universitas Gadjah Mada, Jl. Teknika Selatan, Sekip Utara, Yogyakarta 55281, Indonesia

³Geological Engineering Department, Faculty of Engineering, Universitas Gadjah Mada, Jl. Grafika No. 2, Bulaksumur, Yogyakarta 55281, Indonesia

* Corresponding author:

tel: +62-274-580839

email: endahr@ugm.ac.id

Received: April 18, 2019

Accepted: October 10, 2019

DOI: 10.22146/ijc.45164

Abstract: This research explored the performance of a fixed-bed anaerobic bioreactor system (FBR) using sulfate-reducing bacteria (SRB) from the sediment of Sikidang Crater in Indonesia. Indonesian natural zeolite was used as an inert medium in this bioreactor system. This bioreactor performance was analyzed based on its sulfate reduction efficiency, Cu removal, pH profile, SRB growth, and the changes in mineral composition of the zeolite surface. Based on a batch experiment, the FBR system was operated at 30 °C with a hydraulic retention time (HRT) of 7 days using a zeolite dose of 100 g/L. After its operation, a large amount of SRB (up to 1.5×10^5 cells/mm²) was entrapped and presented in the zeolite. This bacterial consortium could reduce sulfate and copper by around 68% and 99.96%, respectively. In addition, the pH value of the bioreactor changed to neutral, which indicated a good performance of the operation. The result of the Energy-Dispersive X-ray (EDX) confirmed that copper removal was caused by the formation of copper-sulfide precipitation. Mapping also revealed that both copper and sulfur were precipitated at the same location.

Keywords: FBR; SRB; natural zeolite; EDX; copper-sulfide

■ INTRODUCTION

The elevated sulfate and metal content in acid mine drainage (AMD) can be very harmful to the environment [1-2]. AMD is formed when sulfide minerals in mine spoils react with water and oxygen (H₂O and O₂) to produce acidic compounds that dissolve toxic waste containing metals and trace elements. Copper (Cu) is a potentially toxic metal that is harmful to most organisms where its concentration in AMD is very high [3-4]. The toxicity of AMD could be reduced by conventional treatment techniques, such as ion-exchange, neutralization, and coagulation-precipitation [5]. However, these treatments require a large amount of chemicals, energy, and can be expensive.

Biological treatment using sulfate-reducing bacteria (SRB) has the potential to be used for the treatment of AMD [6]. The use of SRB has several advantages over conventional treatments as it is more efficient, relatively

inexpensive, and more environmentally friendly [7]. SRB has the capability to reduce sulfate to sulfide, and then sulfide reacts with the dissolved metals forming insoluble metal precipitates [8].

The fixed-bed anaerobic bioreactor system is one of the faster anaerobic treatment methods of industrial wastewater. This system is a generally accepted in the industry due to its stability and resistance to AMD. Several researchers reported that the characters of the support medium greatly affect the performance of the anaerobic fixed-bed reactor [9-10]. The support medium provides a source of attachment for the bacterial biomass, acts as a bio-filtration bed, and helps prevent the wash-out of the biomass from the reactor. In addition, the SRBs attachment to the support medium promotes cell growth, a shorter generation time, greater products, and less inhibition products, and easier separation of the product and the medium [11].

Previous research explored the properties of various supporting media, such as polyvinyl alcohol gel beads, ceramic, polyethylene, clay, and activated carbon [12-14]. However, recent studies showed that zeolite had good potential if applied to the fixed-bed anaerobic bioreactor system [15]. In addition, zeolite materials can be obtained in very large quantities from some areas of Indonesia [16]. Therefore, the utilization of indigenous bacterial consortium and Indonesian natural zeolite in the FBR system was very effective. These components were very suitable to be applied to tropical environments in Indonesia, and could also reduce the costs during the application process.

Previous investigations have also reported that the volume and the particle size of the support medium influenced the performance of the bioreactor [17-21]. This performance also depends on the hydraulic residence time (HRT). A long HRT induces high sulfate reduction efficiencies and complete oxidation of the electron donor used. However, a short HRT may decrease the time available for the SRB to metabolize the substrate perfectly and cause biomass washout from the bioreactor [22].

Sediment from Sikidang Crater, located in Dieng Highland, Banjarnegara, Central Java, has unique physicochemical properties, such as pH values in the range of 2 to 3, a temperature between 30 °C and 100 °C, and high sulfate content. Therefore, SRB isolated from Sikidang Crater may potentially be applied to treat AMD [23]. It is important to evaluate the activity of SRB from the Sikidang Crater sediment attached to the Indonesian natural zeolite medium (as their inert support) within the FBR system. The purpose of this research was to explore the performance of the FBR using the consortium of SRB from the Sikidang Crater sediment using Indonesian natural zeolite as the medium. The performance of the bioreactor was analyzed based on the sulfate reduction efficiency, Cu removal, pH profile, SRB growth, and the changes in mineral composition of the zeolite surface.

■ EXPERIMENTAL SECTION

Materials

The SRB consortium used in this experiment was isolated from Sikidang Crater, Dieng Highland, Banjarnegara district in Central Java. The culture was

incubated in a glass bottle with Postgate B medium at 30 °C. The medium consisted of the following nutrients (in g/L): 8 mL $\text{NaC}_3\text{H}_5\text{O}_3$, 1.0 MgSO_4 , 0.5 NH_4Cl , 1.0 KH_2PO_4 , 0.1 FeSO_4 , 0.5 $\text{C}_6\text{H}_8\text{O}_6$, 0.1 $\text{C}_6\text{H}_{12}\text{O}_6$, 0.1 CaCl_2 , 0.5 Na_2SO_4 , 0.1 yeast extract [24]. Previously, this medium was adjusted to pH 5 and aerated with nitrogen gas to regulate anaerobic conditions. Every 3 weeks, 20% of the SRB culture in the flask was replaced by fresh medium. After two months, a high density bacterial consortium was obtained. Modified Postgate B medium was used for batch and continuous culture experiments. In this experiment, 0.1 g of FeSO_4 was excluded from the media to allow for the assessment of the Cu metals precipitation. This FeSO_4 was replaced by 0.078 g of $\text{CuSO}_4 \cdot 5\text{H}_2\text{O}$ and 2.56 g of Na_2SO_4 , which were added to the medium. The concentration of sulfate and copper (Cu) in the modified medium was 3000 ppm and 20 ppm, respectively.

The natural zeolite used as an inert support for the SRB was collected from a zeolite mine located in the Gunungkidul district, Yogyakarta, Indonesia. The zeolite chemical composition (in % w/w) consists of: SiO_2 86.3%; Al_2O_3 13.7%; Fe_2O_3 2.4%; CaO 2.3%; MgO 0.4%; Na_2O 1.7%; and K_2O 1.8%. The mineral composition consists of clinoptilolite, mordenite, and montmorillonite. The diameter, surface area, pore volume, and pore size of the zeolite were 2–5 mm, 20.0 m^2/g , 12.4 mL/g , and 23.8 Å, respectively. Impurities in the zeolite were removed by washing twice and soaking in deionized water for 24 h at 30 °C. After that, the zeolite was dried for 24 h at 80 °C and used as a support for the immobilization of SRB consortium cultures for both batch and continuous experiments [16].

Instrumentation

Centrifuged (Eppendorf, 5810R) apparatus was used for the separation of bacterial cells and medium. For the analysis of sulfate and manganese removal, a spectrophotometer (Shimadzu UV-1601) and an Atomic Absorption Spectroscopy (AAS) apparatus (Hitachi, Z-2000) were used, respectively. The decrease in pH values in the bioreactor was measured using a pH meter (Metrohm). The characteristics of the biofilm and the copper interacted on the zeolite surface were

observed using Scanning Electron Microscope - Energy Dispersive X-ray (SEM-EDX) (JEOL JSM-T300).

Procedure

SRB cultures

The SRB consortium used in this study was isolated from the Sikidang Crater sediment. About 50 g of wet sediment was transferred to a 1 L flask, which was then completely filled with Postgate B medium, sealed with a rubber stopper, and incubated in the dark at 30 °C. After 7 days of incubation, 200 mL of the culture was inoculated into a fresh medium at 30 °C for 7 days. This sub-culturing into the fresh medium was conducted repeatedly over 3 weeks to maintain a high density of SRB in culture.

Anaerobic batch experiment

The SRB consortium was inoculated into 450 mL of the modified Postgate B medium at anaerobic conditions. Five different doses of zeolite (20, 40, 60, 80, and 100 g/L) was added to each batch of SRB culture and incubated at 30 °C for 14 days. This batch reactor setup was conducted in Erlenmeyer flasks, which were incubated in the incubator. During incubation, samples were collected at 0, 1, 3, 7, 10, and 14 days for further analysis. There were three replications for each of the treatment groups. Anaerobic batch experiments were carried out to determine the optimal zeolite dose and HRT for the anaerobic continuous experiment, which uses a fixed-bed anaerobic bioreactor.

Anaerobic continuous experiment

A continuous laboratory-scale fixed-bed anaerobic bioreactor system was used in this experiment, with Indonesian natural zeolite as supporting material. The bioreactors used in this study were constructed using plastic tubes with an internal diameter of 7 cm and a length of 67 cm (Fig. 1). The adherence of the active SRB biofilm onto the natural zeolite was carried out over one month. For this purpose the Postgate medium was inoculated with SRB consortium culture containing $\sim 3 \times 10^5$ cells/mL (20% v/v) [25]. The modified Postgate B medium was used as a synthetic AMD and was fed into the reactor at a rate of 15.34 mL/h. This bioreactor was then operated with the optimal conditions (temperature, HRT, and zeolite dose) obtained from the batch experiment.

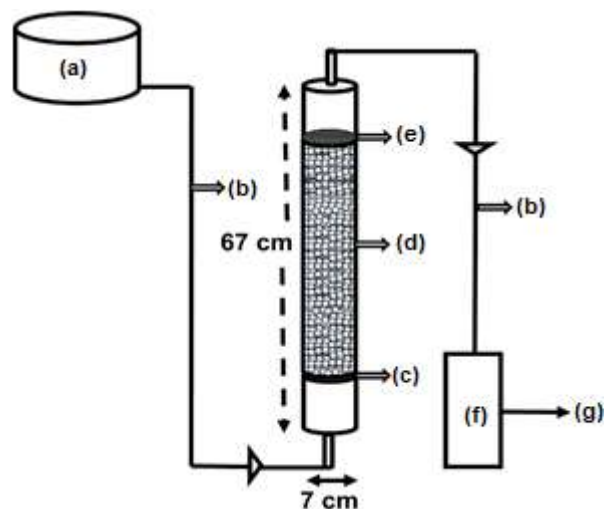


Fig 1. The experimental design of continuous laboratory-scale of the fixed-bed anaerobic bioreactor system: (a) synthetic AMD, (b) connector pipe, (c) stainless steel sieve and filter, (d) SRB biofilm on zeolite surface, (e) filter, (f) outlet, (g) measurements

Chemical analysis

At several time intervals (0, 1, 3, 7, 10, 14 days), 10 mL of a sample from both the batch experiment and continuous experiments were collected using a syringe. These samples were then centrifuged at 5000 rpm at 4 °C for 15 min to obtain the cell-free supernatant. The supernatant was analyzed for their sulfate and copper metal concentrations. Sulfate concentration was analyzed based on the turbid metric method at a wavelength of 420 nm using a spectrophotometer (Shimadzu UV-1601) [25]. To determine the dissolved copper concentration, the supernatant was acidified with HNO₃ and measured through AAS using a spectrometer (Hitachi Z-2000). The pH samples were measured immediately without centrifugation using a pH meter (Metrohm). In addition, the pH during the operation of the bioreactor was also measured.

Characterization of developed SRB population

The SRB consortium in the batch experiments was taken and characterized during both the planktonic phase and the biofilm phase (after 1, 3, 7, 10, and 14 days). Up to 1 mL of the consortium was taken for the planktonic phase, which was diluted with 9 mL sterile water. Whereas, samples of the biofilm phase were collected by

scraping 1 cm² of the zeolite surface using a sterile scraped and then suspended in 10 mL sterile water. The number of SRB consortium were then analyzed in the three-tube Most Probable Number assay with serial dilution [24].

EDX analysis

EDX is a chemical characterization technique used in conjunction with scanning electron microscopy (SEM). JEOL JSM-T300 (environmental scanning electron microscope interfaced with EDAX digital controller) was used. Zeolite (mounted on an aluminum stub that had been covered by colloidal graphite and carbon tape) was placed in the SEM and analyzed under low vacuum mode by tilting to an angle of 15° toward the X-ray gun. A working distance of 10 mm and an accelerating voltage of 15 keV were used for all EDX analyses, and the EDX spectra were collected over 270 sec (i.e., live count time) [26].

Statistical analysis

The data were analyzed statistically using SPSS (v. 20, IBM). A p-value of less than 0.05 was considered to be significantly different. The data were evaluated using one-way ANOVA, followed by a post-hoc Duncan test to analyze the significance of differences across the treatments.

■ RESULTS AND DISCUSSION

Effect of Natural Zeolite Doses on the pH Change, Sulfate Reduction and Cu Precipitation in the Batch Experiment

For the batch experiment, the effects of zeolite dosage on pH, the removal of both sulfate and Cu over time are presented in Fig. 2. Sulfate removal, pH change, and Cu removal are sequential processes that developed during SRB metabolism. The SRB oxidize simple organic compounds, such as lactate, acetate, butyrate, and other fermentation products under anaerobic conditions using sulfate as a terminal electron acceptor. The sulfate is then reduced to hydrogen sulfide and bicarbonate. Hence, this bicarbonate neutralizes the acidity of the medium and produces hydrogen sulfide, which reacts with dissolved copper to form insoluble copper sulfides (CuS) [27].

The zeolite doses had significant effects on SRB activities ($p < 0.05$). The optimal condition was observed in a zeolite dose of 100 g/L. These observations were

consistent with previous investigations [16]. For other bacterial groups, zeolite also plays a role as an adsorbent media in the batch reactor, causing an increase in NH₄-N adsorption capacity that impacts on nitrogen transformation and microbial abundance [28]. Another study reported that a moving bed biofilm reactor (MBBR) using simultaneous bacteria nitrification and denitrification (with zeolite powder-based polyurethane sponges as bio-carriers) could remove 10% more total N in wastewater compared to conventional MBBR [29]. Zeolite also increased methane production by 32 to 97% in the hydrothermal liquefaction processes. Whereas, in laboratory scale investigations over 60 days, swine manure was digested anaerobically using a natural zeolite dose of 40 g/L that produced the highest amount of methane [30].

During the experiments, the removal of sulfate was followed by an increase in pH and a decrease in Cu concentration. The zeolite increased the pH value significantly, which reached a neutral condition in 7 days of operation. Moreover, the Cu concentration decreased significantly after 1 day of operation ($p < 0.05$), and its removal efficiency was around 99.96%. The faster Cu removal after 5 min of operation was also reported by Janyasuthiwong et al. who found removal efficiencies of more than 95.0% [31]. A similarly high Cu removal rate of around 99% was also reported by other researchers [32].

Effect of Natural Zeolite Doses on the Growth of SRB Consortium in the Batch Experiment

It was demonstrated that the SRB consortium developed planktonic and biofilm phases in the bioreactor system. As shown in Fig. 3, the bacterial cell number was higher with zeolite addition than without ($p < 0.05$). This difference was caused by the growth of the biofilm phase, which was shorter compared to the planktonic phase. In addition, the biofilm phase had a shorter lag phase that was observed within 1 day of incubation. In comparison, the planktonic phase was observed at 7 days of incubation. Therefore, the SRB consortium in the biofilm phase was more adaptive to the new environment and the stressful conditions [33]. This phenomenon was observed in previous research

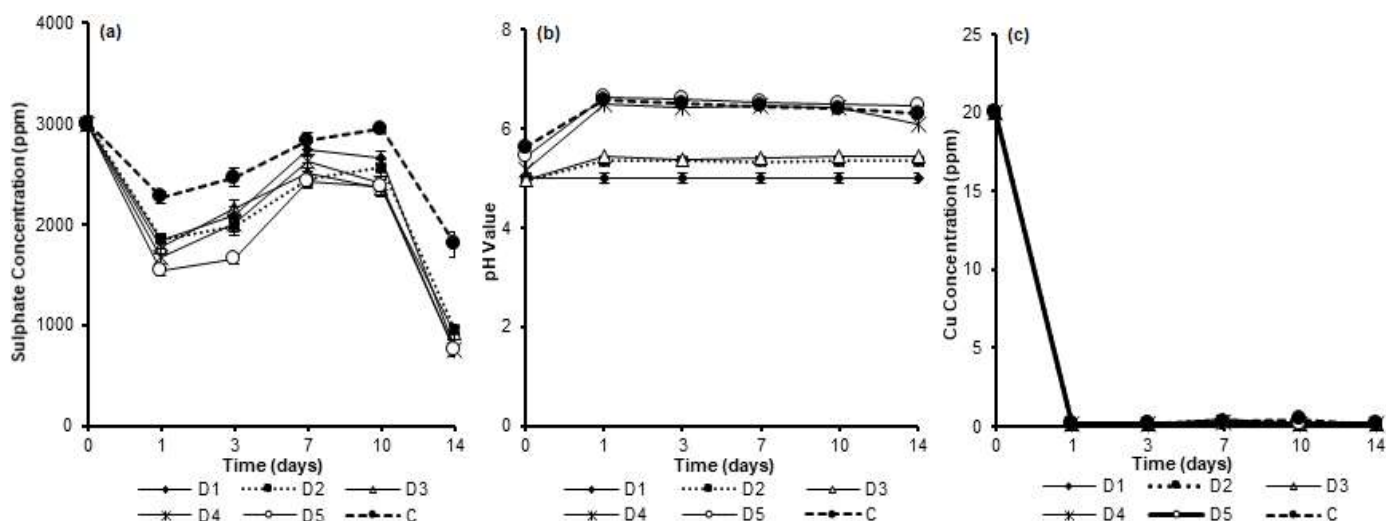


Fig 2. The effect of different zeolite doses on the SRB activity at batch experiment as function of time: (a) the removal of sulfate, (b) change in pH value, (c) the removal of Cu. The treatments D1, D2, D3, D4, and D5 represent zeolite at doses of 20, 40, 60, 80, and 100 g/L, respectively, whereas the control (C) was without zeolite addition

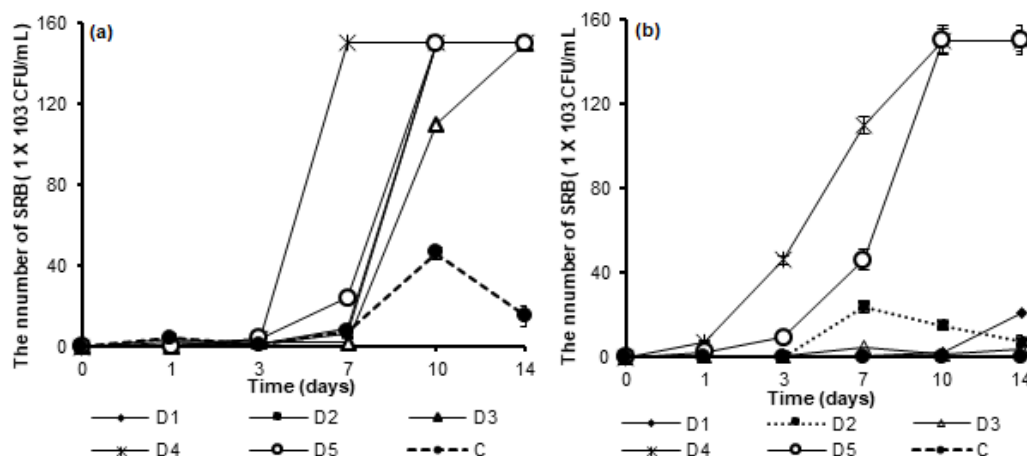


Fig 3. The effect of different zeolite doses on the growth of SRB consortium in the batch experiments, (a) planktonic phase, (b) biofilm phase. The treatments of D1, D2, D3, D4, and D5 represents zeolite doses of 20, 40, 60, 80, and 100 g/L, respectively, whereas the control (C) was without zeolite addition

investigating the formation of the biofilm phase with *Streptococcus mutans*, which was shorter than the planktonic phase. This was due to microorganisms that formed biofilm had several favorable responses in the system. Hence, the microorganisms had higher active biomass, tolerance to toxic compounds, and greater plasmid stability of microbial genes [34].

A large amount of the bacterial biomass was entrapped and attached to the zeolite surface as a biofilm. The highest density of cells was measured at 1.5×10^5 cells/mm². This highest number was observed at zeolite doses of 80 and

100 g/L. However, a zeolite dose of 100 g/L was more adaptive compared with a zeolite dose of 80 g/L.

The Performance of Fixed-bed Anaerobic Bioreactor Experiments

In the continuous experiments, the pH value and copper and sulfate concentrations were measured at various times over a period of 7 days under optimum conditions (30 °C). As demonstrated in Fig. 4, the performance of the bioreactor treatment with a zeolite dose of 100 g/L was more effective compared to the

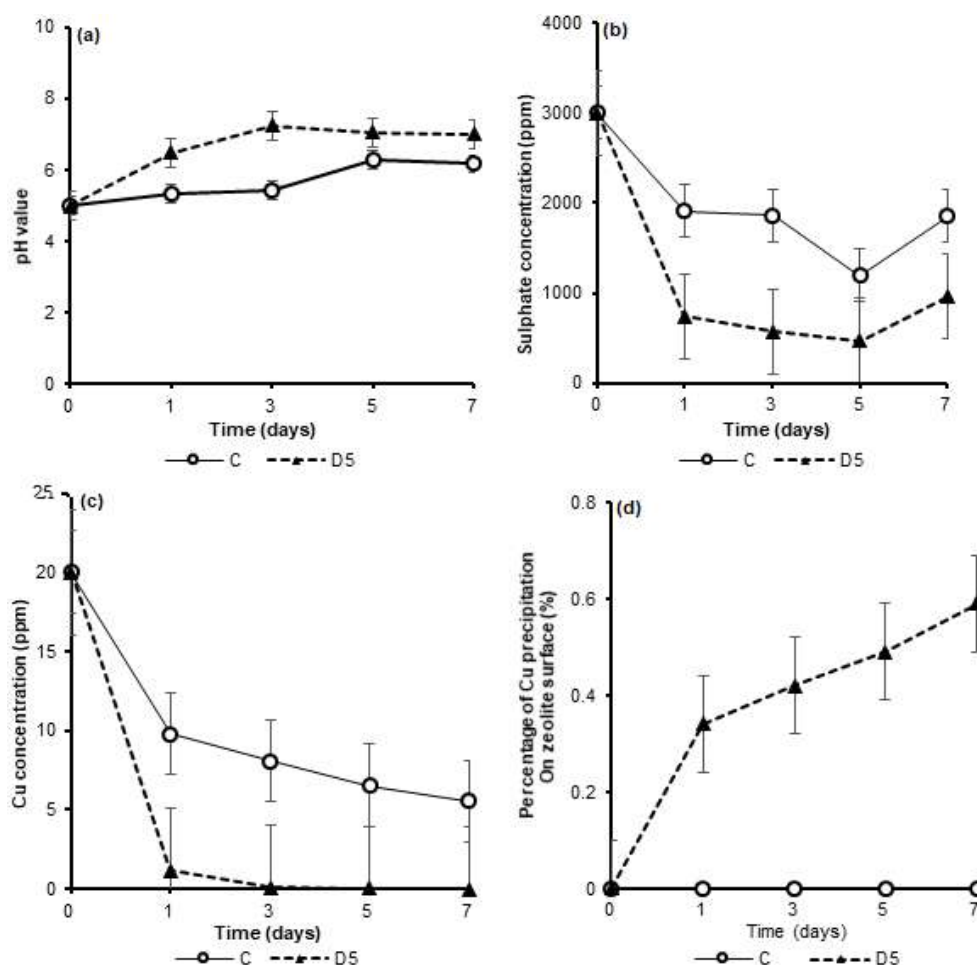


Fig 4. The performance of the fixed-bed anaerobic bioreactor for the treatment of synthetic AMD using the sulfate reducing bacteria consortium from Sikidang Crater sediments (1.5×10^5 cells/mm²) and a natural zeolite dose of 100 g/L with a hydraulic retention time of 7 days at 30 °C. (a) The change of pH values, (b) sulfate concentration, (c) Cu concentration, (d) the percentage of Cu precipitation on the zeolite surface at a dose of 100 g/L. D5: zeolite dose of 100 g/L, and C: without zeolite addition

bioreactor without zeolite as a control for all parameters ($p < 0.05$).

After 7 days of operation, the sulfate concentration of the reactor treatment with a zeolite dose of 100 g/L declined sharply to 920 ppm with 68% removal efficiency, whereas the sulfate concentration of reactor treatment without zeolite was 1848 ppm with 38.4% removal efficiency. These sulfate reduction processes generated hydrogen sulfide and bicarbonate. The bicarbonate neutralizes the acidity of the medium in the bioreactor [25].

The pH values measured after 7 days of operation with a zeolite dose of 100 g/L and without zeolites were 7.0 and 6.61, respectively. In these reactors, hydrogen sulfide

reacts with dissolved copper to form insoluble CuS. Consequently, the Cu concentrations were diminished. The Cu concentration of the reactor treatment with a zeolite dose of 100 g/L was almost completely diminished (99.96%). On the other hand, in the reactor treatment without zeolite, Cu the concentration was reduced by 72.35%. These decreases of Cu in the aqueous solution were followed by the accumulation of Cu in the biofilm surface. The Cu accumulation process on the zeolite surface was dominated by metalloids precipitation caused by the activities of the SRB [35]. In addition, the biofilm extracellular polymeric substances of SRB could entrap the metal sulfide particles [36].

A previous study reported that acid wastewaters at a sulfate loading rate 88 mg/L/h containing 100 mg/L Cu could be remediated by SRB in a fixed-bed anaerobic bioreactor with a metal removal of 94% [37]. The tolerance to heavy metals, pH value, heavy metals, and sulfate removal of immobilized SRB beads was also reported to be significantly enhanced compared with planktonic SRB when the bioreactor was fed with acidic medium containing multiple metals [38]. Another study reported that Indonesian natural zeolite was good inert material for SRB in a laboratory-scale down-flow fluidized-bed reactor. After 9 days of operation, the pH changed to neutral, and sulfate and manganese reduced to 23% and 15.4%, respectively [16].

SEM-EDX Analysis

The composition of the metal precipitates that were accumulated on the surface of zeolite in the bioreactor was determined by SEM-EDX (Fig. 5). The biofilm developed on the support material was investigated after 7 days of incubation. The analysis revealed that Cu was entrapped in both the biofilm and zeolite surface. This observation implies that the metal removal process mainly occurs via sulfide precipitation. The EDX spectra of spots on the zeolite surface revealed the predominance of copper and sulfur at the same precipitation location. This result proved that copper sulfide had been precipitated on the zeolite surface. In addition, this precipitation was confirmed by the results

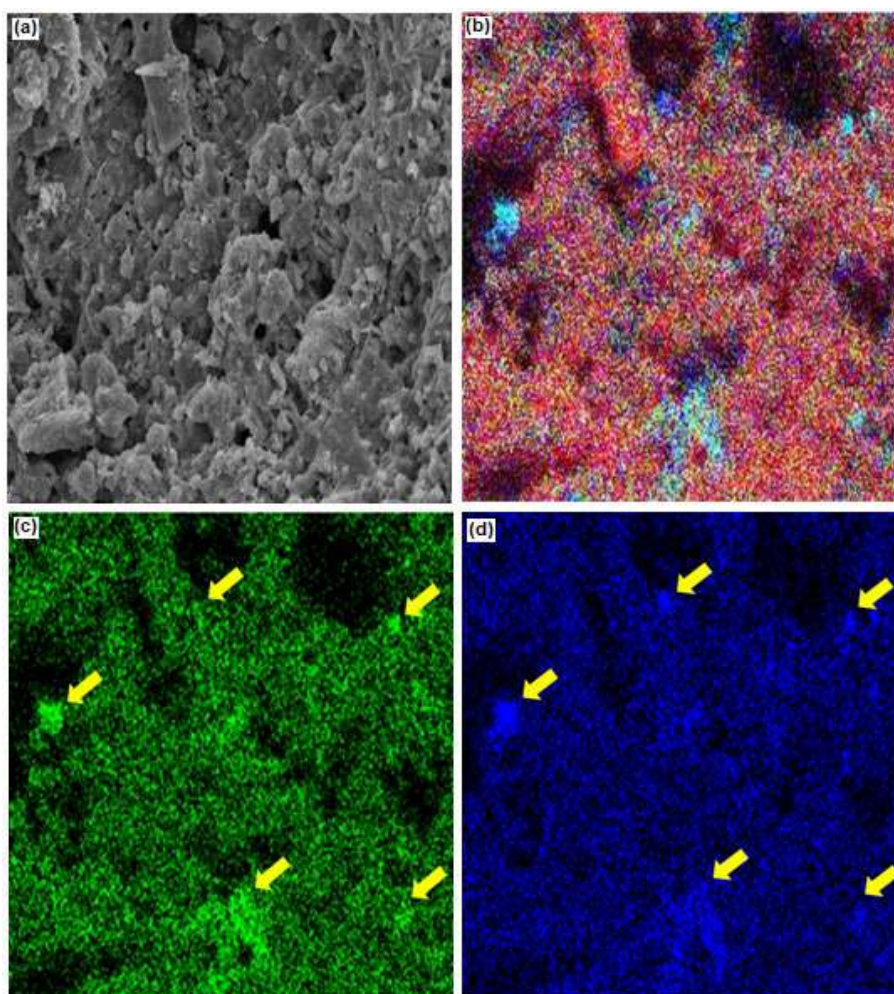


Fig 5. The biofilms developed on zeolites and the composition of their compounds and elements. (a) SEM image of the consortium of SRB biofilms, (b) EDX mapping image of CuS, (c) EDX mapping image of elemental Cu, (d) EDX mapping image of elemental S. The yellow arrows indicate solid CuS precipitants

of the SEM mapping image of copper-sulfides (CuS) in the SRB biofilms consortium. The CuS was precipitated and accumulated on the zeolite surface.

As reported previously, bacterial biofilms could decrease heavy metal pollution in wastewater by several mechanisms, including biosorption, precipitation as sulfides or phosphates, and bacterial reductive precipitation [39]. Therefore, the precipitation process decreased the Cu concentration in the bioreactor. This precipitation was caused by the reaction between Cu and the sulfide produced by SRB. This Cu removal mechanism via CuS precipitation in the SRB biofilm was consistent with previous studies [40]. This precipitation was also reported to be an efficient method for separating toxic metals from wastewater due to the very low solubility of CuS [41].

■ CONCLUSION

The optimal performance of the fixed-bed anaerobic bioreactor was obtained by operating at 30 °C with HRT over 7 days using SRB consortium from Sikidang Crater sediments and a zeolite dose of 100 g/L. The bioreactor could reduce sulfate and Cu concentrations by 68% and 99.96%, respectively. The SRB biomass formed a biofilm on the zeolite surface. Based on the Energy-Dispersive X-ray analysis (EDX), the Cu precipitate was in the form of CuS. In addition, EDX mapping of both Cu and S elements showed that they were precipitated at the same location in the biofilm section.

■ ACKNOWLEDGMENTS

The authors acknowledge the financial support by the KEMENRISTEK DIKTI Indonesia with the Research Implementation Letter No: 663/UN1-P.III/LT/DIT-LIT/2016. We also thank the Laboratorium Penelitian Pusat Terpadu, Universitas Gadjah Mada, Yogyakarta for the SEM-EDX analysis.

■ REFERENCES

- [1] Jamal, A., Yadav, H.L., and Pandey, S.S., 2015, Heavy metals from acid mine drainage in coal mines-A case study, *Eur. J. Adv. Eng. Technol.*, 2 (8), 16–20.
- [2] Hurtado, C., Viedma, P., and Cotoras, D., 2018, Design of a bioprocess for metal and sulfate removal from acid mine drainage, *Hydrometallurgy*, 180, 72–77.
- [3] Larrson, M., Nosrati, A., Kaur, S., Wagner, J., Baus, U., and Nydén, M., 2017, Copper removal from acid mine drainage-polluted water using glutaraldehyde-polyethyleneimine modified diatomaceous earth particles, *Heliyon*, 4 (2), e00520.
- [4] Park, I., Tabelin, C.B., Jeon, S., Li, X., Seno, K., Ito, M., and Hiroyosi, N., 2019, A review of recent strategies for acid mine drainage prevention and mine tailings recycling, *Chemosphere*, 219, 588–606.
- [5] Najib, T., Solgi, M., Farazmand, A., Heydarian, S.Y., and Nasernejad, B., 2017, Optimization of sulfate removal by sulfate reducing bacteria using response surface methodology and heavy metal removal in a sulfidogenic UASB reactor, *J. Environ. Chem. Eng.*, 5 (4), 3256–3265.
- [6] Kumar, A., Bisht, B.S., Josdhi, V.D., and Dhewa, T., 2011, Review on bioremediation of polluted environment: A management tool, *Int. J. Environ. Sci.*, 1 (16), 1079–1093.
- [7] Benedetto, J.S., de Almeida, S.K., Gomes, H.A., Vazoller, R.F., and Ladeira, A.C.Q., 2005, Monitoring of sulfate-reducing bacteria in acid water from uranium mines, *Min. Eng.*, 18 (13-14), 1341–1343.
- [8] Gadd, G.M., and White, C., 1993, Microbial treatment of metal pollution-A working biotechnology?, *Trends Biotechnol.*, 11 (8), 353–359.
- [9] de Aquino, S., Fuess, L.T., and Pires, E.C., 2017, Media arrangement impacts cell growth in anaerobic fixed-bed reactors treating sugarcane vinasse: Structured vs. randomic biomass immobilization, *Bioresour. Technol.*, 235, 219–228.
- [10] Kousi, P., Remoundaki, E., Hatzikioseyan, A., Battaglia-Brunet, F., Joulain, C., Kousteni, V., and Tsezos, M., 2011, Metal precipitation in an ethanol-fed, fixed-bed sulphate-reducing bioreactor, *J. Hazard. Mater.*, 189 (3), 677–684.
- [11] Pandey, S., and Sarkar, S., 2017, Anaerobic treatment of wastewater using a two-stage packed-bed reactor containing polyvinyl alcohol gel beads as biofilm carrier, *J. Environ. Chem. Eng.*, 5 (2), 1575–1585.
- [12] Kumar, G., and Buitrón, G., 2017, Fermentative biohydrogen production in fixed bed reactors using

- ceramic and polyethylene carriers as supporting material, *Energy Procedia*, 142, 743–748.
- [13] Muri, P., Marinšek-Logar, R., Djinović, P., and Pintar, A., 2018, Influence of support materials on continuous hydrogen production in anaerobic packed-bed reactor with immobilized hydrogen producing bacteria at acidic condition, *Enzyme Microb. Technol.*, 111, 87–96.
- [14] Zheng, H., Li, D., Stanislaus, M.S., Zhang, N., Zhu, Q., Hu, X., and Yang, Y., 2015, Development of a bio-zeolite fixed-bed bioreactor for mitigating ammonia inhibition of anaerobic digestion with extremely high ammonium concentration livestock waste, *Chem. Eng. J.*, 280, 106–114.
- [15] Chen, W.S., Tsai, C.Y., Chen, S.Y., Sung, S., and Lin, J.G., 2019, Treatment of campus domestic wastewater using ambient-temperature anaerobic fluidized membrane bioreactors with zeolites as carriers, *Int. Biodeterior. Biodegrad.*, 136, 49–54.
- [16] Retnaningrum, E., and Wilopo, W., 2017, Removal of sulphate and manganese on synthetic wastewater in sulphate reducing bioreactor using Indonesian natural zeolite, *Indones. J. Chem.*, 17 (2), 203–210.
- [17] Encina, P.A.G., and Hidalgo, M.D., 2005, Influence of substrate feed patterns on biofilm development in anaerobic fluidized bed reactors (AFBR), *Process Biochem.*, 40 (7), 2509–2516.
- [18] Sheoran, A.S., Sheoran, V., and Choudhary, R.P., 2010, Bioremediation of acid-rock drainage by sulphate-reducing prokaryotes: A review, *Miner. Eng.*, 23 (14), 1073–1100.
- [19] Zhang, M., Wang, H., and Han, X., 2016, Preparation of metal-resistant immobilized sulfate reducing bacteria beads for acid mine drainage treatment, *Chemosphere*, 154, 215–223.
- [20] Ahmad, M., Liu, S., Mahmood, N., Mahmood, A., Ali, M., Zheng, M., and Ni, J., 2017, Effects of porous carrier size on biofilm development, microbial distribution and nitrogen removal in microaerobic bioreactors, *Bioresour. Technol.*, 234, 360–369.
- [21] Wijesinghe, D.T.N., Dassanayake, K.B., Scales, P.J., Sommer, S.G., and Chen, D., 2018, Effect of Australian zeolite on methane production and ammonium removal during anaerobic digestion of swine manure, *J. Environ. Chem. Eng.*, 6 (1), 1233–1241.
- [22] Kaksonen, A.H., Plumb, J.J., Robertson, W.J., Vanhanen, M.R., Franzman, P.D., and Puhakka, J.A., 2006, The performance, kinetics and microbiology of sulfidogenic fluidized-bed treatment of acidic metal- and sulfate-containing wastewater, *Hydrometallurgy*, 83 (1-4), 204–213.
- [23] Gupta, G.N., Srivastava, S., Khare, S.K., and Prakash, V., 2014, Extremophiles: An overview of microorganism from extreme environment, *Int. J. Agric. Environ. Biotechnol.*, 7 (2), 371–380.
- [24] Kolmert, Å., Wikström, P., and Hallberg, K.B., 2000, A fast and simple turbidimetric method for the determination of sulfate in sulfate-reducing bacterial cultures, *J. Microbiol. Methods*, 41 (3), 179–184.
- [25] Postgate, J.R., 1984, *The Sulphate Reducing Bacteria*, 2nd Ed., University Press, Cambridge, UK, 20–30.
- [26] Cardell, C., and Guerra, I., 2016, An overview of emerging hyphenated SEM-EDX and Raman spectroscopy systems: Applications in life, environmental and materials sciences, *TrAC, Trends Anal. Chem.*, 77, 156–166.
- [27] Cabrera, G., Pérez, R., Gómez, J.M., Abalos, A., and Cantero, D., 2006, Toxic effects of dissolved heavy metals on *Desulfovibrio vulgaris* and *Desulfovibrio* sp. strains, *J. Hazard. Mater.*, 135 (1-3), 40–46.
- [28] Chen, J., Wang, R., Wang, X., Chen, Z., Feng, X., and Qin, M., 2019, Response of nitrification performance and microbial community structure in sequencing biofilm batch reactors filled with different zeolite and alkalinity ratio, *Bioresour. Technol.*, 273, 487–495.
- [29] Song, Z., Zhang, X., Ngo, H.H., Guo, W., Song, P., Zhang, Y., Wen, H., and Guo, J., 2019, Zeolite powder based polyurethane sponges as biocarriers in moving bed biofilm reactor for improving nitrogen removal of municipal wastewater, *Sci. Total Environ.*, 651 (1), 1078–1086.
- [30] Li, R., Liu, D., Zhang, Y., Zhou, J., Tsang, Y.F., Liu, Z., Duan, N., and Zhang, Y., 2019, Improved methane production and energy recovery of post hydrothermal liquefaction waste water via

- integration of zeolite adsorption and anaerobic digestion, *Sci. Total Environ.*, 651 (1), 61–69.
- [31] Janyasuthiwong, S., Rene, E.R., Esposito, G., and Lens, P.N.L., 2015, Effect of pH on Cu, Ni and Zn removal by biogenic sulfide precipitation in an inversed fluidized bed bioreactor, *Hydrometallurgy*, 158, 94–100.
- [32] Welch, K., Cai, Y., and Strømme, M.A., 2012, Method for quantitative determination of biofilm viability, *J. Funct. Biomater.*, 3 (2), 418–431.
- [33] Retnaningrum, E., and Wilopo, W., 2016, Performance and bacterial composition of anodic biofilms in microbial fuel cell using dairy wastewater, *AIP Conf. Proc.*, 1744 (1), 020018.
- [34] Martins, M.M., Faleirob, L., Barros, R.J., Veríssimo, A.R., Barreiros, M.A., and Costa, C.M., 2009, Characterization and activity studies of highly heavy metal resistant sulphate reducing bacteria to be used in acid mine drainage decontamination, *J. Hazard. Mater.*, 166 (2-3), 706–713.
- [35] Miran, W., Jang, J., Nawaz, M., Shahzad, A., Jeong, S.E., Jeon, C.O., and Lee, D.S., 2017, Mixed sulfate-reducing bacteria-enriched microbial fuel cells for the treatment of wastewater containing copper, *Chemosphere*, 189, 134–142.
- [36] Raj, K.K., Sardar, U.S., Bhargavi, E., Devi, I., Bhunia, B., and Tiwari, O.N., 2018, Advances in exopolysaccharides based bioremediation of heavy metals in soil and water: A critical review, *Carbohydr. Polym.*, 199, 353–364.
- [37] Bratkova, S., Koumanova, B., and Beschkov, V., 2013, Biological treatment of mining wastewaters by fixed-bed bioreactors at high organic loading, *Bioresour. Technol.*, 137, 409–413.
- [38] Hullebusch, E.D., Zandvoort, M.H., and Lens, P.N.L., 2003, Metal immobilisation by biofilms: Mechanisms and analytical tools, *Rev. Environ. Sci. Biotechnol.*, 2 (1), 9–33.
- [39] White, C., and Gad, G.M., 2000, Copper accumulation by sulfate-reducing bacterial biofilms, *FEMS Microbiol. Lett.*, 183 (2), 313–318.
- [40] Kiran, M.G., Pakshirajan, K., and Das, G., 2017, Heavy metal removal from multicomponent system by sulfate reducing bacteria: Mechanism and cell surface characterization, *J. Hazard. Mater.*, 324, 62–70.
- [41] Chang, J.C., 1993, “Solubility product constants” in *CRC Hand Book of Chemistry and Physics*, Eds. Lide, D.R., CRC Press, Boca Raton, 8–39.

Overexpression of Lipase Gene from *Alcaligenes* sp. JG3 and its Activity toward Hydrolysis Reaction

Norman Yoshi Haryono, Winarto Haryadi, and Tri Joko Raharjo*

Department of Chemistry, Faculty of Mathematics and Natural Sciences, Universitas Gadjah Mada, Sekip Utara BLS 21, Bulaksumur, Yogyakarta 55281, Indonesia

* **Corresponding author:**

email: trijr_mipa@ugm.ac.id

Received: May 8, 2019

Accepted: July 18, 2019

DOI: 10.22146/ijc.45663

Abstract: Bacterial lipase holds an important role as a new source for many industrial catalysts. The investigation and understanding of the lipase-encoding gene become apparent as the key step for generating high-quality lipase as biocatalyst for many chemical reactions. In this study, bacterial lipase from *Alcaligenes* sp. JG3 was produced via overexpression gene method. This specific lipase was successfully overexpressed using pQE-30 vector and *E. coli* M15[pREP4] as host, producing His-tagged protein sized 46 kDa and was able to hydrolyze triacylglycerol from olive oil with the calculated unit activity and specific activity of 0.012 U and 1.175 U/mg respectively. The *in silico* investigation towards lipase JG3 revealed that it was categorized as ABC transporter protein as opposed to the conventional hydrolase family. Lastly, amino acid sequences SGSGKTT from lipase JG3 was highly conserved sequences and was predicted as the ATP-binding site but the catalytic triad of serine, histidine, and aspartate has not been solved yet.

Keywords: *Alcaligenes*; lipase gene; enzyme activity; a transporter protein

■ INTRODUCTION

Lipases (EC 3.1.1.3) are lipolytic enzymes that are able to perform as a biocatalyst for hydrolysis reaction of triacylglycerol to glycerol and free fatty acid [1]. Not only hydrolysis reaction, but a wide range of chemical reactions could also be assisted by lipase, namely acidolysis, transesterification, esterification, and aminolysis, which make lipase vastly used in various fields of industry. Even to this day, lipase is placed third behind protease and amylase for the most demanded enzyme for industry [2-3]. A more beneficial tendency on lipase study is involving microbial lipase as it has many advantages over lipase from plants and animals, such as; easy to grow, relatively low cost and has higher stability [4]. Looking at these properties, many explorations of microbial lipase have been reported, for example the cold-active lipase from *Candida albicans* [5], organic solvent-tolerant lipase from *Bacillus licheniformis* [6] and thermostable lipase from *Geotrichum candidum* [7].

The mechanism of chemical reaction catalyzed by lipase involves the specific active site that is highly

conserved as pentapeptide Sm-X-Nu-X-Sm, where Sm (small residue) is usually glycine, X could be any residue and Nu (nucleophilic residue) is generally serine [8]. Although the active site of lipase usually remains the same, the homology and protein length of bacterial lipase may vary. Many reported that the protein size of bacterial lipase ranges from 20–60 kDa as determined by electrophoresis SDS-PAGE [3,9-10]. In Indonesia, a certain soil bacterium, *Alcaligenes* sp. JG3 was confirmed to have an extracellular lipase activity toward hydrolysis of olive oil which was up to 5.61 U/mg with the presence of organic solvent *n*-hexane [11-12]. For this bacterium, a particular name has been proposed based on the phylogenetic analysis and the morphological and biochemical tests which is *Alcaligenes javaensis* JG3 [13-14].

An attempt to understand the *Alcaligenes* sp. JG3's lipase (defined as Lip.JG3) have been carried out including investigation of its characteristic and activity as a catalyst, mapping its nucleotide and amino acid sequences and also cloning of the gene [11,15-17]. In this report, overexpression of Lip.JG3 has been carried out

successfully. By doing so, purified Lip.JG3 could be obtained and was able to be put on hydrolysis reaction in order to confirm the gene sequence ability as a lipase enzyme. The overexpressed Lip.JG3 were meant for possible further studies such as kinetics of lipase-catalyzed reaction determination and stability of over expressed Lip.JG3 investigation in order to be the new source of lipase for producing biodiesel or flavoring agent.

■ EXPERIMENTAL SECTION

Materials

Alcaligenes sp. JG3 bacterium samples were a collection of Laboratorium Penelitian dan Pengujian Terpadu UGM, originally isolated from the root of *Zea mays* in the agricultural land of Purwokerto, Central Java, Indonesia [18]. Primer forward Fjg3 (5'-ATGACCGAGC TGA CTGTAG-3'), Fexp (5'-GGATCCACCGAGCTGA CTGTAGAC-3') and reverse Rjg3 (5'-TCAGGAGGGGT AAATCCAC-3'), Rexp (5'-AAGCTTGGAGGGGTAAA TCCACAG-3'), agarose, proteinase-K, ethidium bromide, DNA marker, nuclease-free water, Quick Miniprep Plasmid Kit (Invitrogen), QIAexpressionist Kit Type IV (Qiagen), BamHI and HindIII restriction kit (Promega), MgCl₂, NaCl, Sodium dodecyl sulfate (SDS), isopropanol, ethanol, tris base (Merck), Triton X-100, Na-EDTA (Sigma), TAE buffer, loading buffer (Vivantis), extra virgin olive oil (Bertolli), Pierce BCA protein assay kit and pre-stained protein marker (Thermo Fisher Scientific), Go taq green PCR mix, SOC medium, LB medium, nutrient agar, nutrient broth (NB), *n*-hexane, acetic acid, ammonium persulfate, tetramethylethylenediamine (TEMED), Coomassie blue, acrylamide, bis-acrylamide,

glycine, phenolphthalein, and also antibiotic ampicillin and kanamycin. All the chemicals used in this study were of pro-analysis laboratory grade.

Instrumentation

The instruments used in this study were Thermal Cycler (Bio-Rad), SDS and Gel electrophoresis (Bio-Rad), Gel Documentation System (Bio-Rad), UV lamp (Bio-Rad), Autoclave (Hirayama HL 36 AE), Vortex (Barnstead), Water Bath Incubator (OSK Seiwa Reiko), Centrifuge (Sorvall Biofuge), UV-Visible Spectrophotometer (Shimadzu Probe), Shaking Incubator Chamber, Ultrasonic Cell Crusher (SJIA-250W), MEGA 7.0 software and bioinformatics online servers e.g. MUSCLE, PSIPRED and I-TASSER.

Procedure

DNA isolation and cloning of the lipase gene

DNA isolation, amplification gene and cloning of Lip.JG3 conducted in this study were derived from the previous research [17].

Construction of lipase gene DNA recombinant onto pQE expression vector

Fifty ng of isolate pGEM-T/Lip.JG3 was amplified using primer Fexp and Rexp by the following conditions: pre-denaturation for 5 min at 95 °C, 35 cycles of denaturation at 95 °C for 30 sec, annealing at 57 °C for 30 sec, extension at 72 °C for 30 sec and post-extension at 72 °C for 10 min. For constructing the pQE-lipase JG3 DNA recombinant, both lipase JG3 DNA and pQE vector needed to undergo restriction reaction to provide the complement nucleotides sites. A set of reactions was prepared (Table 1) and then incubated in a water bath at

Table 1. Composition mixtures for restriction reaction

Component	Volume (μL)	Component	Volume (μL)
Ultrapure water	0.8	Ultrapure water	14.8
Buffer E	2	Buffer E	2
Acetylated BSA	0.2	Acetylated BSA	0.2
Lip.JG3 DNA	15	pQE vector	1
Gently mixed by pipetting		Gently mixed by pipetting	
BamHI	1	BamHI	1
HindIII	1	HindIII	1
Gently mix by pipetting (final volume 20 μL)		Gently mix by pipetting (final volume 20 μL)	

37 °C for 4 h. After the reaction was finished, both lipase JG3 DNA and pQE vector were analyzed with electrophoresis agarose 1.5% and purified using Pure Link™ Quick Gel Extraction Kit. The ligation reaction was performed with a mixture of 15 and 5 µL of restricted lipase JG3 and pQE vector respectively, 8 µL 2xRapid Ligation Buffer and 2 µL T4 DNA ligase and then incubated overnight at 4 °C to generate pQE-lipase JG3 DNA recombinant.

Overexpression of lipase protein

Before the Lip.JG3 could be overexpressed, the recombinant DNA needed to be cloned into a compatible host. The gene transformation was carried out via a heat-shock procedure. Ten µL of the ligation mix was put on the sterile 1.5 mL microtube and 50 µL of the thawed *E. coli* M15[pREP4] aliquot was added to the tube. The mixture was then mixed gently and kept on ice for 20 min. After that, the tube was transferred to a 42 °C water bath for 90 sec and immediately returned to the ice for another 2 min. To the mixture, 940 µL SOC medium was added and incubated at 37 °C for 1.5 h with shaking. The *E. coli* aliquot was plated on LB-agar medium containing ampicillin 100 µg/mL and kanamycin 25 µg/mL incubated overnight at 37 °C.

For lipase protein overexpression, a single colony from LB-agar plate was picked, transferred into 5 mL LB-broth containing antibiotic and incubated overnight at 37 °C. Five hundred µL of overnight cultures then inoculated into 200 mL LB-broth and incubated with shaking until the OD₆₀₀ was 0.5–0.7. After the desired OD₆₀₀ was reached, IPTG was added to the cultures (to a final concentration of 1 mM) to induce expression and incubated at 37 °C with shaking for another 5 h. The cells were harvested by centrifugation (6000 rpm for 15 min) and washed twice using PBS buffer to remove all the medium. The harvested cells were then resuspended using 2 mL PBS buffer and sonicated for 4 min using 2 sec bursts and 1 sec cooling down between each burst to break down the cell. The lysate was centrifuged for 5 min at 6000 rpm and the supernatant was collected as crude protein extract.

Since the expressed lipase protein was tagged with 6xHistidine protein, it can be purified using Ni-NTA matrices. Five hundred µL Ni-NTA agarose slurry was loaded into purification column and 500 µL crude protein

extract was transferred into the column, then the mixture was centrifuged at 2000 rpm for minutes (this process was repeated until all the crude extract was loaded into the column). The lysate-Ni-NTA mixture was washed three times using 400 µL PBS buffer containing 20 µM imidazole and then the lipase JG3 protein was eluted using 200 µL PBS buffer containing 250 µM imidazole. Each flow-through was collected separately for further analysis.

Concentration quantification of each flow-through was performed using bicinchoninic acid (BCA) protein assay. For the standard curve, a series of BSA (Bovine Serum Albumin) was made with the concentration ranging from 0–2000 µg/mL. As for the sample, 50 µL of each flow-through was mixed with 1 mL working reagent and then incubated for 30 min at 37 °C and then the absorbance of each sample was measured at wavelength 562 nm. The protein concentration can be calculated as the slope of the standard curve equation. For qualitative analysis, each sample was examined using electrophoresis SDS-PAGE (10% polyacrylamide) at 100 volts and visualized with Coomassie blue.

Determination of lipase activity via a hydrolysis reaction

Determination of lipase activity was conducted using the titrimetric method by measuring the free fatty acid formed from hydrolysis reaction. One gram of olive oil was diluted to a final volume of 10 mL using *n*-hexane. Five hundred µL of purified lipase was added to the mixture and incubated for 5 h on shaker incubator (37 °C, 150 rpm). After the reaction was completed, the polar phase was separated and diluted with the addition of 10 mL ethanol and 2–3 drops of PP indicator was added to the solution. The free fatty acid was titrated with NaOH 0.0125 M (standardized by oxalic acid). As a control reaction, the same mixture composition was used without lipase enzyme. The lipase activity can be calculated by the following equations:

$$\text{Unit activity (U)} = \frac{(V_{\text{NaOH sample}} - V_{\text{NaOH standard}}) M_{\text{NaOH}}}{\text{time of reaction}} \quad (1)$$

$$\text{Specific activity (U / mg)} = \frac{\text{unit activity}}{\text{enzyme mass}} \quad (2)$$

Analysis of lipase protein structure and function

In silico approximation was used to analyze the homology, structure, and function of Lip.JG3 [15]. Alignment of multiple lipase sequences was performed using MUSCLE (<https://www.ebi.ac.uk/Tools/msa/muscle/>), the distribution of secondary structure of Lip.JG3 was carried out using PSIPRED server (<http://bioinf.cs.ucl.ac.uk/psipred/>) and prediction of 3D for Lip.JG3 was conducted using I-TASSER (<https://zhanglab.ccmb.med.umich.edu/I-TASSER/>).

RESULTS AND DISCUSSION

Construction of DNA Recombinant

Based on the restriction map and restriction enzyme list of the vector multi-cloning sites, a pair of expression primer was designed by adding the chosen enzyme restriction sites (G-GAT and A-AGC that would be cleaved by BamHI and HindIII restriction enzymes respectively) to the prior primer pair (Fjg3 and Rjg3). Cutting the pQE-30 vector plasmid using this restriction enzyme, two sticky-end sites were created making the recombination DNA prone to be successful. The appearance of the cleaved plasmid (only one band appeared) was somewhat different compared to the initial plasmid (three bands appeared) as shown in Fig. 1(a) and (b). This phenomenon occurred due to the three typical conformations of plasmid that no longer exist after being cleaved by restriction enzymes. The isolated DNA of pGEM-T/Lip.JG3 were amplified using primer Fexp and Rexp resulting ~1100 bp amplicon as can be seen in Fig. 1(c). To this amplicon, the restriction procedure was also performed creating the compliment of the cleaved plasmid.

Overexpression of Lipase JG3

Prior to overexpression, the cut pQE-30 and Lip.JG3 were ligated and transformed into the host cell of *E. coli* [M15pREP4]. This pQE-30 vector has many features like consisting of strong T5 promoters, containing two strong transcriptional terminators (t_0) to prevent read-through transcription and ensure the stability of the expressed protein and providing multiple cloning sites and 6xHis-tag coding sequence to ease the purification of the protein

target. Since the T5 promoter can initiate a high transcription rate, the existence of high-level repressor becomes crucial to regulate the expression. Thus, any *E. coli* host strain containing the repressor [pREP4] shall be used for the production of recombinant protein.

The transformed *E. coli* containing recombinant of pQE30/Lip.JG3 was inoculated on LB-agar medium in the presence of ampicillin antibiotic (Fig. 2(a)). DNA recombinant was isolated and cut using the previously restricted enzyme to check the availability of pQE-30/Lip.JG3. The enzyme restriction produced two bands of DNA sized ~3 and ~1.1 kb representing the pQE-30 vector and Lip.JG3 gene (Fig. 2(b)). Having confirmed the presence of pQE-30/Lip.JG3 in the host, a single colony of *E. coli* was rejuvenated until OD₆₀₀ was 0.5–0.7 before induced by the addition of IPTG. Analysis of crude and purified lipase using SDS-PAGE is presented in Fig. 3. The lipase JG3 protein appeared as a single band at ~46 kDa. Many comparable molecular weight from bacterial lipases have been reported, for instance, lipase from *B. stearotheophilus*, *T. atroviride* LipB, *Acinetobacter* sp. AU07, *B. thermoleovorans* ID-1, *Cohnella* sp. A01, which were 67.0 kDa, 57.0 kDa, 45.0 kDa, 34.0 kDa, 29.5 kDa, respectively, as determined using SDS-PAGE electrophoresis [19-21].

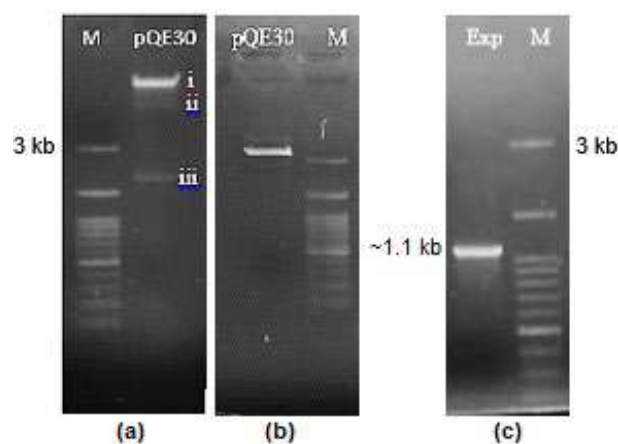


Fig 1. Electrophoresis visualization of (a) uncut pQE-30 vector, symbol i, ii and iii indicating three plasmid conformation state of relaxed, linear and supercoiled, (b) cut pQE-30 vector, (c) amplified Lip.JG3 using expression primer

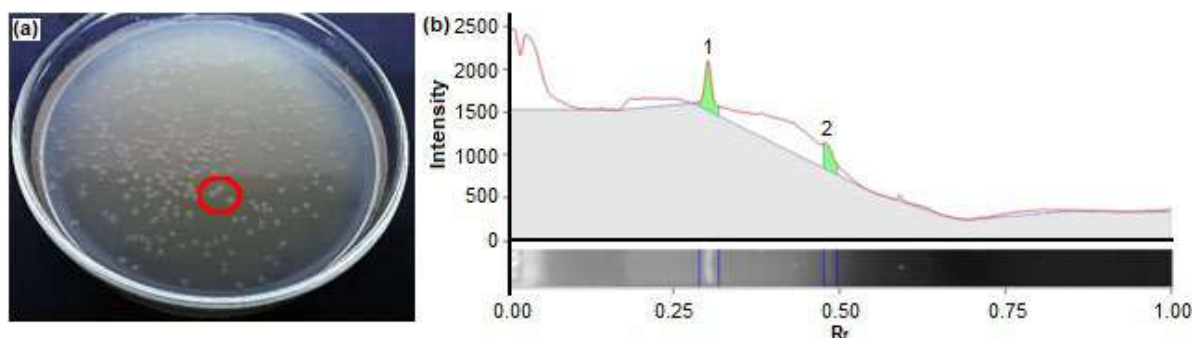


Fig 2. (a) Representative of the transformed *E. coli* colonies containing DNA recombinant of pQE-30/Lip.JG3 (circled in red) and (b) Visualization of BamHI and HindIII restriction using Gel Documentation System; peak 1 was the pQE-30 vector and peak 2 was Lip.JG3 gene

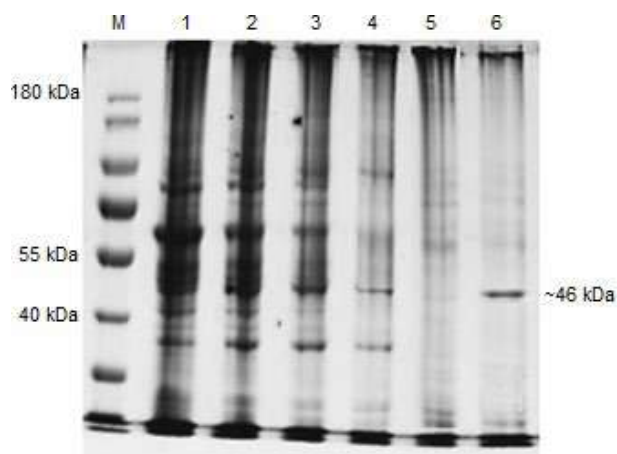


Fig 3. Visualization of SDS-PAGE analysis. Lane M: protein marker, 1: crude extract protein, 2: flow through from initial binding, 3: first wash, 4: second wash, 5: third wash and 6: purified Lip.JG3 protein from the Ni-NTA resin column

Lipase JG3 Activity on Hydrolysis Reaction

Determination of Lip.JG3 unit activity and specific activity were carried out via hydrolysis reaction toward extra virgin olive oil to produce a free fatty acid. Extra virgin olive oil was chosen instead of regular olive oil due to the high percentage of unsaturated long-chained ester in it and lipase favors such substrate [22]. The purification

and activity of Lip.JG3 is summarized in Table 2. Both of the unit activity and specific activity for crude extract and second washed protein was lower than purified Lip.JG3 due to the presence of many other proteins that might interfere with the hydrolysis reaction although the amount of the protein itself was higher. On another report, a similar pattern of hydrolysis activity from purified lipase had higher activity than the crude extract from *Bacillus amyloliquefaciens* PS35 [23].

The specific activity of purified Lip.JG3 was lower than the previous study which was up to 5.61 U/mg [11]. This phenomenon might occur due to the incubation time of the previous study that was much longer (12 h) resulting in a more significant amount of lipase. Besides that, overexpression of Lip.JG3 involved washing steps that may reduce the amount of purified lipase, hence the lower the specific activity. Nevertheless, Lip.JG3 was proven to be able to catalyze the hydrolysis reaction and therefore can be put into consideration as the new source of microbial lipase. To increase the activity of His-tagged expressed enzyme, one may remove the histidine sequences. By doing so, the activity of lipase without histidines was able to increase up to 1.58 fold on pNPP assay [24].

Table 2. Summary of the purification of lipase and enzyme activity

Sample	Protein concentration (mg/mL)	Protein used on hydrolysis reaction (mg)	Unit activity (U)	Specific activity (U/mg)
Crude extract	2.173	1.086	0.005	0.005
Second washed protein	0.215	0.043	0.005	0.116
Purified Lip.JG3	0.051	0.010	0.012	1.175

Prediction of Lipase JG3 3D Structure

Structural knowledge of biomolecules is a vital key to comprehend the function and mechanism of action, because the different structure of one protein to another may lead to the differentiation of act. Bioinformatics is a recent approach to predict the structure and function of a protein [25]. Amino acids vary in their ability to form various secondary structure elements. This secondary structure can be used to enhance the multiple sequences alignment between proteins as it gives more accurate information than the simple sequence that is sometimes unalignable [26]. Fig. 4 shows the distribution of Lip.JG3 secondary structure that possessed 41.67, 25.89 and 32.44% of coil, strand and helix conformation, respectively.

I-TASSER, an automated protein structure, and function were used to predict the 3D model of Lip.JG3 as shown in Fig. 5(a). I-TASSER generates full-length atomic structural models from multiple threading alignments and iterative structural assembly simulations followed by atomic-level structure refinement [27]. Using multiple protein-protein network and structure comparison, I-TASSER deduced Lip.JG3 to have the most similar function with template protein of Fe^{3+} ions import ATP-binding protein FbpC since it showed a high score in C-Score (0.89). Although this template protein (PDB Hit: 3fvqA) acts as a transport protein, it is classified into hydrolase superfamily since ABC Transporter Protein is able to hydrolyze ATP to power up

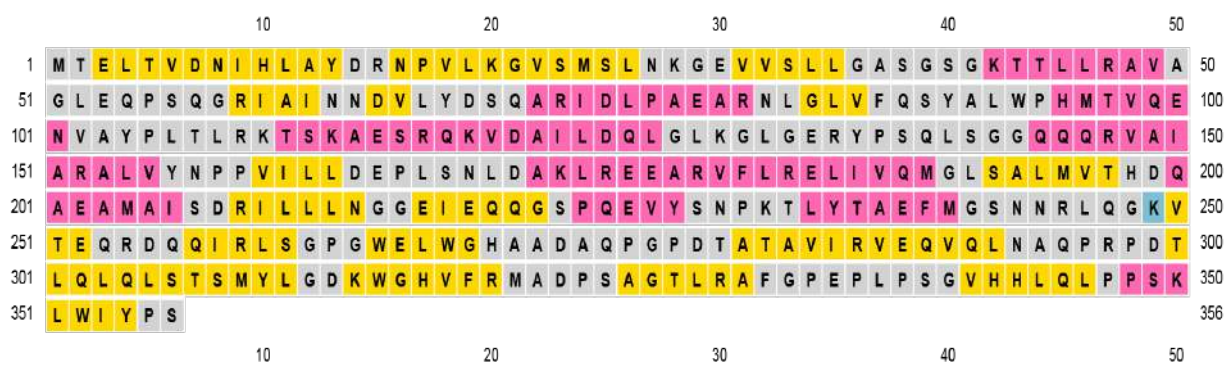


Fig 4. Distribution of secondary structure conformation for Lip.JG3, where the conformation of sheet, helix and coil are represented by the color of yellow, pink and grey respectively

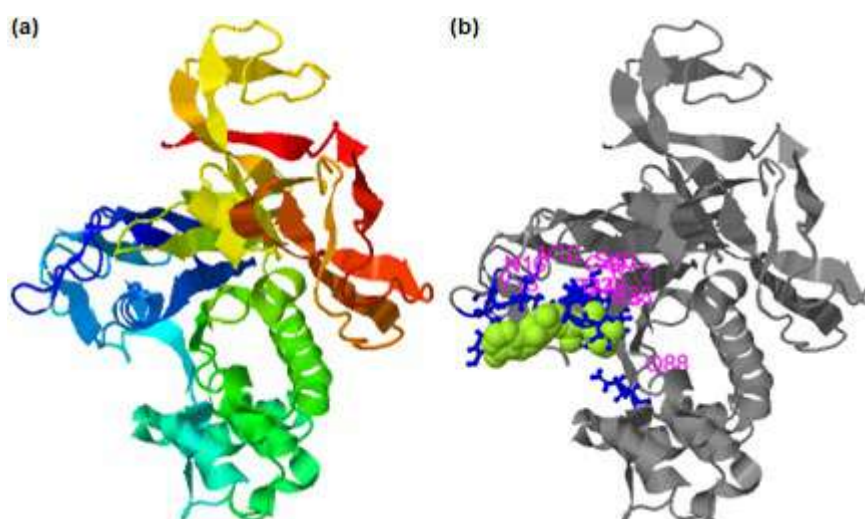


Fig 5. (a) Lip.JG3 3D structure prediction; blue to red color implies N- to C- termini (b) Predicted interaction of Lip.JG3 with ligand ATP, green and blue color represent ligand amino acid binding sites based on the template of PDB Hit: 3fvq

its act [28-29]. On the other hand, Lip.JG3's 3D model has the highest similarity with ABC-ATPase (PDB Hit: 1OXT) based on TM-align structural alignment program to match the model of all structures in the PDB library with TM score up to 0.939 [30].

Homology of Lipase JG3 Protein

Based on the similarity of sequence, structure, and function, lipases may be classified into different groups. There are eight known classes of microbial lipase based on the conserved amino acids sequence and biochemistry properties. Lip.JG3 consists of 357 amino acids and share 98% similarity with lipase from *Alcaligenes faecalis* subsp. *faecalis* NCIB 8687 but the nucleotide sequence share not as high similarity, due to the fact that one amino acid is encoded by more than one possible codon. That is why the nucleotide sequence of the lipase gene is varied although the conserved sequence is still able to be observed [31].

As stated above, Lip.JG3 has the characteristic of protein that comes from an ABC Transporter family. To validate that statement, homology analysis was performed

towards other ABC Transporter lipases such as *Serratia marcescens* and *Alcaligenes faecalis* and is shown in Fig. 6. Based on the homology analysis of the three lipases, they share the conserved sequences of Walker-A (LLGASGSGKTT) and Walker-B (VILLDEP) motif and also ABC signature nucleotides (LSGGQQQRVAIA) underlined in red.

Active Site of Lipase JG3

Generally, lipases from hydrolase family have the catalytic triad of serine, histidine, and aspartate [32]. Since Lip.JG3 was suggested as ABC Transporter Protein, it might be difficult to pinpoint the catalytic triad precisely without Molecular Dynamic (MD) simulation. However, previous studies reported that lipase from *Serratia marcescens* has a loop or helical lid which is responsible for the lipase activation. The presence of this lid over the lipase's active site contribute lipase activity in the interphase of water-oil, when the lid is open lipase active site may bind substrate and convert it into desirable product [33-34].

```

Ser    MIELSVENLHLTYGDNFVLKGVSMDLKRGVVSLLGSPSGSGKTTLLRAVAGLEKPSQGRI
Fae    MTELTVENIHLAYDRNFVLKGVSMNLKGEVVSLLGASGSGKTTLLRAVAGLEQPSQGRI
JG3    MTELTVDNIHLAYDRNFVLKGVSMNLKGEVVSLLGASGSGKTTLLRAVAGLEQPSQGRI
      * * * * * * * * * * * * * * * * * * * * * * * * * * * * * * * * * * * *
Ser    VIGNSAVYNGSARSEI PAEERNLGLVFQSYALWPHKTVFENVAYPLKLRKTASAEIAQRV
Fae    TINNDVLYDSQARIDLPAEARNLGLVFQSYALWFHMTVQENVAYPLTLRKTSKAESRQKV
JG3    AINNDVLYDSQARIDLPAEARNLGLVFQSYALWFHMTVQENVAYPLTLRKTSKAESRQKV
      * * * * * * * * * * * * * * * * * * * * * * * * * * * * * * * * * * * *
Ser    QAVLDQLGLGHLAKRHPHQLSGGQQQRVAIGRALVYNPPFVILLDEPLSNLDAKLREEARV
Fae    EAILDQLGLKGLGERYPQLSGGQQQRVAIARALVYNPPFVILLDEPLSNLDAKLREEARV
JG3    DAILDQLGLKGLGERYPQLSGGQQQRVAIARALVYNPPFVILLDEPLSNLDAKLREEARV
      * * * * * * * * * * * * * * * * * * * * * * * * * * * * * * * * * * * *
Ser    FLRELI IKLGLSALMVTHDQNEAMAI SDRILLNNGKIEQQGTPOEMYGSPPTLFTAEFM
Fae    FLRELIVEMGLSALMVTHDQAEAMAI SDRILLNNGNIEQQGTPOEVYSNPKTYLTAEFM
JG3    FLRELIVQMGLSALMVTHDQAEAMAI SDRILLNNGEIEQQGSPQEVYSNPKTYLTAEFM
      * * * * * * * * * * * * * * * * * * * * * * * * * * * * * * * * * * * *
Ser    GSNNRLPGKVVALEGDRARIEGKDWALWGKAGEGVQVQEGTAVIRVERVRLGEDPQGNQ
Fae    GSNNRLQGTVSEQREQQTRLSGPGWELWGHAAAPLTPGQQATAVIRVEQVQLNTPGPGPET
JG3    GSNNRLQGVTEQRDQQIRLSGPGWELWGHAAADAQPDPDTATAVIRVEQVQLNAQPRPDT
      * * * * * * * * * * * * * * * * * * * * * * * * * * * * * * * * * * * *
Ser    LELPLLSTMYLGDREWEYLFRTVAEDF-VVRAYGHEARDRALCRLSLPAEHLWIFPKA
Fae    LQLHLSTMYLGDKWEHVFRMADPSAGTLRAFGEPLPGGVHHLQLPPSKLWIYPS-
JG3    LQLQLSTMYLGDKWEHVFRMADPSAGTLRAFGEPLPSGVHHLQLPPSKLWIYPS-
      * * * * * * * * * * * * * * * * * * * * * * * * * * * * * * * * * * * *

```

Fig 6. Alignment of Lip.JG3 amino acid sequence against lipase/ABC Transporter from *Serratia marcescens* (NCBI ID: WP_025304186.1) and *Alcaligenes faecalis* (NCBI ID: HCA17200.1)

Many suggestions have been proposed to solve the mechanism of ABC protein to hydrolyze the appropriate substrate. The Walker-B motif, specifically the glutamic acid residue is predicted as the active site as it directly binds into the phosphodiester bond resulting hydrolysis reaction [15]. Residues of T⁴³, Q⁸⁸, D1⁶⁴, and E¹⁶⁵ from Lip.JG3 amino acid sequence was predicted to have the ability to bind Mg²⁺, as well as from another ABC Transporter protein. The presence of Mg²⁺ enhances the binding ability of phosphate residue on ATP. While the residues of Y¹³, N¹⁶, V¹⁸, S³⁸, G³⁹, S⁴⁰, G⁴¹, K⁴², T⁴³, T⁴⁴, and Q⁸⁸ are predicted to be the binding site for Ca²⁺ and the activity of crude extract lipase from *Alcaligenes* sp. JG3 is enhanced by 1.38 times with the addition of Ca²⁺ [11]. This type of metal ion bond implies that the act of this enzyme is supported by metal ion cofactors [35].

The classification of ABC transporter for Lip.JG3 might be highlighted due to the possibility of the protein secretion via ABC exporter pathway [36]. Although the amino acid sequences of Lip.JG3 responsible for ATP-binding was able to be defined and it is also able to catalyze hydrolysis reaction, the true catalytic sequences responsible to bind with the triacylglycerol has yet to be confirmed. Further simulation of the interaction between Lip.JG3 and oil substrate is still needed to be investigated.

■ CONCLUSION

The overexpression of lipase gene from *Alcaligenes* sp. JG3 was successfully carried out with *E. coli* M15[pREP4] as host, producing lipase protein sized 46 kDa. The Lip.Jg3 was able to hydrolyze olive oil with calculated unit activity and specific activity of 0.012 U and 1.175 U/mg respectively. From 3D protein structure analyses, Lip.JG3 belonged to the ABC transporter protein superfamily, indicating that it might be secreted via the ABC pathway.

■ ACKNOWLEDGMENTS

This research was fully funded by the Ministry of Research, Technology and Higher Education of the Republic of Indonesia with the contract number 2033/UN1/DITLIT/DIT-LIT/LT/2018. Surajiman, Istini

and Tri Purwanti are acknowledged for laboratory technical assistance.

■ REFERENCES

- [1] Lajis, A.F.B., 2018, Realm of thermoalkaline lipases in bioprocess commodity, *J. Lipids*, 2018, 5659683.
- [2] Singh, R., Kumar, M., Mittal, A., and Mehta, P.K., 2016, Microbial enzymes: Industrial progress in the 21st century, *3 Biotech*, 6 (2), 174.
- [3] Boshale, H., Shaheen, U., and Kadam, T., 2016, Characterization of a hyperthermostable alkaline lipase from *Bacillus sonorensis* 4R, *Enzyme Res.*, 2016, 4170684.
- [4] Patil, K.J., Chopda, M.Z., and Mahajan, R.T., 2011, Lipase biodiversity, *Indian J. Sci. Technol.*, 4 (8), 971–982.
- [5] Lan, D., Yang, N., Wan, W., Shen, Y., Yang, B., and Wang, Y., 2011, A novel cold-active lipase from *Candida albicans*: Cloning, expression, and characterization of the recombinant enzyme, *Int. J. Mol. Sci.*, 12 (6), 3950–3965.
- [6] Anbu, P., and Hur, B.K., 2014, Isolation of an organic solvent-tolerant bacterium *Bacillus licheniformis* PAL05 that is able to secrete solvent-stable lipase, *Biotechnol. Appl. Biochem.*, 61 (5), 528–534.
- [7] Sangeetha, R., Geetha, A., and Arulpandi, I., 2010, Concomitant production of protease and lipase by *Bacillus licheniformis* VSG1: Production, purification, and characterization, *Braz. J. Microbiol.*, 41 (1), 179–185.
- [8] Anobom, C.D., Pinheiro, A.S., De-Andrade, R.A., Aguiéiras, E.C.G., Andrade, G.C., Moura, M.V., Almeida, R.V., and Freire, D.M., 2014, From structure to catalysis: Recent development in the biotechnological applications of lipases, *Biomed. Res. Int.*, 2014, 684506.
- [9] Bora, L., and Bora, M., 2012, Optimization of extracellular thermophilic highly alkaline lipase from thermophilic *Bacillus* sp. isolated from hot spring of Arunachal Pradesh, India, *Braz. J. Microbiol.*, 43 (1), 30–42.

- [10] Shu, C.H., Xu, C.J., and Lin, G.C., 2006, Purification and partial characterization of a lipase from *Antrodia cinnamomea*, *Process. Biochem.*, 41 (3), 734–738.
- [11] Lestari, P., Handayani, S.N., and Oedjijono, O., 2009, Sifat-sifat biokimiawi ekstrak kasar lipase ekstraseluler dari bakteri *Azospirillum* sp. JG3, *Molekul*, 4 (2), 73–82.
- [12] Ethica, S.N., 2014, Determination of genes involved in glycerol metabolism of *Alcaligenes* sp. JG3, *Dissertation*, Universitas Gadjah Mada, Yogyakarta, Indonesia.
- [13] Ethica, S.N., Oedjijono, Semiarti, E., Widada, J., and Raharjo, T.J., 2018, Genotypic and phenotypic characterization of *Alcaligenes javaensis* JG3 potential as an effective biodegrader, *BIOTROPIA*, 25 (1), 1–10.
- [14] Ethica, S.N., Nataningtyas, D.R., Lesteri, P., Istini, Semiarti, E., Widada, J., and Raharjo, T.J., 2013, Comparative evaluation of conventional versus rapid methods for amplifiable genomic DNA isolation of cultured *Azospirillum* sp. JG3, *Indones. J. Chem.*, 13 (3), 248–253.
- [15] Nataningtyas, D.R., Raharjo, T.J., and Astuti, E., 2019, Three-dimensional structural modeling of the lipase-encoding gene from soil bacterium *Alcaligenes* sp. JG3 using automated protein homology analysis, *Indones. J. Chem.*, 19 (3), 565–574.
- [16] Raharjo, T.J., Haryono, N.Y., Nataningtyas, D.R., Alfiraza, E.N., and Pranowo, D., 2016, Characterization of lipase gene fragment from *Alcaligenes* sp. JG3 bacterium, *Am. J. Biochem. Mol. Biol.*, 6 (2), 45–52.
- [17] Haryono, N.Y., Haryadi, W., and Raharjo, T.J., 2018, Characterization of a putative lipase gene from *Alcaligenes* sp. JG3 bacterium via cloning, *J. Biol. Sci.*, 18 (5), 216–222.
- [18] Ethica, S.N., Semiarti, E., Widada, J., Oedjijono, O., and Raharjo, T.J., 2017, Characterization of *moaC* and nontarget gene fragments of food-borne pathogen *Alcaligenes* sp. JG3 using degenerate colony and arbitrary PCRs, *J. Food Saf.*, 37 (4), e12345.
- [19] Golaki, B.P., Aminzadeh, S., Kharkane, A.A., Yakhchali, B., Farroch, P., Khaleghinejad, S.H., Tehrani, A.K., and Mehrpooyan, S., 2015, Cloning, expression, purification and characterization of lipase 3646 from thermophilic indigenous *Cohnella* sp. A01, *Protein Expression Purif.*, 109, 120–126.
- [20] Bacha, A.B., Moubayed, N.M.S., and Abid, I., 2015, Thermostable alkaline and detergent-tolerant lipase from a newly isolated thermophilic *Bacillus stearothermophilus*, *Indian J. Biochem. Biophys.*, 52, 179–188.
- [21] Fotouh, D.M.A., Bayoumi, R.A., and Hassan, M.A., 2016, Production of thermoalkaliphilic lipase from *Geobacillus thermoleovorans* DA2 and application in the leather industry, *Enzyme Res.*, 2016, 9034364.
- [22] Rogalska, E., Dochet, I., and Verger, R., 1997, Microbial lipases: Structures, function and industrial applications, *Biochem. Soc. Trans.*, 25 (1), 161–164.
- [23] Kanmani, P., Kumaresan, K., and Aravind, J., 2015, Gene cloning, expression and characterization of the *Bacillus amyloliquefaciens* PS35 lipase, *Braz. J. Microbiol.*, 46 (4), 1235–1243.
- [24] De Simone, A., 2016, Engineering the genetic code of *Escherichia coli* with methionine analogues and bioorthogonal amino acids for protein immobilization, *Thesis*, Freie Universität Berlin, Germany.
- [25] Mala, J.G.S., and Takeuchi, S., 2008, Understanding structural features of microbial lipase-An overview, *Anal. Chem. Insights*, 3, 9–19.
- [26] Simossis, V.A., and Herina, J., 2004, Integrating protein secondary structure prediction and multiple sequence alignment, *Curr. Protein Pept. Sci.*, 5 (4), 249–266.
- [27] Yang, J., and Zhang, Y., 2015, Protein structure and function prediction using I-TASSER, *Curr. Protoc. Bioinf.*, 52 (1), 5.8.1–5.8.15.
- [28] Newstead, S., Fowler, P.W., Bilton, P., Carpenter, E.P., Sadler, P.J., Campopiano, D.J., Sansom, M.S., and Iwata, S., 2009, Insights into how nucleotide-binding domains power ABC transport, *Structure*, 17 (9), 1213–1222.
- [29] Orelle, C., Durmort, C., Mathieu, K., Duchene, B., Aros, S., Fenaille, F., Andre, F., Junot, C., Vernet, T., and Jault, J.M., 2018, A multidrug ABC transporter with a taste for GTP, *Sci. Rep.*, 8 (1), 2309.

- [30] Verdon, G., Albers, S.V., Dijkstra, B.W., Driessen, A.J., and Thunnissen, A.M., 2003, Crystal structures of the ATPase subunit of the glucose ABC transporter from *Sulfolobus solfataricus*: Nucleotide-free and nucleotide-bound conformations, *J. Mol. Biol.*, 330 (2), 343–358.
- [31] Bell, P.J., Sunna, A., Gibbs, M.D., Curach, N.C., Nevalainen, H., and Bergquist, P.L., 2002, Prospecting for novel lipase gene using PCR, *Microbiology*, 148 (1), 2283–2291.
- [32] Arpigny, J.L., and Jaeger, K.E., 1999, Bacterial lipolytic enzymes: Classification and properties, *Biochem. J.*, 343 (1), 177–183.
- [33] Meier, R., Drepper, T., Svensson, V., Jaeger, K.E., and Baumann, U., 2007, A calcium-gated lid and a large beta-roll sandwich are revealed by the crystal structure of extracellular lipase from *Serratia marcescens*, *J. Biol. Chem.*, 282 (43), 31477–31483.
- [34] Barbe, S., Lafaquière, V., Guieysse, D., Monsan, P., Reamud-Siméon, M., and André, I., 2009, Insights into lid movements of *Burkholderia cepacia* lipase inferred from molecular dynamics simulations, *Proteins*, 77 (3), 509–523.
- [35] Wilken, S., 2015, Structure and mechanism ABC transporter, *F1000Prime Rep.*, 7, 14.
- [36] Akatsuka, H., Kawai, E., Omori, K., and Shibatami, T., 1995, The three genes lipB, lip C and lipD involved in the extracellular secretion of the *Serratia marcescens* lipase which lacks an N-terminal signal peptide, *J. Bacteriol.*, 177 (22), 6381–6389.

Optimization Model on the Effect of Clove Oil, Formaldehyde, and Chitosan Added to Batik Fabric Colored with Gambier (*Uncaria gambir* Roxb): Antifungal Properties and Stability

Edia Rahayuningsih^{1,*}, Felix Arie Setiawan², Conny Julanda Ayanie¹, Ambrosius Aditya Antoko¹, Yosephine Intan Ayuningtyas¹, and Himawan Bayu Petrus¹

¹Department of Chemical Engineering, Universitas Gadjah Mada, Jl. Grafika No 2, Yogyakarta 55281, Indonesia

²Department of Chemical Engineering, Universitas Jember, Jl. Kalimantan No. 37, Kampus Tegalboto, Jember, Jawa Timur 68121, Indonesia

*** Corresponding author:**

email: edia_rahayu@ugm.ac.id

Received: May 21, 2019

Accepted: June 20, 2019

DOI: 10.22146/ijc.46038

Abstract: Triggered by the concept of sustainability, the use of natural dyes in batik fabric processing has increased recently. To inhibit fungus growth on batik fabric colored with natural dyes, either clove oil or formaldehyde was added as an antifungal agent. To increase the stability of the interaction between the antifungal agent and the batik fabric, chitosan was used as a crosslinker. A modified version of the standard tests American Association of Textile Chemists and Colorists (AATCC) 30 and Response Surface Methodology (RSM) was applied as the characterization method. The results showed that the growth percentage of fungi in Batik treated with either clove oil or formaldehyde was much lower than that in the control sample. Growth of *Aspergillus niger* could be prevented by about 32% using clove oil and 94% using formaldehyde. The optimal condition was obtained with 1% chitosan as a crosslinking reagent, 15.91 ppm of formaldehyde, and 60-min immersion time, with absorbance intensity of formaldehyde crosslinking solution and fungus growth areas being 0.159 and 2.47%, respectively.

Keywords: Gambier natural dye; crosslinking; antifungal; chitosan; clove oil; formaldehyde

■ INTRODUCTION

Known for its diverse cultures and art, Indonesia originated the use of Batik as a cultural art medium. Since October 2nd, 2009, batik has been designated as an element of non-material global cultural heritage [1]. Batik is a patterned fabric made using a wax-resistant dyeing technique. The patterned designs display an important and intimate philosophy regarding social life. Aside from batik motifs, designs, and philosophies, the charm of the beauty of batik is also enhanced by the coloring used.

Both natural and synthetic dyes have been used in the coloring process of batik fabric. Before the mid-19th century, batik coloring was done using natural dyes derived from plant extracts such as stems, bark, leaves, seeds, flowers, and other parts of plants. After the discovery of synthetic dyes, the use of natural dyes in the

coloring process of batik fabric was abandoned because synthetic dyes were affordable and easy to use [2]. In the early 20th century, the development of natural dyes for textiles re-emerged. Meanwhile, public awareness of the health and environmental impacts of synthetic dyes led to increasingly strict regulations implemented by governments [3-4]. The use of synthetic textile dyes which contain heavy metals can have environmental impacts such as water, soil, and air pollution [5]. In addition, the content of heavy metals in synthetic dyes can have a direct effect on humans, such as skin cancer and other types of cancers, brain damage, cerebrovascular disease, and lung disease, so that the use of natural dyes becomes an option to overcome these problems.

Natural dyes can be obtained from various sources such as insects, minerals, fungi, and different parts of plants such as leaves, roots, flowers, fruit, and skin [6].

As natural derivative products, natural dyes have several advantages such as being environmentally friendly, non-toxic, have unique color, and high degradability [7-8]. These advantageous properties are also supported with antimicrobial properties contained in several natural dyes. Antimicrobial activity is an important property to make long-lasting and favorable batik fabric especially in tropical countries with high humidity.

Gambier extract as a natural dye derived from the Gambier plant (*Uncaria gambir* Roxb) contains antimicrobial activity [9]. The chemical constituent on Gambier which is responsible for the antimicrobial activity is tannins. Gambier extract consists of 24.56% tannins, which produces brownish color [10]. The humid environment during storage and usage of fabric enhances the growth of microorganisms such as bacteria and fungi [11]. Fungi and mold worsen the fabric quality by ripping and damaging the fabric fiber; meanwhile, bacteria are responsible for unpleasant odor [12]. Antimicrobial agents can be classified into compounds that are biocidal (killing microorganisms) and biostatic (inhibiting adhesion and growth) [11,13]. For customer comfort and satisfaction, the addition of antifungal agents has been conducted for several natural dyes coloring processes to inhibit fungi growth on the fabric. Several antifungal agents are sufficient to inhibit or kill microorganism such as clove oil and formaldehyde [14-16]. Clove oil has antifungal properties against yeast, filamentous fungi, and pathogenic fungi in humans [15,17]. Phenolic compounds as clove oil constituents have antimicrobial and phytotoxic properties, and can kill insects [16]. Another study also reported that clove oil has antifungal properties against mold, yeast, and fungi on the human pathogen [17]. On the other hand, formaldehyde has disinfectant properties that can inhibit microbial activity such as bactericide, tuberculocide, fungicide, virucide, and sporicide [10,14,18-21].

The crosslinking between cellulose and the antifungal compound is one of the critical stabilization processes in the textile industry. A suitable crosslinking method can prevent the release of the antifungal compound from the cellulose fiber. In this study, either clove oil or formaldehyde was immobilized on the

Gambier-colored batik fabric, using chitosan as the crosslinker. The possible reaction of crosslinking between chitosan to cellulose using formaldehyde and clove oil have not been proposed yet. The optimum condition was examined using Response Surface Methodology (RSM) as a fastness test, Analysis of Variance (ANOVA) as a significance test, and Least Significant Difference (LSD) for fungal growth. Furthermore, *Aspergillus niger*, a well-known and fast growing fungus, was used to study the antifungal activity. As mentioned above, the application of antimicrobials, especially antifungals, to fabrics would increase the quality of the fabric. The study should serve as a reference for the beneficial use of Gambier natural dyes and other natural dyes to gain stable and long-lasting batik products.

■ EXPERIMENTAL SECTION

Materials

The materials used in this study are presented in Table 1. In this research, commercially-available Gambier powder derived from natural Gambier leaves as illustrated in Fig. 1 was used to maintain the same quality of coloring agent material during the entire study.

Procedure

Material preparation

Gambier powder was diluted in a stirring flask using distilled water with feed-solvent ratio (w/v) 0.048 g/L for 2 h at 100 °C. The solution was cooled and stabilized for one day to precipitate insoluble solid. After filtration, the filtrate became the coloring agent. Cotton fabric was uniformly cut into a rectangular size 5 cm × 5 cm. The coloring process was carried out by soaking the fabric samples on the coloring solution as illustrated in Fig. 2 for 30 min at 95 °C continued by the drying process. The dry fabric was soaked in 20 g/L alum solution for 30 min followed with prolonged drying. The fabric was washed with hot water and rinsed with cold water continued by the drying process. Chitosan 0.1% (w/v) was dissolved in 1% acetic acid solution. Either clove oil-Tween 80 or formaldehyde was added into a chitosan solution with a predetermined concentration to

Table 1. List of materials

Material	Source	Brand	Purity
Gambier powder	Local Market - Yogyakarta	Bulk	-
Cotton fabric	Workshop Batik Indigo - Yogyakarta	Bulk	-
Chitosan	Chem-mix Pratama - Yogyakarta	Bulk	-
Clove oil	Local Market - Yogyakarta	Lansida	100%
Formaldehyde	Workshop Batik Indigo - Yogyakarta	Bulk	35%
Sodium sulfate	Chemical Engineering Laboratory - UGM	Merck	99.99%
Acetylacetone	Local Market - Yogyakarta	Merck	99.5%
Acetic acid	Chemical Engineering Laboratory - UGM	Merck	96%
Ammonium sulfate	Chemical Engineering Laboratory - UGM	Merck	99.9%
Alum	Workshop Batik Indigo - Yogyakarta	Bulk	-
Tween 80 n-nonionic	Local Market - Yogyakarta	Sigma-Aldrich	-
Distilled water	Chemical Engineering Laboratory - UGM	Bulk	-
<i>Aspergillus niger</i>	Microbiology Laboratory - UGM	-	-
Potato Dextrose Broth	Microbiology Laboratory - UGM	Sigma-Aldrich	-



Fig 1. Gambier as (a) raw leaves and (b) powder extract

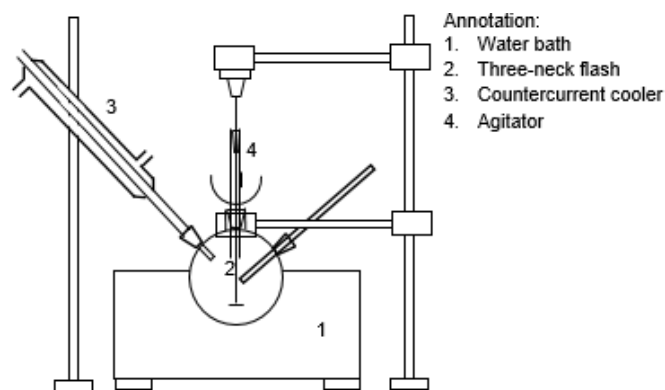


Fig 2. Batch coloring process

produce the antifungal compound solution. Tween 80 was used as an emulsifier for clove oil to be attached into chitosan.

Antifungal application

The fabric was dipped in each antifungal solution. The fabric was then dried at room temperature. The dipping process duration was varied by 10, 25, and 60 min.

Measurement of absorbance on crosslinking strength using fastness test. To examine crosslinking strength, each clove oil-treated fabric was dissolved with a 0.3% (w/v) Tween 80 solution at 30 °C and left overnight. Then, 5 mL samples were taken and analyzed using UV-VIS Spectrophotometer. The absorbance of each sample was measured by UV-VIS Spectrophotometer

at 396.4 nm wavelength [22]. Meanwhile, absorbance test method on formaldehyde was conducted using EN ISO 14184-1 standard method. Each sample treated with formaldehyde as the antifungal agent was contacted with distilled water at 40 °C for 1 h. Set of apparatus was applied to maintain temperature. The liquid phase was filtered and reacted with acetylacetone, namely Nash reactive, to produce a yellow solution. The absorbance of each formaldehyde-treated sample was measured with UV-VIS Spectrophotometer at 412.9 nm wavelength.

Antifungal analysis

The Modified American Association of Textile Chemists and Colorists (AATCC) Test Method 30 was used to observe the antifungal activity. The positive control that has been colored with Gambier natural dyes

Table 2. Experimental design and level of independent variables

Independent Variable	Range of level		
	-1	0	1
^{1,2} Chitosan concentration (CA), %	0.1	0.225	1
¹ Clove oil concentration (CB), %	0.5	1.5	2.5
² Formaldehyde concentration (CF), ppm	10	22.5	50
^{1,2} Time (T), min	10	25	60

¹optimization variable for clove oil crosslinking²optimization variable for formaldehyde crosslinking

was also performed in this study. Each treated sample was cut in a circular shape with a 6 cm diameter about the size of a petri dish. *Aspergillus niger* cultured in Potato Dextrose Broth (PDB) growth medium was used in the antifungal test. PDB was used to evaluate the spore germination and the growth of *Aspergillus niger* [23]. PDB medium 0.75 µL and *Aspergillus niger* suspension were dropped-coated on the fabrics using an inoculation needle. Furthermore, fungal growth was observed for 72 h.

Data analysis

In accordance to the modified AATCC 30, the fungal growth analysis was conducted visually with the colony diameter measurement. The diameter size of each replication had been carried out by measuring the average diameter of six samples of fungal growth. Calculation of sample area percentage was then evaluated using the following equation:

$$\text{Inhibition percentage} = \frac{\text{inhibition diameter}^2}{\text{cloth diameter}^2} \times 100\% \quad (1)$$

The optimization was determined by three-level factorial design using Response Surface Methodology (RSM) in the Minitab® program on the absorbance data. The dependent variable in this study was the absorbance measured by UV-Vis Spectrophotometer. Meanwhile, the individual independent variables could be seen in Table 2 for every antifungal agent. The optimum chitosan and clove oil concentration to inhibit the microbial growth are 0.225% and 1.5% respectively [22,24]. Moreover, the limit of formaldehyde concentration is below 75 ppm for fabrics used in clothing [25].

The non-linear polynomial equation is generally used to correlate the variables, with the responses as dependent variables and the factor as an independent variable. The

basic equation for the second-order response surface model followed [26-28]:

$$Y = \beta_0 + \sum_{i=1}^k \beta_i x_i + \sum_{i=1}^k \beta_{ii} x_i^2 + \sum_{1 < i < j}^k \beta_{ij} x_i x_j + \varepsilon \quad (2)$$

where, Y: response; β_0 : constant coefficient; β_i , β_{ii} and β_{ij} : the coefficients for the linear, quadratic and interaction effect respectively; x_i and x_j : factors (i and j are the range from 1 to k); and ε : error.

A coefficient of determination (R^2) was observed during the optimization process [29]. Mushroom growth can also be classified with several scales [16], namely: 0: No fungal growth is seen using microscopic observation, 1: Fungal growth is seen using microscopic observation, however, is not seen using bare eyes, 2: Fungal growth covers 25% of the test area, 3: Fungal growth covers 50% of the test area, 4: Fungal growth covers 75% of the test area, 5: Fungal growth covers 100% of the test area.

RESULTS AND DISCUSSION

In this study, the quality of the antifungal agent was evaluated using two analytical methods. The first method analyzed the ability of the substance to attach on the fabric using fastness tests. The second method analyzed the capability of the antifungal agent using antifungal analysis. To enhance the interaction strength between the antifungal compound and the cellulose fiber, both on the first method and second method, chitosan was used as the crosslinker. These two methods were very useful to describe the quality of antifungal agents on the application process. The proposed reaction mechanism of cellulose and clove-oil or formaldehyde using chitosan as crosslinker can be seen in Fig. 3(a) and (b) respectively.

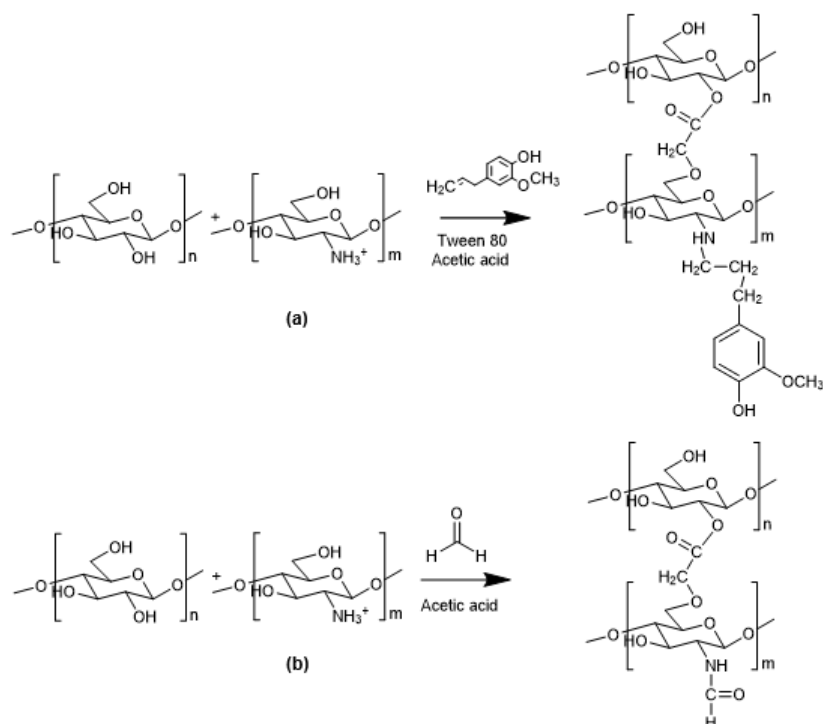


Fig 3. Proposed crosslinking reaction in the study (a) cellulose-chitosan-clove oil and (b) cellulose-chitosan-formaldehyde

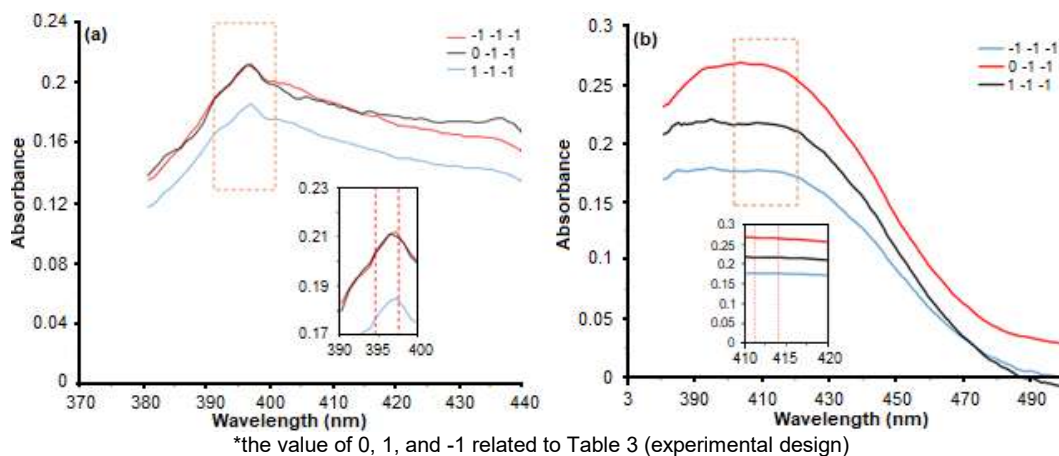


Fig 4. UV-Vis Spectrophotometry results of (a) clove oil crosslinking sample and (b) formaldehyde crosslinking sample

Identification of Clove Oil and Formaldehyde Using UV-Vis Analysis

Fastness tests were conducted using UV-Vis spectrophotometer on clove oil and formaldehyde crosslinking with chitosan. The selected spectrophotometry results are presented in Fig. 4(a) and (b). The figures also present the similarity trend of chitosan concentration variation when other variables were defined at the lowest value. Fig. 4(a) shows optimum

absorption (λ_{max}) around wavelength 394.4–397.5 nm that fits the wavelength of clove oil-chitosan crosslinking solution. Meanwhile, the same tendency occurred in the formaldehyde-chitosan crosslinking solution measurement with maximum absorption around wavelength 411.3–414.1 nm shown in Fig. 4(b). Thus, the selected wavelength for each analysis could be used to evaluate the optimum condition of crosslinking strength using the fastness test.

Determination of Crosslinking Strength Using Fastness Test

The absorbance of the samples was used to determine the amount of antifungal agent released from the cotton fabric into a liquid phase. Absorbance resulted from UV-Vis Spectrophotometry generally represents the concentration of a substance in a specific wavelength. Thus, the correlation between absorbance and targeted substance concentration was assumed to be linear. Model fitting was also performed to obtain the predicted value of each absorbance using Minitab®. The predicted absorbance as responses of optimization could be seen in Table 3 with the empirical equation described below.

Optimum condition from the data on the presence of

clove oil^a and formaldehyde^b with a crosslinking method; with i: input, R: input response, and O = output.

$$YB = 0.2456 + 0.109CA - 0.0480CB - 0.00087T - 0.158CA^2 + 0.0153CB^2 + 0.000013T^2 - 0.0084CA \times CB - 0.000795CA \times T + 0.000098CB \times T \quad (3)$$

$$YF = 0.1739 + 0.444CA - 0.00151CF - 0.00185T - 0.338CA^2 + 0.000025CF^2 + 0.000032T^2 + 0.001559CA \times CF - 0.001984CA \times T - 0.000014CF \times T \quad (4)$$

where CA is chitosan concentration, CB is clove oil concentration, CF is formaldehyde concentration, T is immersion time, YB is clove oil absorbance, and YF is formaldehyde absorbance. The most stable interaction between the antifungal compound and the fabric is demonstrated by the lowest absorbance data which was represented at run code 24 for clove oil addition and run

Table 3. Absorbance result as a parameter to quantify the degree of fastness

Run code	ⁱ CA, %	ⁱ T, min	Clove oil			Formaldehyde		
			ⁱ CB, %	^R YB data*	^O YB model	ⁱ CF, ppm	^R YF data*	^O YF model
1	0.100	10	0.5	0.211	0.227	5.00	0.172	0.191
2	0.100	25	0.5	0.227	0.220	5.00	0.188	0.176
3	0.100	60	0.5	0.228	0.228	5.00	0.195	0.198
4	0.100	10	1.5	0.225	0.209	22.5	0.178	0.177
5	0.100	25	1.5	0.259	0.204	22.5	0.185	0.158
6	0.100	60	1.5	0.218	0.216	22.5	0.205	0.171
7	0.100	10	2.5	0.226	0.223	50.0	0.143 ^b	0.186
8	0.100	25	2.5	0.195	0.219	50.0	0.151	0.161
9	0.100	60	2.5	0.192	0.234	50.0	0.161	0.161
10	0.225	10	0.5	0.212	0.232	5.00	0.264	0.231
11	0.225	25	0.5	0.208	0.224	5.00	0.237	0.212
12	0.225	60	0.5	0.216	0.229	5.00	0.200	0.225
13	0.225	10	1.5	0.240	0.214	22.5	0.178	0.220
14	0.225	25	1.5	0.217	0.207	22.5	0.164	0.198
15	0.225	60	1.5	0.217	0.216	22.5	0.171	0.202
16	0.225	10	2.5	0.225	0.226	50.0	0.266	0.235
17	0.225	25	2.5	0.173	0.221	50.0	0.251	0.207
18	0.225	60	2.5	0.295	0.233	50.0	0.197	0.197
19	1.000	10	0.5	0.184	0.157	5.00	0.215	0.244
20	1.000	25	0.5	0.145	0.140	5.00	0.200	0.203
21	1.000	60	0.5	0.150	0.123	5.00	0.171	0.162
22	1.000	10	1.5	0.077	0.132	22.5	0.305	0.255
23	1.000	25	1.5	0.107	0.117	22.5	0.183	0.210
24	1.000	60	1.5	0.059 ^a	0.103	22.5	0.182	0.160
25	1.000	10	2.5	0.159	0.138	50.0	0.320	0.303
26	1.000	25	2.5	0.146	0.124	50.0	0.217	0.251
27	1.000	60	2.5	0.121	0.114	50.0	0.183	0.188

code 7 for formaldehyde addition. Linear plotting of absorbance data with absorbance responses could be seen in Fig. 5. To give a clear explanation of each parameter effect in every treatment, the correlation of each parameter on absorbance was conducted as seen in Fig. 6.

Both Fig. 6(a) and (b) show that chitosan concentration (CA) gives the most significant effect on the absorbance changes. This can be seen from the range of mean values between the significant upper and lower levels. This observed phenomenon indicates that crosslinking strength significantly increases with a significant increase in chitosan concentration during material preparation and antifungal application. However, the higher chitosan concentration in formaldehyde increased the absorbance after fastness test, which was not preferable. We believe that the crosslinking process had not yet been established, leading to a higher

release of the compounds from the fabric into the solution, and thus higher observed absorbance in the solution after the fastness test. Furthermore, both clove oil and formaldehyde show similar trend on the absorbance. While time (T) only had a significant effect on the formaldehyde addition, time duration reflected the immersion time of the cotton fabrics in the crosslinking solution (Fig. 6(b)). The results showed that clove oil crosslinking solution does not need extended time to infiltrate cotton fabric while formaldehyde crosslinking solution does require a longer time to stabilize on the cotton fabric surfaces.

Afterwards, the best condition for the crosslinking solutions was analyzed further. Lowest absorbance in each treatment had been targeted by optimization using response surface methodology (RSM). The three-level factorial design had been performed with F-value, and

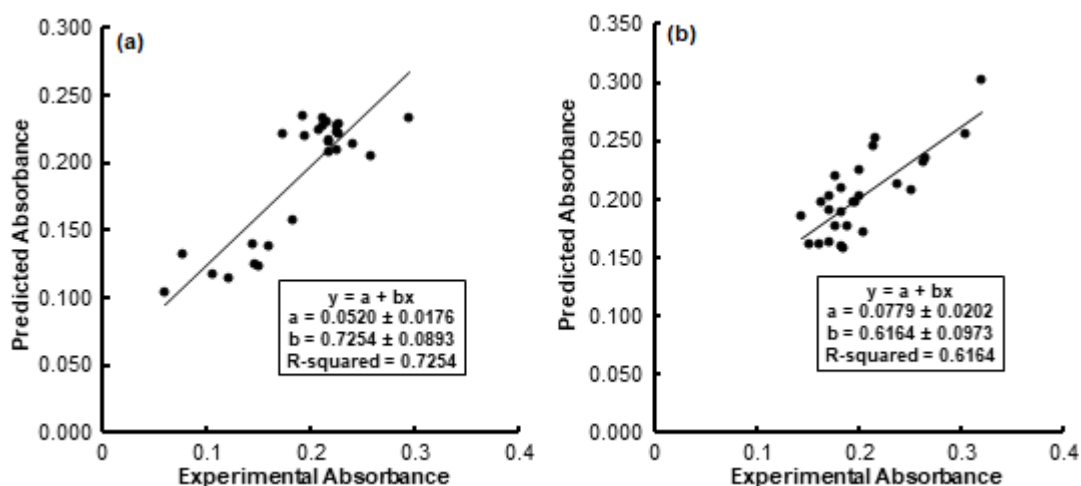


Fig 5. Linear fitting plot of absorbance data and absorbance response from the model, (a) clove oil crosslinking solution and (b) formaldehyde crosslinking solution

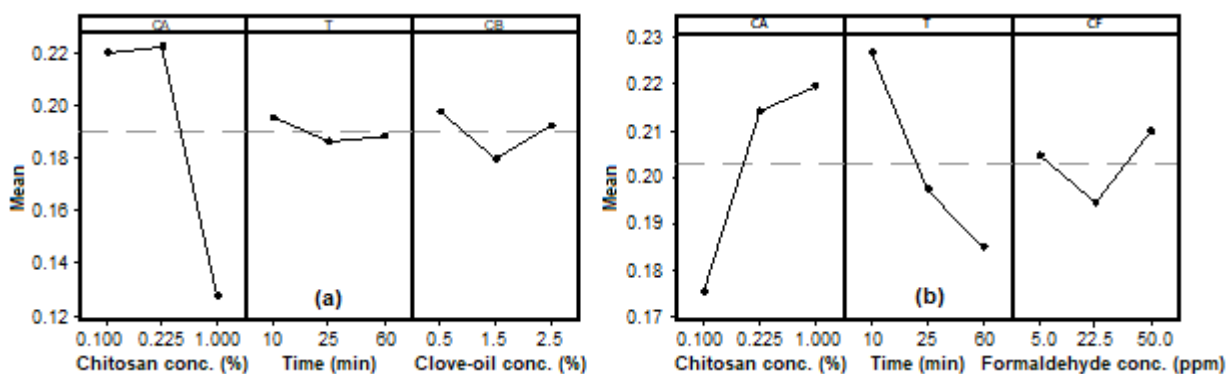


Fig 6. Each parameter effect on the responses, (a) clove oil and (b) formaldehyde addition

Table 4. Analysis of variance on fastness test of the crosslinking solution

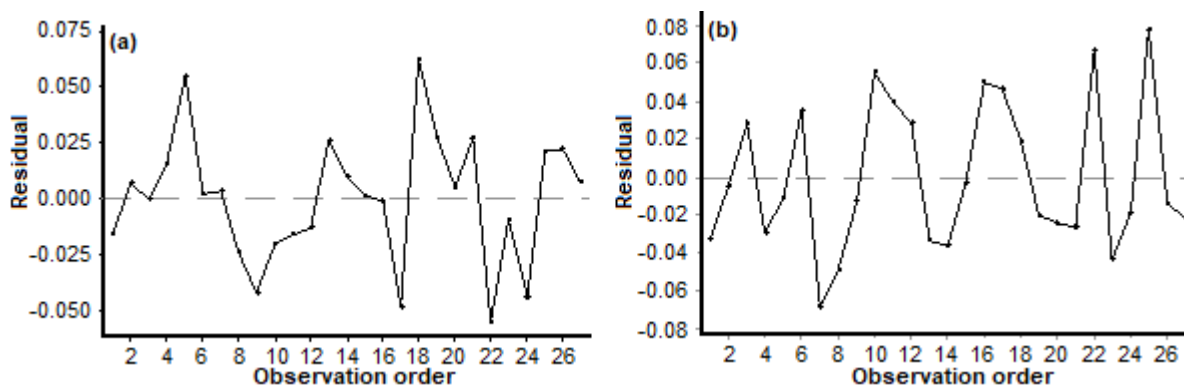
Source	Clove oil crosslinking solution		Formaldehyde crosslinking solution	
	F-value	P-value	F-value	P-value
Model	4.99	0.002	3.07	0.022
Linear	0.51	0.681	5.76	0.007
CA	0.33	0.575	5.96	0.026
CB	1.05	0.32	0.43	0.52
T	0.16	0.696	10.29	0.005
Square	0.77	0.528	2.33	0.111
CA×CA	0.96	0.342	4.77	0.043
CB×CB	1.12	0.305	0.80	0.383
T×T	0.22	0.642	1.42	0.25
2-Way Interaction	0.39	0.762	3.46	0.04
CA×CB	0.16	0.695	3.28	0.088
CA×T	0.95	0.344	6.43	0.021
CB×T	0.06	0.809	0.66	0.427
R-squared	72.54%		61.64%	

P-value as seen in Table 4. Analysis of variance (ANOVA) for clove oil crosslinking solution gives better result compared to formaldehyde crosslinking solution if P-value is used to evaluate the model. However, the proposed adequacy models for Equation (3) and (4) are represented by P-value 0.002 and 0.022 respectively which shows statistical significance due to the small number of P-value of lower than 0.05. This indicates that the model proposed in Equation (3) and (4) is appropriate to reflect the effect of each parameter to the degree of fastness.

The low R-squared values (Fig. 5 and Table 4), < 75%, indicates that the dependent parameters of the model did not show the trend of the independent parameters. However, a high R-squared-valued model

does not always mean a good model. To evaluate this R-squared value, residual plots were conducted to further explain the model. The residual plot in Fig. 7 indicates that the models showed good predictive value as the residual plots for both the clove oil and formaldehyde models were scattered without a discernible trend. The initial hypothesis that the dependent variables would affect the independent variable can thus be accepted.

The left side of the graph in Fig. 8 presents the minimum absorbance of < 0.12 at 1.0% chitosan concentration and 0.75–2.5% clove oil concentration for the first graph, and for 40–60 min immersion in 1.0% chitosan for the second graph. The last figure on the left indicates a minimum absorbance of 0.18–0.20 at 0.75–2.4%

**Fig 7.** Residual plot of the model (a) clove oil crosslinking solution and (b) formaldehyde crosslinking solution

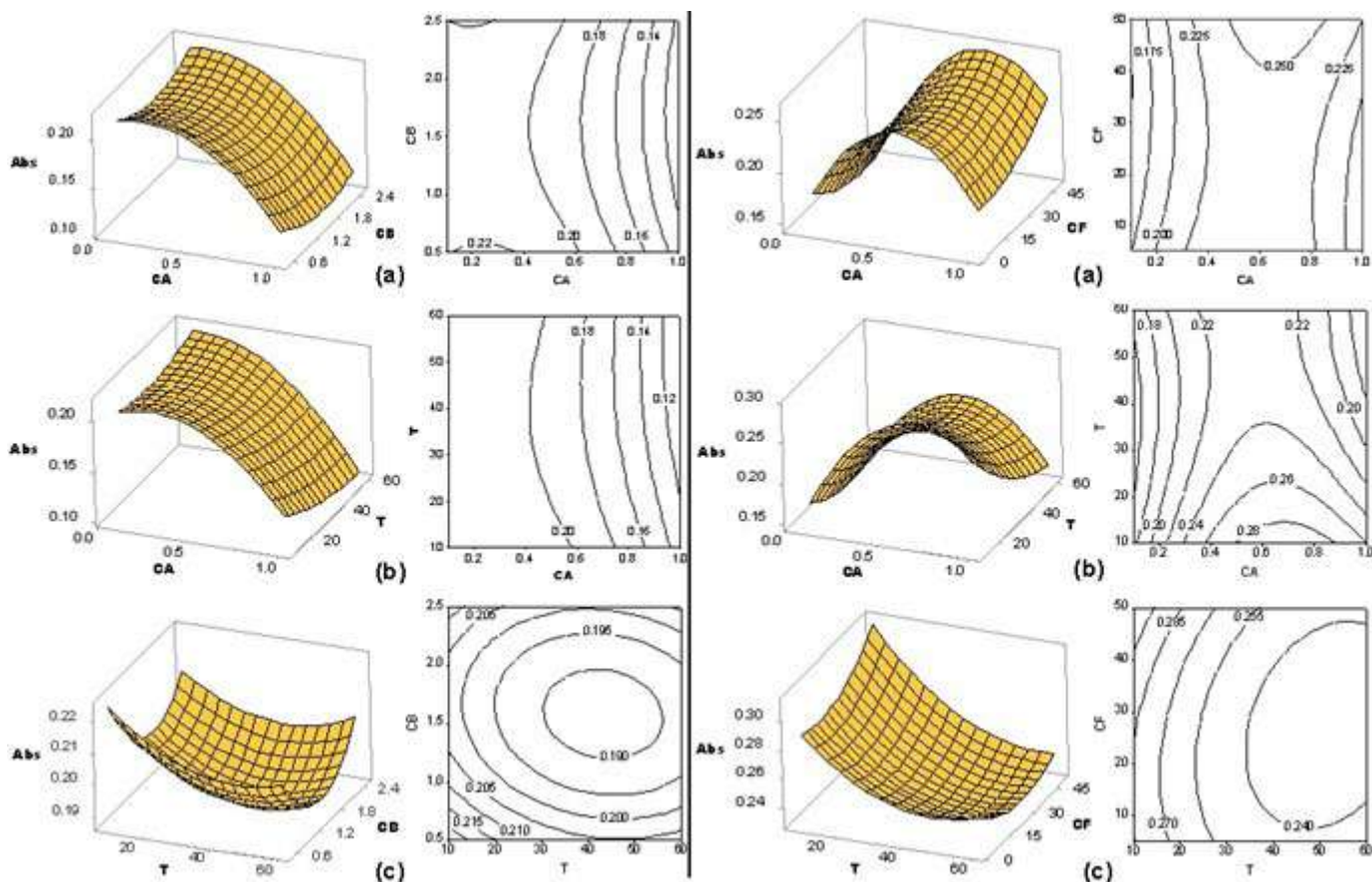


Fig 8. Contour and surface plot of parameters against the response; left image for clove oil and the right image for chitosan (a) CA vs CF, (b) CA vs T, and (c) T vs CB

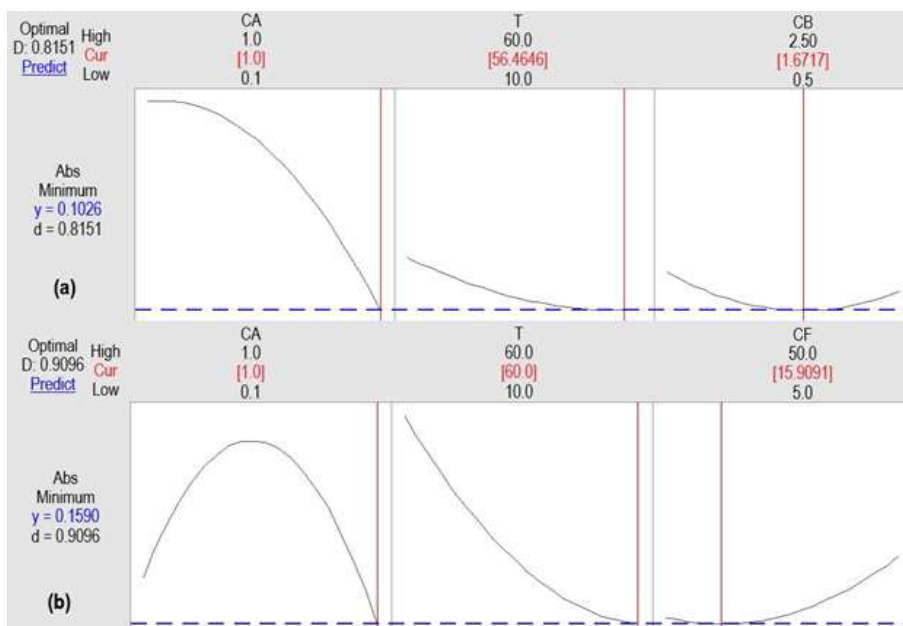


Fig 9. The optimum condition for (a) clove oil crosslinking solution and (b) formaldehyde crosslinking solution

clove oil concentration and 20–60 min immersion. The right side of the graph presents a minimum absorbance of < 0.16 at 0.1% chitosan concentration and 10–50 ppm formaldehyde concentration for the first graph, and 20–60 min immersion in 1.0% chitosan concentration. The third graph on the right side reflects minimum absorbance at a value of 0.24 at 5–45 ppm formaldehyde concentration and 40–60 min of immersion time.

Optimization for all parameters was also conducted to determine the best conditions for the two crosslinker solutions. The result of optimization, as can be seen in Fig. 9, resulted in the lowest absorbance at 0.103 and 0.159 for clove oil and formaldehyde crosslinking solutions, respectively. The optimum condition for the clove oil crosslinking solution occurred at 1% chitosan concentration, 1.672% clove oil concentration, and 56.5 min immersion time. Meanwhile, the optimum parameters for the formaldehyde crosslinking solution took place at 1% chitosan concentration, 15.91 ppm formaldehyde, and 60 min immersion time. The ideal concentration of chitosan for both crosslinking methods was 1%. It reflected that at 1% chitosan concentration, the fabric was totally covered in the bonding of cellulose-chitosan-antifungal agent. Moreover, the optimum concentration of clove oil was not significantly different from that in Muresan et al. [22] and Chinta et al. [24]. The optimum formaldehyde concentration in this study is observed below the limit for infant's fabric, 20 ppm [25].

Determination of Antifungal Properties

To test the antifungal properties of clove oil and formaldehyde, antifungal testings were carried out against *Aspergillus niger* for 72 h. The results for control, clove oil-treated, and formaldehyde-treated samples are shown in Fig. 10(a), (b), and (c) respectively. Colony growth measurement and the percent area of fungal growth were also analyzed in this study. Table 5 shows the area of fungal

growth and the significance levels obtained using ANOVA test and LSD calculation. Significance level test was used to describe the differences in colony growth and the percentage area of fungal growth in every treatment to confirm the antifungal properties of the modified fabric.

The results shown in Table 5 indicate that formaldehyde was very effective in inhibiting fungal growth. Clove oil, on the other hand, presented insignificant results compared to the control sample. Thus, clove oil was not a suitable antifungal compound to combat *Aspergillus niger* growth in this study. Furthermore, formaldehyde showed statistically significant results and gave the lowest scale of bacteria growth compared to control and clove oil treatment. It is well known that formaldehyde is a remarkable substance for disinfection and sterilization of inactive microorganisms. It has been reported that formaldehyde could alkylate amino and sulfhydryl groups contained on protein and purine bases [30]. It is worthwhile to note that chitosan is also an antifungal compound with biostatic properties against fungi, which might enhance the antifungal effect.

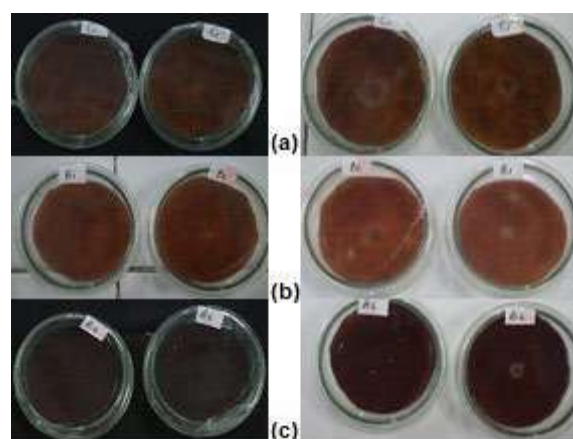


Fig 10. Fungal growth on potato dextrose broth medium (a) control, (b) clove oil crosslinking treatment, and (c) formaldehyde crosslinking treatment for 48 h and 72 h

Table 5. Antifungal test results on crosslinking of clove and formaldehyde oils after 72 h

Treatment	Initial fabric diameter, cm	Diameter, cm		Average, cm	Growth, %	Scale
		Test 1	Test 2			
C1	6.00	4.32	3.54	3.93±0.55 ^c	42.90±12.89 ^c	3
Clove oil	6.00	3.20	3.32	3.26±0.08 ^c	29.52±1.56 ^c	2
Formaldehyde	6.00	1.08	0.78	0.93±0.21 ^a	2.40±1.22 ^a	1

Table 6. The optimum condition of crosslinking solution consideration

Treatment	Chitosan concentration, %	Time, min	Antifungal concentration, ppm	Absorbance	Fungus growth area, %	Restriction
Clove oil	1	56.5	16717.20	0.103	29.53 ^c	Cost
Formaldehyde	1	60.0	15.91	0.160	2.47 ^a	Safety and Environment

Based on Fig. 9, Table 5, and Fig. 10, the optimal conditions for the preparation of clove oil-based and formaldehyde-based antifungal fabrics are summarized in Table 6. The excessive amount of clove oil was ten thousand times larger than formaldehyde. Restriction parameter was also made to give a brief comparison of the crosslinking solution.

The application of clove oil would boost the price of batik while formaldehyde would pose environmental concerns given its toxicity. The maximum safe exposure to formaldehyde is 0.75 ppm by inhalation, measured as an 8 h time-weighted average (TWA), and 2 ppm for a short-term exposure limit (STEL) of 15 min [31-32]. Despite the fact that the formaldehyde is stabilized with a crosslinking agent, textiles employees need to be limited from direct exposure using standard safety equipments. Closed-process systems could be constructed to minimize exposure to formaldehyde, but this would be costly. With all safety and environmental considerations, the optimal conditions in this study were achieved with the application of the formaldehyde crosslinking solution. The use of formaldehyde and clove oil in the crosslinking solutions in this study were reliable for cotton fabric application because the reaction mechanisms do not involve natural dyes. We believe that research into other optimal processes could potentially lead to other antifungal crosslinking methods.

■ CONCLUSION

This study aimed at finding the most suitable conditions for the preparation of antifungal Batik fabrics colored with Gambier-based natural dye. Either clove oil or formaldehyde was used as antifungal compounds, and chitosan was used as a crosslinker that facilitates the immobilization through bonding between the antifungal compounds and the cellulose fiber of the fabric. The results showed that formaldehyde is better than clove oil

to use in conjunction with Gambier extracts as natural dyes. The optimal conditions for the preparation of a stable antifungal batik fabric were at 1% chitosan concentration, 15.91 ppm formaldehyde, and 60 min immersion time, with absorbance intensity of released antifungal substances after fastness test of 0.159 and fungal growth areas of 2.47%. Although the application of formaldehyde as an antifungal agent still requires environmental and safety considerations regarding its toxicity, it showed better antifungal properties compared to clove oil in this study and could significantly suppress *Aspergillus niger* growth with a statistically significant result. In general, this study contributes to forwarding optimal conditions for the incorporation and immobilization of antifungal compounds to natural dye-colored fabrics, using crosslinker in the immobilization strategy.

■ ACKNOWLEDGMENTS

The Department of Chemical Engineering, Universitas Gadjah Mada is gratefully acknowledged for the support and facility.

■ REFERENCES

- [1] The Jakarta Post, 2009, *Batik selected for UNESCO cultural heritage list*, <https://www.thejakartapost.com/news/2009/09/08/batik-selected-unesco-cultural-heritage-list.html>, accessed on 4 May 2019.
- [2] Widiawati, D., 2018, The utilization of batik pattern and natural dyes as valuation of the local value in batik society, *Jurnal Sositologi*, 17 (2), 208–219.
- [3] Shahid, M., Islam, S., and Mohammad, F., 2013, Recent advancements in natural dye applications: A review, *J. Cleaner Prod.*, 53, 310–331.
- [4] Islam, S., Shahid, M., and Mohammad, F., 2013, Perspectives for natural product based agents

- derived from industrial plants in textile applications—a review, *J. Cleaner Prod.*, 57, 2–18.
- [5] Kasiri, M.B., and Safapour, S., 2013, “Natural dyes and antimicrobials for textiles” in *Green materials for energy, products and depollution. Environmental chemistry for a sustainable world*, Eds. Lichtfouse, E., Schwarzbauer, J., and Robert D., vol. 3, Springer, Dordrecht, 229–286.
- [6] Haji, A., Mehrizi, M.K., and Sharifzadeh, J., 2016, Dyeing of wool with aqueous extract of cotton pods improved by plasma treatment and chitosan: Optimization using response surface methodology, *Fibers Polym.*, 17 (9), 1480–1488.
- [7] Kiumarsi, A., Gashti, M.P., Salehi, P., and Dayeni, M., 2017, Extraction of dyes from *Delphinium Zalil* flowers and dyeing silk yarns, *J. Text. Inst.*, 108 (1), 66–70.
- [8] Gashti, M.P., Katozian, B., Shaver, M., and Kiumarsi, A., 2014, Clay nanoadsorbent as an environmentally friendly substitute for mordants in the natural dyeing of carpet piles, *Color. Technol.*, 130 (1), 54–61.
- [9] Dhalimi, A., 2015, Permasalahan Gambir (*Uncaria gambir* L.) di Sumatera Barat dan alternatif pemecahannya, *Perspektif*, 5 (1), 46–59.
- [10] Gove, P.B., 1966, *Webster's third new international dictionary of the English language, unabridged*, G. & C. Merriam, Springfield, Mass.
- [11] Gao, Y., and Cranston, R., 2008, Recent advances in antimicrobial treatments of textiles, *Text. Res. J.*, 78 (1), 60–72.
- [12] Paul, R., 2014, *Functional finishes for textiles: Improving comfort, performance and protection*, 1st Ed., Woodhead Publishing.
- [13] Rahman, M.A., Ahsan, T., and Islam, S., 2010, Antibacterial and antifungal properties of the methanol extract from the stem of *Argyreia argentea*, *Bangladesh J. Pharmacol.*, 5 (1), 41–44.
- [14] Rubbo, S.D., Gardner, J.F., and Webb, R.L., 1967, Biocidal activities of glutaraldehyde and related compounds, *J. Appl. Bacteriol.*, 30 (1), 78–87.
- [15] Sarkar, R.K., De, P., and Chauhan, P.D., 2003, Bacteria-resist finish on cotton fabrics using natural herbal extracts, *Indian J. Fibre Text. Res.*, 28 (3), 322–331.
- [16] Walentowska, J., and Foksowicz-Flaczyk, J., 2013, Thyme essential oil for antimicrobial protection of natural textiles, *Int. Biodeterior. Biodegrad.*, 84, 407–411.
- [17] Pinto, E., Vale-Silva, L., Cavaleiro, C., and Salgueiro, L., 2009, Antifungal activity of the clove essential oil from *Syzygium aromaticum* on *Candida*, *Aspergillus* and dermatophyte species, *J. Med. Microbiol.*, 58 (11), 1454–1462.
- [18] Emmons, C.W., 1933, Fungicidal action of some common disinfectants on two dermatophytes, *Arch. Derm. Syphilol.*, 28 (1), 15–21.
- [19] Klein, M., and Deforest, A., 1983, “Principles of viral inactivation” in *Disinfection, Sterilization, and Preservation*, Eds., Block, S.S., 3rd Ed., Lea & Febiger, Philadelphia, 422–434.
- [20] McCulloch, E.C., and Costigan, S., 1936, A comparison of the efficiency of phenol, liquor cresolis, formaldehyde, sodium hypochlorite and sodium hydroxide against *Eberthella typhi* at various temperatures, *J. Infect. Dis.*, 59 (3), 281–284.
- [21] Sagripanti, J.L., Eklund, C.A., Trost, P.A., Jinneman, K.C., Abeyta Jr., C., Kaysner, C.A., and Hill, W.E., 1997, Comparative sensitivity of 13 species of pathogenic bacteria to seven chemical germicides, *Am. J. Infect. Control*, 25 (4), 335–339.
- [22] Muresan, A., Cerempei, A., Dunca, S., Muresan, R., and Butnaru, R., 2009, Aromatherapeutic characteristics of cotton fabrics treated with rosemary essential oil, *Cellul. Chem. Technol.*, 43 (9–10), 435–442.
- [23] Kang, H.C., Park, Y.H., and Go, S.J., 2003, Growth inhibition of a phytopathogenic fungus, *Colletotrichum* species by acetic acid, *Microbiol. Res.*, 158 (4), 321–326.
- [24] Chinta, S.K., Landage, S.M., Abhishek, A., Sonawane, K.D., and Jalkate, C., 2012, Medical textiles—application of essential oil as antimicrobial agent on nonwoven, *GJBB*, 1 (1), 75–80.
- [25] United States Government Accountability Office,

- 2010, *Formaldehyde in textiles: While levels in clothing generally appear to be low, allergic contact dermatitis is a health issue for some people*, <http://www.gao.gov/products/GAO-10-875>, accessed on 28 November 2018.
- [26] Bezerra, M.A., Santelli, R.E., Oliveira, E.P., Villar, L.S., and Escaleira, L.A., 2008, Response surface methodology (RSM) as a tool for optimization in analytical chemistry, *Talanta*, 76 (5), 965–977.
- [27] Montgomery, D.C., 2017, *Design and analysis of experiments*, 9th Ed., John Wiley & Sons, Inc., Hoboken, New Jersey, USA.
- [28] Rahayuningsih, E., Pamungkas, M.S., Olvianas, M., and Putera, A.D.P., 2018, Chlorophyll extraction from suji leaf (*Pleomele angustifolia* Roxb.) with ZnCl₂ stabilizer, *J. Food Sci. Technol.*, 55 (3), 1028–1036.
- [29] Vedaraman, N., Sandhya, K.V., Charukesh, N.R.B., Venkatakrishnan, B., Haribabu, K., Sridharan, M.R., and Nagarajan, R., 2017, Ultrasonic extraction of natural dye from *Rubia Cordifolia*, optimisation using response surface methodology (RSM) & comparison with artificial neural network (ANN) model and its dyeing properties on different substrates, *Chem. Eng. Process.*, 114, 46–54.
- [30] Favero, M., 1991, “Chemical disinfection of medical and surgical materials” in *Disinfection, Sterilization, and Preservation*, Eds. Block, S.S., 4th Ed., Lea & Febiger, Philadelphia, 617–641.
- [31] Occupational Safety and Health Administration, 1991, *OSHA amends formaldehyde standard*, United States Department of Labor.
- [32] Occupational Safety and Health Administration, 2007, *Toxic and hazardous substances. Formaldehyde*, United States Department of Labor, Code of Federal Regulations: 29 CFR 1910.1048.

Conceptual Difficulties Experienced by First-Year Undergraduate Chemistry Students in Assigning Oxidation Number: A Case Study of High School Chemistry Textbooks

Rahmat Basuki

Department of Chemistry, Faculty of Science and Technology, University of Jambi,
Jl. Jambi-Muara Bulian Km. 15, Mendalo, Jambi 36361, Indonesia

* **Corresponding author:**

tel: +62-85743213964

email: rhmtbsq@gmail.com

Received: July 4, 2018

Accepted: January 3, 2019

DOI: 10.22146/ijc.36695

Abstract: The purpose of this research was to investigate first-year undergraduate chemistry students' understanding in assigning oxidation number following a case-study course instruction. A list of multiple choice question and interview section was formulated to identify the initial knowledge as representative of their conceptual understanding in assigning oxidation number obtained from their chemistry textbooks. This study revealed that most of 34 students who participated were confused about the nature of oxidation number. In the section of the interview which focused on applying "The Rules", many students experienced more problems in assigning oxidation number of sulfur in $S_2O_3^{2-}$ ion. Several misconceptions relating to the inappropriate assumption in assigning oxidation number were identified. The data illustrated how students attempt to make sense of the concept obtained from High School with the knowledge they had already constructed in solve of a given question. The research implied that the teachers, lecturers, curriculum developers, and High School Chemistry textbooks authors need to be cognizant of the importance of related concept (electronegativity and dot-Lewis structure) with oxidation number. The high school and chemistry textbook authors were recommended to introduce this interconnection (including formal charge) to minimize the misconception and conceptual difficulties experienced by first-year undergraduate chemistry students in assigning oxidation number.

Keywords: conceptual difficulties; assigning oxidation number; misconception; case study of chemistry program students

■ INTRODUCTION

During the past three decades, although there has been considerable research into students' understanding of chemistry, there has been relatively limited research focusing on undergraduates' understanding of chemistry concepts. Although there were studies carried out previously on primary and secondary students' understandings of chemistry, and teaching basic chemical concepts effectively [1-2], in recent years research has started to concentrate on undergraduates' (and prospective teachers') understanding of basic and advanced concepts in chemistry, such as chemical equilibrium [3], chemical kinetics [4], phase changes [5], vaporization, vapor pressure and vaporization rate [6-7], enthalpy [8], entropy [9-10], Gibbs free energy [11],

chemical bonding [12], colligative properties [13] and also how to teach the concepts of chemistry effectively [14]. Overwhelmingly, evidence suggests that undergraduates' understanding of advanced ideas in chemistry is very poor because of lacks of basic concept understanding. Part of the difficulty rests with the nature of chemistry itself, but more seems to stem from how the concepts are customarily taught without regard to what is known about students' learning and the content structure of the domain [15].

The conceptual understanding of chemistry by students is an important issue. There are several concepts in chemistry at basic and advanced levels that are difficult to understand, because their operational definitions involve sophisticated reasoning [16]. The

concepts of Oxidation Number (ON) are among those. Many students tend to memorize numerical equations or algorithms rather than learn the concepts. Therefore, they can solve numerical problems, but fail to answer conceptual questions. A review of the literature reveals that there are many misconceptions within the domain of chemistry [16-18]. The study of the oxidation-reduction concept has been a fundamental part of higher education chemistry courses for many years [19-20]. This topic includes the ON concepts, which seem to give high school students trouble because they involve abstract concepts. Assigning ON in high school was firstly taught in grade X after they learn chemical bonding, atomic theory, and the periodic table of elements. Mastery of the concepts associated with ON facilitates the mastery of these other chemical concepts. However, most of the commonly used high school chemistry textbooks perform only "The Rules" approach to assigning ON, without connecting with the previous chapter. Besides, the fundamental concept of determining ON was much related to the previous concept.

In the constructivist concept, whenever a concept has restricted meaning, this gives a false notion that concepts are single units. ON concept, in this case, should be differentiated in the mind of a person. As more and new relationships to other concept are acquired, the respective concepts take on new meaning [21]. Limited explanation of assigning ON only through "The Rules" will result in misleading interpretations or misconception [22]. Redox material misconception had been experienced by students, for example: they had a difficulty on distinguishing the definition of the oxygen and electrons transfer, they often experience an error in the determination of the oxidation number of atom in molecule. They did not know the key concept of oxidation and its relation to another concept, i.e. electronegativity; and related to that concept they had a difficulty on how to apply the equalization to the redox reactions [23]. Misleading interpretation on determining ON will affect the students in the understanding and application of redox concept.

Assigning ON study in high school studied in grade X for the first time, after they learn chemical bonding,

atomic theory, and the periodic table of element. "The Rules" approach was the only method used in common high school chemistry textbooks in Indonesia. Simple molecules which have relatively higher electronegativity differences, such as, HF, H₂S, H₂SO₄, PCl₃, and so forth, "The Rules" successfully worked. However, it has not given satisfying results when "The Rules" applied to a molecule with more covalent character which has fewer electronegativity differences CH₃COOH, C₂H₅OH, S₂O₄²⁻, POBr₃, H₂O₂, etc. It needed another related concept (dot-Lewis structure and electronegativity). Caused by this behavior of assigning ON using only "The Rule" in high school without mastering the fundamental concept of ON, the student frequently experiences difficulties in learning concept relating the ON i.e. formal charge in university level. This research aims to explore the initial knowledge of assigning ON that student's brought from high school as represent of a chemistry textbook that they have learned. The research question answered in this study is: What misconceptions in initial knowledge – if any – about assigning oxidation number (ON) are found among first-year chemistry student in University of Jambi?

■ EXPERIMENTAL SECTION

Materials

The material as a subject-sample of the study was 34 students of Chemistry Program in the first semester (2017/2018) of University of Jambi. They joined the Basic Chemistry I course subject. Based on constructivist principles of knowing by Von Glasersfeld (1995) knowledge is actively built up from within by a thinking person; knowledge is actively received through the senses or by any form of communication [24-27]. So, the new student was assumed to have initial knowledge of redox concept from their textbooks which actively communicated by the teacher in high school. It was also assumed that what they learn in high school represent by chemistry textbooks that they used [28-36].

Instrumentation

The research instruments were 15 multiple choice questions (Table 1) transformed from some common used

Table 1. Fifteen (15) multiple choice questions as research instruments were transformed from some common used chemistry textbooks in Indonesia

Name:	
High School chemistry mark:	
1. Oxidation number of N in HNO_3 (a) +5 (b) +3 (c) +1	9. Oxidation number of P in POBr_3 (a) 0 (b) +3 (c) +5
2. Oxidation number of Mn in KMnO_4 (a) +1 (b) +5 (c) +7	10. Oxidation number of both C in CH_3COOH (a) -3 and +3 (b) -4 and +4 (c) 0 and 0
3. Oxidation number of both Cr in $\text{K}_2\text{Cr}_2\text{O}_7$ (a) +3 and +3 (b) +6 and +6 (c) +12 and +12	11. Oxidation number of I in ICl_5 (a) +7 (b) +5 (c) 0
4. Oxidation number of O in KO_2 (a) -2 (b) -1 (c) -1/2	12. Formal Charge of both S in $\text{S}_2\text{O}_3^{2-}$ (a) +2 and +2 (b) +5 and -1 (c) 0 and 0
5. Oxidation number of H in NaH (a) -1 (b) 0 (c) +1	13. Formal charge of P in POBr_3 (a) 0 (b) +3 (c) +5
6. Oxidation number of O in H_2O_2 (a) -2 (b) -1 (c) +2	14. Formal charge of both C in CH_3COOH (a) -3 and +3 (b) -4 and +4 (c) 0 and 0
7. Oxidation number of O in OF_2 (a) -2 (b) -1 (c) +2	15. Formal charge of I in ICl_5 (a) +7 (b) +5 (c) 0
8. Oxidation number of both S in $\text{S}_2\text{O}_3^{2-}$ (a) +2 and +2 (b) +5 and -1 (c) 0 and 0	
Note:	

chemistry textbooks in Indonesia and a list of question for interview protocol (Table 2). Fifteen multiple choice problems were given in the test before entering the Redox Reaction chapter (pre-test) and then followed by an interview section.

Procedure

This research was conducted by descriptive analysis study with a form of case study research to address the research question and fulfill the purpose of the study.

Identification and validation of conceptual and propositional knowledge

The procedure of the study was the students finish off the 15 multiple choice questions and then followed by individually interview section. This procedure designed to answer the purpose of the study involved the identification of conceptual and propositional knowledge about what they know. After the completion of each question, students reflect on the abstract knowledge gained [37]. This stage can be used by an instructor (lecturer) as a foothold to give additional knowledge which is necessary for students to fully understand oxidation number and related concept. Several senior high school chemistry textbooks were examined to formulate 15 multiple choice questions. The questions were reviewed by an expert in chemistry education and a high school chemistry teacher. Their comments were used to revise the original list of problems. The purposes for undertaking this task were threefold. First, the problems provided a scientifically accurate body of knowledge so that student's responses could be compared with scientifically accurate views. Second, the problems provide a complete and comprehensive list of the knowledge required by students to understand oxidation number concept. Third, the problem provided the framework for the development of the interview protocol and data analysis procedure.

Development of the interview protocol

The purpose of the interview was to explore a sample of students' understandings of oxidation number concept and identify any difficulties or misconception in initial knowledge. The questions of interview protocol

(Table 2) were not limited and may be expanded depending on the necessity. A semi-constructed interview protocol was developed based on the list of 15 multiple choice questions as conceptual and propositional knowledge. The interview process was carried out individually directly after the students finish off 15 multiple choice questions.

Sample size and selection

Thirty-four new chemistry students in first academic year 2018/2019 in University of Jambi have been asked to solve 15 multiple choice questions based on their knowledge before entering The Redox Reaction chapter in Basic Chemistry I course (pre-test). The students were classified into top, medium and bottom rank in class based on their mark in high school and author's objective observation. This classification aims to strengthen the representation of students' responses. The answer given by the students was assumed as a reflection of their thinking ability and their understanding on the previous concept that has been learned (in high school). The result was then discussed how the students respond to clarify the reason for their answers through interview section.

Analysis of data

The interviews were recorded on digital audio and analyzed within a few days of the event. The tapes were played twice, and each student's responses were summarized question by question. The dialogue was then classified based on the similarity respond. The selected dialogue was transcribed verbatim from the record and represented into a short conversation. The classified students' response is presented in Table 3.

Table 2. List of question for interview protocol

1.	What "tools" do you use to assign the ON?
2.	How do you assign ON of molecule in the question? Show the explanation.
3.	Where did you have "The Rules" to assign ON? If it is from chemistry textbooks, mention the title/author/publisher.
4.	Is any other "tools" to assign the ON beside "The Rules"?
5.	Is the association of two atoms or more always have same ON each atom?
6.	How do you confirm that the ON of each atom was correct?
7.	Do you know that ON has assign based on its Lewis structure and electronegativity?
8.	Do you know Formal Charge?

Table 3. Summary of the students' responses results to interview section

Student	Position in Class*	Students' Response
Herman	Middle	ON of Cr in $K_2Cr_2O_7$ was +12. Doubt the ON is +12 or must divide +12 by 2 because the amount of Cr is 2. (Doubt about ON was for on atom or group of atoms).
Gita	Bottom	Confused ON of chromium atom in $K_2Cr_2O_7$ was +12 or +6
Rawel	Top	ON always an average of total ON of group atom divided by its subscript
Reza	Top	Know that KO_2 was superoxide, so the ON of O was -1/2 (Should know the exceptional atom first, other ON will follow).
Dea	Bottom	Confused what should assign first, O or K in KO_2 and Na or H in NaH, didn't familiar the exceptional.
Kiranti	Top	Never learn before that ON of atom in molecule was related to its Lewis structure.

*Students were designated as being in the top, middle, or bottom third of their class

Summaries such as these were examined for common and disparate replies and were used to identify students' misconceptions. Clearly, responses from Herman, Gita, Rawel, Reza, Dea, and Kiranti revealed confusion about the nature of ON and related concept (electronegativity and dot-Lewis structure). Quotes from them presented in the results section and added support to the documentation of students' misconceptions about assigning ON. Interpretations made from the summaries were confirmed or rejected by referring to individual student summaries and the audio record. This procedure was carried out twice by the author to ensure reliability.

■ RESULTS AND DISCUSSION

In this article, the discussion of the results focused on two areas of student's difficulties: assigning ON by

using "The Rules" and correlation ON with related concept (dot-Lewis structure and electronegativity). These difficulties give rise to misconceptions which are discussed below. The results of students' answer in 15 multiple choices question presented in Fig. 1.

Assigning Oxidation Number

In response to question 1, all students successfully gave the correct answer and explain well how they got ON of nitrogen atom in HNO_3 using "The Rule". As stated before, common used high school chemistry textbooks use the "Rules" to determining ON. Here is the summary of these "Rules" from commonly used high school chemistry textbooks [28-36]: (1) ON of free atom is zero; (2) ON of metal always has a positive sign. For example, ON of primary group (A) should be determined

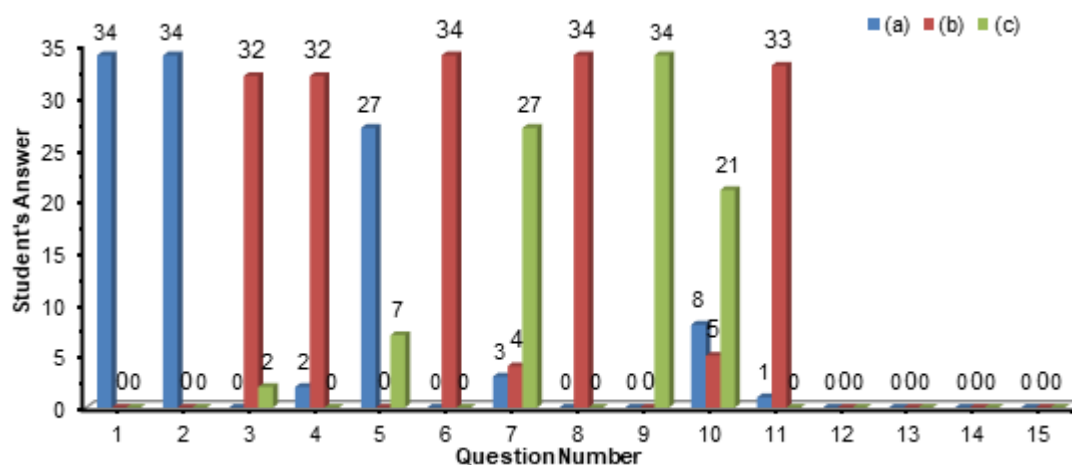


Fig 1. Students' answer results of 15 multiple choice questions as representation of common high school textbooks which was given before entering the Redox Reaction chapter (pre-test)

from its group, such as group IA generally is +1, IIA is +2, IIIA is +3, VIIA generally is -1, and so forth. Metal of transition group has varied value of ON, such as Fe: +2 and +3, Cu: +1 and +2, and so forth (3) Sum of ON in neutral molecule is zero; (4) ON of monoatomic ion is equal to its charge; (5) Sum of ON in polyatomic ion is equal to its charge; (6) ON of oxygen atom is commonly -2, but it is -1 in peroxide, and -1/2 in superoxide; (7) ON of hydrogen atom is commonly +1, but it is -1 in hydride; and (7) ON of another atom, determined from its group, such as group IA generally is +1, IIA is +2, IIIA is +3, VIIA generally is -1 etc.

It is mentioned in these textbooks [28-36], how to determine ON of nitrogen atom in HNO_3 as shown by the students using rule number (2), (5), and (6), the calculation can be expressed:

$$(1 \times \text{ON of H}) + (1 \times \text{ON of N}) + (2 \times \text{ON of O}) = 0$$

$$(1 \times +1) + (\text{ON of N}) + (3 \times -2) = 0$$

$$(+1) + \text{ON of N} + (-6) = 0$$

$$\text{ON of N} = +5$$

The other examples that can be solved using "The Rules" were a question no. 2: KMnO_4 , and another molecule, such as NaCl , H_3PO_4 , SO_3 , and so forth (the underlined atom was atom would be determined its ON). The simpler method represents "The Rule" can be seen in Fig. 2. These results indicate the good understanding of some simple molecule that it's ON can be solved only by "The Rules".

Misconception 1: ON belongs to a group of the atom.

Misconception 2: ON of atom in group's atom is always average of total ON of group atom

divided by the subscript of that group atom.

Based on the author's experience, misconception 1 frequently was experienced by many students. In response to question 3, Herman and Gita got the wrong answer caused by mistake assumption that ON belong to a group of atom:

Interviewer: Show me, how did you assigning ON Cr in $\text{K}_2\text{Cr}_2\text{O}_7$.

Herman : (explain how he got ON by using methods in Fig. 2 as a representation of "The Rules")

Interviewer: So, the ON of Cr in $\text{K}_2\text{Cr}_2\text{O}_7$ is +12 or +6?

Herman : I think it is +12. Actually, I doubt the ON is +12 or we must divide +12 by 2 because the amount of Cr is 2.

Two students (Herman and Gita) was answered +12 (option c in question 2) for ON of chromium in $\text{K}_2\text{Cr}_2\text{O}_7$. Gita has referred the similar answer with Herman. They confused ON of chromium atom in $\text{K}_2\text{Cr}_2\text{O}_7$ was +12 or +6. The right concept was that ON belongs to the only single atom. So, +12 should be for the two atoms of chromium because the subscript represents the amount of an atom in one molecule.

Misconception 2 was experienced almost in all high school students. Rawel is one of an outstanding student in Basic Chemistry class and based on the author's observation and his chemistry mark in high school, Rawel was ranked in the top of the class. He correctly stated that ON belongs to one atom, but experienced conceptual conflict when trying to explain the ON of each atom in a group of atom:

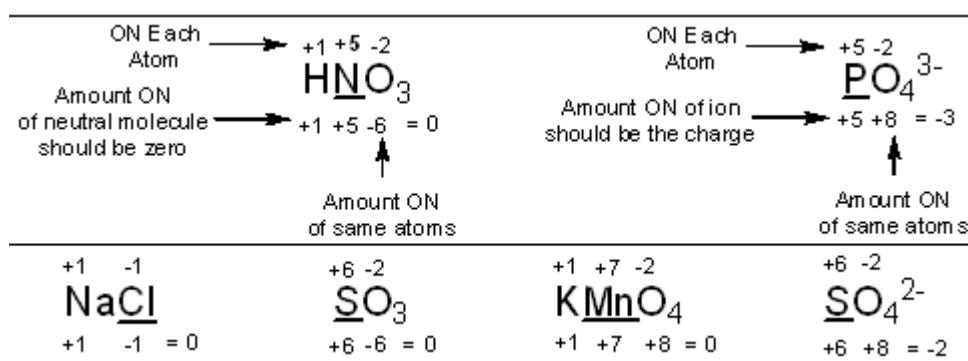


Fig 2. Sketch of simplification methods to assigning ON as "The Rule" representation applies in common molecules/ions

Interviewer: are you sure the ON of both Cr in $K_2Cr_2O_7$ was +6?

Rawel : Yes, I am. Because one atom has one value of ON.

Interviewer : Is the ON always an average of total ON of group atom divided by its subscript?

Rawel : Yes, I am. Initially, I was pretty much sure. But, after I saw the answer option, I hesitate that it is always the average. I do not know. I never been taught this in high school.

The student's answers on question 1-3 proved that using only "The Rules" was worked for certain molecules (most of simple molecule). The misconception was rise from inadequate knowledge of redox concept. The misconception might cause by the high school chemistry textbooks was not provide additional explanation besides "The Rules" and teacher was not emphasize this section [38-39].

The ON of Exceptional Atom

Misconception 3: The exceptional atom has to be known first, and then ON will follow

Rule number (5) and (6) stated that there was any exceptional ON for hydride (-1), peroxide (-1), and superoxide (-1/2). A misconception emerged when students try to solve question 4-7. In fact, question 4 still can be solved only using "The Rule". Thirty-two (32) students who have the correct the answers mostly stated that alkaline group (IA group) must have ON = +1 (IA group only have ON = +1) and the other atom (oxygen) will follow. So based on "The Rules", the correct answers were ON of K = +1, and O = -1/2. The confusing the rest of them (Dea and Bella) was what atom was to be determined first. Dea achieved low rank in class, and she also answered +1 (option C) in question 5. In the following dialogue she revealed that she did not regard the exceptional O and H:

Interviewer: Why did you choose -2 (option A) for oxygen atom in KO_2 ?

Dea : I did not know. I have confused what should assign first, O or K.

Interviewer: For question 5, NaH you did the wrong answer too. Why you finally choose that answer?

Dea : I only familiar with ON H: +1 and ON O: -2.

The interview with Reza, whose get top rank in class, supports misconception 3:

Interviewer: Why did you choose -1/2 (option C) for oxygen atom in K_2O ?

Reza : Because I know it was peroxide. Beside, K only has ON +1.

Interviewer: You did the same method to NaH and H_2O_2 ?

Reza : Yes, I did.

Interviewer: Could you explain, why the ON O of peroxide is -1, peroxide -1/2, and H in hydride is -1?

Reza : Hmm... I do not know why. I think it is exceptional.

In question 7, 27 students choose the correct answer, and the rest split to option A (3 students) and B (4 students). But, most of them were confused to assign ON of each atom especially its sign, (+) or (-). Even though almost 80% of students gave the correct answers, but they were just guessing. They were doubtful because they have no fundamental concept to confirm their results. It is evident in answering question 7 that they cannot give a precise reason why they choose the answer. Most of them answered "The Rules" without any explanation because they have no knowledge other than "The Rules". Some students responded it was "exceptional", when they asked why. But still, they didn't know for sure when using "The Rules" as an exceptional and common one. Only two students, Rawel and Reza which state "*It was because F located after right O, so the ON F is -1 and O is +2*". But they did not mention the electronegativity. Based on the work of Garnett and Treagust [40], this phenomenon was common since in High School, and several misconceptions related to the inappropriate use of definitions of oxidation and reduction were identified.

Question 4-7 shows us that ON is strongly related with other concepts. The concepts that so related with ON were electronegativity and dot-Lewis structure. The definition by its terminology of ON is the charge remaining on an atom when all ligands are removed

heterolytically in their closed form, with the electron being transferred to the more electronegative partners; homonuclear bonds do not contribute to the ON [41]. On the other hand, for a formal charge (FC), in any combining two or more different atoms, it is assumed that there is always full equally sharing of electrons between the two atoms. Fig. 3 shows the explanation of where the ON was known based on electronegativity by Pauling

scale (Table 4) on several selected atom [42].

For this superoxide case, three electrons should be in sharing between the two oxygen atoms in O_2^- as bonding electrons and it is impossible to break this bond heterolytically for exactly the same atoms (O), but it is also impossible to break homolytically an odd number of electrons. Basically ON and FC is “imaginary numeric value” because it could not break one electron to be in a $\frac{1}{2}$.

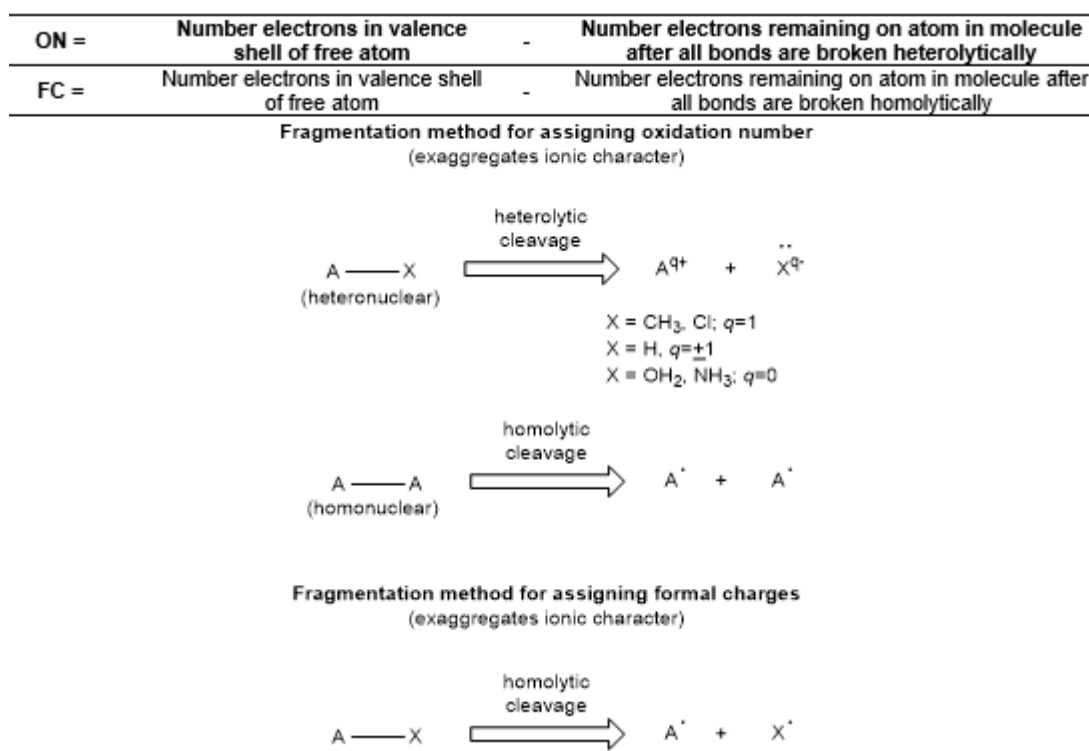


Fig 3. The differences between fragmentation methods for assigning oxidation number (ON) and formal charge (FC)

Table 4. Electronegativity of Pauling Scale several selected atoms [36]

1	2	12	13	14	15	16	17	18
H								He
2.300								4.160
Li	Be		B	C	N	O	F	Ne
0.912	1.576		2.051	2.554	3.066	3.610	4.193	4.787
Na	Mg		Al	Si	P	S	Cl	Ar
0.869	1.293		1.613	1.916	2.253	2.589	2.689	3.242
K	Ca	Zn	Ga	Ge	As	Se	Br	Kr
0.734	1.034	1.588	1.756	1.994	2.211	2.424	2.685	2.966
Rb	Sr	Cd	In	Sn	Sb	Te	I	Xe
0.706	0.963	1.521	1.656	1.824	1.984	2.158	2.359	2.582
Cs	Ba	Hg	Tl	Pb	Bi	Po	At	Rn
0.659	0.881	1.765	1.789	1.854	(2.01)	(2.19)	(2.39)	(2.60)

There is no choice besides using an average of ON even in this odd number of electron. Even though, there was no different result in ON value conducted by both only “The Rules” and sketch dot-Lewis structure. However, using sketch dot-Lewis structure term of “imaginary numeric value” seems logical and can be explained clearly to the students. The chemistry students should reach this level of understanding in ON and FC concept.

The Correlation of ON, Lewis Structure and Electronegativity

Based on the sketch of redox definition as presented in Fig. 3, two things could be concluded: (1) ON can be determined from differences between electronegativity values. “The Rules” is a simplification of concept to assigning ON, and it is really powerful to assign ON of simple molecule. However, uses of “The Rule” should be completed by related concept because of the nature of ON was differences of electronegativity values [43]. The amounts of differences of electronegativity lead to the type of chemical bonds, if it were high, the substance tend to ionic, otherwise if slight, it tends to covalent. (2) ON concept is designated for a substance that has any –even a little– electronegative differences (bonding between different atoms), so the substance assumed tends to ionic. However, it was also could be applied to the covalent substance as long as they have any electronegative differences. These electronegative differences cause the heterolytic cleavage, where electron will move to atom with greater electronegativity. If the atom in substance has the same electronegativity, so the substance tends to be covalent and cause the homolytic cleavage, where the electron will be shared equally to each atom/ligands. This condition obtains a new unit called formal charge (FC).

In response to question 8, all of 34 students answer option A. This response revealed that they assume the ON of an atom in the group of atom was always the average value. This assumption express as misconception 2. The Interview with Kiranti, whose chemistry result was best in class, supports misconception 2:

Interviewer: How about question 8, what ON of both S in $S_2O_3^{2-}$?

Kiranti : My answer is A (+2 and +2). But now, I was querying my answer. I do not know, I think there was another method to solve it.

Interviewer: The correct answer was B, +5 and -1.

Kiranti : (shocked)... How it was possible?!

Interviewer: Did you know that ON of atom in molecule was related to its Lewis structure?

Kiranti : I did not know. I never learned it in high school, even in Olympiad class. I just found out.

Assigning ON based on this concept requires drawing the dot-Lewis structure (electron-dot) that molecule. Whereas, electron in covalent polar bond is not fully shared, to simplify the ON calculation it is assumed that an electron “is fully transferred to” atom with greater electronegativity. Example assigning ON of varied chlorine atom (Fig. 4) explains that is why the sum of ON of free molecule has zero. Chlorine atom in Cl_2 molecule has the same electronegativity, so it will have homolytically cleavage, where electron shared equally. So, ON of both Cl atoms can be counted as $7 - 7 = 0$. The same principle can be applied to Fig. 5 that electron as if “belong to” the more electronegative atom. Uses only “The Rule” will fail to assign the correct value of ON in question 8. They need a related concept: electronegativity and dot-Lewis structure. These concepts must be mastered well to avoid the misconception. Therefore, insufficiency of any concept and its related concept will lead to misconception [22,44].

The entire students in this study think that ON of sulfur atom in $S_2O_3^{2-}$ ion has the same value, +2. Using only “The Rules” they used to calculate $2 \times (\text{ON S}) + 2 \times (-2) = -2$. It was reasonable because they did not know if dot-Lewis structure will assign the ON value. They confess that they never been taught in High School to assign ON through drawing the dot-Lewis structure first. So the students might only think the ON was always average. So, using only “The Rule” for particular molecule –usually called exceptional, as long as they knew that it was exceptional– will lead to wrong ON value. Without drawing dot-Lewis structure, this calculation cannot be accepted because each of sulfur has

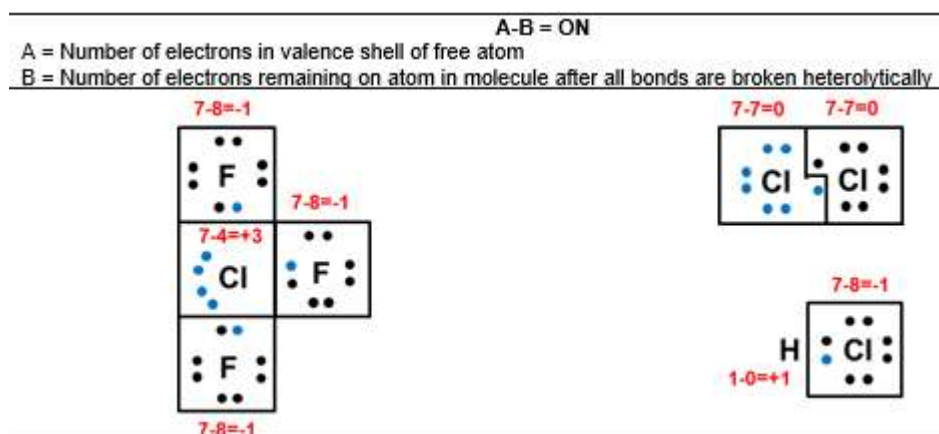


Fig 4. Assigning ON of varied chlorine atom that electron(s) were always fully transfer from atom having less electronegative to that more electronegative

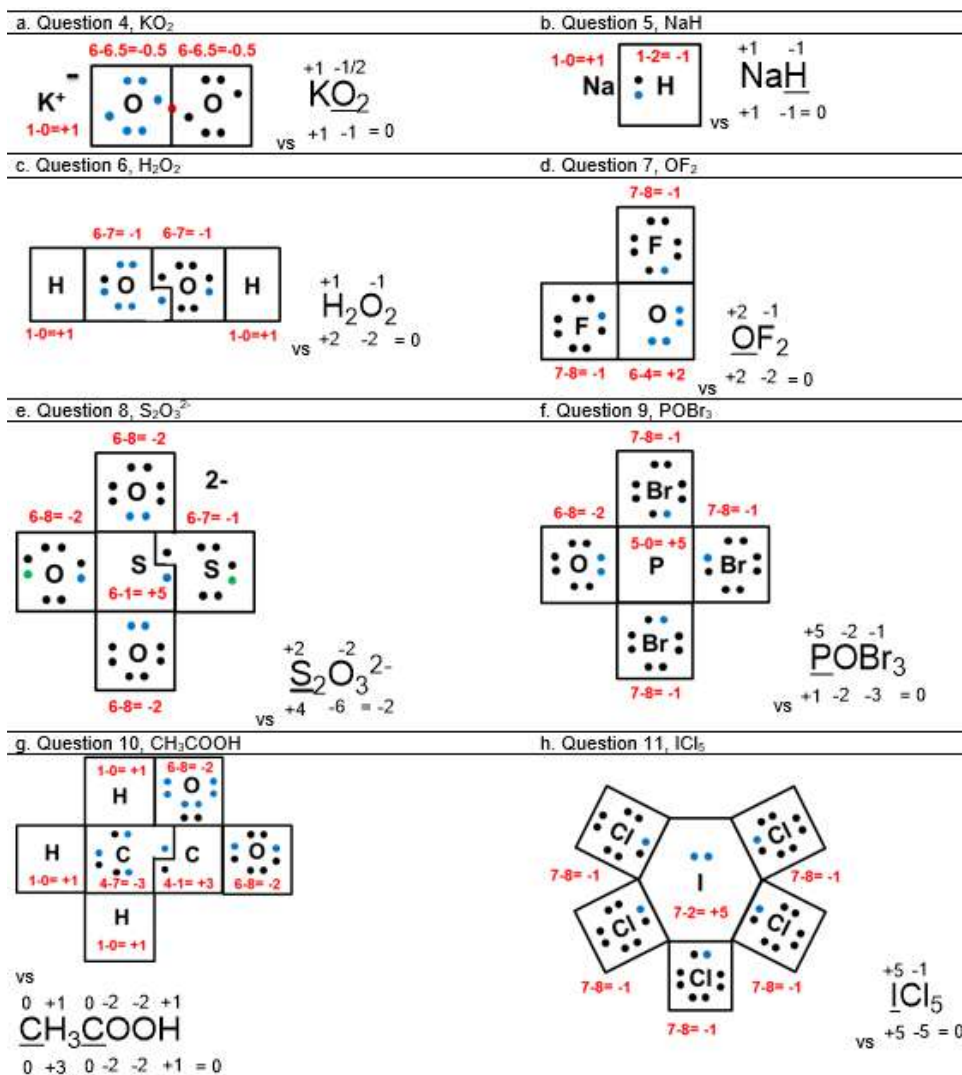


Fig 5. Assigning ON by electron(s) were always fully transfer from atom having less electronegative to that more electronegative vs. only "The Rules" of Question 4-11

different environment. ON of S (center) has only 1 electron left because it is bonding with 3 oxygen atoms which have higher electronegativity than S and 1 S atom which have equal electronegativity. So, calculation can be written $ON\ S\ (\text{center}) = 6 - 1 = +5$, for S (side) $ON = 6 - 7 = -1$. ON of atom in group's atom was not always average of total ON of group atom divided by the subscript of that group atom. Assigning ON of question 4-11 can be seen in Fig. 5.

The Correlation of ON and Formal Charge (FC)

All of 34 students in this study coincide to response "Just heard that term, never learn formal charge (FC) in high school" for question 12-15. The response was normal because FC does not exist in the high school chemistry syllabus. However, chemistry teacher/textbooks may introduce the nature of ON and related concept so that the formal charge term will familiar to students. The lack of this knowledge will be one of the reasons why many students at all levels struggle to learn chemistry, but they are often unsuccessful. Discovering the concept and its connection with another concept has been the target of many studies. One possible answer that is beginning to emerge is that many students cannot construct appropriate understandings of fundamental chemical concepts from the very beginning of their studies caused by there is no further explanation about the related concept from textbooks/teachers. Therefore, they cannot fully understand the more advanced concepts that build upon the fundamentals [45].

The difference of fundamental approach between ON and FC has an important perspective: ON is constant, and it is not dependent on resonance structure, unchanged even the dot-Lewis structure was changed (resonance). But FC is changed depending on its resonance structure. The example of this phenomenon can be seen in resonance of thiocyanate ion (Fig. 6). Applying only "The Rules" to assigning ON was not so helpful if dealing with a group of atom in the molecule. It was only can be solved with the combination of dot-Lewis structure and electronegativity. According to interviewed students, the most used high school chemistry textbooks among the 9 textbooks [28-36] was authored by Purba and

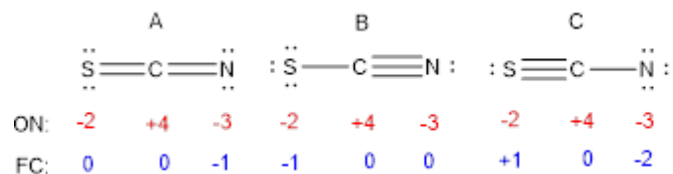


Fig 6. ON and FC of thiocyanate ion resonance. FC was changed analogously with resonance changing but ON was not

Sarwiyati [34]. These textbooks were also the only one from 9 textbooks that provide the information of electronegativity role in assigning ON even in a limited way. But still, there was some mistake in a molecule as an example of these textbooks [28-36]. Sketch of assigning ON by only "The Rules" versus by the dot-Lewis structure and electronegativity of these molecules presented in Fig. 6. Because of the interconnection among related concept is very important, the connection between related concepts to ON should be taught in the beginning of High School and deepened in University. The high school chemistry textbooks are better to provide enrichment matter/additional information about this. Besides, the chemistry instructor/teacher/lecturer is often neglecting to emphasize the importance of this relation [46-47]. From a constructivist perspective, students and instructor/teacher/lecturer must consider this related concept in redox as they become engaged in the subject of chemistry.

CONCLUSION

"The Rules" is a powerful method to assigning ON. However, used only "The Rules" have any limitation. "The Rules" should be completed with a related concept to nature of oxidation number: electronegativity and dot-Lewis structure. This study concluded that most of students only know "The Rules" to assigning ON as initial knowledge from High School because their chemistry textbook was not completed by additional information related ON concept. Additionally, the chemistry instructors/teacher/lecturer was often negligent to emphasize the importance of this relation. This condition was vulnerable to lead the misconception of ON in particular molecule as identified in this study. As a suggestion, the instructors/teacher/lecturer must

consider this related concept in redox as they become engaged in the subject of chemistry. Learning ON in High School (or in the beginning year in university) should be taught by a related concept: electronegativity and dot-Lewis structure supported by chemistry textbook containing complete related concept. Without learning these connection concepts, misconceptions tend to occur, and the student will struggle to learn chemistry. The publisher/textbook author's was also considering this to revise the book.

■ ACKNOWLEDGMENTS

The author thanks Dr. Madyawati Latief and Dr. Ngatijo to facilitate this research; Dr. Yusnaidar and Netri Mardia, S.Pd. for the review and validating the research instrument.

■ REFERENCES

- [1] Tytler, R., 2000, A comparison of year 1 and year 6 students' conceptions of evaporation and condensation: Dimensions of conceptual progression, *Int. J. Sci. Educ.*, 22 (5), 447–467.
- [2] Zikovelis, V., and Tsaparlis, G., 2006, Explicit teaching of problem categorisation and a preliminary study of its effect on student performance – the case of problems in colligative properties of ideal solutions, *Chem. Educ. Res. Pract.*, 7 (2), 114–130.
- [3] Van Driel, J.H., 2002, Students' corpuscular conceptions in the context of chemical equilibrium and chemical kinetics, *Chem. Educ. Res. Pract.*, 3 (2), 201–213.
- [4] Cakmakci, G., Leach, J., and Donnelly, J., 2006, Students' ideas about reaction rate and its relationship with concentration or pressure, *Int. J. Sci. Educ.*, 28 (15), 1795–1815.
- [5] Azizoğlu, N., Alkan, M., and Geban, Ö., 2006, Undergraduate pre-service teachers' understandings and misconceptions of phase equilibrium, *J. Chem. Educ.*, 83 (3), 947–953.
- [6] Canpolat, N., 2006, Turkish undergraduates' misconceptions of evaporation, evaporation rate, and vapour pressure, *Int. J. Sci. Educ.*, 28 (15), 1757–1770.
- [7] Canpolat, N., Pinarbasi, T., and Sozbilir, M., 2006, Prospective teachers' misconceptions of vaporization and vapor pressure, *J. Chem. Educ.*, 83 (8), 1237–1242.
- [8] Sozbilir, M., and Bennett, J.M., 2006, Turkish prospective chemistry teachers' misunderstandings of enthalpy and spontaneity, *Chem. Educ.*, 11 (5), 355–363.
- [9] Carson, E.M., and Watson, J.R., 2002, Undergraduate students' understanding of entropy and Gibbs free energy, *Univ. Chem. Educ.*, 6, 4–12.
- [10] Bennett, J.M., and Sozbilir, M., 2007, A study of Turkish chemistry undergraduates' understanding of entropy, *J. Chem. Educ.*, 84 (7), 1204–1208.
- [11] Sozbilir, M., 2002, Turkish chemistry undergraduate students' misunderstandings of Gibbs free energy, *Univ. Chem. Educ.*, 6, 73–83.
- [12] Frailich, M., Kesner, M., and Hofstein, A., 2009, Enhancing students' understanding of the concept of chemical bonding by using activities provided on an interactive website, *J. Res. Sci. Teach.*, 46 (3), 289–310.
- [13] Pinarbasi, T., Sozbilir, M., and Canpolat, N., 2009, Prospective chemistry teachers' misconceptions about colligative properties: Boiling point elevation and freezing point depression, *Chem. Educ. Res. Pract.*, 10 (4), 273–280.
- [14] Tsaparlis, G., 2005, Non-algorithmic quantitative problem solving in university physical chemistry: A correlation study of the role of selective cognitive factors, *Res. Sci. Technol. Educ.*, 23 (2), 125–148.
- [15] Cakmakci, G., Leach, J., and Donnelly, J., 2006, Students' ideas about reaction rate and its relationship with concentration or pressure, *Int. J. Sci. Educ.*, 28 (15), 1795–1815.
- [16] Harle, M., and Towns, M., 2011, A review of spatial ability literature, its connection to chemistry, and implications for instruction, *J. Chem. Educ.*, 88 (3), 351–360.
- [17] Singer, S., and Smith, K.A., 2013, Discipline-based education research: Understanding and improving learning in undergraduate science and engineering, *J. Eng. Educ.*, 102 (4), 468–471.

- [18] Taber, K.S., 2013, Revisiting the chemistry triplet: drawing upon the nature of chemical knowledge and the psychology of learning to inform chemistry education, *Chem. Educ. Res. Pract.*, 14 (2), 156–168.
- [19] Doymus, K., Karacop, A., and Simsek, U., 2010, Effects of jigsaw and animation techniques on students' understanding of concepts and subjects in electrochemistry, *Educ. Technol. Res. Dev.*, 58 (6), 671–691.
- [20] Regan, Á., Childs, P., and Hayes, S., 2011, The use of an intervention programme to improve undergraduate students' chemical knowledge and address their misconceptions, *Chem. Educ. Res. Pract.*, 12 (2), 219–227.
- [21] Cakir, M., 2008, Constructivist approaches to learning in science and their implications for science pedagogy: A literature review, *Int. J. Environ. Sci. Educ.*, 3 (4), 193–206.
- [22] Widarti, H.R., Permana, A., and Mulyani, S., 2016, Student misconception on redox titration (a challenge on the course implementation through cognitive dissonance based on the multiple representations), *Indones. J. Sci. Educ.*, 5 (1), 56–62.
- [23] Taber, K.S., 2001, Building the structural concept of chemistry: Some consideration from educational research, *Chem. Educ. Res. Pract.*, 2 (2), 123–158.
- [24] Tobin, K.G., 1994, "Constructivism as a Referent for Teaching and Learning" in *The Practice of Constructivism in Science Education*, 1st Ed., Routledge, New York, 20.
- [25] Wheatly, G.H., 1991, Constructivist perspectives on science and mathematics learning, *Sci. Educ.*, 75 (1), 9–21.
- [26] Michael, J., 2006, Where's the evidence that active learning works?, *Adv. Physiol. Educ.*, 30 (4), 159–167.
- [27] Park, S., and Oliver, J.S., 2007, Revisiting the conceptualization of Pedagogical Content Knowledge (PCK): PCK as a conceptual tool to understand teachers as professionals, *Res. Sci. Educ.*, 38 (3), 261–284.
- [28] Setyawati, A.A., 2009, *Kimia – Mengkaji fenomena Alam untuk Kelas X SMA/MA*, Pusat Perbukuan Departemen Pendidikan Nasional, Jakarta, 131–140.
- [29] Permana, I., 2009, *Memahami Kimia 1: SMA/MA untuk Kelas X Semester 1 dan 2*, Pusat Perbukuan Departemen Pendidikan Nasional, Jakarta, 105–112.
- [30] Sunarya, Y., and Setiabudi, A., 2009, *Mudah dan Aktif Belajar Kimia 1 untuk Kelas X SMA/MA*, Pusat Perbukuan Departemen Pendidikan Nasional, Jakarta, 123–137.
- [31] Utami, B., Saputro, A.N.C., Mahardiani, L., Yamtinah, S., and Mulyani, B., 2009, *Kimia 1 untuk Kelas X SMA/MA*, Pusat Perbukuan Departemen Pendidikan Nasional, Jakarta, 143–164.
- [32] Harnanto, A., and Ruminten, 2009, *Kimia 1 untuk Kelas X SMA/MA*, Pusat Perbukuan Departemen Pendidikan Nasional, Jakarta, 131–142.
- [33] Sudarmo, U., and Sariwati, E., 2015, *Buku Siswa: Kimia untuk Kelas X SMA/MA (kelompok peminatan matematika dan ilmu alam) K2013*, Erlangga, Jakarta.
- [34] Purba, M., and Sarwiyati, E., 2016, *Kimia 1 untuk Kelas X SMA/MA (kelompok peminatan matematika dan ilmu alam) K2013*, Erlangga, Jakarta. p. 208-228.
- [35] Muchtariadi, 2016, *Kimia 1 Kelas X SMA (edisi revisi 2016)*, Yudhistira, Jakarta. 181–193.
- [36] Watoni, H., Kurniawati, D., and Juniastri, M., 2016, *Kimia untuk kelas X SMA/MA kelompok peminatan matematika dan ilmu-ilmu alam*, Yrama Widya, Bandung.
- [37] Hmelo-Silver, C.E., 2004, Problem-Based Learning: What and How Do Students Learn?, *Educ. Psychol. Rev.*, 16 (3), 235–266.
- [38] Özkaya, A.R., 2002, Conceptual difficulties experienced by prospective teachers in electrochemistry: Half-cell potential, cell potential, and chemical and electrochemical equilibrium in galvanic cells, *J. Chem. Educ.*, 79 (6), 735–738.
- [39] Mahaffy, P., 2004, The future shape of chemistry education, *Chem. Educ. Res. Pract.*, 5 (3), 229–245.
- [40] Garnet, P.J., and Treagust, D.F., 1992, Conceptual

- difficulties experienced by senior high school students of electrochemistry: Electric circuits and oxidation-reduction equations, *J. Res. Sci. Teach.*, 29 (2), 121–142.
- [41] Parkin, G., 2006, Valence, oxidation number, and formal charge: three related but fundamentally different concept, *J. Chem. Educ.*, 83 (5), 791–799.
- [42] Mann, J.B., Meek, T.L., and Allen, L.C., 2000, Configuration energies of the main group elements, *J. Am. Chem. Soc.*, 122 (12), 2780–2783.
- [43] Pauling, L., 1960, “The Partial Ionic Character of Covalent Bonds and the Relative Electro-negativity of Atoms” in *The Nature of the Chemical Bond and the Structure of Molecules and Crystals: An Introduction to Modern Structural Chemistry*, 3rd Ed., Cornell University Press, New York, 64–107.
- [44] Shehu, G., 2015, Two ideas of redox reaction: Misconceptions and their challenges in chemistry education, *IOSR-JRME*, 5 (1), 15–20.
- [45] Nakleh, M.B., 1992, Why some student don't learn chemistry, *J. Chem. Educ.*, 69 (3), 191–196.
- [46] Basuki, R., Amanda, H., Bemis, R., Lisma, A., and Yusnaidar, Y., 2018, Incomplete explanation in determining oxidation number: A case study on chemistry program students, *Indones. J. Sci. Educ.*, 7 (3), 333–340.
- [47] Francisco, J.S., Nakleh, M.B., Nurrenbern, S.C., and Miller, M.L, 2002, Assessing student understanding of general chemistry with concept mapping, *J. Chem. Educ.*, 79 (2), 248–257.

Review:**Thermal Process of Castor and Plant Based Oil****Mohammad Haniff Ahmad¹, Wan Asma Ibrahim², Jahirah Sazali¹, Izirwan Izhab¹, and Zulkafli Hassan^{1,*}**¹Faculty of Chemical and Natural Resources Engineering, Universiti Malaysia Pahang, 26300 Gambang, Pahang, Malaysia²Forest Research Institute Malaysia (FRIM), 52109 Kepong, Selangor Darul Ehsan, Malaysia*** Corresponding author:**

tel: +609-5492920/2889

email: zulkafli@ump.edu.my

Received: June 25, 2018

Accepted: November 2, 2018

DOI: 10.22146/ijc.39711

Abstract: Castor oil is an oil derived from castor seed from the plant *Ricinus communis*. The versatility of castor oil is highly attributed by the 12-hydroxy-9-octadecenoic acid (ricinoleic acid) and its functional groups. It is an oil that cannot be consumed by humans. However, castor oil actually can be used to produce many valuable products such as chemicals, paint, and cosmetics due to its unique characteristic which contains a high percentage of ricinoleic acid that helps in producing many valuable products. The utilization of vegetable oils is currently in the highlight of the chemical industry, as they are one of the most important renewable resources due to their universal availability, inherent biodegradability, low price, and eco-friendliness. Therefore, the main aim of this paper is to focus on the thermal cracking of castor oil with Zeolite ZSM-5 as the catalyst generates products consisting alcohol, methyl esters and fatty acids which are valuable raw materials for industries. The background, characteristics, composition, properties and industrial application of castor oil have also been discussed. The important properties and various applications of castor oil which can be obtained from toxic seeds have much greater potential than other available vegetable oils.

Keywords: castor oil; ricinoleic acid; composition; industrial application

■ INTRODUCTION

Nowadays, Asia can be considered as the leader for oils and fats in the oleochemical industry. Specifically, 75% of the total production of castor oil was conquered by India and then followed by China and Brazil each accounting for 12.5 and 5.5%, respectively as shown in Fig. 1 [1]. This has made India the world's largest producer of castor oil. The world castor oil production has increased from 2003 to 2013 with the values from 1.055 to 1.440 million tons while India is leading it [4]. In a decade, the production has increased about 36% due to castor oil's easy availability, low cost, non-food competition, high boiling point, high viscosity and other environmental considerations [1]. As previously mentioned, Fig. 1 shows that Asia is truly leading the production of castor oil with India alone contributing most of it. To support more of this statement, castor oil Derivatives Market Global

Market Analysis Opportunity Outlook 2021 reported that Asia-Pacific dominates the global castor oil and derivatives market due to increasing healthcare spending and continuous expansion of personal care. Countries such as India and China are expected to further dominate the global market of castor oil and derivatives and flourish at a compound annual growth rate (CAGR) of 5.0% during 2015–2021 [2].

Castor plant grows well in wet tropics to the dry subtropical regions with an optimum temperature of 20–25 °C. Warm climate condition can attribute to the high content of oil, but temperatures over 35 °C can cause poor seed setting while lower temperatures can induce the formation of frost which can destroy the plant [3]. The poor climate adaptability of the plant to cold weather conditions has restricted the pursue of castor plantation. Besides that, high toxicity of the castor seed is also the reason why U.S. farmers do not pursue

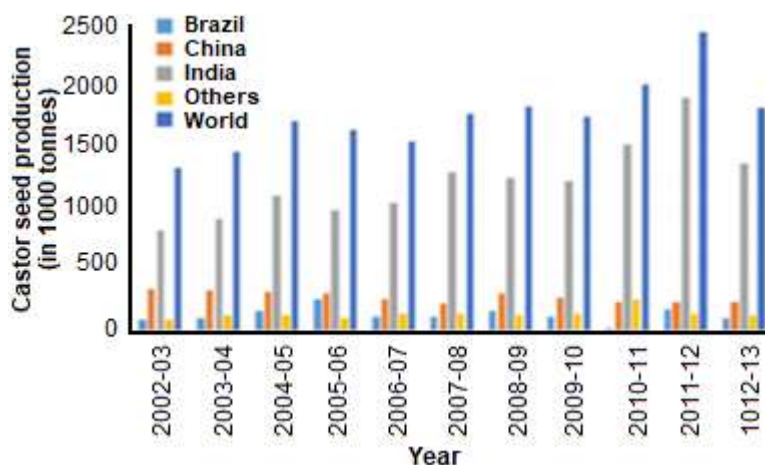


Fig 1. Production amount of castor oil by major countries. Reprinted (adapted) from Mubofu [1] with permission from Springer International Publishing



Fig 2. Castor plant, *Ricinus communis* (on the left) and Castor seeds (on the right)

castor plantation due to ricin that presents in the seed, where 1 mg of it can actually kill an adult [4]. Castor plant is mostly found in India where it grows wild on wastelands and is also cultivated for its oily seeds. Although castor plant is native to the Ethiopian region of tropical east Africa, it is becoming an increasingly abundant weed in the southwestern United States and also in tropical and warm temperate regions throughout the world [5]. Around 6000 years ago in Egypt, castor plant had already been grown for its oil [6].

In terms of physical appearance, castor plant can be grown as a large shrub or tree up to 12 m in height depending on the suitability of the climate. The stems of castor plant are hollow and pale green while the leaves are glossy reddish brown with obvious veins and are 10–40 cm

in length. The seeds are capsulated in a reddish green spiny fruit and dispersed by water and wind [2]. It takes around 95–180 days for the fruits to be ripe. The castor seed crop can be harvested when all the capsules are dry, and the leaves have fallen from the plants [7]. It is a crop that has potential in hot climates, and the yield is greatly affected by the soil moisture, photoperiod, and temperature of the production area [8].

Castor oil, *Ricinus communis* L., is originally a member of the tropical plant family Euphorbiaceae. Castor plant is usually planted and cultivated mostly in the temperate countries of the globe. Castor oil is a viscous, pale yellow, non-volatile and non-drying oil with a bland taste [4]. Castor oil is a non-drying oil with no odor, and it has high viscosity. It is yellowish brown

in nature as shown in Fig. 2. This oil comes from the castor seed of a plant called *R. communis* or generally called castor plant. The oil was obtained from the seed through a process of extracting or expressing it. Moreover, the castor seeds usually consist of 50% castor oil which can simply be extracted from its seeds. The versatility of castor oil has been applied in various sectors such as specialty chemicals, perfume, and medicine [9]. The interest for castor oil products in the market value is increasing which might be caused by their sustainability, biodegradability, eco-friendliness and their reasonable price [9].

The flexibility of castor oil is focused on its high composition of ricinoleic acid as well as the existence of the three functional groups. The carboxyl group can enlarge the esterification limit in which the unsaturation can be adjusted by hydrogenation, epoxidation or vulcanization process. The hydroxyl group plays an important role for the oil in producing a semi-drying state by making it acetylated or alkoxyated. Furthermore, the reactivity of the hydroxyl position allows the molecule to split through the extreme temperature of pyrolysis. Caustic fusion process helps to shorten the carbon chain to obtain products. The double bond, on the other hand, contributes to the ability for chemical reactions and it allows the modification process to happen. The hydroxyl group contributes to the high viscosity of castor oil [10]. Castor oil has an unsaturated bond, high molecular weight (298), low melting point (5 °C) and a very low solidification point (-12 to -18 °C). Thus, these characteristics make it industrially marketable, as it has the most stable viscosity among the other vegetable oils which brings a lot of advantages to castor oil [11]. Therefore, the suitable thermal process such as thermal catalytic cracking is crucial in order to obtain castor oil since the unique structure of castor oil contributes to the various industrial applications of castor oil.

■ EXTRACTION, COMPOSITION, AND PROPERTIES OF CASTOR OIL

The oil from castor seed can be extracted either by mechanical pressing and solvent extraction or a combination of both [12]. Firstly, the seed was crushed into small pieces and then dried in a steam-jacketed vessel so that the moisture content in the castor seed can be removed. Then, the crushed seed was inserted into hydraulic presses and pressed hard in order to extract the oil [4]. However, the oil recovered was not much, only around 45%, but there were still around 10% of the oil that can be extracted from the cake [12-13]. Therefore, further steps were taken to further extract the oil inside the cake by using a solvent extraction method. Through this method, most of the studies done by other researchers used Soxhlet extractor to extract the remaining oil inside the cake [4,14-15]. There is also a study which has been done by Mgudu et al. [16] where they performed a solvent extraction method assisted by microwave as the heating medium. Most of the solvent used from other studies for the solvent extraction method was hexane, but another solvent can also be used like heptane and petroleum ethers which then will help to remove the remaining oil inside the cake [3]. Table 1 shows the yield of castor oil obtained from several studies through the extraction process by a solvent extraction method using hexane as the solvent for the process. It was reported that cold-pressed oil has low acid value, low iodine value and a slightly higher saponification value than solvent-extracted oil and is lighter in color. However, there was still no information on which oil from these methods was used for the industries [4].

Castor seed usually contains about 30–35% of oil [17] but there are also studies stating that castor seed contains between 45–55 % of oil, but it depends on the

Table 1. The yield of castor oil through a solvent extraction process

Parameter	Warra [18]	Abdelaziz et al. [19]	Nangbes et al. [17]	Abitogun et al. [15]
Weight of seed (g)	50	910	-	-
Oil yield (%)	42.23 ± 0.208	31.99	48.32 ± 1.85	48.39 ± 2.00
Method	Solvent extraction	Solvent extraction	Solvent extraction	Solvent extraction

Table 2. Properties of castor oil

Properties	Yusuf et al. [21]	Salimon et al. [15]	Abitogun et al. [15]
Specific gravity	0.959	-	0.948
Lipid content (%)	-	43.30	-
Moisture content (%)	-	0.20	0.30
Iodine value (mg/g)	84.18	84.50	58.39
Acid value (mg/g)	2.07	4.90	14.80
% free fatty acid	-	3.40	7.40
Peroxide value (mq/kg)	38.00	10.20	158.64
Saponification value (mg/g)	175.31	182.90	178.00
Viscosity (cP)	-	332.00	-
Refractive index at 25°C	1.472 (30°C)	1.47	1.792
Average molecular weight	-	937.70	-
Fire point (°C)	-	-	256.00
Flash point (°C)	-	-	225.00
Smoke point (°C)	-	-	215.00
pH	6.16	-	5.80
Congealing temperature (°C)	-	-	18.00

Table 3. Compositions of fatty acids from various studies

Type of fatty acid	Ogunniyi [4] (%)	Mutlu [6] (%)	Salimon et al. [15] (%)	Abitogun [15] (%)
Ricinoleic	89.0	87.7 – 90.4	84.2	81.94
Palmitic	1.0	0.8 – 1.1	1.3	0.46
Oleic	3.0	2.2 – 3.3	5.5	2.28
Linoleic	4.2	4.1 – 4.7	7.3	0.61
Linolenic	0.3	0.5 – 0.7	0.5	0.30
Stearic	1.0	0.7 – 1.0	1.2	0.50
Dihydrostearic	0.7	-	-	0.24

method of extraction used and the geographical area [1]. Hence, various compositions and physical-chemical properties of castor oil were observed from castor seed in different climatic conditions [20]. For example, castor oil from Malaysia has a total lipids value of 43.3% per dry weight and saponification value of 182.96 mg KOH/g [12] whereas Nigerian castor oil contains total lipid value of 48% per dry weight and saponification value of 178.00 mg KOH/g [1].

In terms of properties, castor oil may have various physical and chemical properties as they depend greatly on the selected method of extraction. Table 2 shows the typical properties obtained from several other studies based on the solvent extraction method. The chemical composition of castor oil remains relatively constant

although it was grown in a different country of origin or season.

Similar to the other plant-based oils, castor oil is also a triglyceride molecule that mostly consists of fatty acids and glycerol [18,22]. What makes the castor oil special and comparatively unique is generally due to its plentiful composition of ricinoleic acid and also the presence of functional groups of hydroxyl and carboxyl with the single point of unsaturation existing in the molecule. Ninety percent of the fatty acids are accounted by the ricinoleic acid and marginal percentages of saturated and unsaturated components. Table 3 shows the composition of fatty acids that exist in castor oil from various studies analyzed through Gas Chromatography-Mass Spectrometry (GC-MS). The presence of ricinoleic

acid is the main factor why the castor oil is more valuable due to the various possible applications in the chemical industry.

The presence of ester linkage, hydroxyl and carboxyl groups of the castor oil aids to the versatility of oil through various chemical reactions and modification by undergoing certain processes with an added reactant to produce many valuable products. Fig. 3 shows the chemical structure of castor oil while Table 4 shows various reactions that castor oil can undergo with their final products from the respective processes.

■ INDUSTRIAL APPLICATION

For industrial purposes, castor oil is the most suitable alternative compared to other plant-based oils because it can be used as a starting or raw material for various industrial high-value-added products, typically due to its impressive chemical structure. Fig. 4 shows the structure of ricinoleic acid in castor oil with the presence

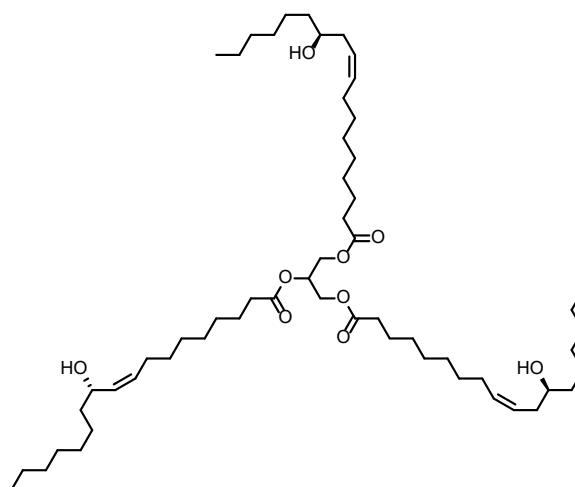


Fig 3. Structure of castor oil

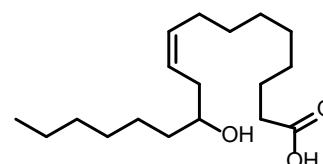


Fig 4. Chemical structure of ricinoleic acid

Table 4. Products from different reactions of castor oil [23]

Functional groups	Type of reaction	Added reactants	Type of products
Ester linkage	Hydrolysis	Acid, enzyme or Twitchell reagent catalyst	Fatty acids, glycerol
	Esterification	Monohydric alcohols	Esters
	Alcoholysis	Glycerol, glycols, pentaerythritol	Mono- and diglycerides monoglycols, etc.
	Saponification	Alkalies, alkalies plus metallic salts	Soluble soaps, insoluble soaps
Double bond	Amidation	Alkylamines, alkanolamines, and other compounds	Amine salts, amides
	Oxidation, polymerization	Heat, oxygen, crosslinking agent	Polymerized oils
	Hydrogenation	Hydrogen (moderate pressure)	Hydroxystearates
	Epoxidation	Hydrogen peroxide	Epoxidized oils
	Halogenation	Cl ₂ , Br ₂ , I ₂	Halogenated oils
	Addition reactions	S, maleic acid	Polymerized oils
	Sulphonation	H ₂ SO ₄	Sulphonated oils
	Hydroxyl group	Dehydration, hydrolysis, distillation	Catalyst (e.g., concentrated sulphuric acid, activated earth) (plus heat)
Caustic fusion		NaOH	Sebacic acid, capryl alcohol
Pyrolysis		High heat	Undecelnic acid, heptaldehyde
Halogenation		PCl ₅ , POCl ₃	Halogenated castor oils
Alkoxylation		Ethylene and/or propylene oxide	Alkoxyated castor oils
Esterification		Acetic-, phosphoric-, maleic-, phthalic anhydrides	Alkyl and alkylaryl esters, phosphate esters
Urethane reactions		Isocyanates	Urethane polymers
Sulfation		H ₂ SO ₄	Sulfated castor oil

of double bond and functional groups of hydroxyl and carboxyl. The high percentage of ricinoleic acid and the existence of the functional groups are the factors why castor oil has more possibilities and versatile applications in the chemical industry compared to the other vegetable oils [6]. Castor oil is usually used in the market as a raw material for various products like paint, lubricant, perfumes and other wide variety of products.

One of the applications of castor oil is in the manufacture of artificial leather. In this process, 50% of castor oil is mixed with 25% nitrocellulose and 25% cellulose and dispersed in a low-boiling solvent to be later applied to cloth [10]. This process has been fully developed until it is hard to differentiate whether the product is artificial or genuine leather. It is because the introduction of castor oil into nitrocellulose helps to yield a good quality of film concerning its strength and pliability [24]. Furthermore, the hydroxyl group also helps to endow it with a higher degree of miscibility with nitrocellulose than other fatty oils [24].

Castor oil was also used in the production of perfume because this oil can produce valuable chemicals such as heptaldehyde and undecylenic acid. The castor oil needs to undergo the transesterification process to obtain the methyl esters by previously mixing it with methanol before proceeding the process. The product will then be distilled and separated to obtain only methyl ester. Hence, the methyl ester will undergo thermal cracking process at a higher temperature around 500 °C to obtain the final product [25].

Lastly, castor oil is also possible to be utilized in paint manufacturing. Usually, paint contains vegetable oil such as linseed and tung oil where its function is to form tough films by covering the coated surface when it is exposed to atmospheric oxygen. This process is known as drying because both of these oils function as drying oils, mainly because they are highly unsaturated compared to castor oil that only has one double bond resulting in the lack of drying properties. According to Gilbert [24], the hydroxyl group of castor was possible to be removed as water which would cause the formation of second olefinic linkage to produce dehydrated castor oil (DCO) product which contains two double bonds in the fatty acid chain.

This dehydrated castor oil will dry paints films faster compared to linseed oil but less rapidly than tung oil [24].

■ THERMAL DEGRADATION

Biomass fuels from vegetable oils can be synthesized by utilizing various types of methods available. The most common methods used are pyrolysis, catalytic cracking [26], transesterification processes with the assistance of catalysts [27] and also hydrocracking reactions [28]. The products from the mentioned methods have high potential to be obtained from the vegetable oil [29]. The products of the thermal process usually consist of petroleum-like fractions such as gasoline, kerosene, diesel and no sulfur or heavy metals present [30].

On top of that, the biofuels produced by the catalytic cracking process are possible to be achieved by using the current infrastructure used in the oil refining industry. This is because the lab-scale catalytic cracking concept is very similar to the oil refining process. Therefore, biofuels have a promising industrial technology to be used and a high market demand.

Castor oil which undergoes thermal cracking process can yield mostly heptaldehyde and undecylenic acid. This happens when the ricinoleic molecule located at the hydroxyl is cleaved to be shorter chain molecules, in which the process is conducted at a high temperature without the presence of oxygen [31]. Both compounds have their applications in the market especially in cosmetics, pharmaceuticals, polymers, and perfumery. Heptaldehyde is also applicable as a solvent for resins and rubber production. According to Ogunniyi et al. [4], heptaldehyde can be used as a plasticizer by going through a hydrogenation process. Heptaldehyde is usually formed from the hydroformylation process of hexane, the esters of undecylenic and ricinoleic acid which has been degraded or through the hydrolysis of methyl undecenoate.

On the other hand, undecylenic acid is normally important in the preparation of insecticides, nylon from polymers and foot remedies. The other main applications of castor oil are paints or coatings. Castor

oil can produce special paint or furniture oil applications by going through dehydration by nonconjugated oil-maleic anhydride [6]. A study by Trevino and Trumbo [31] proved that the castor oil could be utilized for coating production by changing the hydroxyl of castor oil to β -ketoesters using *t*-butyl acetoacetate. This reaction is found to be comparatively fast and can be proceeded to high yield under delicate conditions. This is because the results showed that the 60° angle glosses of the films and film flexibilities were sensible. Castor oil is also most commonly used as biodegradable polyesters. Carothers has prepared the first synthetic condensation polymers in the 1930s [32]. Polyesters are highly biodegradable and environmentally friendly, with wide applications in the biomedical field, preparation of elastomers and packaging materials.

■ ZEOLITE ZSM-5 CRACKING

Zeolite catalyst ZSM-5 is one of the most efficient catalysts used for hydrocarbon cracking. It is made up of silica-alumina pentagon chains connected by oxygen atoms [33]. HZSM-5 is known for its ability to react with any materials to obtain aromatic and gasoline products. This catalyst will further assist the vegetable oils to obtain up to gasoline boiling range compounds. Other than that, the selectivity of zeolites fully depends on the acidity, pore shape, and size [34]. The usage of acidic zeolite catalyst such as ZSM-5 in catalytic cracking processes can be a promising choice to acquire olefins. In addition, the crystalline catalyst will provide a large surface area. This allows the cracking process to be initiated by the presence of active acid sites [35]. The selective characteristics of HZSM-5 based on shape will cause minor cracking which eventually produces a high amount of organic liquid products (OLP) and low amount of gaseous products [36].

Furthermore, catalysts with oxides such as calcium oxide will cause the delay in the decomposition of long-

chain oxygenated hydrocarbons. Therefore, the reactions using basic catalysts will obtain similar products as thermal cracking. However, secondary cracking is needed to form aromatic compounds.

The product to be obtained might differ greatly due to the presence of a catalyst. Zeolites are mostly used in major sectors such as petrochemical and pollution control. Furthermore, the high acidity contributes to the high efficiency in selectivity as well as the activity of zeolites, as compared to other amorphous silica-alumina catalysts. Zeolites are better as it is more powerful in cracking ability [37]. Few past works have been done using zeolites in order to crack vegetable oils [38]. Therefore, heterogeneous catalysis has the advantage by depending on the properties of the zeolites' materials used [33,35]. Different types of zeolites have also shown the impressive ability in catalytic cracking of different plant-based oils, such as HZSM-5 with supported metals [38]. Cracking, aromatization, isomerization of hydrocarbons, and alkylation reactions can easily happen when zeolite ZSM-5 is used. Some metals are commonly used to enhance zeolites effectiveness because of their ability to withstand the zeolites' acidity. Zeolite ZSM-5 has high silica over aluminum ratio. For instance, the catalytic cracking of camelina oil to yield biofuels using a different concentration of zinc incorporated into ZSM catalyst shows that higher concentration of zinc added did not give higher yield. The suitable zinc concentration must be less, around 20 wt.% in which this resulted in higher yield [39]. Besides, the incorporation of zinc into ZSM-5 can expedite decarbonylation and dehydrogenation processes [40-41]. However, the catalyst used might also become a constraint to the catalytic cracking process. Therefore, it is always encouraging to discard impurities as well as minimizing the viscosity of the oils used.

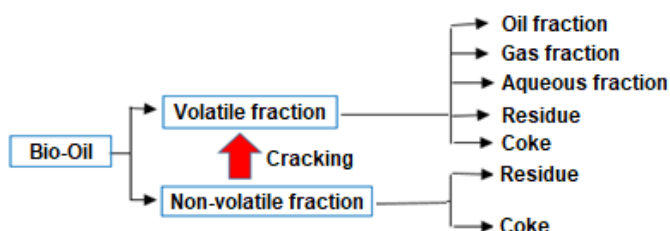
The thermal cracking process is used to observe the conversion of light olefins when it is being tested using

Table 5. Products obtained by using different types of ZSM-5 catalyst.

Catalyst type	Types of oil	Metal	Product	Reference
ZnZSM-5	Camelina	Zn	Acids, alcohols, esters, hydrocarbons	[39]
NaZSM-5	Crude soybean	Na	Aromatics, cyclics, aliphatics, acids, ketones	[43]
HZSM-5	Jatropha	-	Aliphatics, aromatics, esters, acids, ketones	[36]

Table 6. Type of catalysts used to yield oil products

Type of catalyst	Reaction temperature(°C)	The yield of oil (wt.%)	Reference
H-mordenite	330	17	[44]
ZnZSM-5	380	19	[45]
HZSM-5	380	24	[45]

**Fig 5.** Reaction chain

four kinds of HZSM-5 catalysts [42]. It is highly favorable to use the hydrogenation reactions to determine the profile of the process and for the deoxygenation of triglycerides to obtain hydrocarbons in a liquid state. Table 5 shows the typical products obtained from several other studies by using different types of ZSM-5 catalysts from three different types of vegetable oils.

■ ZEOLITES AS CATALYST FOR CRACKING REACTIONS

Generally, thermal cracking occurs at the ranges of temperature from 400 to 600 °C. Higher temperature tends to make lower oil product and higher gas product. This is because a higher temperature will increase the rate of reactions and thus, smaller volatile compounds can be formed. Oxygen content can also be decreased to an acceptable amount depending on the temperature needed. Zeolite cracking mechanism can be done through a few reactions. Firstly, hydrocarbons are cracked to smaller fractions. Next, oxygen is eliminated by dehydration as the main path through decarboxylation, and decarbonylation processes [40].

Further reaction mechanism of the zeolite cracking can be simplified into a reaction chain as shown in Fig. 5. Initially, bio-oil will be divided into a volatile and a non-volatile fraction conducted at 200 °C in vacuum condition [44]. The non-volatile fraction which underwent cracking can become volatiles, or it can become condensate through a polymerization process. It can also become the residue as it does not evaporate in the process. The volatile

fraction can consist of oil, liquid, and gaseous fractions. The volatiles can polymerize or condense in order to become residue as well. Table 6 shows the type of catalysts used to yield oil products.

■ CONCLUSION

In conclusion, castor oil is proved to be an important renewable source. Although it was not edible to be consumed by human, like other vegetable oils, there are so many uses that castor oil can be utilized in other industries to produce more valuable end products. The impressive composition of ricinoleic acid and the availability of the three functional groups of hydroxyl, carboxylate and double bond makes it as a highly potential renewable resource when it undergoes various chemical reactions, modifications, and transformations to produce derivative products. The thermal cracking approach is recognized as an efficient method to produce different kinds of specialty chemicals. In addition, thermal cracking is absolutely a reliable alternative for various sectors especially in the processing of specialty chemicals. Other than that, zeolite ZSM-5 has also displayed great potential as cracking catalysts. It is suggested to let the activity of cracking catalyst to be further improved by combining microporous zeolites with mesoporous materials in order to increase its thermal and hydrothermal stability and also its selectivity towards organic liquid products (OLP).

In this short review, it is outlined the background, characteristics, composition and various industrial uses of castor oil in the industries. However, there are still other chemicals or side products derived from the castor oil that can be produced which did not manage to be mentioned in this paper. For future directions, the non-edible oils like castor oil or other non-edible oils in the market should be further discovered through researches so that those edible oils in the market can be focused on as a source of food for human only. In order to secure

the availability of castor oil, fertile agricultural land should be allocated for edible oil plantation whereas waste or fallow land should be used for non-edible oil crops as it has simpler and easier ecological requirements. Limited land areas, especially in developed countries, should be fully utilized for non-edible oil plantation such as castor oil in which it will eventually increase the oil production for the country's economic assurance [46].

■ ACKNOWLEDGMENTS

This study was financially supported by the internal grants of Universiti Malaysia Pahang (RDU170351 and 170334).

■ REFERENCES

- [1] Mubofu, E.B., 2016, Castor oil as a potentially renewable resource for the production of functional materials, *Sustainable Chem. Processes*, 4, 11.
- [2] Castor Oil & Derivatives Market: *Global Market Analysis & Opportunity Outlook 2021*, 2018, <https://www.researchnester.com/reports/castor-oil-derivatives-market-global-market-analysis-opportunity-outlook-2021/128>, accessed on 12 September 2018.
- [3] Patel, V.R., Dumancas, G.G., Viswanath, L.C.K., Maples, R., and Subong, B.J.J., 2016, Castor oil: Properties, uses, and optimization of processing parameters in commercial production, *Lipid Insights*, 9 (1), 1–12.
- [4] Ogunniyi, D.S., 2006, Castor oil: A vital industrial raw material, *Bioresour. Technol.*, 97 (9), 1086–1091.
- [5] Ladda, P.L., and Kamthane, R.B., 2014, *Ricinus communis* (Castor): An overview, *IJRPP*, 3 (2), 136–144.
- [6] Mutlu, H., and Meier, M.A.R., 2010, Castor oil as a renewable resource for the chemical industry, *Eur. J. Lipid Sci. Technol.*, 112 (1), 10–30.
- [7] Oil Seed Crops Food & Energy, 2013, *Castor bean*, <http://www.oilseedcrops.org/castor-bean>, accessed on 20 August 2018.
- [8] Armendáriz, J., Lapuerta, M., Zavala, F., García-Zambrano, E., and Ojeda, M.C., 2015, Evaluation of eleven genotypes of castor oil plant (*Ricinus communis* L.) for the production of biodiesel, *Ind. Crops Prod.*, 77, 484–490.
- [9] Shridhar, B.S., Beena, K.V., Anita, M.V., and Paramjeet, K.B., 2010, Optimization, and characterization of castor seed oil, *Leonardo J. Sci.*, 9 (17), 59–70.
- [10] Scholz, V., and da Silva, J.N., 2008, Prospects and risks of the use of castor oil as a fuel, *Biomass Bioenergy*, 32 (2), 95–100.
- [11] Shrirame, H.Y., Panwar, N.L., and Bamniya, B.R., 2011, Bio-diesel from castor oil – A green energy option, *LCE*, 2 (1), 1–6.
- [12] Dasari, S.R., and Goud, V.V., 2013, Comparative extraction of castor seed oil using polar and nonpolar solvents, *Int. J. Curr. Eng. Technol.*, 1, 121–123.
- [13] Muzenda, E., Kabuba, J., Mdletye, P., and Belaid, M., 2012, Optimization of Process Parameters for Castor Oil Production, *Proceedings of the World Congress on Engineering*, WCE, Vol. III, 4-6 July 2012, London, U.K.
- [14] Salimon, J., Mohd Noor, D.A., Nazrizawati, A.T., Mohd Firdaus, M.Y., and Noraishah, A., 2010, Fatty acid composition and physicochemical properties of Malaysian castor bean *Ricinus communis* L. seed oil, *Sains Malays.*, 39 (5), 761–764.
- [15] Abitogun, A., Alademeyin, O., and Oloye, D., 2008, Extraction and characterization of castor seed oil, *Internet J. Nutr. Wellness*, 8 (2), 1–5.
- [16] Mgudu, L., Muzenda, E., Kabuba, J., and Belaid, M., 2012, Microwave - Assisted extraction of castor oil, *International Conference on Nanotechnology and Chemical Engineering (ICNCS'2012)*, 21-11 December 2012, Bangkok, 47–51.
- [17] Nangbes, J.G., Nvau, J.B., Buba, W.M., and Zukdimma, A.N., 2013, Extraction and characterization of castor (*Ricinus communis*) seed oil, *Int. J. Eng. Sci.*, 2 (9), 105–109.
- [18] Warra, A.A., 2015, Physico-chemical and GC/MS analysis of castor bean (*Ricinus communis* L.) seed oil, *Chem. Mater. Res.*, 7 (2), 2224–3224.
- [19] Abdelaziz, A.I.M., Elamin, I.H.M., Gasmelseed, G.A., and Abdalla, B.K., 2014, Extraction, refining

- and characterization of sudanese castor seed oil, *J. Chem. Eng.*, 2 (1), 1–4.
- [20] Omari, A., Mgani, Q.A., and Mubofu, E.B., 2015, Fatty acid profile and physicochemical parameters of castor oils in Tanzania, *Green Sustainable Chem.*, 5 (4), 154–163.
- [21] Yusuf, A.K., Mamza, P.A.P., Ahmed, A.S., and Agunwa, U., 2015, Extraction and characterization of castor seed from wild *Ricinus communis* Linn, *Int. J. Sci. Environ. Technol.*, 4 (5), 1392–1404.
- [22] Alwaseem, H., Donahue, C.J., and Marincean, S., 2014, Catalytic transfer hydrogenation of castor oil, *J. Chem. Educ.*, 91 (4), 575–578.
- [23] *Castor Oil and its Chemistry*, 2000, [https://www.chem.uwec.edu/chem491_w01/Pharma cognosy491/castor bean chemistry.pdf](https://www.chem.uwec.edu/chem491_w01/Pharma%20cognosy491/castor%20bean%20chemistry.pdf), accessed on 5 May 2018.
- [24] Gilbert, E.E., 1941, The unique chemistry of castor oil, *J. Chem. Educ.*, 18 (7), 338–341.
- [25] Botton, V., de Souza, R.T., Wiggers, V.R., Scharf, D.R., Simionatto, E.L., Ender, L., and Meier, H.F., 2016, Thermal Cracking of methyl esters in castor oil and production of heptaldehyde and methyl undecenoate, *J. Anal. Appl. Pyrolysis*, 121, 387–393.
- [26] Fréty, R., da Rocha, M.G.C., Brandão, S.T., Pontes, L.A.M., Padilha, J.F., Borges, L.E.P., and Gonzalez, W.A., 2011, Cracking and hydrocracking of triglycerides for renewable liquid fuels: Alternative processes to transesterification, *J. Braz. Chem. Soc.*, 22 (7), 1206–1220.
- [27] Kazemian, H., Turowec, B., Siddiquee, M.N., and Rohani, S., 2013, Biodiesel production using cesium modified mesoporous ordered silica as a heterogeneous base catalyst, *Fuel*, 103, 719–724.
- [28] Nam, L.T.H., Vinh, T.Q., Loan, N.T.T., Tho, V.D.S., Yang, X.Y., and Su, B.L., 2011, Preparation of bio-fuels by catalytic cracking reaction of vegetable oil sludge, *Fuel*, 90 (3), 1069–1075.
- [29] Yigezu, Z.D., and Muthukumar, K., 2015, Biofuel production by catalytic cracking of sunflower oil using vanadium pentoxide, *J. Anal. Appl. Pyrolysis*, 112, 341–347.
- [30] Tian, H., Li, C., Yang, C., and Shan, H., 2008, Alternative processing technology for converting vegetable oils and animal fats to clean fuels and light olefins, *Chin. J. Chem. Eng.*, 16 (3), 394–400.
- [31] Trevino, A.S., and Trumbo, D.L., 2002, Acetoacetylated castor oil in coatings applications, *Prog. Org. Coat.*, 44 (1), 49–54.
- [32] Sivaram, S., 2017, Wallace Hume Carothers and the birth of rational polymer synthesis, *Resonance*, 22 (4), 339–353.
- [33] Xu, R., Pang, W., Yu, J., Huo, Q., and Chen, J., 2010, *Chemistry of Zeolites and Related Porous Materials: Synthesis and Structure*, John Wiley & Sons (Asia) Pte Ltd.
- [34] Rahimi, N., and Karimzadeh, R., 2011, Catalytic cracking of hydrocarbons over modified ZSM-5 zeolites to produce light olefins: A review, *Appl. Catal., A*, 398 (1-2), 1–17.
- [35] Vichaphund, S., Aht-ong, D., Sricharoenchaikul, V., and Atong, D., 2015, Production of aromatic compounds from catalytic fast pyrolysis of Jatropha residues using metal/HZSM-5 prepared by ion-exchange and impregnation methods, *Renewable Energy*, 79, 28–37.
- [36] Deshpande, D.P., Haral, S.S., and Sarode, P.B., 2013, Hydrocarbon liquid from castor Oil, *Res. J. Chem. Sci.*, 3 (7), 87–89.
- [37] Sadrameli, S.M., and Green, A.E.S., 2007, Systematics of renewable olefins from thermal cracking of canola oil, *J. Anal. Appl. Pyrolysis*, 78 (2), 445–451.
- [38] Cheng, J., Li, T., Huang, R., Zhou, J., and Cen, K., 2014, Optimizing catalysis conditions to decrease aromatic hydrocarbons and increase alkanes for improving jet biofuel quality, *Bioresour. Technol.*, 158, 378–382.
- [39] Zhao, X., Wei, L., Cheng, S., Huang, Y., Yu, Y., and Julson, J., 2015, Catalytic cracking of camelina oil for hydrocarbon biofuel over ZSM-5-Zn catalyst, *Fuel Process. Technol.*, 139, 117–126.
- [40] Corma, A., Mengual, J., and Miguel, P.J., 2013, IM-5 zeolite for steam catalytic cracking of naphtha to

- produce propene and ethene. An alternative to ZSM-5 zeolite, *Appl. Catal., A*, 460-461, 106–115.
- [41] Benson, T.J., Hernandez, R., French, W.T., Alley, E.G., and Holmes, W.E., 2009, Elucidation of the catalytic cracking pathway for unsaturated mono-, di-, and triacylglycerides on solid acid catalysts, *J. Mol. Catal. A: Chem.*, 303 (1-2), 117–123.
- [42] Li, L., Quan, K., Xu, J., Liu, F., Liu, S., Yu, S., Xie, C., Zhang, B., and Ge, X., 2014, Liquid hydrocarbon fuels from catalytic cracking of rubber seed oil using USY as catalyst, *Fuel*, 123, 189–193.
- [43] Zandonai, C.H., Yassue-Cordeiro, P.H., Castellã-Pergher, S.B., Scaliante, M.H.N.O., and Fernandes-Machado, N.R.C., 2016, Production of petroleum-like synthetic fuel by hydrocracking of crude soybean oil over ZSM5 zeolite - Improvement of catalyst lifetime by ion exchange, *Fuel*, 172, 228–237.
- [44] Adjaye, J.D., Katikaneni, S.P.R., and Bakhshi, N.N., 1996, Catalytic conversion of a biofuel to hydrocarbons: Effect of mixtures of HZSM-5 and silica-alumina catalysts on product distribution, *Fuel Process. Technol.*, 48 (2), 115–143.
- [45] Mortensen, P.M., Grunwaldt, J.D., Jensen, P.A., Knudsen, K.G., and Jensen, A.D., 2011, A review of catalytic upgrading of bio-oil to engine fuels, *Appl. Catal., A*, 407 (1-2), 1–19.
- [46] Timilsina, G.R., and Shrestha, A., 2010, Biofuels: Markets, Targets and Impacts, *World Bank*, 1–47.